Dipl.-Ing. Madeleine Bali

# Magnetic material degradation due to different cutting techniques and its modeling for electric machine design

vorgelegt als

## DISSERTATION

zur Erlangung des akademischen Grades
Doktor der technischen Wissenschaften

eingereicht an der

Technischen Universität Graz

1. Gutachter

Prof. Dr.-Ing. Annette Mütze
Institut für Elektrische Antriebstechnik und Maschinen, TU Graz, Österreich

2. Gutachter

Prof. Dr.-Ing. Herbert De Gersem
Institut für Theorie Elektromagnetischer Felder, TU Darmstadt, Deutschland

Graz, April 2016

# AFFIDAVIT

I declare that I have authored this thesis independently, that I have not used other than the declared sources/resources, and that I have explicitly indicated all material which has been quoted either literally or by content from the sources used. The text document uploaded to TUGRAZonline is identical to the present doctoral thesis.

........................  ........................
Date  Signature

*for my family*

# Contents

# Abstract

The magnetic properties of electrical steel sheets, such as those typically used in electric machines, are adversely affected by cutting. Different cutting techniques are available, such as mechanical (punching, guillotining), laser, wire and water-jet cutting. The last two are are rarely used for reasons of time and thus cost. Punching is the most common cutting technique in industry. However, laser cutting has been increasingly used, too. The degrading effect of laser cutting on the material's magnetic characteristics is much less understood than that of mechanical cutting.

The degrading effect of the cutting process on the magnetic properties is still difficult to determine theoretically and depends on many parameters, notably the material investigated (chemical composition and grain size) and the settings of the cutting technology (clearance, blade radii, tool wear, cutting speed, cutting mode, power). The statements differ on the degrading effect of a specific cutting technique in literature and how the effects of different cutting techniques compare. Many statements are derived from a select number of investigations of only one material and/or operating point/frequency and hence generalizations are difficult to make.

For design applications, a model is desirable to describe the degrading effect due to different cutting techniques in an easy and straightforward way which is applicable to arbitrary geometries and which considers, at least indirectly, the influences of different materials and settings. Additionally, this model should be based on input data which are relatively easy to obtain (wide-spread, standardized and fast-to-perform measurement methods and easily manufactured test samples in contrast to custom-designed setups and/or time-consuming and cost-consuming sample preparation (e.g. annealing, winding)).

This work presents a systematic analysis of the degrading influence of mechanical and laser cutting on the magnetic properties of the cut steel sheets. The analysis includes three non-oriented steel sheet materials commonly used in electric machines (M270-35A, M400-50A and M800-65A), different frequencies (quasi-static, 50 Hz, 250 Hz and 500 Hz) and cut geometries (steels strips, stator lamination stacks). Notably, the influences of the cutting techniques are compared among each other. Furthermore, a new modeling approach is presented which meets the desired requirements.

Chapters 1-3 give an overview of the state of knowledge of the degradation effect, the materials investigated and the measurement series carried out: Chapter 1 reviews the existing results and opinions on the degradation effect due to mechanical and laser cutting. Chapter 2 summarizes the test samples investigated and presents the measurements carried out and the respective setups. In Chapter 3, the chemical composition and the average grain size diameter of the electrical steel sheets investigated are analyzed.

Chapters 4-6 examine the degrading effects of mechanical and laser cutting on the magnetic properties (specific losses, magnetization curves and relative permeabilities): Chapter 4 shows results of quasi-static measurements of strip samples with different widths and cutting directions obtained by a remagraph. A significantly different shape of the hysteresis curve of small laser-cut in contrast to mechanically-cut samples is found. In Chapter 5, the same steel strips are further investigated in an Epstein frame at different frequencies. Chapter 6 analyzes the magnetic behavior of stator lamination stacks which originate from the same mother coils and are cut by the same cutting methods as the strip samples. All these Chapters highlight that a point of intersection (POI) may occur. Above this POI magnetic behavior of the laser-cut samples is better than that of the mechanically-cut samples. This applies for all magnetic characteristics investigated, the specific losses as well as for the magnetization curves and the relative permeabilities. The POIs of the specific losses are shifted to lower magnetic flux densities with increasing frequency and material thickness (here, also with decreasing grain size). Thus, the operating point, the material and also the cut geometry influence which cutting technique is the most appropriate for a given case.

Chapters 7 and 8 concern the modeling of the degradation effect due to cutting: Chapter 7 classifies the previously proposed modeling approaches to describe the degradation effect induced by cutting, studies their differences and analyzes the respective implementation efforts. Subsequently, Chapter 8 proposes a new Epstein frame based modeling of the degradation effect for arbitrary geometries and without needing to know the exact deterioration depth. This method is validated for different materials and at different frequencies, leading to sufficiently accurate results. Furthermore, the Epstein frame technique provides a simple and straightforward way to quantify the input parameters.

# Zusammenfassung

Die magnetischen Eigenschaften von Elektroblechen, die typischerweise in elektrischen Maschinen und Transformatoren zum Einsatz kommen, werden durch den Schneidprozess negativ beeinflusst. Für das Schneiden von Elektroblechen können unterschiedliche Schneidtechnologien eingesetzt werden, z. B. mechanisches Schneiden (Stanzen, Schlagschere), Laserschneiden, elektroerosives oder Wasserstrahlschneiden. Die beiden letztgenannten werden, aufgrund zeit- und somit auch kostenintensiver Faktoren, eher selten eingesetzt. Das Stanzen ist die in der Industrie meistverwendete Schneidtechnik. Allerdings gewinnt auch das Laserschneiden zunehmend an Bedeutung. Dabei ist der verschlechternde Einfluss des Laserschneidens auf die magnetischen Eigenschaften lange noch nicht so gut verstanden und untersucht worden wie jener des mechanischen Schneidens.

Es ist schwierig, die Verschlechterung der magnetischen Eigenschaften aufgrund des Schneidens theoretisch zu beschreiben oder darzustellen, da sie von verschiedenen Parametern abhängt, z. B. vom geschnittenen Material (chemische Zusammensetzung und mittlerer Korngrößendurchmesser) oder den Schnitteinstellungen (Schneidspalt, Klingenradius, Werkzeugverschleiß, Schneidgeschwindigkeit, Betriebsart, Laserleistung, etc.). Die Meinungen darüber, welche Schneidtechnik den größten nachteiligen Einfluss auf die magnetischen Eigenschaften hat, gehen auseinander. Viele der hierbei zugrunde gelegten Schlussfolgerungen basieren jedoch auf vereinzelten Untersuchungen, in denen beispielsweise nur ein bestimmtes Material und/oder ein bestimmter Betriebspunkt oder eine bestimmte Frequenz untersucht wird. Deshalb ist es schwierig, ein allgemeingültiges Verhalten abzuleiten.

Für den Entwurf elektrischer Maschinen ist ein Modell notwendig, das den negativen Einfluss unterschiedlicher Schneidtechniken auf die magnetischen Eigenschaften auf einfache und schnelle Weise berücksichtigt. Zudem sollte es auf unterschiedliche Geometrien anwendbar sein und die Unterschiede aufgrund unterschiedlicher Materialien oder Schnitteinstellungen implizit berücksichtigen. Des Weiteren sollte es möglich sein, die Eingangsdaten schnell und einfach zu ermitteln. Eine weitverbreitete, standardisierte und schnell durchzuführende Messmethode mit einfach herzustellenden Materialproben ist somit gegenüber sonderangefertigten Messaufbauten und/oder zeit- und kostenintensiven Probenvorbereitung (z. B. Spannungs-

armglühen, spezielle Wicklungen) von Vorteil.

Die vorliegende Arbeit präsentiert eine systematische Analyse der Verschlechterung der magnetischen Eigenschaften von Elektroblechen, hervorgerufen durch mechanisches sowie Laserschneiden. Im Falle des Laserschneidens werden sowohl die Auswirkungen der Carbondioxidlaser- als auch der Festkörperlaserschneidtechnik analysiert. Die Untersuchung umfasst drei nichtkornorientierte Bleche, die typischerweise in elektrischen Maschinen eingesetzt werden (M270-35A, M400-50A, M800-65A), verschiedene Frequenzen (quasi-statisch, 50 Hz, 250 Hz und 500 Hz) und unterschiedlich geschnittene Geometrien (Blechstreifen, Ständerblechpakete). Großes Augenmerk wird auf den Vergleich der verschlechternden Einflüsse auf die magnetischen Eigenschaften aufgrund unterschiedlicher Schneidarten gelegt. Abschließend wird ein neuer Modellansatz vorgestellt, der die oben genannten Anforderungen erfüllt.

Die Kapitel 1-3 geben einen Überblick über den derzeitigen Stand der Technik bezüglich der Verschlechterung der magnetischen Eigenschaften aufgrund des Schneidens und präsentieren die untersuchten Materialien und die verwendeten Messaufbauten: In Kapitel 1 werden die bereits existierenden Ergebnisse und Meinungen, die mit dem verschlechternden Einfluss durch mechanisches und Laserschneiden zusammenhängen, zusammengefasst. Kapitel 2 stellt die untersuchten Materialproben und die durchgeführten Messungen sowie deren Aufbau vor. Anschließend werden in Kapitel 3 die chemische Zusammensetzung und der mittlere Korngrößendurchmesser der hier untersuchten Materialien ermittelt.

Die Kapitel 4-6 untersuchen den zerstörenden Einfluss des mechanischen sowie des Laserschneidens auf die magnetischen Eigenschaften (spezifische Verluste, Magnetisierungskurven und relative Permeabilität): Kapitel 4 präsentiert die Ergebnisse quasi-statischer Messungen, die mittels eines Remagraphen ermittelt wurden, an unterschiedlich breiten Blechstreifen. Zusätzlich wurde der Einfluss der Schnittrichtung analysiert. Bei den schmalen lasergeschnittenen Blechstreifen wurde eine erhebliche Beeinflussung in der Form der Hysteresekurve festgestellt, verglichen mit denen der schmalen, mechanisch geschnittenen Materialproben. In Kapitel 5 werden die gleichen Blechstreifen in einem Epsteinrahmen und bei verschiedenen Frequenzen untersucht. Kapitel 6 analysiert das magnetische Verhalten der Ständerblechpakete, die von der gleichen Elektrobandrolle (Muttercoil) für das jeweilige Material stammen und mit den gleichen Schneidtechniken geschnitten wurden wie die in Kapiteln 3-5 untersuchten Blechstreifen. All diese Kapitel zeigen, dass ein Schnittpunkt (engl. "point of intersection", POI) aufteten kann, oberhalb dessen das magnetische Verhalten der lasergeschnittenen Proben besser ist als das der mechanisch geschnittenen. Diese Charakteristik wurde bei allen untersuchten magneti-

schen Eigenschaften beobachtet, sowohl bei den spezifischen Verlusten als auch bei den Magnetisierungskurven und relativen Permeabilitäten. Die Schnittpunkte der spezifischen Verluste treten mit zunehmender Frequenz und Blechdicke (in dieser Arbeit setzten sich die dickeren Materialien auch aus kleineren mittleren Korngrößendurchmessern zusammen) bei immer kleineren magnetischen Flussdichten auf. Somit bestimmen Parameter der Anwendung wie z. B. der Betriebspunkt, das verwendete Material und die geschnittene Geometrie, welche Schneidtechnik für eine bestimmte Anwendung am besten geeignet ist.

Kapitel 7 und 8 beschäftigen sich mit der Modellierung des verschlechternden Einflusses auf die magnetischen Eigenschaften, der durch das Schneiden hervorgerufen wird: Kapitel 7 unterteilt die bisherigen vorgeschlagenen Modellierungsansätze, um den Schneideffekt zu berücksichtigen, untersucht deren Unterschiede und analysiert den jeweiligen Implementierungsaufwand. Anschließend wird in Kapitel 8 ein neuer, auf einfachen Epsteinmessungen beruhender Modellierungsansatz vorgestellt, der auf unterschiedliche Geometrien anwendbar ist und für den kein exakter Wert der Zerstörungstiefe bekannt sein muss. Diese Methode wurde für verschiedene Materialien und Frequenzen mit hinreichender Genauigkeit verifiziert.

# Chapter 1

# State of the art

## 1.1 Electrical steel sheets

For most electric machines both the stator and the rotor core are made from stacks of thin electrical steel sheets. Worldwide the manufacturing of electrical steel sheets and strips has been increasing (see Fig. 1.1). Most of the production is located in Asia, particulary in China (Fig. 1.1). Between 2005 and 2014, the World Steel Association [209] reported an increase of about 150 % in the electrical steel sheet production. According to the standard DIN EN 10106 [52], the material designation contains the following information: the letter M indicates an electrical sheet, the first number is a hundred times the maximum loss at 1.5 T and 50 Hz in W/kg, the second number is a hundred times the nominal thickness of the sheet in millimeters and a letter A depicts a non-oriented electrical steel in the final annealed condition. In addition to non-oriented electrical steel sheets, grain-oriented electrical steel sheets are also used, most commonly, in (distribution) power transformers. These sheets have a magnetically preferred direction. In contrast, non-oriented electrical steel sheets can be identified by their uniformly distributed magnetic characteristic. Thus, these steels are the clear choice for electric machines.

Table 1.1: Structure of an electrical steel sheet's designation [52].

| Name | M | 270 | 35 | A |
|---|---|---|---|---|
| Identifying | electrical sheet | loss at 1.5 T and 50 Hz | sheet thickness | final annealed condition |

### 1.1.1 Texture, domain walls and magnetization

*Texture*

As soon as molten iron has cooled, crystallites with crystal lattices form, built from multiple small unit cells (see Fig. 1.2) [177]. Iron crystallizes in a cubic structure (see Fig. 1.3) [177]. At the beginning of the solidification process, disordered atoms begin
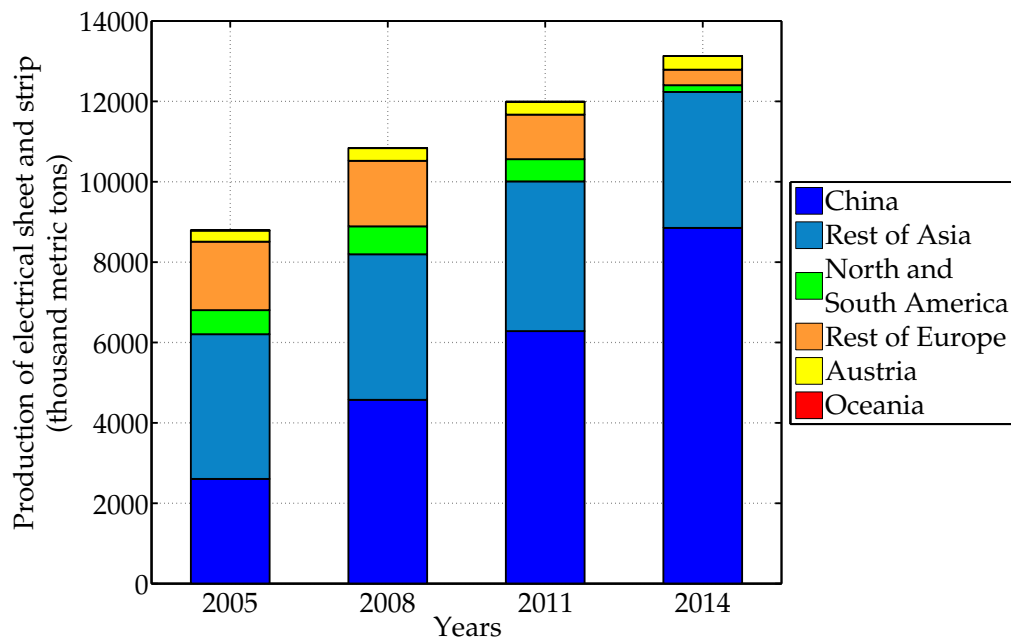
Figure 1.1: Annual production of electrical steel sheets and strips [209]. Note, the bar of 2014 does not include Germany, as no data was available.

to form which give rise to further crystals, until all atoms are set (see Fig. 1.2) [177]. From these crystals, grains are formed which are bound to each other (the crystal lattices of each grain are tilted against each other), Fig. 1.2 [177], until solidification is finished. The final grain size depends, among other factors, on the cooling rate and the presence of high-melting compounds, such as aluminum and nitrogen or aluminum and oxygen [177]. The entirety of the crystallites' orientation is called texture [14]. In the case of electrical steel sheets, the Goss and the cubic texture arises (Fig. 1.3). The Goss texture is found in grain-oriented steels with the magnetically easy axis parallel to the rolling direction [23, 140]. Non-oriented steel sheets with the cubic texture have two magnetically preferred directions in the sheet plane [23, 140]. Note, the magnetically easy axes are the cube edges; the cubic diagonal is the magnetically hard axis or worst direction [10, 23], see Fig. 1.3. The surface diagonal is magnetically situated between the cube edges and cubic diagonal and is called the magnetically medium axis [26].[1]

---

[1]Using terms of material sciences, the cube edges are denoted with the Miller indices e.g. "[100]", the cubic diagonal with e.g. "[110]" and the surface diagonal with "[111]". The family of all cristallographic equivalent directions is denoted as "<100>, <110>, and <111>" respectively. [130]

(a) Started solidification from the molten iron

(b) Finished solidification
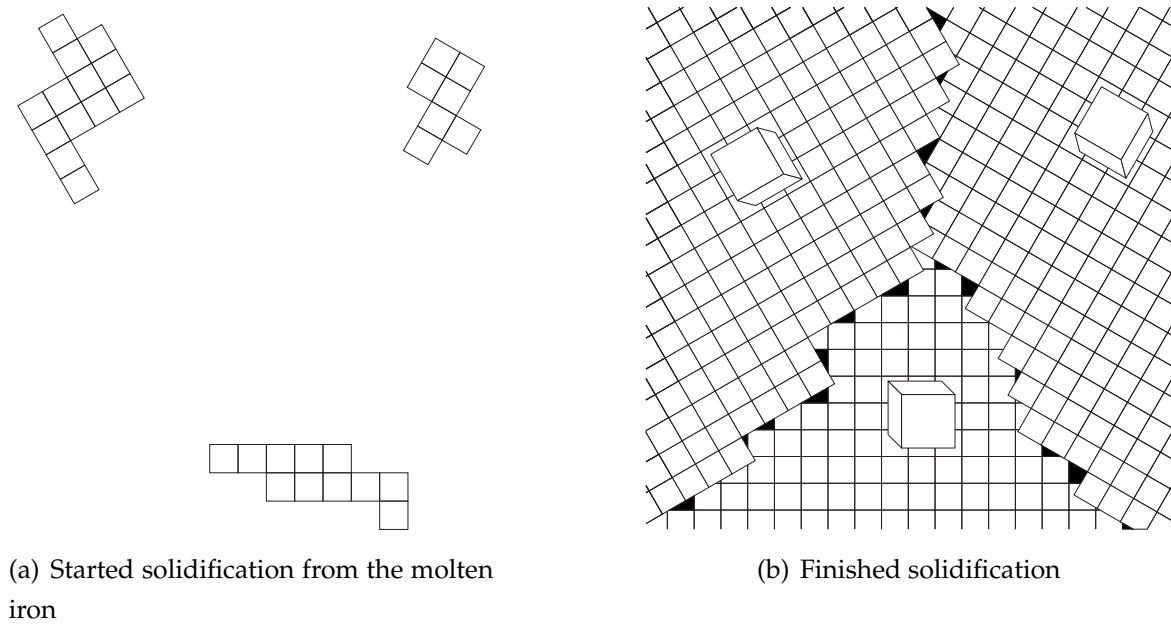
Figure 1.2: Started and completed solidification, from [177].
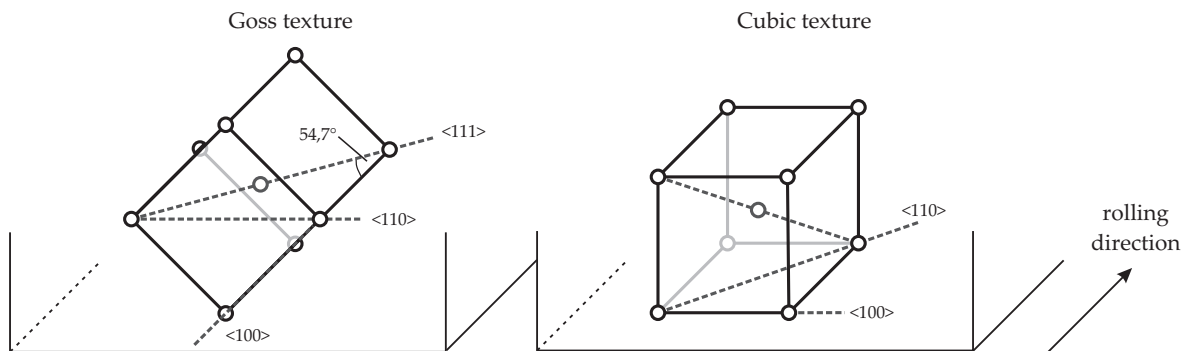


Figure 1.3: Orientation of the crystallites of Goss and cubic texture, from [23, 140].
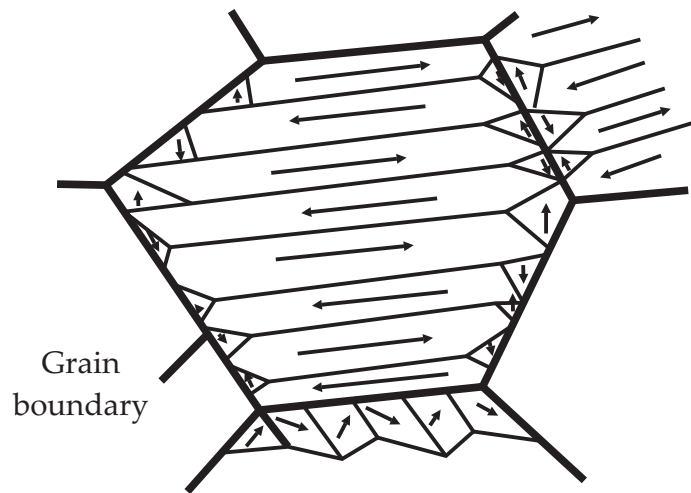
Figure 1.4: Grains and their domains, from [10].

*Magnetic domains*

The microstructure (size and distribution of crystal lattice domains [14]) of the steel sheets "superimposes with the magnetic domain structure" [10]. The model of magnetic domains was first introduced by the French physician Pierre Weiss, after whom these domains are named (Weiss domains). According to this model, the grains of a ferromagnetic material consist of several magnetic domains[2] (small atomic magnets [26]), see Fig. 1.4. In each domain, "the atoms are aligned [in] parallel and the domain is thus saturated, even when no [external] field is applied" [26]. This effect is called 'spontaneous magnetization' [26]. The structure of these domains (e.g. domain width, number of domains) results of the minimization of the total free energy, consisting of the energy of exchange, anisotropy energy and magnetic energy (including magnetoelastic energy, magnetostatic energy, magnetic potential energy) [10]. (More detailed explanations are given in [10, 111].) Therefore, a crystal with magnetic poles (high magnetostatic energy) does not consist of one domain only (Fig. 1.5, left), but is partitioned into several domains (Fig. 1.5) and forms flux closure domains (Fig. 1.5, right) to minimize stray field energy and thus the magnetic energy [10, 78].

The individual domains are separated by walls. In these walls, the atomic magnets change their orientation gradually from the direction of the first to the second domain [23] (Fig. 1.6, left). Bloch and Néel walls are distinguishable (Figs. 1.6, left and 1.7). However, the latter only occur below a defined critical layer thickness (see [47]). Above this layer thickness, only Bloch walls occur [47]. The thickness of these domain walls results from "the equilibrium between the exchange energy and

---

[2]The size of one domain is in the range of 0.1 $\mu$m – 1 mm and contains from millions up to hundreds of billions of atoms [78].
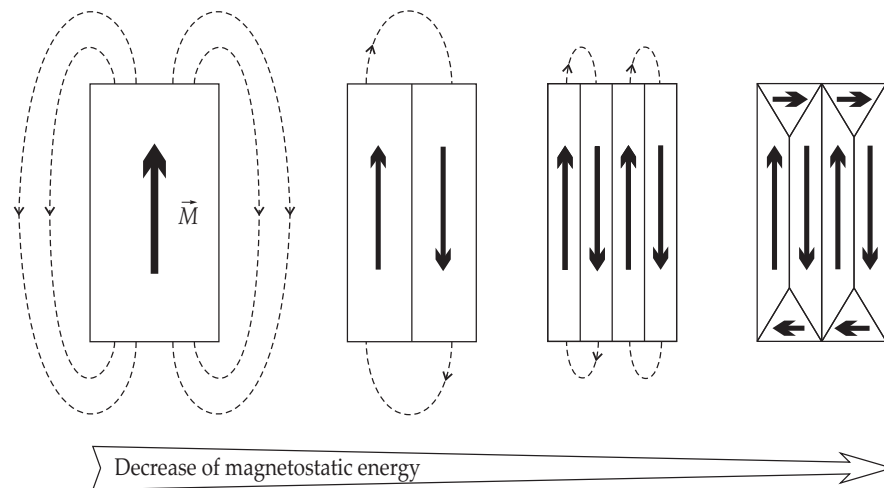
Figure 1.5: Minimization of magnetostatic energy, from [10, 198].
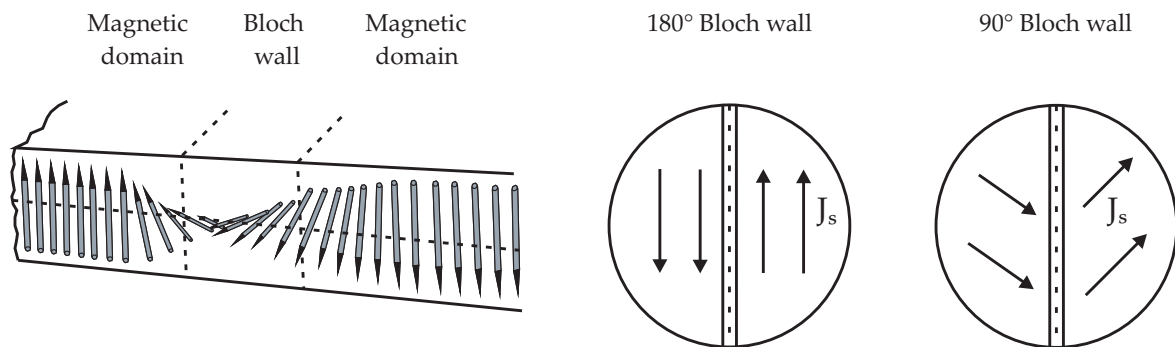


Figure 1.6: Bloch walls, from [23, 78].

the energy of magnetic anisotropy" [10]. The Bloch walls are further distinguishable according to the angle between the magnetization direction on both sides, for example 90° or 180° domain walls [23], see Fig. 1.6.

*Magnetic domain behavior in an external field*

If an external field is applied to a ferromagnetic material, the Bloch walls of the magnetic domains begin to move. Bloch walls are pinned on e.g. impurities, defects or faults inside the lattice [23]. Thus, a certain magnetic energy, correlating with a specific magnetic field, is necessary to overcome these pinning defects. Below this energy, the Bloch wall movement is defined as reversible motion of domain walls (The Bloch walls return to their starting position when the magnetic field is turned off.) (see Fig. 1.8). Above this energy, the Bloch walls break away until they reach pinnings that can only be overcome with a higher energy [23]. These Bloch wall jumps are called Barkhausen jumps [23]. Here, the irreversible motion of domain walls begins (see Fig. 1.8). Magnetic domains which are already oriented in the direction of the applied external field, grow through domain wall motion at the expense of the
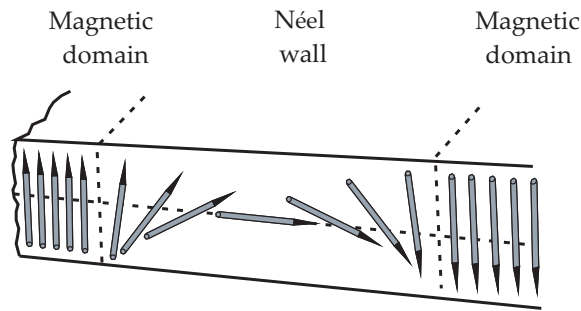
Figure 1.7: Néel wall, adapted from [55].

other domains [23] (Fig. 1.8). Considering the whole material, the global magnetization increases further [23]. After the Bloch wall motion is completed ("unfavorably oriented domains have disappeared" [78]), the reversible domain rotation begins at higher magnetic fields [23, 78]. The magnetic moments of the domains rotate into the final direction of the external applied field [23]. The material is saturated: all magnetic moments are parallel to the magnetic field.

*Magnetostriction and Villari effect*

Applying an external field to a ferromagnetic material results, once the movement of the Bloch walls vanishes, in a rotation of the magnetic domains, which in turn changes the dimensions of the material [198]. This is called magnetostriction $\lambda(H)$, characterized "by longitudinal changes in length" $l$ [198] (see Eq. (1.1) and Fig. 1.9). This effect is attributed to the rotation of magnetization, but not associated with the 180° domain wall movement [78]. The magnetostriction itself depends on its direction. For FeSi electrical steel sheets it applies[3]: $\lambda_{[100]}$: positive; $\lambda_{[110]}$: positive up to $H \gg 40000$ A/m, then negative; $\lambda_{[111]}$: negative [122]. Thus, the magnetostriction is a tensor [78]. In the case of a cubic lattice, the saturation magnetization $\lambda_s$ is derived from Eq. (1.2). Consequently, electrical steel sheets with medium silicon content have positive saturation magnetostrictions: $\lambda_{s,\,\text{SiFe 3.2\% Si}} = +9 \cdot 10^{-6}$ [198][4]. However, FeSi steel sheets with high silicon contents (SiFe 6.5 % Si) have $\lambda_s \approx 0 \cdot 10^{-6}$ [7], [198][4].

$$\lambda = \frac{\Delta l}{l} \tag{1.1}$$

$$\lambda_s = \frac{1}{5}(2\lambda_{100} + 3\lambda_{111}) \tag{1.2}$$

The Villari effect is the inverse effect of the magnetostriction [198]. Here, the domains which are oriented in the direction of the applied mechanical stress $\sigma$ change their size [198].

---

[3]For the notation indices "[...]", see footnote [1, p.2].
[4]Referring to [129].
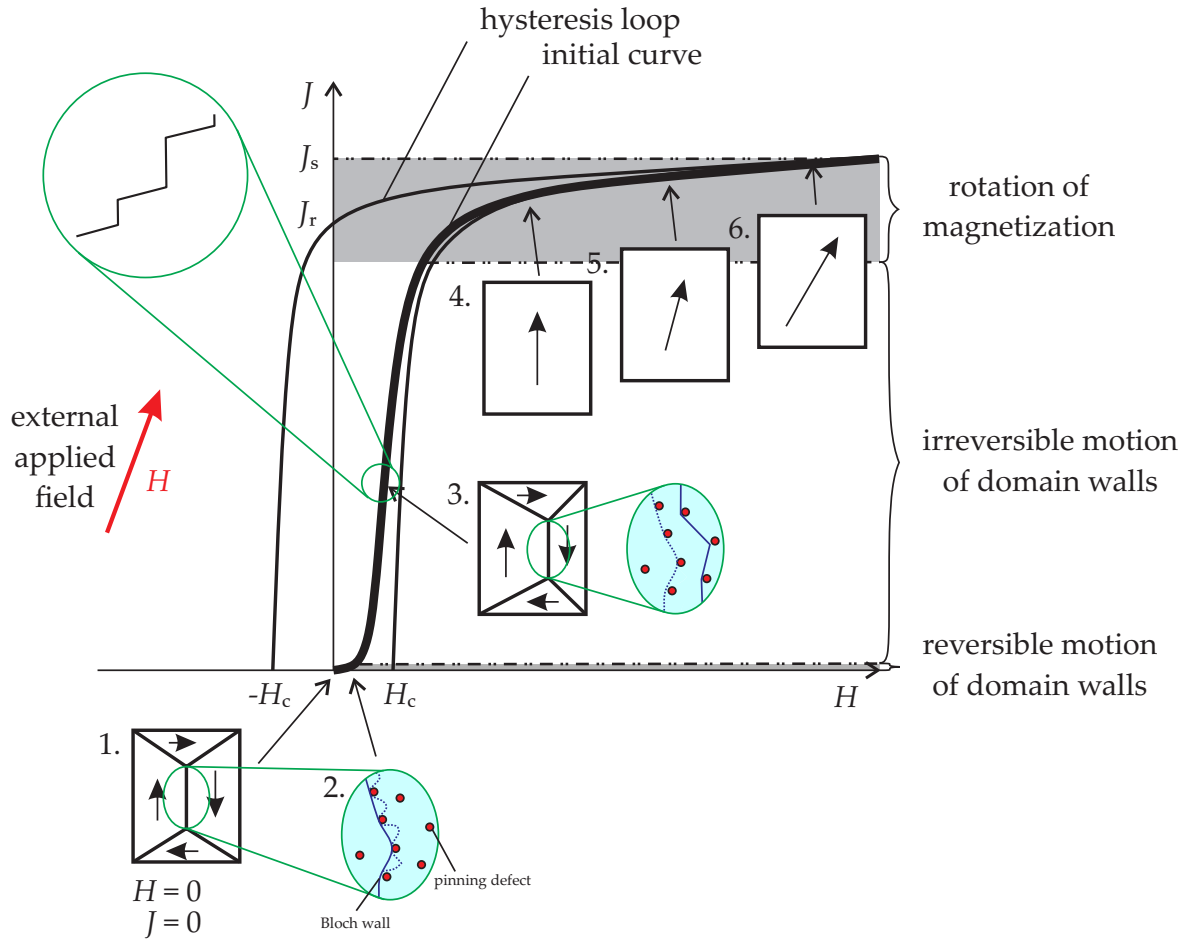
Figure 1.8: Domain wall behavior with increasing external magnetic field, from [23, 28, 55, 78, 140].
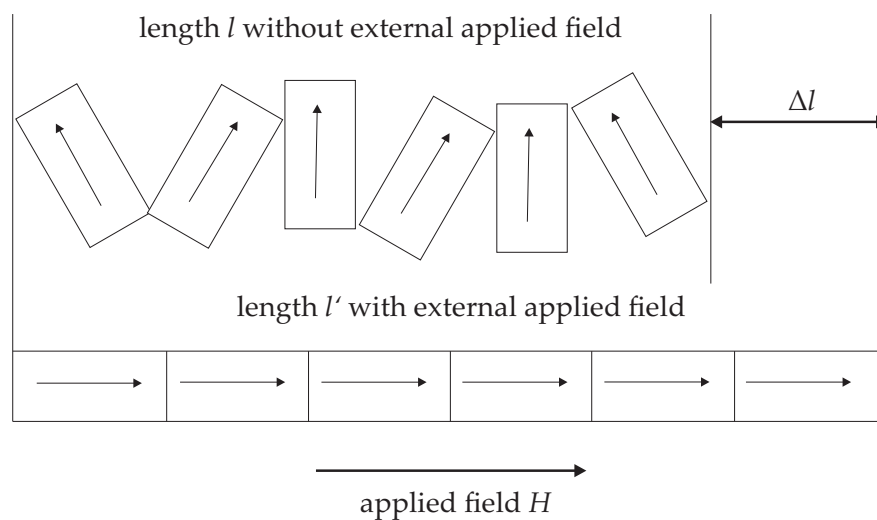


Figure 1.9: Schematic presentation of the magnetostriction effect, from [75].

## 1.1.2 Iron losses

The specific losses of electrical steel sheets $p_s$, comprise *static* hysteresis loss $p_h$ and *dynamic* eddy current loss $p_e$. The latter can be further distinguished between the classical eddy current loss $p_{ec}$ and the anomalous $p_a$ or excess loss $p_{exc}$ [16] (see Eq. (1.3) and Fig. 1.10). The hysteresis losses result from the energy required for the Barkhausen jumps and the irreversible rotation of the domains [140]. The classical eddy currents (macroscopic eddy currents) originate from the change of the magnetic flux density in time which, in turn, induces a voltage and results in an eddy current (Faraday's law) [140] (Fig. 1.11 a)). This loss depends on the magnetic polarization $J$, frequency $f$, steel sheet thickness $w_z$ as well as on the material's density $\rho$ and specific electrical resistance $\rho_E$ (Eq. (1.4)). The anomalous losses are microscopical eddy current losses: When the externally applied field causes magnetic domain wall motion, local changes in magnetization and then local eddy currents in the area of the moved domain wall occur [140] (Fig. 1.11 b)). However, in contrast to the classical eddy current loss, the anomalous loss depends on the magnetic structure of the material (in particular the domain wall spacing $2L$ in the demagnetized state[5] and the steel sheet thickness $w_z$) [16, 24, 25].



$$p_s = p_h + p_e \qquad (1.3)$$
$$= p_h + p_{ec} + p_a$$
$$= p_h + p_{ec} + p_{exc}$$
$$p_{ec} = \frac{(\pi J f w_z)^2}{6\rho\rho_E}. \qquad (1.4)$$
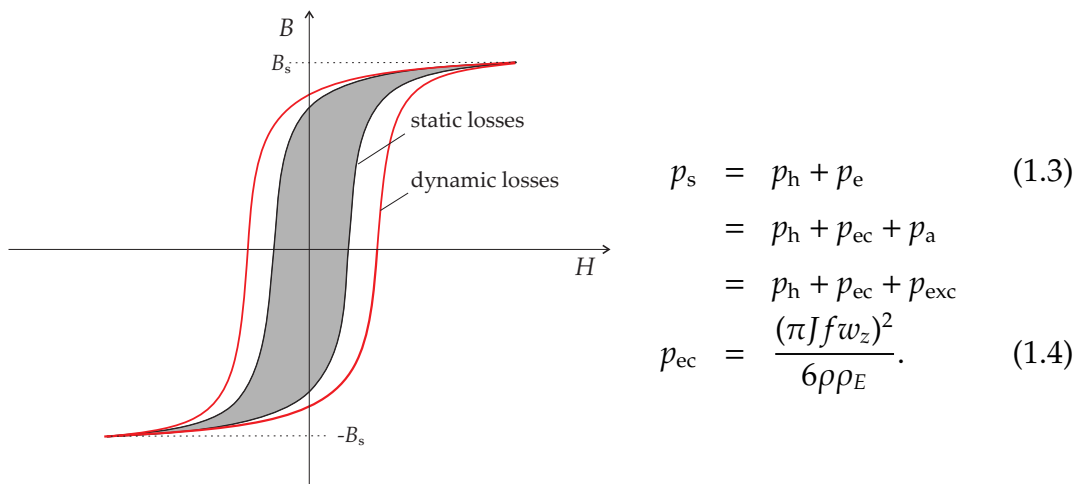
Figure 1.10: Hysteresis curve including static and dynamic losses, from [23].

---

[5]Further information is given in [16, 24].

(a) Classical eddy currents      (b) Anomalous eddy currents
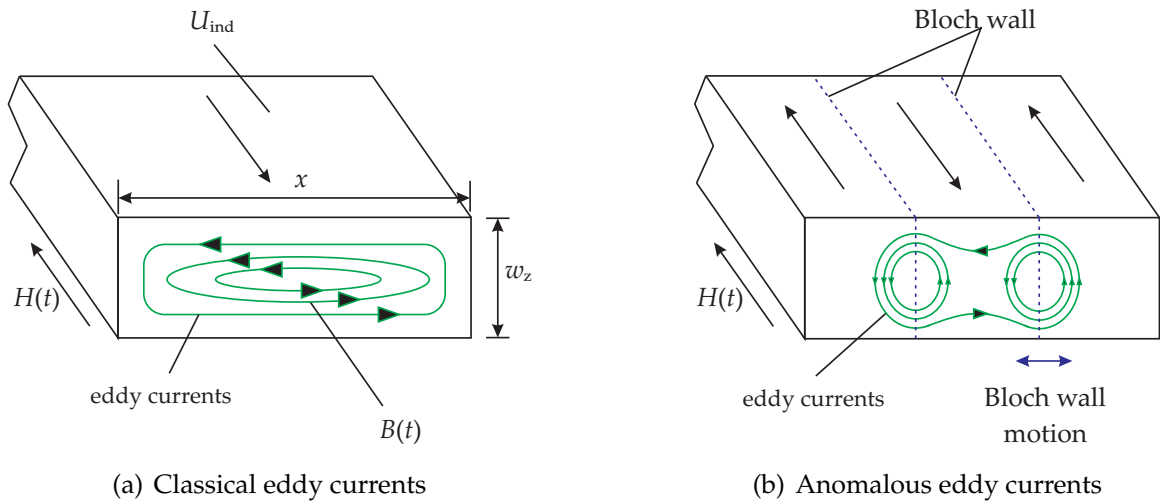
Figure 1.11: Principles of classical and anomalous eddy currents, from [140, 198].
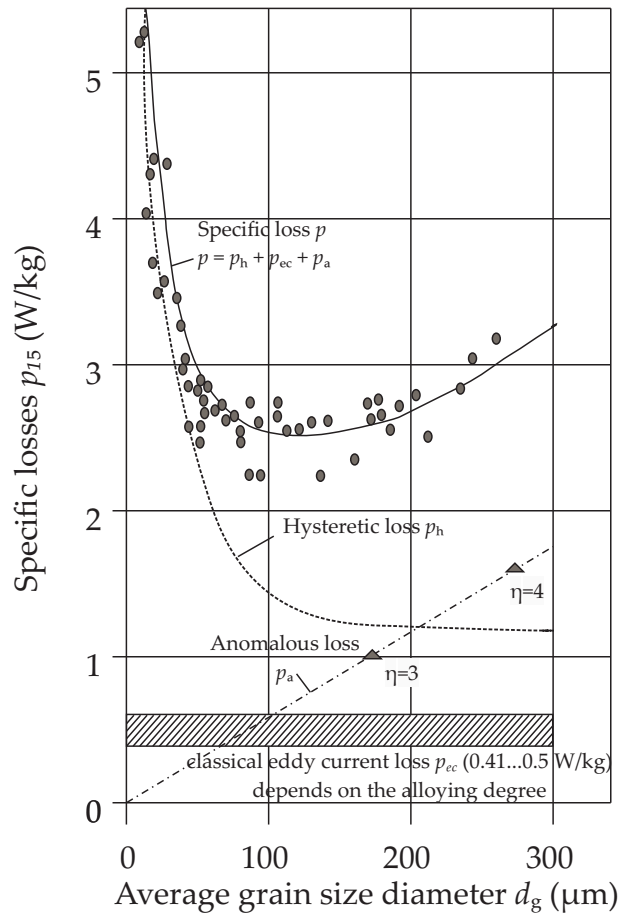


Figure 1.12: Different loss components as a function of average grain size diameter (material thickness: $0.5\,\mathrm{mm}$, Si+Al$\geq$ 3%), from [24]; $\eta = 2L/w_z$.

## 1.2 Influence of grain size, material composition and temperature on the magnetic characteristics

### 1.2.1 Grain size

Fig. 1.12 shows the specific losses versus averaged grain size diameter $d_\mathrm{g}$ of an electrical steel sheet [24]: The hysteresis losses decrease, but the anomalous losses increase with increasing grain size. Thus, a minimum of total losses occurs for grain sizes around $100\,\mu$m[6] [24]. The author of [127] presented a very similar diagram, including the total loss, hysteresis loss and eddy current loss in relation to the grain diameter. He identified an optimal grain size diameter of about $150\,\mu$m [127]. The results of [24, 127] are also confirmed by the results presented in [112]: The larger the grain size is, the smaller the quasi-static hysteresis loop and thus the losses and the coercive field strength. Note, for small frequencies the hysteresis dominates, whereas for high frequencies the eddy current losses dominate [25, 115]. At $50\,$Hz hysteresis and eddy current losses are within the same range [25]. All grains produce "localised losses around their boundaries" [185]. Therefore, small grains cause an increase in hysteresis losses [196, 210]. With larger grain sizes, the magnetic domain widths increase, which, in turn, results in higher eddy currents [35, 144]. Hence, low loss steels are usually characterized by large grain sizes [185]. The ideal grain-texture for a non-oriented electrical steel sheet is a polycrystalline structure with grain-sizes between 20 and $200\,\mu$m, without impurities and imperfections [210], as these impede the Bloch wall movements. Furthermore, considering e.g. [196], "the optimization of grain size relative to the sheet thickness is important," due to the anomalous loss.

### 1.2.2 Contents and alloys

The magnetic properties of electrical steel sheets can be improved by adding several alloys in a specific quantity. Commonly used alloys include silicon, aluminum, manganese and phosphor [81]:

*Silicon* (Si) is the most important alloy when it comes to electrical steel sheets [24]. As highlighted in [25], adding silicon to steel led to the largest improvement in the losses of electrical steel sheets between 1890 and 1980. Silicon reduces the hysteresis losses [25] as a larger content of silicon increases the grain size [170] and thus reduces the grain boundaries responsible for localized losses (see Chapter 1.2.1). Furthermore, the silicon content has also a beneficial effect on the eddy currents [24]: with increasing silicon content, the resistivity of the material increases, thereby

---

[6]The occurrence of the loss minimum at around $100\,\mu$m is independent of the alloy grade [24].

| Processing step | Low silicon grades | Medium silicon grades | High silicon grades |
|---|---|---|---|
| Cutting | low | medium | high |
| Pressing (coated) | none | none | none |
| Pressing (uncoated) | none | very low | low to medium |
| Welding | very low | low | medium |

Table 1.2: Comparison of the influence of different manufacturing steps on material degradation; different grades of non grain oriented steel; adapted from [172, 210].

suppressing the classical eddy currents (see Eq. (1.4)) [10,23,79,115,211]. The author of [153] mentions that this increase in resistivity also leads to a decrease in excess losses. Note, the investigated anomalous losses for silicon steel sheets after box annealing in [81] decreased with increasing silicon content at 1.5 T, but increased at 1 T. However, considering the total iron losses, electrical steel sheets with 6 % (mass percentage rate) silicon are desirable. Applications exist which use materials with silicon contents of up to 6.5 % [105]. At this silicon content "the magnetostriction is almost zero" [7]. Other induced characteristics which result from adding silicon, include the increase of the maximum permeability[7] (significantly in the range of $3 - 6.5 \%$ silicon [23][p.30]) and the decrease of the anisotropy constant, which is desired for non-oriented steels [23][p.572], [79, 153]. However, by increasing silicon the cold formability is reduced (the material ductility is reduced, so the material becomes brittle), wherefore the silicon content in steel sheets is mostly limited to 3.5 % [7, 10, 24, 25]. Thus, commonly used electrical steel sheets have a silicon content between $0.5 - 3 \%$ [105] or less than 3.2 % [210][8]. Furthermore, the increasing silicon content decreases the magnetic saturation and the magnetostriction [7,23,26,115,189].

In the extensive studies of [173,210] the authors exemplarily analyze the influence of the silicon content on the material degradation for different manufacturing steps (Table 1.2): The lower the silicon content, the less susceptible the material is to the manufacturing steps.

*Aluminum* (Al) is a further alloy which decreases the losses of steel sheet [24]. Adding aluminum in the range of $0.3 - 0.4 \%$ induces a well grain growth which reduces again the hysteresis loss [10]. In general, Al influences the magnetic properties

---

[7]Silicon, as well as, aluminum increases the permeability at small magnetic flux densities, but decreases the permeability at saturation (larger than 1.5 T) [79,214].

[8]The authors of [120] propose a concentration gradient of Si alloys in electrical steel sheets, decreasing the Si content from the surface (where the eddy currents occur) to the center, reporting on a 50% reduction of iron loss at acceptable magnetic saturation for lamination material with a concentration gradient from 6.5 wt% Si at the edge to 3 wt% Si in the center of the steel sheet.

similarly to silicon relating to e.g. losses, crystalline anisotropy constant, resistivity and saturation magnetic flux density [127]. When compared to silicon, the influence of aluminum on the resistivity and ductility is greater [7]. According to [27] the losses, the polarization at saturation as well as the thermal conductivity all decrease and the hardness increases with elevated Si+Al content. The statement on the first two aspects are in line with the findings for increasing silicon content presented in [23][p.30], [127]. To ensure a good cold workability (e.g. cold rollability, punchability) the total alloy degree of Si+Al should be smaller than 4.2 % [24] or 4 % [127]. The author of [27] mentions alloys of Si+Al of up to 5 % in electrical steel sheets. However, according to [10] the aluminum content should be less than 0.5 % due to its affinity with oxygen.

Next to the silicon content, also the alloys of aluminum, *manganese* and *phosphorus* increase the resistivity of the material [11, 81], contributing to smaller eddy current losses. The main function of manganese is to "increase the ductility and hence aid in fabrication," but concerning the magnetic properties, manganese has a negligible influence [26]. Small contents of "steel hardening phosporus" are used to improve the mechanical cutting process [214].

*Impurities*

The magnetic properties of an electrical steel sheet are also affected by impurities, such as carbon, sulfur, nitrogen, oxygen, titanium and zirconium [81], [127][9]. These "readily form carbide, nitride, sulfide and oxide inclusions" [81], which in turn impedes the Bloch wall movement [10] and grain growth [127] and thus the adjustment of the 'optimal' grain size [24, 81, 115]. Thus, the width of the hysteresis loop, the coercive field strength and the hysteresis loss increase [115], see also Table 1.4.

The author of [127] classified the effects due to the impurities into three categories:
1. *Inhibition of grain growth:* fine precipitates (e.g. MnS, AlN) obstruct grain growth. An example for the sulfur content and the grain diameter is given in [127], which seems to decrease linearly with increasing sulfur content (decrease of $d_g$ about 33 % when changing the sulfur content from 10 to 30 ppm). The results in [144] confirm that with low sulfur content (4 ppm), the grain growth is improved, as this includes a reduction of MnS.
2. *New magnetic domains produced by impurities lower the magnetostatic energy and inhibit domain wall movement:* domain walls are pinned (unmovable) by the inclusions.
3. *Recrystallized texture is negatively influenced by the impurities:* during the process of annealing crystals with a plethora of orientations settle around the inclusions. For

---

[9]Referring to [181].

[10]Next to inclusions, also further defects and barriers such as dislocations, grain boundaries and precipitations lead to an impairment of the bloch wall movements [115].

Table 1.3: Exemplary contents of several elements in conventional electrical steel sheets.

| Element | Content in ppm or % |
|---|---|
| Silicon | $0.5 - 3.5\,\%$ [215] |
| Aluminum | $< 0.8\,\%$ [215] |
| Carbon | $< 0.02\,\%$ [215] |
| Sulfur | $30 - 50\,\mathrm{ppm}$ [144], $< 0.02\,\%$ [215] |
| Manganese | $0.1 - 0.4\,\%$ [215] |

Table 1.4: Options to influence the resulting loss characteristics of non-oriented electrical steel sheets during material manufacturing, from [25].

| Material characteristic | Affecting | Influenceable by |
|---|---|---|
| Degree of purity ↗ | hysteresis loss ↘ | steel production: annealing |
| Precipitates ↗ | hysteresis loss ↘ | steel production: hot rolling, annealing |
| Grain size ↗ | hysteresis loss ↘ | steel production: cold forming, annealing |
| Grain size ↘ | eddy current loss ↘ | steel production: cold forming, annealing |
| Mechanical stresses ↘ | hysteresis loss ↘ | annealing, further manufacturing steps |
| Crystal anisotropy ↘ | hysteresis loss ↘ | alloy grade |
| Magnetostriction ↘ | hysteresis loss ↘ | alloy grade |
| Specific electric resistance ↗ | eddy current loss ↘ | alloy grade |
| Steel sheet thickness ↘ | eddy current loss ↘ | |

example, the "nucleus with (222) orientation increases" as the content of impurities rises. This texture detriments the magnetic properties (e.g. produces higher losses than other textures), thereby leading to higher losses.

Thus, smaller contents of impurities result in better magnetic properties [210]. The acceptable content of carbon in non-oriented electrical steel for use with electric machines is in the range of 20 to 50 ppm, depending on the overall composition of the alloy [48]. If the carbon content remains in this range, then the resistance to aging is additionally ensured [48]. Further conventional contents of impurities are presented in Table 1.3.

### 1.2.3 Temperature effects

Temperature may also influence the magnetic properties of electrical steel sheets. During operation, the material temperature within an electric machine deviates from the ambient temperature. The author of [36] reports that the coercive force, the remanence, and the losses decrease with increasing temperature (see Fig. 1.13), but the effect ceases above a certain temperature (in [36] above $300\,°\mathrm{C}$) which depends
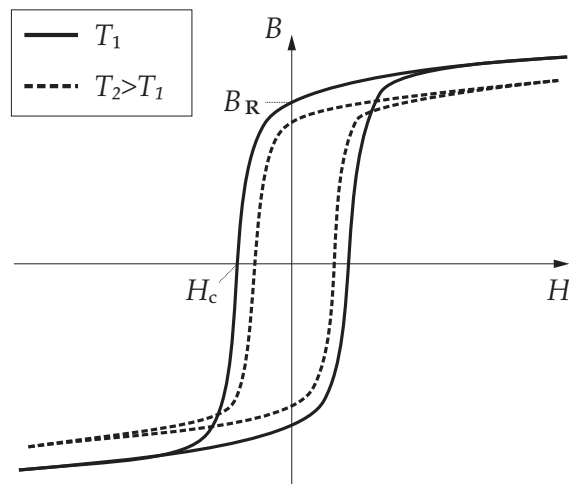
Figure 1.13: Schematic drawing of the influence of temperature on the hysteresis loop, from [23, 176].

on the maximum magnetization. Furthermore, as the temperature increases, the magnetic flux density increases at low fields, but decreases above the knee point area [36]. Additionally, the maximum relative permeability increases with temperature. The author of [36] investigated his samples in the temperature range of $30 - 700\,°C$. Electrical machines are commonly operated below $150\,°C$ (depending e.g. on the temperature stability of all used materials inside the machine). However, also in this range, the author of [36] obtained a decrease up to $6\,\%$ in total core loss, $15\,\%$ in hysteresis loss, both respectively at $1.2\,T$, and a maximum permeability increase of $9\,\%$. Except for the ceasing of the effect above a certain temperature, these findings are all confirmed by the study of [195] who investigated $6.5\,\%$ Si steel (10JNEX900) and by [135] who studied non-oriented silicon steel. The measurement results of [105] confirm that with increasing temperature the coercive magnetic field strength, the loss and the saturation magnetic flux density decrease.

The author of [195] showed with loss separation that both hysteresis as well as eddy current losses are reduced as the temperature increases. For the eddy current loss, this is attributed to the almost linear increase of the material's resistivity or rather the decrease of the conductivity [185, 195] with temperature (compare with Eq. (1.4)). Thus, the temperature has a similar effect on the eddy current loss as alloying elements (see Chapter 1.2.2). The hysteresis loss decreases as the atomic motion increases with temperature and thus "less polarization energy for the Weiss domains is needed" [176].
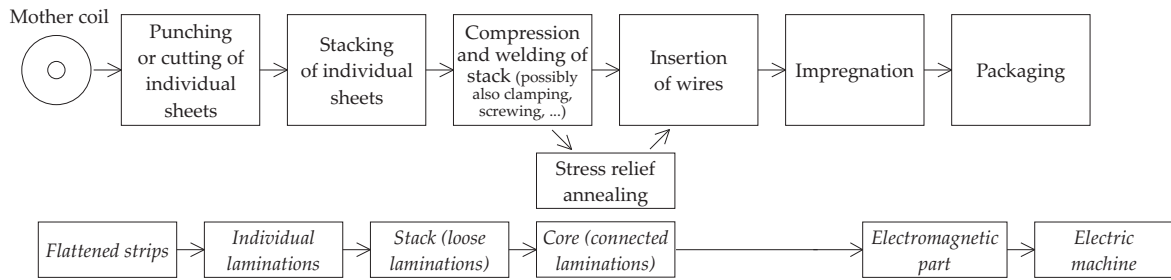
Figure 1.14: Flowchart of manufacturing process and corresponding conditions of laminations; expanding a schematic proposed in [211].

# 1.3 Magnetic material degradation during manufacturing process

## 1.3.1 Processing of the laminations during electric machine manufacturing process

Fig. 1.14 illustrates the manufacturing process of an electric machine, focusing on the processes the magnetic material is subjected to: The laminations of electric machines are made from electrical steel usually delivered in rolled strips that are unrolled and flattened before the strips are cut into individual electrical steel sheets. A number of these laminations are stacked. The stack is typically compressed and welded together, and possibly submitted to stress-relief annealing. Then, the windings are inserted, the machine is assembled, and the assembly is impregnated and/or submitted to epoxy treatment. All of these manufacturing steps may influence – and likely degrade – the steel's magnetic characteristics, evidently with varying intensity and depending on the details of the process applied.

## 1.3.2 Overview of cutting techniques

Different cutting techniques are available, such as mechanical cutting (punching[11], guillotine), laser cutting, chemical etching, electric discharge machining, water-jet cutting and photocorrosion [51, 66, 110, 119, 157, 171]. Electric discharge machining, water-jet cutting and photocorrosion are known to be less detrimental on the magnetic properties when compared with mechanical and/or laser cutting [51, 110, 171]. However, these three cutting techniques are rarely ever used, if at all, for research purposes, and even then, only for prototypes. This is mostly due to the extremely slow cutting speed (e.g. in the case of water-jet cutting 800 mm/min for a material

---

[11]Different forms of punching can be distinguished, e.g. die stamping, single stage stamping and single slot notching [210].

thickness of 0.5 mm [171]) and hence due to the very high cost.

Punching is frequently reported as the most widely used approach due to low cost [5, 110, 153, 157] (although initial investment is high, production cost is low and the production is fast, resulting in its use for high production volumes [66]). However, laser cutting, which is more time consuming [59], is commonly used for prototyping as well as for small series production. Nevertheless, the advantage to laser cutting is the possibility of rapidly changing or modifying the cut geometry at low cost. (Initial investment is low [66].) In contrast, the punching machine requires a new manufactured cutting tool as soon as the geometry changes and is thus not flexible with respect to a change of geometries. Further disadvantages of punching includes the bluntness of the cutting tool which increases with the number of punched samples, as well as the burr evoked at the cut edge [153]. With increasing clearance and a more worn-out cutting tool[12], the height of the burr increases as well [153, 169]. These shearing burrs must be kept small or be removed (implying an additional processing step and, as a consequence, additional costs), as such burrs may damage the isolation on the lamination surface and lead to short circuits (hot spots) between the individual sheets in the lamination stack [69, 180]. Furthermore, due to the burrs the stacking factor is reduced [45].

Considering laser-cut samples, the statements are not consistent: some authors report that no burr occurs e.g. [10, 13, 59], others state that even for such samples burrs exist [43, 45]. However, these burrs are normally smaller than those of mechanically-cut samples (laser induced burr $< 30\,\mu$m; $35\,\mu$m $<$ mechanically induced burr $< 95\,\mu$m (see [45])). Dickmann [45] further reports that solid state laser cutting leads to smaller burrs than $CO_2$-laser cutting. Furthermore, the occurrence and size of the laser-induced burrs depend on the laser settings (e.g. gas quantity, gas pressure, laser beam output, cutting speed) [45, 164]. In general, the cutting process induces mechanical and/or thermal stresses, especially close to the cut edges [146, 151, 169], influencing, and generally degrading, the magnetic properties in the affected zones. The degrading effects of laser cutting are optically less obvious than those of mechanical cutting.

### 1.3.3 Mechanical cutting

Mechanical cutting includes guillotining and punching. According to [153] "punching is a [...][special] case of guillotining, i.e. when cutting is conducted without rake angle."

---

[12]The harder the material (again depending on the material's composition and alloys, see Chapter 1.2.2), the larger the wear of the cutting tool; however, the burr size decreases as harder material is more fractured than teared by punching, [214] referring to [137].
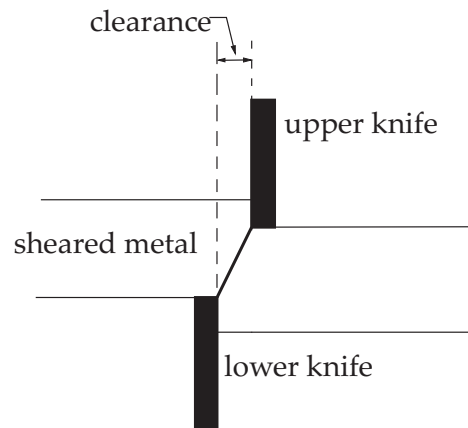
Figure 1.15: The clearance influences the degradation effect on the material, from [10].
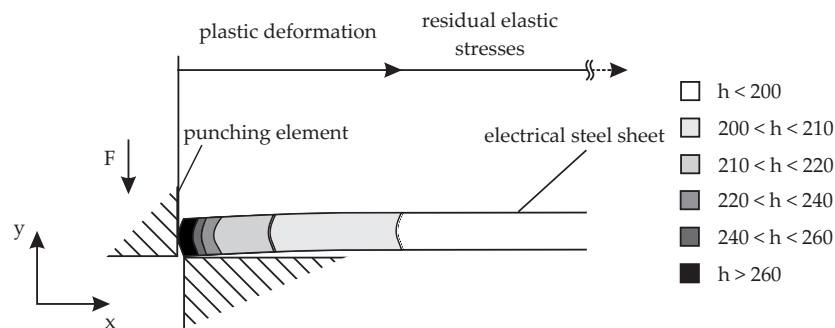


Figure 1.16: Area of influence of plastic and elastic degradation, based on [82]; $h$ = Vickers microhardness.

Electrical steel sheet samples which are cut mechanically, obtain inhomogeneous stresses inside the material which results in plastic deformation along the cut edge [105, 153]. However, both plastic as well as elastic stresses are induced in the material due to cutting [57, 148], see Fig. 1.16. Through the mechanical cutting, the lattice absorbs the mechanical energy which results in a movement of the neighboring layers and micro-structural defects [154]. These "further operate as pinning sites for the domain walls." [154]. These changes, in turn, degrade and influence the magnetic as well as the mechanical properties of the steel sheets [154].

Referring to [50], [169] explains the change of the magnetic properties as a result of the tensions induced within the material as follows: First, elastic deformation occurs at the moment the tool is applied to the sheet. As the tool further enters into the material, increased localized plastic deformation occurs. The increasing pressure leads to a consolidated zone with a high deformation ability because of the high compression the material is subjected to. Once the tension within the material exceeds the shear strength of the material, cracks are initiated, running towards the
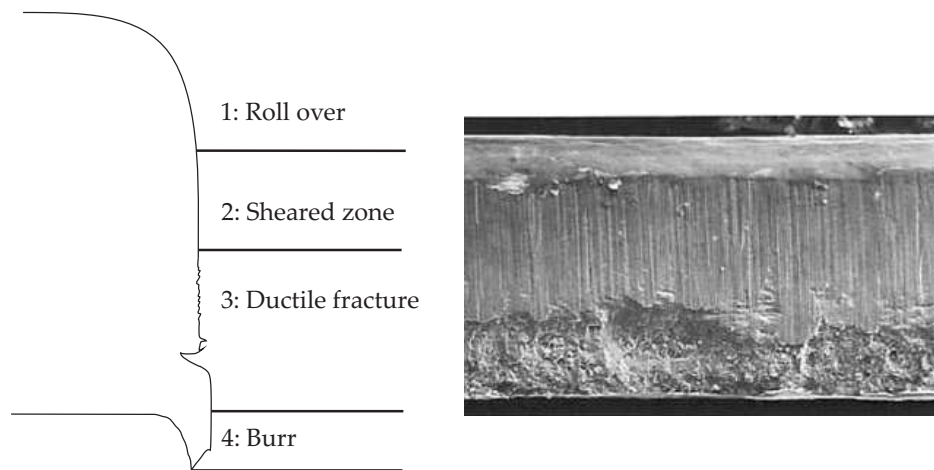
Figure 1.17: Regions of the cut edge, from [12, 110].

perpendicular cut edges. Several authors report that the punching process further results in a change of grain morphology near the cut edge (e.g. [4, 51, 110, 170]). In Fig. 1.17 the characteristic areas of the cut edge due to mechanical cutting are presented [12]. The respective proportions depend on the settings of the cutting technique (see e.g. [153]).

***Previous experiments to identify the deterioration depth induced by cutting***
In the literature a variety of different measurement methods have been used to determine the deterioration depth along the cut edge which is induced by mechanical cutting[13]. These methods are [64]:

- microhardness measurements (e.g. [146]),
- microscopy (e.g. crystallographic or Kerr microscopy), e.g. [178],
- method of drilled holes, e.g. [134, 138, 148, 170],
- needle probe method, e.g. [39],
- neutron gratering interferometry with neutron dark field image [183, 184],
- investigation of samples with different widths and additional measurement of the magnetic properties e.g. [178].

***Results of the deterioration depths presented in literature***
*1) Microhardness measurements*
Several authors e.g. [4, 12, 146, 154] have performed microhardness measurements to obtain the deterioration depth due to mechanical cutting: [146] investigated a non-oriented electrical sheet (M330-50A) and calculated the plastic strain from the microhardness. He divided the degraded region into an obviously damaged region

---

[13]A detailed summary of experimentally investigated magnetic flux density distributions within cut samples is presented in Chapter 7.

(smaller than 0.4 mm) and a region with small strains (0.4 -1 mm) [146]. The authors of [154] investigated samples (FP800-65A) which are cut with and without compression. They found out that the deterioration depth is decreased with additional compression (guillotine-cut without compression: until 10 mm; with compression: < 1 mm or respectively smaller than the sample's thickness) [154]. The authors of [12] investigated several steels. They came to the conclusion that the "large deformation affected zone [...] can extend as far as 8 mm" with a very large deformed area of $500 - 1000\,\mu$m from the cut edge [12]. In the paper of [4] larger microhardnesses are observed until $1000\,\mu$m or higher. In [153], the author presents microhardness measurements for different electrical steel sheets and obtained deterioration depth ranges of $0.4-0.8$ mm, $1-2.8$ mm and < 1 mm (depending on the respective sample). This author of [153] concludes that the degraded zone due to punching correlates with the thickness of the sheet. According to [57] the plastically deformed zone correlates with half the thickness of the electrical steel. The author of [170] found out that the hardened zone for low silicon steel is smaller ($0.2 - 0.4$ mm in width) than that for high silicon steels (with up to 2 mm). This is in line with [167] who stated that with increasing grain boundary density, the plastic deformation decreases[14]. The results of [169] showed a degraded zone of 0.35 mm for a material with 1 % silicon content (this deterioration depth is in line with that of the low silicon material presented in [170]). Interestingly, this degraded zone width was found to be independent of the quality of the cutting tool [169][15]. However, the hardnesses of these degraded areas, which had been induced by a sharp and a blunt cutting tool, differed.

*2) Microscopes*

The authors of [178] investigated the domain patterns of the electrical steel sheet (50A400) by Kerr effect microscopy to draw conclusions on the depth of the deteriorated area due to shearing (guillotine). As a reference probe they further investigated a stress-relief annealed sample [178]. With this method they determined an affected area of $1 - 1.4$ mm. The authors of [64] analyzed the investigated material also by measuring the crystallographic structure. They observed smaller grain sizes along the cut edge in contrast to those in the middle part. They stated the area with such smaller grains of about $500\,\mu$m from the cut edge [64].

*3) Method of drilled holes*

Nakata *et al.* [138] applied a measurement technique presented in [126] on silicon steel sheet samples (35A250[16]) to investigate the change of flux distribution due to

---

[14]With increasing silicon content the average grain size increases [170][p. 45].

[15]Probably materials with small grain sizes (derivating from the low silicon content [170]) are less sensitive to the settings of the cutting technique as e.g. the wear of the cutting tool.

[16]This corresponds to material M250-35A.

mechanical cutting. He reports on two different measurement techniques, the first of which is a method with search coils which are placed through holes inserted in the test sample [138]. The disadvantage is that the holes affect the flux distribution in their vicinity [138]. Therefore, he modified this measurement technique by inserting conical holes in the surface of the sheet which are filled with a conducting paste and twisted magnet wires [138]. The measurements were carried out at 50 Hz [138]. He observed that the deteriorating effect on the magnetic flux density distribution concerns a region of up to 10 mm [138]. However, he also mentions that the rapid deterioration occurs within 5 mm from the cut edge. [138]. The author of [119] also examined several non-oriented steel sheets with the method of drilled holes. He determined a degradation depth of $5 - 6$ mm (strongly influenced) and a small or negligible influence of mechanical cutting in the range of $5/6 - 10$ mm from the cut edge [119]. From the results presented in [148] it can be assumed that the zone affected by cutting is smaller than 4 mm, as in the case of M800-50A, at 1.5 T and 50 Hz. According to [163] the degraded area of large grain and high silicon material reaches up to 15 mm and in the case of low silicon and small grain material is smaller than 10 mm[17]. The measurements were performed at 50 Hz.

*4) Needle probe method*

In contrast to the method of drilled holes, the needle probe method is a non-destructive method [39, 150] and bases on the patent of [206]. The author of [153] investigated punched samples with this method and determined the affected zone to about 5 mm [153][p. 198].

*5) Neutron grating interferometer combined with neutron dark field image*

Siebert [183, 184] used the neutron grating interferometer in combination with the neutron dark field image method to obtain the distribution of the magnetic flux density across the width of the investigated sample. He achieved a parabolic distribution for his mechanically-cut samples [183, 184]. According to [184] the width of the affected zone due to mechanical cutting extends half of the sample, in the respective case 5 mm (sample width: 10 mm). This is also backed up with the results presented in [183] for smaller sample widths.

*6) Samples with different widths and magnetic property measurements*

The authors of [178] measured samples (50A400) with varying widths at 50 Hz in a single sheet tester, at different magnetic field strengths and flux densities. From

---

[17]This fits again with the results of [170] that the degraded zone of high silicon material is larger than that of low silicon material.

the flux density, they determined degraded depths of $< 1 - 5$ mm, depending on the respective magnetic field strength [178]. From the iron losses, the degraded region is estimated to be $1.5 - 2.5$ mm at 1.5 T. Again this depth changes with smaller flux densities. The variation of degradation depth with considered parameter illustrates well the challenge of proper definition.

*7) Combination of magnetic property measurements and simulation*

The authors of [64] derived the deterioration depth due to punching from experimental data to 1.87 mm, for their respective material [64]. Using an analytic model they obtained a depth of 1.4 mm [62].

*8) Further investigated deterioration depths with no exact allocation*

According to [134], the author of [33] mentions a 1 mm wide degraded area due to mechanical cutting. Wilczynski [207] presented a model based on measurement data to obtain the width of the stressed zones induced by cutting. In the case of the punched non-oriented sample (EP330-50A) he calculated a depth of 0.6 mm [207].

**Reasons for the differences of detected deterioration depths**

As seen above, the determined deterioration depths presented in literature differ. This may be explained by several reasons:

1. *Measurement method:* Some of the measurement methods determine an indirect characteristic/property from which the magnetic deterioration depth is derived. Some methods might induce further internal stresses which might influence the result obtained for the magnetic deterioration depth. An example: In the work of [178] the deterioration depth of a given sample is investigated with three different approaches: in regard to the magnetic flux density, the iron losses, and by Kerr microscopy. The first approach led to $< 1-5$ mm depending on the magnetic field strength, the second approach estimated $1.5 - 2.5$ mm at 1.5 T, and the microscopy suggested $1 - 1.4$ mm. Since the deterioration observed by microscope mirrors only the plastic deformation [64], the difference between the deterioration depth determined by microscope and by analysis of magnetic properties reflects the existence of elastic residual stresses [153]. Also other authors state that the results of investigated deterioration depth differ depending on the measurement method: E.g. Schoppa [170] mentions that the investigated depth by the method of drilled holes is larger than that obtained by microscopy.

2. *Definition of deterioration depth:* Some authors present the depth at which the investigated material property changes significantly. However, others define

the deterioration depth as the depth at which the material property is again the same as that of the reference (non-deteriorated) sample (see e.g. [12]: large deformation affected zone and very deformed area). Furthermore, some methods only represent the depth of plastically deformed areas (e.g. microhardness measurements; sheared zone ≅ magnetically deteriorated zone) in contrast to others which also represent the zone of residual elastic stresses[18] , but this unsheared area may also be affected by the mechanical cutting process (Fig. 1.16). According to [128] residual stresses "may spread over the whole lamination." These residual stresses only have a small local influence on the permeability in comparison to plasticity, but the residual stresses affect a larger volume of the material [128]. The plasticity dominates directly at the cut edge "whereas at some distance residual stresses do" [128], and are stated to be of equal relative influence on the global magnetic influence as the plasticity. The degree of degradation due to residual stresses or plasticity depends on the magnetic field strength [128]: the former has the larger influence at fields up to a certain field strength and the latter is the main factor of influence beyond that field strength. In the material analyzed (non-oriented FeSi steel with 3 % silicon and 0.5 mm thickness) in [128], this crossover takes place at around $H = 400$ A/m.

3. *The material investigated:* The chemical composition as well as the material texture influence the deterioration depth. For example, cutting has a larger adverse influence on the deterioration depth and the magnetic properties of materials with large grain sizes and high silicon contents [64, 148, 163]. However, the author of [163] states that the silicon content influence is smaller than that of the grain size[19]. Also Schoppa [170] refers to the dependence of the size of the magnetically deteriorated zone on the grain size and silicon content. In [172] he further states that the effect of cutting on the magnetic properties is greater for materials with large grains. Additionally considering Chapter 1.2.2, the alloy affects the ductility of the material. This in turn influences the degree to which the material is sensitive to deterioration during the mechanical processing and hence, the difficulty to exactly predict the degree of deterioration for a given process. (This fits also with Table 1.2.)

4. *Sample width and geometry:* The smaller the sample width is, the higher the possibility that the degraded zones of the different cut edges might overlap and thus "falsify" the deterioration depth determined, assuming a cutting effect on one side only. Furthermore, the more 'complicated' the sample geometry

---

[18]Compare e.g. the results of [153][p. 198 and p. 62].

[19]Note, the silicon content, in turn, influences the average grain size diameter of the material [170].
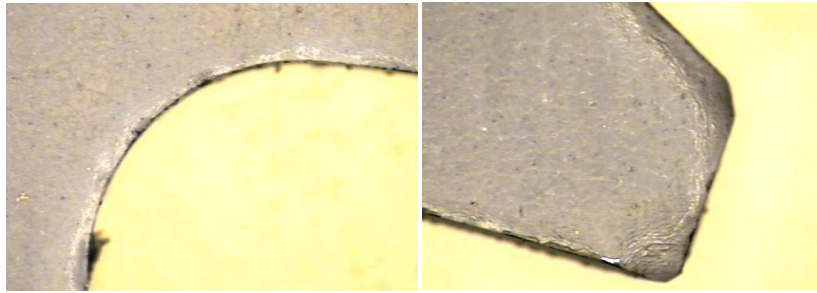
Figure 1.18: Punched edges at slot bottom and tooth tip, from [43].

is (deviating from long straight lines e.g. small edges, notches), the more the deterioration depth might vary (see e.g. the punched laminations of [43] in Fig. 1.18).

5. *The cutting method and its settings:* Although both guillotine as well as punching are mechanical cutting techniques, they (slightly) differ with respect to the deterioration effects. Furthermore, the settings of each cutting technique influence the degrading effects on the material, as for example clearance size, blade radii, frictional contact, tool wear, blank holder force/additional compression to the sample [10, 124, 154, 169]: For example, the authors of [12] showed that with increasing clearance, the deformation, the hardness, the bended volume as well as the degradation of the magnetic properties increase (the remanent magnetic flux density and relative permeability both decrease, while the coercive magnetic field strength and the specific losses increase). Again, the optimum clearance depends on the chemical composition of the material, e.g. silicon content [12]. The results of [71] showed that with decreasing punch velocity and increasing clearance, the losses of the material increased. Thus, this confirms the results of [12]. However, according to [153] the difference in cutting parameters "affect stronger the height of burr than the size of the deformation affected zone." The author of [169] states that worn-out tools lead to increased pressure and material hardening. Other researchers also confirm the effect of the wear of the tool and/or the sharpness of the punch [5, 185, 210] and the increase of the punching burr with increased wear of the punching element [210].

6. *Operation point:* The point of operation (magnetic field strength/magnetic flux density, frequency) also influences the experimentally determined deterioration depth. For example, the authors of [178] stated that the width of the degraded area decreases with increased magnetic field strength $H$. This behavior is also reflected in the mathematical modeling of [170]. Also the results

presented in [119, 138] show that the deterioration depth decreases with increasing magnetic flux density. This is attributed to the degree of saturation: with increased saturation "the difference between the permeabilities in areas where the characteristic is deteriorated and where it is not is no longer large, and flux flows uniformly through both types of region" [deteriorated and non-deteriorated zones] [138]. The author of [153] further showed, that the magnetic flux density, which is forced to the middle of the sheet at low frequencies due to the cut edge degradation, is "pushed backed to the cut edge" with increasing frequency due to larger eddy currents and thus in turn due to the skin effects. As already seen in Chapter 1.2.3 also the temperature of the material investigated may affect the results. The temperature of the material again depends on the point of operation and on the measurement method (see e.g. [192]).

## 1.3.4  Laser cutting

Laser cutting is a thermal separation technology for cutting e.g. metals [164]. The laser cutting technology cuts with focused beams and is free of wear [164]. The laser beam heats up the material locally and transforms it into a liquid or gaseous form [164]. Caused by the relative motion a cutting kerf occurs [164]. In the case of laser beam fusion cutting, an assisting cutting gas, e.g., nitrogen blows the fused material, slag and its vapors out of the gap (Fig. 1.19) [164, 207]. Thus, laser cutting induces a thermal shock wave into the material, resulting in residual thermal stresses within the affected material [4, 153, 207]. This is due to the rapid heating to high temperature[20] followed by a fast cooling which results in a large temperature gradient [148, 207]. This leads to dislocations in grains along the cut edge [207]. Furthermore, it may happen that "grains slide over one another" which may introduce micro-cracks [207]. This may further lead to an increase of "dislocations and stresses at the material edge, [to an] decrease of crystallites and, consequently, [to a larger] deterioration of magnetic properties." [207].

Different types of laser cutting technologies exist. In the following, the solid state as well as the carbon dioxide laser are shortly explained. These two types are commonly used in industry for cutting electrical steel sheets and are further investigated in this work[21].

---

[20]The authors of [207] mention a temperature gradient of about 5000 °C.

[21]When the expression 'in this work' is used, the results of this dissertation are referred to.
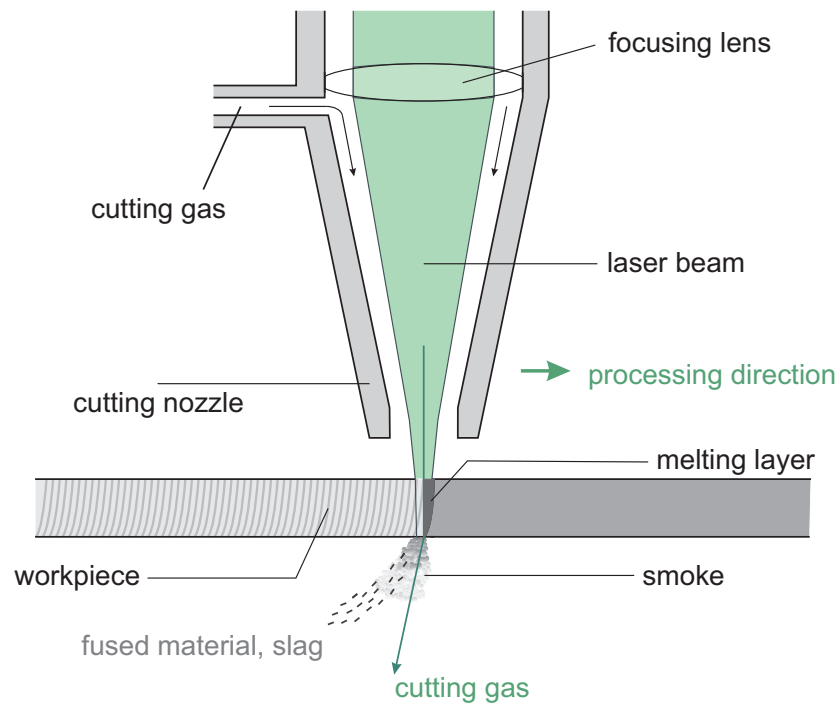
Figure 1.19: Schematic representation of the laser beam fusion cutting technology, from [31, 61].

*Solid state laser*

The active medium of a solid state laser is a solid (glass or host crystal) [31]. This host crystal is doped with foreign ions, commonly neodymium (Nd) or ytterbium (Yb) [31]. Considering Nd:YAG laser (neodymium-doped yttrium aluminum garnet laser): With light of arc lights or diode lasers, the electrons of the neodymium ions are brought up to a high energy level [31]. By returning from the upper to the lower energy level, laser light with $1.06\,\mu$m is emitted [31]. Note, here a four energy level system (high, upper, lower, ground) is considered. During the transition between the other levels (high to upper and low to ground energy state), heat is emitted to the crystal. The emitted photons have the same physical properties and thus the same wavelengths, same directions of propagation and their electromagnetic radiations are in phase [164].

*Carbon dioxide laser*

The laser-active medium of the $CO_2$-laser is a gas mixture of carbon dioxide ($CO_2$), helium (He) and nitrogen ($N_2$) [31, 164]. Electrical gas discharges (caused by direct voltage or high-frequency alternating voltage) induce free electrons, which "excites the nitrogen molecules by pushing them" [31, 164]. These molecules start to oscillate and release their energy to the $CO_2$-molecules by pushing them (indirect excitation) [31, 164]. Thus, the latter are raised from the ground level to the high energy
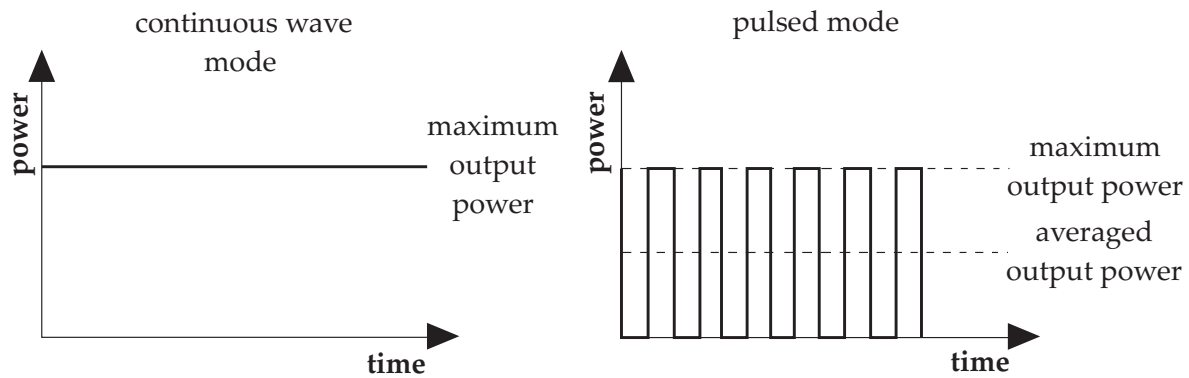
Figure 1.20: Continuous wave and pulsed laser mode, from [31].

level [31]. By moving to the lower laser level, the $CO_2$-molecules emit light of a nominal wavelength of 10.6 $\mu$m [31]. By returning to the ground energy state, heat is emitted [31].

*Pulsed or continuous wave(cw)-mode*

By now, most lasers are able to operate in continuous wave (cw) or in pulsed mode. Thus, in the case of cw-mode, the active medium is continuously excited and a continuous laser beam is generated [31]. In the quasi-cw-mode, the active medium is excited with pulses but with high frequency (a multiple of 10 kHz) [31]. The pulse break is so short that the laser beam is still continuous. During the pulsed mode the active medium is excited with short pulses [31]. Duration, power and frequency of these pulses define the average laser power which is smaller than that of the laser pulses [31].

***Results of the deterioration depths presented in literature***

*1) Microhardness measurements:*

Araujo *et al.* [4] investigated the microhardness of not only mechanically-cut samples, but also that of laser-cut samples. They found no significant change of microhardness from the cut edge to the middle of the sample. Thus, they concluded that laser cutting does not induce a change of hardness inside the material. Considering the hardness profiles of laser-cut samples investigated by [110], the hardness does again not change significantly in the zone of the cut edge in contrast to that of the mechanically-cut sample. However, the authors of [110] explain the small increase observed in hardness at the cut edge with thermal strains. The authors of [2] cite [200] that a solid state laser-cut sample resulted in an increased microhardness within a depth of 0.1 mm from the cut edge. The authors of [2] state the same width for the thermally influenced zone of $CO_2$-laser cut samples. This supports the results of the author of [45] who analyzed the microhardness of $CO_2$-laser and FKL-laser as well

as mechanically-cut samples: In the case of laser-cut samples, the microhardness at the cut edge increases not as much as that of mechanically-cut samples. The maximum reported increase in hardness is about 14 % for the $CO_2$-laser cut sample, 28.5 % for the FKL-laser cut sample and 86 % for the mechanically-cut sample [45]. In general, changes in the microhardness for laser-cut samples are observed within 100 $\mu$m from the cut edge [45]. This increase in microhardness is also explained by stresses in the lattice structure, but now due to the thermal gradient [45]. The authors of [13] showed a microhardness increase of up to 1600 $\mu$m from the cut edge in the case of the fully processed non-oriented steel sheet, depending on the laser settings (e.g. cutting speed, power, gas pressure).

*2) Microscopes:*

Most researchers agree that laser cutting does not change or deform the grain morphology of the material in the cut edge area (e.g. [2, 4, 51, 110]). They state that the grain morphology remains unchanged by laser cutting and is the same near the cutting line [4] and inside the material far away from the cut edge. Nevertheless, the author of [148] expects that laser cutting may cause grain growth at the cut edge due to the thermal treatment. Dickmann [45] investigated $CO_2$-laser cut samples (V940-65A) using a magneto-optical procedure based on the Kerr-effect for the visualization of the Weiss domains [23]. He determined a deteriorated magnetic zone (more degraded mobility of the domains) of up to 400 $\mu$m from the cut edge at magnetic field strengths of 1 A/cm. With larger magnetic field strengths this zone decreases [45].

*3) Method of drilled holes*

The method of drilled holes is also applied to laser-cut samples in [119]. Magnetic flux density distributions from the cut edge to the middle of the sheet are presented for four different materials, which are commonly used in electrical machines at 1 T and 1.5 T at 50 Hz. In contrast to the mechanically-cut samples, the laser-cut samples (in particular a laser-milling machine with slow cutting speed and low power) of all materials investigated showed no significant deterioration of the magnetizing condition in the vicinity of the cut edge [119]. Thus, it is difficult to determine a deterioration depth from these measurements.

*4) Neutron grating interferometer combined with neutron dark field image*

Siebert [183] presented the distribution of magnetic flux density of both mechanically-cut samples and laser-cut (solid state laser) samples (M330-35A), at several magnetic field strengths, obtained with the neutron grating interferometry. In con-

trast to the mechanically-cut samples, "no such [...] decrease at the cut [...] edge" of laser-cut samples is observed, but a decrease of the magnetic flux density "over the total [sample] width" is recognized [183]. Thus, no symmetric parabolic distribution with a maximum in the middle of the sample is found; however, an asymmetric distribution with its maximum at the first and its minimum at the second laser-cut edge is found. This applies to both sample sizes investigated (10 mm and 5 mm). The difference of the flux densities at both cut edges decreases with increasing field strength and larger sample width [183]. Thus, no specific deterioration depth can be given, as the magnetic flux density distribution of the whole sample is affected. A similar behavior is observed for $CO_2$-laser cut samples, presented in [184].

*5) Further investigated deterioration depths with no exact allocation*
The authors of [207] applied the same model as used for the mechanically-cut samples (see p. 21) to $CO_2$-laser cut samples for determining the deterioration depth. In the case of the laser-cut non-oriented sample (EP330-50A), they calculated a depth of 4 mm [207].

The previous investigations showed that it is more complicated to determine a deterioration depth for laser-cut than for mechanically-cut samples: No radical decrease in the vicinity of the cut edge is found for laser-cut samples, but rather a decrease of magnetic properties which spreads over the whole sample width. Furthermore, the results of literature show that not every measurement method used to identify the degradation depth known from mechanically-cut samples may be applicable to laser-cut samples. For example, the determination of the changed grain sizes (microscopy) is not evident, as according to some authors e.g. [2] laser cutting does not change the grain size of the material.

**Further reasons of differences of detected deterioration depths**
Most of the aforementioned reasons in the abstract for the mechanically-cut samples apply also to laser-cut samples. Here, additional aspects applying to laser cutting are given.

1. *Laser method:* The investigations of [45, 46] showed that the laser cutting methods might differ with respect to their deteriorating effects on the magnetic properties. For example, according to the investigations of [45, 46] the $CO_2$-laser technology degrades the relative permeability of the material investigated more intensely than solid state laser cutting.

2. *The material investigated:* In addition to the chemical composition, other factors may also influence the deterioration effect due to laser cutting. For instance,

the author of [46] states that laser cutting has a more detrimental effect on the magnetic properties in the case of grain oriented steel sheet samples in contrast to non-oriented steel sheets. Furthermore, note that it has not yet been possible to manufacture non-oriented materials with perfect isotropic properties [210]: Non-oriented ferromagnetic materials have shown to still exhibit slightly better magnetic behavior into the rolling direction[22]. For example, it has been found that the power losses are lowest if the sheets are cut in parallel to the rolling direction [79, 172]. According to [210] this is at most 10 %.

3. *Sample width and geometry:* Considering Fig. 1.21 (which has been obtained optically), the deterioration edge seems to be more uniform and independent of a more 'complicated' geometry, as is the case with mechanically-cut samples (Fig. 1.18). However, the thermally induced stresses may vary in their distribution. Furthermore, the observed uniform cut edge may also result from a special laser method or setting. According to [30, 164], small curves may cause additional deterioration as small edges must be cut with a loop (no abrupt change of direction possible).

4. *Laser settings:* In [45, 46] the influence of different settings on the deterioration effect of the magnetic properties is presented. Thus, with increased laser cutting speed, the increase of specific losses decreases [46]. The measurement results of [40, 171] confirm the less detrimental effect on the magnetic properties with increasing cutting speed. The slower the cutting speed is, the larger the affected material zone, as "more thermal stresses are introduced [per material volume] when cutting [...] at low speed" [39]. The microhardness measurements of [13] showed that the zone with increased microhardness shrinks with e.g. increasing cutting speed. However, the maximum possible cutting speed depends again on the thickness of the material (the thicker the material, the slower the possible cutting speed) and on the geometry to cut (at small or complicated curvatures, the cutting speed has to slow down). A smaller laser power in combination with a smaller laser beam diameter leads to a smaller thermal load on the material and thus to a smaller increase of losses [46]. By increasing gas pressure, the increase of specific losses is reduced [46]. Additional parameters as, for example, the pulse duration and pulse frequency are further discussed in [45, 46]. The authors of [59] investigated different detrimental effects on the magnetic properties by comparing two different assisting gases as air and nitrogen. They conclude that laser cutting with air

---

[22]Some manufacturers rotate the individual sheets around the axis of the machine, into circumferential direction, to reduce the effect of this remaining anisotropy.
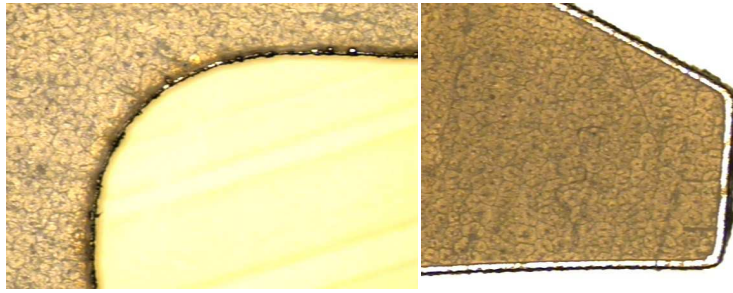
Figure 1.21: Fiber laser-cut edges at slot bottom and tooth tip, from [43]. Fiber laser is a special kind of solid state laser.

deteriorates the magnetic properties more than with nitrogen [59]. Also, the author of [45] investigated the different influence on the magnetic properties of laser-cut samples by changing the gas.

***Varying opinions about laser and mechanical cutting***

Today, no general agreement exists as to whether laser or mechanical cutting has a less degrading effect on the magnetic properties of steel sheets. The authors of [2,13,51,59,157] conclude that the detrimental effect on the magnetic properties is greater for laser-cut samples than for mechanically-cut samples, whereas the authors of [119,148] state that laser cutting deteriorates the magnetic characteristics less than mechanical cutting. The authors of [5] mention that losses in laser-cut samples are higher for low, and are lower for high inductions when compared with samples cut on a metal sheet cutting machine. The same authors report on similar behavior for the permeability [5]. This suggests that the operating point of the electric machine affects which cutting technique is to be preferred. Furthermore, a difference might occur between semi-processed and fully-processed steel: the studies reported in [13] (referring to the results for semi-processed steel mostly) also contain a few results on fully-processed electrical steel in which the degradation due to laser cutting is smaller than that due to mechanical cutting. Further, the grain orientation might also lead to another result: considering the work of [114], laser cutting leads to smaller coercive magnetic field strengths and smaller hysteresis losses compared to mechanical cutting. However, [114] investigated grain-oriented Fe-Si ribbons. In [119], further differing results of other authors concerning mechanical and laser cutting are presented.

Since it is reasonable to expect that the specific laser cutting technique and its parameters, in particular the laser cutting speed and energy, as well as the other stated 'reasons of differences' (see above) will influence the effect on the material, such parameters/reasons will also affect the comparison with the punching technique.

*Influence of mechanical and laser cutting on the magnetic domains*
The authors of [114] report that mechanical cutting generates compressive stresses along the cut edge, which results in a changed domain orientation within the compression region. In particular, the 90° domain walls are increased at the cut edge [114]. According to [59, 207], both mechanical as well as laser cutting induce compressive stresses inside the material which result, for both cut samples, in an "expansion of 90° [...] at the expense of 180° domains" [207]. As previously mentioned, mechanical cutting as well as laser cutting induces stresses, defects and dislocations inside the material [207], which again results in a worse domain movability (e.g. [45]).

## 1.3.5 Other cutting methods

As previously mentioned, in addition to mechanical and laser cutting, other cutting methods concerning the magnetic properties of steel sheets are investigated in the literature, as for instance water-jet cutting and electric discharge machining (wire cutting). A main reference for water-jet cutting is given by [171]: The authors point out that water-jet cutting degrades the magnetic properties less than mechanical cutting. The largest difference between these two cutting techniques is found in the range of 0.5 to 1.6 T. With water-jet cutting, the ferromagnetic material suffers from a smaller deformation at the cut edge than with mechanical cutting. Furthermore, the cooling effect of the water reduces the degree of deterioration. The main disadvantages of water-jet cutting are cited to be the slow cutting speed and the "limitation in segment shape" [171].

The electric discharge machining (EDM) technique is, if at all, only used for "small-lot production" [110], prototyping [43], or for scientific studies. An exemplary cut edge of EDM is presented in Fig. 1.22. The work reported on in [110] states that steel sheets cut by wire electric discharge machining have a lower hardness at the cutting edge than the samples cut by laser cutting or punching. According to [146], in reference to [116], the hardness of a material "can be used to determine an equivalent plastic strain." Thus, considering only the hardness, wire electric discharge machining has a less detrimental effect on the cut material than laser cutting or punching. (Note that in this case, no reference is made to residual stresses.) Considering the detrimental effect on the magnetic properties due to different cutting techniques, the iron losses and the magnetizing force (i.e. the permeability) at 1.5 T, 50 Hz were the lowest for wire electric discharge machining when compared to laser as well as mechanical cutting [110, 211]. The results of [157] confirm better magnetic characteristics for EDM-cut samples than for laser-cut samples. According to [153] the material which is cut by electroerosion is "free of any stresses." However, the author of [110] investigated his samples after cutting and further after stress relief anneal-
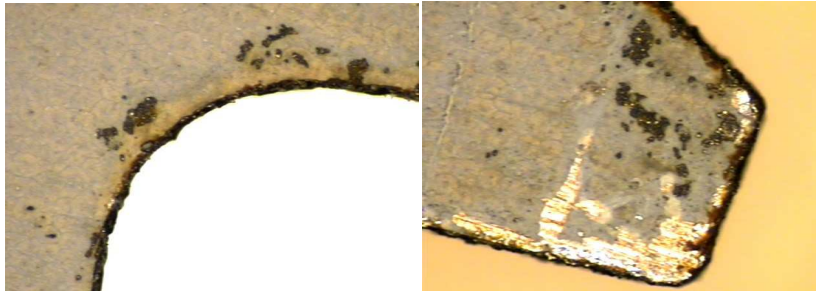
Figure 1.22: Wire-cut edges at slot bottom and tooth tip, from [43].

ing. He obtained, even in the case of EDM, differences of the magnetic properties before and after stress relief annealing. This indicates that also the electroerosion technique induces stresses inside the material and deteriorates the magnetic properties. Nevertheless, the author of [43] investigated three PM motor types with differently cut stators. The best agreement between measurements and simulation was achieved for the motor with the wire-cut stator. The authors attribute this to the smaller material deformation and smaller burr size as compared to the laser-cut and mechanically-cut stator samples [43]. Thus, the advantages of this cutting method are the smaller detrimental effect on the magnetic properties and smaller burrs. However, the disadvantages are the slow cutting speed [153] as well as the possibility of a burned coating due to "high local temperatures" [43].

## 1.4 Further (possible) manufacturing steps

### 1.4.1 Stacking and interconnecting

Following the cutting process, the individual sheets are stacked, compressed and connected by e.g. welding, clamping, riveting, gluing and screwing/bolting (see also Fig. 1.14). All these mentioned manufacturing steps lead to further degraded magnetic properties [5, 106, 110, 132, 133, 145, 170, 173]. The respective extent of this degradation depends, among other factors, on the sample geometry and size, interconnecting method (e.g. placement, size and number of bolts or welding seams [105, 110, 170, 174]), point of operation (e.g. [5]) and material investigated (e.g. materials with large grains and high silicon contents are more sensitive to welding than those with small grains and without silicon [170]).

Again, the degradation of the magnetic properties is caused by the introduced mechanical stresses inside the material due to the interconnecting method and, as in the case of welding, also as a result of the thermal stresses [105, 173]. Furthermore, the interconnection might further introduce short circuits between the laminations due

to burrs at the lamination edges or destroyed insulation, leading to small contacts between the sheets and thus an increase in eddy current losses [174, 211]. Note, the welding seam itself is a connection between the laminations which leads to short circuits [105, 170].

## 1.4.2 Stress relief annealing

After the manufacturing step of stacking and interconnecting, stress relief annealing may be performed to reduce or remove already induced internal stresses and local plastic strains due to the manufacturing process inside the material [80, 99, 110, 138, 149, 211], leading to an improvement of magnetic properties, e.g. decrease of iron loss and increase of permeability and remanent magnetic flux density [13, 22, 110, 158, 183, 207, 211]. Considering the mechanically-cut samples in [110], the annealing forwards grain growth in the previously plastically deformed area due to cutting and thus induces a recrystallized structure[23]. However, with stress relief annealing adding a further step to the manufacturing process, its positive effects evidently come at additional cost and time [171].

The measurement results reported in [22] show that such an annealing process can decrease iron losses by up to 60 %. This change is mainly attributed to the hysteresis contribution with the eddy current contribution evaluated as constant. However, the loss reduction reported for a finished machine (a conventional 4-pole 380 V, 11 kW induction machine) is only 15 %. This is explained, among others, by the additional no load losses, which modify the percentage reduction due to annealing [22]. Also the author of [80] reports on an improved efficiency of the motors investigated due to annealing. The fully-finished samples investigated in [13] achieved a decrease in losses of 40 % in the case of laser-cut samples and about 33 % in the case of mechanically-cut samples after stress relief annealing. However, the author of [114] reports no significant effect on saturation magnetization $M_\mathrm{s}$ of laser-cut samples due to annealing. In [110] and [211] the beneficial effect of annealing is also presented for wire-cut samples.

After the manufacturing step(s) of stacking and interconnection (and stress relief annealing), the wires are inserted inside the lamination package, which induces stresses and strains around the slots [211].

---

[23]The extent of grain growth and microstructural recovery depends on the settings of the annealing as e.g. the temperature and duration of the annealing [113].

### 1.4.3 Shrink fitting/housing

Typically, the last manufacturing step is the housing or shrink fitting process: the core is fitted into the motor frame by heat shrinkage or press fitting [211]. The inner diameter of the frame is slightly smaller than the outer diameter of the core [65]. Thus, large compressive stresses are introduced in radial and tangential directions along the circumference of the core [170, 211].

Several studies have shown that the compression of shrink fitting and/or compression inserted in longitudinal or transverse direction to the rolling direction in steel sheets[24] lead to an increase of the iron loss and to a decrease of the material's permeability and remanent magnetic flux density [57,118,127,133,192–194,212]. The respective degrading effect due to shrink fitting again depends on several conditions as for example the material of the cylinder in which the lamination package is shrink fitted in (see e.g. [212]).

### 1.4.4 Relative influence of different manufacturing steps

In [170], the different manufacturing steps are evaluated due to their degrading influence on the magnetic properties. Table 1.5 shows an extract of the results presented in [170]. In light of Table 1.5, cutting is the most detrimental part of the manufacturing steps presented in Fig. 1.14. This is also confirmed by the authors of [38] who identified the increase of the specific power losses through punching to be larger than that due to compression and welding. Nevertheless, the respective relative influence of different manufacturing steps might again vary with the samples' geometry, number of welding seams, etc. However, as the cutting is mostly presented as the step introducing the largest material degradation on the steels' magnetic properties, this work focuses on different cutting techniques and their degrading influence.

---

[24]Note, considering the radial compression of shrink fitting at the teeth of the core, this stress is once longitudinal and then perpendicular to the rolling direction (depending on the respective teeth). Hence, the average of these two characteristics may provide an estimate of the influence of shrink fitting (see e.g. [194]).

| *Magnetization* Processing step | Operating range $J < 0.5\,\mathrm{T}$ | Operating range $0.5\,\mathrm{T} < J < 1.5\,\mathrm{T}$ | Operating range $J > 1.5\,\mathrm{T}$ |
|---|---|---|---|
| Cutting | low | high | very low |
| Pressing | none | low to medium | none |
| Welding | low | medium | none |
| Housing | very low | low to medium | very low |
| *Loss* Processing step | Operating range $J < 0.5\,\mathrm{T}$ | Operating range $0.5\,\mathrm{T} < J < 1.5\,\mathrm{T}$ | Operating range $J > 1.5\,\mathrm{T}$ |
| Cutting | low | medium | high |
| Pressing (uncoated) | none | very low | low to medium |
| Welding | very low | low | medium |
| Housing | low | low | medium |

Table 1.5: Comparison of the influence of the different manufacturing steps on the magnetization and loss behavior; adapted from [170].

# Chapter 2

# Experimental work

## 2.1 Introduction

The influence of three different cutting techniques on the magnetic properties of electrical steel sheets is studied. The investigated cutting techniques are:

- Mechanical cutting (guillotine or punching)
- Carbon dioxide laser cutting ($CO_2$) and
- Solid state laser cutting (FKL).

The following aspects have been of particular interest:

- What are the main differences between the deteriorating effects of mechanical and laser cutting concerning the magnetic properties and losses of electrical steel sheets?
- Do the degrading effects on the magnetic properties and losses of $CO_2$-laser and FKL-laser cutting differ?
- Is it possible to state which cutting technique is best?
- To what extent does the effect of aging have an influence on the magnetic properties and losses of mechanically-cut and laser-cut samples?

This dissertation is amply supported by measurements. Sections 2.1.1 – 2.1.3 report on the test samples, the cutting techniques used and the measurements carried out. Chapters 2.2 – 2.6 present the different measurement methods and setups in detail.

## 2.1.1 Test samples

The measurement samples consist of three different non-oriented steel sheet materials, which are typically used in electric machines: M270-35A, M400-50A and M800-65A. The samples are cut from three mother coils (MC) for the Epstein and
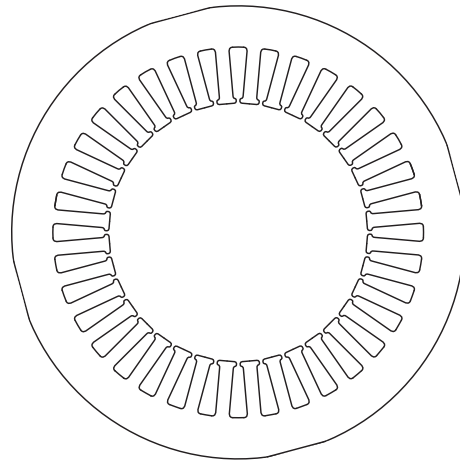
Figure 2.1: Cross sectional area of the analyzed stator cores. (For the dimensions see Chapter 2.6, p. 53.)

stator specimens. Thus, each specimen of a given material derives from the same mother coil (three materials – three mother coils). This is important as "the variation from MC to MC is much larger" than "the variation caused by the manufacturing process" as Clerc [38] stated.

The dimensions of the first set of Epstein samples are in accordance with the standard IEC 60404-2 [86] with a width of 30 mm and a length of 305 mm. The second set has only a width of 7.5 mm for samples cut by guillotine and by FKL-laser and a width of 7 mm for specimens cut by $CO_2$-laser. The length of 305 mm remains unchanged. The smaller samples are thus modified Epstein specimens. All Epstein specimens are cut in rolling (LL) and transverse (QQ) direction.

The stator samples consist of a length of about 100 mm composed of stacked and pressed laminations. The cross-sectional area of the stator is shown in Fig. 2.1.

The specimen nomenclature in the following chapters (can) contain the information below: sheet material, specimen width, cutting technique (SS = guillotine, punched, $CO_2$ = carbon dioxide laser, FKL = solide state laser), cutting direction (LL = rolling direction, QQ = transverse direction), signal frequency of measurement and additional variations of the measurement setup (e.g., power amplifier with or without sense lines, see Fig. 2.2).

## 2.1.2  Cutting techniques

The Epstein specimens are cut by guillotine, $CO_2$-laser and FKL-laser. The stator sheets are cut by $CO_2$-laser and FKL-laser as well, however for the mechanical cutting, a punching machine is used. In contrast to the Epstein specimens, the stator steel sheets are packaged, pressed and glued after cutting, at a pressure of
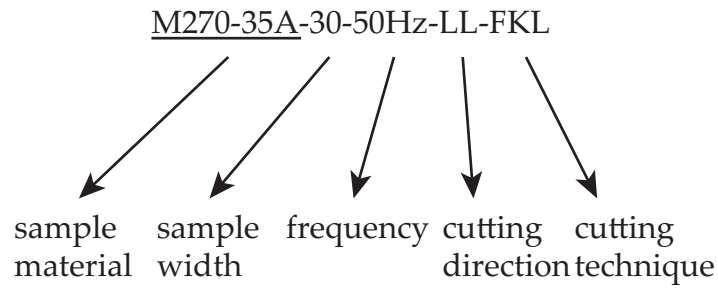
Figure 2.2: Specimen nomenclature.

about 0.3 MPa. For a better comparison of the behavior of the laser-cut samples of this study and also with results already investigated by other researchers, the laser settings of the two lasers used are presented in Table 2.1.

Table 2.1: Laser settings.

| Laser | Mode | Power (W) | Max. cutting speed (m/min) for Epstein specimen | Max. cutting speed (m/min) for stator probes | Gas | Gas pressure | Laser beam diameter |
|---|---|---|---|---|---|---|---|
| $CO_2$ | pulsed, pulsed frequency 5000 Hz | 2000 | 12 | 12 | $N_2$ | 10 bar | 3.75" 0.15 mm (at cutter head) |
| FKL (Nd:YAG) | approx. cw-mode (20 kHz) | 6000 | 32 | 32 (for 0.35 mm and 0.5 mm thickness) 15 (for 0.65 mm thickness) | | | 150 $\mu$m |

### 2.1.3 Types of measurements

To analyze the influences of the different cutting techniques on the magnetic behavior of the electrical steel sheets mentioned above, five different types of measurements are carried out:

1. With the help of optical emission spectrometry (OES), the chemical composition of the material is analyzed (see Chapter 2.2).

2. The average grain size diameter $d_g$ is determined for each type of material by electron backscatter diffraction (EBSD, Chapter 2.3).

3. The quasi-static hysteresis curves of the Epstein specimens are measured by a so-called remagraph (for more detailed information, see Chapter 2.4).

4. The Epstein frame measurements (see Chapter 2.5) are carried out to identify the magnetic properties and iron losses of the Epstein specimens.

5. The stator measurement setups (see Chapter 2.6) determine the magnetic properties and iron losses of the stator yoke (due to the way the windings are inserted, only the losses of the stator back/yoke are measured).

An overview of all measurements is provided in Tables 2.2, 2.3 and 2.5.

## 2.2 Optical emission spectrometry

Optical emission spectrometry, also called spark emission spectrometry, is a method for measuring the chemical composition of metals and electrical steels in particular. While energy is supplied by electric spark discharges, atoms of the material investigated, and thus electrons, are excited and emit radiation with defined wavelengths [121]. Each element emits an element-specific line spectrum and is thus allocatable [121]. Most of the metallic elements emit spectral lines in the wavelength range of 0.36-0.80 $\mu$m [121].

The chemical compositions of electrical steels is left to the manufacturer's discretion. Standards (IEC EN 60404-8-6 [89] and IEC EN 60404-1 [84]) do not require the compositions to be explicitly stated. However, for the analysis carried out in this work, it is important to know its chemical composition as each element and its relative volume and mass may influence the properties, including the magnetic properties (see Chapter 1.2.2).

A selection of the measured samples was degreased, ground and investigated with OES (see Table A.1 in Appendix A.1). Three or four areas were ground in the middle of the strip. Afterwards, measurements were carried out on each of the ground areas and averages as well as standard deviations were calculated[1]. The corresponding bar charts show the mean of these measurements with their standard deviations (Chapter 3). The results are discussed in Chapter 3.

## 2.3 Electron backscatter diffraction (EBSD)

The EBSD technique is used to obtain and analyze the microstructure of, e.g., metallic samples based on a crystallographic analysis [3, 74]. "A scanning electron micro-

---

[1]These measurements were performed by [72].
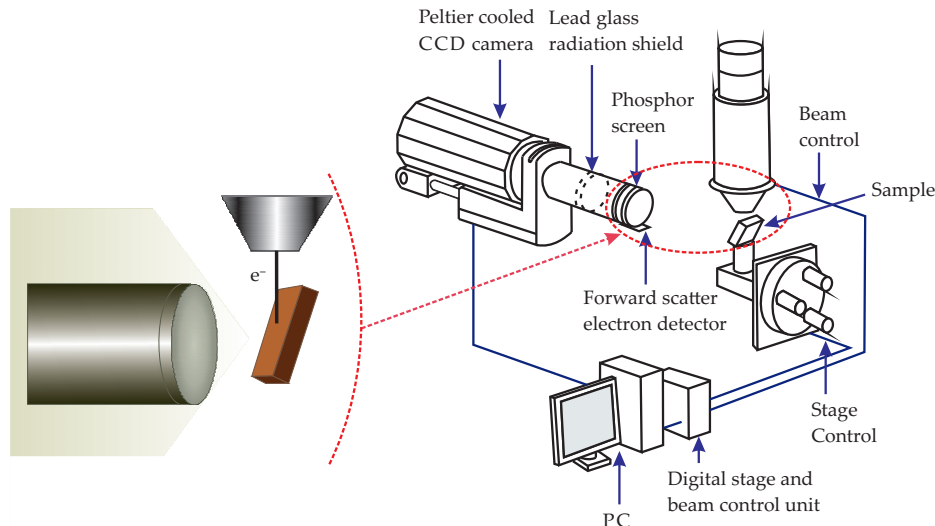
Figure 2.3: EBSD system, from [3,74].

scope (SEM) fires a [stationary,] tightly-focused beam of electrons at" [74] the tilted[2] specimen to be investigated (Fig. 2.3). According to the crystalline structure of the sample, "some of the electrons in the beam are diffracted [...] and hit a phosphor screen [...], generating patterns of light that are detected and recorded by a digital camera" [74] (Fig. 2.3). Among others, these patterns provide information of crystal orientation, grain sizes, grain boundary misorientations and local crystalline perfections [3].

In this work[21,p.24], the EBSD technique was mainly used to determine the (average) grain size diameter(s) of all three investigated materials and to gain insight into the arrangement of the grains. The samples were investigated in a Zeiss Ultra 55 FEG SEM with the EBSD system from EDAX (Mahwah, USA) [56]. The scanning electron microscope was operated at 20 kV [56]. Before the investigation, the samples were prepared by "mounting in conductive resin, mechanical grinding, diamond polishing [using a 0.25 $\mu$m diamond paste] and final polishing" [91] using a 0.04 $\mu$m SiO$_2$ emulsion. Thus, a smooth surface of the sample was obtained.

Since EBSD samples were mounted in electrically non-conductive material, a conductive adhesive tape or the coating with, e.g., carbon was necessary to avoid electrostatic charging. The first option was used for the samples extracted from the surface at the middle of the sheet, the latter for those extracted from the cross section (including the cut edge area) (see Fig. 2.4). Furthermore, the coating thickness must be taken into account, as with increasing coating thickness, the pattern quality decreases (see e.g. [108])[3].

---

[2]The sample is tilted at 70° from the horizontal so that most of the diffracted electrons reach the phosphor screen.

[3]The preparations of the samples as well as the measurements with the EBSD were performed by

EBSD sample extracted
from the surface at the
middle of the steel sheet

EBSD sample extracted
along the cut edge

EBSD sample extracted
from the cross section
including the cut edge

$w_z$

30 mm
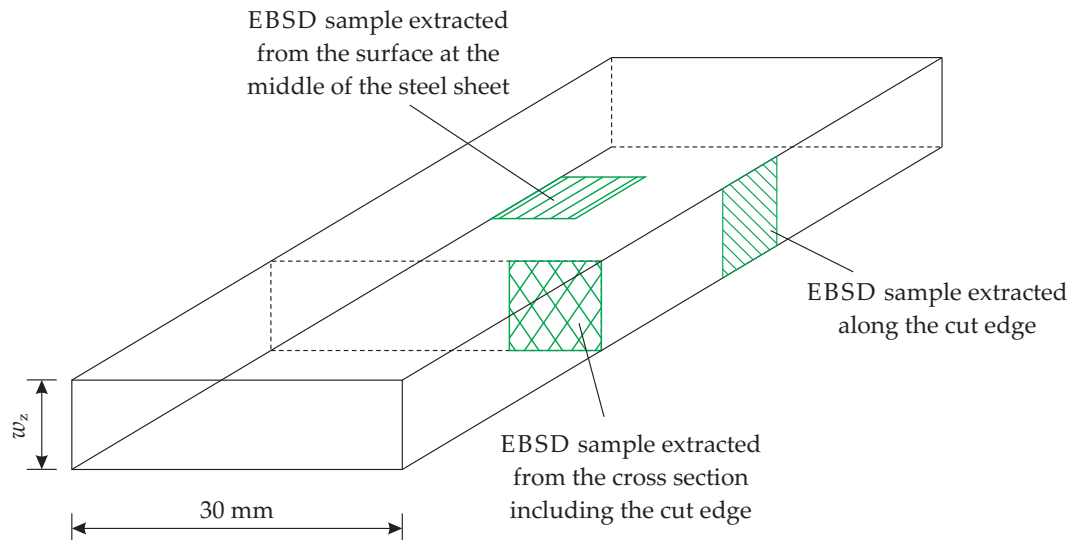
Figure 2.4: EBSD samples extracted.

## 2.4  Remagraph/Permeameter

The remagraph (in IEC 60404-4 [88] also called permeameter type B) measurement setup according to IEC 60404-4 [88] and as used in the measurements reported herein, is used for measuring the (quasi-static) hysteresis curve of magnetically soft materials [60].  It consists of a yoke, two coils for the magnetization of the samples and two for the measurements of the magnetic field strength $H$ and flux density $B$: a $J$-compensated surrounding coil and an $H$-potential coil (see Fig. 2.5) [60]. The measuring coils are respectively connected to a fluxmeter [60], in this case to a fluxmeter from Brockhaus Messtechnik [103].  Various measurement coils are available for different kinds of specimens, e.g., for flat or round specimens.

The following measurements were made on a subset of the electrical steel strips which are also used for the Epstein tests.  The number of strips in the remagraph is smaller than the number in the Epstein frame.  The number was chosen to obtain nearly the same cross-sectional area for all steel strips in the remagraph which are of the same width (detailed numbers see Table 2.2).  These strips were stacked together, taped at the ends to avoid shifting, and clamped between the yoke.  The measurement method refers to the standard IEC 60404-4 [88].  All measurements were performed at a frequency of 1 Hz.  As this frequency is smaller than the Wolman frequency[4] for all three investigated materials, the obtained hysteresis curves are 'quasi-static' [23].

the Institute for Electron Microscopy and Nanoanalysis at TU Graz [56].

[4]Hysteresis curves measured with a frequency below the Wolman frequency differ only slightly from the static curves, therefore they can be defined as 'quasi-static' [23]. Beyond this frequency, eddy current losses need to be taken into account.  Thus, the Wolman frequency is a cut-off frequency for eddy currents [208].

**A:** specimen

**B:** yoke

**C:** field generating coils

**D:** J-compensated surrounding coil

**E:** potential coil for *H* measurement

**F:** connection *J*-Fluxmeter

**G:** connection *H*-Fluxmeter
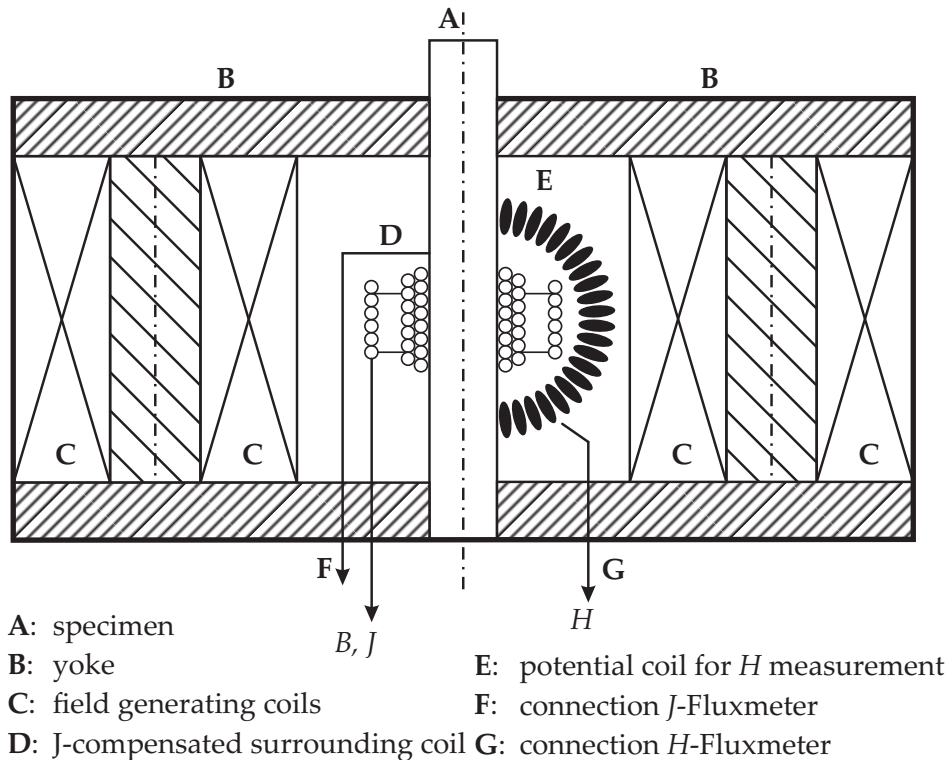
Figure 2.5: Composition of remagraph, based on [60].

Table 2.2 gives an overview of the measurements carried out.

Before each measurement, the samples were demagnetized by an AC magnetic field with continuously decreasing amplitude down to zero [23, 60]. Afterwards, the hysteresis loop was measured. Two measurements were taken for each sample. The second measurement differs in that the vertical specimen is turned upside-down (top and bottom are reversed). This was done to ensure that the material behaves magnetically similarly in both directions. As seen in Fig. 2.6, the steel strips mostly show a very good reproducible magnetic behavior, independent of the clamping direction. This different clamping direction is defined by an additional "u" (clamping downwards) or "o" (clamping upwards) at the measured samples' names (see diagrams in Chapter 4.1).

To facilitate the comparison between the results in Chapter 4 and to provide a tool to better describe the observation, the common hysteresis loop has been divided into different parts, as shown in Fig. 2.7.

For the calculation of the relative permeability, the initial magnetization is used, as this curve is nearly identical to the commutation curve [23, 73].
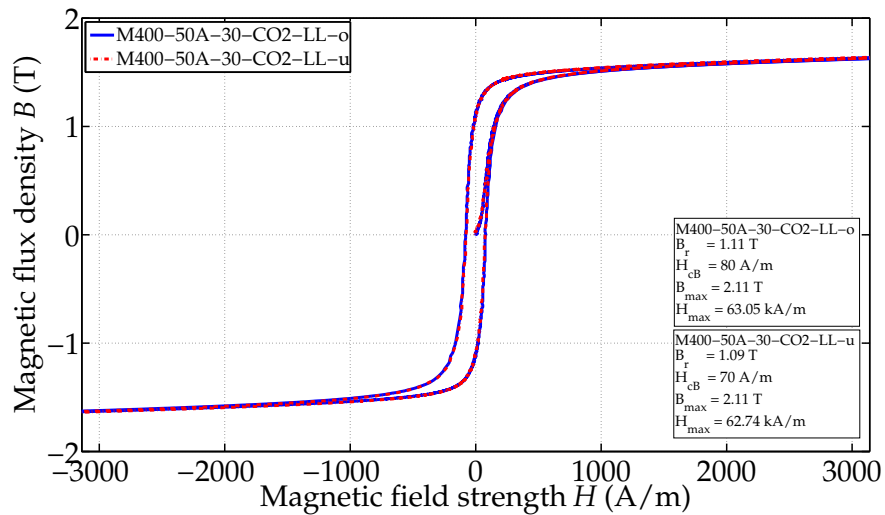
(a) M400-50A-30-CO2-LL
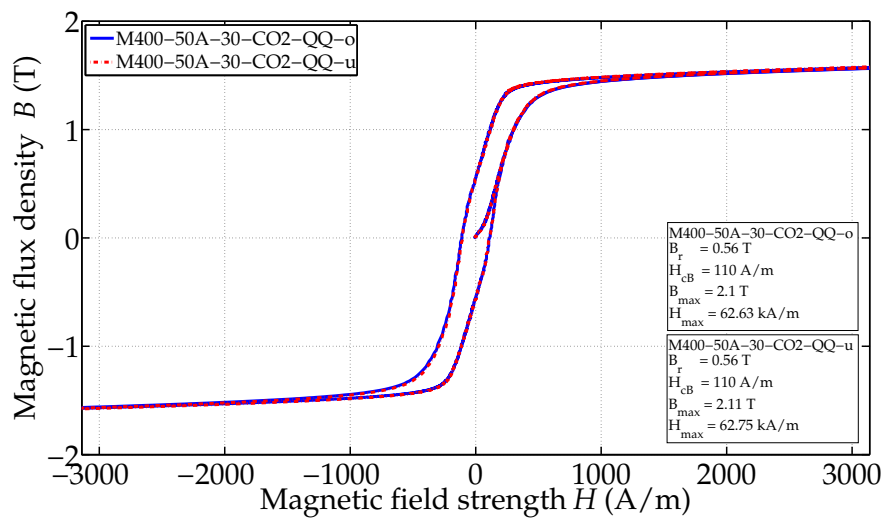


(b) M400-50A-30-CO2-QQ

Figure 2.6: Reproducibility of Epstein specimens in the remagraph clamped in two directions.

Table 2.2: Overview of remagraph measurements.

| Material | Number of electrical steel sheets | Cross-sectional area of the specimen in $mm^2$ | Amplitude of voltage in V | J-compensated surrounding coil | H-potential coil |
|---|---|---|---|---|---|
| **Small specimens** | | | | | |
| M270-35A-7.5-SS-LL | 9 | 23.625 | 30 V | $w = 207$ | $S_w = 1036e^{-4}\,mm^2$ |
| M270-35A-7.5-SS-QQ | | | 30 V | $R = 11\,\Omega$ | $R = 96.5\,\Omega$ |
| M270-35A-7-$CO_2$-LL | 9 | 22.05 | 30 V | $w = 207$ | $S_w = 1036e^{-4}\,mm^2$ |
| M270-35A-7-$CO_2$-QQ | | | 30 V | $R = 11\,\Omega$ | $R = 96.5\,\Omega$ |
| M270-35A-7.5-FKL-LL | 9 | 23.625 | 30 V | $w = 207$ | $S_w = 1036e^{-4}\,mm^2$ |
| M270-35A-7.5-FKL-QQ | | | 30 V | $R = 11\,\Omega$ | $R = 96.5\,\Omega$ |
| M400-50A-7.5-SS-LL | 6 | 22.5 | 30 V | $w = 207$ | $S_w = 1036e^{-4}\,mm^2$ |
| M400-50A-7.5-SS-QQ | | | 30 V | $R = 11\,\Omega$ | $R = 96.5\,\Omega$ |
| M400-50A-7-$CO_2$-LL | 6 | 21 | 30 V | $w = 207$ | $S_w = 1036e^{-4}\,mm^2$ |
| M400-50A-7-$CO_2$-QQ | | | 30 V | $R = 11\,\Omega$ | $R = 96.5\,\Omega$ |
| M400-50A-7.5-FKL-LL | 6 | 22.5 | 30 V | $w = 207$ | $S_w = 1036e^{-4}\,mm^2$ |
| M400-50A-7.5-FKL-QQ | | | 30 V | $R = 11\,\Omega$ | $R = 96.5\,\Omega$ |
| M800-65A-7.5-SS-LL | 5 | 24.375 | 30 V | $w = 207$ | $S_w = 1036e^{-4}\,mm^2$ |
| M800-65A-7.5-SS-QQ | | | 30 V | $R = 11\,\Omega$ | $R = 96.5\,\Omega$ |
| M800-65A-7-$CO_2$-LL | 5 | 22.75 | 30 V | $w = 207$ | $S_w = 1036e^{-4}\,mm^2$ |
| M800-65A-7-$CO_2 - QQ$ | | | 30 V | $R = 11\,\Omega$ | $R = 96.5\,\Omega$ |
| M800-65A-7.5-FKL-LL | 5 | 24.375 | 30 V | $w = 207$ | $S_w = 1036e^{-4}\,mm^2$ |
| M800-65A-7.5-FKL-QQ | | | 30 V | $R = 11\,\Omega$ | $R = 96.5\,\Omega$ |
| **Wide specimens** | | | | | |
| M270-35A-30-SS-LL | 7 | 73.5 | 30 V | $w = 184$ | $S_w = 1700e^{-4}\,mm^2$ |
| M270-35A-30-SS-QQ | | | 30 V | $R = 67.5\,\Omega$ | $R = 164.1\,\Omega$ |
| M270-35A-30-$CO_2$-LL | 7 | 73.5 | 30 V | $w = 184$ | $S_w = 1700e^{-4}\,mm^2$ |
| M270-35A-30-$CO_2$-QQ | | | 30 V | $R = 67.5\,\Omega$ | $R = 164.1\,\Omega$ |
| M270-35A-30-FKL-LL | 7 | 73.5 | 30 V | $w = 184$ | $S_w = 1700e^{-4}\,mm^2$ |
| | | | 30 V | $R = 67.5\,\Omega$ | $R = 164.1\,\Omega$ |
| M270-35A-30-FKL-QQ | | | | | |
| M400-50A-30-SS-LL | 5 | 75 | 30 V | $w = 184$ | $S_w = 1700e^{-4}\,mm^2$ |
| M400-50A-30-SS-QQ | | | 30 V | $R = 67.5\,\Omega$ | $R = 164.1\,\Omega$ |
| M400-50A-30-$CO_2$-LL | 5 | 75 | 30 V | $w = 184$ | $S_w = 1700e^{-4}\,mm^2$ |
| M400-50A-30-$CO_2$-QQ | | | 30 V | $R = 67.5\,\Omega$ | $R = 164.1\,\Omega$ |
| M400-50A-30-FKL-LL | 5 | 75 | 30 V | $w = 184$ | $S_w = 1700e^{-4}\,mm^2$ |
| M400-50A-30-FKL-QQ | | | 30 V | $R = 67.5\,\Omega$ | $R = 164.1\,\Omega$ |
| M800-65A-30-SS-LL | 4 | 78 | 30 V | $w = 184$ | $S_w = 1700e^{-4}\,mm^2$ |
| M800-65A-30-SS-QQ | | | 30 V | $R = 67.5\,\Omega$ | $R = 164.1\,\Omega$ |
| M800-65A-30-$CO_2$-LL | 4 | 78 | 30 V | $w = 184$ | $S_w = 1700e^{-4}\,mm^2$ |
| M800-65A-30-$CO_2$-QQ | | | 30 V | $R = 67.5\,\Omega$ | $R = 164.1\,\Omega$ |
| M800-65A-30-FKL-LL | 4 | 78 | 30 V | $w = 184$ | $S_w = 1700e^{-4}\,mm^2$ |
| M800-65A-30-FKL-QQ | | | 30 V | $R = 67.5\,\Omega$ | $R = 164.1\,\Omega$ |

$w$ = number of turns; $S_w$ = total winding cross-sectional area
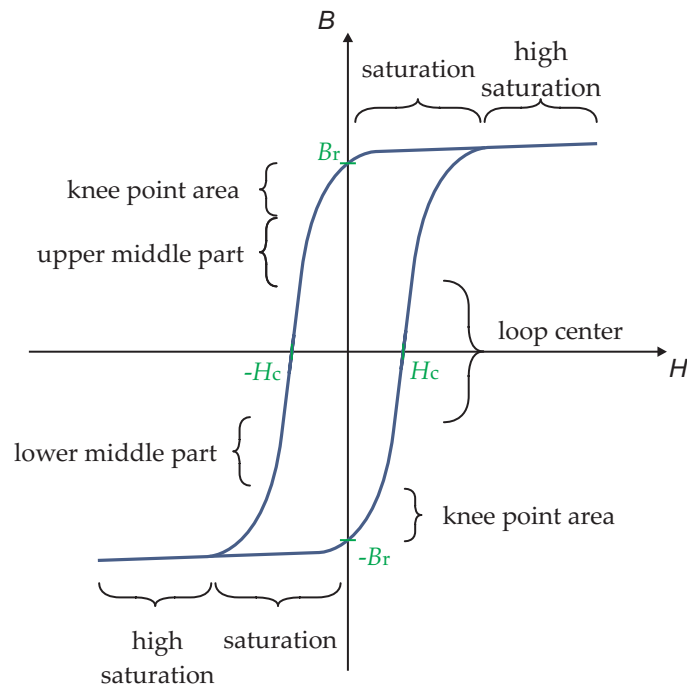
Figure 2.7: For a better description, the hysteresis loop is divided into several parts.

## 2.5  Epstein frame

The Epstein frame measurement setup (Fig. 2.8) is used for measuring the magnetic properties of electrical steel sheets, e.g., the specific losses for different magnetic polarizations $J$. The whole setup is composed of the Epstein frame, a power amplifier (PAS 5000, Spitzenberger + Spies, detailed data in Appendix F.1) and a wide band power analyzer (Norma D 6100, LEM NORMA GmbH) and bases on the wattmetric procedure of [86]. The frame itself consists of four coils and of a mutual inductance $M$ for air magnetic flux correction [86]. Each coil contains a primary and a secondary winding [86], each with $N_1 = N_2 = 700$ windings. The Epstein frame measurements were conducted according to the standards IEC 60404-2 [86] for frequencies up to 400 Hz, and IEC 60404-10 [85] for frequencies between 400 Hz and 10 kHz.

According to the standard IEC 60404-2, the number of strips in an Epstein frame must be a multiple of four [86]. All measurements presented in Chapter 5 were carried out for 16 strips for the 30 mm wide samples (4 strips per coil) and for 64 strips for the small samples (16 strips per coil). The exact arrangement of the strips in the Epstein frame is shown in Fig. 2.9.

The measurements were taken at an ambient temperature of 23 °C ± 5 °C [86]. Before the samples were measured in an alternating field, they were weighted and demagnetized by an AC magnetic field. The primary voltage was then adjusted by a ramp function to the set value and after a few seconds, the primary voltage was
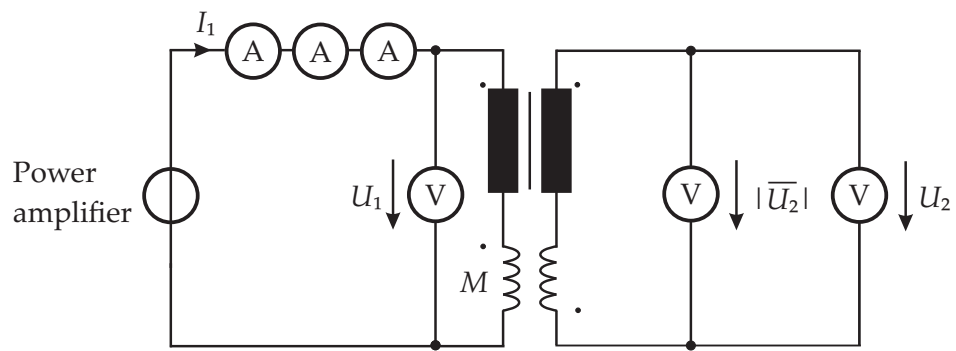
*M*...mutual inductance

Figure 2.8: Electric circuit of Epstein frame measurement setup based on [86] with amperemeter and voltmeter of the power analyzer.
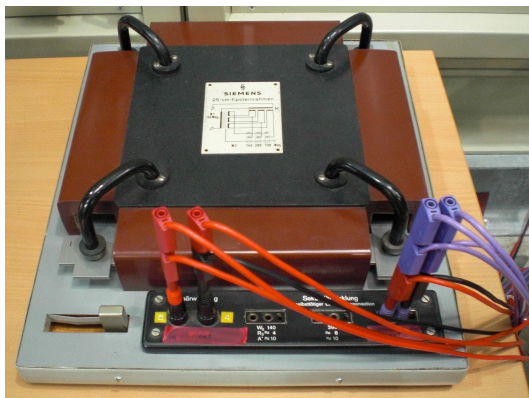


(a) top view



(b) standard samples



(c) small samples
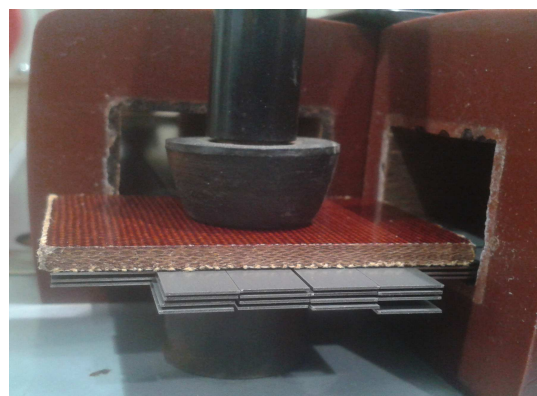


(d) small samples

Figure 2.9: Equipped Epstein frame.

samples cut in transverse direction

samples cut in logitudinal direction

coil with primary and secondary winding
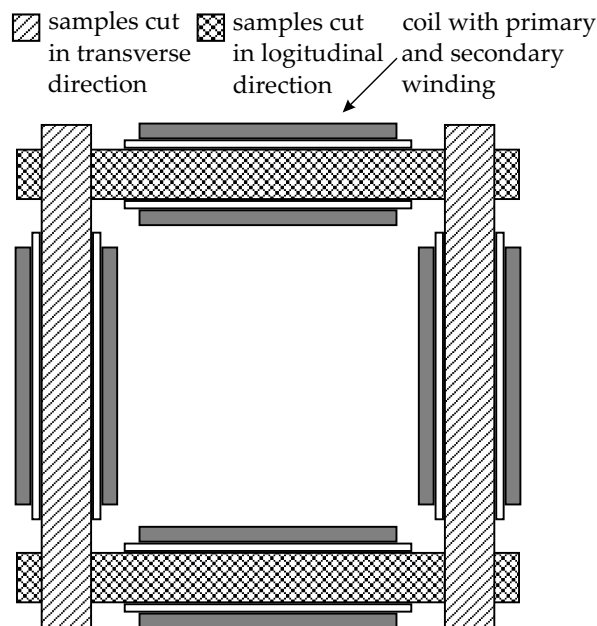
Figure 2.10: Arrangement of steel strips in the Epstein frame, based on [86].

again decreased by the ramp function. After each measurement, the samples were once again demagnetized.

According to the standard [86], the form factor of the secondary voltage must be $1.111 \pm 1\,\%$. To ensure this, the measurement setup was amended by two sense lines (plus and minus) of the power amplifier on the secondary winding of the Epstein frame (method 1: 'Epsteinframe' method = with sense lines).

Additionally, some samples were measured without sense lines; consequently, the form factor no longer meets the requirements of the standard with increasing polarization $J$ (method 2: 'modified Epsteinframe' method = without sense lines). The sample name is extended by 'without sense lines' for the samples measured without sense lines.

With the power analyzer the root mean squares, the average rectified values as well as the peak values of the primary and secondary voltage, primary current, power derived from primary current and secondary voltage, primary power derived from primary current and primary voltage and the frequency are measured. For redundancy against measurement errors, the primary current is measured by three channels; two channels are equipped each with a 10 A shunt and one channel with a 30 A shunt. The secondary voltage is measured by two channels. The input impedance of the voltage channel is $10\,\mathrm{M}\Omega$. Thus, its influence on the measured values of $I_1$ and $U_2$ can be neglected.

When both cutting directions are investigated, it is to ensure that the longitudinally-cut specimens take place in two opposite coils of the Epstein frame and also the transversely-cut specimens are placed in two opposite coils [86], see Fig. 2.10. The

identifier name of these measured samples then consists of 'Mix', instead of 'QQ' or 'LL' (compare with Chapter 2.1.1, Fig. 2.2).

All Epstein samples were measured at three frequencies: 50 Hz, 250 Hz and 500 Hz, with a few samples also at 800 Hz (see Table 2.3). The specific loss $p_s$, the magnetic field strength $H$ and the magnetic polarization $J$ were calculated from the measurement data in accordance with the standards IEC 60404-2 and IEC 60404-10 [85, 86]. Table 2.3 gives an overview of all performed Epstein measurements.

Table 2.3: Overview of the performed Epstein measurements.

| Overview of Epstein measurements with and without sense lines on the secondary winding | | | | | | |
|---|---|---|---|---|---|---|
| Material | Sample width in mm | Frequency in Hz | Cutting direction | Cutting technique | With sense lines on secondary winding | Without sense lines on secondary winding |
| M270-35A | 30.0 | 50 | Mix | SS | x | x |
| M270-35A | 30.0 | 250 | Mix | SS | x | x |
| M270-35A | 30.0 | 500 | Mix | SS | x | x |
| M270-35A | 30.0 | 800 | Mix | SS | x | |
| M270-35A | 7.5 | 50 | Mix | SS | x | x |
| M270-35A | 7.5 | 250 | Mix | SS | x | x |
| M270-35A | 7.5 | 500 | Mix | SS | x | x |
| M270-35A | 7.5 | 800 | Mix | SS | x | |
| M270-35A | 30.0 | 50 | Mix | $CO_2$ | x | x |
| M270-35A | 30.0 | 250 | Mix | $CO_2$ | x | x |
| M270-35A | 30.0 | 500 | Mix | $CO_2$ | x | x |
| M270-35A | 30.0 | 800 | Mix | $CO_2$ | x | x |
| M270-35A | 30.0 | 50 | LL | $CO_2$ | x | |
| M270-35A | 30.0 | 250 | LL | $CO_2$ | x | |
| M270-35A | 30.0 | 500 | LL | $CO_2$ | x | |
| M270-35A | 7.0 | 50 | Mix | $CO_2$ | x | x |
| M270-35A | 7.0 | 250 | Mix | $CO_2$ | x | x |
| M270-35A | 7.0 | 500 | Mix | $CO_2$ | x | x |
| M270-35A | 30.0 | 50 | Mix | FKL | x | x |
| M270-35A | 30.0 | 250 | Mix | FKL | x | x |
| M270-35A | 30.0 | 500 | Mix | FKL | x | x |
| M270-35A | 30.0 | 800 | Mix | FKL | x | |
| M270-35A | 30.0 | 50 | LL | FKL | x | |
| M270-35A | 30.0 | 250 | LL | FKL | x | |
| M270-35A | 30.0 | 500 | LL | FKL | x | |
| M270-35A | 30.0 | 50 | QQ | FKL | x | |
| M270-35A | 30.0 | 250 | QQ | FKL | x | |
| M270-35A | 30.0 | 500 | QQ | FKL | x | |
| M270-35A | 7.5 | 50 | Mix | FKL | x | x |
| M270-35A | 7.5 | 250 | Mix | FKL | x | x |
| M270-35A | 7.5 | 500 | Mix | FKL | x | x |

| Overview of Epstein measurements with and without sense lines on the secondary winding | | | | | | |
|---|---|---|---|---|---|---|
| *Material* | *Sample width in mm* | *Frequency in Hz* | *Cutting direction* | *Cutting technique* | *With sense lines on secondary winding* | *Without sense lines on secondary winding* |
| M400-50A | 30.0 | 50 | Mix | SS | x | |
| M400-50A | 30.0 | 250 | Mix | SS | x | |
| M400-50A | 30.0 | 500 | Mix | SS | x | x |
| M400-50A | 7.5 | 50 | Mix | SS | x | x |
| M400-50A | 7.5 | 250 | Mix | SS | x | x |
| M400-50A | 7.5 | 500 | Mix | SS | x | x |
| M400-50A | 30.0 | 50 | Mix | $CO_2$ | x | |
| M400-50A | 30.0 | 250 | Mix | $CO_2$ | x | |
| M400-50A | 30.0 | 500 | Mix | $CO_2$ | x | x |
| M400-50A | 30.0 | 50 | LL | $CO_2$ | x | |
| M400-50A | 30.0 | 250 | LL | $CO_2$ | x | |
| M400-50A | 30.0 | 500 | LL | $CO_2$ | x | |
| M400-50A | 30.0 | 50 | QQ | $CO_2$ | x | |
| M400-50A | 30.0 | 250 | QQ | $CO_2$ | x | |
| M400-50A | 30.0 | 500 | QQ | $CO_2$ | x | |
| M400-50A | 7.0 | 50 | Mix | $CO_2$ | x | x |
| M400-50A | 7.0 | 250 | Mix | $CO_2$ | x | x |
| M400-50A | 7.0 | 500 | Mix | $CO_2$ | x | x |
| M400-50A | 7.0 | 50 | LL | $CO_2$ | x | |
| M400-50A | 7.0 | 250 | LL | $CO_2$ | x | |
| M400-50A | 7.0 | 500 | LL | $CO_2$ | x | |
| M400-50A | 7.0 | 50 | QQ | $CO_2$ | x | |
| M400-50A | 7.0 | 250 | QQ | $CO_2$ | x | |
| M400-50A | 7.0 | 500 | QQ | $CO_2$ | x | |
| M400-50A | 30.0 | 50 | Mix | FKL | x | |
| M400-50A | 30.0 | 250 | Mix | FKL | x | |
| M400-50A | 30.0 | 500 | Mix | FKL | x | x |
| M400-50A | 30.0 | 50 | LL | FKL | x | |
| M400-50A | 30.0 | 250 | LL | FKL | x | |
| M400-50A | 30.0 | 500 | LL | FKL | x | |
| M400-50A | 30.0 | 50 | QQ | FKL | x | |
| M400-50A | 30.0 | 250 | QQ | FKL | x | |
| M400-50A | 30.0 | 500 | QQ | FKL | x | |
| M400-50A | 7.5 | 50 | Mix | FKL | x | x |
| M400-50A | 7.5 | 250 | Mix | FKL | x | x |
| M400-50A | 7.5 | 500 | Mix | FKL | x | x |

| | Overview of Epstein measurements with and without sense lines on the secondary winding | | | | | |
|---|---|---|---|---|---|---|
| *Material* | *Sample width in mm* | *Frequency in Hz* | *Cutting direction* | *Cutting technique* | *With sense lines on secondary winding* | *Without sense lines on secondary winding* |
| M800-65A | 30.0 | 50 | Mix | SS | x | |
| M800-65A | 30.0 | 250 | Mix | SS | x | |
| M800-65A | 30.0 | 500 | Mix | SS | x | x |
| M800-65A | 7.5 | 50 | Mix | SS | x | x |
| M800-65A | 7.5 | 250 | Mix | SS | x | x |
| M800-65A | 7.5 | 500 | Mix | SS | x | x |
| M800-65A | 30.0 | 50 | Mix | $CO_2$ | x | |
| M800-65A | 30.0 | 250 | Mix | $CO_2$ | x | |
| M800-65A | 30.0 | 500 | Mix | $CO_2$ | x | x |
| M800-65A | 30.0 | 50 | LL | $CO_2$ | x | |
| M800-65A | 30.0 | 250 | LL | $CO_2$ | x | |
| M800-65A | 30.0 | 500 | LL | $CO_2$ | x | |
| M800-65A | 30.0 | 50 | QQ | $CO_2$ | x | |
| M800-65A | 30.0 | 250 | QQ | $CO_2$ | x | |
| M800-65A | 30.0 | 500 | QQ | $CO_2$ | x | |
| M800-65A | 7.0 | 50 | Mix | $CO_2$ | x | x |
| M800-65A | 7.0 | 250 | Mix | $CO_2$ | x | x |
| M800-65A | 7.0 | 500 | Mix | $CO_2$ | x | x |
| M800-65A | 7.0 | 50 | LL | $CO_2$ | x | |
| M800-65A | 7.0 | 250 | LL | $CO_2$ | x | |
| M800-65A | 7.0 | 500 | LL | $CO_2$ | x | |
| M800-65A | 7.0 | 50 | QQ | $CO_2$ | x | |
| M800-65A | 7.0 | 250 | QQ | $CO_2$ | x | |
| M800-65A | 7.0 | 500 | QQ | $CO_2$ | x | |
| M800-65A | 30.0 | 50 | Mix | FKL | x | |
| M800-65A | 30.0 | 250 | Mix | FKL | x | |
| M800-65A | 30.0 | 500 | Mix | FKL | x | x |
| M800-65A | 30.0 | 50 | LL | FKL | x | |
| M800-65A | 30.0 | 250 | LL | FKL | x | |
| M800-65A | 30.0 | 500 | LL | FKL | x | |
| M800-65A | 30.0 | 50 | QQ | FKL | x | |
| M800-65A | 30.0 | 250 | QQ | FKL | x | |
| M800-65A | 30.0 | 500 | QQ | FKL | x | |
| M800-65A | 7.5 | 50 | Mix | FKL | x | x |
| M800-65A | 7.5 | 250 | Mix | FKL | x | x |
| M800-65A | 7.5 | 500 | Mix | FKL | x | x |

## 2.6 Stator lamination stacks

The stator measurement setup is used for analyzing the magnetic properties of 'cores made of soft magnetic materials' [90]. Three different approaches are taken to determine the losses of the different cut stators. These methods are further explained in the section below.

The electrical steel sheets of all stators belong to the same mother coils as the Epstein and remagraph specimens (see Chapter 2.1.1). After cutting, the steel sheets are stacked, glued manually and compressed with $0.3\,N/mm^2$ [165].

In general, all setups consist of the stator with primary and secondary winding, a power amplifier (PAS 5000, Spitzenberger + Spies, further data in Appendix F.1) and a wide band power analyzer (Norma D 6100, LEM NORMA GmbH), again with three current shunts in the current measurement path to increase measurement accuracy: two channels equipped with a 30 A shunt and one channel with a 100 A shunt. As for the Epstein frame measurements, the input impedance of the voltage channel is large (10 MΩ), and thus the influence on the measured values of $I_1$ and $U_2$ are negligible. The respective circuit diagram is presented in Fig. 2.11. Both the primary and the secondary winding are wound around the stator yoke. Thus, the magnetic flux is located in the yoke region. The number of windings for the primary winding is $N_1 = 43$ and for the secondary winding $N_2 = 50$. The winding of the primary coil has a cross-section of $4\,mm^2$. Before and after each measurement, the stators are demagnetized, as required for the Epstein samples (see Chapter 2.5).
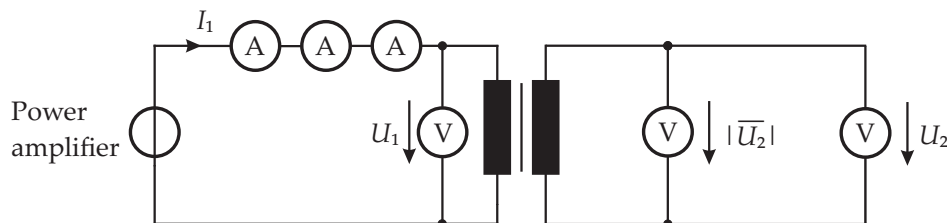


Figure 2.11: Electric circuit of the stator measurement setup.

Eight different stators are investigated (Table 2.4). All stators have the same dimensions: an outer diameter of $D_a = 135\,mm$, a yoke height of $h_{yoke} = 12\,mm$, and an iron length $l_{Fe}$ of about 100 mm (see Chapter 2.1.1, Fig. 2.1). The only differences are the material and the cutting techniques used. At the outer diameter of the stator, a temperature sensor is attached to control the temperature behavior.

Three different measurement methods are carried out.

1. The first method is in accordance with standard IEC 62044-3 [90].

2. As the first method differs slightly from the Epstein procedure (see paragraph
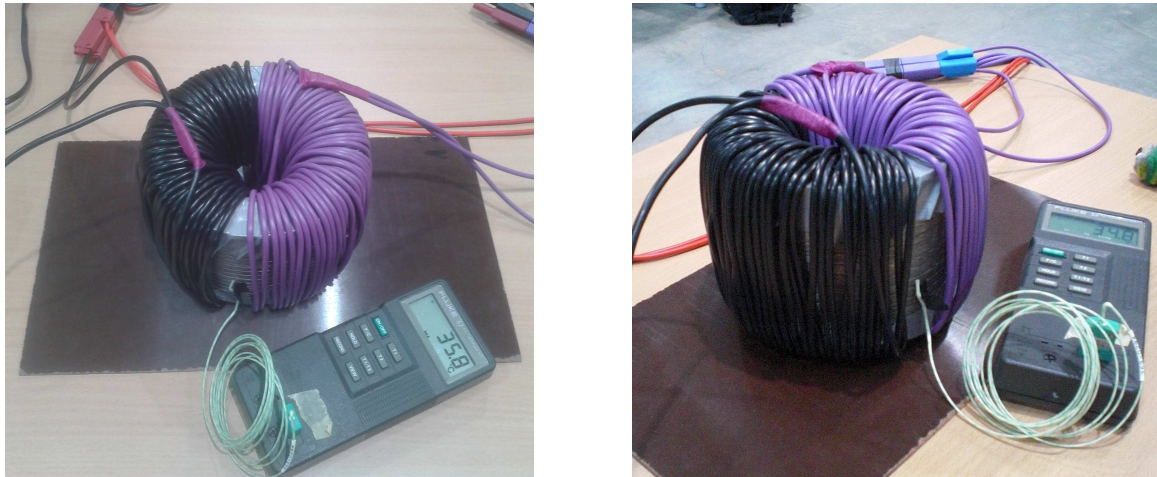
Figure 2.12: Stator under test with primary and secondary coil.

Table 2.4: Investigated stators.

|  | **M270-35A** | **M400-50A** | **M800-65A** |
|---|---|---|---|
| **Punched** |  | x | x |
| **CO$_2$-laser** | x | x | x |
| **FKL-laser** | x | x | x |

x = available stators for measuring the losses at different operating points.

'Measurement method: 'IEC 62044-3''), a further measurement method based on the Epstein frame procedure [86] is performed (see paragraph 'Measurement method: 'Epsteinframe'') to allow a better comparison with the Epstein results of Section 2.5.

3. For the sake of complete comparability, the stators are also measured based on the second method but without sense lines (see paragraph 'Measurement method: 'modified Epsteinframe'').

**1) Measurement method: 'IEC 62044-3'**

This method follows the standard IEC 62044-3 [90]. The setup consists of two separate windings, the primary coil (field excitation) and the secondary coil (voltage measuring winding). The windings are close to and distributed equally around the core [90]. In contrast to the Epstein standards [85, 86] the primary voltage must contain a harmonic content smaller than 1 % if the output is sinusoidal [90]. Therefore, the sense lines of the power amplifier are connected to the primary winding.

Another difference to the Epstein standards is the exact procedure required for the measurement of the individual points. Within the time of 2 ± 0.5 seconds, the output source must be set to the time dependent parameters (frequency, waveform
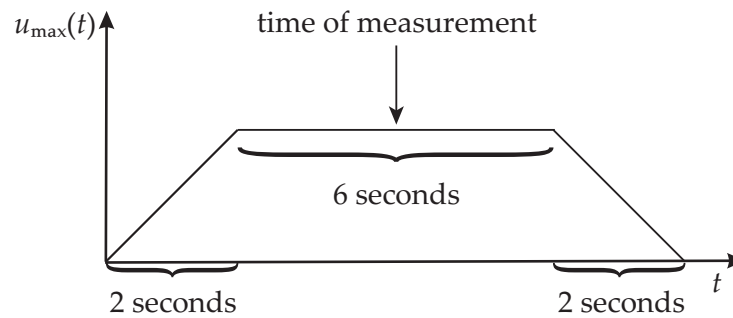
Figure 2.13: Applied voltage amplitude over time to comply with the standard [90].

and output amplitude) [90]. At the time $t_{\mathrm{m}}$ the measurement must be taken [90]. Then, the output source must be turned off immediately [90]. In total, the field must not be excited longer than ten seconds [90]. This is to avoid self-heating of the core [90]. Corresponding to this requirement, the measurement points are adjusted with an output voltage ramp of two seconds to obtain the desired measurement point (see Fig. 2.13). After a further three seconds, the measurement is taken. Shortly thereafter, the output source is turned off with a ramp. The voltage over time of the measurement setup is shown in Fig. 2.13.

The temperature of the stator is monitored by a sensor. Before the next reading is taken, the sample must reach ambient temperature: 25±3 °C ( [84]). Thus, the influence on the measurement data by self-heating of the stator is almost excluded.

The specific losses are calculated based on IEC 62044-3 [90].

**2) Measurement method: 'Epsteinframe'**

This measurement method follows the Epstein standard [86], the secondary voltage is required to be a pure sine wave (see Chapter 2.5). Thus, the sense lines of the power amplifier are connected to the secondary winding. Furthermore, the measurements of the series are taken in succession, in contrast to IEC 62044-3 [90] in which each measurement point is aimed at individually. Apart from that, the measurement setup is identical to the method of IEC 60404-2 (see Chapter 2.5). The 'Epsteinframe' measurement method is applied for a better comparison with the Epstein results of the Epstein specimens.

**3) Measurement method: 'modified Epsteinframe'**

As the Epstein specimens are also measured without sense lines on the secondary winding (see Chapter 2.5), the stator specimens are also measured according to the 'Epsteinframe' method, the only difference being that no sense lines are used, either on the primary or on the secondary winding. This approach is chosen to determine the effect of the secondary sense lines on the specific losses.

with secondary sense lines     without sense lines     with primary sense lines
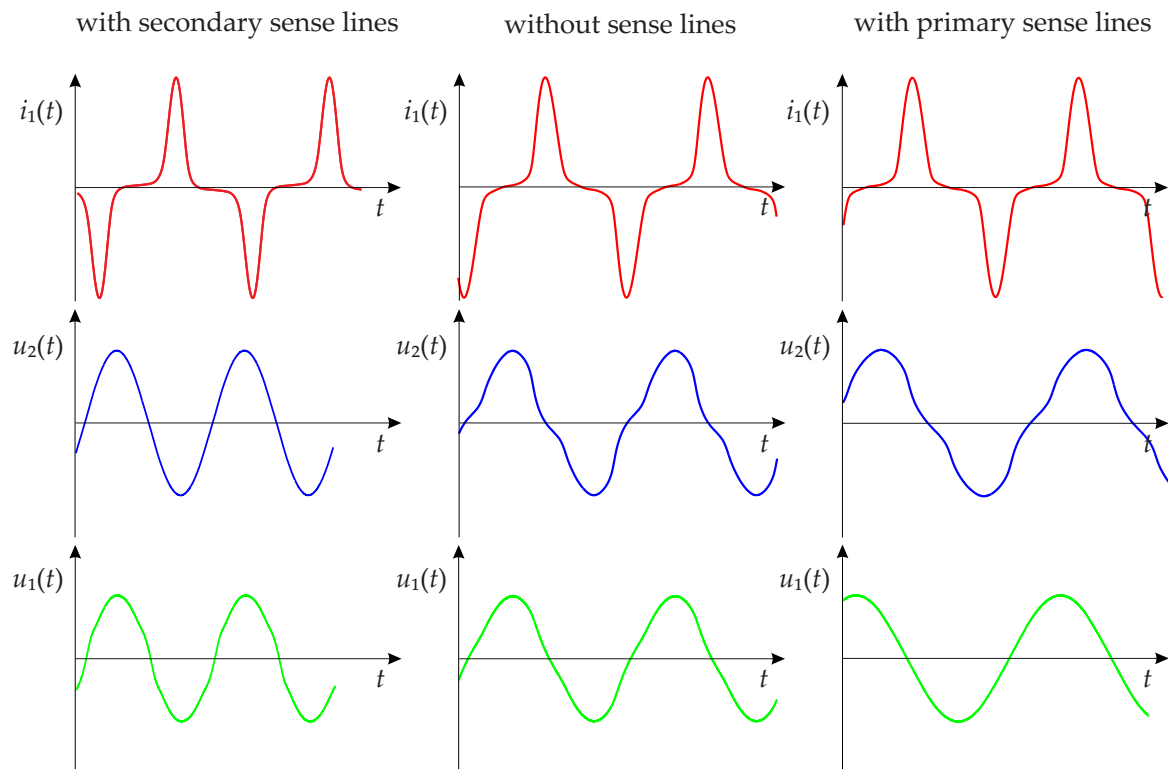


Figure 2.14: Effect of sense lines on the shape of voltages and current.



(a) without sense lines        (b) with sense lines
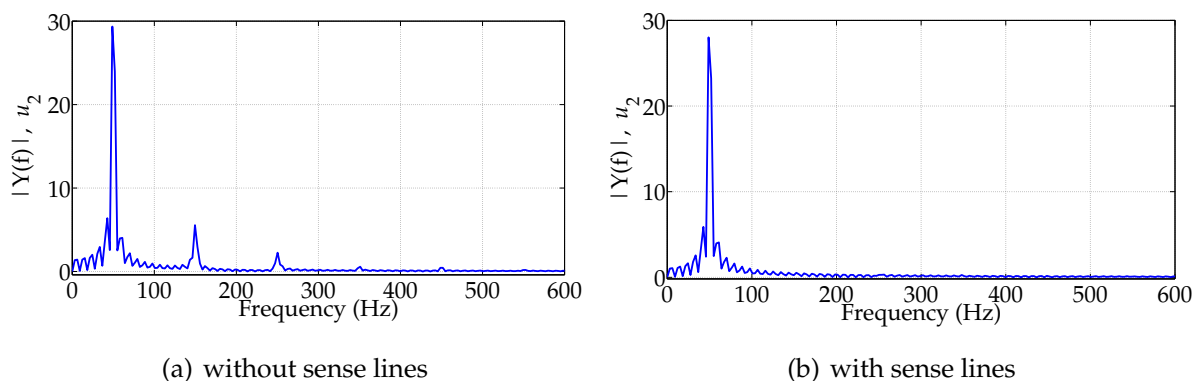
Figure 2.15: Effect of sense lines on the secondary winding.

The influence of sense lines on the primary current and both voltage shapes is shown in Fig. 2.14. The effect of secondary sense lines applied or not applied to the harmonics of the secondary voltage is presented in Fig. 2.15. Ideally, the 'Epstein-frame' method only produces the first harmonic, as the sense lines are connected to the secondary winding. This is mostly ensured for small frequencies, e.g., 50 Hz. With higher frequencies and saturated materials, harmonic components may occur, too. Thus, in this area no pure sinusoidal of the secondary voltage is producible. Note, the form factor of the secondary voltage of $1.111 \pm 1\%$ is an indicator for the quality of the sinusoidal shape of the secondary voltage.

For the 'modified Epsteinframe' method, additional harmonics are expected as this method measures without sense lines. Hence, the harmonics already occur at small frequencies (50 Hz). Of course, these harmonics have a higher amplitude at higher frequencies compared with those produced by the 'Epsteinframe' method. With increasing order, the amplitudes of the harmonics decrease.

The signals produced by the method 'IEC 62044-3' show a similar harmonic content as those of the 'modified Epsteinframe' method. The primary voltage of the 'modified Epsteinframe' method is nearly sinusoidal, as supplied by the power amplifier (Fig. 2.14). Table 2.5 gives an overview of all performed stator measurements.

Table 2.5: Overview of the stator measurements.

| Stator material | Cutting technique | Frequency | Measuring method: 'IEC 62044-3' | Measuring method: 'Epsteinframe' | Measuring method: 'modified Epsteinframe' |
|---|---|---|---|---|---|
| M270-35A | $CO_2$-laser | 50 Hz | x | x | x |
| M270-35A | $CO_2$-laser | 250 Hz | x | x | x |
| M270-35A | $CO_2$-laser | 500 Hz | x | x | x |
| M270-35A | FKL-laser | 50 Hz | x | x | x |
| M270-35A | FKL-laser | 250 Hz | x | x | x |
| M270-35A | FKL-laser | 500 Hz | x | x | x |
| M400-50A | punched | 50 Hz | x | x | x |
| M400-50A | punched | 250 Hz | x | x | x |
| M400-50A | punched | 500 Hz | x | x | x |
| M400-50A | $CO_2$-laser | 50 Hz | x | x | x |
| M400-50A | $CO_2$-laser | 250 Hz | x | x | x |
| M400-50A | $CO_2$-laser | 500 Hz | x | x | x |
| M400-50A | FKL-laser | 50 Hz | x | x | x |
| M400-50A | FKL-laser | 250 Hz | x | x | x |
| M400-50A | FKL-laser | 500 Hz | x | x | x |
| M800-65A | punched | 50 Hz | x | x | x |
| M800-65A | punched | 250 Hz | x | x | x |
| M800-65A | punched | 500 Hz | x | x | x |
| M800-65A | $CO_2$-laser | 50 Hz | x | x | x |
| M800-65A | $CO_2$-laser | 250 Hz | x | x | x |
| M800-65A | $CO_2$-laser | 500 Hz | x | x | x |
| M800-65A | FKL-laser | 50 Hz | x | x | x |
| M800-65A | FKL-laser | 250 Hz | x | x | x |
| M800-65A | FKL-laser | 500 Hz | x | x | x |
| x = performed measurements | | | | | |

# Chapter 3

# Experimental results: chemical composition and grain size

## 3.1 Optical emission spectrometry

For each investigated sample, three measurements were taken (see Chapter 2.2). The standard deviation of each measurement is indicated in Fig. 3.1 and listed in Appendix A.1, Table A.1. As Fig. 3.1 shows, the largest relative standard deviation was found for material M270-35A, especially for the measured carbon and aluminum contents. However, considering all results of one material (e.g. M270-35A, carbon content, first four bars), all bars are in the same range (see Fig. 3.1).

### 3.1.1 Results

The optical emission spectrometry was carried out by [72]. As the ground and measured areas are placed in the middle of the strips (see Chapter 2.2), the different cutting techniques have no effect on the spectrometry results, wherefore this aspect is not discussed in this section.

The results by optical emission spectrometry show no unexpected characteristics for the electrical steel sheets. They reveal the differences of material compositions of the three studied materials M270-35A, M400-50A and M800-65A. The complete set of results is listed in Appendix A.1.

M270-35A is characterized by a higher carbon ($0.0075\,\text{wt\%}/0.003\,\text{wt\%} \rightarrow 250\,\%$), silicon ($2.83\,\text{wt\%}/1.58\,\text{wt\%} \rightarrow 179\,\%$) and aluminum ($1.03\,\text{wt\%}/0.13\,\text{wt\%} \rightarrow 792\,\%$) content than M400-50A and M800-65A whereas the manganese content is the lowest for M270-35A (see Fig. 3.1 and Appendix A.1). The materials M400-50A and M800-65A differ primarily in their manganese contents (see Figs. 3.1).

(a) Carbon content

(b) Silicon content

(c) Manganese content

(d) Aluminium content
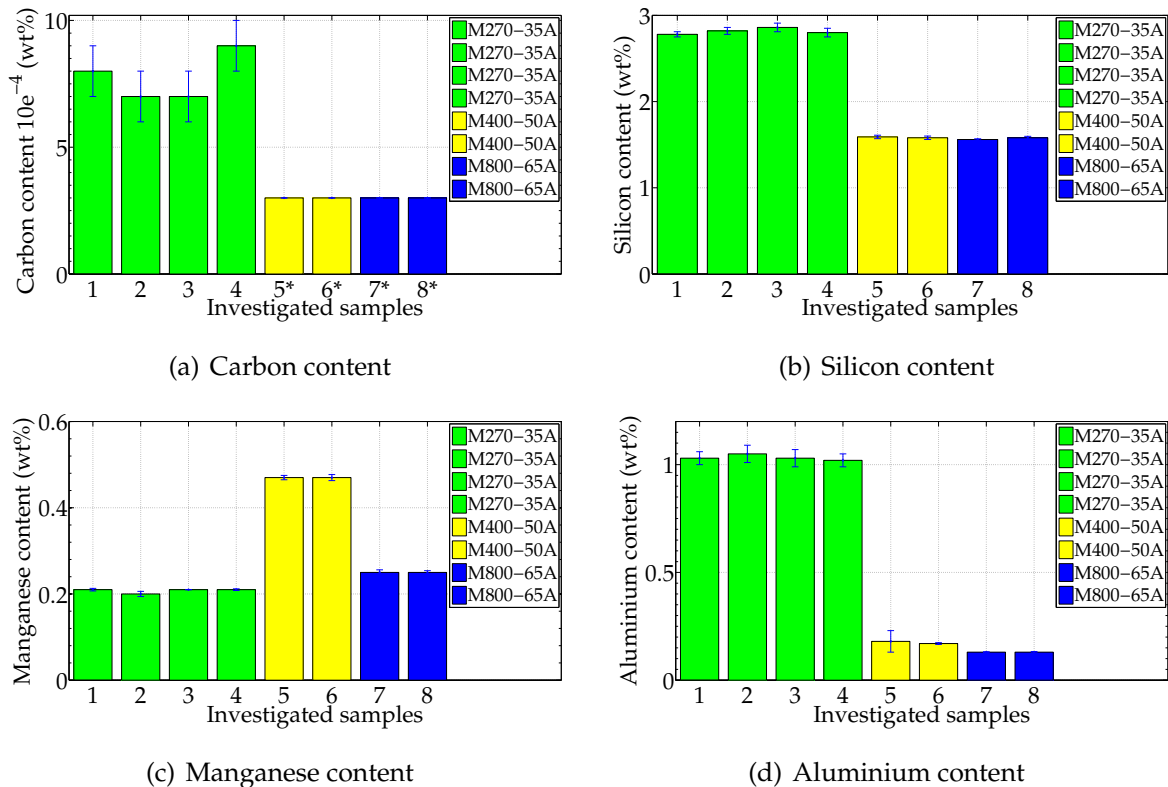
Figure 3.1: Results measured by optical emission spectrometry (∗ = content is smaller than the value specified in the diagram, compare with Table A.1 in Appendix A.1).

---

Conclusions:
- Material M270-35A has higher contents of carbon, silicon and aluminium than materials M400-50A and M800-65A.
- Materials M400-50A and M800-65A differ primarily in their manganese contents.

---

## 3.2  Grain size identification

The EBSD measurements were performed by [56]. To obtain the average grain size $d_g$ of the non-deteriorated material, EBSD samples were extracted from the surface at the center of the electrical steel sheets and investigated as described in Chapter 2.3. Thus, it is expected that the sample obtained from the center is unaffected by the respective cutting technique (virgin material). Since all samples of a given material derive from the same MC, the average grain size diameters determined from the center of several sheets of one material are assumed to be in the same range. This is confirmed by the measurement results obtained (see Table A.2

Table 3.1: Grain size diameter determined in the center and at the cut edge of the steel sheets. The rounded values of all respective measurements (see Tables A.2 and A.3 in Appendix A.2) are presented.

| Material | Average grain size diameter in the sample's center in $\mu$m | Average grain size diameter at the samples's cut edge in $\mu$m |
|---|---|---|
| M270-35A | 81 | |
| M270-35A_SS | | 57 |
| M270-35A_CO$_2$ | | 64 |
| M270-35A_FKL | | 52 |
| M400-50A | 54 | |
| M400-50A_SS | | 45 |
| M400-50A_CO$_2$ | | 46 |
| M400-50A_FKL | | 47 |
| M800-65A | 27 | |
| M800-65A_SS | | 29 |
| M800-65A_CO$_2$ | | 26 |
| M800-65A_FKL | | 30 |

in Appendix A.2). For these measurements, the 30 mm wide Epstein samples were used. Subsequently, further EBSD samples are taken from the cut edge area for determining the potentially changed grain size due to the cutting process. This was carried out for all different cut samples. In Table 3.1 the rounded average grain size diameters of the respective measurements of Tables A.2 and A.3 are presented.

## 3.2.1 Results

*Grain size diameter*

Table 3.1 presents the average grain size diameters $d_{\mathrm{g}}$ for the determined investigated materials[1]. At first, it is obvious that the non-affected material of M270-35A has the largest grain size diameter with a mean of 81 $\mu$m, followed by material M400-50A with 54 $\mu$m and subsequently material M800-65A with 27 $\mu$m. This difference in grain size is also reflected in Fig. 3.2.

When comparing the average grain size diameters at the cut edges with those at the center, it is apparent that the sizes of the grains at the cut edge are decreased, especially for materials M270-35A and M400-50A. This applies for all cutting techniques investigated. The smaller the grain size of the virgin material, the smaller is

---

[1]In Appendix A.2 more detailed information is provided.

the decrease of the grain size at the cut edge due to the cutting. In the case of the material with the smallest grains (M800-65A), no apparent change in grain size is found. This suggests that the materials' sensitivities to change the grain size due to cutting decreases with decreasing grain size (see Table 3.1).

Furthermore, no significant difference of grain size reduction between mechanical and laser cutting is observed. The image quality figures (non-published) show that in the case of mechanically-cut samples, no diffraction information is obtainable from some areas at the cut edge. This is due to the grains which are strongly deformed or frayed. The larger the deformation of a grain is, the more difficult it is to obtain a diffraction information of this specific grain. Hence, grains with which no diffraction information are obtained, are not used in the determination of the grain size. Thus, the evaluated cut edge grain size diameters of mechanically-cut samples have to be used with caution. In contrast, the image quality figures of the laser-cut samples indicate better reliability, as the grains at the cut edges are less deformed (see also next Subsection "Grain images").

*Grain images*

Different images were taken: IPF (inverse pole figure) and GOS (grain oriented spread) images. The IPF images depict "the distribution of a selected direction in the specimen, in relation to the crystal axes" [191]. The GOS figures represent the average misorientation to the average orientation, both originating from all measurement points within one grain [191] and are thus a measure for the uniformity of orientations within one grain.

Fig. 3.2 shows the images resulting from the EBSD samples obtained from the surface at the center of the steel sheet (see Fig. 2.4). These images mirror the differently sized grains in the respective material.

The cut edges of differently cut samples are presented in Figs. 3.3 and 3.6. Those of mechanically-cut and laser-cut samples differ significantly in their appearance: Those mechanically-cut are more frayed and plastically deformed in contrast to the laser-cut samples with a more uniform cut edge (Figs. 3.3 and 3.6). Furthermore, Fig. 3.3 shows that the mechanical cutting induces larger misorientations inside the respective cut edge grains compared with those of the laser-cut samples, which in turn mirrors the intensity of stress and dislocations within the grain due to the cutting. These larger misorientations for grains in mechanically-cut in contrast to laser-cut samples is also obvious along the cut edge (Figs. 3.4 and 3.5). The cut edges of FKL-laser and $CO_2$-laser cut samples look almost identical. For all samples, it applies: The larger the distance from the cut edge is, the smaller the deviations are from the average orientation within a grain (Fig. 3.3, indicated by blue color).
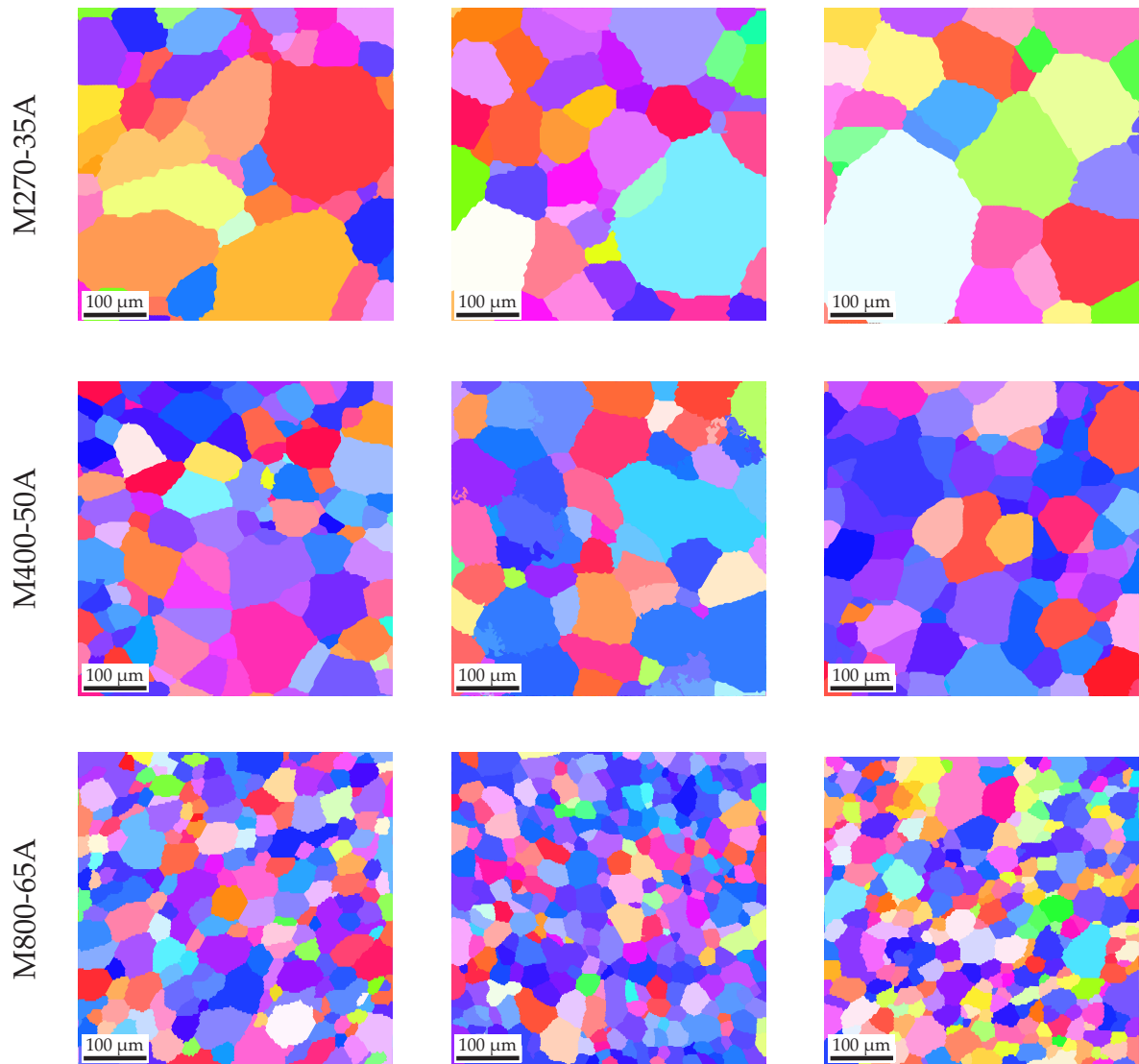
Figure 3.2: Examples of grains at the surface of all three materials investigated (IPF).
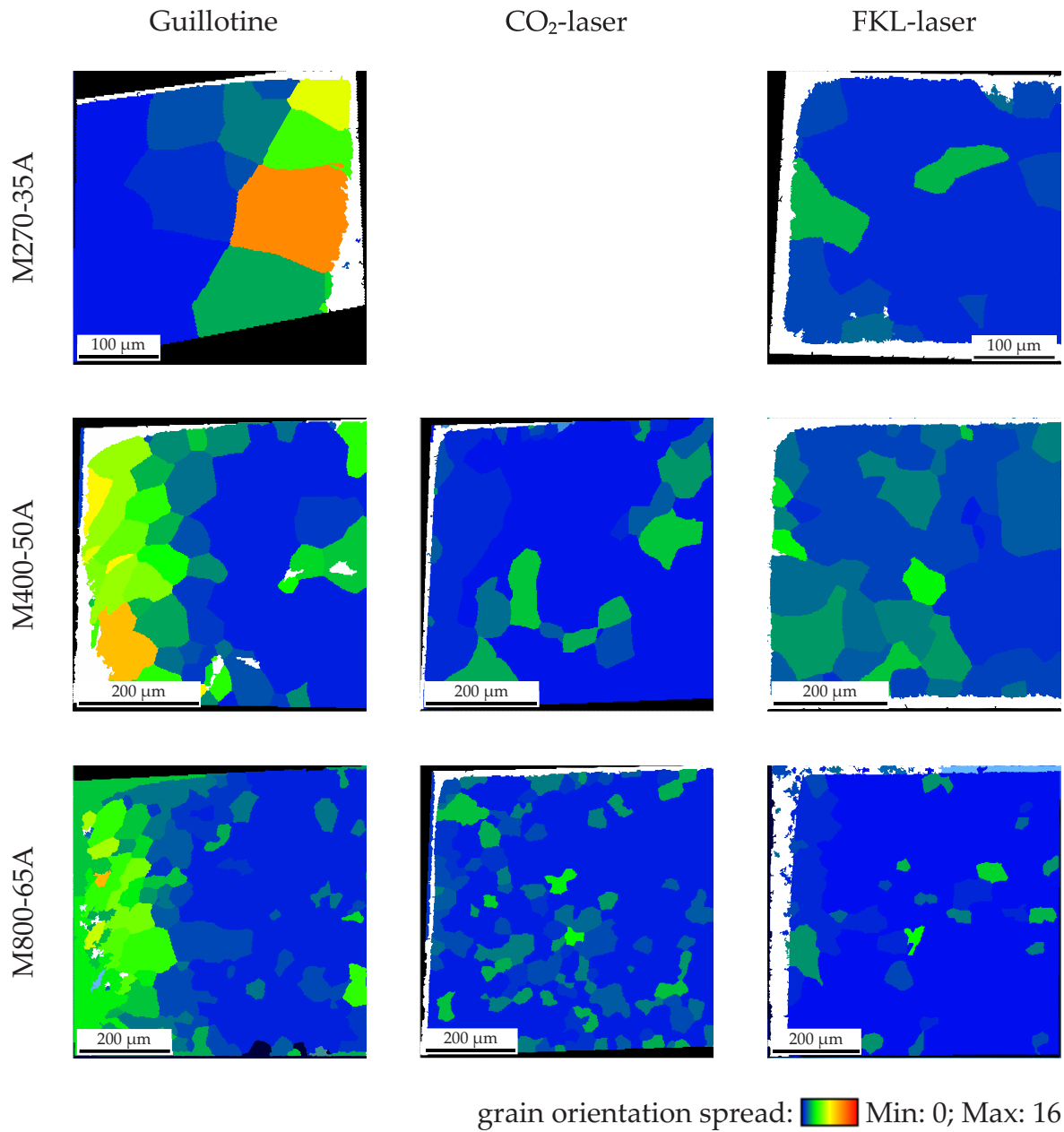
Figure 3.3: Grains at the cut edge for all materials and cutting techniques investigated (GOS).
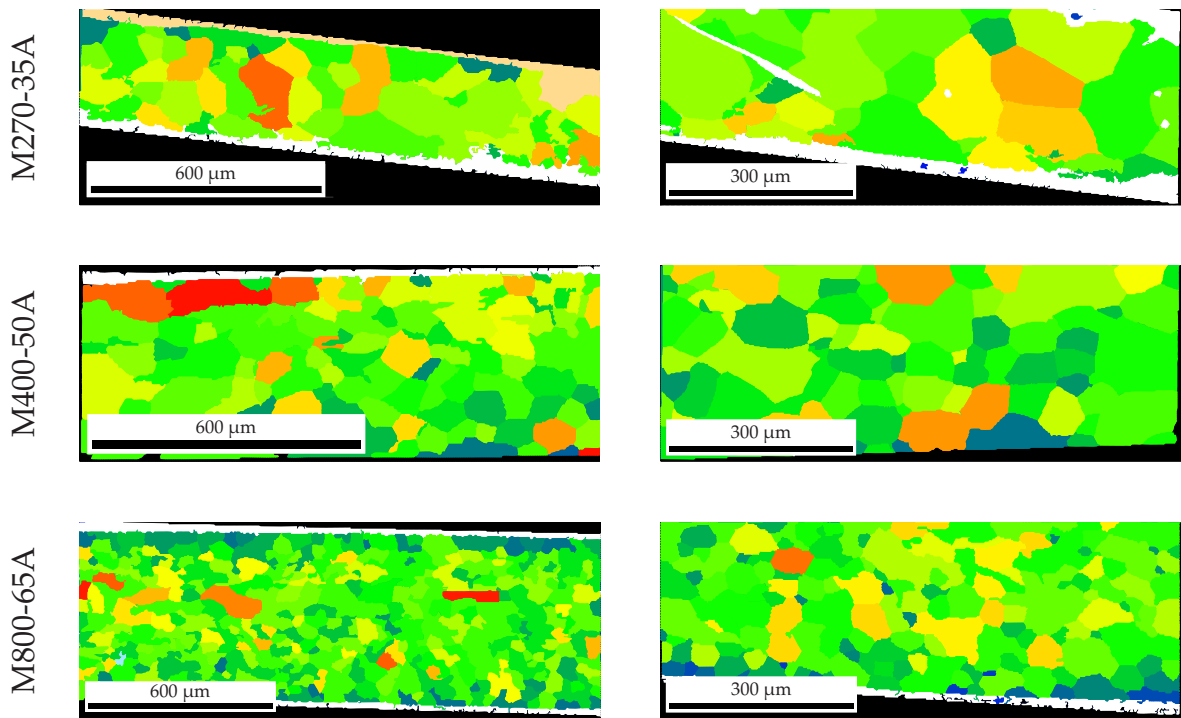
grain orientation spread: Min: 0; Max: 16

Figure 3.4: Examples of grains along the cut edge for mechanically-cut materials (GOS).
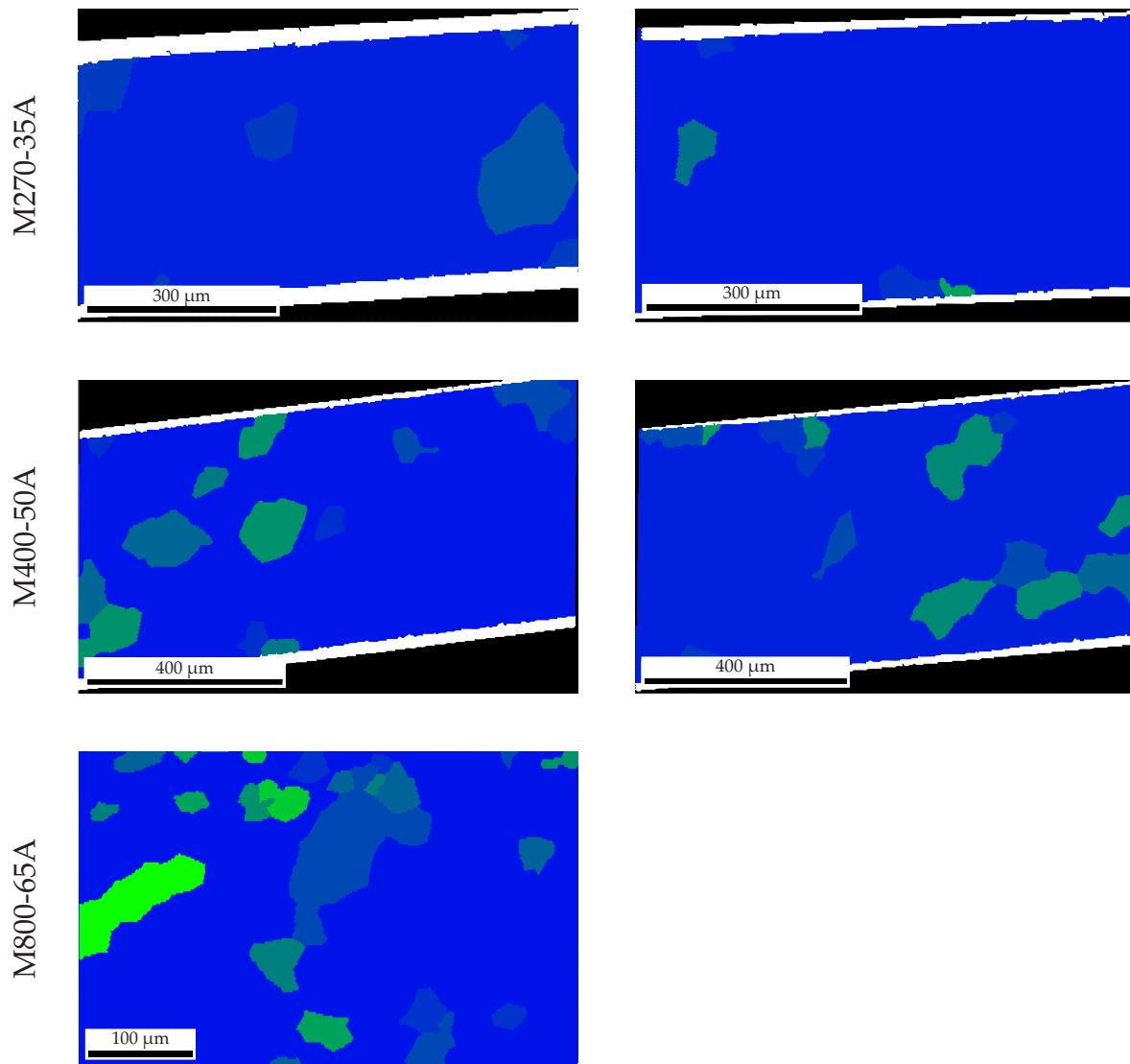
grain orientation spread: ▮ Min: 0; Max: 16

Figure 3.5: Examples of grains along the cut edge for FKL-laser cut materials (GOS).

Guillotine                    CO$_2$-laser                    FKL-laser

M270-35A

100 μm

100 μm

M400-50A

200 μm

200 μm

200 μm

M800-65A

200 μm

200 μm

200 μm

111

Inverse Pole Figure [001]

001          101
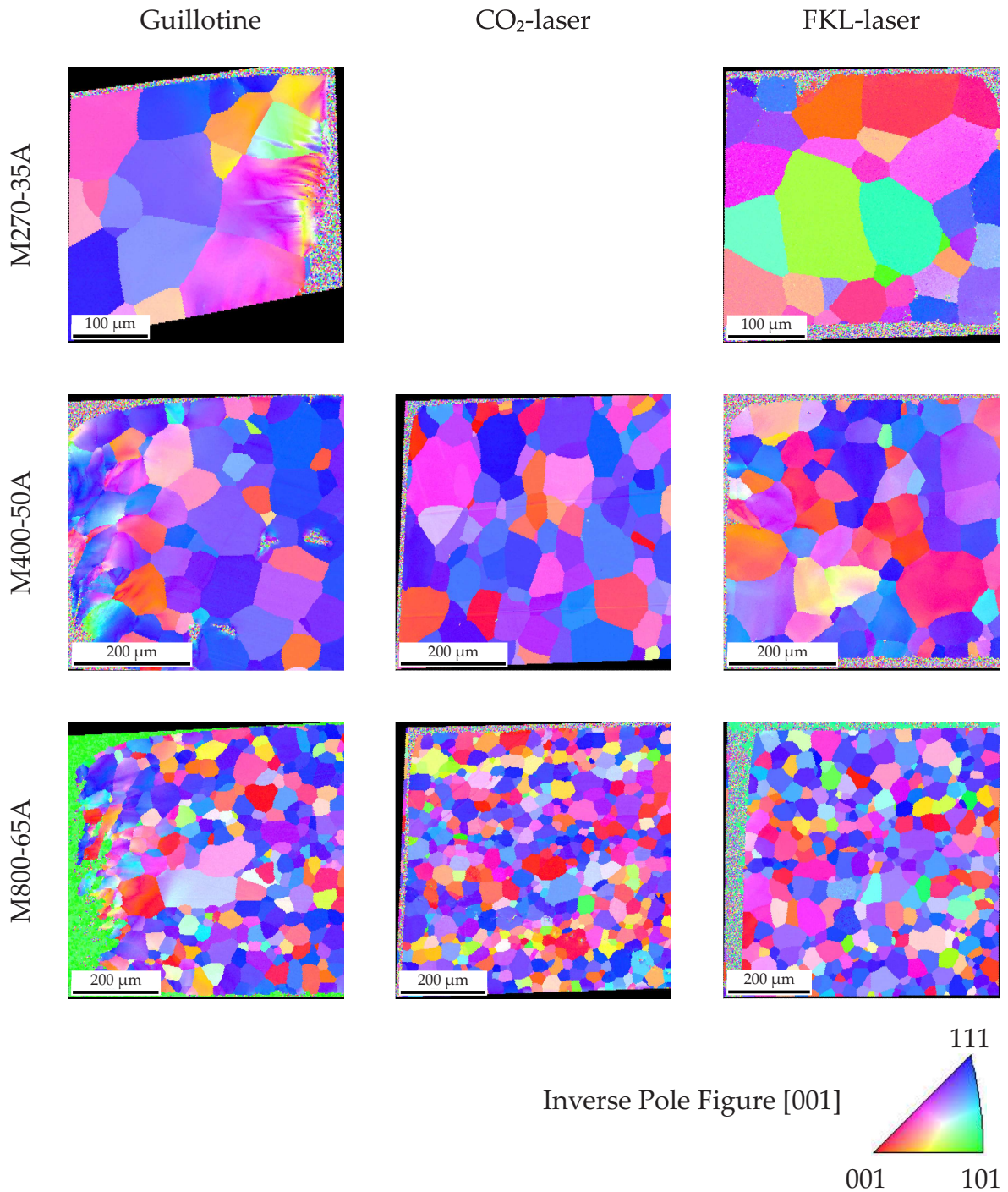
Figure 3.6: Grains at the cut edge for all materials and cutting techniques investigated (IPF). The very small colored dots are ascribed to impurities caused during EBSD sample preparation.
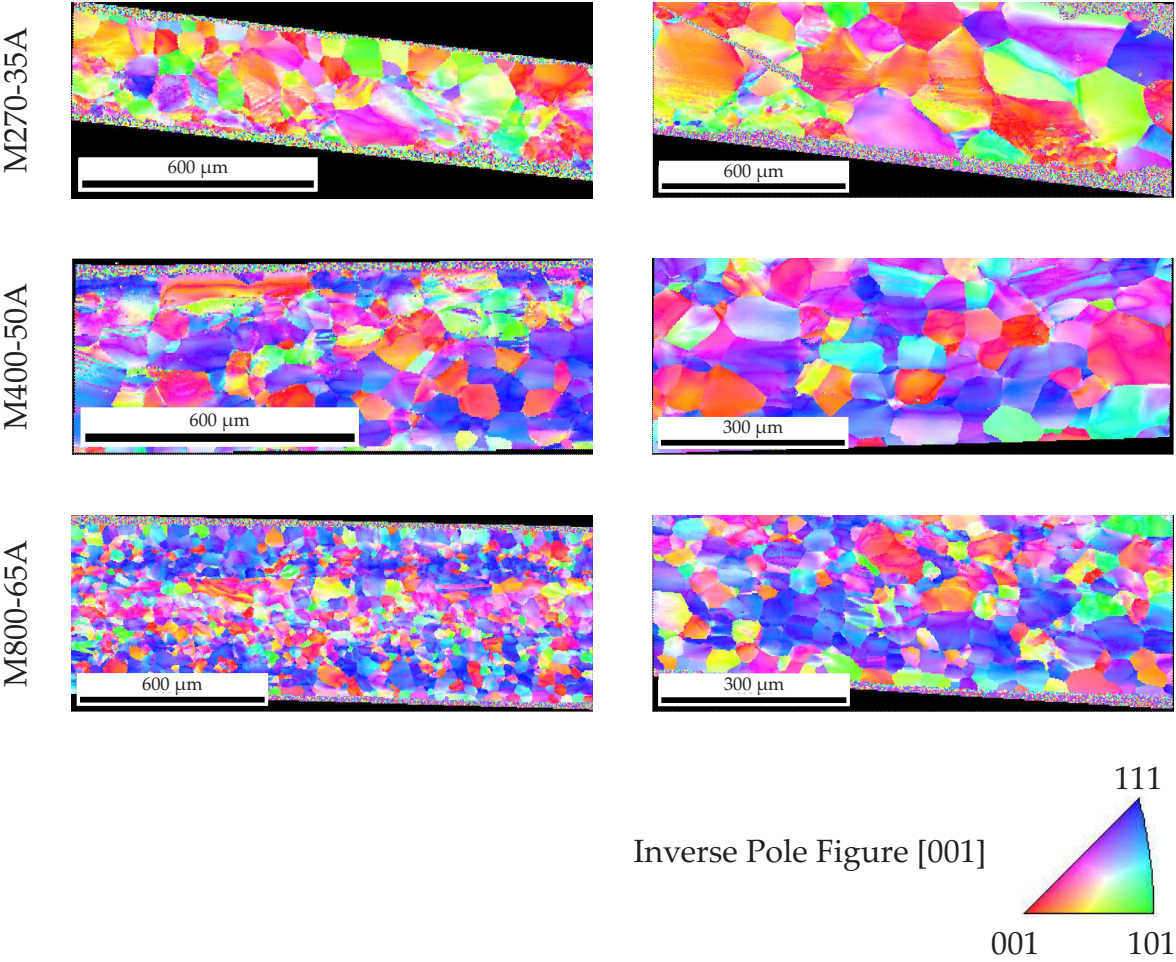
Figure 3.7: Examples of grains along the cut edge for mechanically-cut materials (IPF).

M270-35A

M400-50A

M800-65A

Inverse Pole Figure [001]

111

001  101
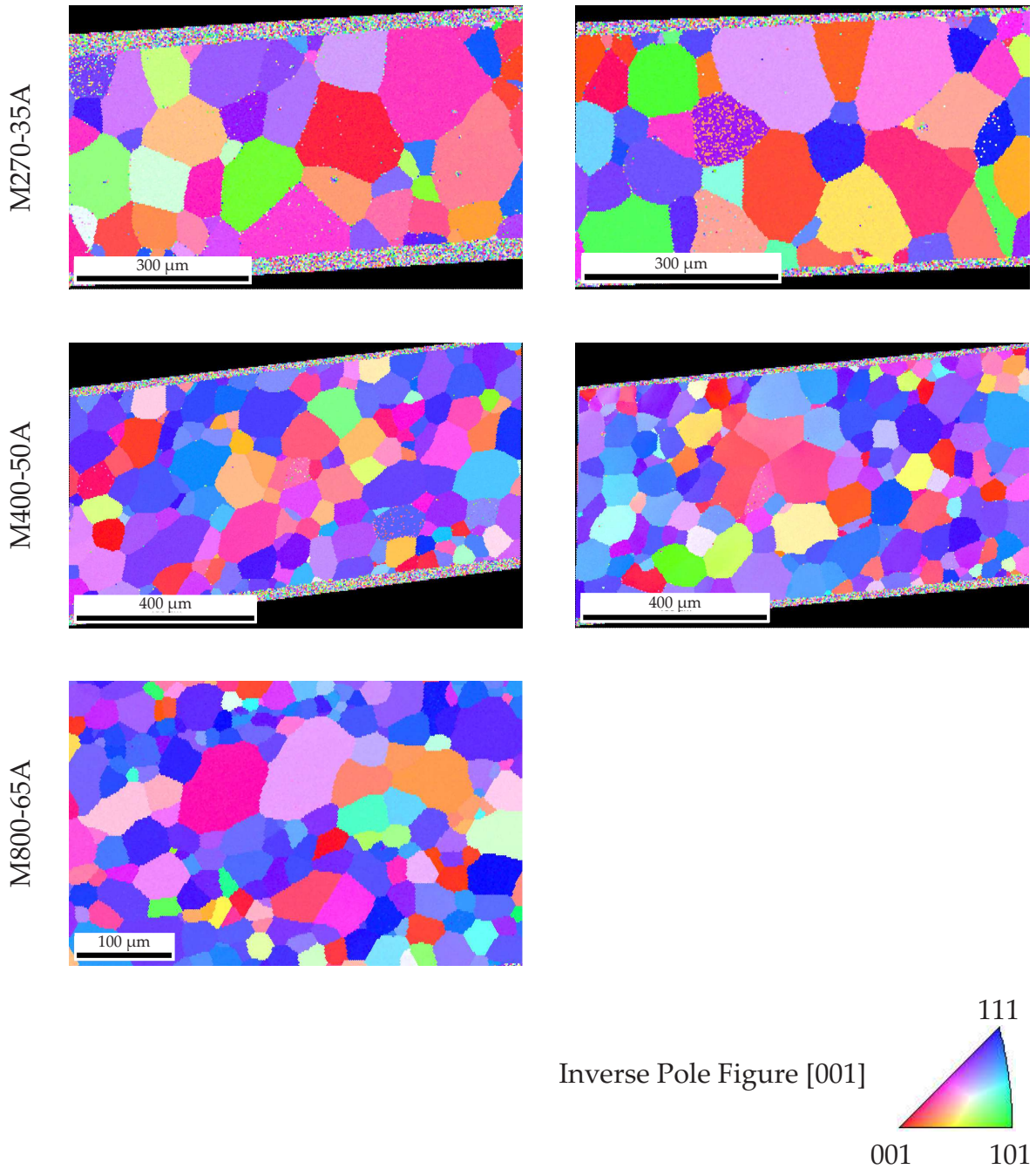
Figure 3.8: Examples of grains along the cut edge for FKL-laser cut materials (IPF).

Conclusions:

- The material with the originally largest grains is most sensitive to the cutting, resulting in the largest decrease of grain size in the cut edge area. Thus, it applies: the smaller the grains are in a material, the smaller the change in grain size is due to cutting. This applies to mechanical as well as laser cutting.

- Below a specific small grain size of the virgin material, no significant change in grain size at the cut edge is observed.

- Mechanical cutting leads to frayed cut edges and to larger misorientations within the grains placed at the cut edge. This suggests larger stresses and dislocations inside the edge grains.

- The cut edges of both laser-cut edges are more uniform, with less pronounced misorientations within the grains compared with mechanically-cut samples.

## 3.3  Discussion

As previously presented in Chapter 1.2, the respective grain size of a material depends, among other factors, on the chemical composition of the steel sheet. Thus, it is reasonable that material M270-35A has the largest average grain size diameter, as this material contains much more silicon and aluminum, which in turn enhance grain growth, compared to materials M400-50A and M800-65A. The last two materials only differ significantly in the content of manganese. However, manganese is "relatively inert in its effect on magnetic properties" [26]. Thus, the difference in grain size of these two materials may be attributed to other grain size influencing factors (e.g. manufacturing steps[2] or its respective performance (annealing treatment)).

The investigations in Chapter 3.2 revealed that the material with the largest grains is most sensitive to the cutting methods. This is in accordance with results presented in literature: According to [170], the author of [167] states that with increasing grain boundary density (and thus decreasing grain size), the extent of deformations is smaller. The authors of [118] showed that materials with larger grains are more sensitive to compressive stress. According to [207], all cutting methods presented in this work induce compressive stresses inside the material. Thus, the statement of [118] confirms the results presented in this work.

Furthermore, it is shown in Chapter 3.2 that the grain size is decreased at the cut

---

[2]Here, only manufacturing steps are referred to which are performed until the MC is finished.

edge for both mechanically as well as laser-cut samples. However, the measurement data of the grain size diameter of the mechanically-cut samples have to be used with caution, as the cut edge does not provide diffraction information entirely. Thus, the grain reduction might differ from that obtained with measurements. The effect of decreasing grain size at the cut edge is also confirmed for mechanically-cut samples by, e.g., [63, 64]. However, most authors report that the grain size did not change at the cut edge of laser-cut samples [4, 51]. Furthermore, the author of [148] expects that laser cutting may even cause grain growth at the cut edge due to the thermal treatment. Both of these assumptions contrast the findings of this work, where the change of grain size due to the cutting (including laser cutting) depends on the grain size of the virgin material.

In principle, the cut edge shapes identified here of mechanically-cut and laser-cut samples in Chapter 3.2 (Figs. 3.3 and 3.6) are in accordance with those presented in [128], [153][p. 60], [110][3] (e.g. frayed edges for mechanically-cut samples). The same applies to the images presented in [4, 51].

## 3.4 Excursion: grain size and specific losses

In this work, three different materials are investigated which differ in their thicknesses $w_z$ and their average grain size diameter $d_g$.[4] The grain size influences the hysteresis as well as the anomalous loss (see Fig. 1.12). However, the thickness only affects the classical eddy currents (see Eq. (1.4)). Thus, the grain size influences the quasi-static[5] hysteresis curves (see Chapter 4). In the case of the Epstein and stator measurements (Chapters 5 and 6), both the thickness and the grain size (might) lead to differences in the magnetic behavior of the different materials investigated. For higher frequencies, the influence of the grain size on the total losses is expected to be limited, as the eddy currents increase with the square (classical eddy currents) and with $\frac{3}{2}$ (anomalous loss) of the frequency (see [16]).

---

[3]Compare with Fig. 4 a, b.

[4]Due to the respective material composition, also further properties such as the resistivity might change from material to material. However, the main differing parameters are the thickness and grain size (also influenced by the material composition (see Chapter 1.2.2)).

[5]No eddy currents must be considered (see Chapter 2.4).

---

# Chapter 4

# Experimental results: remagraph

In the following, the investigated samples are analyzed with respect to the influence of cutting technique, cutting direction and ratio $V_{dg}/(V_{nd} + V_{dg})$. This ratio illustrates the relation between the volume of material deteriorated due to cutting and the total material volume of the sample.

## 4.1 Influence of cutting technique

In addition to selected results in this Chapter, illustrating the main findings, comprehensive sets of measurement results are presented in Appendix B.1.

### 4.1.1 Small specimens

The analyzed samples are rather small (7.0 or 7.5 mm in width, see Chapter 2.1.1). Based on the assumption that the deteriorated volume induced by cutting has a constant deterioration depth $\delta$ (e.g. about 2 mm, see Chapter 1), the ratio of the deteriorated volume to the total material volume, $V_{dg}/(V_{nd} + V_{dg})$, is rather large. Therefore, the deteriorating effect of the individual cutting techniques is expected to show a more significant influence on these small samples than on the wide samples (compare with Subsection 4.1.2).

**Hysteresis curve**

*Laser versus mechanical cutting*
The laser cutting technique (mainly thermally induced stresses) deteriorates the magnetic properties in a different way than mechanical cutting (mechanically induced stresses; here guillotine cutting); see, for example, the hysteresis loops in Fig. 4.1. In Fig. 4.1 the material (M270-35A) was cut in rolling direction. The loop center of the *B-H* curve of the **guillotine-cut sample** is thinner than its middle parts
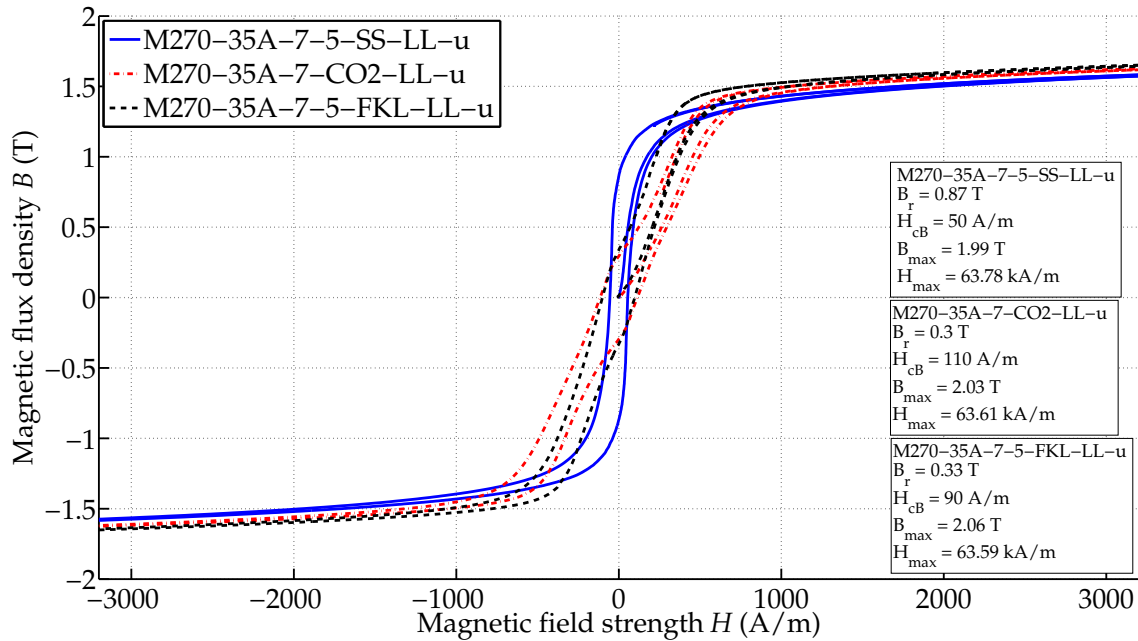
Figure 4.1: *B-H* curves for small samples of M270-35A-LL-u, all three investigated cutting techniques.

(see also Fig. 2.7). This characteristic is reduced with increasing material thickness[1] (here, also with decreasing grain size). The slope of the initial curve (representing the differential permeability) in the loop center area and in the middle parts is steep. For example, the gradient $\frac{\Delta B}{\Delta H}$ of the initial curve in the loop center area is up to four times higher in the case of guillotine-cut samples than the same gradient of the FKL-laser cut sample, see Fig. 4.1. This factor varies of course with the type of material, sample size and thus ratio $V_{dg}/(V_{nd} + V_{dg})$ and cutting direction.

The *B-H* curves of the **laser-cut samples** behave differently: The loop centers of the laser-cut samples are expanded and wider than the other parts of the hysteresis curve, leading to larger coercive field strengths $H_c$ when compared to those of the guillotine-cut samples (see legends in Fig. 4.1). The loop centers of all measured small laser-cut samples are in the area of $\pm0.20\,\text{T}$ and $\pm0.45\,\text{T}$ (see Appendix B.1). In addition, the *B-H* curves are shifted into a clockwise direction in relation to those of the guillotine-cut samples (Fig. 4.1), wherefore the remanent flux densities $B_r$ of the laser-cut samples are smaller than those of the guillotine-cut specimen (see

---

[1]Note that in this work three different materials, each of a different thickness, are investigated. However, these three materials also differ in their grain size (see Chapter 3.2), which, in turn, influence the hysteresis losses (see Chapter 1.2.1 and Fig. 1.12). Thus, when it is stated that some characteristics increase or decrease with material thickness, this relationship may originally result from the material compositions and/or the different grain sizes of the materials. This applies to all Chapters.
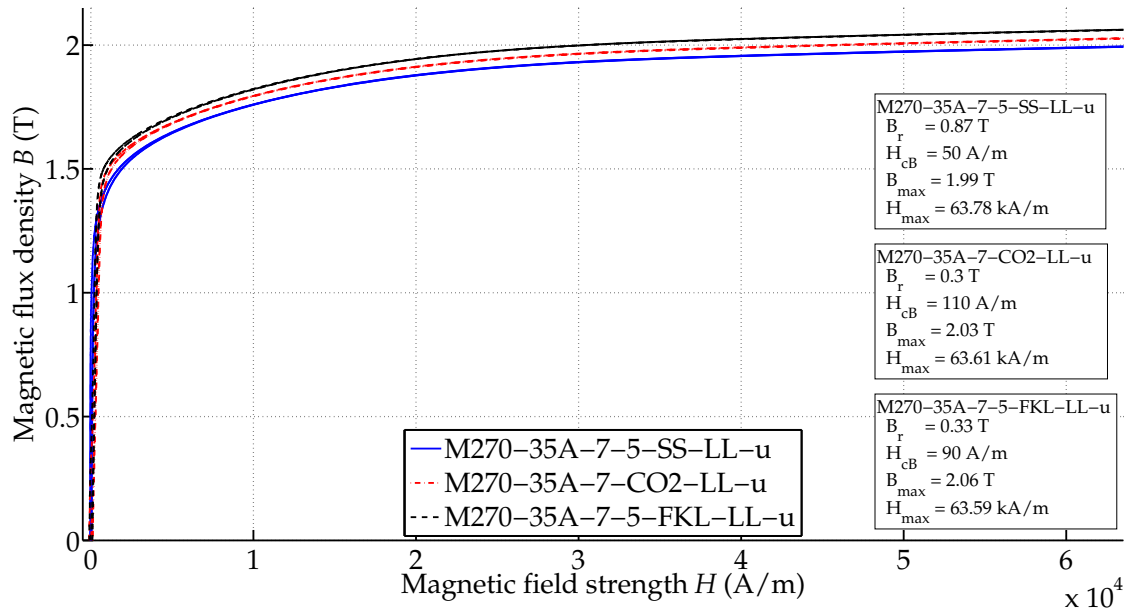
Figure 4.2: *B-H* curves of M270-35A-LL-u including the high saturation area, all three investigated cutting techniques.

legends in Fig. 4.1). Considering [26][2] and [100], this larger shifting may indicate that laser cutting induces larger internal stresses than mechanical cutting inside the material samples[3]. The remanent magnetic flux densities $B_r$ of both small laser-cut samples differ much less than those of the small laser-cut and guillotine-cut specimens, even though both small laser-cut samples have different widths (see Tables in Appendix B.2). Thus, the loop center areas of the small laser-cut samples do not change sharply with further increasing ratio $V_{dg}/(V_{nd} + V_{dg})$. Hence, the following applies: $B_{r,\text{guillotine-cut}} > B_{r,\text{laser-cut}}$.

Until around 1 T, the $B/H$-slope of the initial curves of the laser-cut samples is lower than that of the guillotine-cut samples (Figs. 4.1 and 4.3). Then, up to the end of the knee-point area (in this case around 1.5 T), it is larger. In the (high) saturation area, the small laser-cut samples reach a higher magnetic flux density $B$ than the small guillotine-cut samples for the same magnetic field strength $H$: $B(H_{\text{saturation}})_{\text{laser}} > B(H_{\text{saturation}})_{\text{guillotine}}$ (Figs. 4.1 and 4.2). This applies to all investigated small samples.

The thicker (here, also smaller grain size of) the material is, the less the *B-H* curves of the laser-cut samples shifted in relation to those of the guillotine-cut samples[4]

---

[2]pp. 625-626.

[3]Note, the internal stresses by laser cutting are thermally induced whereas those of mechanical cutting are mechanically induced (see Chapters 1.3.3 and 1.3.4).

[4]Considering the work of [100], the shifting reflects the internal sate of internal stresses. Thus, the smaller shifting might suggest, that materials with many, small grains are less sensitive to stresses induced by laser cutting than those with large grains.

(see Appendix B.2). Furthermore, the thicker (here, also smaller grain size of) the material is, the more the *B-H* curves increase in width and thus the characteristic of the 'laser-effect' is less obvious[5].

The shape of the hysteresis loop of the small laser-cut specimens differs evidently from that of the guillotine-cut samples. Thus, in this work[21,p.24], this distinctive curve with a *wide loop center area* and *thin, strongly inclined middle parts* and *knee point areas* is referred to as the **'laser-effect'**. This effect is triggered by the stresses which are induced by the laser and which might differ (in type and/or extent) from the stresses induced by mechanical cutting. This definition might differ from other definitions used in literature (compare Chapter 4.3). Furthermore, it is important to mention that some of these characteristics can also be caused by stacking compression [179] or tensile deformation mechanism [93]. According to [59, 207], stresses induced by different cutting techniques (punching, laser cutting) are compressive stresses. Thus, the compressive components of laser-cut induced stresses must be larger than those induced by guillotine cutting.

*Comparison of the two laser cutting techniques*
The hysteresis curve of the $CO_2$-laser cut sample is more shifted than that of the FKL-laser cut sample (see Fig. 4.1), because the ratio $V_{dg}/(V_{nd} + V_{dg})$ of the $CO_2$-laser cut sample is larger (different widths of laser-cut samples, see Chapter 2.1.1).

The characteristic parameters for the loop center area, $B_r$ and $H_c$, are still in the same range. The remanent flux density $B_r$ is smaller[6], and the coercive magnetic field strength $H_c$ is equal or larger for the $CO_2$-laser cut samples, due to the larger ratio $V_{dg}/(V_{nd} + V_{dg})$: The thicker (here, also the smaller the grain size of) the material is, the more $H_{c,CO_2} \approx H_{c,FKL}$[7] (see Appendix B.1). At high saturation the FKL-laser cut samples reach higher magnetic flux densities $B$ for the same magnetic field strength $H$ than the $CO_2$-laser cut specimens: $B(H_{saturation})_{FKL} > B(H_{saturation})_{CO_2}$ (see Fig. 4.2).

Overall, the hysteresis loops of the two laser cutting techniques have very similar shapes. This suggests that the curves would be nearly identical if the samples had the same widths and that the deterioration effect of the two laser cutting techniques on the hysteresis loop and consequently also on the characteristic parameters and the specific losses can be considered rather similar. This assumption is further investigated in Chapter 4.1.2, 'Hysteresis curve'.

---

[5]Note, in this Chapter only the quasi-static hysteresis losses are studied. These losses decrease with increasing grain size (see Fig. 1.12). Eddy currents (classical and anomalous) can be neglected because quasi-static measurements are carried out (see Chapter 2.4).

[6]Whether this difference only depends on the difference in sample width is further investigated in Chapter 4.1.2.

[7]As concluded before, materials with small grains might be less sensitive to cutting and thus less sensitive to small differences of the laser cutting technologies.
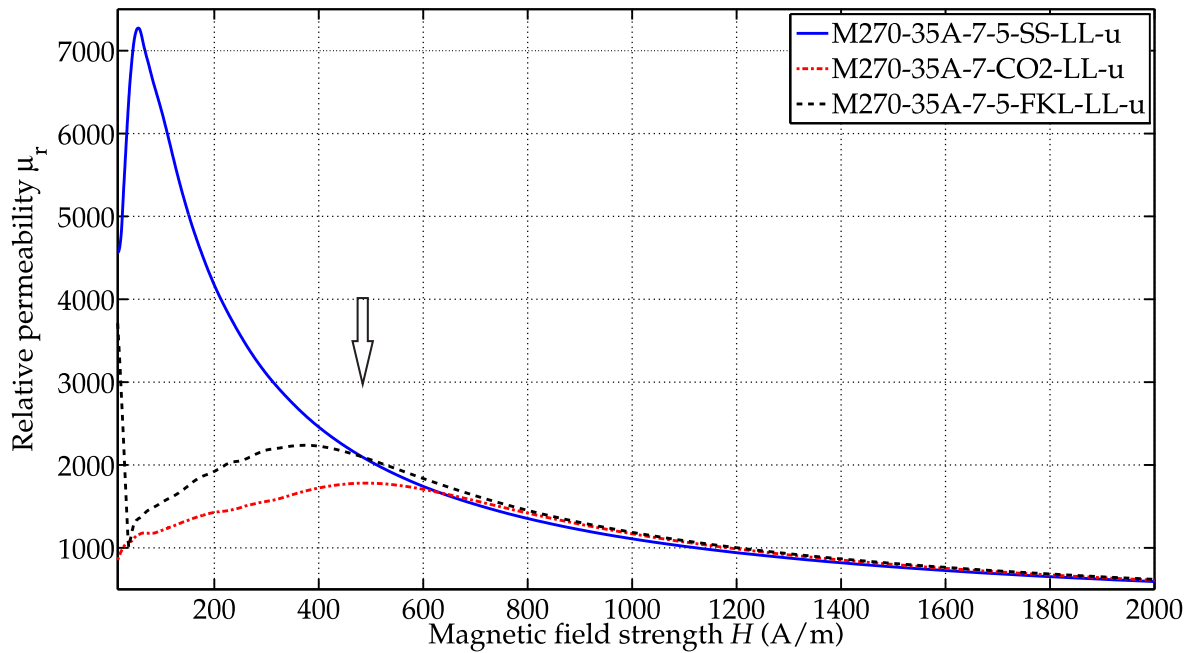
Figure 4.3: Relative permeability for different cutting techniques.

**Relative permeability**

*Laser versus mechanical cutting*

The relative permeability $\mu_r$ computed from the measurement data of Fig. 4.1 is presented in Fig. 4.3. At low magnetic field strengths $H$, the relative permeability is larger for guillotine-cut samples. Later, a point of intersection (POI) occurs (for the investigated samples here in the range of 450 to 1000 A/m, depending on difference in sample width[8], type of material and cutting direction) and the relative permeability of mechanically-cut samples is smaller than those of the two laser-cut samples (see also Fig. B.21).

By considering the maximum permeabilities (see e.g. Fig. 4.3) the following applies: $\mu_{r, max, small, guillotine} > \mu_{r, max, small, laser}$. Fig. 4.3 also shows that the relative permeabilities of laser-cut samples loose the distinctive maximum with increasing ratio $V_{dg}/(V_{nd} + V_{dg})$.

For most investigated samples the following applies: The smaller the maximum relative permeability $\mu_{r,max}$ is, the more $\mu_{r,max}$ shifted to higher magnetic field strength $H$. This behavior disappears for samples with lost distinctive maximum (discussed in more detail in the following Subsections).

---

[8]Note, the mentioned difference in sample width here refers only to the investigated samples in this work. Of course, with smaller or wider sample sizes this POI may occur at other magnetic field strengths $H$.

### Comparison of the two laser cutting techniques

For all small laser-cut samples, the following applies: $\mu_{\text{r, max, small, FKL}} > \mu_{\text{r, max, small, } CO_2}$.
This difference is especially significant in the range of 0 to 800 A/m. Above 800 A/m,
the difference of relative permeabilities of FKL-laser and $CO_2$-laser cut samples is less
than 50. As the small $CO_2$-laser cut samples have a smaller width than the FKL-laser
cut samples (see Chapter 2.1.1), the relative permeability of the small $CO_2$-laser cut
samples is more deteriorated. However, further study of the wide samples shows
that this order also exists for samples of same width (see Chapter 4.1.2).

The POIs of guillotine-cut with $CO_2$-laser cut samples are always at larger
magnetic field strengths $H$ than those with the FKL-laser cut specimen. This is
mainly associated with the difference in sample width.

### Specific losses

### Laser versus mechanical cutting

As the area enclosed by the hysteresis loop is proportional to the specific losses [16],
the latter can be computed from the hysteresis loops by

$$\frac{p}{f} = \oint H dB. \tag{4.1}$$

From the hysteresis loop results (see Figs. 4.1 and 4.7), it can be derived that the
specific losses of the laser-cut samples in the loop center area are larger than that of
guillotine-cut samples, as the area enclosed is larger. Thus, for low magnetic flux
densities $p_{\text{laser-cut}} > p_{\text{guillotine-cut}}$ (first assumption) applies. However, the widths of
the middle parts of the laser-cut specimens are smaller compared to those of the
guillotine-cut samples. Especially for materials with higher thicknesses (here, also
smaller grain size, e.g. M800-65A) this effect is recognized. The specific losses of the
differently cut samples may thus approach each other with increasing magnetic flux
density and that of the laser-cut samples may also become the smaller one. Thus,
at medium and/or high magnetic flux densities (depending also on the respective
material [e.g. composition and grain size]), it may apply $p_{\text{laser-cut}} \approx p_{\text{guillotine-cut}}$ or
even $p_{\text{laser-cut}} < p_{\text{guillotine-cut}}$ (second assumption).

Both assumptions are confirmed by the stepwise computed specific losses (see
Figs. 4.4 and 4.5). At low magnetic flux densities $B$ the laser-cut samples have a
larger energy density than the guillotine-cut samples (see Figs. 4.4 and 4.5). Then,
the gradient of the energy density for laser-cut samples decreases, at high mag-
netic flux densities it increases again[9]. In contrast, in the case of longitudinally-cut
samples, the gradient of the guillotine-cut samples increases continuously; thus, at

---

[9]In this work, this characteristic is defined as 'wave' shape.

moderate to high magnetic flux densities a POI may occur (see Figs. 4.4 and 4.5, compare guillotine-cut with FKL-laser cut samples, as the $CO_2$-laser cut samples have smaller widths). In the case of transversely-cut samples, the gradient of guillotine-cut samples increases much more sharply from about 1/1.2 T, wherefore the POI occurs[10]. This POI does not occur for all investigated samples. It should be noted that the computation of the energy densities is based on approximation only and may introduce inaccuracies due to the filtering method and the subsequent computation of the losses. The filtering is used to smooth the read hysteresis loop i.e. eliminate nonsmoothness due to the barkhausen jumps. A more precise evaluation of the occurrence of the POI is performed with the results of the Epstein and stator measurements (see Chapters 5 and 6).

The 'wave' shape is observed for the specific losses of all small laser-cut samples including both transverse and longitudinal cutting direction (see Subsection "Cutting direction - Specific losses"[p. 88]). The losses of the small guillotine-cut samples have continuously increased behavior in the case of longitudinally-cut samples. Note, for transversely guillotine-cut samples the 'wave' shape also occurs, but at large it is less pronounced compared with the laser-cut samples. However, for guillotine-cut samples, in the case of material M800-65A, both effects (continuous increasing, 'wave' shape) are less pronounced and might result in a more 'linear' behavior (see Fig. 4.6).

### Comparison of the two laser cutting techniques

The two curves of the two laser cutting techniques indicate a similar degrading effect on the loss behavior of the investigated samples: The curves themselves have the same characteristics (compare with Figs. 4.5 and 4.6). The differences between the results is primarily explained by the difference in sample widths (7.5 versus 7 mm, compare Chapter 2.1.1) and thus the different ratios $V_{dg}/(V_{nd} + V_{dg})$.

As mentioned in Subsection "Hysteresis curve", the loop centers of both laser-cut specimens seem to be in the same range and consequently depend, only to a small extent, on the small difference in samples widths. Thus, the energy densities of both laser-cut samples at small magnetic field strengths $H$ overlap, or are closely related. This is confirmed for almost all investigated samples (see for instance Fig. 4.6, low magnetic flux densities).

---

Conclusions - small samples:
- Laser cutting deteriorates the magnetic material properties in a different way than mechanical cutting (compare hysteresis loops, relative perme-

---

[10]This stronger increase is observed for material M270-35A and M400-50A. Thus, this behavior is reduced for material M800-65A.
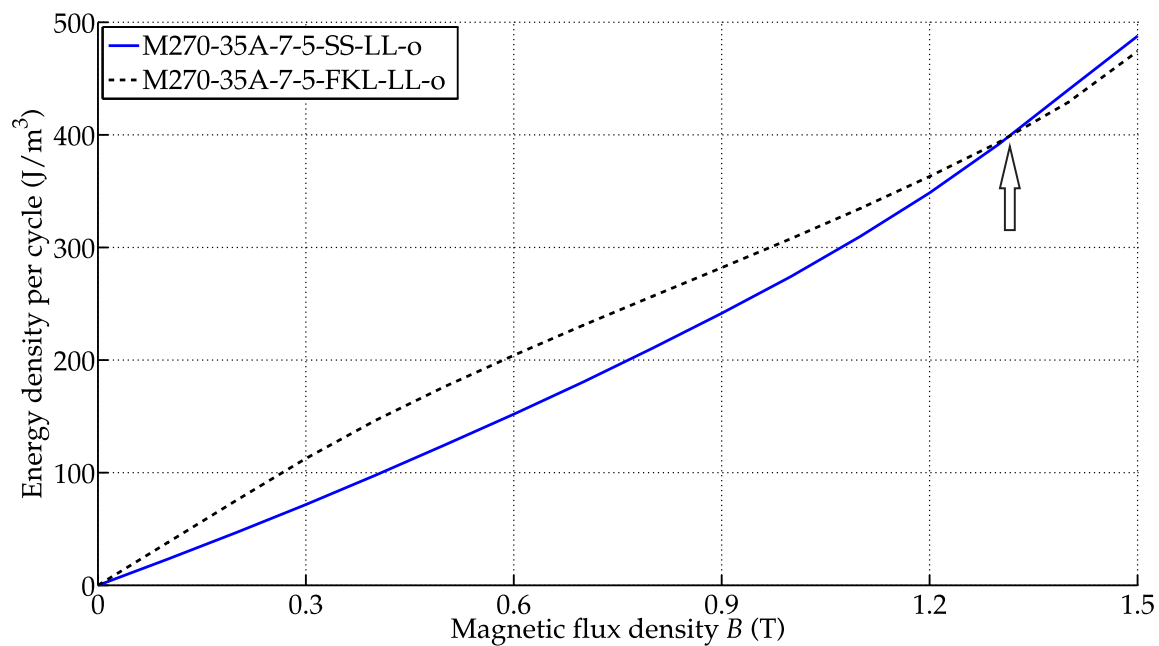
Figure 4.4: Energy densities of the hysteresis curves over magnetic flux density $B$, M270-35A-75-LL-o.
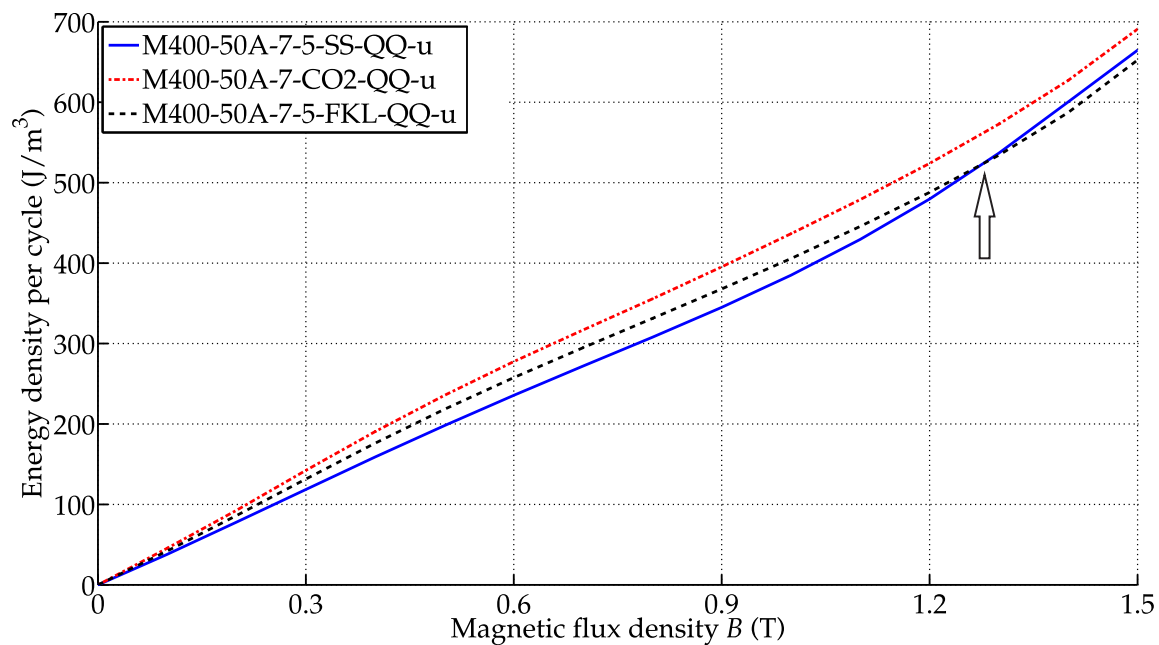


Figure 4.5: Energy densities of the hysteresis curves over magnetic flux density $B$, M400-50A-75-QQ-u.
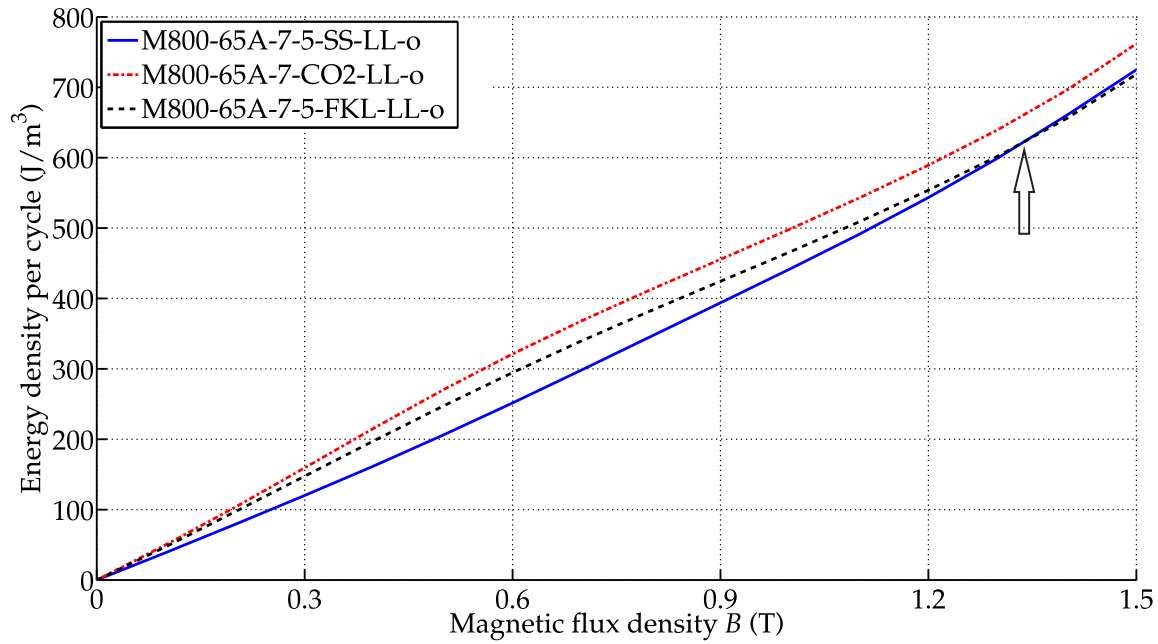
Figure 4.6: Both laser-cut samples show similar behavior with respect to the energy density of the hysteresis curve. The difference between the curves is mainly explained by the difference in sample widths.

- ability and loss behavior).
- Laser-cut samples differ from guillotine-cut samples by more shifted middle parts and knee point areas.
- The hysteresis curves of laser-cut samples are characterized by wide loop center areas and thin, strongly inclined upper and lower middle parts and knee point areas (here designated as 'laser-effect').
- The thicker (here, also smaller the grain size in) the material was, the less the *B-H* curves of the laser-cut samples shifted in relation to the guillotine-cut samples.
- It applies: $B_{r,\text{guillotine-cut}} > B_{r,\text{laser-cut}}$ and $H_{c,\text{guillotine-cut}} < H_{c,\text{laser-cut}}$, but $B(H_{\text{saturation}})_{\text{guillotine-cut}} < B(H_{\text{saturation}})_{\text{laser-cut}}$.
- Considering the maximum relative permeabilities, it applies:

  $\mu_{r,\text{max, small, guillotine}} > \mu_{r,\text{max, small, FKL}} > \mu_{r,\text{max, small, } CO_2}$.
- A POI for the relative permeabilities of laser-cut and guillotine-cut samples occurs at the knee point areas of the laser-cut specimens.
- It applies: $\mu_{r,CO_2} < \mu_{r,\text{FKL}}$.
- A POI may occur at the energy densities of guillotine-cut and laser-cut samples.

> - Due to the larger loop center, the laser-cut samples have larger energy densities than the guillotine-cut samples in the loop center area.
> - The energy density shapes of both laser-cut samples lead to the assumption that the $CO_2$-laser as well as the FKL-laser degrade the specific losses of electrical steel sheet in a similar way.

**Cutting direction - Hysteresis curve**

*Laser versus mechanical cutting*

Fig. 4.7 shows the same measurement as Fig. 4.1 with samples of the same material but cut into the transverse direction. Here, the loop center of the hysteresis curve of the guillotine-cut sample is wider than the middle parts of the curve (Fig. 4.7). Again, this characteristic disappears with increasing material thickness (here, also with decreasing grain size). The width of the loop center ($w_{lc}$) is closer to the width of the laser-cut samples ($\Delta w_{lc,QQ,SS \rightarrow laser} < \Delta w_{lc,LL,SS \rightarrow laser}$). Thus, the coercive magnetic field strength $H_c$ is closer to those of the laser-cut samples (see legends in Fig. 4.7). This is in contrast to the longitudinally-cut samples (Fig. 4.1). The loop center sizes of longitudinally guillotine-cut and laser-cut samples differ significantly and thus also the coercive magnetic field strengths $H_c$. The hysteresis loop area of the transversely guillotine-cut sample in total is increased compared with that of the longitudinally guillotine-cut sample (compare also with Subsection "Cutting direction - Specific losses"[p. 88]). The increase of the loop center area for transversely-cut specimens decreases for thicker material (here, also with decreasing grain size).

The *B-H* curve of the transversely guillotine-cut sample is shifted into a clockwise direction to higher magnetic field strengths $H$ and smaller magnetic flux densities $B$ when compared to that of the longitudinally-cut specimen. Thus, the relative permeability is worse than in the case of the sample cut in rolling direction (see Fig. 4.8 and Subsection "Cutting direction - Relative Permeability"[p. 86]). Through this shifting and the larger loop center area, the remanent magnetic flux density $B_r$ of the guillotine-cut sample changes strongly (see Table B.1). Comparing, for example, the material M270-35A presented in Figs. 4.1 and 4.7, it is about 50 % (see Table B.1 in Appendix B.2). With increasing material thickness (here, also with decreasing grain size), $\Delta B_{r, guillotine, small, LL \rightarrow QQ}$ decreases (see Table B.1 in Appendix B.2). Thus, the influence of the cutting direction on the relative shifting of the hysteresis curve is reduced. The change from the 0.35 mm to the 0.5 mm thick steel sheet is smaller than that from the 0.5 mm to the 0.65 mm thick steel sheets (see Table B.1 in Appendix B.2).

The hysteresis loops of transversely and longitudinally laser-cut samples are partly different: The loop center area remains unchanged, independent of its cutting di-
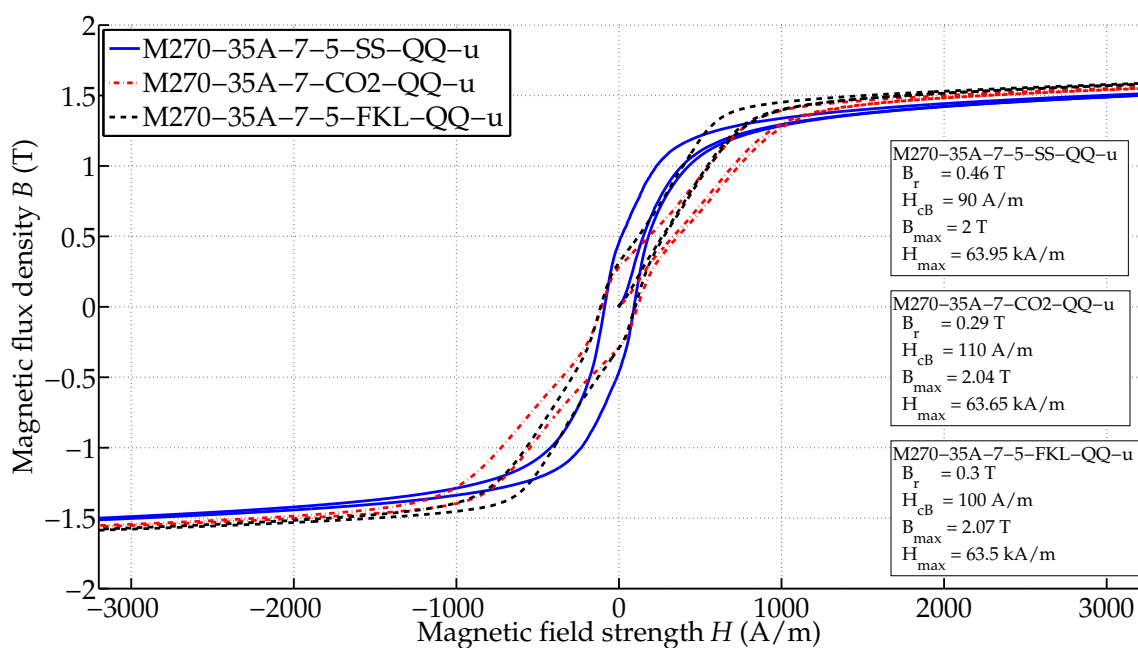
Figure 4.7: *B-H* curves of M270-35A-QQ-u, small samples.
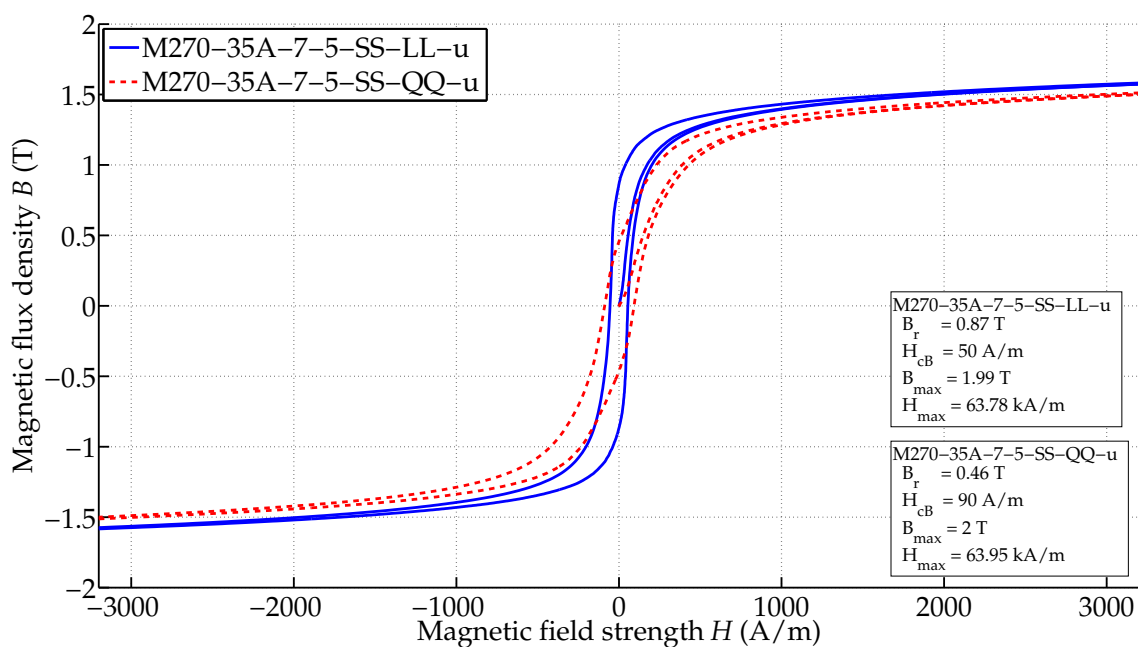


Figure 4.8: *B-H* curves of small longitudinally and transversely guillotine-cut samples: M270-35A-7.5-SS-u.

rection (no shifting of the loop center observed between both samples, see Figs. 4.9 and 4.10). Thus, the remanent magnetic flux density $B_r$ and the coercive magnetic field strength $H_c$ are almost independent of the cutting direction (see legends in Fig. 4.9). It follows that $\Delta B_{r,\,laser,\,small,\,LL\,\rightarrow\,QQ}$ is much smaller than those of the guillotine-cut samples (see Appendix B.2, Tables B.2 and B.3). Presumedly, the degradation induced by the laser seems to be already so high for the small longitudinally-cut samples that a further degradation induced by the transverse cutting direction has little or no impact. The loop center size[11] of the laser-cut samples seems to be material-specific. M400-50A has the largest loop center area interval (magnetic flux density). However, the influence of the cutting direction is certainly apparent in the middle parts, in the knee point and saturation areas, as these parts are more shifted to lower magnetic flux densities $B$ and higher magnetic field strengths $H$ in the case of the transversely-cut samples compared to the longitudinally-cut probes (see Figs. 4.9 and 4.10). Overall, the hysteresis curves of small laser-cut samples (without considering the loop center) are more shifted into a clockwise direction with respect to the vertical axis than those of the small guillotine-cut samples.

It is observed that the transversely-cut specimens have higher magnetic flux densities $B$ at high saturation than the longitudinally-cut probes. This applies especially for laser-cut samples (for guillotine-cut samples this is only true for material M270-35A). Thus, a POI might appear and the behavior might reverse. With increasing material thickness (here, also with decreasing grain size), the POI is shifted to higher magnetic flux densities (exception $CO_2$-laser cut samples from M400-50A to M800-65A). However, these POIs are at high saturation (32000 A/m-50000 A/m) which are less important, as the differences of magnetic properties of samples with different cutting directions are small.

*Comparison of the two laser cutting techniques*

By comparing the hysteresis curves of both laser-cut samples with respect to the cutting direction, no significant difference is obvious, except the larger shifting of the upper and lower middle parts as well as the knee point and saturation areas of the $CO_2$-laser cut samples (compare Figs. 4.9 and 4.10). This larger shifting is associated with the smaller sample width of these samples (see Chapter 2.1.1) and thus a larger ratio of $V_{dg}/(V_{nd} + V_{dg})$, wherefore the assumption is made that both laser cutting techniques have almost the same influence on the hysteresis curve considering different cutting directions if they have the same sample width. This assumption is to be verified further by examining "wide specimens" (see Chapter 4.1.2).

---

[11]Here, the range of magnetic flux density is referred to.
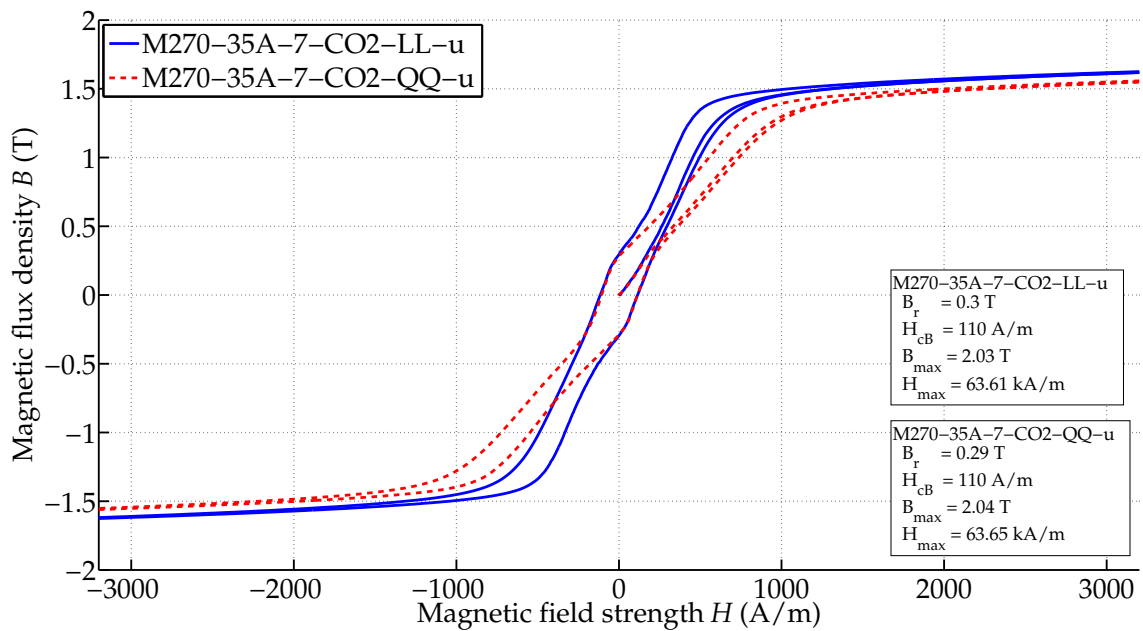
Figure 4.9: *B-H* curves of small longitudinally and transversely CO$_2$-laser cut samples: M270-35A-7.5-CO$_2$-u.
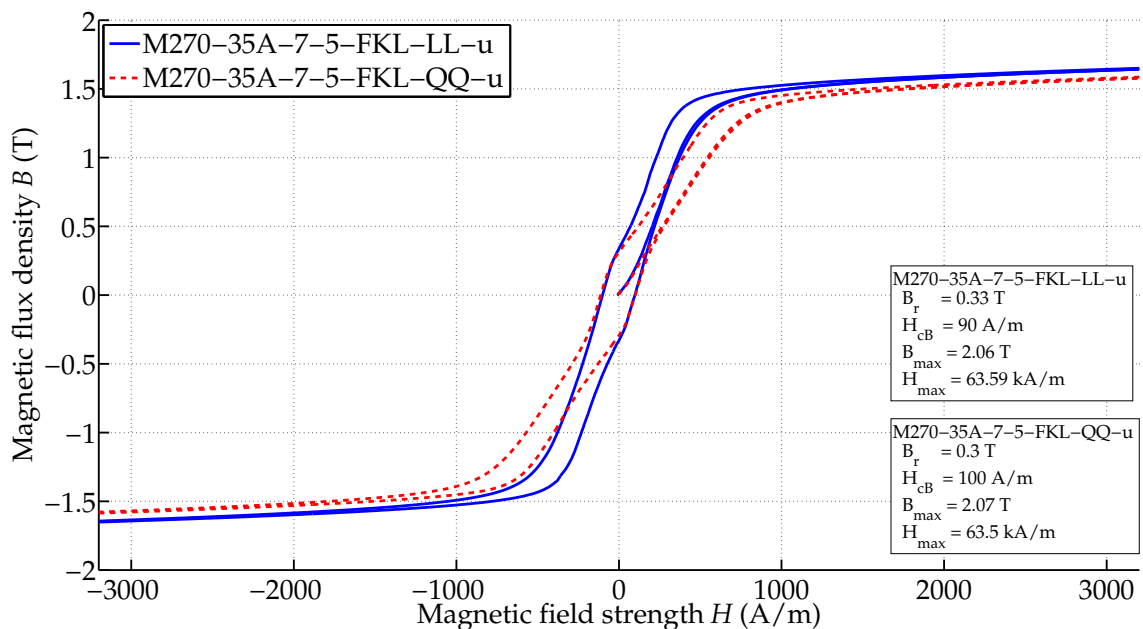


Figure 4.10: *B-H* curves of small longitudinally and transversely FKL-laser cut samples: M270-35A-7.5-FKL-u.
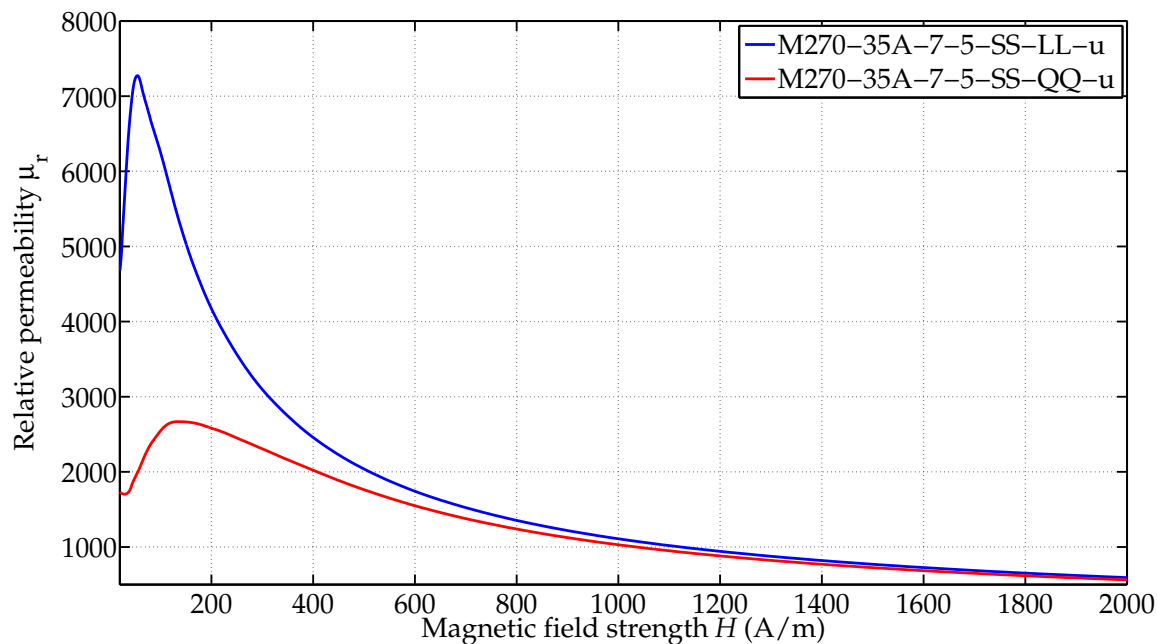
Figure 4.11: Relative permeabilities of small guillotine-cut samples cut into two directions.

## Cutting direction - Relative Permeability

### *Laser versus mechanical cutting*

It has already been mentioned that the hysteresis curve of the transversely guillotine-cut samples is shifted into a clockwise rotation compared to that of the longitudinally-cut samples. Thus, the relative permeability is also influenced. The computed relative permeability of small guillotine-cut samples in rolling and transverse direction is presented in Fig. 4.11. It is apparent that the maxima of the relative permeabilities of longitudinally guillotine-cut samples are significantly higher (exact values depend on the type of material and ratio $V_{dg}/(V_{nd} + V_{dg})$) than those of samples cut in transverse direction. For both cutting directions a distinct extrema of $\mu_r$ is visible. Furthermore, the maxima of the relative permeability of the transversely guillotine-cut samples are shifted to larger magnetic field strengths $H$ compared with those of the longitudinally-cut samples. This applies to all guillotine-cut samples.

As mentioned in Subsection "Cutting direction - Hysteresis curve" the hysteresis curves of the laser-cut samples are more shifted to the vertical axis than those of the guillotine-cut samples. Thus, also the relative permeabilities of the small laser-cut samples are obviously smaller below the knee point area than those of guillotine-cut samples (compare Figs. 4.11 and 4.12).

The influence of cutting direction on the relative permeability $\mu_r$ of the small laser-cut samples is presented in Fig. 4.12. As with the guillotine-cut samples, the largest

reduction of relative permeability is in the area of small magnetic field strengths $H$. However, the decrease of relative permeability caused by the different cutting directions is significantly smaller for laser-cut samples. In the case of material M270-35A a reduction of up to 33 % occurs for small laser-cut samples in contrast to small guillotine-cut samples with a reduction of up to 64 % (see Figs. 4.11 and 4.12). With increasing material thickness (here, also with decreasing grain size) this reduction of maximum relative permeability as a function of the cutting direction for the small guillotine-cut samples is decreased (for example M400-50A reduction of up to 49 %, M800-65A reduction of up to 33 %). Of course, the relative permeability of the small longitudinally laser-cut samples is already many times lower than that of the longitudinally guillotine-cut sample (compare Figs. 4.11 and 4.12). Thus, at small magnetic field strengths $H$, laser cutting deteriorates the relative permeability more than guillotine cutting, whereas the further influence due to the cutting direction is smaller.

The relative permeability of the longitudinally laser-cut specimens still show distinct extrema, in contrast to those of the transversely laser-cut small samples which exhibit more of a plateau. Thus, the relative permeabilities of the laser-cut samples loose the distinctive maximum with increasing ratio $V_{dg}/(V_{nd} + V_{dg})$ (see conclusion above in "Relative permeability") and additionally with the cutting direction deviating from the rolling direction. This is explained by a larger extent of compressive stresses (see Chapter 4.3). This behavior is most pronounced for the thinnest material (here, also the material with the largest grains)[12].

*Comparison of the two laser cutting techniques*

Also in the case of relative permeability, the two different laser cutting techniques influence the material in a similar way. The difference in absolute values which is also reflected by more shifted middle parts and knee point areas of the hysteresis curves (see Subsection "Cutting direction - Hysteresis curve") is mainly attributed to the difference in sample widths (Chapter 2.1.1) and thus to the influence of the ratio $V_{dg}/(V_{nd} + V_{dg})$. This needs to be clarified finally with the wide samples. However, the distinct extrema $\mu_{r,\,max}$ of the $CO_2$-laser cut sample is shifted to higher magnetic field strengths $H$ (see Fig. 4.12). However, this behavior does not apply for all investigated samples. It is observed that this behavior disappears as soon as the characteristic of a lost distinctive maximum becomes more apparent (see e.g. Fig. 4.12, transversely-cut samples).

---

[12]Thus, materials with large grains may be more sensitive to compressive stresses than those built up of small grains.
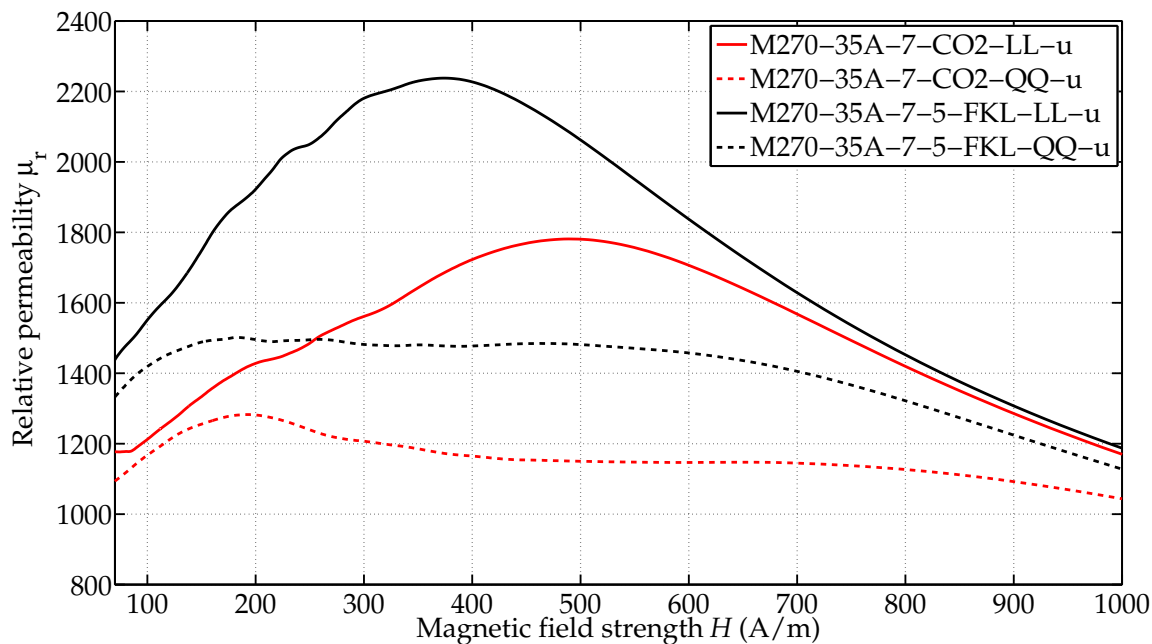
Figure 4.12: Relative permeabilities of small laser-cut samples cut into two directions.

## Cutting direction - Specific losses

### *Laser versus mechanical cutting*

The losses (computed according to Eq. (4.1)) of the small guillotine-cut samples are higher for transverse cutting direction (see Fig. 4.13). This applies for all cutting techniques (Fig. 4.14). The difference of guillotine-cut samples starts right from the beginning (loop center, see Fig. 4.13, remember the difference in loop center size (Fig. 4.8)). This is in contrast to the laser-cut specimens (see Fig. 4.14) in which the differences of cutting direction is, if at all, first obvious at magnetic flux densities above the loop center. In Subsection "Cutting direction - Hysteresis curve" it is mentioned that the hysteresis curves of the transversely guillotine-cut specimens have a larger width in the loop center than in the middle parts. This is reflected in Fig. 4.13, as the gradient of the transversely-cut specimen first increases (at low magnetic flux densities), then decreases (at medium magnetic flux densities) and subsequently again increases (at medium to high magnetic flux densities)[13]. In contrast, the gradient of the longitudinally guillotine-cut specimen increases rather continuously; as for longitudinally guillotine-cut samples the middle parts of the hysteresis curve are wider than the loop center (see Fig. 4.13). Furthermore, as mentioned above, the width of the loop center of the transversely small guillotine-cut samples is closer to the width of the transversely laser-cut specimen. This is also

---

[13]'wave' shape behavior, see p. 78.
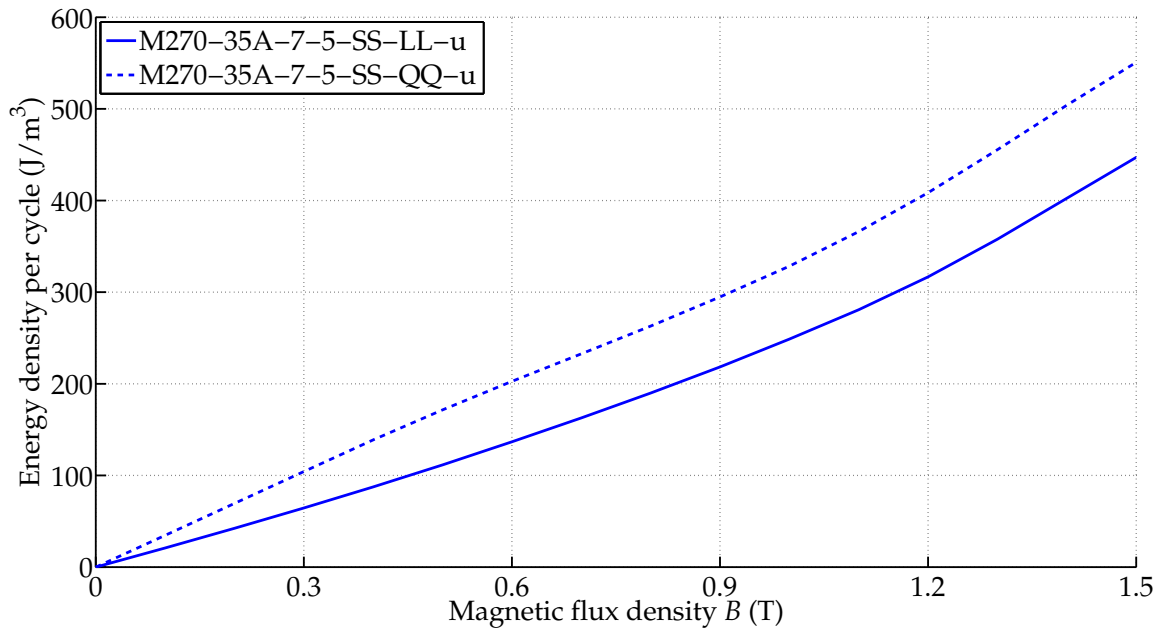
Figure 4.13: The difference in energy densities for small longitudinally and transversely guillotine-cut samples is apparent from the beginning (loop center).

confirmed by comparing Figs. 4.4 and 4.15.

The specific loss curves of the laser-cut samples have a similar characteristic as those of the transversely guillotine-cut samples (compare Figs. 4.13 and 4.14)

The 'wave' shape of the specific losses is observed for the small longitudinally and transversely laser-cut samples, as well as the small transversely guillotine-cut samples, as the loop centers of the hysteresis curves are larger than the middle parts (Figs. 4.13 and 4.14). Furthermore, the loss curves of the laser-cut samples in longitudinal and transverse cutting directions overlap at low magnetic flux densities (see Fig. 4.14). This again reflects the compliance of these two loop centers which are unaffected by the cutting direction (Fig. 4.9). The difference of energy densities between the two cutting directions of one cutting method is more pronounced for guillotine-cut samples.

Again, as for the longitudinally-cut samples, a POI of the specific losses of laser-cut and guillotine-cut samples may occur for the transversely-cut samples (Fig. 4.15).

*Comparison of the two laser cutting techniques*

In the loop center area, the computed energy densities of both small laser-cut specimens are almost identical (see Figs. 4.15 and 4.16). At medium magnetic flux densities, the energy densities of both laser-cut samples differ, but still have the same shape. Once again, it is assumed that this difference is mainly due to the
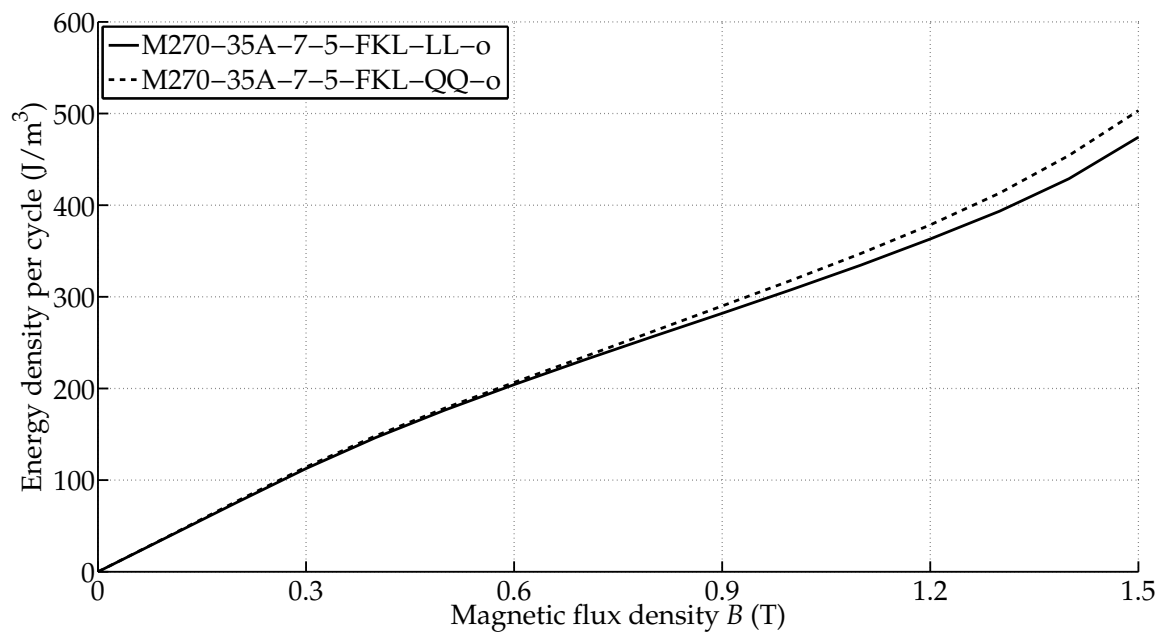
Figure 4.14: The difference in energy densities for small longitudinally and transversely laser-cut samples is first apparent for magnetic flux densities above the loop center.
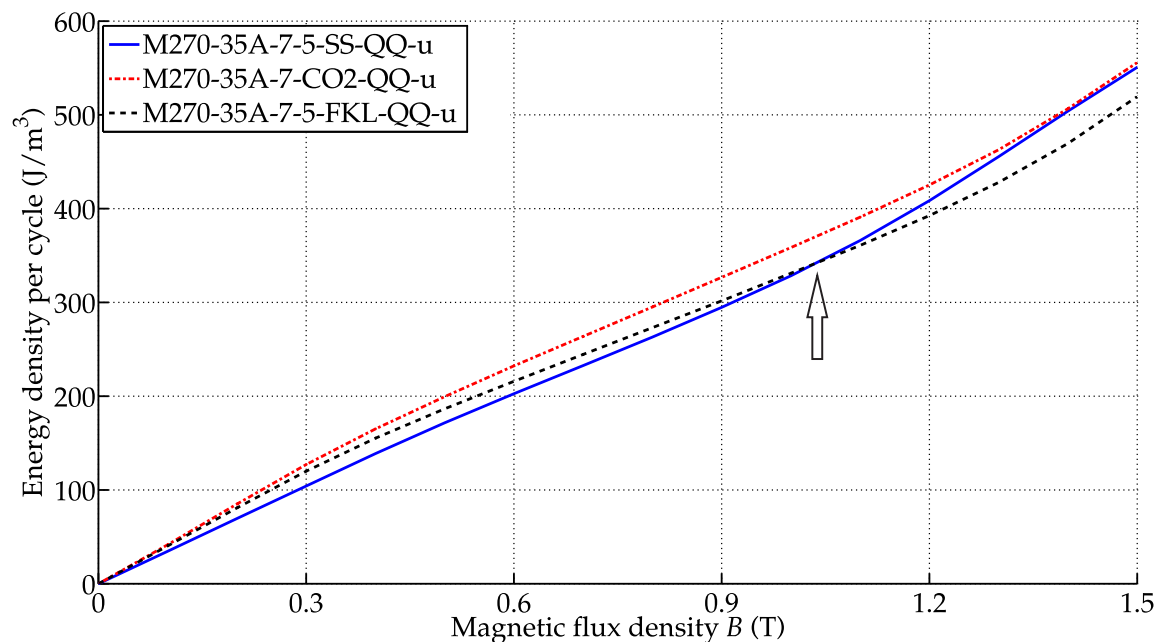


Figure 4.15: Energy densities for small transversely-cut samples, M270-35A, all cutting techniques.
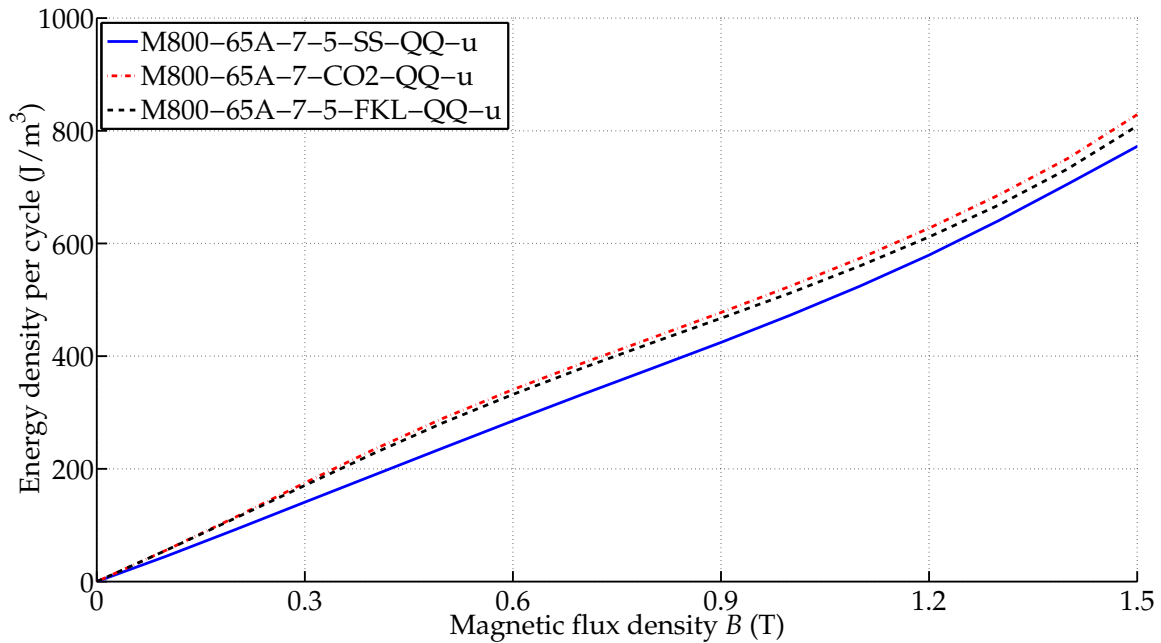
Figure 4.16: Energy densities for small transversely-cut samples, M800-65A, all cutting techniques .

different sample widths of the small laser-cut specimens. Whether this difference is also affected by the different laser cutting techniques will be investigated further in "wide samples" (see Chapter 4.1.2). The larger slopes of the small laser-cut samples at low, in contrast to medium, magnetic field strengths $H$, again reflect that the loop center area of laser-cut samples is larger than the middle parts.

The disparity mentioned between guillotine and laser-cut samples with respect to the changed cutting direction show the different deterioration effects on the magnetic material.

Conclusions - small samples:
- The thicker (here, also the smaller the grains of) the material is, the smaller the shifting of the hysteresis curves between transversely and longitudinally-cut specimens.
- Guillotine-cut samples: The hysteresis curves of the transversely-cut specimens are shifted into a clockwise direction in relation to those of the longitudinally-cut samples. Additionally, the transversely-cut probes have a wider loop center area than the longitudinally-cut specimens.
- The remanent magnetic flux densities of the *guillotine-cut* samples change strongly from the longitudinal to the transverse direction.

- The loop center areas of the small *laser-cut samples* remain unaffected by the cutting direction, but it leads to more shifted lower middle and upper middle parts as well as knee point and saturation areas.
- For small laser-cut specimens the following applies: $B_{\text{r,LL}} \approx B_{\text{r,QQ}}$.
- It applies: $\Delta\mu_{\text{r, max, guillotine, small, LL} \rightarrow \text{QQ}} > \Delta\mu_{\text{r, max, laser, small, LL} \rightarrow \text{QQ}}$.
- The distinctive maximum of $\mu_{\text{r}}$ of laser-cut samples disappears with increasing ratio $V_{\text{dg}}/(V_{\text{nd}} + V_{\text{dg}})$ and increasing deviation from the longitudinally cutting direction.
- The specific losses of transversely-cut guillotine probes are larger than those of longitudinally-cut specimens.
- As the loop center area of laser-cut samples is unaffected by the cutting direction, the specific losses of transversely-cut as well as for longitudinally-cut specimens are rather the same at low magnetic flux densities (loop center area).
- A POI of guillotine-cut and laser-cut samples may also occur for transversely-cut samples.

## 4.1.2  Wide specimens

Assuming that the deterioration depth $\delta$ of one cutting technique remains constant, the wider specimens consist of more non-deteriorated volume compared to the small samples. Therefore the ratio $V_{\text{dg}}/(V_{\text{nd}} + V_{\text{dg}})$ is smaller and the properties of the non-deteriorated volume (e.g. stress state, grain size, cutting direction) have more influence on the overall magnetic behavior, and the influence of cutting becomes, in relative terms, smaller. It can therefore be concluded that the influence and the difference between the different cutting techniques is not as clearly seen as for the small specimens.

**Hysteresis curve**

*Laser versus mechanical cutting*
The 'laser-effect' defined in Chapter 4.1.1, is no longer apparent as was the case with the small specimens (see Fig. 4.17), as expected from the smaller ratio $V_{\text{dg}}/(V_{\text{nd}} + V_{\text{dg}})$. If at all, these characteristics are only slightly noticeable for transversely-cut samples (for example Fig. 4.18), as the middle parts become thinner in comparison to the loop center and are shifted to the right, whereas the hysteresis curve of the guillotine-cut sample has a smoother transition between the hysteresis loop parts.
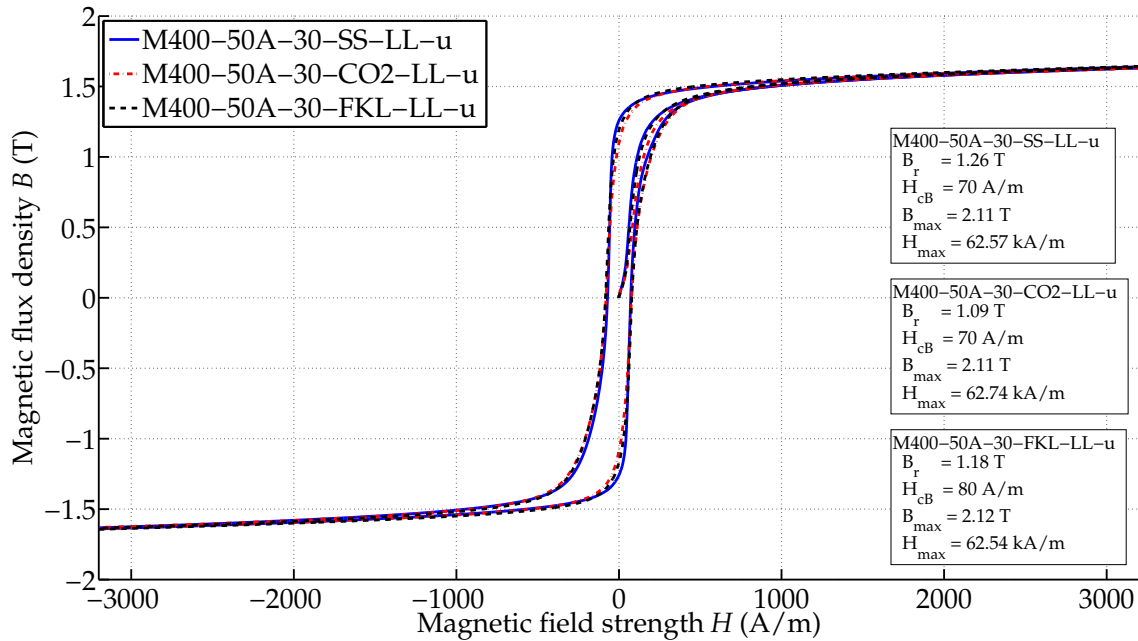
Figure 4.17: *B-H* curves for different cutting techniques, wide samples M400-50A-30-LL-u.

For longitudinally-cut wide samples no influence on the hysteresis curve of the 'laser-effect' is observed (Fig. 4.17), thus guillotine-cut as well as laser-cut samples have a more similar magnetic behavior.

However, the loop centers of the guillotine-cut samples are still thinner (in a few exceptional cases of the same width) than those of the laser-cut samples, even if not as obvious as for small samples (compare the coercive magnetic field strengths $H_c$ in the legends of the diagrams in Appendix B.1). Also, the differences between the remanent magnetic flux densities $B_r$ of guillotine-cut and laser-cut samples strongly decreased. It applies: $\Delta B_{r, small, guillotine \rightarrow laser} > \Delta B_{r, wide, guillotine \rightarrow laser}$ (compare with the tables in Appendix B.2). As for the small specimens it still applies $B_{r, guillotine-cut} > B_{r, laser-cut}$ (see Appendix B.2). The middle parts of the guillotine-cut samples are smaller than those of the laser-cut samples. The hysteresis loops of the laser-cut samples are still, albeit slightly, shifted to those of the guillotine-cut samples, which may indicate that for laser-cut samples the internal stresses are still higher (compare with [26][14] and [100]). Among other characteristics, this is reflected by the remanent flux densities $B_r$ (compare with Tables B.4, B.5 and B.6 in Appendix B.2). Furthermore, the gradients of the initial curves of the differently cut samples still differ in the loop center area, but considerably less than those of the small samples (for example, the gradient $\frac{\Delta B}{\Delta H}$ of the wide guillotine-cut sample of material

---

[14]pp. 625-626.
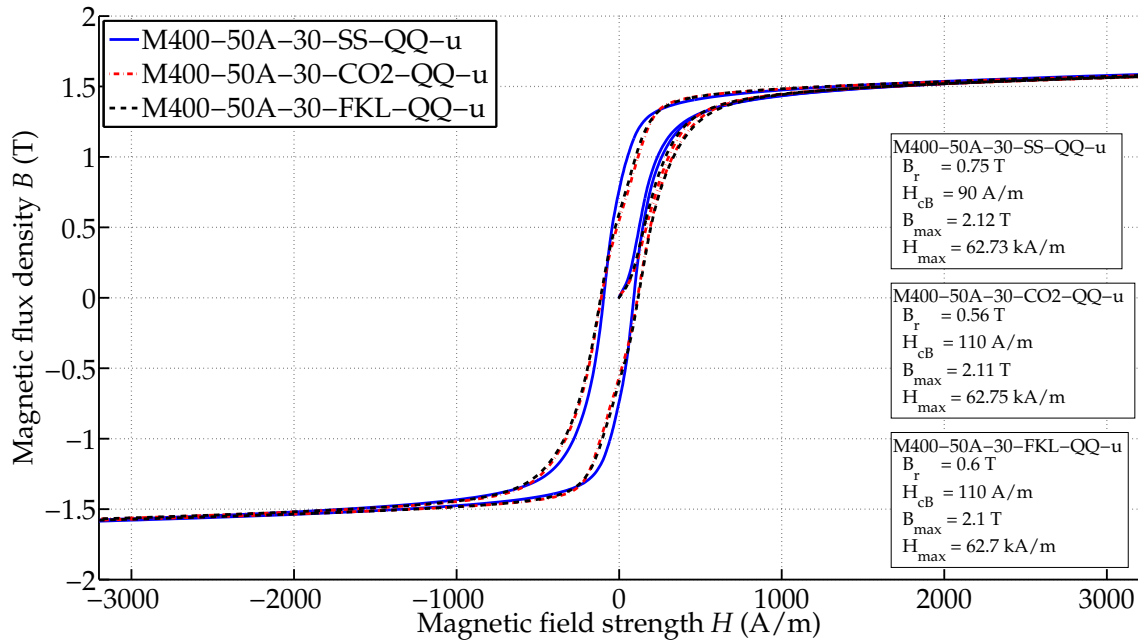
Figure 4.18: *B-H* curves for different cutting techniques, wide samples M400-50A-30-QQ-u.

M270-35A-30-LL-u is higher than the same gradient of the wide laser-cut samples by a factor of about 1.15; it is thus essentially smaller than the investigated factor for the same material but in small samples (see Chapter 4.1.1))[15]. Even at the middle parts and knee point areas, a larger gradient is expected for guillotine-cut than for laser-cut samples (further clarification in Subsection 'Relative permeability'). This larger gradient also contributes to the fact that $B_{r, \text{guillotine-cut}} > B_{r, \text{laser-cut}}$.

The hysteresis loops are widened with increasing material thickness (here, also with decreasing grain size)[16](see Appendix B.1). For M800-65A at (high) saturation areas, the wide FKL-laser cut specimens reach higher magnetic flux densities for the same magnetic field strengths $H$ as the guillotine-cut or $CO_2$-laser cut samples. This is in accordance with the small samples (see Chapter 4.1.1). However, for material M270-35A the guillotine-cut samples reach higher magnetic flux densities $B$ at high saturation than the laser-cut samples. This is in contrast to the results of the small samples (Chapter 4.1.1), in which guillotine-cut samples always approach the smallest magnetic flux density $B$ at high magnetic field strength $H$ compared to laser-cut samples. As will be discussed in Chapter 4.2, the effect of increasing ratio $V_{\text{dg}}/(V_{\text{nd}} + V_{\text{dg}})$ leads, in the case of guillotine-cut samples, to a decreased magnetic flux density in the saturation area. This is in contrast to laser-cut samples (Chapter 4.2). Therefore, it might occur that some wide guillotine-cut samples reach

---

[15]For transversely-cut samples this shifting is larger than for longitudinally-cut samples.

[16]Smaller grains provide larger hysteresis losses (see Fig. 1.12) and thus the hysteresis loop is widened.

larger magnetic flux densities than the FKL-laser cut samples and in the case of small samples, lower magnetic flux densities $B$ compared to those of the laser-cut specimens. For M400-50A, the longitudinally FKL-laser cut samples reach higher magnetic flux densities $B$ at high magnetic field strengths $H$ than the guillotine-cut samples. This behavior reverses for the transversely-cut samples. The $CO_2$-laser cut samples always reach smaller magnetic flux densities than the guillotine-cut and FKL-laser cut samples. This applies to all three investigated materials. Overall, for both wide and small samples it applies: $B(H_{\text{saturation}})_{\text{FKL}}, B(H_{\text{saturation}})_{\text{guillotine}} > B(H_{\text{saturation}})_{\text{CO}_2}$.

In the case of material M270-35A, the hysteresis loops of wide laser-cut and guillotine-cut samples differ least. Especially in the case of the wide transversely-cut samples of M400-50A, the largest differences are observed (Fig. 4.18).

*Comparison of the two laser cutting techniques*
A closer look at all measured hysteresis loops of both wide laser-cut samples shows that the hystersis curves of the $CO_2$-laser cut samples are slightly more shifted to those of the the guillotine-cut samples than those of the FKL-samples. With one exception (M800-65A-30-LL-o), this applies to all wide measured samples (compare with Appendix B.1). Thus, the remanent magnetic flux densities $B_r$ of $CO_2$-laser cut samples are smaller than (or equal to) those of FKL-laser cut samples, although both laser-cut samples have the same width (see Chapter 2.1.1). Thus, the larger shifting of the hysteresis curves of the wide $CO_2$-laser cut samples indicates that this behavior is not only due to differences in sample width, as previously assumed in Chapter 4.1.1, but also due to the cutting technique itself. However, for the most part, the difference between guillotine-cut and laser-cut samples is much higher.

In most cases, the coercive magnetic field strengths $H_c$ of the wide FKL-laser and $CO_2$-laser cut samples are about the same. Thereafter, the coercive magnetic field strengths of the $CO_2$-laser cut samples are rather larger than those of the FKL-laser cut samples. The same behavior of $B_r$ and $H_c$ was observed with the small laser-cut samples (compare with Chapter 4.1.1). However, for small laser-cut samples this was still attributed to the difference in sample width. As the same characteristic is now observed for the wide laser-cut samples (identical sample width!), it is attributed to the different cutting techniques.

The FKL-laser cut samples reach higher magnetic flux densities $B$ for the same magnetic field strength $H$ than the $CO_2$-laser cut samples at high saturation areas. This is in accordance with the results of the small samples. Thus, this observation is also attributed to the difference in cutting technique.
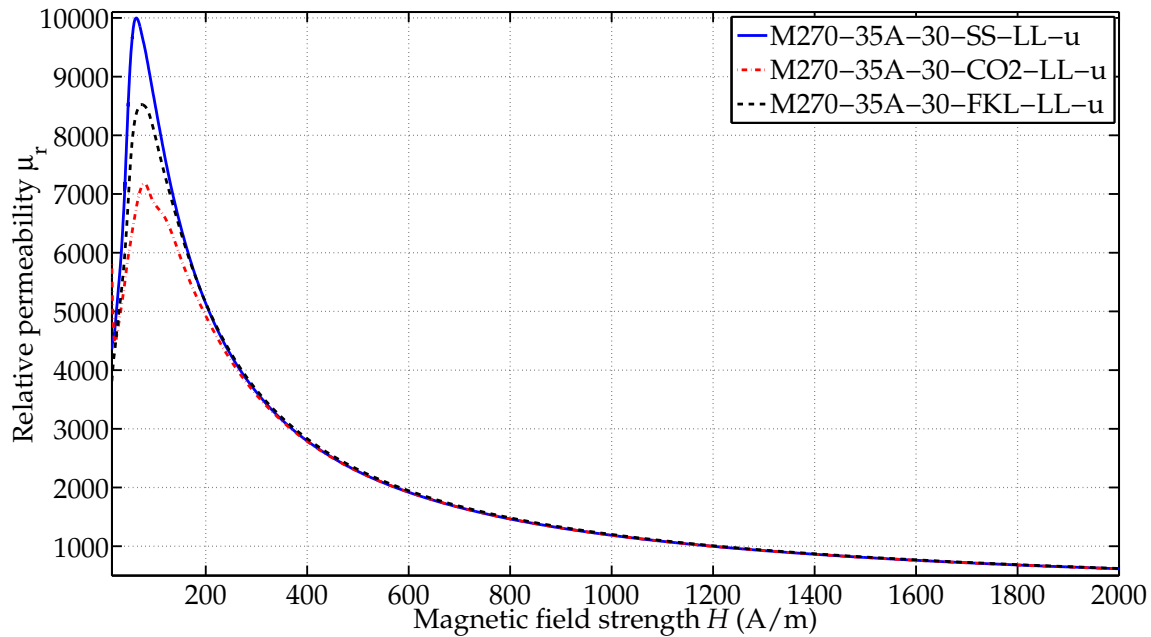
Figure 4.19: Relative permeability for different cutting techniques.

**Relative permeability**

*Laser versus mechanical cutting*

The following applies to the maxima of the relative permeability (see Fig. 4.19): $\mu_{r,max,guillotine} > \mu_{r,max,laser}$. This is in line with the results of the small samples (Chapter 4.1.1). Also a POI occurs in the range of 160 to 800 A/m (again depending on the type of material and cutting direction), where the relative permeability of guillotine-cut samples is smaller than that of the laser-cut samples. However, the POI of guillotine-cut and $CO_2$-laser cut samples occurs at larger magnetic field strengths $H$ than those with the FKL-laser cut specimens (in line with small samples), but near to the POI of guillotine-cut and FKL-laser cut samples. In most cases with wide samples, it appears at lower magnetic field strengths $H$ than with small samples (hysteresis curves of the small samples are relatively more shifted to those of the guillotine-cut samples as in the case of the wide samples).

Furthermore, $\mu_{r,max}$ is shifted to higher magnetic field strengths $H$, the smaller the extrema (see Figs.4.19 and B.22). This behavior is in line with the small samples, as long as a distinctive maximum exists.

Both, for wide laser-cut as well as for wide guillotine-cut samples, distinctive maxima of the relative permeabilities occur (Fig. 4.19). This distinctive maximum for laser-cut samples disappears with increasing ratio $V_{dg}/(V_{nd} + V_{dg})$ and with cutting direction deviating from the rolling direction (see small samples in Chapter 4.1.1).

The relative permeabilities of laser-cut and guillotine-cut samples at smaller mag-

netic field strengths $H$ (maximum area) differ significantly[17]. The field strength $H$ where both relative permeabilities of wide laser-cut as well as guillotine-cut samples only differ less than 50 is above 500 A/m for all three investigated materials. The same applies for the small samples (see Chapter 4.1.1): above the range of 700 A/m, hardly any difference for the relative permeabilities ($\Delta\mu_r \leq 50$) is observed.

*Comparison of the two laser cutting techniques*

The following applies for all measured wide samples: $\mu_{r, max, FKL} > \mu_{r, max, CO_2}$. Additionally, the extrema of the $CO_2$-laser cut samples occur at higher magnetic field strengths $H$ than those of the FKL-laser cut samples. In Chapter 4.1.1 the order of the maximum permeabilities was referred to as the difference in samples widths. Here, all samples have the same width, wherefore the different degrading effects on the relative permeability are additionally attributed to the cutting techniques themselves. Thus, the $CO_2$-laser cutting technique has a larger degrading impact on the relative permeability than the FKL-laser technique. This difference is especially significant in the range of 0 to 500 A/m.

**Specific losses**

*Laser versus mechanical cutting*

The computed energy densities of the wide guillotine-cut samples are smaller than those of the wide laser-cut samples (Fig. 4.20). The POIs of the guillotine- and the laser-cut curves occur only in some cases, in contrast to the case of the small specimens. With increasing ratio $V_{dg}/(V_{nd} + V_{dg})$ the occurrence of these POIs increases. In Fig. 4.4, a significant difference between the loss curves of longitudinally laser-cut and guillotine-cut samples was obvious, as the loop center area of small laser-cut specimens is wider than the rest of the curve. The same material, but with larger sample width, is now presented in Fig. 4.20. Here, this previously observed 'wave' shape characteristic for the small laser-cut samples is hardly observed for the wide samples (see Figs. 4.20 and 4.22, compare with Chapter 4.1.2, Subsection 'Hysteresis curve'), as the dominant 'laser-effect' has disappeared on the longitudinally wide samples (see Chapter 4.1.2, 'Hysteresis curve'). Instead of the 'wave' shape on the longitudinally laser-cut samples, a more 'linear' shape occurs at moderate flux densities (Figs. 4.20 and 4.22). For transversely-cut samples (see Fig. 4.21) this 'wave' shape characteristic still exists (slightly) and is in accordance with Chapter 4.1.2, Subsection 'Hysteresis curve'[p. 92]. However, in the case of longitudinally-cut samples,

---

[17]Note, each difference $\Delta\mu_r \geq 50$ is considered "significant" here. Of course, this definition depends on the application.
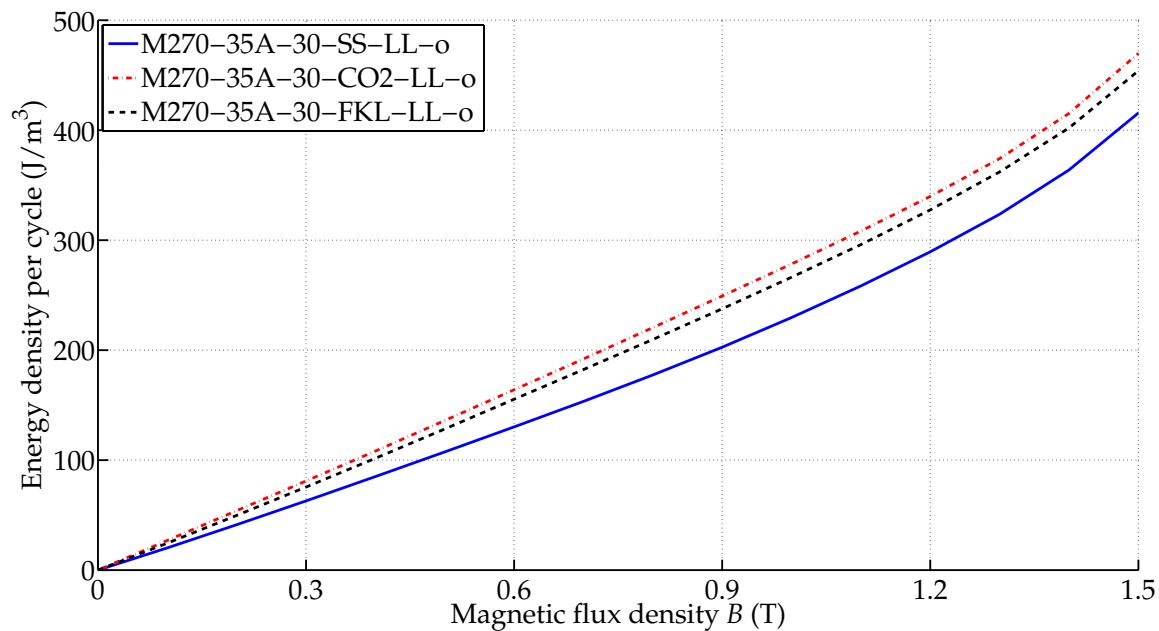
Figure 4.20: Energy densities of the hysteresis curves over the magnetic flux density *B*, wide samples M270-35A-30-LL-o.

the loss behavior between the guillotine-cut and the laser-cut samples still differs: The shape of the loss curves of the longitudinally guillotine-cut samples is still more curved (Figs. 4.20 and 4.22).

*Comparison of the two laser cutting techniques*

The characteristics of the energy densities of the wide $CO_2$-laser and FKL-laser cut samples are again very similar (same shape), in line with the results obtained for the small samples.

However, in most cases (concerning all measurements of the wide samples) the $CO_2$-laser cut specimens have (slightly) larger energy densities and thus specific losses than the FKL-laser cut samples (see Figs. 4.20 and 4.22). The few exceptions (three exceptions in total from all measured wide samples) are contributed to the fault tolerance of the filtering and calculation method of the hysteresis curve areas. This difference concerning the different cutting technique is in most cases relatively small (see Figs. 4.20 and 4.22).

Thus again, the difference in specific losses of $CO_2$-laser and FKL-laser cut samples is not only a consequence of different sample widths (as assumed for the small samples), but also a consequence of the cutting technique itself. Thus, the different laser cutting techniques degrade the specific losses to a different extent. It is expected that this difference due to the cutting technique will disappear with higher frequencies (to be investigated in Chapter 5).
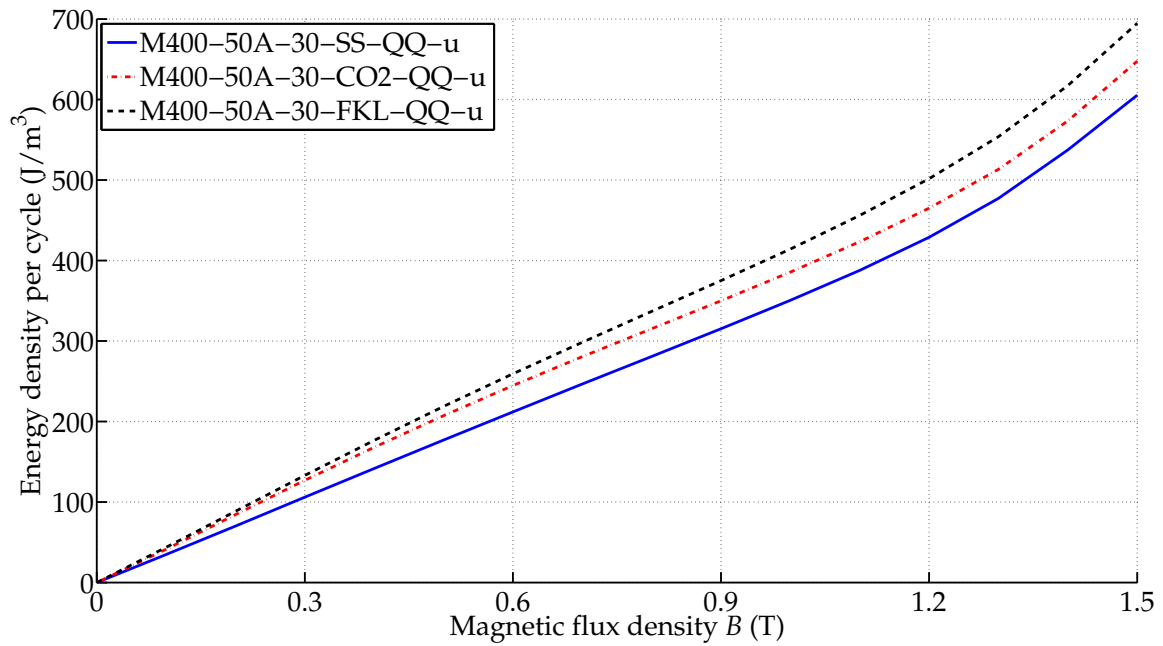
Figure 4.21: Energy densities of the hysteresis curves over the magnetic flux density $B$, wide samples M400-50A-30-QQ-u.
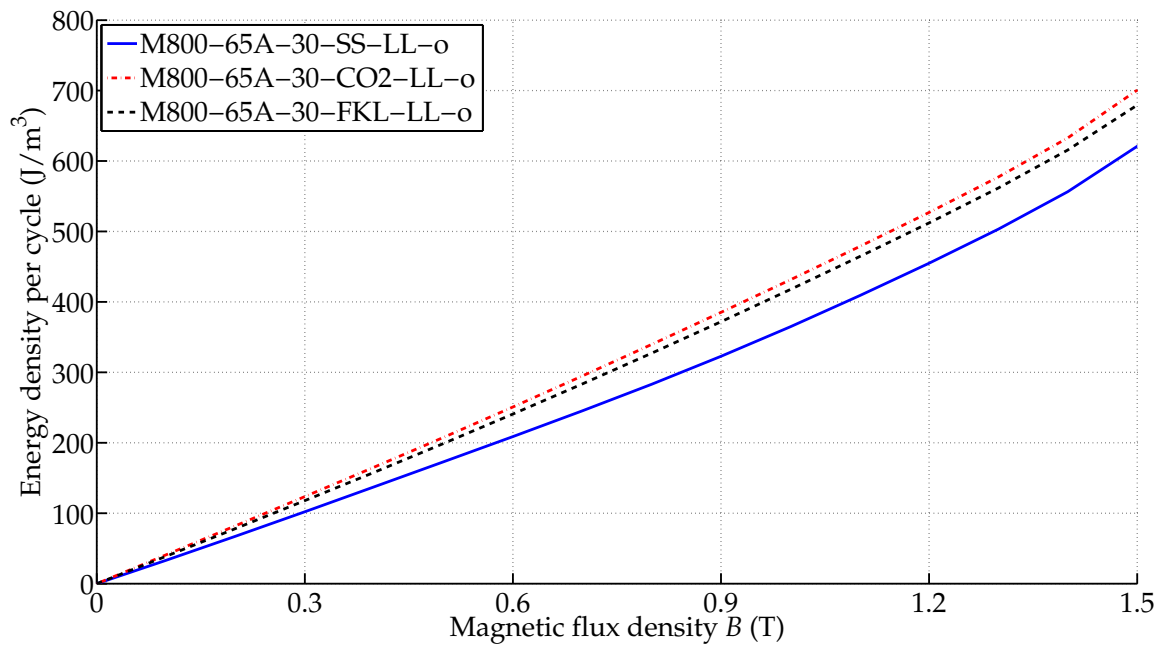


Figure 4.22: Energy densities of the hysteresis curves over the magnetic flux density $B$, wide samples M800-65A-30-LL-o.

Conclusions - wide samples:

- The laser-effect is not as clearly visible as for the small specimens, as this effect reduces with increasing ratio $V_{dg}/(V_{nd} + V_{dg})$.
- It applies: $B_{r,\text{guillotine-cut}} > B_{r,\text{laser-cut}}$.
- The following applies: $B_{r,CO_2} \leq B_{r,FKL}$ and $H_{c,CO_2} \approx H_{c,FKL}$.
- The hysteresis curves of the $CO_2$-laser-cut samples are slightly more shifted than those of the FKL-laser cut samples.
- It applies: $\mu_{r,\text{max, guillotine}} > \mu_{r,\text{max, FKL}} > \mu_{r,\text{max, }CO_2}$. In the same order the maximum is shifted to higher magnetic field strengths $H$.
- The energy densities of the guillotine-cut sample are smaller than those of the laser-cut samples. POIs occur only rarely.
- The characteristics of the energy densities of both laser-cut samples are rather close, but in most cases these energy densities are larger for $CO_2$-laser-cut samples.
- Overall, the $CO_2$-laser cutting technique deteriorates the magnetic properties more than the FKL-laser technique. The relative permeability at small magnetic field strengths $H$ is affected most. The influence on the losses and the characteristic data of the hysteresis curve is much smaller.

**Cutting direction - Hysteresis curve**

*Laser versus mechanical cutting*

The wide guillotine-cut as well as the laser-cut samples show a larger loop center area for transversely-cut samples in contrast to longitudinally-cut samples (see Figs. 4.24 – 4.26). Thus, the transversely-cut specimens have a larger loop center and in reference to this a thinner middle part and the longitudinally-cut samples have a thinner loop center part than the lower knee point areas (see Figs. 4.23, 4.24 and 4.26). Overall, the hysteresis loops of both guillotine-cut as well as laser-cut samples become more similar with decreasing ratio $V_{dg}/(V_{nd} + V_{dg})$ (the influence of laser-effect disappears). Thus, the differences in loop center size of laser-cut and mechanically-cut samples are in the same range for longitudinally-cut as well as transversely-cut samples. This is in contrast to the small samples, in which a significant difference of the loop center widths of the laser-cut and guillotine-cut samples is observed for the investigated longitudinally-cut strips (see Chapter 4.1.1). Therefore, it also applies: $\Delta B_{r,\text{guillotine, LL, wide} \to \text{small}} < \Delta B_{r,\text{laser, LL, wide} \to \text{small}}$. Furthermore, the loop center area of laser-cut samples no longer remains unchanged for different cutting directions as with the small samples (see Chapter 4.1.1). Thus, the change of remanent magnetic

flux density $B_r$ of wide samples from longitudinal to transverse direction is considerably larger than that of the small samples ($\Delta B_{r,\text{ laser, small, LL} \rightarrow \text{QQ}} \ll \Delta B_{r,\text{ laser, wide, LL} \rightarrow \text{QQ}}$, see as well Appendix B.2). This is again explained by the small ratio $V_{dg}/(V_{nd} + V_{dg})$: The deterioration introduced by the laser reduces the influence of the cutting direction.



(a) M270-35A-30-SS-LL-o

(b) M270-35A-30-FKL-LL-o
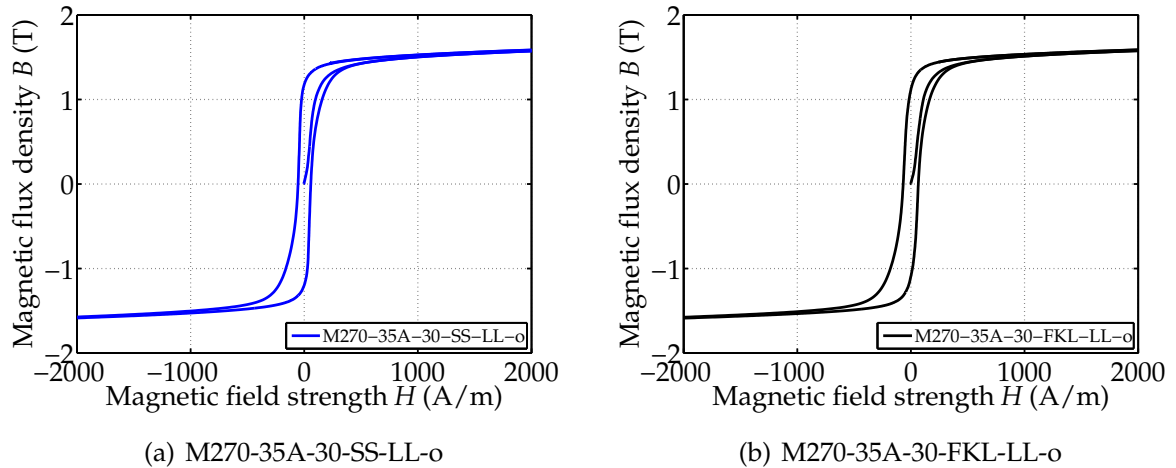
Figure 4.23: The longitudinally-cut wide samples have a thinner loop center than the width at the lower knee point areas.

As for the small samples, the hysteresis curves of the transversely-cut samples are shifted into a clockwise direction to those of the longitudinally-cut samples (see Figs. 4.24 and 4.26). This shifting is less pronounced for material M800-65A and more pronounced for M400-50A (absolute values are compared). Furthermore, the shifting with regard to the vertical axis is larger for the small than for the wide samples, notably for the laser-cut samples. This behavior is again explained by the ratio $V_{dg}/(V_{nd} + V_{dg})$. With this shifting also the remanent magnetic flux density $B_r$ decreases for both laser-cut as well as guillotine-cut samples (see Appendix B.2). This is in contrast to the small laser-cut samples in which the remanent flux density is not influenced by the cutting direction, as the loop center area is "fixed" (see Chapter 4.1.1).

*Comparison of the two laser cutting techniques*

The hysteresis curves of the transversely wide $CO_2$-laser cut samples are slightly more shifted into a clockwise direction, in contrast to those of the wide FKL-laser cut specimens. Therefore, the remanent flux densities $B_r$ of the FKL-laser cut samples are larger for both cutting directions than those of the $CO_2$-laser cut samples, see Appendix B.2.
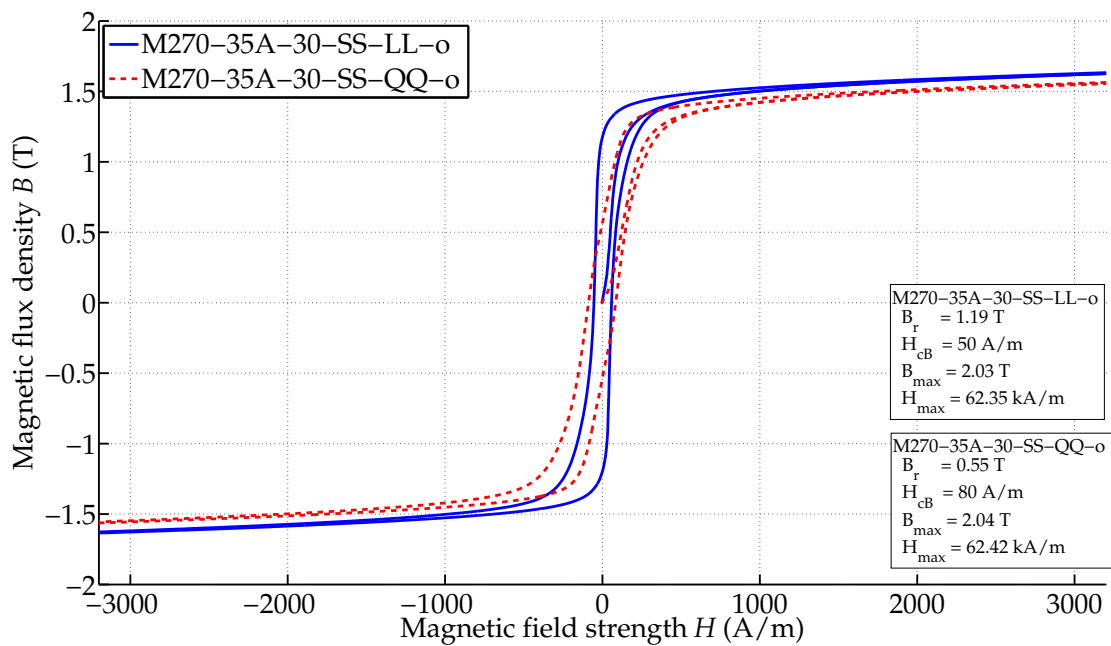
Figure 4.24: Comparison of wide longitudinally and transversely guillotine-cut samples, M270-35A-30-SS-o.
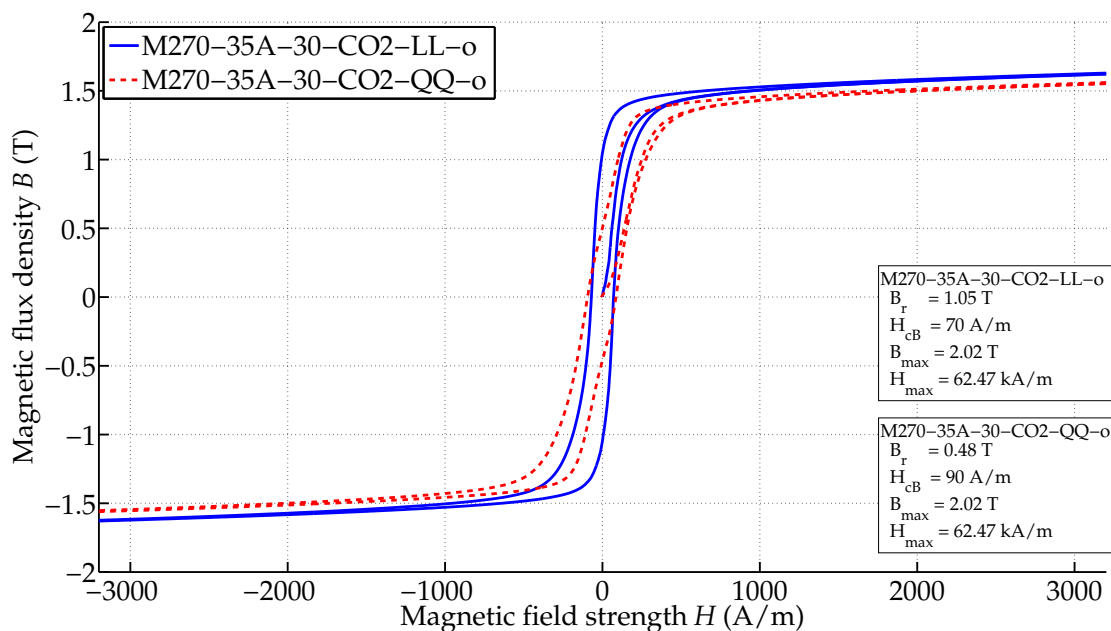


Figure 4.25: Comparison of wide longitudinally and transversely CO$_2$-laser cut samples, M270-35A-30-CO$_2$-o.
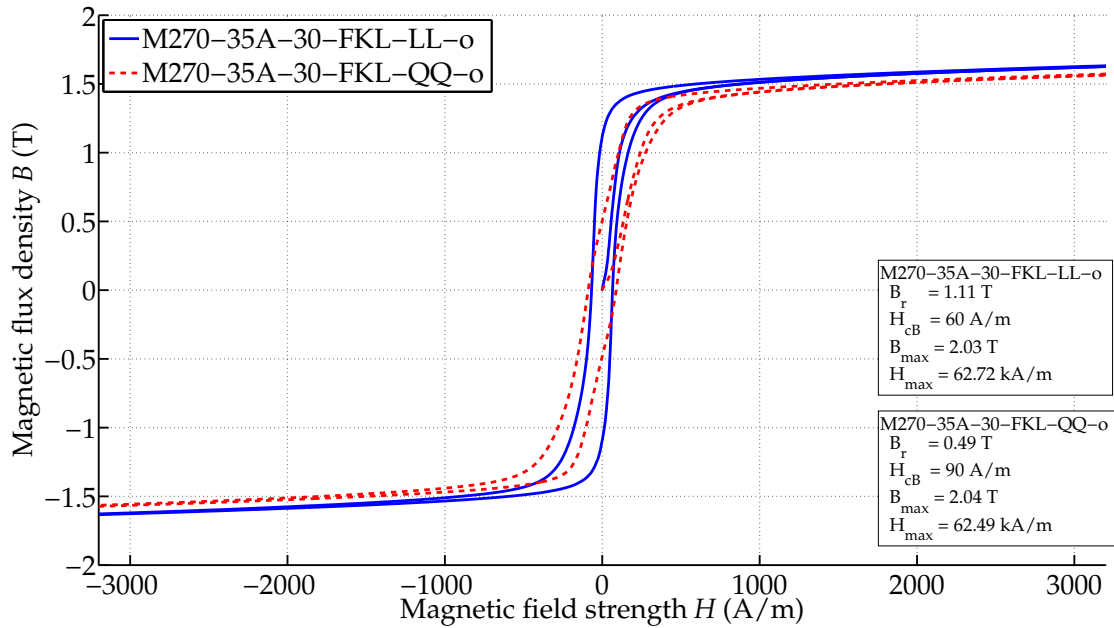
Figure 4.26: Comparison of wide longitudinally and transversely FKL-laser cut samples, M270-35A-30-FKL-o.

**Cutting direction - Relative Permeability**

*Laser versus mechanical cutting*

As for the small samples, the maximum relative permeabilities of the wide samples decrease from longitudinal to transverse cutting direction for both guillotine-cut as well as laser-cut samples (see Figs. 4.27 and 4.28). Again, it applies: $\Delta\mu_{r, max, guillotine, LL \rightarrow QQ} > \Delta\mu_{r, max, laser, LL \rightarrow QQ}$ (absolute values), but with less intensity than for the small samples. The relative permeability still shows a maximum, even for the transversely laser-cut specimens, even if not as obvious as for the longitudinally-cut samples (see Fig. 4.28), but also no plateau (compare with Chapter 4.1.1, small specimens). This confirms the assumption that the distinct extremum disappears with increasing ratio $V_{dg}/(V_{nd} + V_{dg})$ and additionally with cutting direction.

Again, the maxima of the relative permeabilities of the transversely guillotine-cut samples are shifted to larger magnetic field strengths $H$ compared to those of the longitudinally-cut samples. This is in line with the small samples and applies to all guillotine-cut samples.

*Comparison of the two laser cutting techniques*

In the case of M400-50A (see Fig. 4.28), the relative permeabilities of $CO_2$-laser cut samples are rather an image of the relative permeabilities of the FKL-laser cut
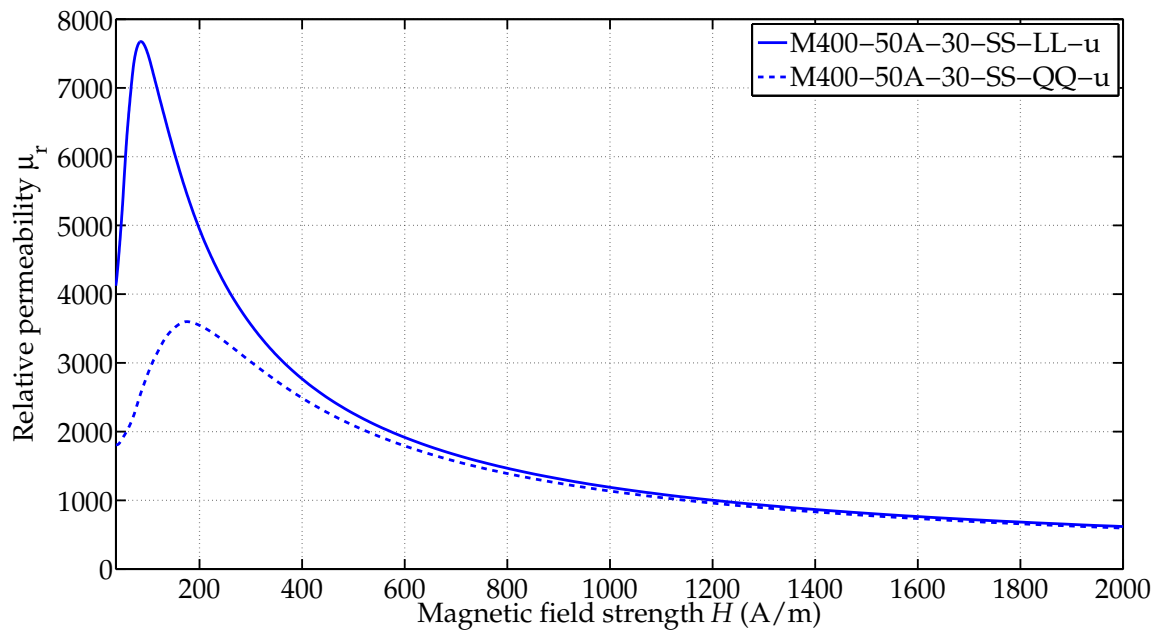
Figure 4.27: Relative permeability of wide guillotine-cut samples in two directions.
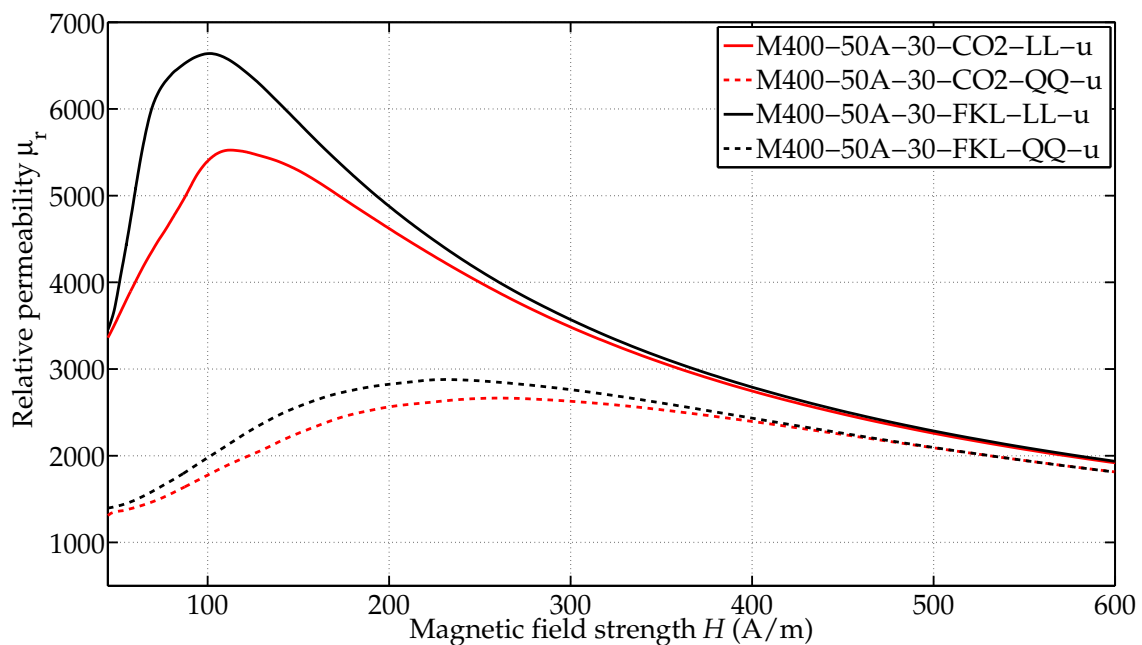


Figure 4.28: Relative permeability of wide laser-cut samples in two directions.

samples with the difference that they are shifted to smaller relative permeabilities $\mu_r$ and larger magnetic field strengths $H$. This is observed for all investigated wide samples.

For the wide laser-cut samples it also applies that with larger deviation from the longitudinal cutting direction, the maxima of the relative permeability are shifted to larger magnetic field strengths $H$, as long as a distinctive maximum exists (compare with small samples). However, in the case of the small transversely-cut samples, the distinct maximum is lost.

Both wide laser-cut samples consist of the same sample width. As the maxima of the relative permeabilities of the two laser-cut samples still differs significantly, this difference is attributed to the cutting technique itself and not only to the sample width as postulated in Chapter 4.1.1.

**Cutting direction - Specific losses**

*Laser versus mechanical cutting*
As with the small specimens, the energy densities of the wide transversely-cut samples are larger than those of the wide longitudinally-cut samples for both guillotine-cut as well as laser-cut samples (see Figs. 4.29 and 4.30), for all magnetic field strengths $H$. Especially, in the case of laser-cut samples, this is in contrast to the small samples (see Chapter 4.1.1) in which the energy densities of both cutting directions are the same at small magnetic flux densities $B$ (loop center area). The wide transversely-cut specimens have a wider loop center than the width at the middle parts (see Subsection "Cutting direction-Hysteresis curve"[p. 100]), wherefore the energy density at low magnetic flux densities $B$ first increases more, then, at medium magnetic flux densities, increases less and finally increases again more ('wave'-shape, see Figs. 4.29 and 4.30). This applies to all investigated cutting techniques of wide transversely-cut samples and is in line with the behavior of the small samples (see Chapter 4.1.1). However, this effect decreases with increasing material thickness (here, also with decreasing grain size).

*Comparison of the two laser cutting techniques*
In contrast to the small specimens, the loop centers of the wide longitudinally and transversely laser-cut samples do not remain constant (see Fig. 4.26), wherefore also the energy densities of these samples differ from the beginning (see Fig. 4.30). This applies for all wide investigated samples.
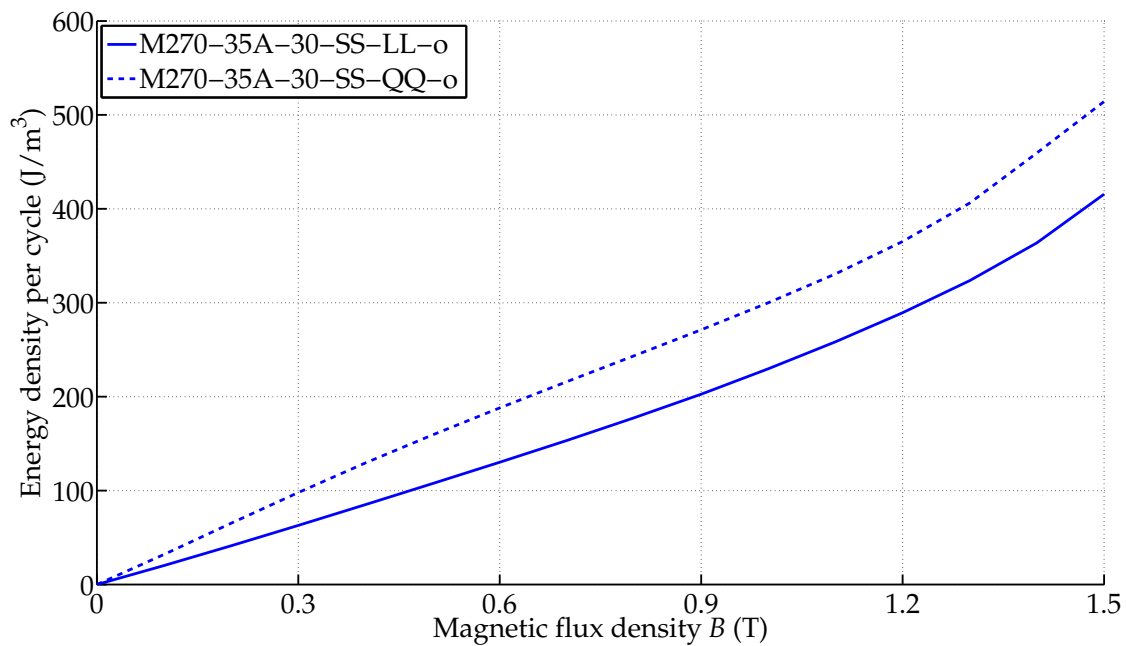
Figure 4.29: Energy densities for wide longitudinally and transversely guillotine-cut samples.
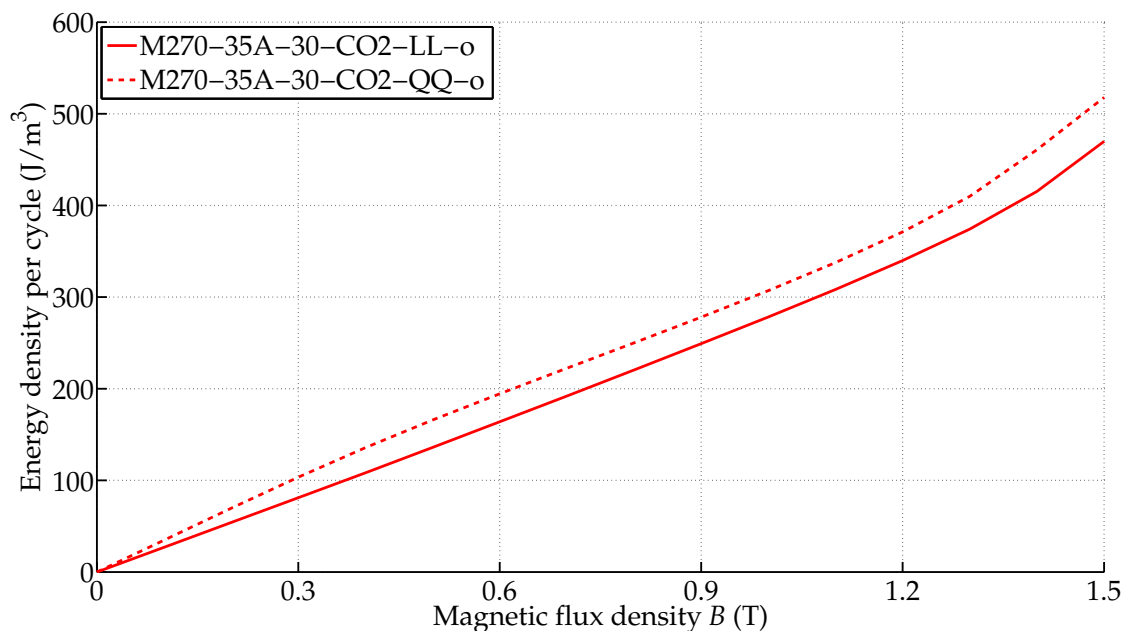


Figure 4.30: Energy densities for wide longitudinally and transversely laser-cut samples.

Conclusions - wide samples:

- Wide longitudinally-cut specimens: loop center is thinner than the width at the lower knee point areas; wide transversely-cut specimens: loop center is wider than the rest of the hysteresis loop.
- For wide laser-cut specimens it applies: $B_{r,LL} \neq B_{r,QQ}$.
- The loop center part of wide laser-cut specimens depends on the cutting direction.
- The whole hysteresis loop of the transversely laser-cut specimens is shifted into a clockwise direction compared to the longitudinally-cut sample, in contrast to the small specimens.
- Comparing wide samples to the small specimens, the hysteresis curves of the small laser-cut specimens are more shifted into a clockwise direction and a specific laser-effect is observed which influences the hysteresis loop dramatically.
- It applies: $\Delta\mu_{r, \text{max, guillotine, LL} \rightarrow QQ} > \Delta\mu_{r, \text{max, laser, LL} \rightarrow QQ}$.
- The differences of relative permeability $\mu_r$ of small laser-cut samples for longitudinally and transversely-cut samples is smaller than for wide laser-cut samples at smaller magnetic field strengths $H$. Thus, for small samples, at small $B$, the effect of cutting direction is impaired by the laser-effect.

## 4.2 Influence of the ratio $V_{dg}/(V_{nd} + V_{dg})$

In the following, the particular influence of the ratio $V_{dg}/(V_{nd} + V_{dg})$ is investigated in further detail.

**Hysteresis curve**

*Laser versus mechanical cutting*
The larger the ratio $V_{dg}/(V_{nd} + V_{dg})$ is, the more the knee point and saturation areas of the hystersis curve of the guillotine-cut samples are shifted to lower magnetic flux densities $B$ and the remanent flux densities $B_r$ decrease as well (see Figs. 4.31 and B.23 in Appendix B.4). Furthermore, the knee point areas experience a slight shifting to higher magnetic field strengths $H$, which comes along with the increasing relative amount of internal stresses. The loop center slightly increases with increasing ratio $V_{dg}/(V_{nd} + V_{dg})$ (compare the coercive magnetic field strengths $H_c$ in Figs. 4.31 and B.23 in Appendix B.4) but is not shifted.

In contrast, the increasing ratio $V_{dg}/(V_{nd} + V_{dg})$ induces a shifting of the knee
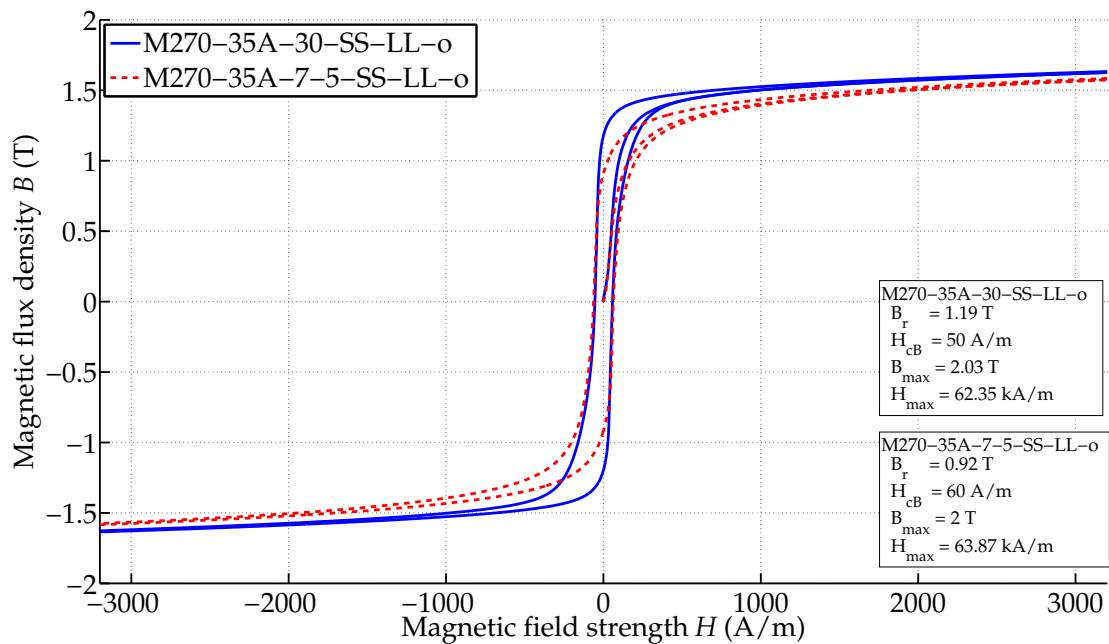
(a) M270-35A
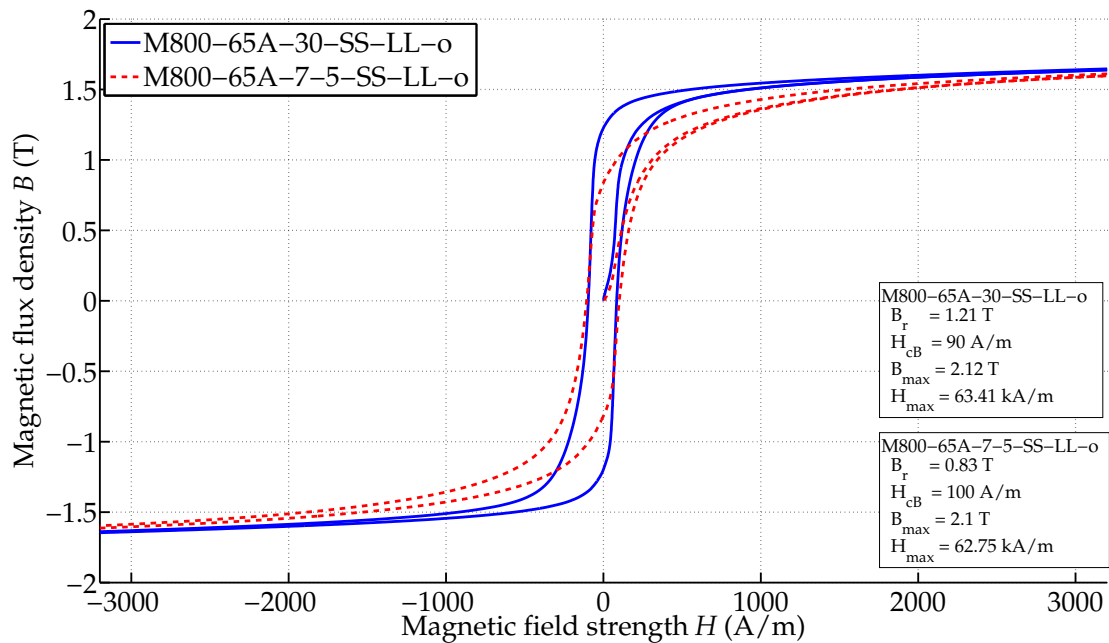


(b) M800-65A

Figure 4.31: Effect of ratio $V_{dg}/(V_{nd} + V_{dg})$ on the magnetic flux density of longitudi-
nally guillotine-cut samples.

point areas to higher magnetic field strengths $H$ on the laser-cut samples (see Figs. 4.32 and B.24 in Appendix B.4), but(!) not to (remarkably) smaller magnetic flux densities $B$ (compare with Figs. B.23 and 4.31). Thus, the *B-H* curve at high saturation (and thus the last part of the domain rotation region) is unaffected by the ratio $V_{dg}/(V_{nd} + V_{dg})$ for laser-cut samples. This applies to all investigated materials and cutting directions. The increasing ratio $V_{dg}/(V_{nd} + V_{dg})$ also affects the middle parts (strongly) as well as the loop center areas by a shifting (see Figs. 4.32 and B.24). For all investigated samples, the loop center area is more shifted for longitudinally laser-cut samples, whereas the middle parts are more shifted for transversely laser-cut samples with increasing ratio $V_{dg}/(V_{nd} + V_{dg})$.

For both guillotine-cut as well as laser-cut samples it applies: $B_{r,wide} > B_{r,small}$. However, this effect is most pronounced for longitudinally-cut samples.

### *Comparison of the two laser cutting techniques*

The previously mentioned characteristics are observed for both FKL-laser and $CO_2$-laser cut samples (see Figs. B.25, B.26, 4.32 and B.24). The middle parts and knee point areas of the small $CO_2$-laser cut samples are more shifted to higher magnetic field strengths $H$ than those of the FKL-laser cut samples mainly due to the difference in width of small laser-cut samples. Apart from that, no further differences are observed.

## Relative permeability

### *Laser versus mechanical cutting*

The relative permeability $\mu_r$ of guillotine-cut samples is decreased at low magnetic field strengths $H$. In the area of saturation, the effect of the ratio $V_{dg}/(V_{nd}+V_{dg})$ on the relative permeability is negligible (compare Figs. 4.31, 4.33 and B.23). This difference is smaller for transversely-cut than for longitudinally-cut samples (see Fig. 4.33).

The relative permeability $\mu_r$ strongly decreases with increasing ratio $V_{dg}/(V_{nd} + V_{dg})$ for laser-cut samples at low magnetic field strengths $H$ (see Fig. 4.34). The relative permeabilities of wide and small laser-cut samples approach faster at smaller magnetic field strengths $H$ than those of the guillotine-cut samples (see Figs. 4.33 and 4.34).

With increasing ratio $V_{dg}/(V_{nd} + V_{dg})$ the difference of transversely and longitudinally-cut samples decreases (see Figs. 4.35 and 4.36). This effect is stronger for laser-cut than for guillotine-cut samples. Furthermore, the change of $\mu_r$ of wide to small transversely guillotine-cut samples is smaller than in the case of laser-cut samples (Figs. 4.35 and 4.36).
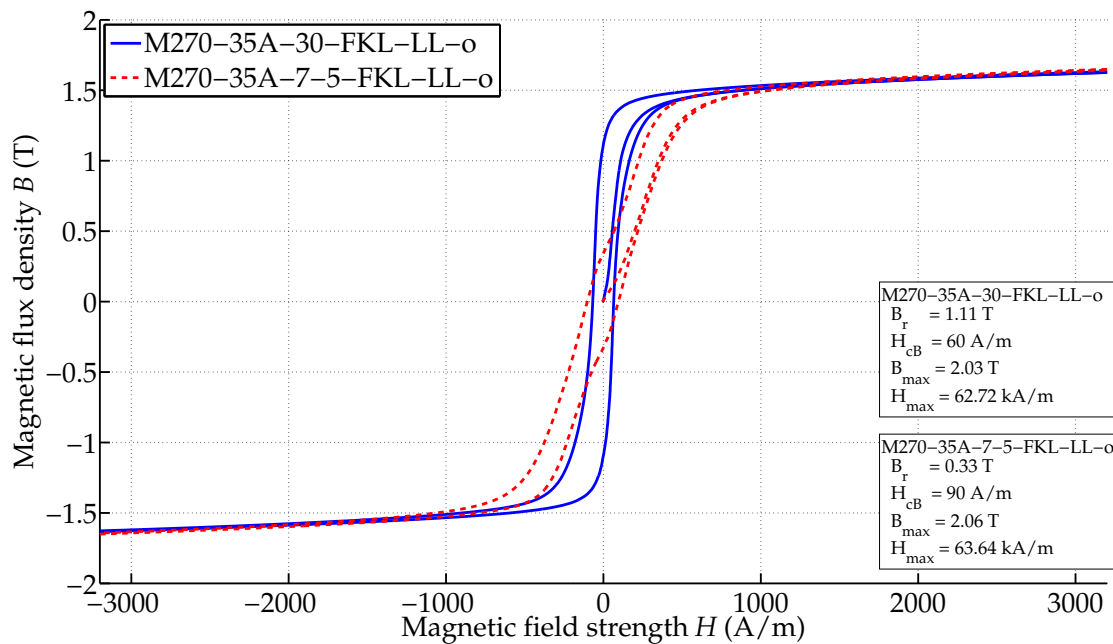
(a) M270-35A
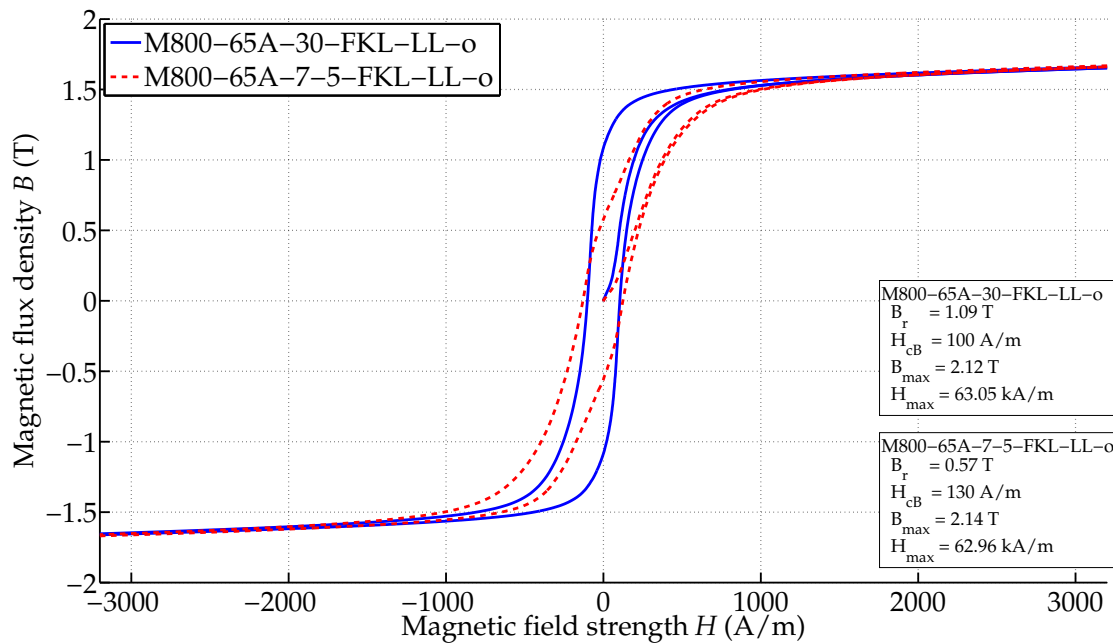


(b) M800-65A

Figure 4.32: Effect of ratio $V_{dg}/(V_{nd} + V_{dg})$ on the magnetic flux density of longitudi-
nally FKL-laser cut samples.
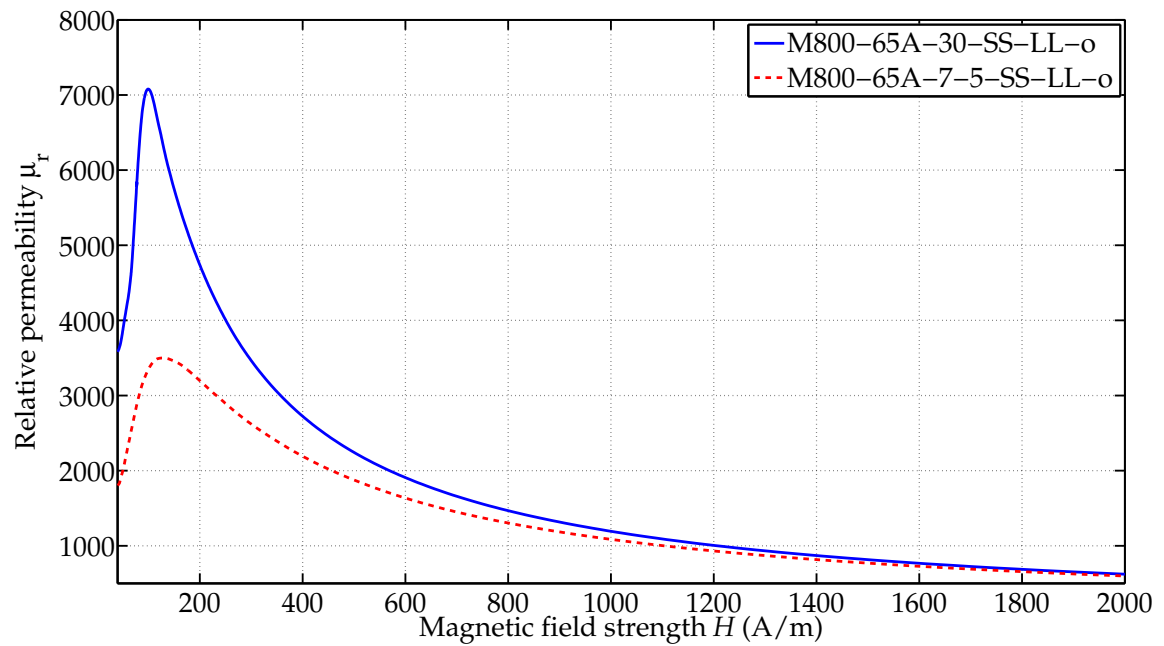
(a) M800-65A-SS-LL-o
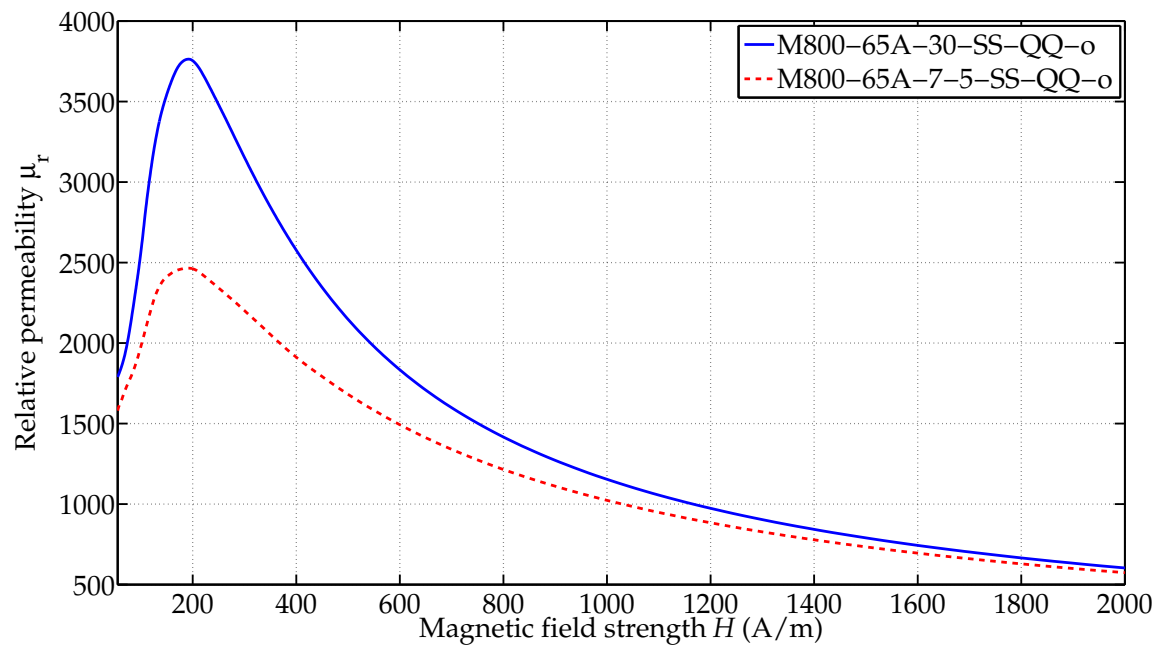


(b) M800-65A-SS-QQ-o

Figure 4.33: Effect of ratio $V_{\mathrm{dg}}/(V_{\mathrm{nd}} + V_{\mathrm{dg}})$ on the relative permeability of guillotine-cut samples.
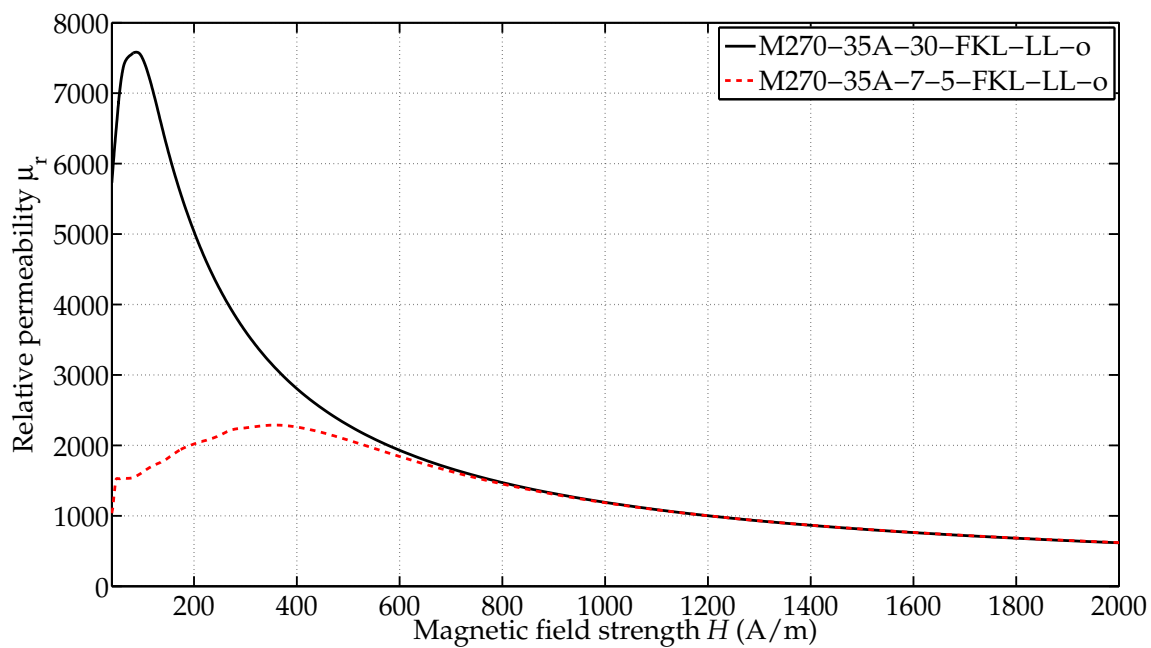
(a) M270-35A-FKL-LL-o
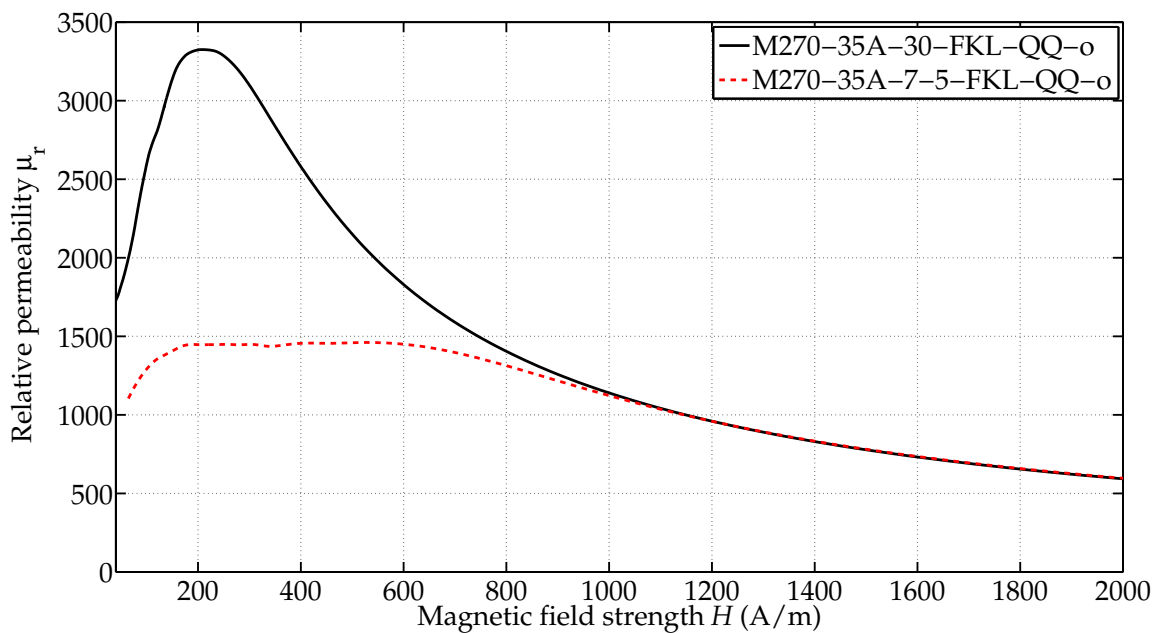


(b) M270-35A-FKL-QQ-o

Figure 4.34: Effect of ratio $V_{\mathrm{dg}}/(V_{\mathrm{nd}} + V_{\mathrm{dg}})$ on the relative permeability of FKL-laser cut samples.

*Comparison of the two laser cutting techniques*
No further differences of the two laser cutting techniques on the relative permeability concerning the ratio $V_{dg}/(V_{nd} + V_{dg})$ are observed in addition to those already previously stated.

**Specific losses**

*Laser versus mechanical cutting*
With increasing ratio $V_{dg}/(V_{nd} + V_{dg})$ the specific hysteresis losses also increase (Fig. 4.37). The difference of these energy densities in the case of longitudinally guillotine-cut samples increases more continuously than that of the laser-cut specimens (see Fig. 4.37). Thus, the largest difference in the case of longitudinally laser-cut samples is at moderate flux densities.

In the case of the laser-cut samples, especially for the transversely-cut samples, the two curves of samples with different ratios $V_{dg}/(V_{nd} + V_{dg})$ may converge or reverse their behavior (POI) at medium or high magnetic flux densities $B$ (see for instance Fig. 4.38). This is not observed for the guillotine-cut samples.

*Comparison of the two laser cutting techniques*
Concerning the ratio $V_{dg}/(V_{nd} + V_{dg})$, the energy densities of both laser-cut samples have the same shape. In addition to those already stated, no further differences between the two laser cutting techniques on the specific losses concerning the different sample sizes are observed.

---

Conclusions:
- The effect of increasing ratio $V_{dg}/(V_{nd} + V_{dg})$ on *guillotine-cut* samples induces a shifting of the knee point and saturation area to smaller magnetic flux densities $B$ with a slight movement to higher magnetic field strengths $H$. The loop center area remains (almost) unaffected.
- The effect of increasing ratio $V_{dg}/(V_{nd} + V_{dg})$ on *laser-cut* samples induces a shifting of the knee point area to higher magnetic field strengths $H$, but not to smaller magnetic flux densities $B$. Thus, the (high) saturation area remains nearly unaffected. However, the loop center area is shifted.
- The relative permeability of the *laser-cut* samples decreases with increasing ratio $V_{dg}/(V_{nd} + V_{dg})$ predominantly in the loop center area and the middle parts.
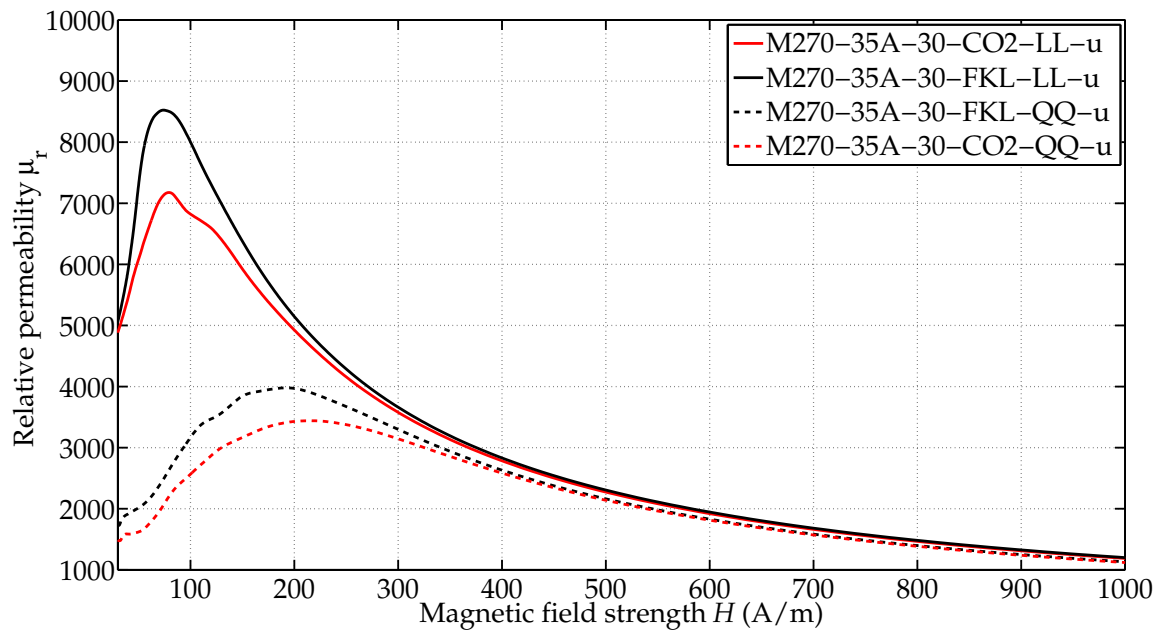
(a) wide laser-cut samples
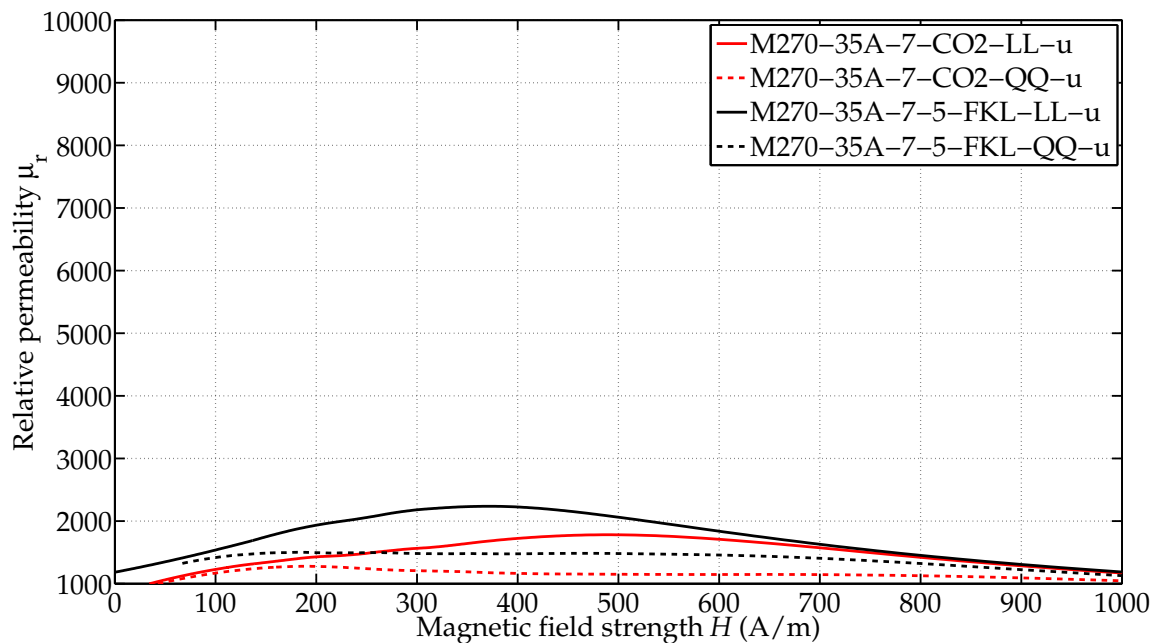


(b) small laser-cut samples

Figure 4.35: Relative permeability $\mu_r$ of laser-cut specimens for different cutting directions for wide and small samples. Range of interest: 0-200 A/m.
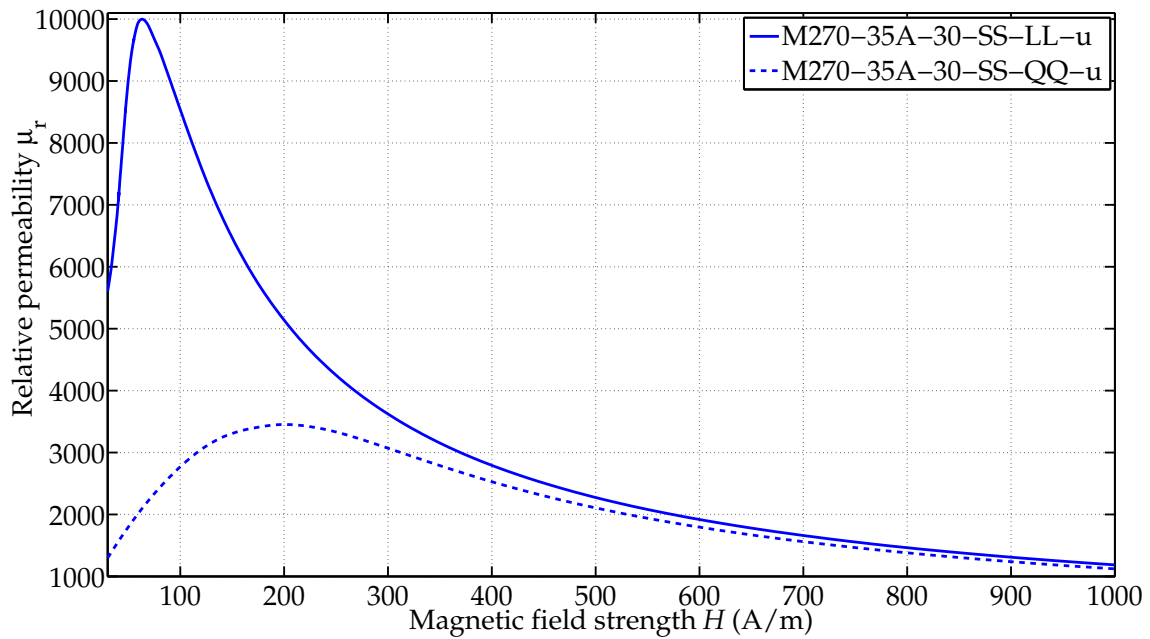
(a) wide guillotine-cut samples
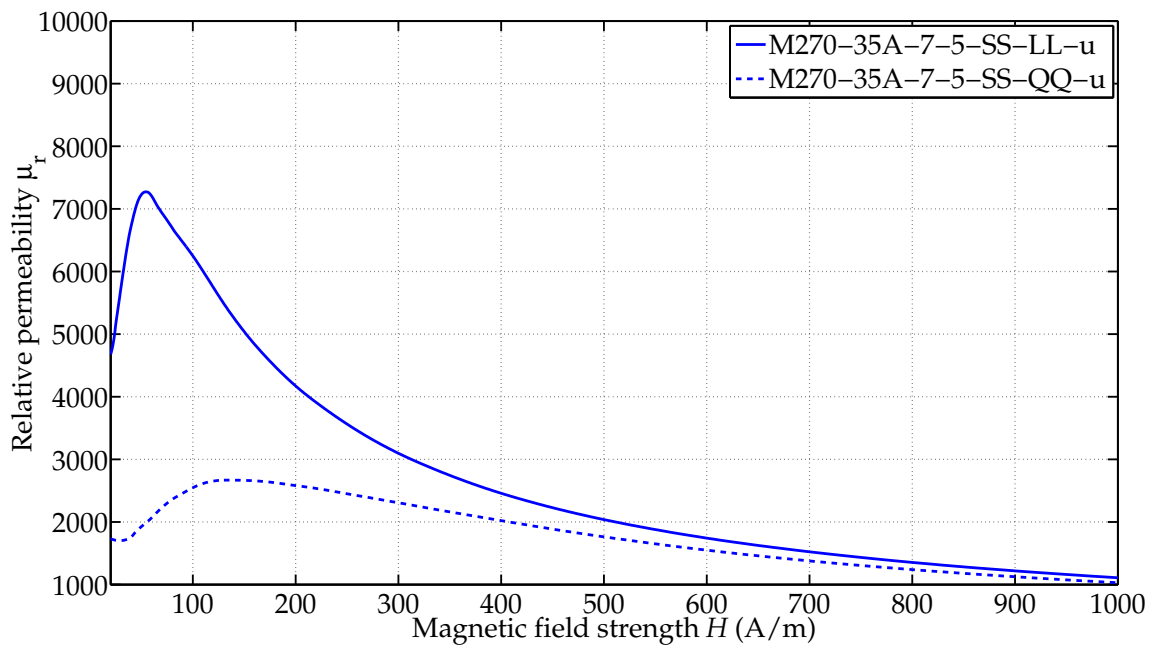


(b) small guillotine-cut samples

Figure 4.36: Relative permeability $\mu_r$ of guillotine-cut specimens for different cutting directions for wide and small samples. Range of interest: $0 - 200$ A/m.
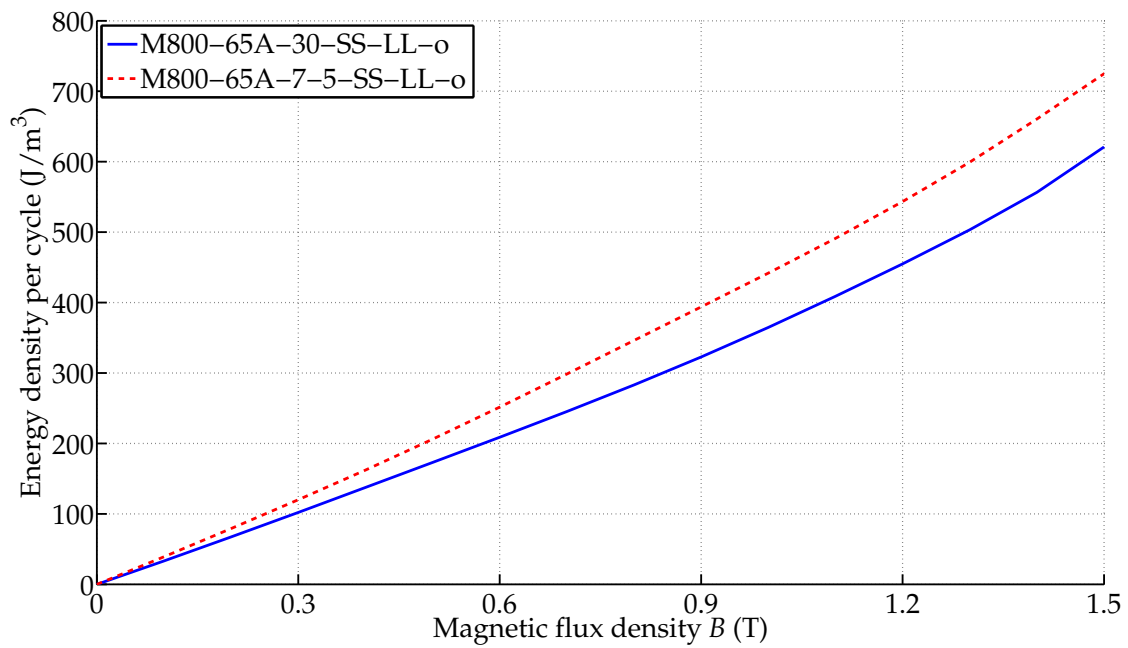
(a) guillotine-cut samples
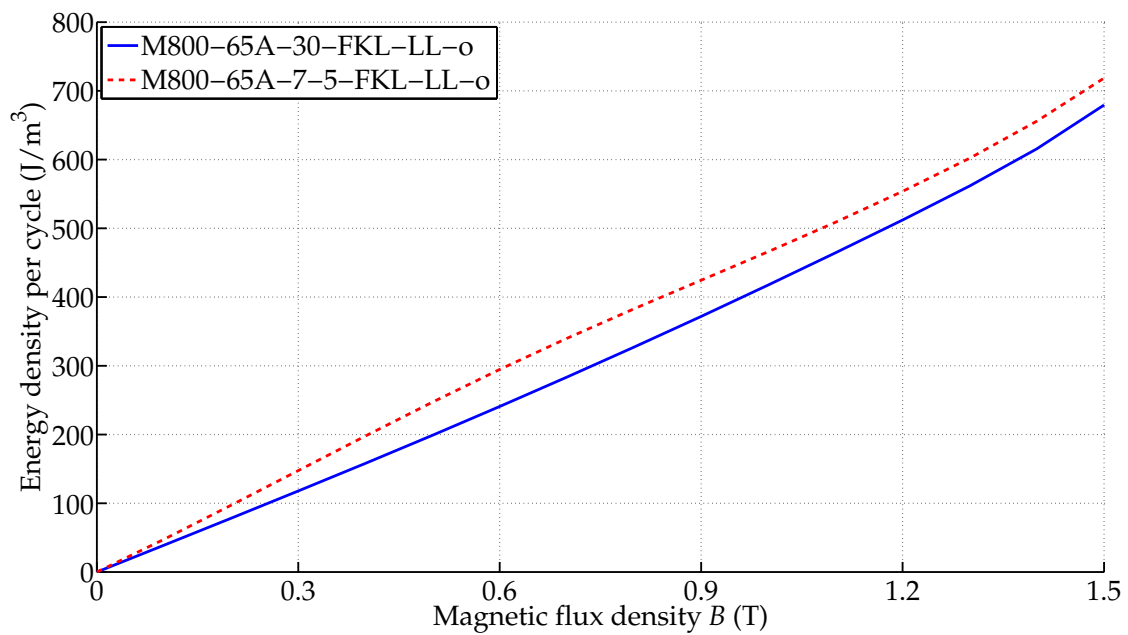


(b) laser-cut samples

Figure 4.37: Energy densities of guillotine-cut and laser-cut samples considering the ratio $V_{\mathrm{dg}}/(V_{\mathrm{nd}} + V_{\mathrm{dg}})$.
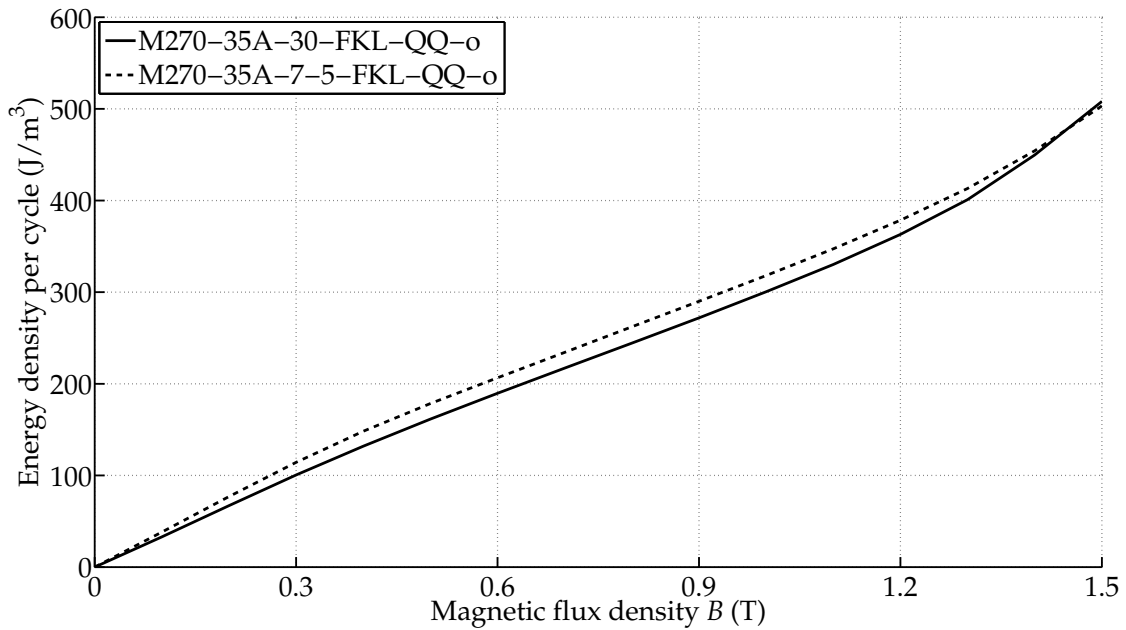
Figure 4.38: The energy densities of wide and small sample width may converge or a POI may occur.

- The relative permeability of *guillotine-cut* samples decreases with increasing ratio $V_{dg}/(V_{nd} + V_{dg})$ both in the loop center area and in the middle parts as well as in the knee point areas. The difference of both permeabilities is negligible in the saturation area.
- It applies: $B_{r,wide} > B_{r,small}$.
- The energy densities of the small samples are larger than those of the wide samples.

## 4.3 Discussion

In this section the results of the measurements presented in Chapters 4.1 and 4.2 are analyzed further and compared with results from literature which have primarily been obtained from hysteresis curve measurements.

**'Laser-effect' on the shape of *B-H* curves**

As discussed in Chapter 4.1 the 'laser-effect' (definition in Chapter 4.1) is mainly apparent in the small laser-cut samples. For the wide specimens this influence is less or not at all significant. This is due to the ratio $V_{dg}/(V_{nd} + V_{dg})$ and the respective cutting direction.

Dickmann [46] also studied the effect of laser cutting on the magnetic properties on V940-65A at 50 Hz, including the effect on the *B-H* curves, investigating ring samples with a width of 15 mm and Epstein samples with a width of 30 mm. A 'laser-effect' according to the definition in Chapter 4.1 is not observed or mentioned. Probably the 'laser-effect' is not yet visible for these two sample sizes, since the damaged area induced by cutting is relatively small. This confirms the result of this work, i.e. that the 'laser-effect' is rarely noticeable for wide specimens. Furthermore, Dickmann [46] analyzed the samples at 50 Hz, in contrast to the quasi-static measurements reported on in this Chapter. Thus, additional eddy currents may have reduced the here observed characteristic 'laser-effect' on the *B-H* curves of [46]. However, in the work of [46] a deformation of the *B-H* curve induced by all cutting techniques which is characterized by a so-called 'shifting' and/or 'shearing' (compare also with Chapter 4.1) of the complete loop is shown. Such a shifting is also illustrated in [32] and [131]. The shifting is explained by the influence of external stresses [131], e.g. stresses by mechanical cutting [105]. According to [113] " 'shearing' must be related to the compressive component of the residual stress." Considering [26, 100] the shifting also reflects the amount of internal stresses inside the material.

Ryckebusch [162] studied the difference of guillotine-cut and laser-cut Epstein strips with widths of 10 mm and 15 mm. No further information of the used laser-technique and its settings is given. The *B-H* curve of the probes, consisting of material M680-50A, were measured by an Epstein frame at a frequency of 100 Hz. The Epstein frame is equipped half with strips cut in rolling direction and half with transversely-cut samples [162].

As in this work, also the author of [162] noticed a 'laser-effect' on the measured *B-H* curves. This effect is defined by a more shifted *B-H* curve of the laser-cut samples compared to those of the guillotine-cut samples and by the need of a higher magnetic field for a specific flux density [162]. The laser-effect is identical for the 10 mm as well as for the 15 mm specimen, but with the difference that the effect is larger for the smaller samples [162]. The latter is in line with the findings of this work and also with [4]: The authors of [4] defined a 'dimensional effect' for the larger influence of cutting on smaller samples [4]. As these authors investigated laser-cut samples, this 'dimensional effect' on small medium silicon content steel samples also reflects the characteristics of the 'laser-effect' as presented in this work.

The definitions of the laser-effect in the work of [162] and this work differ in some points. The definitions agree on the shifting of the *B-H* curve of the laser-cut samples into a clockwise direction (compare e.g. Fig. 4.1). But, as observed in this work, for small transversely-cut samples this shifting is mainly recognized for the upper and lower middle parts and the knee point and saturation areas (compare

e.g. Fig. 4.7), but not for the loop center. In the case of longitudinally-cut samples, a shifting is also observed in the loop center area (see e.g. Fig. 4.1). However, the author of [162] measured transversely-cut and longitudinally-cut samples together in one measurement (see above), wherefore the characteristic of the transverse cutting direction is overlapped by that of the longitudinally-cut samples. Thus, both results do not necessarily contradict each other.

However, the samples investigated in [162] show no significant loop center, which differs from the rest of the *B-H* curve, and no special body shape for laser-cut specimens is identified. This is in contrast to the findings from this work. Furthermore, the author of [162] stated that "a higher magnetic field is needed to reach a given value of the induction" [162] for laser-cut samples, whereas in this work this does not apply to all parts of the *B-H* curve (compare e.g. parts of (high) saturation and knee-point areas of guillotine-cut and FKL-laser cut samples in Figs. 4.1, 4.2 and 4.7). These differences to the results of this work are possibly due to the following reasons:

1. Possibly different laser-techniques and settings[18].
2. Measurement frequency (100 Hz vs. quasi-static measurement): Additional eddy current losses may reduce the distinctive 'laser-effect' on the hysteresis shape.
3. Material (M680-50A vs. M400-50A) and its composition and thus grain size.
4. Different width of the samples and thus different ratios $V_{\mathrm{dg}}/(V_{\mathrm{nd}} + V_{\mathrm{dg}})$ (15 mm and 10 mm vs. 30 mm and 7.5 mm/7 mm).
5. Measured samples (combination of longitudinally-cut and transversely-cut samples vs. only longitudinally-cut or transversely-cut samples).
6. Measurement method (Epstein frame vs. remagraph).

Regarding the hysteresis shape, results of Araujo *et al.* [4] (measurements taken at 50 Hz) the 'laser-effect' according to the definition presented in Chapter 4.1 is confirmed for conventional FeSi samples. For samples with a higher silicon content, FeSi 6.5 samples (6.5 wt% silicon), the degrading effect by the laser equals the shape presented in [162]. Thus, according to [4], the material composition, the Si-content in particular, influences the degrading effect on the hysteresis shape. The author of [4] explains this with magnetostriction: The higher silicon material has a lower magnetostriction than the medium silicon material. Consequently, the material composition would be one possible explanation for the 'laser-effect' differences of Ryckebusch [162] and this work. However, the silicon content of the analyzed material M680-50A (Surahammars Bruks AB) by [162] is 1 wt%, according to the information provided by [1]. Therefore, this material does not belong to the high

---

[18]Influences on the *B-H* curve caused by different laser settings on ring samples (yoke width: 15 mm) are shown in [46].

silicon materials and thus the different hysteresis shape found by [162] must have another explanation than the silicon content (possibly one of those listed in the enumeration above).

However, the results of this work show that laser-cut electrical steel sheets with a silicon-content smaller than 3 wt% (precise information is given in Chapter 3) contain a 'laser-effect' on the quasi-static hysteresis shape which dominates with increasing ratio $V_{dg}/(V_{nd} + V_{dg})$. For sample widths of 30 mm, the ratio $V_{dg}/(V_{nd} + V_{dg})$ is already so small that this 'laser-effect' is not visible. This explains why no laser-effect is detectable in the results of [51]. Typically steel sheets in electric machines contain less than 3.5 wt%, wherefore the studied FeSi 6.5 sample of [4] is not of real interest in this case.

Schoppa [170, 173] found that with increasing silicon content in steel sheets, the sensitivity of effects induced by cutting increases. He explains this by the larger grain growth of high-silicon iron [170]. With high grain boundary density the deterioration depth of cutting is smaller ( [170] from [167]). This conclusion of [170] contradicts with the results of [4], in which the high-silicon material showed less influence of the cutting technique concerning the shape of the *B-H* curves. However, the author of [170] investigates this behavior at mechanically-cut probes. According to the results of this work (e.g. differences in hysteresis shapes) and those of other authors (e.g. [183, 207]), laser cutting deteriorates the magnetic properties differently than mechanical cutting, and therefore it is also possible that the sensitivities of effects by laser cutting at high-silicon content behave differently.

However, it should be noted that Araujo's high silicon content material (FeSi 6.5) has a thickness of 0.2 mm, in contrast to his second investigated sample, a conventional FeSi steel sheet of 0.5 mm thickness [4]. The question arises as to whether or not the laser cutting speed and hence energy volume introduced into the material was the same for both sample types (see for example [46] for the influence of different cutting speed on the *B-H* curve of electric steel ring samples).

In [207] different hysteresis curves of punched and laser-cut material are presented. The sample width is 16 mm and is thus between the widths of the wide and small samples investigated in this work. Thus the 'laser-effect' should be stronger compared to the wide samples and less pronounced compared to the small samples. This is the case, since the loop center of the laser-cut sample is wider than that of the guillotine-cut samples (compare with small samples above) and the upper and lower middle parts are thinner than the loop center. Furthermore, the hysteresis loop of the laser-cut sample is more shifted into a clockwise rotation compared to those of the guillotine-cut samples. This is congruent with the results of this work. Of course the 'laser-effect' is smaller than in the case of the small samples.

The characteristics of the 'laser-effect' (defined in Chapter 4.1) are identical or similar to characteristics caused by compression [118, 166] or tensile deformation mechanism [93]. Therefore, it might be concluded that the 'laser-effect' induces internal stresses inside the material which may also arise in the material as well for compression and tensile deformation. Considering [59] and [207] the stresses induced by different cutting techniques (punching, laser cutting) are compressive stresses. Thus, the results of this work suggest that the compressive component of laser-cut induced stresses is larger than that of guillotine-cut samples.

Since the shape of the hysteresis curve depends on the magnetic domains and their movement [168], and both again depend on the microstructure, material composition, texture and the stress state of the material, the results of this work confirm that the (thermal) degradation by laser cutting changes the magnetic domains differently and/or to a different extent than mechanical cutting.

**Remanent flux density and coercive field strength**

In this work, it has been observed that $B_{r,\text{guillotine-cut}} > B_{r,\text{laser-cut}}$. This behavior occurs mostly for small, longitudinally-cut samples and least for wide, transversely-cut samples. The author of [183] examined longitudinally-cut samples with different widths of up to 30 mm at a frequency of 50 Hz and for all samples obtained smaller remanent magnetic flux densities $B_r$ for laser-cut than for guillotine-cut samples. Thus, this confirms the results of this work. Emura *et al.* [51] also studied the difference of different cutting techniques on normal Epstein strips (30 mm width). These authors also mention a lower remanence $B_r$ and higher coercive force $H_c$ for laser-cut specimens [51]. However, in this work an increased coercive force $H_c$ for laser-cut samples compared to guillotine-cut samples first appears significantly for the small specimens (compare Chapter 4.1). According to the authors of [114] laser-cut samples (in their case samples with 4 mm width) have smaller coercive field strengths $H_c$ compared to mechanically-cut samples. This contrasts with the findings in this work. However, these authors [114] investigated grain-oriented steel sheets.

The author of [4] stated that the coercive magnetic field strength is "practically the same" for all analyzed laser-cut samples of different widths (from 5 mm to 30 mm). However, no exact values of the magnetic field strengths $H$ are given, but a diagram including four hysteresis curves of different sample sizes is provided. This does not fit with our observation (see e.g. Fig. 4.39). The smaller the strip is, the larger the difference of $H_c$ to wider samples. The latter is also confirmed by the results of [183]. Taking these results into account, this difference becomes already obvious for laser-cut samples smaller than 10 mm when comparing to 30 mm wide samples. In this
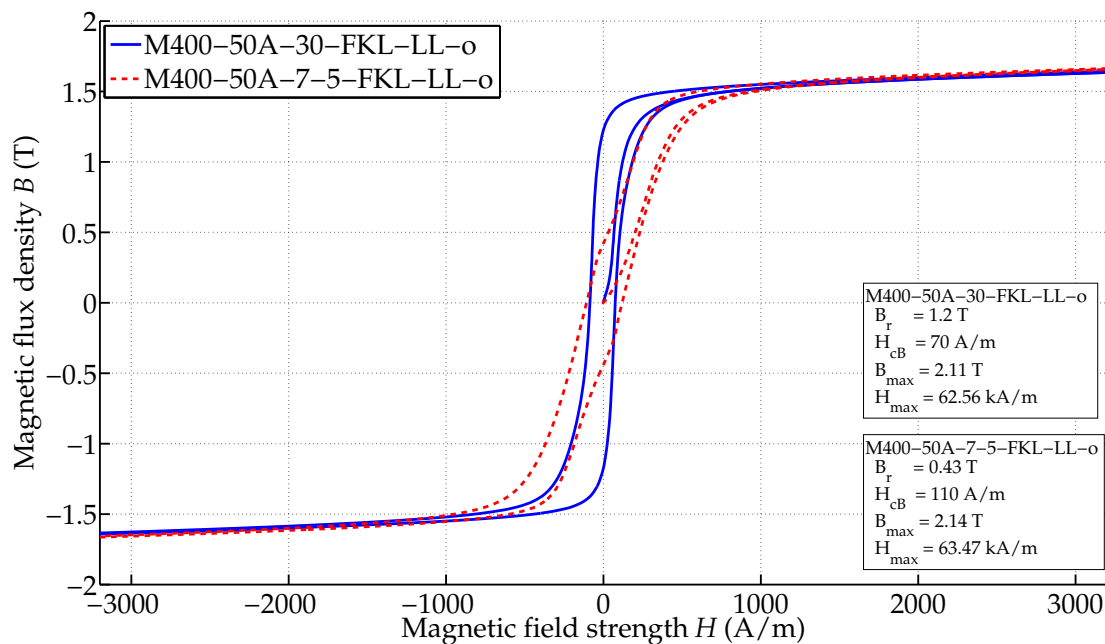
Figure 4.39: Dimensional effect on the coercive magnetic field strength $H_c$ of FKL-laser cut sample of M400-50A.

work, this increase of $H_c$ with increasing ratio $V_{dg}/(V_{nd} + V_{dg})$ is larger for laser-cut than for guillotine-cut samples. The results of [183], where longitudinally-cut samples are analyzed, confirm this behavior. However, this characteristic is smaller for the transversely-cut samples (see e.g. Figs. 4.32 and B.24). Considering [168], the coercive field strength $H_c$ depends on the residual stress state inside the material, the magnetostriction and the microstructure of the material (e.g. grain size). With increasing local stress and magnetostriction, the coercive magnetic field strength $H_c$ increases [168][19]. With the assumption that the grain size remains constant for both the laser-cut as well as the guillotine-cut samples (considering one material), the larger coercive magnetic field strengths $H_c$ of the laser-cut samples would thus indicate that the internal stress inside the respective material for laser-cut samples is larger[20]. Of course, this is more pronounced for small samples (see e.g. Table 4.1).

**Relative permeability**

The relative permeabilities of laser-cut samples decrease with increasing ratio $V_{dg}/(V_{nd} + V_{dg})$, with the smallest influence on the knee point or (high) saturation area. Thus, the loop center as well as the middle parts are affected most, especially

---

[19]Note, this relationship is also shown in [45], which refers to [101, 102].

[20]Certainly, the grain size may change in the cut edge area, depending on the respective cutting technique (see Chapters 1.3 and 3.2).

for small samples. The exact magnetic flux density range depends on the material. Also Araujo [4], who studied laser-cut samples, mentions a decreased permeability of conventional FeSi samples with decreased sample width. However, Araujo [4] limits this decreasing behavior to the range of 0.5 T and 1.5 T, what corresponds to the middle parts and the knee point area of the hysteresis loop for the material analyzed. Thus, this is not completely in line with the findings presented in this work.

Furthermore, it is also observed that the maxima of the relative permeabilities of different cutting techniques are in the following order: $\mu_{r,\,max,\,guillotine} > \mu_{r,\,max,\,FKL} > \mu_{r,\,max,\,CO_2}$. In the same order, the maxima are shifted to higher magnetic field strengths $H$. This applies to all investigated materials (see Chapter 4.1.1), as long as a distinctive maximum occurs. Dickmann confirms this order in [46], although the laser settings differ from the laser settings used in this work (e.g. large differences in cutting speed).

It is observed that the relative permeabilities of the small laser-cut samples are worse in the middle parts of the hysteresis loop than those of the guillotine-cut samples of the same width. This order can change in the knee point and/or saturation area, a POI occurs (see Figs. 4.3 and B.21). For the wider specimens this effect is not nearly as relevant (see Figs. 4.19 and B.22). This applies to all analyzed materials. [162] also state that the difference of permeability between laser-cut and guillotine-cut samples depends on the polarization. He found the largest difference in the range of 1.1 T and 1.3 T for samples with widths of 10 mm and 15 mm. This range correlates with the knee point area.

Dickmann [46] states that the cutting process has a more significant influence on the permeability than on the loss behavior. This is confirmed by the results of this work. At high magnetic field strengths $H$, no difference in relative permeabilities can be observed between differently cut samples [46]. This assumption concurs with the results of the samples investigated in this work. However, the permeabilities at high magnetic field strengths $H$ of guillotine-cut and laser-cut samples converge less strongly for the small samples than in the case of the wide samples (see e.g. Figs. B.21 and B.22).

The results of the previous Chapters showed that with increasing ratio $V_{dg}/(V_{nd} + V_{dg})$ and deviation from the longitudinal cutting direction, the permeabilities of laser-cut samples loose their distinctive maxima. Considering, for example, the results of [192], this behavior may be associated with larger compressive stresses in the case of laser-cut compared with guillotine-cut samples. This characteristic is further investigated in Chapter 5.

**Specific losses**

The hysteresis curves of the small laser-cut samples consist of a wider loop center area than those of the small guillotine-cut samples. Thus, the laser-cut samples have higher losses for small magnetic flux densities. However, it is also observed that the area widths of the middle parts of the laser-cut samples are (slightly) smaller compared to those of the guillotine-cut samples, wherefore it is assumed that the specific losses of the differently cut samples approach each other and/or reverse their order (POI occurs) with increasing magnetic flux density. The reversing behavior of losses can also be observed in [46] and [162]. Dickmann [46] shows that the laser settings, as e.g. the cutting speed, have an influence on the loss behavior induced by the laser cutting technique. In this respect, it is possible to obtain lower losses for laser-cut samples by choosing the most appropriate settings [46]. This also results in lower losses at some magnetic flux densities compared with guillotine-cut samples, whereas a POI occurs (see diagram 9 in [46]). The author of [182] concludes, from his investigated Epstein strips, that for high flux densities solid state laser cutting produces better results than mechanical cutting. This finding supports the existence of a POI, even for the wide samples.

**Cutting direction**

In this work it has been established that the loop center area of *small laser-cut* specimens remains unaffected by the cutting direction, and it applies $B_{r,LL} \simeq B_{r,QQ}$. However, the cutting direction leads to more shifted lower middle and upper middle parts as well as knee point and saturation areas (Figs. 4.9 and 4.10). This shifting results in higher magnetic field strengths $H$ and lower magnetic flux densities $B$. In contrast, the small transversely guillotine-cut hysteresis shapes are completely shifted (the loop center area included) into a clockwise direction when compared to the small longitudinally guillotine-cut hysteresis shapes (Fig. 4.8). Note, that the shifting of the knee point for the transversely-cut guillotine samples in relation to the small longitudinally-cut guillotine samples results in lower magnetic flux densities $B$ in contrast to the shifting of the transversely laser-cut samples, which is characterized by higher shifting to magnetic field strengths $H$ than to lower magnetic flux densities $B$ (compare Figs. 4.8, 4.9 and 4.10). The thicker (here, also the smaller the grain size of) the material is, the smaller the relative shifting of the hysteresis curves between transversely and longitudinally-cut samples[21].

As the hysteresis curves of the transversely guillotine-cut probes show a wider loop

---

[21]Again, this may suggest that materials consisting of small grains are less sensitive to influences which further degrade the magnetic properties, e.g. the cutting direction.

center area than those of the longitudinally guillotine-cut specimens, it follows that the specific losses of transversely-cut guillotine probes are higher for low magnetic flux densities than the specific losses of longitudinally-cut guillotine specimens. Afterwards these specific losses approach each other with higher magnetic flux densities $B$. The difference between these losses decreases with increasing thickness (here, also with decreasing grain size) of the material.

The loop center area of *small laser-cut* samples is independent of the cutting direction. Thus, it follows that the specific losses of small transversely-cut as well as for small longitudinally-cut specimens tend to be very similar, even at low magnetic flux densities.

As the 'laser-effect' is not significant for the wide samples, it applies $B_{r,LL} \neq B_{r,QQ}$. This is also confirmed by the results of [182]. In this work, the hysteresis loops of the wide transversely guillotine-cut and laser-cut samples are completely shifted into a clockwise direction compared to those of the longitudinally-cut samples (Figs. 4.24 and 4.25). The loop center area for samples cut in transverse direction is wider compared to the samples cut in rolling direction. This behavior is also reflected by the investigated samples of [182]. As shown in this work, this behavior decreases with increasing material thickness (here, also with decreasing grain size). This applies for guillotine-cut as well as for laser-cut samples. Thus, the specific losses of the wide transversely laser-cut specimens are supposed to be higher at low flux densities compared to the wide longitudinally-cut samples (this is in contrast to the small laser-cut samples). This difference in specific losses decreases with higher magnetic flux densities $B$ and thicker (here, also with smaller grains of the) material.

Also Ryckebusch [162] stated that the losses at low magnetic flux densities differ significantly, comparing 30 mm wide Epstein samples in transverse and longitudinal cutting direction. This difference decreases with increasing frequency and polarization [162]. Thus, the results of this work extend the knowledge that the specific losses of small longitudinally and transversely laser-cut samples do not differ significantly, even at low magnetic flux densities. Furthermore, for small guillotine-cut samples this difference reduces with increasing material thickness (here, also with decreasing grain size).

The maximum relative permeabilities decrease more sharply from longitudinal to transverse cutting direction in the case of guillotine-cut samples, in contrast to laser-cut samples ($\Delta\mu_{r,\,max,\,guillotine,\,LL\,\to\,QQ} > \Delta\mu_{r,\,max,\,laser,\,LL\,\to\,QQ}$). Additionally, the reduction of relative permeability at small magnetic field strengths $H$ of laser-cut samples caused by the cutting direction decreases with decreasing sample width ($\Delta\mu_{r,\,laser,\,wide,\,LL\,\to\,QQ} > \Delta\mu_{r,\,laser,\,small,\,LL\,\to\,QQ}$).

**Ratio $V_{dg}/(V_{nd} + V_{dg})$**

The studies of this work showed that the specific losses increase with increasing ratio $V_{dg}/(V_{nd} + V_{dg})$ and thus with decreasing sample width. Many other authors refer to the 'specific cutting length' (cutting length referred to the mass of the sample (CL)). Thus, the small samples in this work have a larger specific cutting length than the wide samples. For instance, Ryckebusch [162] points out that with increasing specific cutting lengths the specific losses increase as well. This is mostly in line with the results of the previous Chapters. Many other authors investigated the specific loss behavior vs. the specific cutting length. As they measured the losses, e.g. by an Epstein frame, these findings are discussed in Chapter 5.5.

For all samples, the larger the ratio $V_{dg}/(V_{nd} + V_{dg})$ is, the more the *B-H* curve shifted, whereas the shifting from the laser-cut differs from the shifting of the guillotine-cut samples (see Chapter 4.3). Emura [51] also states that cutting in general creates a 'shearing'-effect on the hysteresis curve to "lower remanence and permeability" [51]. According to [182], which refers to [112] and [32] "a sheared loop is an evidence for induced stress" [182]. As the relative extent of induced stresses is larger for smaller samples, the curves of the small samples are more shifted. This 'shifting' of the *B-H* curve with increasing ratio $V_{dg}/(V_{nd} + V_{dg})$ can also be observed in the diagrams presented in [183, 192] and [197]. Dickmann [46] studied Epstein probes with 30 mm width and compared them to an annealed specimen, defining this reference sample as a non-deteriorated sample, thus the ratio $V_{dg}/(V_{nd} + V_{dg})$ moves towards zero. He previously mentioned a shearing behavior for all cut samples, independent of the cutting technique. Hence, the results of Dickmann [46] support the results of this work. The results in this work show that the ratio $V_{dg}/(V_{nd} + V_{dg})$ according to Chapter 4.2 reduces the knee point area from guillotine-cut samples to lower magnetic flux densities *B* and slightly to higher magnetic field strengths *H*. In contrast, the knee point area of laser-cut samples is shifted predominantly to higher magnetic field strengths *H*. This behavior can also be seen in the diagrams of [4] and [183], where laser-cut samples with different widths of conventional FeSi material are presented.

A similar shifting behavior of laser-cut samples is presented in [51], but only for laser-cut samples which had been annealed before they were cut. The shifting of the *B-H* curve of the presented normal (without annealing before or after cutting) laser-cut sample [51] leads to knee-point areas which are shifted to smaller magnetic flux densities *B*. These different characteristics must thus result from residual stresses inside the material which have already been caused from previous manufacturing steps.

Baudouin *et al.* [11] also analyzed the influence of two sample sizes and thus

different ratios $V_{\mathrm{dg}}/(V_{\mathrm{nd}} + V_{\mathrm{dg}})$, on the characteristic magnetic properties $B_{\mathrm{r}}$, $\mu$ and $H_{\mathrm{c}}$. Additionally, they compared mechanical and laser-cut samples. According to their measurements, $H_{\mathrm{c}}$ of the fully processed materials is more deteriorated, and thus increased by mechanical cutting, than by laser cutting when considering wide versus small samples (in their case 20 mm to 5 mm width) [11]. This is not in agreement with our findings (see Table 4.1). The authors of [11] further report a reduced influence on $H_{\mathrm{c}}$ for SC samples, cut with a continuous laser. However, these samples only contain 0.31 % Si, which might influence the change of magnetic properties due to the cutting technique. In this work, no case is found where the coercive field strength $H_{\mathrm{c}}$ decreases with increasing ratio $V_{\mathrm{dg}}/(V_{\mathrm{nd}} + V_{\mathrm{dg}})$ neither for the mechanically-cut nor the laser-cut samples. However, here, samples with larger silicon contents are investigated compared to the SC sample in [11]. Thus, possible reasons for this different influence on $H_{\mathrm{c}}$ might be differences in laser settings and the material investigated. Baudouin *et al.* [11] conclude on the base of the characteristic magnetic properties ($B_{\mathrm{r}}$, $\mu$ and $H_{\mathrm{c}}$) that "laser cutting appears more appropriate for the smaller samples" [11]. However, in this work, it is shown that each magnetic property is influenced by the different cutting techniques to another extent and that the point of operation (of the final devices/ electric machine) is important to evaluate which cutting technique is the best for the respective case (remember POIs).

Table 4.1: Change of coercive magnetic field strength from wide to small longitudinally-cut samples.

|  | M270-35A_SS_LL_o wide → small | M270-35A_CO$_2$_LL_o wide → small | M270-35A_FKL_LL_o wide → small |
|---|---|---|---|
| $H_{\mathrm{c}}$ in $\frac{\mathrm{A}}{\mathrm{m}}$ | 50 → 60 | 70 → 100 | 60 → 90 |
|  | M400-50A_SS_LL_o wide → small | M400-50A_CO$_2$_LL_o wide → small | M400-50A_FKL_LL_o wide → small |
| $H_{\mathrm{c}}$ in $\frac{\mathrm{A}}{\mathrm{m}}$ | 80 → 80 | 80 → 110 | 70 → 110 |
|  | M800-65A_SS_LL_o wide → small | M800-65A_CO$_2$_LL_o wide → small | M800-65A_FKL_LL_o wide → small |
| $H_{\mathrm{c}}$ in $\frac{\mathrm{A}}{\mathrm{m}}$ | 90 → 100 | 100 → 130 | 100 → 130 |

Conclusions:
- All materials investigated in this work (Si-content always smaller than 3 wt%) reflect with increasing ratio $V_{\mathrm{dg}}/(V_{\mathrm{nd}} + V_{\mathrm{dg}})$ the 'laser-effect' (according to the definition in Chapter 4.1) on the hysteresis shape.
- In the case of laser-cut samples, the distinctive maximum of the relative permeability disappears with increasing ratio and larger deviation from

the longitudinal cutting direction.

- The characteristics of the 'laser-effect' on the hysteresis curve and permeability indicate that laser cutting induces more compressive stresses than guillotine cutting.

- With increasing ratio $V_{dg}/(V_{nd} + V_{dg})$ the relative permeability of laser-cut and guillotine-cut samples is decreased, but with less impact in the knee point or (high) saturation area.

- With increasing ratio $V_{dg}/(V_{nd}+V_{dg})$ the knee point area of laser-cut samples is shifted to higher magnetic field strengths $H$. This is in contrast to the behavior of guillotine-cut samples, in which the knee point area is shifted to lower magnetic flux densities $B$ and, if at all, slightly to higher magnetic field strengths $H$.

- With larger ratio $V_{dg}/(V_{nd} + V_{dg})$, $H_c$ increases and $B_r$ decreases.

- The loop center area of small laser-cut samples is unaffected by the cutting direction. Therefore, it applies $B_{r,LL} \approx B_{r,QQ}$ and $p_{LL} \approx p_{QQ}$ at low magnetic flux densities. This is in contrast to the guillotine-cut samples.

- The additional decreasing influence of cutting direction on the maximum permeability is smaller for laser-cut than for guillotine-cut samples.

- Both investigated laser cutting techniques degrade the magnetic properties very similarly (compare e.g. shapes of hysteresis curves and permeability), with the difference that the magnetic properties of $CO_2$-laser cut samples are degraded to a larger extent.

# Chapter 5

# Experimental results: Epstein frame

Measurements performed with the Epstein frame supply the magnetic polarization $J$ due to the mutual inductance of the frame which compensates the air flux (see Fig. 2.8 and [86]). However, the measurements presented in Chapters 4 and 6 provide the magnetic flux density $B$. For a better comparison of all measurements, the magnetic polarizations $J$ obtained with the measurements reported on in this Chapter are converted to and presented for the corresponding magnetic flux densities $B$.

The diagrams of the specific losses $p_s$ are presented up to $B = 1.6\,\text{T}$. Above this value, uncertainties of the measurement results may occur due to the following reasons:

- The compliance of the form factor [86] may no longer be ensured (exact values of the individual measurements are given in Appendix C.4). This leads to further harmonics, which result in higher losses (see also Chapter 5.1).

Leakage flux:

- Leakage flux around the overlapping corners.
- A special characteristic of the losses at high magnetic flux densities occurs due to the Epstein frame used here. An aluminum plate is mounted on the frame of the air compensating area (see Fig. 2.9 a)). The more the material is saturated, the more magnetic flux flows also through this plate, wherefore the losses decrease at higher magnetic flux densities and falsify the measured values.
- As soon as the material is highly saturated, the relative permeability decreases and approaches one, whereas the magnetic flux may also flow through the surrounding air.

Comprehensive sets of measurement results (magnetization curves and specific losses) are presented in Appendix C. Specific values such as the specific losses at 1 T and 1.5 T, are listed in the Tables in Appendix C.1.

# 5.1 Measurement results with and without sense lines

As mentioned in Chapter 2.5, the Epstein frame measurements were performed with and without sense lines on the secondary winding. The following observations were made:

In general, the loss curves measured with and without sense lines do not show a noteworthy difference below the form factor limitation. This limit is at 1.12211 [86] and is the ratio of the root mean square and the average rectified value of the secondary voltage. Thus, this limitation differs for each measurement series and needs to be calculated individually (see Appendix C.4). This form factor limit occurs at smaller magnetic flux densities $B$ for the measurements taken without sense lines compared to those with sense lines (compare Tables C.3 and C.4). Remarkable differences between the results of these two measuring methods occur above this form factor limitation (in most cases from 1.4 T/1.5 T onward, depending on the individual measurement). From this point of high magnetic saturation onward the power amplifier has to adjust the primary voltage forcing it to be non-sinusoidal to achieve a sinusoidal secondary voltage. Thus with sense lines, the form factor is ensured up to larger magnetic flux densities more than for the measurements without sense lines. Because of the added harmonics, the measured losses without secondary sense lines are higher at high magnetic flux densities $B$ than those measured with secondary sense lines (see Fig. 5.1).

The measurements with and without sense lines reflect the good reproducibility below the form factor limitation of the investigated sample sets.

> Conclusions:
> - The difference between the loss curves measured with and without sense lines on the secondary winding is only significant for magnetic flux densities above the form factor limitation. This limit varies with the investigated material, sample width and frequency.
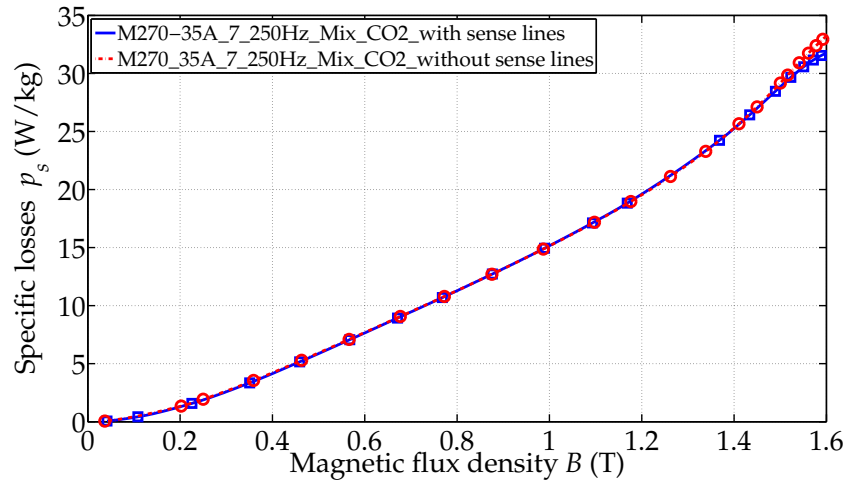
(a) M270-35A
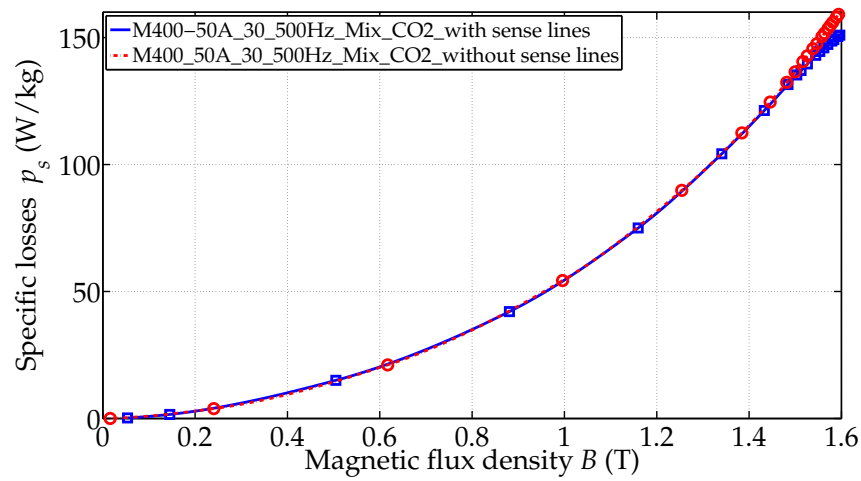


(b) M400-50A
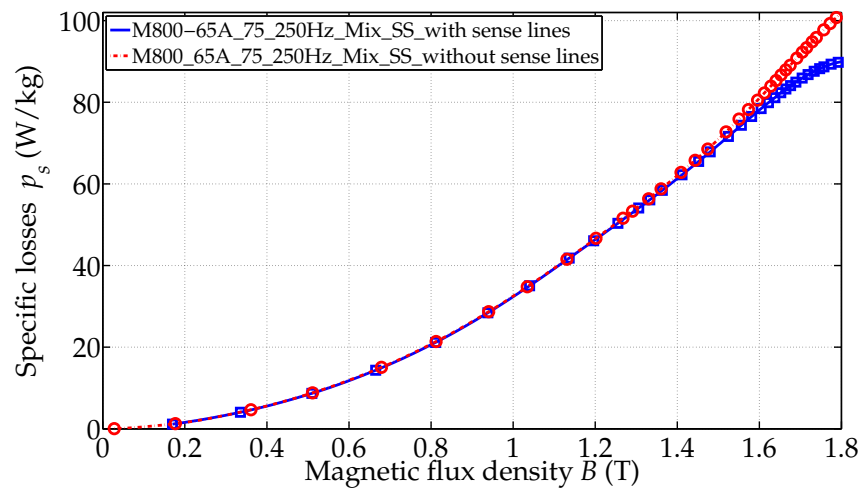


(c) M800-65A

Figure 5.1: Specific losses measured with and without sense lines on the secondary winding.

# 5.2  Influence of cutting technique

## 5.2.1  Small samples

**Specific losses**

*Laser versus mechanical cutting*

The results shown in Fig. 5.2 illustrate well that the deteriorating effect of the laser cutting techniques on the specific losses differs from those of the mechanical cutting (in this case, guillotine cutting).

As known from literature (e.g. [207]), both the mechanical and laser cutting processes induce compressive stresses inside the material, leading to inhomogeneities, dislocations and defects in the lattice structure [23]. The stresses due to mechanical cutting result from cold forming [45]. In contrast, in the case of laser cutting, the large thermal gradient between the melted material and remaining material induces stresses inside the material [45]. Thus, the extent and the distribution of the induced compression stresses and hence the loss characteristics, likely differ significantly inside the differently cut samples (as shown in Fig. 5.2). The specific losses of the guillotine-cut samples increase more with a square of the magnetic flux density (see for instance Fig. 5.2). In contrast, the specific losses of the laser-cut samples show an almost 'linear' behavior[1] at moderate flux densities (in case of Fig. 5.2 in the range of about (0.4...1.2)T (domain wall movement area) at 50 Hz). This effect decreases with increasing frequency (see e.g. Appendix C.2), material thickness[2] (see for instance Fig. 5.3) and sample width (compare Fig. 5.2 with Figs. 5.7 and 5.8). All these parameters reduce the influence of the laser-effect and/or induced stresses by cutting on the specific losses.

A POI between the loss curves of the guillotine-cut and laser-cut samples may occur: At smaller magnetizations, the specific losses of laser-cut samples are larger than those of guillotine-cut samples; however, these do increase more rapidly. Then,

---

[1]Note, this 'linear' behavior results from the already linear (see Fig. 4.20) or 'wave' shape characteristic (see for instance Fig. 4.14) of the quasi-static loss curves. The latter is now damped by the eddy currents, therefore it also appears more 'linear'. Whether the 'linear' or the 'wave' shape behavior is present in Chapter 4 depends, in addition to the cutting technique, on the material, sample size and cutting direction. It is assumed that this characteristic results from the internal compressive stresses. The more intensive the 'wave' shape, the more compressive stresses are inside the material. Even in the case of guillotine-cut samples such a curve shape may occur (see Fig. 4.13), but mainly for transversely-cut samples. However, this behavior is already reduced/eliminated by composing transversely-cut and longitudinally-cut samples (in this Chapter 'mixed' samples are measured) and by the additional occurrence of eddy currents when compared with Chapter 4. Therefore, here (Chapter 5), this characteristic only appears for laser-cut samples.

[2]Possibly, here also with decreasing grain size, see Chapter 3.4.
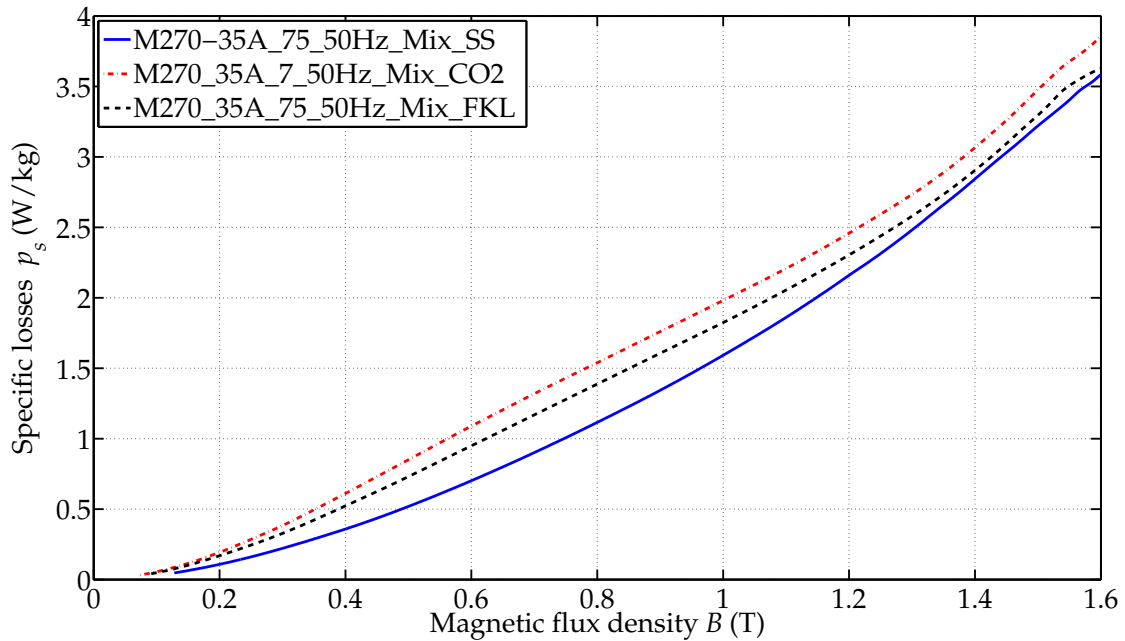
Figure 5.2: The laser-cut samples have the same curve shape. The $CO_2$-samples have higher losses because the sample width is smaller compared to FKL-laser and guillotine-cut sample.

at a certain degree of magnetization, a POI may occur (see Fig. 5.3, the POI is highlighted by the arrows in the diagrams)[3] after which the specific losses of the guillotine-cut samples are larger. Thus, with higher frequency, the degrading effect of guillotine cutting on the specific losses may be worse when compared to laser cutting. This is in line with the results obtained in Chapter 4.1.1. The occurrence of such a POI depends on the material itself, its width (ratio $V_{dg}/(V_{nd} + V_{dg})$), and the frequency of operation. With increasing frequency and increasing material thickness (possibly here, also with decreasing grain size), this POI is shifted to smaller magnetic flux densities $B$ (see Table 5.1 and Fig. 5.3). These characteristics apply to both laser cutting techniques analyzed.

Considering the shapes of the hysteresis curves and of the hysteresis losses (Chapter 4), the compressive stresses are interpreted to be larger for the laser-cut than for the mechanically-cut samples (compare the quasi-static loss curves presented in Chapter 4 and [118]). With increasing frequency and material thickness, the eddy current losses increase and thus the relative influence of the hysteresis losses, the linear loss behavior, disappears more and more. The larger compressive stresses in the case of laser-cut samples indicate more dislocations and defects inside the lattices of the material. This, in turn, leads to a larger electric resistance [109,115] and thus

---

[3]Compare FKL-laser and guillotine-cut samples, as they have the same width (Chapter 2.1.1).

(a) 50 Hz



(b) 250 Hz



(c) 500 Hz
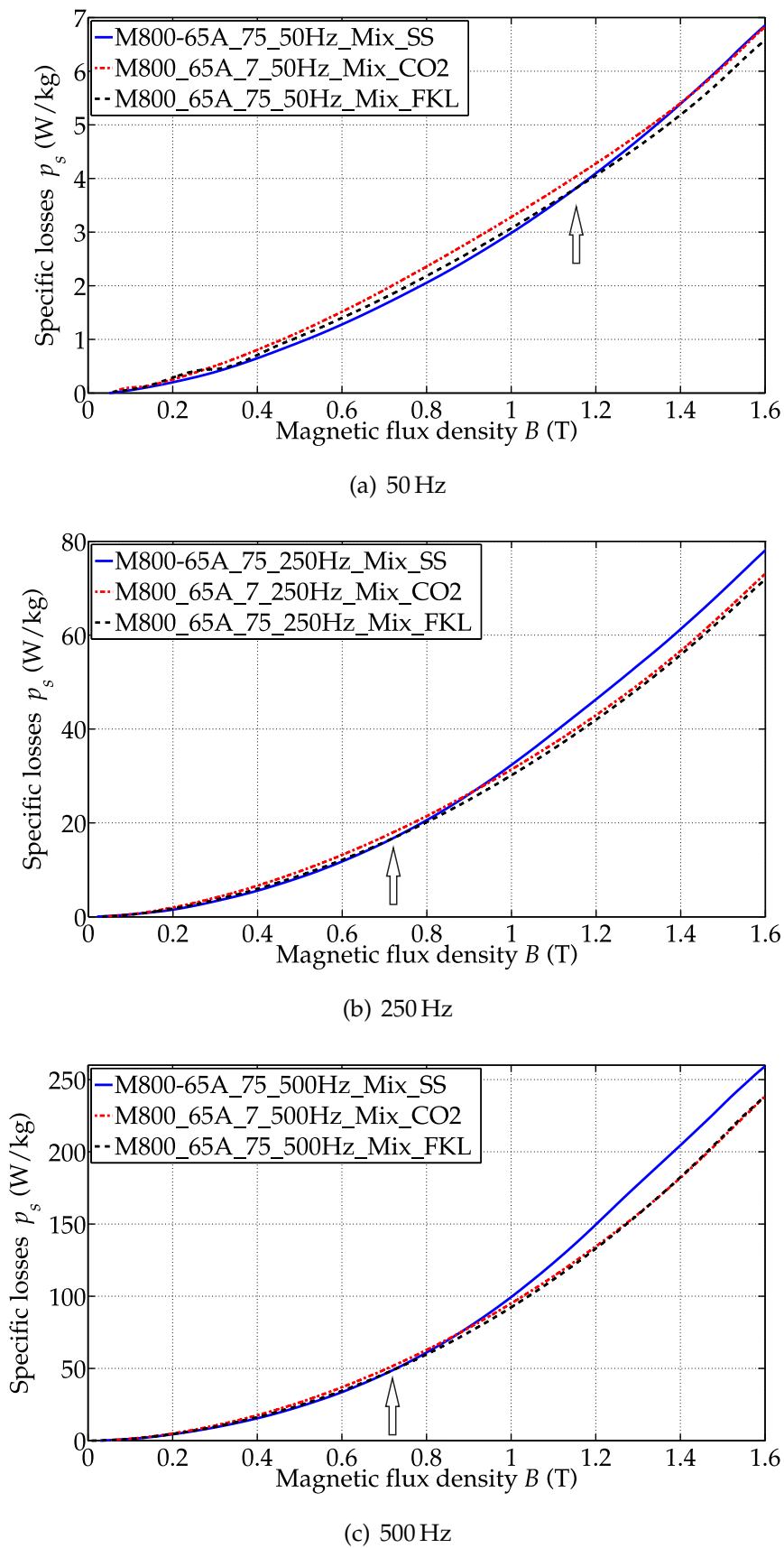
Figure 5.3: Specific losses of small samples of M800-65A measured at different frequencies.

Table 5.1: POIs at different frequencies, seen here for the small samples in 'Mix'-order. Note: $CO_2$-samples are smaller than FKL-samples.

|  | **M270-35A_75** | **M400-50A_75** | **M800-65A_75** |
|---|---|---|---|
| 50 Hz | - ($CO_2$ - SS) | - ($CO_2$ - SS) | 1.42 T ($CO_2$ - SS) |
|  | - (FKL - SS) | 1.58 T* (FKL - SS) | 1.15 T (FKL - SS) |
| 250 Hz | - - | - ($CO_2$ - SS) | 0.91 T ($CO_2$ - SS) |
|  |  | 1.07 T (FKL - SS) | 0.72 T (FKL - SS) |
| 500 Hz | - ($CO_2$ - SS) | 1.10 T ($CO_2$ - SS) | 0.88 T ($CO_2$ - SS) |
|  | 1.22 T (FKL - SS) | 0.95 T (FKL - SS) | 0.72 T (FKL - SS) |

∗ = to be considered with caution, see introduction of Chapter 5.

the degree to which the classical eddy currents increase with frequency and material thickness (see Eq. (1.4)[4]). Thus, the POI is shifted to smaller flux densities $B$.

This finding is in contrast to a still wide-spread understanding that laser cutting has a larger deteriorating effect on the specific losses of electrical steel sheets than mechanical cutting. As a matter of fact, at specific, rather low magnetizations, the deteriorating effect of laser cutting can be much smaller than that of mechanical cutting.

*Comparison of the two laser cutting techniques*
Considering for instance Fig. 5.2, the two curves of the FKL-laser and the $CO_2$-laser cut samples show a very similar curve shape and thus loss behavior. This is confirmed for all small samples measured in the Epstein frame (see Appendix C.2) and is consistent with the results presented in Chapter 4.1.1. However, the $CO_2$-laser cut samples show higher losses than the FKL-laser cut samples. As for the results of the small samples obtained in Chapter 4, the distinction between the results is mainly attributed to the samples' difference in widths (7.5 versus 7 mm), since the specific losses increase with the relative amount of degraded material of the overall sample. Thus, it is concluded that both laser cutting techniques have a very similar influence on the specific losses of the materials investigated. It might be assumed that the loss curves of $CO_2$-laser and FKL-laser cut samples would be almost 'identical' if they had the same sample width. This is investigated further with the wide samples in Chapter 5.2.2. Furthermore, both obtained loss curves of the two laser cutting technologies indicate that with increasing ratio $V_{dg}/(V_{nd} + V_{dg})$ (difference in sample size of small $CO_2$-laser and FKL-laser cut samples), the specific losses increase as well (for more detail, see Chapter 5.4).

---

[4]Resistivity $\rho_{E, \text{laser-cut}}$ > resistivity $\rho_{E, \text{guillotine-cut}} \rightarrow p_{ec, \text{laser-cut}} < p_{ec, \text{guillotine-cut}}$.

**Magnetization curves and relative permeability**

*Laser versus mechanical cutting*

Fig. 5.4 shows an example of the measured magnetization curves of small guillotine-cut and laser-cut samples. Figs. 5.5 b) and 5.6 depict the relative permeabilities from these measurements.

The magnetization curves of guillotine-cut and laser-cut samples show significantly different shapes. Fig. 5.4 a) represents the characteristics of the magnetization curves of almost all investigated small samples: At lower magnetic field strengths, up to the knee point, the guillotine-cut specimen has a larger gradient and thus a higher permeability, as can be seen in Fig 5.5 b). Just, before the POI of the guillotine-cut sample with the laser-cut sample (FKL), the gradient of the guillotine-cut sample is smaller than the gradient of the laser-cut samples (Fig. 5.4 a)). Thus, also a POI of the relative permeabilities occurs (see Fig 5.5 b)). At higher saturation, the magnetization curves approach each other and also the gradients tend to converge from the knee point area onward. Thus, at these magnetic field strengths $H$ the permeabilities are very similar.

Of particular interest is material M800-65A: At 50 Hz, the characteristic of the *B-H* curve is almost identical to those presented in Fig. 5.4 a). However, at 250 Hz and 500 Hz, the gradient of the guillotine-cut sample is much closer to that of the laser-cut sample[5] at low magnetic field strength $H$ (in Fig. 5.4 b) in the range of $0\,T - 1.3\,T$; see further Appendix C.2[5]). By considering the corresponding relative permeability (see Fig. 5.6), this difference of guillotine-cut and FKL-laser cut specimens is still obvious at low magnetic field strengths $H$. However, compared to the permeabilities in Fig. 5.5 c), the total difference is smaller.

Again, the knee-point areas of the guillotine-cut samples starts at lower magnetic flux densities $B$ than those of the laser-cut samples (Fig. 5.4 b)) and the POIs of the relative permeabilities of guillotine-cut and laser-cut samples still exist (see Fig. 5.6).

Considering the POIs of the magnetization curves in Table 5.2, points of intersection for one material remain in the same range, so they are most likely almost independent of the frequency. The different POIs for $CO_2$-laser and FKL-laser cut samples are attributed to the different sample widths.

Figs. 5.5 and 5.6 show that the maximum relative permeabilities of the small laser-cut samples are smaller (considering e.g. Fig. 5.5 b), by about a factor of two) than those of the small guillotine-cut sample. Thus, it applies: $\mu_{\text{max,guillotine}} > \mu_{\text{max,laser}}$ (consistent with Chapter 4).

For the materials M400-50A and M800-65A, the following applies: With higher

---

[5]Compare guillotine-cut with FKL-laser cut samples, as these samples have the same width.
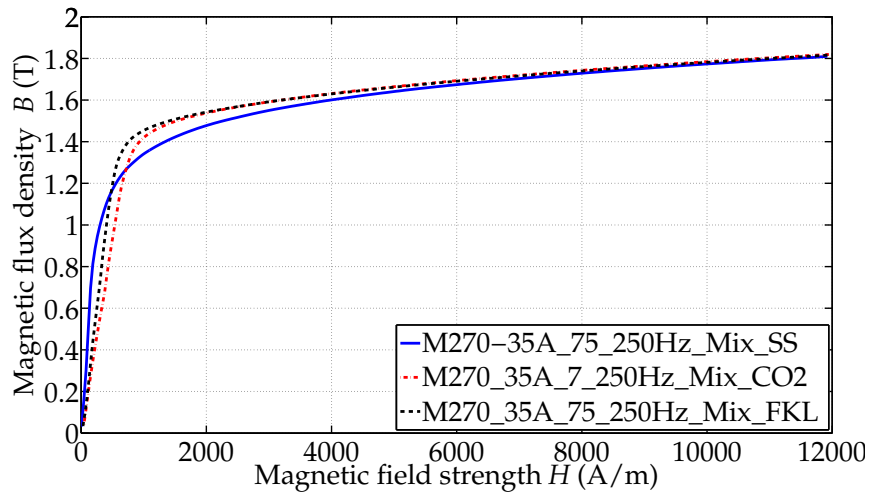
(a) M270-35A
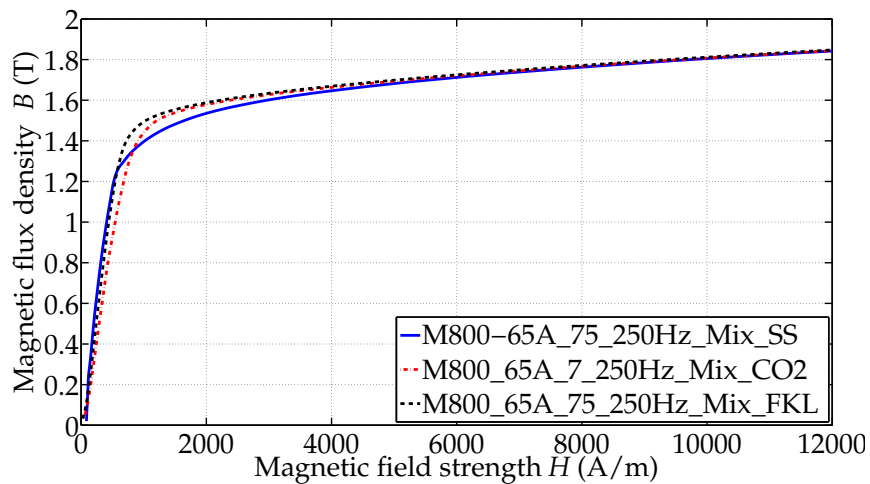


(b) M800-65A

Figure 5.4: *B-H* curves of the small Epstein-samples, comparing the different cutting techniques.
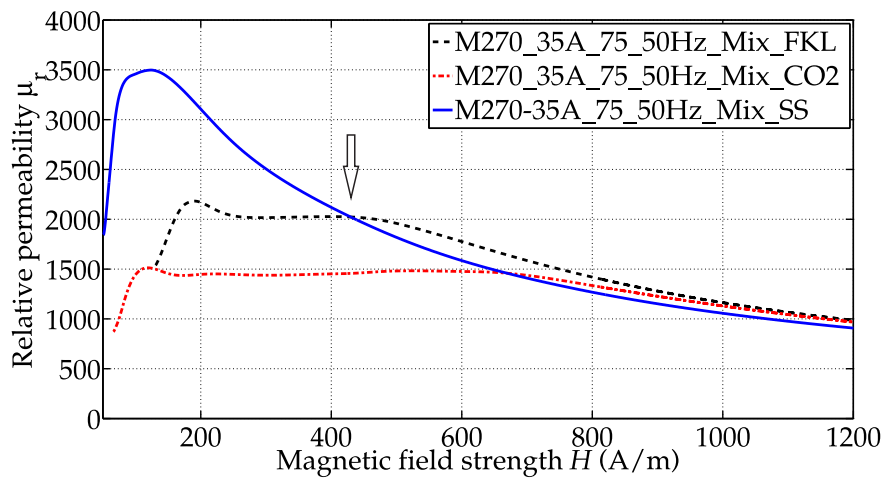
(a) 50 Hz
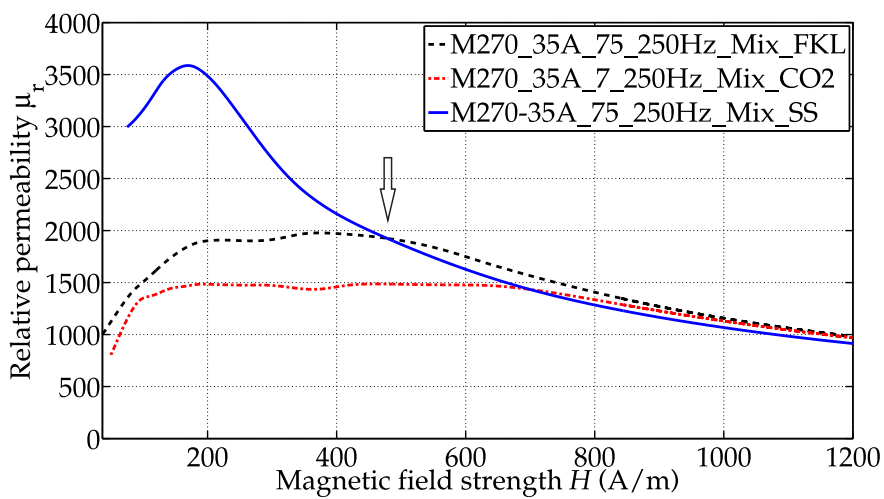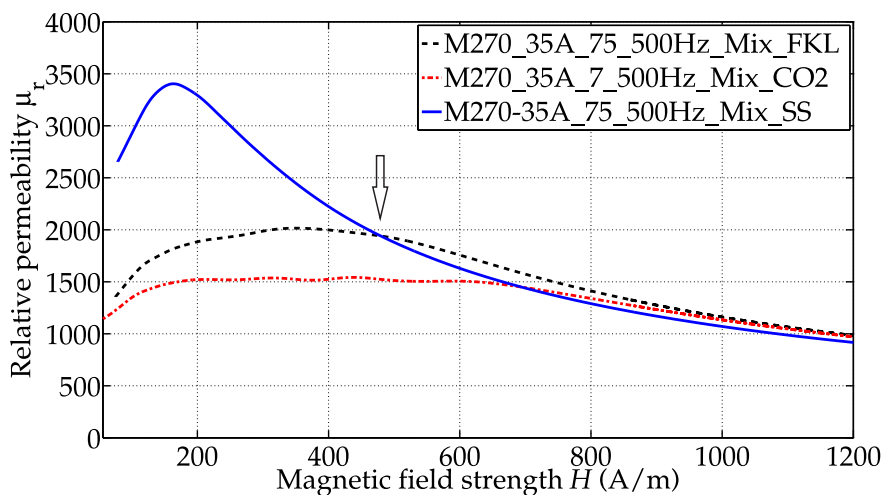


(b) 250 Hz



(c) 500 Hz

Figure 5.5: Relative permeability of the small Epstein-samples, comparing the different cutting techniques.
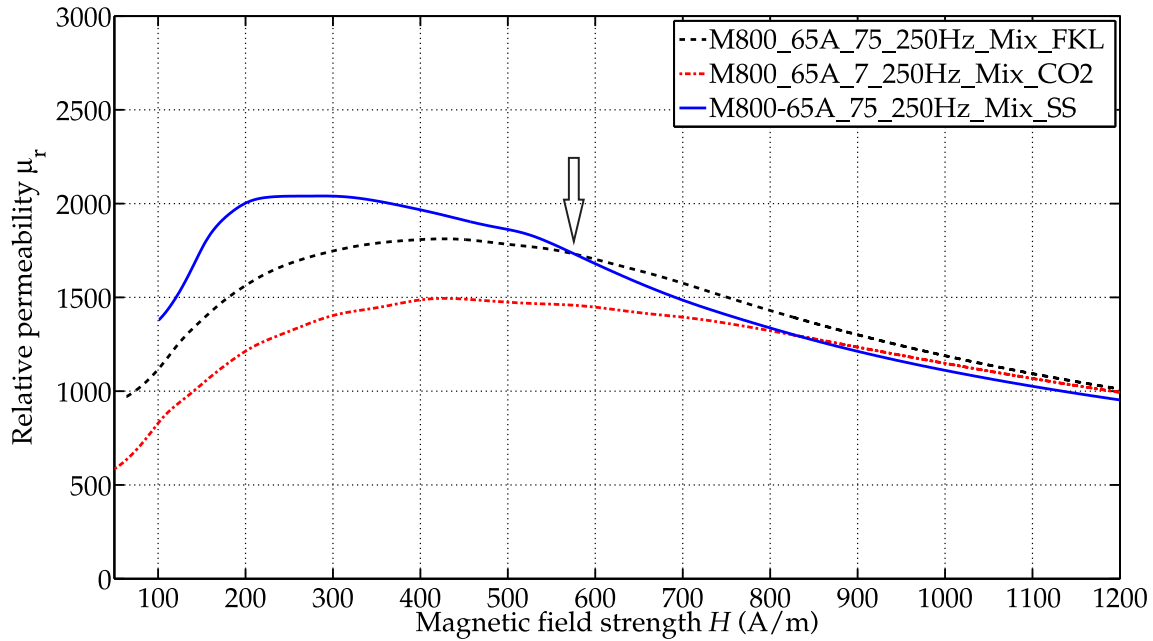
Figure 5.6: Relative permeability of M800-65A_75_250Hz_Mix.

frequency the difference of the maximum relative permeabilities of laser-cut and guillotine-cut samples decreases, and the maximum relative permeabilities (occurring as a peak or as a plateau) themselves decrease, too (see Table 5.4). This effect increases with the thickness (here, also with the decreasing grain size) of the material. Only material M270-35A_75 shows an exception (see Fig. 5.5), as the maximum permeabilities of the laser-cut samples stay almost in the same range, independently of the frequency. Furthermore, the maximum permeability of the guillotine-cut sample is larger at 250 Hz than at 50 Hz. It can be assumed that this maximum must be larger for the guillotine-cut samples of material M270-35A, at 50 Hz.

Considering Fig. 5.5, the maximum relative permeability of the laser-cut samples is not well pronounced (losing the distinctive maximum (in accord with Chapter 4.1.1)), and almost similar to a plateau, in contrast to that of the small guillotine-cut samples. This 'plateau' is shifted to lower relative permeabilities with increasing ratio $V_{dg}/(V_{nd} + V_{dg})$ (compare $CO_2$- and FKL-laser cut samples).

As with the specific losses, a POI of the laser and mechanically-cut samples for the relative permeabilities occurs, which also seems to depend on the material investigated (Table 5.3; these values of flux density $B$ agree with the POIs of the measured *B-H* curves). This is in line with the results obtained in Chapter 4.1.1. This POI occurs at the magnetic field strength of the knee point area of the laser-cut samples.

### Comparison of the two laser cutting techniques
The measured difference between the magnetization curves of the two laser-cut sam-

Table 5.2: POIs (magnetization curve) at different frequencies, seen here for the small samples in 'Mix'-order.

|  | M270-35A_75 | M400-50A_75 | M800-65A_75 |
|---|---|---|---|
| 50 Hz | 1.23 T ($CO_2$ - SS) | 1.34 T ($CO_2$ - SS) | 1.33 T ($CO_2$ - SS) |
|  | 1.09 T (FKL - SS) | 1.23 T (FKL - SS) | 1.26 T (FKL - SS) |
| 250 Hz | 1.27 T ($CO_2$ - SS) | 1.36 T ($CO_2$ - SS) | 1.35 T ($CO_2$ - SS) |
|  | 1.16 T (FKL - SS) | 1.27 T (FKL - SS) | 1.25 T (FKL - SS) |
| 500 Hz | 1.26 T ($CO_2$ - SS) | 1.38 T ($CO_2$ - SS) | 1.40 T ($CO_2$ - SS) |
|  | 1.17 T (FKL - SS) | 1.32 T (FKL - SS) | 1.12 T (FKL - SS) |

ples concerns mainly the area up to the knee point (see Fig. 5.4): The magnetization curve of the $CO_2$-laser cut sample is shifted to higher magnetic field strengths than that of the FKL-laser cut sample. Thus, up to around 1000 A/m, the $CO_2$-laser cut samples have a smaller relative permeability than the FKL-laser cut samples (Fig. 5.5 b)). This shifting of the magnetization curve below the knee point and the resulting lower permeability for $CO_2$-laser cut samples at low magnetic field strengths $H$ may be mainly attributed to the difference in sample size (7.5 versus 7 mm width) and thus larger ratio $V_{dg}/(V_{nd} + V_{dg})$. However, as known from Chapter 4, it may also be due to the different cutting techniques used. This is investigated further with the wide samples (Chapter 5.2.2). Concerning all results of the small samples, it applies: $\mu_{max,guillotine} > \mu_{max,FKL} > \mu_{max,CO_2}$. This concurs with Chapter 4.1.1. Also this behavior is investigated further with the wide samples.

Table 5.3: POIs for permeability at different frequencies, seen here for the small samples in 'Mix'-order.

|  | M270-35A_75 | M400-50A_75 | M800-65A_75 |
|---|---|---|---|
| 50 Hz | 669 $\frac{A}{m}$ (1.22 T) ($CO_2$ - SS) | 805 $\frac{A}{m}$ (1.34 T) ($CO_2$ - SS) | 708 $\frac{A}{m}$ (1.33 T) ($CO_2$ - SS) |
|  | 430 $\frac{A}{m}$ (1.09 T) (FKL - SS) | 502 $\frac{A}{m}$ (1.21 T) (FKL - SS) | 542 $\frac{A}{m}$ (1.26 T) (FKL - SS) |
| 250 Hz | 699 $\frac{A}{m}$ (1.25 T) ($CO_2$ - SS) | 849 $\frac{A}{m}$ (1.35 T) ($CO_2$ - SS) | 831 $\frac{A}{m}$ (1.35 T) ($CO_2$ - SS) |
|  | 478 $\frac{A}{m}$ (1.16 T) (FKL - SS) | 597 $\frac{A}{m}$ (1.27 T) (FKL - SS) | 577 $\frac{A}{m}$ (1.25 T) (FKL - SS) |
| 500 Hz | 694 $\frac{A}{m}$ (1.26 T) ($CO_2$ - SS) | 990 $\frac{A}{m}$ (1.39 T) ($CO_2$ - SS) | 1098 $\frac{A}{m}$ (1.45 T) ($CO_2$ - SS) |
|  | 480 $\frac{A}{m}$ (1.17 T) (FKL - SS) | 699 $\frac{A}{m}$ (1.32 T) (FKL - SS) | 709 $\frac{A}{m}$ (1.12 T) (FKL - SS) |

Conclusions - small samples:
- The losses of the mechanically-cut samples increase more with a square, in contrast to those of the laser-cut samples, which have a more 'linear'[1,p.132] characteristic at moderate flux densities.

Table 5.4: Maximum of permeability at different frequencies, as seen for the small samples in 'Mix'-order.

|  | **M270-35A_75** | **M400-50A_75** | **M800-65A_75** |
|---|---|---|---|
| | 3498 (SS) | 4527 (SS) | 3610 (SS) |
| 50 Hz | 1513 ($CO_2$) | 1880 ($CO_2$) | 1910 ($CO_2$) |
| | 2182 (FKL) | 2236 (FKL) | 2158 (FKL) |
| | 3587 (SS) | 3073 (SS) | 2041 (SS) |
| 250 Hz | 1485 ($CO_2$) | 1596 ($CO_2$) | 1495 ($CO_2$) |
| | 1977 (FKL) | 1972 (FKL) | 1812 (FKL) |
| | 3404 (SS) | 2329 (SS) | 1536 (SS) |
| 500 Hz | 1542 ($CO_2$) | 1366 ($CO_2$) | 1180 ($CO_2$) |
| | 2015 (FKL) | 1658 (FKL) | 1294 (FKL) |

- This 'linear' characteristic decreases with increasing frequency, material thickness[2,p.132] and sample width.
- A POI occurs for the specific losses of guillotine-cut and laser-cut samples.
- This POI is shifted to lower magnetic flux densities with increasing frequency and increasing material thickness[2,p.132].
- The specific losses of both small laser-cut Epstein samples show the same curve shape. The different absolute values are mainly attributed to the difference in the samples' widths.
- With increasing ratio $V_{dg}/(V_{nd} + V_{dg})$ the specific losses increase as well.
- Below the knee-point area, guillotine-cut samples have a larger permeability than laser-cut samples. It applies: $\mu_{max,guillotine} > \mu_{max,laser}$.
- The knee-point area of guillotine-cut samples is at lower magnetic flux densities $B$ compared to those of laser-cut samples.
- For a given material, the POIs of the magnetization curves for small samples seems to be independent of the frequency.
- The distinct extrema of the relative permeabilities flattens to a 'plateau' in the case of the small laser-cut samples.
- It applies: $\mu_{max,laser\,(FKL)} > \mu_{max,laser\,(CO_2)}$. However, this is mainly attributed to the difference in sample widths of the two laser-cut samples.
- $\mu_{max}$ decreases with increasing ratio $V_{dg}/(V_{nd} + V_{dg})$.
- $\Delta\mu_{max,\,guillotine\text{-}cut \rightarrow FKL\text{-}laser\,cut}$ decreases with increasing frequency and material thickness[2,p.132].

## 5.2.2 Wide samples

**Specific losses**

*Laser versus mechanical cutting*

Considering the wide samples, the laser-cut samples still follow a different loss trend compared to the guillotine-cut samples (see for instance Figs. 5.7 and 5.8). This concurs with the results presented in Chapter 4.1.1. The curve of specific losses of guillotine-cut samples is still more curved than those of the laser-cut samples, whereas the guillotine-cut samples show mostly lower losses at small and medium magnetic flux densities (see Figs. 5.7 and 5.8). Beyond this area the losses of the guillotine-cut and the laser-cut samples are almost equal (see Fig. 5.7,b)) or, a POI occurs above which the guillotine-cut samples show higher losses (see Fig. 5.8). The area of lower losses for guillotine-cut samples and thus the POI are shifted to lower magnetic flux densities with increasing frequency (see also Figs. 5.9 and 5.10) and for thicker material (possibly also with decreasing grain size) (see Table 5.5 and Figs. 5.7 to 5.10). Thus, at higher frequencies the laser cutting technology becomes a viable alternative to mechanical cutting, when the specific losses $p_s$ are of interest.

Furthermore, the POI is moved to lower magnetic flux densities with smaller sample widths (compare only wide with small samples with Tables 5.1 and 5.5). This applies for both laser cutting techniques investigated. However, this assumption is not true when comparing the POIs of the small FKL-laser with the smaller $CO_2$-laser cut sample. Under the assumption that both laser cutting techniques degrade the specific losses to almost the same extent, if they had the same sample width (see next Subsection - 'Comparison of the two laser cutting techniques', p. 147), the small $CO_2$-laser cut samples, which have a larger ratio $V_{dg}/(V_{nd} + V_{dg})$ than the small FKL-laser cut samples, should have their POIs at smaller magnetic flux densities than the small FKL-laser cut samples. This, however, is not the case (see Fig. 5.11).

Additionally, Tables 5.1 and 5.5 indicate that the interval of the points of intersection from 50 Hz to 250 Hz is larger than the interval from 250 Hz to 500 Hz. Thus, the shifting of the POIs to lower magnetic flux densities $B$ with increasing frequency is non-linear.

The 'linear' characteristic of the specific losses of the laser-cut samples, as observed for the small samples at moderate flux densities, is strongly reduced for the wide samples and only slightly seen for material M270-35A at low frequency (see Fig. 5.7). Thus, this characteristic disappears with decreasing ratio $V_{dg}/(V_{nd} + V_{dg})$, as well as with increasing material thickness and frequency. Both material thickness and frequency increase the eddy currents, whereas the characteristic properties of the hysteresis losses are reduced (see also Chapter 3.4).
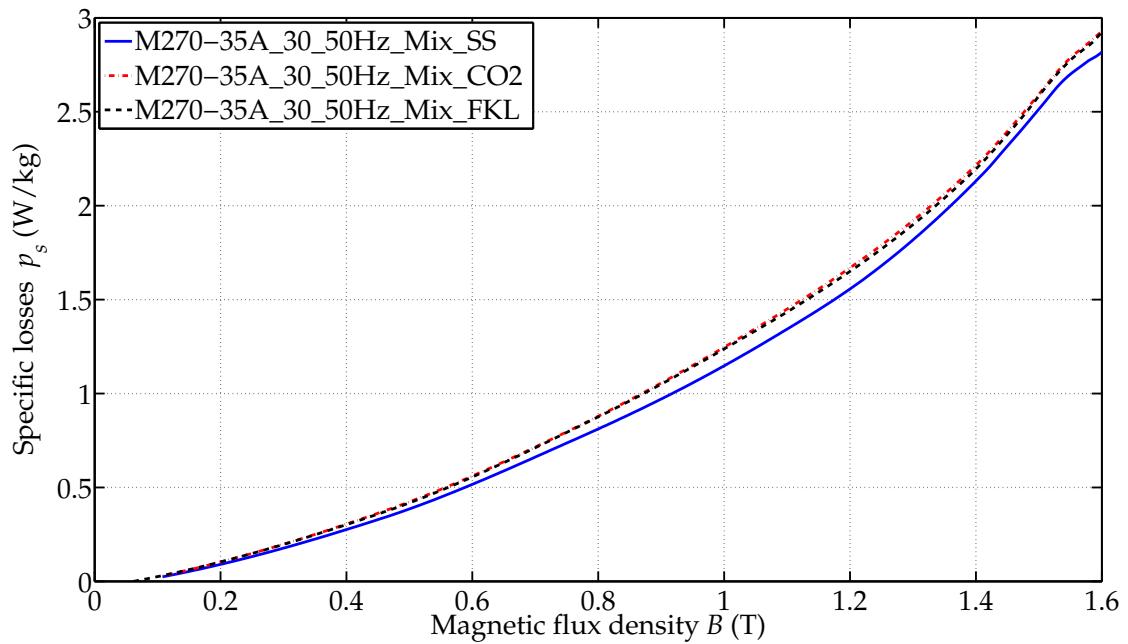
(a) 50 Hz
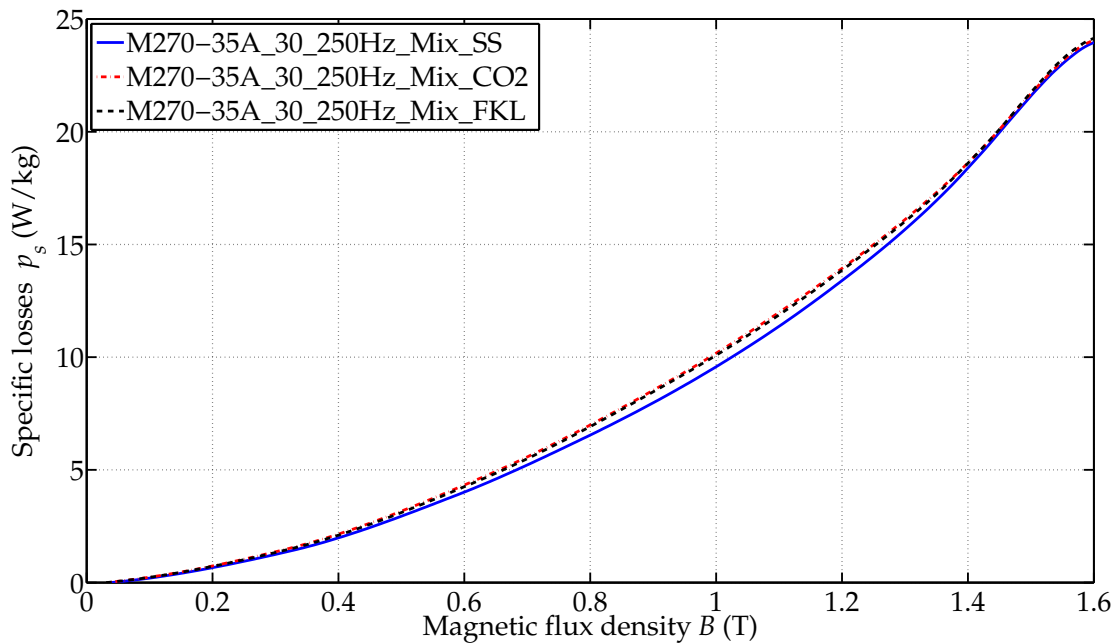


(b) 250 Hz

Figure 5.7: Specific losses of M270-35A wide samples produced by different cutting techniques.
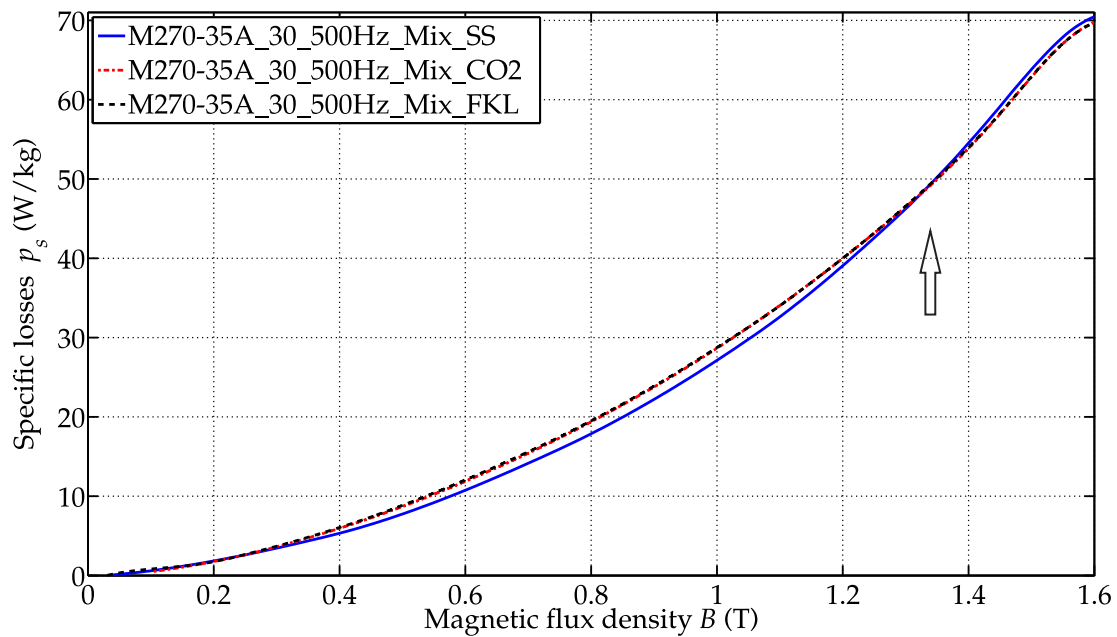
(a) 500 Hz
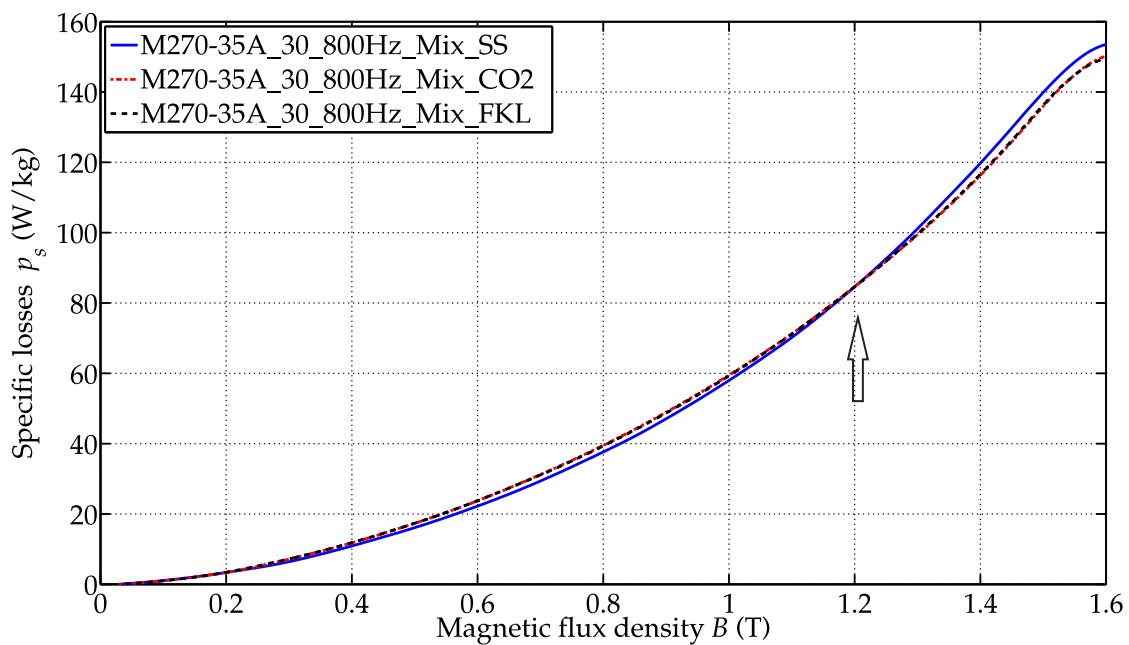


(b) 800 Hz

Figure 5.8: Specific losses of M270-35A wide samples produced by different cutting techniques.
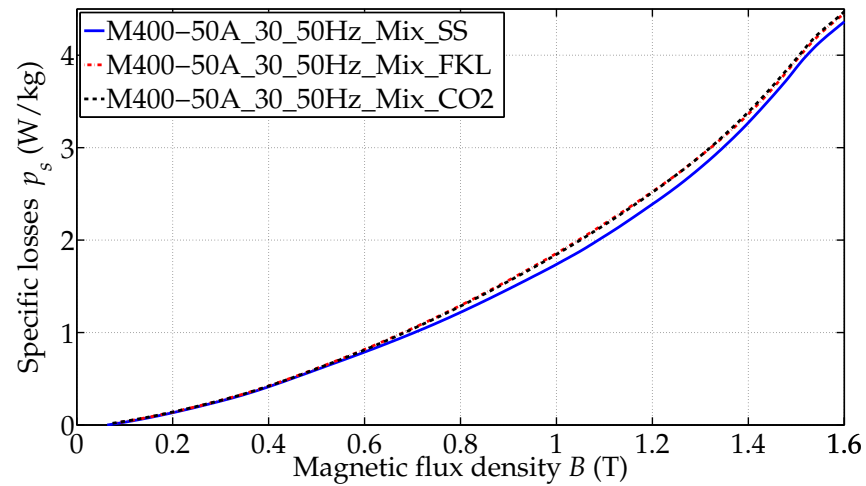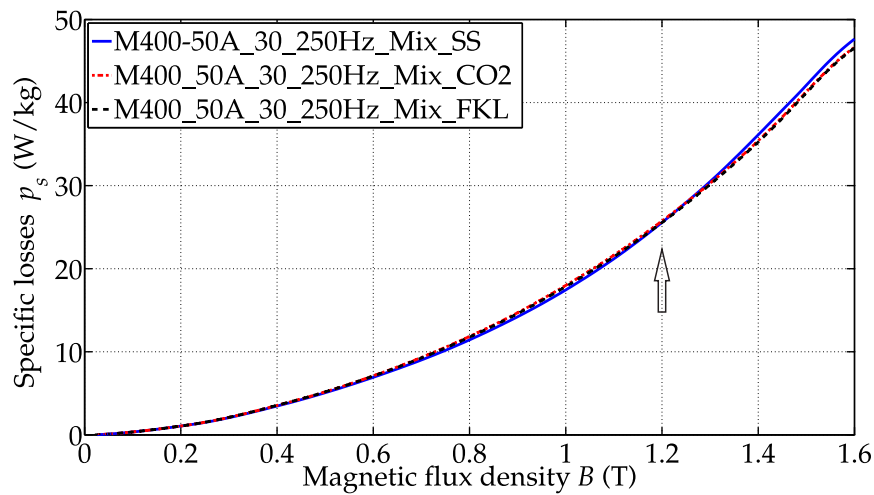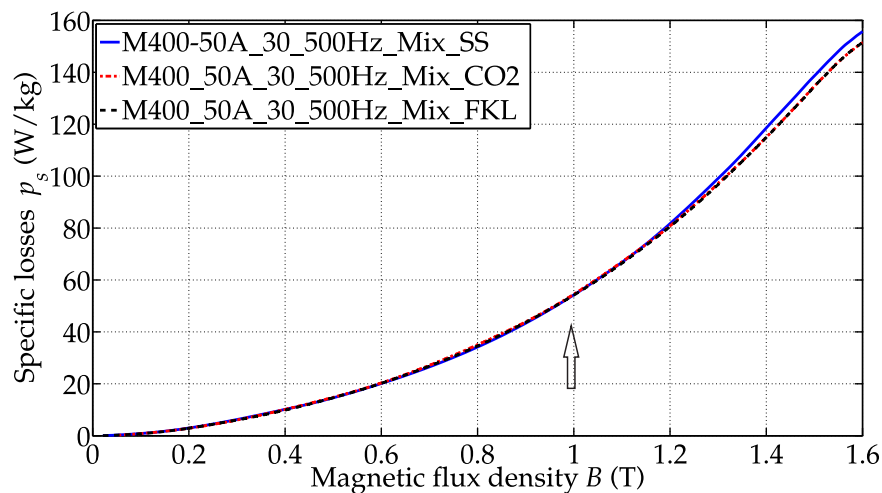
(a) 50 Hz



(b) 250 Hz



(c) 500 Hz

Figure 5.9: Specific losses of M400-50A wide samples produced by different cutting techniques.
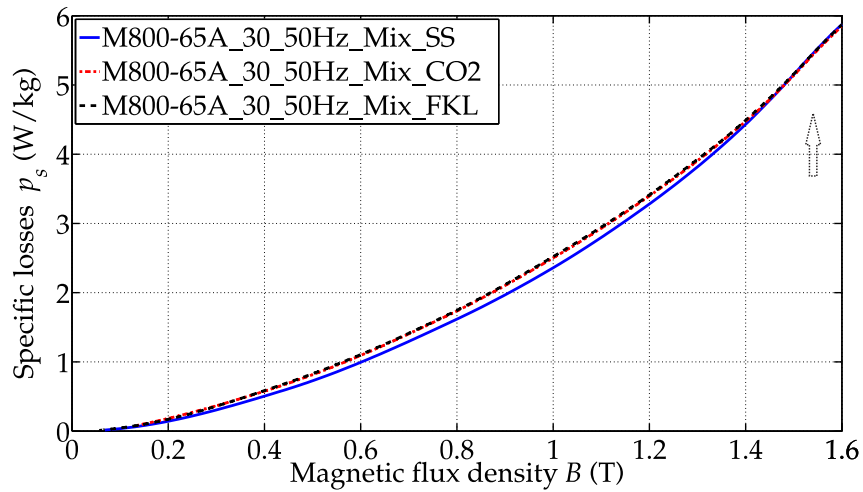
(a) 50 Hz
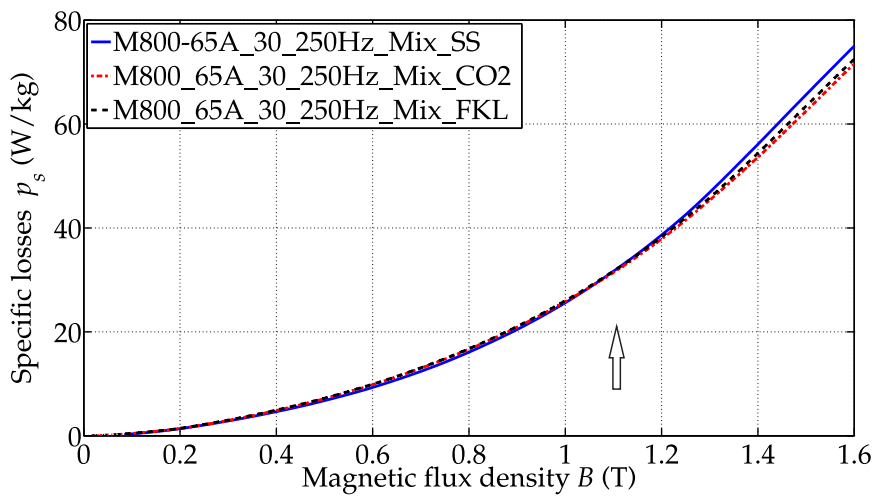


(b) 250 Hz
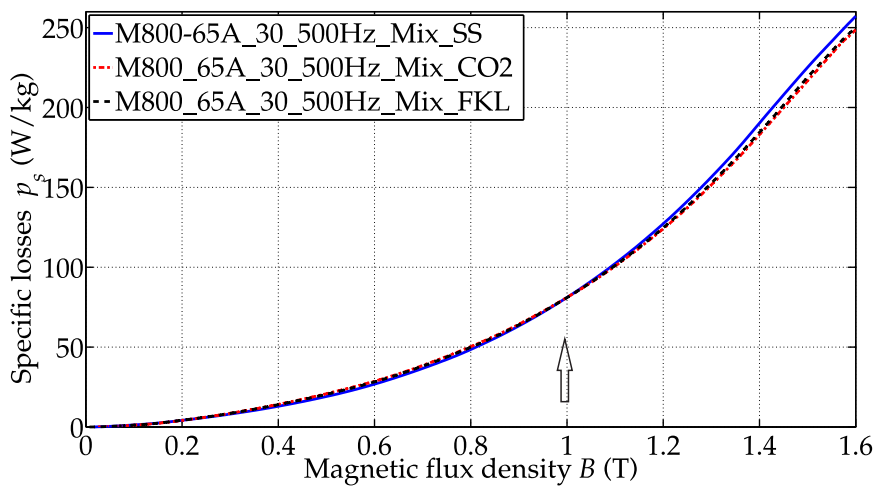


(c) 500 Hz

Figure 5.10: Specific losses of M800-65A wide samples produced by different cutting techniques.
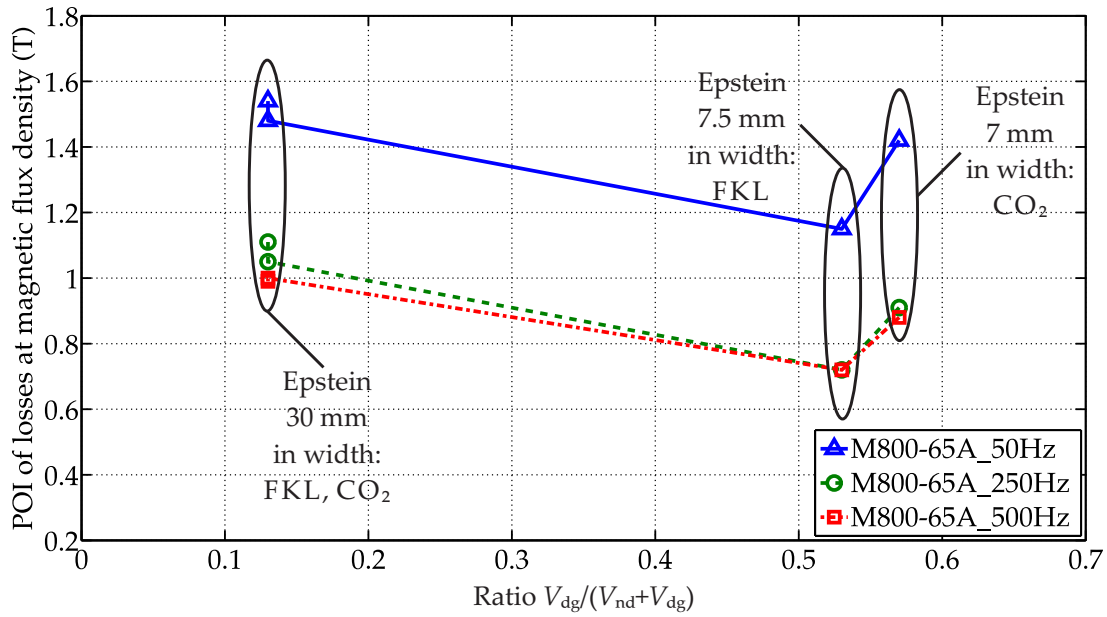
Figure 5.11: POI versus ratio $V_{dg}/(V_{nd} + V_{dg})$ under the assumption that both lasers deteriorate the material in the same way. Ratio $V_{dg}/(V_{nd} + V_{dg})$ bases on a deterioration depth of 2 mm.

Table 5.5: POIs (loss curves) at different frequencies, seen here for the wide samples in 'Mix'-order.

|        | **M270-35A_30** | **M400-50A_30** | **M800-65A_30** |
|--------|-----------------|-----------------|-----------------|
| 50 Hz  | - -             | - -             | 1.48 T ($CO_2$ - SS) <br> 1.54 T* (FKL - SS) |
| 250 Hz | - -             | 1.25 T ($CO_2$ - SS) <br> 1.20 T (FKL - SS) | 1.05 T ($CO_2$ - SS) <br> 1.11 T (FKL - SS) |
| 500 Hz | 1.32 T ($CO_2$ - SS) <br> 1.34 T (FKL - SS) | 1.14 T ($CO_2$ - SS) <br> 0.99 T (FKL - SS) | 1.00 T ($CO_2$ - SS) <br> 0.99 T (FKL - SS) |
| 800 Hz | 1.21 T ($CO_2$ - SS) <br> 1.20 T (FKL - SS) | N/A             | N/A             |

∗ = to be considered with caution, see introduction of Chapter 5.

### Comparison of the two laser cutting techniques

Both laser-cut samples have (almost) the same curve shape and gradients (see Figs. 5.7 to 5.10). This applies to all investigated wide samples, measured in the 'Mix' arrangement (see Chapter 2.5). It can therefore be concluded that both laser cutting techniques deteriorate the material, in terms of the specific losses, in the same way. This is apparently in conflict with the results of Chapter 4, where the wide $CO_2$-laser cut samples still have slightly higher losses than the FKL-laser cut

samples. However, it is assumed that this difference in losses due to the different laser cutting techniques disappears with increasing eddy currents and thus becomes more and more negligible (Note that in Chapter 4 only hysteresis losses were measured in contrast to the Epstein frame measurements presented here).

However, differences in the specific losses are observed with the following samples: M270-35A_30_50Hz_LL (from about 1 T: $p_{s,FKL} < p_{s,CO_2}$), M400-50A_30_50Hz_LL ($p_{s,FKL} < p_{s,CO_2}$), M800-65A_30_500Hz_QQ (from about 1 T: $p_{s,FKL} > p_{s,CO_2}$). These differences may be due to the following reasons: measurement errors, the sample set of one cutting direction includes (a) sample(s) with a deviating characteristic[6], and/or both differences of the laser-cut specimens measured in one cutting direction overlap and cancel each other in the case of the mixed samples.

**Magnetization curves and relative permeability**

*Laser versus mechanical cutting*

Fig. 5.12 shows a representative *B-H* curve for material M270-35A (further diagrams are presented in Appendix C.3). The magnetization curves of the guillotine-cut samples differ from those of the laser-cut samples most obviously in the knee point area. The knee-point area of the guillotine-cut samples still occurs at smaller magnetic flux densities *B* than those of the laser-cut samples. This is in line with the results of the small samples. The gradients below the knee point area of all three curves are closer together than those of the small samples. The corresponding relative permeabilities are shown in Fig. 5.13 c). According to this diagram, the largest differences are in the range below 200 A/m.

Considering all results of the wide samples at large, the guillotine-cut samples have the largest maximum relative permeabilities compared to those of the laser-cut samples (see Table 5.7). This is in accord with the results obtained by the small samples and those of Chapter 4. Furthermore, the maximum permeabilities are shifted to higher magnetic field strengths *H* with decreasing amplitude (Figs. 5.13 a), b)). This is in line with the results of Chapter 4.

With increasing frequency the maximum permeability decreases and is less pronounced but still distinct. However, a 'plateau', as observed for the small laser-cut samples, is not visible. Thus, the latter laser characteristic only occurs for samples with large ratio $V_{dg}/(V_{nd} + V_{dg})$. This is in accord with Chapter 4.

POIs of the relative permeability of wide guillotine-cut and laser-cut samples

---

[6]As the 'Mix' arrangement of wide samples only contains eight samples of each cutting direction, it may be possible that a sample strip with deviating characteristic is present in the measurement of one cutting direction (16 samples), but not in the mixed measurement.
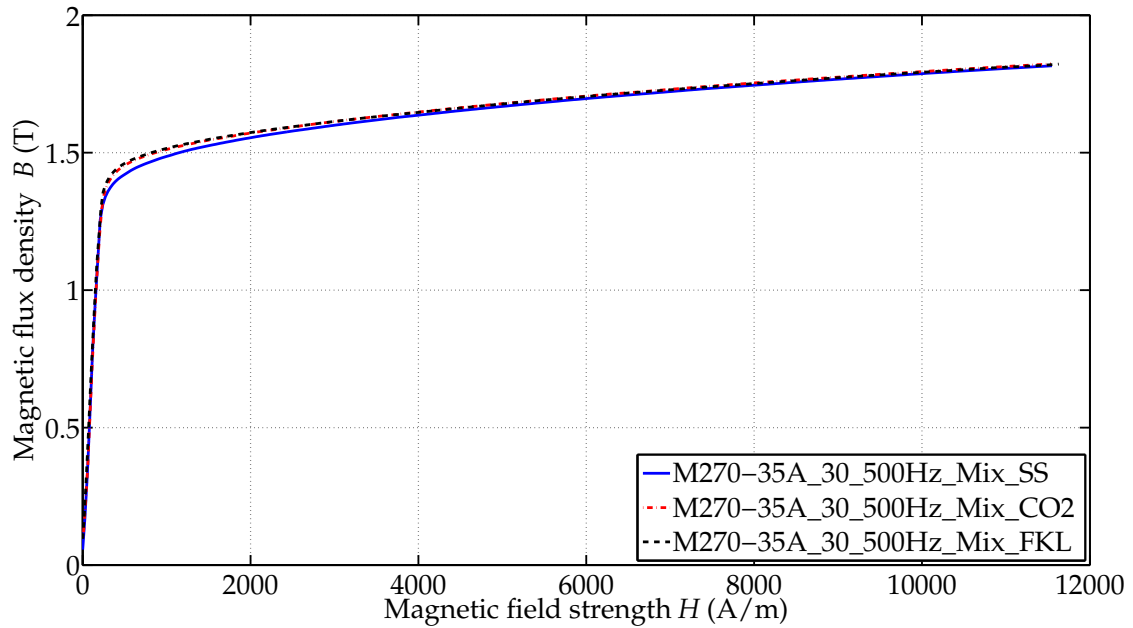
Figure 5.12: Exemplary *B-H* curve of M270-35A_30_500Hz_Mix.

also exist. However, these mostly occur where the difference between the relative permeabilities of both cutting techniques is small and thus are not of further interest here.

The POIs of losses and permeability do not occur at the same magnetic field strengths *H* and hence not at the same magnetic flux densities *B*. This applies both to the small and the wide samples. This is also an indication that the degradation induced by cutting on the permeability differs from that on the loss behavior.

*Comparison of the two laser cutting techniques*

According to Fig. 5.12 the curve shapes of the laser-cut samples are nearly the same. Considering the related relative permeability (Fig. 5.13), the significant differences of FKL-laser and $CO_2$-laser cut specimens occur at magnetic field strengths *H* below 300 A/m (exact values depend on the material and frequency).

Again, the $CO_2$-laser cut samples have the lowest maximum permeabilities (see Table 5.7). Thus, it applies $\mu_{max,guillotine} > \mu_{max,FKL\text{-}laser} > \mu_{max,CO_2\text{-}laser}$ (Fig 5.13), although the wide samples of $CO_2$-laser and FKL-laser cut samples have the same width. Especially in the range below the knee point area (magnetic domain moving region), FKL-laser cutting deteriorates the relative permeability less than $CO_2$-laser cutting. This can be seen clearly by the location of the maxima and their amplitudes, independent of the sample width. This is in agreement with the results presented in [46] and with the results obtained in Chapter 4.

The difference of the influences of the two laser cutting techniques may be at-
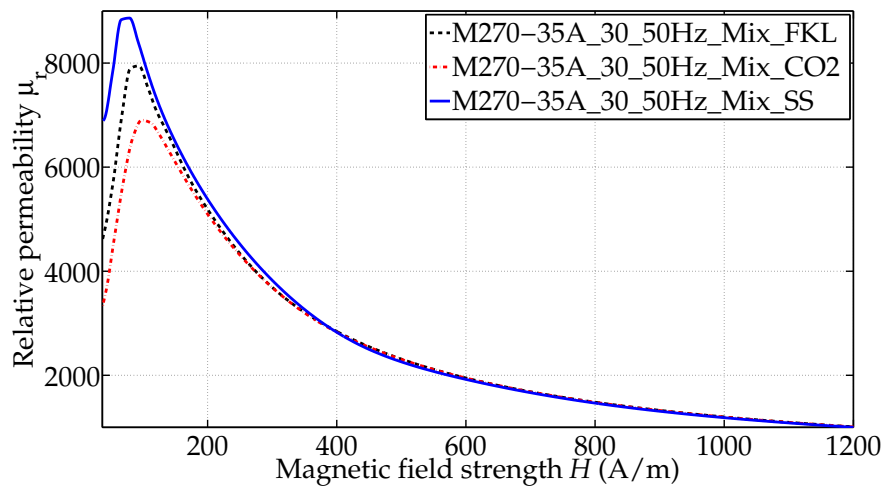
(a) 50 Hz
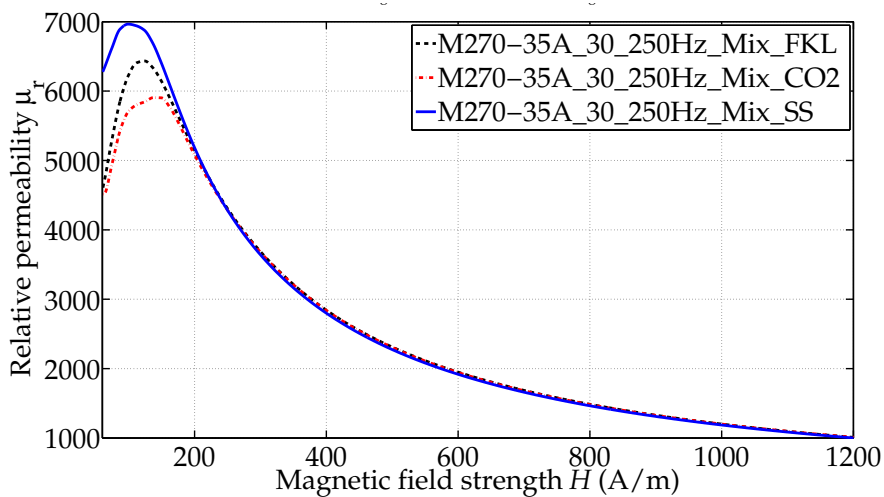


(b) 250 Hz
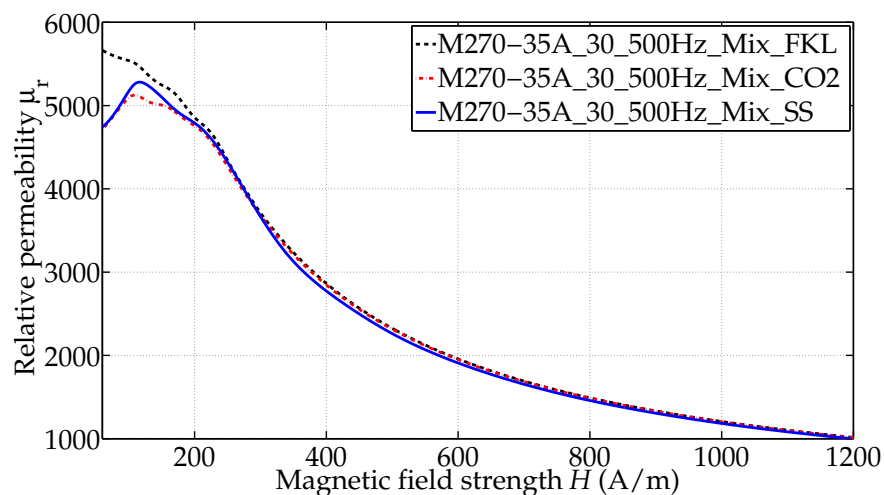


(c) 500 Hz

Figure 5.13: Relative permeability of M270-35A wide samples produced by different cutting techniques.

tributed to the different laser settings as, for example, the cutting speed (see Table 2.1). A further explanation may be that the relative permeability is more affected by the laser cutting process than the specific losses [45], wherefore a difference between the two laser cutting techniques still occurs for the relative permeability, but for the specific losses it is negligible.

Table 5.6: POIs of permeability at different frequencies, seen here for the wide samples in 'Mix'-order.

| | M270-35A_30 | M400-50A_30 | M800-65A_30 |
|---|---|---|---|
| 50 Hz | $398 \frac{A}{m}$ (1.42 T) ($CO_2$ - SS) | $412 \frac{A}{m}$ (1.39 T) ($CO_2$ - SS) | $252 \frac{A}{m}$ (1.31 T) ($CO_2$ - SS) |
| | $387 \frac{A}{m}$ (1.42 T) (FKL - SS) | $295 \frac{A}{m}$ (1.35 T) (FKL - SS) | $226 \frac{A}{m}$ (1.3 T) (FKL - SS) |
| 250 Hz | $247 \frac{A}{m}$ (1.35 T) ($CO_2$ - SS) | $875 \frac{A}{m}$ (1.48 T) ($CO_2$ - SS) | $354 \frac{A}{m}$ (1.14 T) ($CO_2$ - SS) |
| | $223 \frac{A}{m}$ (1.32 T) (FKL - SS) | $854 \frac{A}{m}$ (1.49 T) (FKL - SS) | $329 \frac{A}{m}$ (1.09 T) (FKL - SS) |
| 500 Hz | $293 \frac{A}{m}$ (1.38 T) ($CO_2$ - SS) | $555 \frac{A}{m}$ (1.44 T) ($CO_2$ - SS) | $236 \frac{A}{m}$ (0.62 T) ($CO_2$ - SS) |
| | ** (FKL - SS) | $486 \frac{A}{m}$ (1.36 T) (FKL - SS) | $213 \frac{A}{m}$ (0.58 T) (FKL - SS) |

∗∗ = x-laser cut samples always show a higher permeability than guillotine-cut samples.

Table 5.7: Maximum permeabilities at different frequencies, seen here for the wide samples in 'Mix'-order.

| | M270-35A_30 | M400-50A_30 | M800-65A_30 |
|---|---|---|---|
| 50 Hz | 8865 (SS) | 7557 (SS) | 5969 (SS) |
| | 6901 ($CO_2$) | 5220 ($CO_2$) | 5155 ($CO_2$) |
| | 7947 (FKL) | 5892 (FKL) | 5549 (FKL) |
| 250 Hz | 6965 (SS) | 4271 (SS) | 2964 (SS) |
| | 5905 ($CO_2$) | 3770 ($CO_2$) | 2823 ($CO_2$) |
| | 6433 (FKL) | 3978 (FKL) | 2907 (FKL) |
| 500 Hz | 5282 (SS) | 4124 (SS) | 2189 (SS) |
| | 5125 ($CO_2$) | 3023 ($CO_2$) | 2127 ($CO_2$) |
| | 5520 (FKL) | 3116 (FKL) | 2189 (FKL) |

Conclusions - wide samples:
- The losses of wide laser-cut and guillotine-cut samples still differ in their curve shapes. This is in agreement with the findings obtained in Chapter 4. However, the 'linear' characteristic is strongly reduced if compared with the small samples.
- POIs still occur for the loss curves of guillotine-cut and laser-cut samples. These are shifted to lower magnetic flux densities $B$ with increasing frequency, material thickness[2,p.132] and ratio $V_{dg}/(V_{nd} + V_{dg})$ (compare small

and wide specimen).

- The losses of both wide laser-cut samples show the same curve shape and have (almost) the same values. Compared to the results of Chapter 4, the additional eddy currents must have 'eliminated' the slight differences, which are still apparent with the quasi-static measurements. Thus, it can be said that both cutting techniques have the same degrading effect on the material loss behavior.

- The knee point area of the guillotine-cut samples still occurs at smaller magnetic flux densities $B$ than those of the laser-cut samples. This is in accord with the results of the small samples.

- For wide samples it still applies: $\mu_{\mathrm{max,guillotine}} > \mu_{\mathrm{max,FKL}} > \mu_{\mathrm{max,CO_2}}$, although both laser-cut samples have the same width. Thus, the relative permeability is more affected by different laser cutting techniques than the specific losses, whereas both laser techniques have a different degrading influence on the permeability, especially in the magnetic domain moving region. The difference in sample width, as it is the case with the small samples, additionally increases the difference of permeabilities between the two laser-cut samples.

- The maximum relative permeability is shifted to larger magnetic field strengths with decreasing amplitude.

- The wide investigated laser-cut samples still show distinct extremes.

- POIs of the permeability still exist.

- $B_{\mathrm{point\ of\ intersection,\ losses}} \neq B_{\mathrm{point\ of\ intersection,\ permeability}}$.

## 5.3 Influence of cutting direction

The influence of the cutting direction is only investigated for some laser-cut samples, as for the guillotine-cut samples, not enough strip samples are available (see Table 2.3 in Chapter 2.5). Therefore, the results may only apply to laser-cut specimens and a comparison with guillotine-cut samples was not possible.

The specimens cut in transverse direction (QQ) show worse magnetization curves and relative permeabilities at low magnetic field strengths $H$ than the measured samples of LL-samples and QQ- samples (Mix) or the samples cut in rolling direction (LL) (see Fig. 5.14 a) and b)). For example, a higher magnetic field strength $H$ is required to obtain the same magnetic flux density $B$ compared to the other two sample sets (Fig. 5.14 a)). However, the samples cut longitudinally obtain the best

results concerning the magnetization curves and the relative permeability. This behavior applies generally to all wide and small laser-cut samples, but to different extents: E.g. the differences in relative permeability at low magnetic field strengths $H$ are reduced for small samples and with higher frequencies.

In many cases, the specimens cut in transverse direction (QQ) show higher specific losses than the measured samples of LL-samples and QQ-samples (Mix) or the samples cut in rolling direction (LL) (see Fig. 5.14 c)). However, different behavior is also observed for the wide samples of material M400-50A at 500 Hz and M800-65A at 250 Hz and 500 Hz (for both laser cutting techniques) and for the small samples for M800-65A at 500 Hz: A POI for the specific losses of transversely-cut and longitudinally-cut samples occurs (see Fig. 5.15: The POI occurs at 1.45 T and 1.4 T, respectively and Fig. 5.16). Thus, transversely laser-cut samples may have smaller losses than longitudinally laser-cut samples at high magnetic flux densities $B$. In the case of M270-35A no POI is observed, either for wide and small samples.

With increasing material thickness[2,p.132], the POI occurs at smaller frequencies and smaller magnetic flux densities. This conclusion derives from the wide samples; as for the small samples, only a POI occurs for material M800-65A at 500 Hz. Furthermore, with smaller sample width the POI for M800-65A at 500 Hz is shifted to higher magnetic flux densities $B$.

Considering the curves as a whole, the differences between the measured curves are larger for M270-35A and decrease with increasing material thickness. As the eddy currents are larger for increasing material thickness, the effect of the cutting direction is reduced. For example, at 1 T and 500 Hz, the losses of the wide transversely FKL-laser cut samples and those of the 'Mix' samples compare as follows: M270-35A -9 %, for M400-50A -6 % and for M800-65A -0.7 % decrease. The losses of the small transversely $CO_2$-laser cut samples and those of the 'Mix' samples show decreases of M400-50A -3.6 %, M800-65A -0.4 %, again at 1 T and 500 Hz.

---

Conclusions:
- A POI of the specific losses of transversely and longitudinally laser-cut samples may occur. It is primarily found for thicker[2,p.132] material at high frequencies and small ratios $V_{dg}/(V_{nd} + V_{dg})$.
- With increasing thickness[2,p.132] of the material, this POI occurs at smaller frequencies and smaller magnetic flux densities.
- With smaller sample width, the POI for M800-65A at 500 Hz is shifted to higher magnetic flux densities $B$.
- The distances between the loss-curves QQ-samples, LL-samples and Mix-samples decreases with increasing material thickness.

---
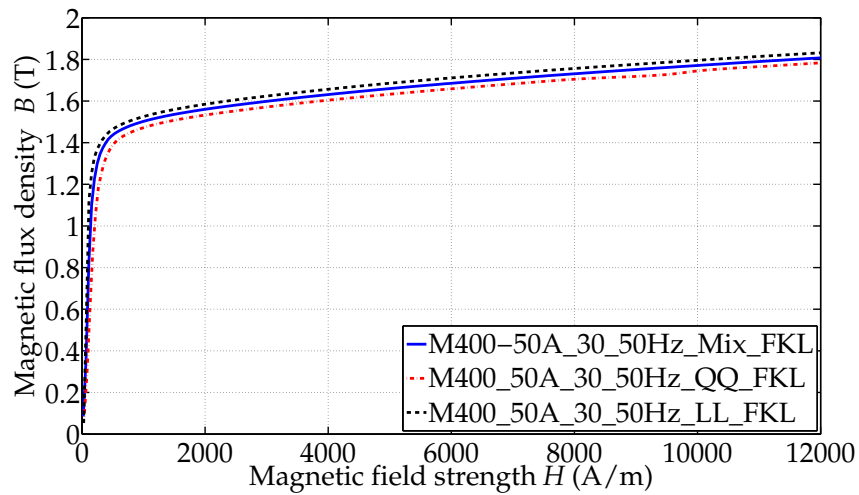
(a) Magnetization curve
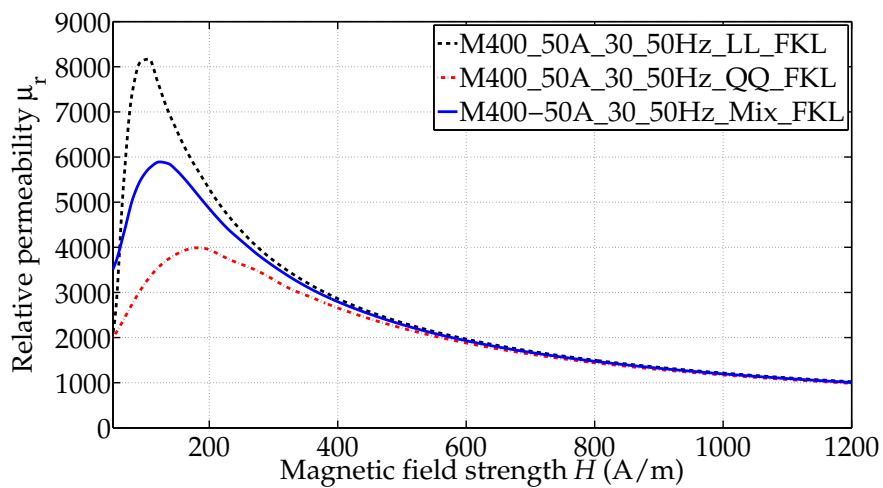


(b) Relative permeability
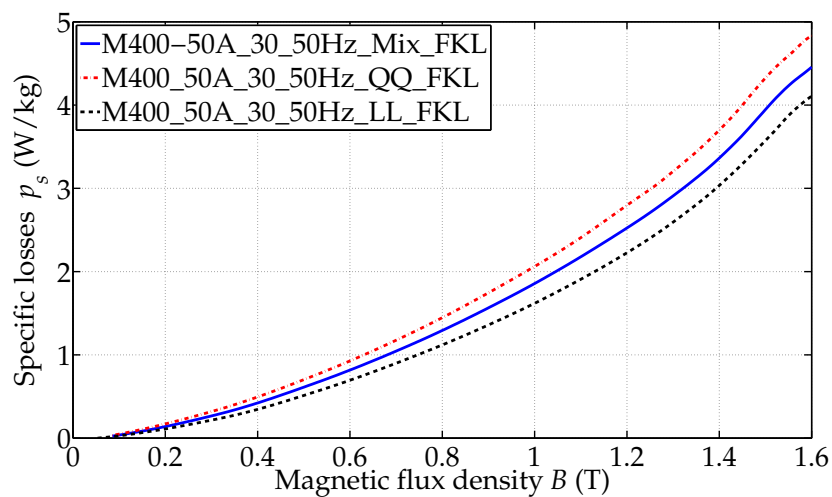


(c) Specific losses

Figure 5.14: Comparison of different cutting directions.
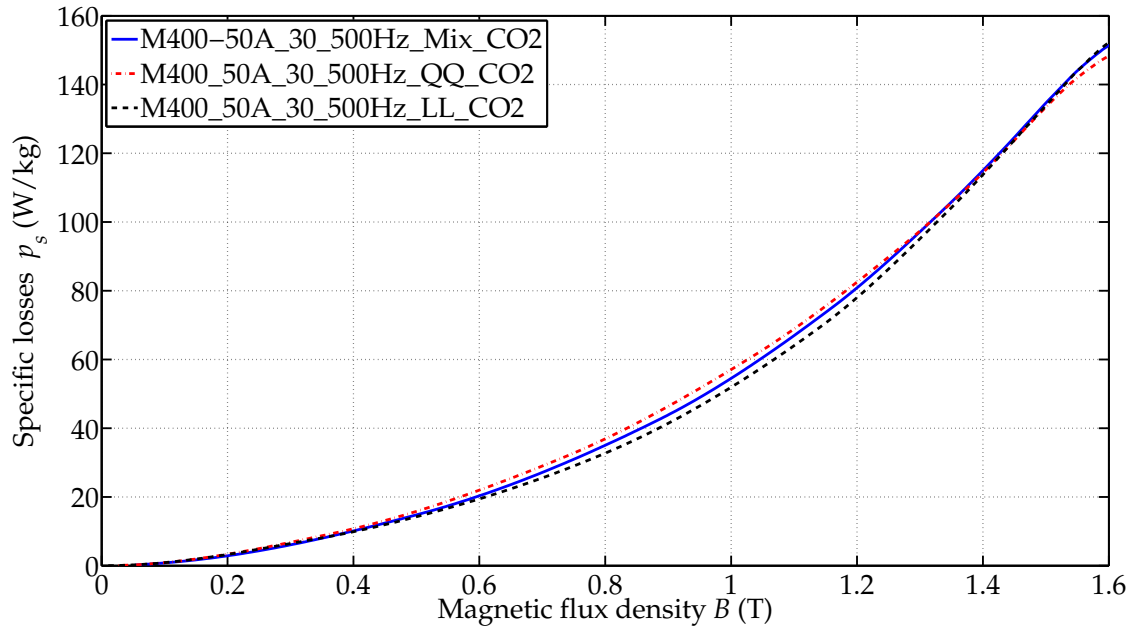
(a) $CO_2$
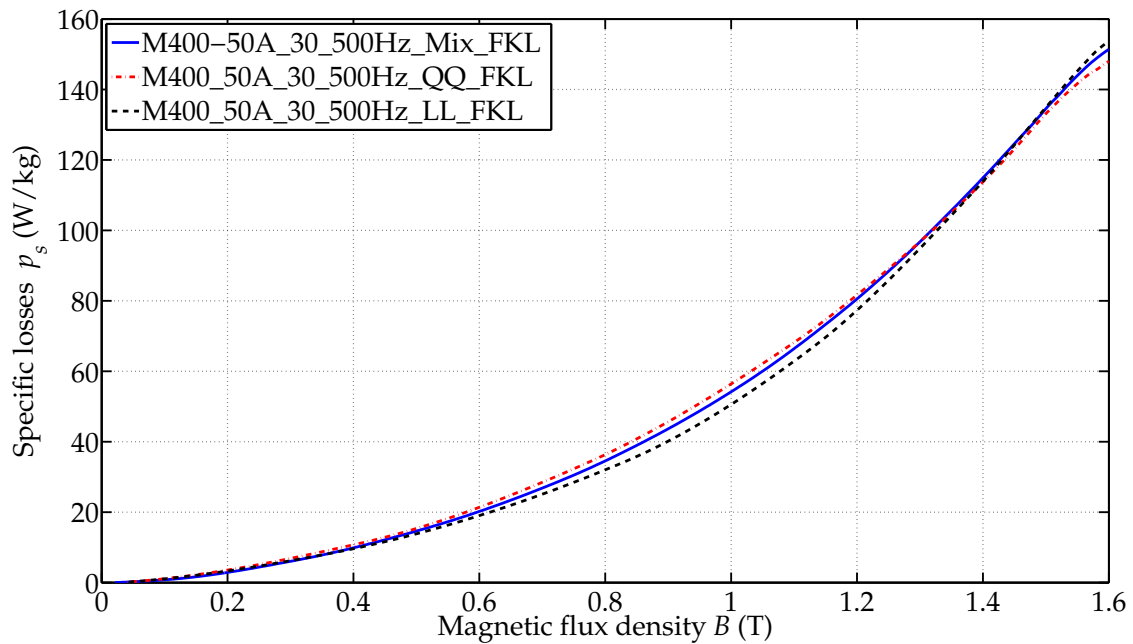


(b) FKL

Figure 5.15: Occurrence of POI for M400-50A at 500 Hz. Up to 1.4 T the longitudi-
nally-cut probe has lower specific losses than the transversely-cut spec-
imen. Above this point, the situation reverses.
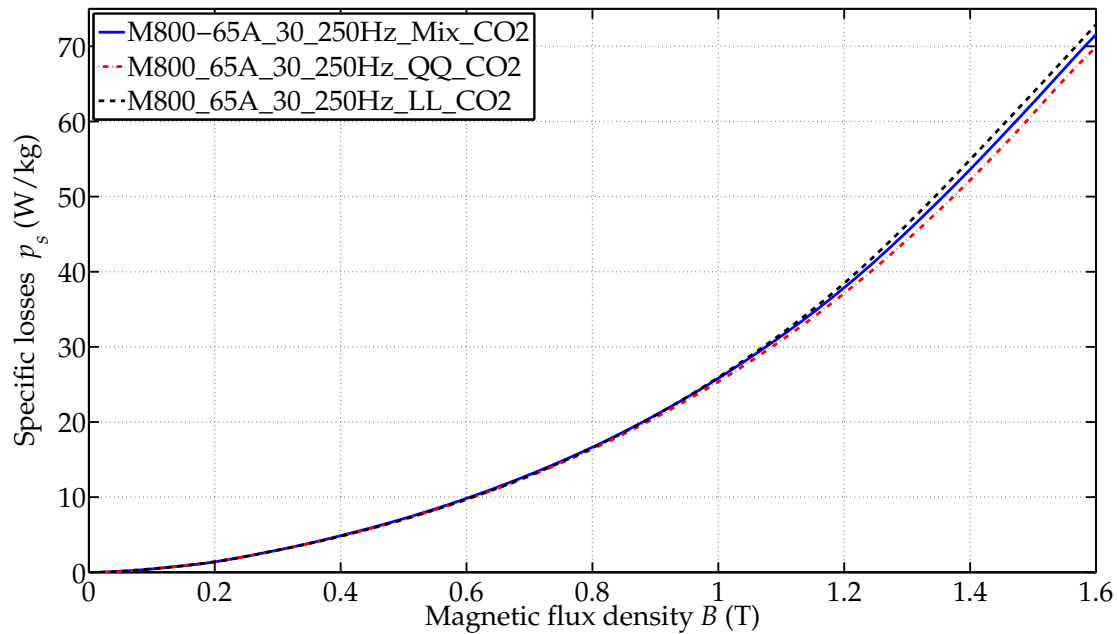
(a) $CO_2$
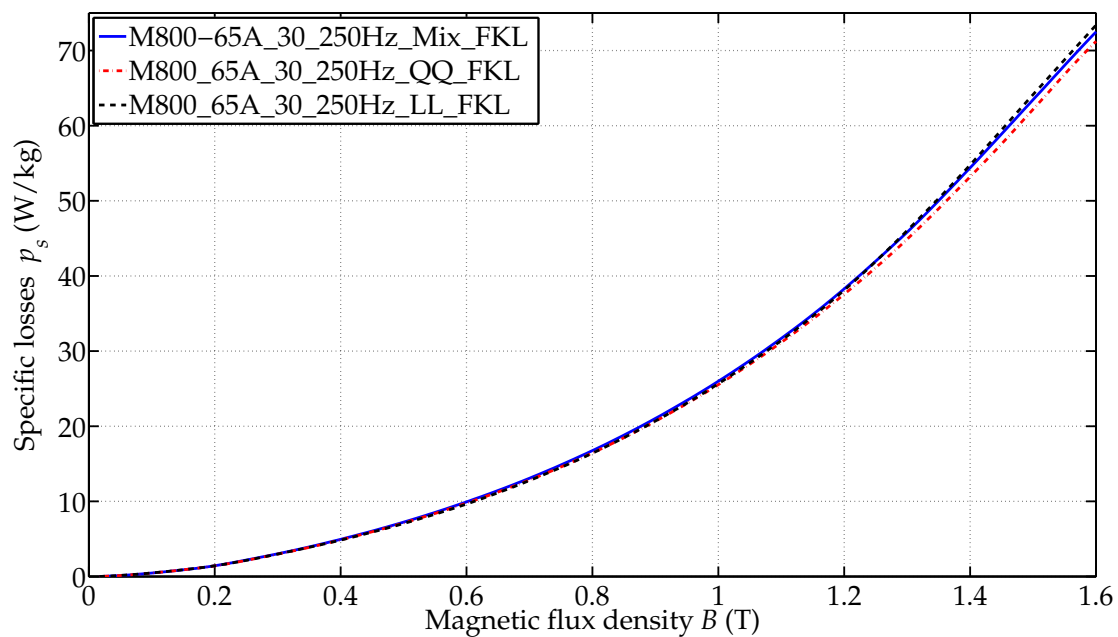


(b) FKL

Figure 5.16: Occurrence of POI for M800-65A at 250 Hz. Up to that point, the longi-
tudinally-cut probe has lower specific losses than the transversely-cut
specimen. Above this point, the situation reverses.

# 5.4  Influence of the ratio $V_{\mathbf{dg}}/(V_{\mathbf{nd}} + V_{\mathbf{dg}})$

In this section, the influence of the ratio $V_{\mathrm{dg}}/(V_{\mathrm{nd}} + V_{\mathrm{dg}})$ on the magnetization curves, the specific losses and the relative permeability are investigated. The calculated ratios between small and wide samples base on the wide samples $(\frac{'x'_{\mathrm{small}}}{'x'_{\mathrm{wide}}})$[7].

**Specific losses**

*Laser versus mechanical cutting*
Figs. 5.17 b) and 5.18 b) compare the ratios $\frac{p_{\mathrm{s,small}}}{p_{\mathrm{s,wide}}}$ of the specific losses of the small samples related to those of the wide samples. These result from the specific losses shown in Figs. 5.17 a) and 5.18 a). The diagrams are presented from 0.4 T onward. The shapes of these ratios $\frac{p_{\mathrm{s,small}}}{p_{\mathrm{s,wide}}}$ of guillotine-cut samples differ from those of the FKL-laser cut samples[8]: At low magnetic flux densities $B$, the ratio $\frac{p_{\mathrm{s,small}}}{p_{\mathrm{s,wide}}}$ of the FKL-laser cut samples is larger than those of the guillotine-cut samples. Also, the FKL-laser cut samples have a larger (negative) slope. This applies to materials M270-35A and M400-50A, at all investigated frequencies.

*Comparison of the two laser cutting techniques*
The ratios $\frac{p_{\mathrm{s,small}}}{p_{\mathrm{s,wide}}}$ of both laser-cut samples show similar shapes, but differ with respect to the absolute values and slopes in their extent (see Fig. 5.17 b)), which is again mainly attributed to the difference in sample width. This applies to all investigated materials and frequencies.

**Magnetization curves**

*Laser versus mechanical cutting*
In Figs. 5.19 and 5.20, the magnetization curves of the small and the wide guillotine-cut and FKL-laser cut samples and their ratios $\frac{H_{\mathrm{small}}}{H_{\mathrm{wide}}}$ are presented. The additional influence of the ratio $V_{\mathrm{dg}}/(V_{\mathrm{nd}} + V_{\mathrm{dg}})$ differs for guillotine-cut and laser-cut samples. In the case of guillotine-cut samples, the largest ratio $\frac{H_{\mathrm{small}}}{H_{\mathrm{wide}}}$ and thus most worsening influence affects the knee point area. In contrast, the magnetization curves of the laser-cut samples are already deteriorated below the knee point area.

Thus, the guillotine-cut samples show an increased ratio $\frac{H_{\mathrm{small}}}{H_{\mathrm{wide}}}$ predominantly in the range of 1-1.5 T, whereas the large values of the FKL-laser cut samples extend

---

[7]Both laser-cut samples are referred to the wide FKL-laser cut samples: $\frac{'x'_{\mathrm{FKL,\,small}}}{'x'_{\mathrm{FKL,\,wide}}}$ and $\frac{'x'_{\mathrm{CO_2,\,small}}}{'x'_{\mathrm{FKL,\,wide}}}$.

[8]Here, only guillotine-cut and FKL-laser cut samples are compared, as the respective small samples have the same width.
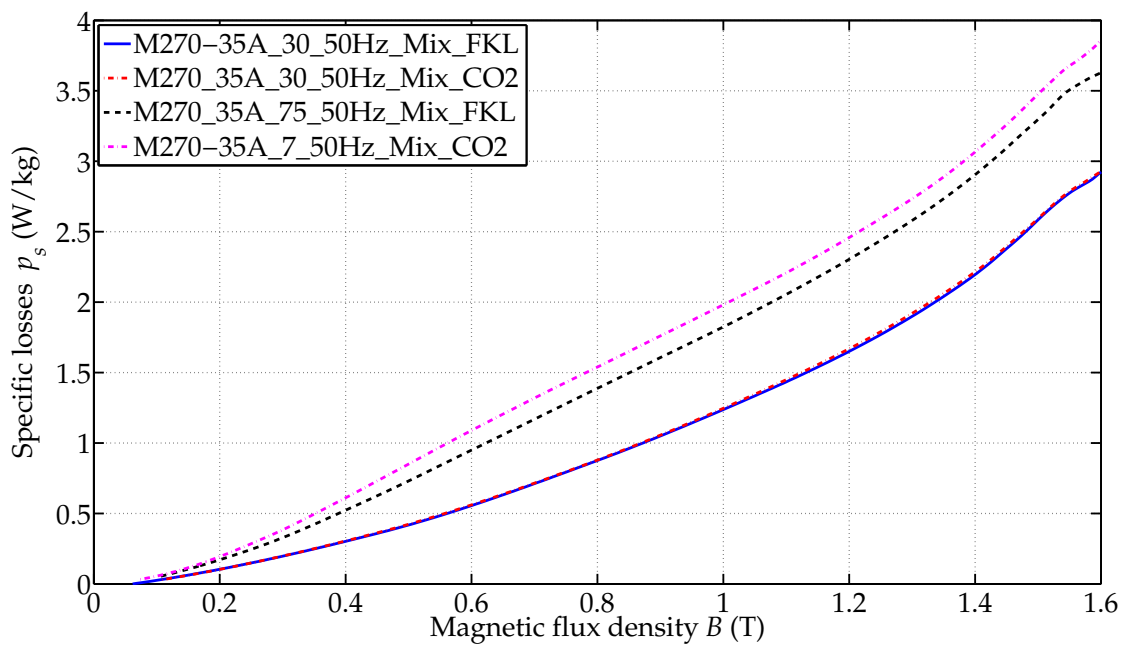
(a) Specific losses of laser-cut samples.
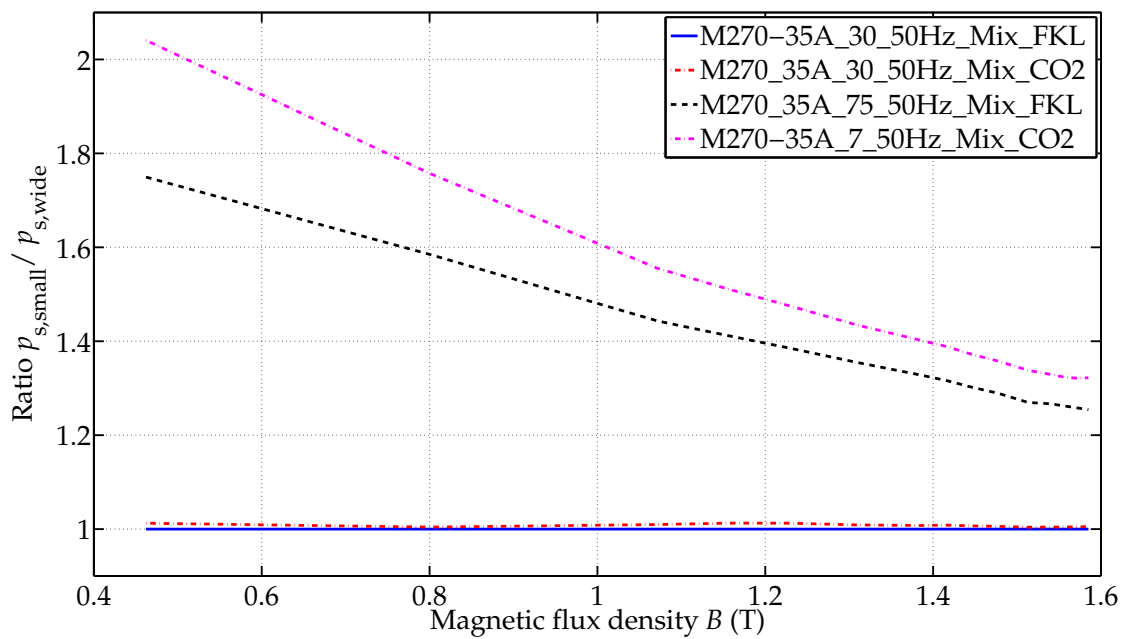


(b) Ratio $\frac{p_{s,\text{small}}}{p_{s,\text{wide}}}$ of the specific losses

Figure 5.17: Specific losses of laser-cut samples.
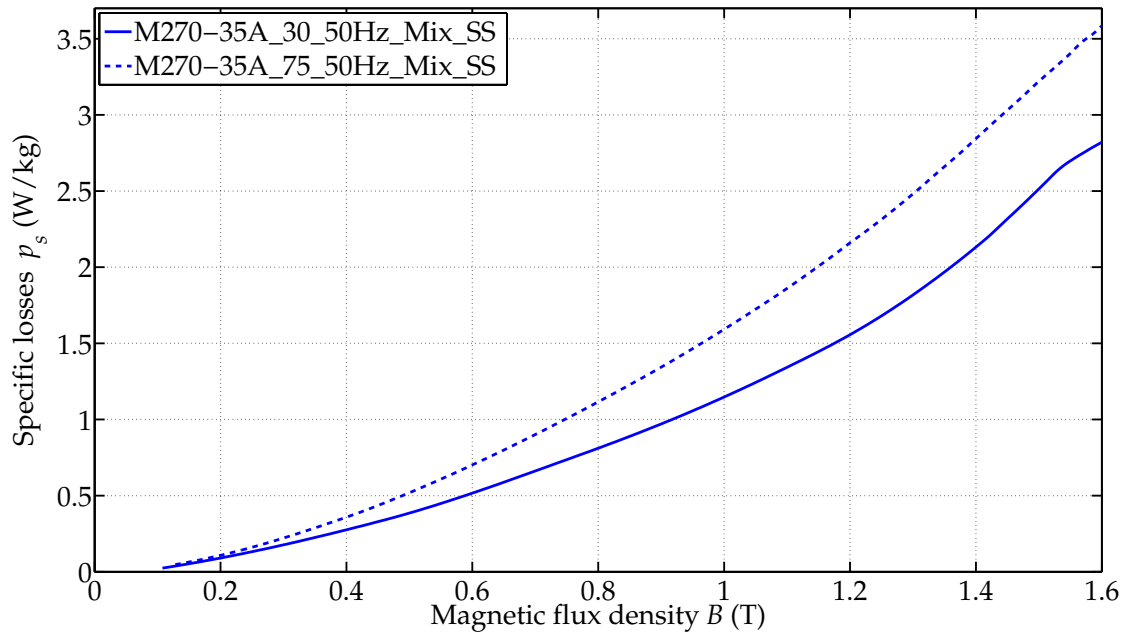
(a) Specific losses of laser-cut samples.
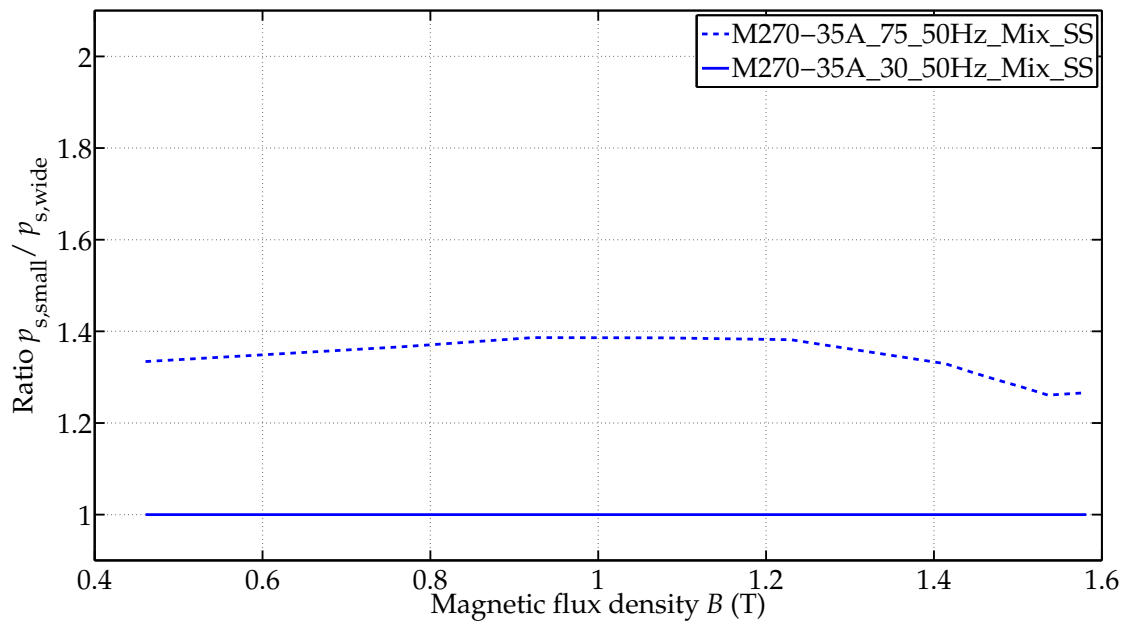


(b) Ratio $\frac{p_{s,small}}{p_{s,wide}}$ of the specific losses

Figure 5.18: Specific losses of guillotine-cut samples.
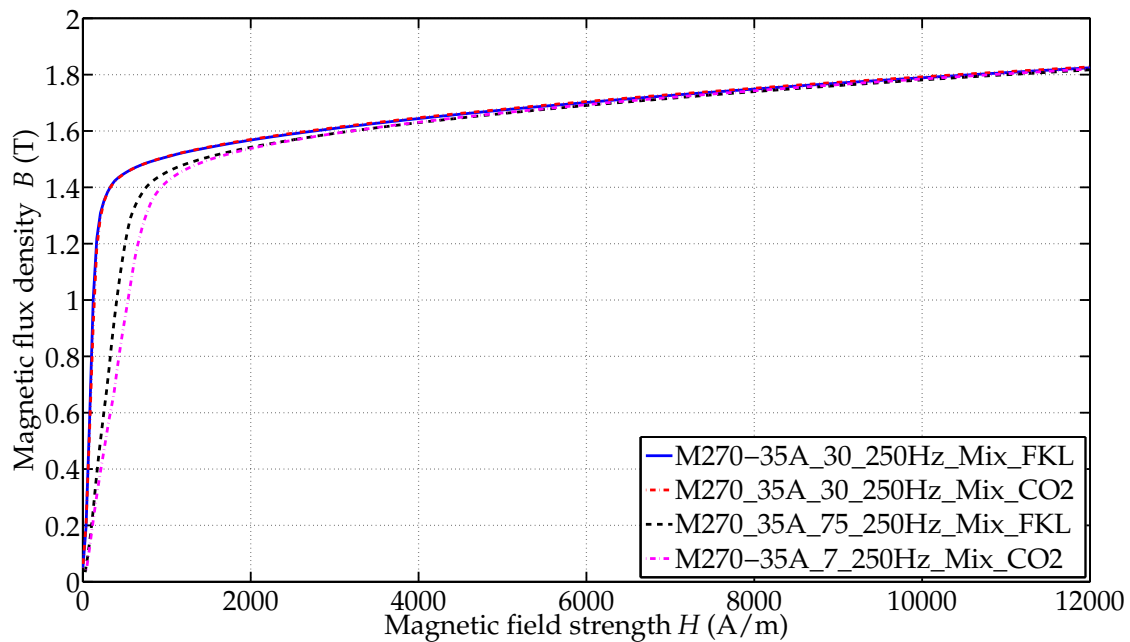
(a) Magnetization curves of laser-cut samples
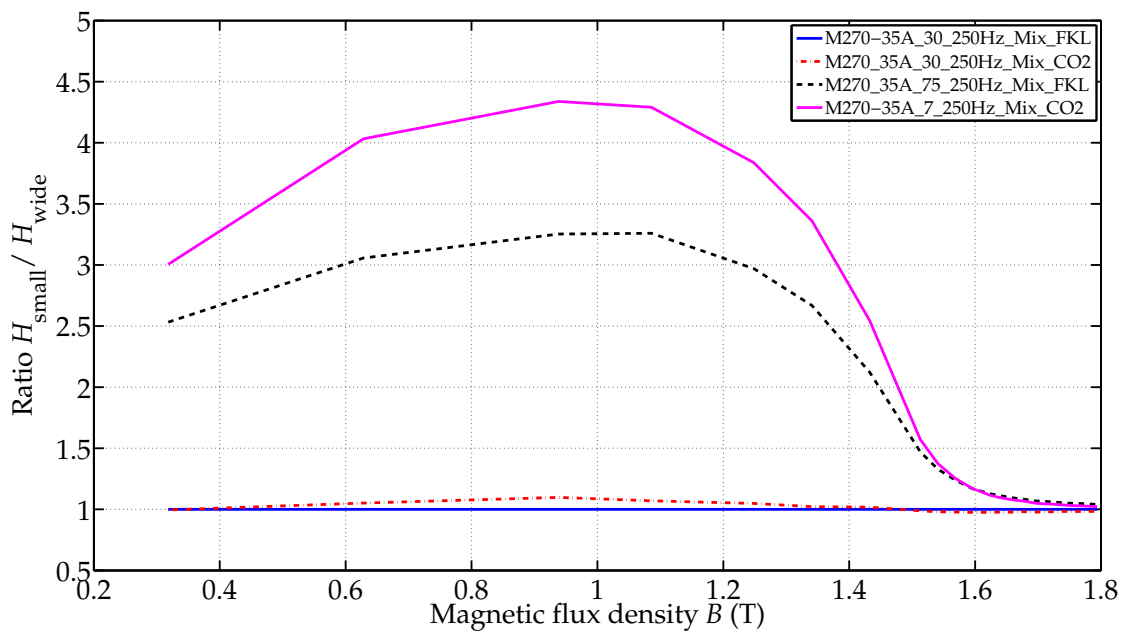


(b) Ratio $\frac{H_{\text{small}}}{H_{\text{wide}}}$ of the magnetization curves

Figure 5.19: Magnetization curves of laser-cut samples.
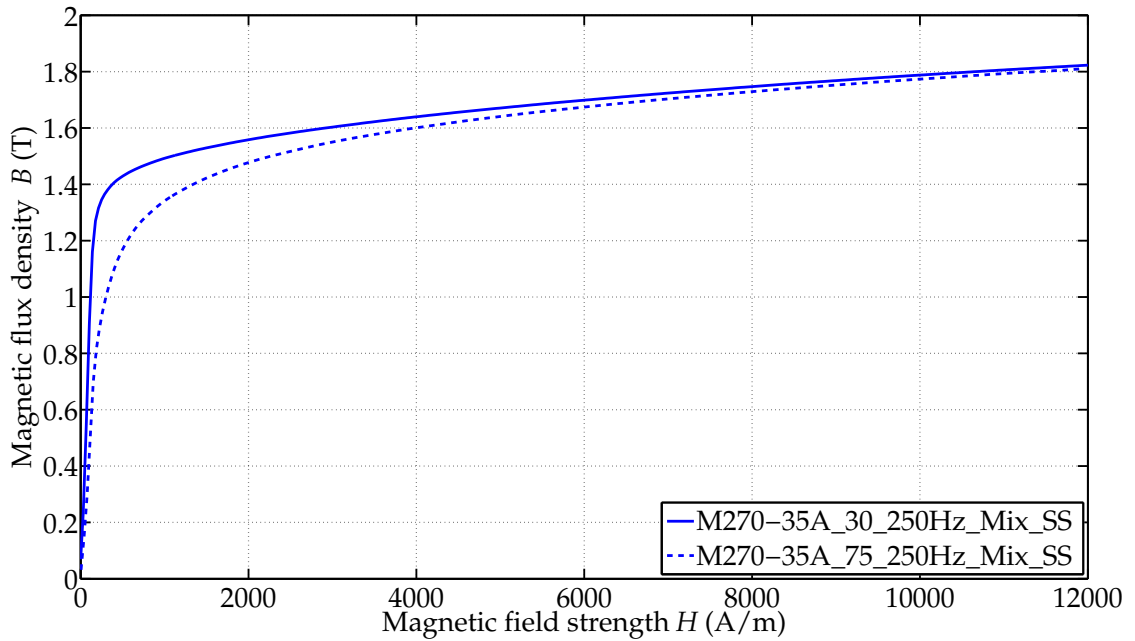
(a) Magnetization curves of guillotine-cut samples
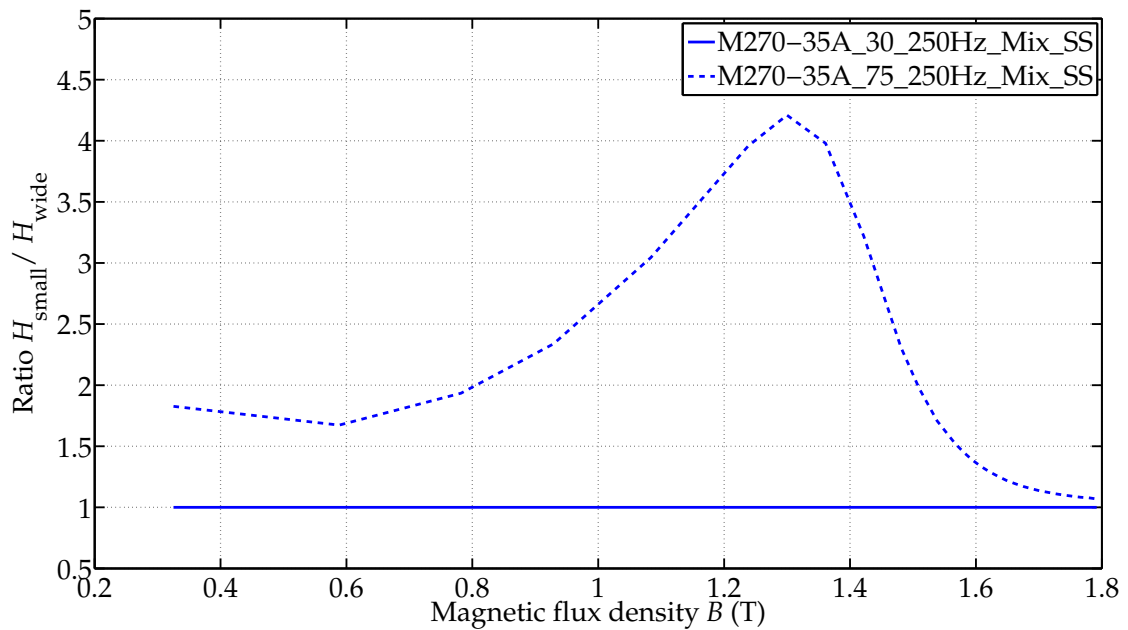


(b) Ratio $\frac{H_{small}}{H_{wide}}$ of the magnetization curves

Figure 5.20: Magnetization curves of guillotine-cut samples.
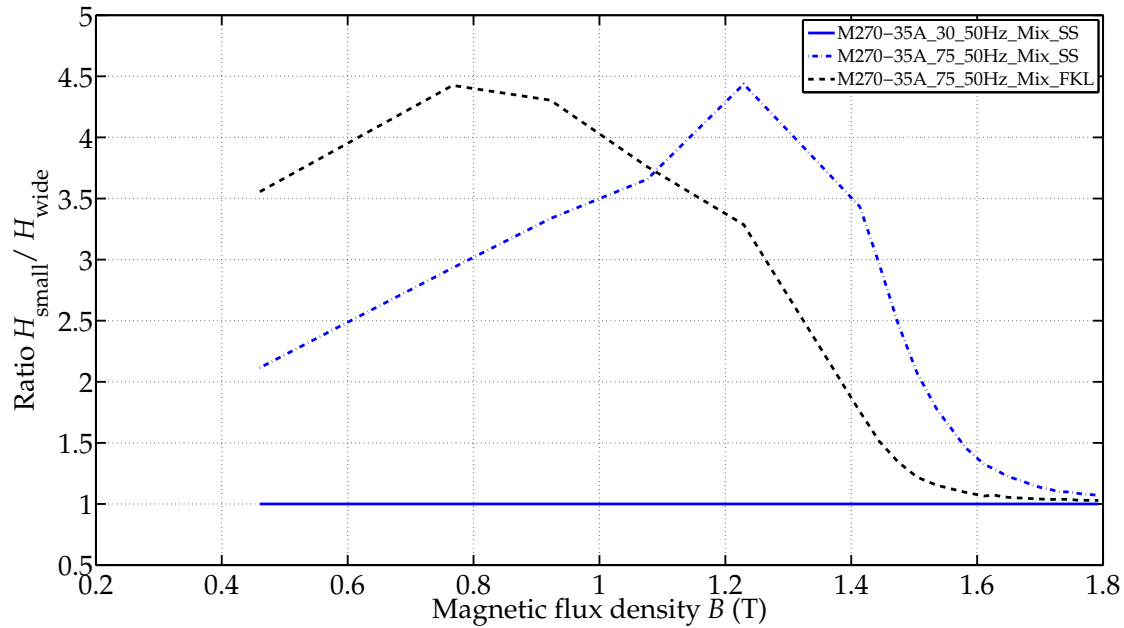
Figure 5.21: Computed ratios $\frac{H_{small}}{H_{wide}}$ of magnetization curves of laser-cut and guillotine-cut samples for M270-35A at 250 Hz, referenced to the wide guillotine-cut samples.

over a larger range of magnetic flux density. This applies to all investigated materials and frequencies. Below 1.1 T, the ratio $\frac{H_{small}}{H_{wide}}$ of FKL-laser cut samples is generally larger than that of the guillotine-cut samples. The difference between both ratios $\frac{H_{small}}{H_{wide}}$ reduces with increasing material thickness (possibly, here also with decreasing grain size). However, considering all three frequencies and materials, the guillotine-cut samples show higher extrema and more distinctive peaks than the FKL-laser cut samples (Figs. 5.19 b) and 5.20 b)). These extrema decrease with increasing frequency and material thickness[2,p.132] (for the latter, only one exception is observed).

Furthermore, the ratio $\frac{H_{small}}{H_{wide}}$ of the guillotine-cut samples approaches 1 at higher magnetic flux densities $B$ than that of the laser-cut sample (see Fig. 5.21: here, all samples are compared to the wide guillotine-cut sample). This applies to all investigated samples and is consistent with the results presented in Chapter 4.2. This direct comparison (Fig. 5.21) highlights also the POI which might occur.

The shape of the ratio $\frac{H_{small}}{H_{wide}}$ of the guillotine-cut samples is similar for all three frequencies and materials. Thus, also the maximum exists almost in the same range of magnetic flux densities. However, the shape of the ratio $\frac{H_{small}}{H_{wide}}$ of the FKL-laser cut samples is similar at 50 Hz and 250 Hz (round curvature), but changes to a shape similar to a plane (the 'distinct' extrema disappear) in the case of 500 Hz (see Fig. 5.22). The latter behavior is also observed for materials M400-50A and M800-65A at 250 Hz and 500 Hz.
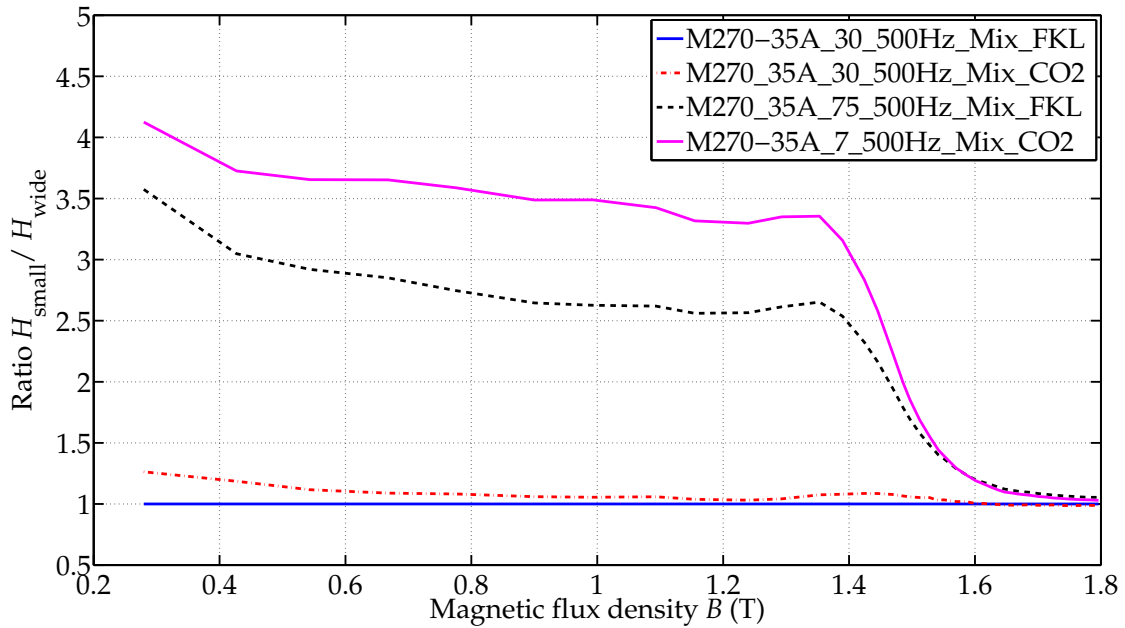
Figure 5.22: Computed ratio $\frac{H_{small}}{H_{wide}}$ of magnetization curves of laser-cut samples for M270-35A at 500 Hz.

*Comparison of the two laser cutting techniques*

The small $CO_2$-laser cut samples are smaller than those of the FKL-laser cut samples (see Chapter 2.1.1). Thus, in the case of the $CO_2$-laser cut specimens the ratio $\frac{H_{small}}{H_{wide}}$ increases further, especially below and in the knee point area. This is in accord with the results of Chapter 4.2. As expected, the shapes of the ratio $\frac{H_{small}}{H_{wide}}$ of both laser-cut samples are very similar (see Fig. 5.19), but the absolute values and slopes differ. This applies to all investigated materials and frequencies. This difference is negligible above 1.6 T. Considering Fig. 5.19 in particular, the further decreased sample width may increase the ratio $\frac{H_{small}}{H_{wide}}$ from about 3.25 to 4.25 at about 0.9 T. Thus, in the case of the 7 mm wide samples, a magnetic field strength $H$ is needed to be about four times larger and in the case of the 7.5 mm wide samples about three times larger, to obtain the same magnetic flux density $B$ as with the wide samples.

**Relative permeablility**

*Laser versus mechanical cutting*

With the computed ratios $\frac{\mu_{r,\,small}}{\mu_{r,\,wide}}$, the difference of laser-cut and guillotine-cut samples is again obvious. The most affected area is at small magnetic field strengths $H$. This lines up with Chapter 4.2. In general, the relative permeabilities at low magnetic field strengths $H$ are less deteriorated with decreasing sample width for guillotine-

cut than for laser-cut samples. However, the ratios $\frac{\mu_{\text{r, small}}}{\mu_{\text{r, wide}}}$ of the guillotine-cut samples need a larger magnetic field strength $H$ to approach the permeability of the wide sample, than the FKL-laser cut samples do[8,p.157](compare Figs. 5.23 b) and 5.24 b)). This is consistent with the results in Chapter 4.2 and applies to all investigated samples. For example, the laser-cut samples reach the ratio $\frac{\mu_{\text{r, small}}}{\mu_{\text{r, wide}}}$ of 0.9 at 600 A/m, whereas the guillotine-cut samples only reach this ratio at 1100 A/m.

### *Comparison of the two laser cutting techniques*

Although, the samples differ in width, the shapes of the ratio $\frac{\mu_{\text{r, small}}}{\mu_{\text{r, wide}}}$ over the magnetic field strength $H$ of both laser-cut samples are related (see Fig. 5.23 b)). However, the $CO_2$-laser cut specimens need a larger magnetic field strength $H$ to approach the relative permeability of the wide sample.

---

Conclusions:

*Specific losses*

- The ratio $\frac{p_{\text{s,small}}}{p_{\text{s,wide}}}$ of the laser-cut samples starts at low magnetic flux densities $B$ at higher values and decreases more strongly with increasing magnetic flux density than that of the guillotine-cut samples. This may lead to the POIs, observed in Chapters 5.2.1 and 5.2.2.

*Magnetization curves*

- The largest ratios $\frac{H_{\text{small}}}{H_{\text{wide}}}$ of guillotine-cut samples occur in the knee point area.

- In contrast, large ratios of laser-cut samples occur already below the knee point area.

- The ratio $\frac{H_{\text{small}}}{H_{\text{wide}}}$ of the guillotine-cut sample shows a distinct maximum in the range of 1 to 1.5 T. In contrast, the maxima of the ratios $\frac{H_{\text{small}}}{H_{\text{wide}}}$ of the FKL-laser cut samples extend over a larger range of magnetic flux densities. This may lead to the POIs, observed in Chapters 5.2.1 and 5.2.2.

*Relative permeability*

- The ratio $\frac{\mu_{\text{r, small}}}{\mu_{\text{r, wide}}}$ of the laser-cut samples is more reduced at low magnetic field strengths $H$, but approaches the permeability of the wide sample at smaller magnetic field strengths $H$ than that of the guillotine-cut samples. Remember again the POIs observed in Chapters 5.2.1 and 5.2.2.

- The shapes of the investigated ratios $\frac{\mu_{\text{r, small}}}{\mu_{\text{r, wide}}}$ of both laser-cut samples are in most cases very similar. The differences are mainly attributed to their difference in sample width.
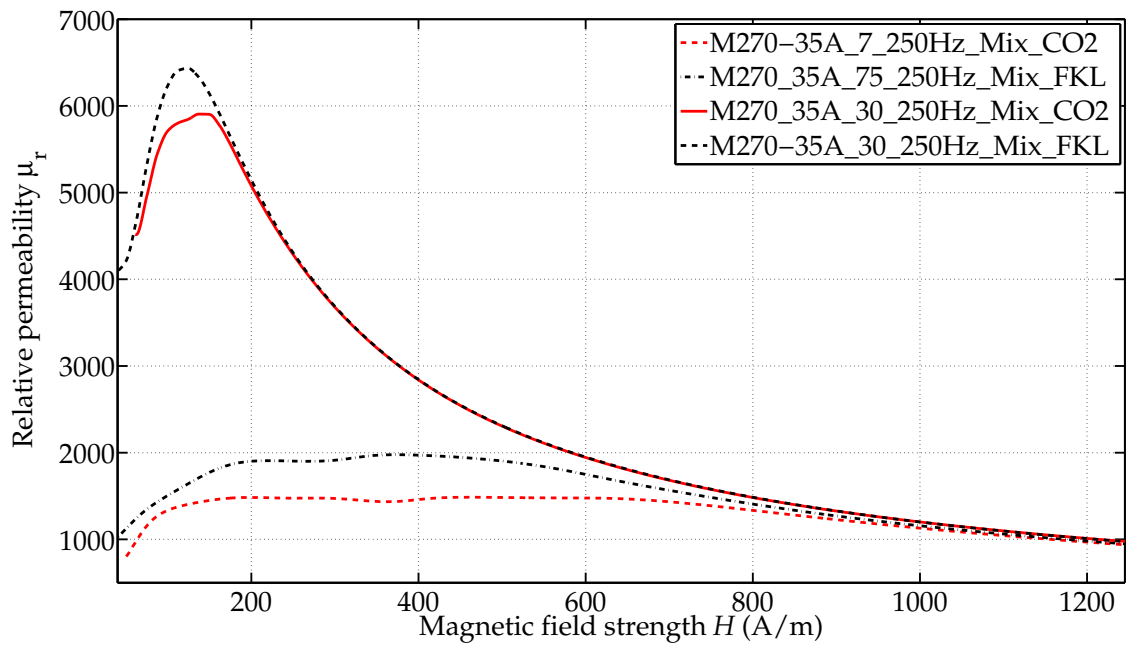
---

(a) Relative permeability of laser-cut samples
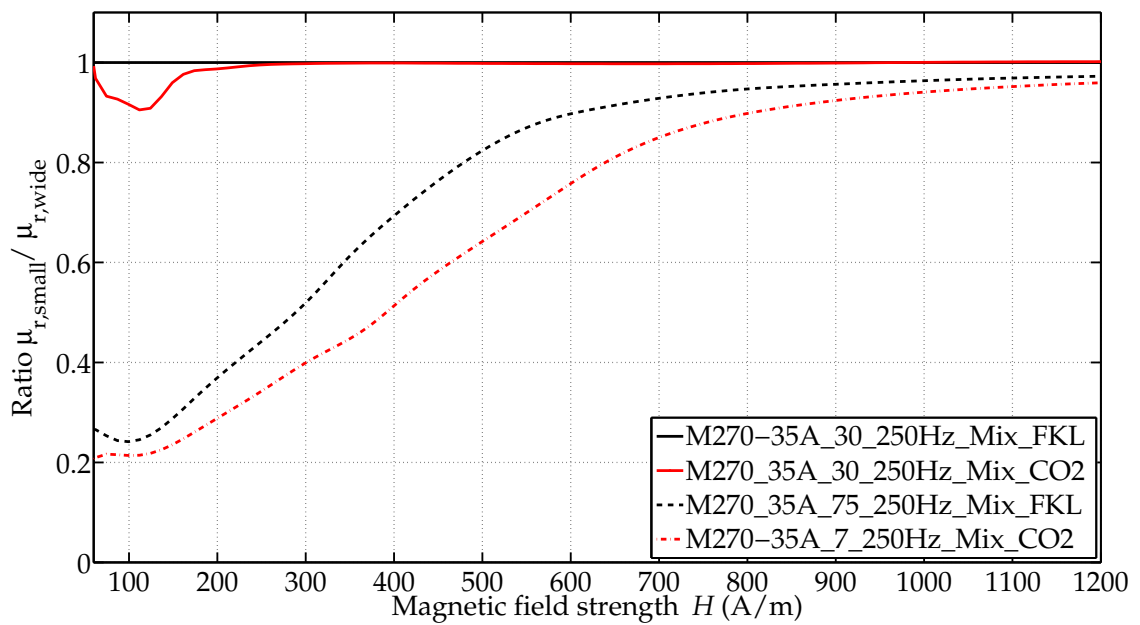


(b) Ratios $\frac{\mu_{r,\,small}}{\mu_{r,\,wide}}$ of the relative permeabilities

Figure 5.23: Relative permeability of laser-cut samples.
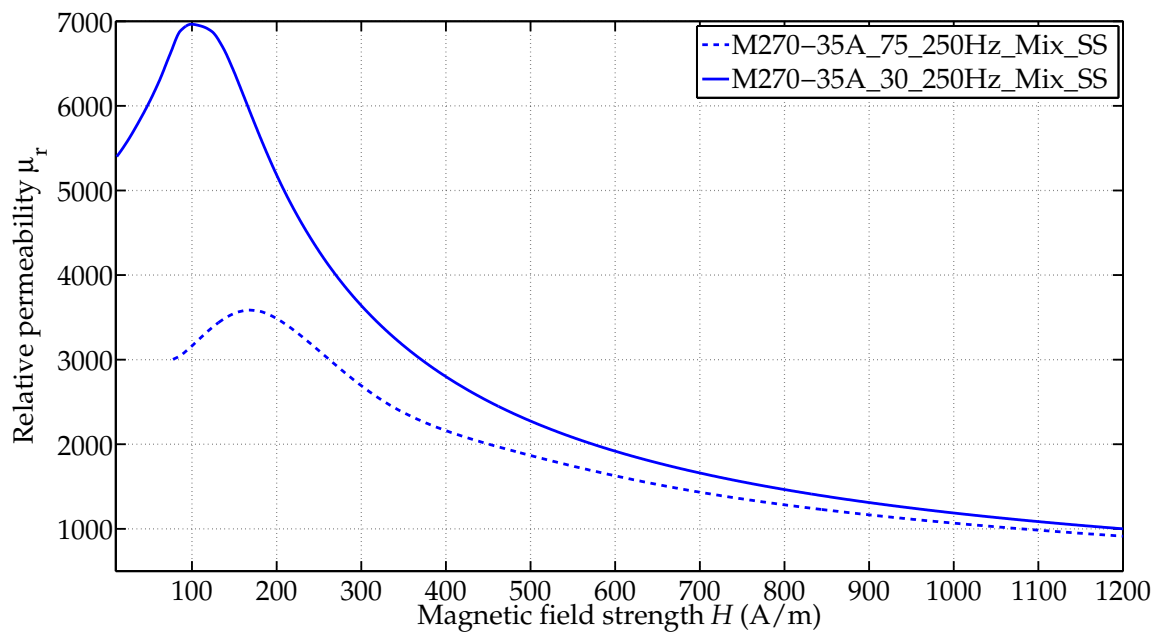
(a) Relative permeability of guillotine-cut samples
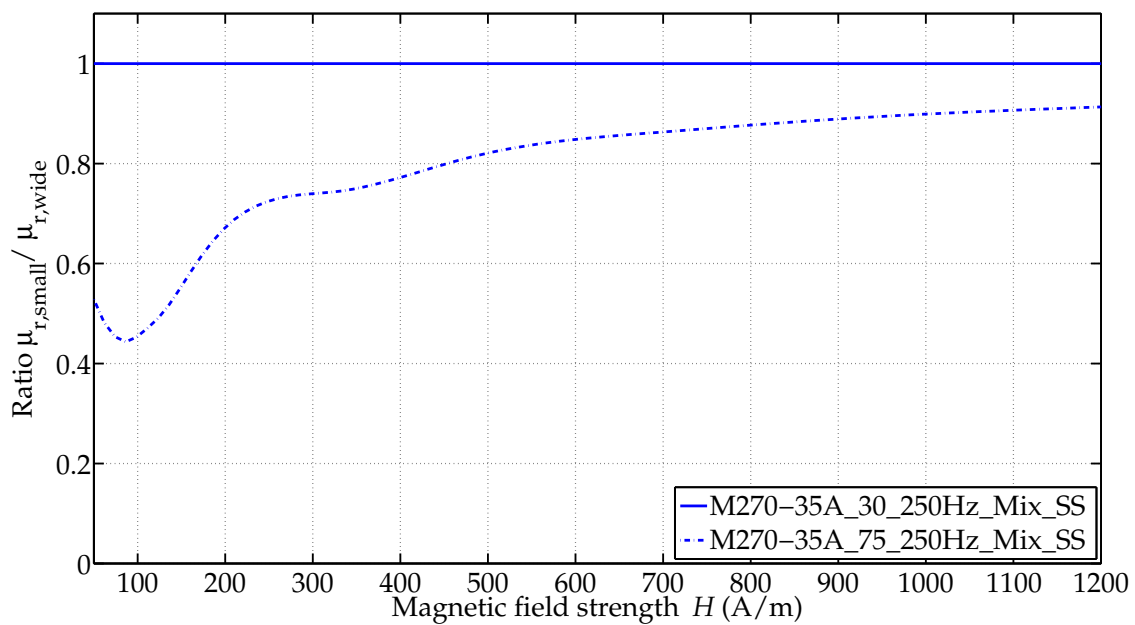


(b) Ratios $\frac{\mu_{r,\text{small}}}{\mu_{r,\text{wide}}}$ of the relative permeabilities

Figure 5.24: Relative permeabilities of guillotine-cut samples.

# 5.5 Discussion

In the following, the results of the measurements of Chapter 5 are analyzed further and compared with results from literature [21,p.24].

**Specific losses**

**Differences due to different cutting techniques**

The specific losses of the guillotine-cut samples increase noticeably with the square of the magnetic flux density. In contrast, the specific losses of the laser-cut samples show an almost 'linear' behavior in the range of medium magnetic flux densities $B$. This effect of 'linear parts' decreases with increasing frequency, material thickness[2,p.132] and sample width (ratio $V_{dg}/(V_{nd} + V_{dg})$). The relationship between the 'linear parts' and the sample width is also confirmed by the results presented in [205]. These authors investigated sample strips with different widths which were cut by a $CO_2$-laser and investigated at 50 Hz. For the smallest strips (4 and 5 mm in width [205]) this 'linear' and/or 'wave' shape of the specific losses at moderate flux densities is also recognizable. However, these authors do not mention or refer to this specific characteristic.

Samples deteriorated by compressive stress show a similar effect: With increasing compressive stress, the shapes of the specific losses presented in [192] also show these 'linear' parts. This supports the conclusion from Chapter 4.3 that compressive stresses induced by laser cutting are larger than those induced by guillotine-cutting.

In this work[21,p.24], the specific losses of samples cut by the two different laser cutting techniques show the same curve shapes and gradient behaviors. The difference observed, albeit only slightly, in curves of these differently laser-cut samples in Chapter 4 (only hysteresis losses measured) shows that this deviation is no longer apparent or is overlapped when eddy currents are added (Epstein frame measurements are performed with frequencies of 50, 250 and 500 Hz). Thus, it is concluded that both laser cutting methods, with the laser settings from Chapter 2.1, deteriorate the loss behavior in almost the same way. This is supported by the losses for $CO_2$-laser and FKL-laser cut samples at 1 and 1.5 T measured at 50 Hz, presented in [182]. However, even if contradictory statements might be found in the literature, the used laser settings and the used laser technology opportunities at the time the measurements were performed, have to be considered before comparisons are made and conclusions are drawn.

Baudouin [11] studied fully-processed and semi-processed steel sheets which were cut by two different laser settings and by mechanical cutting. The measured specific losses showed that for 1.5 T and 50 Hz the pulsed laser mode combined with

less power leads to lower specific losses for the fully-processed material than the continuous laser mode and the mechanical cutting [11]. The samples cut by continuous laser and by mechanical cutting reached the same losses [11]. This is in agreement with the author [45] who showed that different laser settings result in different deterioration of the material properties. Some authors conclude that laser cutting is much worse for loss behavior than mechanical cutting, e.g. [2,207]. This is mostly due to the choice of laser settings, sample sizes (ratio $V_{dg}/(V_{nd} + V_{dg})$) and measurement settings (frequency $f$, magnetic flux density $B$) and not in line with the findings of this work, according to which no general statement can be made (see also the discussions of the POIs).

**Point of intersection**

The results in this work show that a POI of the specific loss curves of the mechanically-cut and laser-cut samples may occur. For both the wide and the small samples, it applies that this POI is shifted to lower magnetic flux densities with increasing frequency and material thickness[2,p.132]. This shifting depends non-linearily on increasing frequency.

This observation of a POI agrees with the results published in [162] (or rather [5]), where the POIs are also moved to lower flux densities with increasing frequency. Note, the author of [162] refers to a 'reversing trend' instead of a point of intersection (the latter is the designation in this work). In the diagram of Dickmann [46], an indirect hint can be found which most likely suggests a point of intersection of specific losses of mechanically-cut and laser-cut samples. [46] showed that at high magnetic flux densities $B$, the percentage increase of laser-cut specimens is lower than that of mechanically-cut probes. This behavior occurs at lower magnetic flux densities $B$ with better and more optimized laser settings, e.g. higher cutting speed [46] (optimized laser settings means less deteriorating influence on the material magnetic properties). Thus, depending on the absolute values of specific losses, a point of intersection may also be possible at high magnetic flux densities for the samples of [46].

This work observed an influence of the material thicknesses[2,p.132] on the loss behavior of the material and on the position of the POI. This contrasts with [170], in which no significant influence of the material thickness on the magnetic behavior of the electrical steel sheets is reported.

**Ratio $V_{dg}/(V_{nd} + V_{dg})$**

As expected, the specific losses increase with increasing ratio $V_{dg}/(V_{nd} + V_{dg})$. Furthermore, the POIs (losses) are shifted to lower (or equal) magnetic flux densities $B$

with increasing ratio $V_{dg}/(V_{nd} + V_{dg})$ when comparing the POIs of mechanically-cut samples with one type of laser cutting technique. Considering the POIs of small samples (FKL-guillotine [sample widths of both: 7.5 mm] vs. $CO_2$-guillotine [sample width of $CO_2$-laser cut sample: 7 mm]), a shifting of the POI to higher magnetic flux densities with increasing ratio $V_{dg}/(V_{nd} + V_{dg})$ is observed (Fig. 5.11).

Previous investigations from other authors are based on the specific cutting length instead of the ratio $V_{dg}/(V_{nd} + V_{dg})$. An increasing specific cutting length also leads to an increasing ratio $V_{dg}/(V_{nd} + V_{dg})$. Hence, these results are often comparable. According to several authors, the specific losses of an electrical steel sheet increase with increasing specific cutting length [22, 127, 134, 162, 169, 170, 172]. Thus, these observations are in agreement with each other. The results of Ryckebusch [162] also confirm that the POI at specific losses of mechanically-cut and laser-cut samples is shifted to lower magnetic flux densities $B$ with increasing cutting length. This is in accordance with the results in this work, when only comparing wide and small samples. However, the author of [162] only investigated two different cutting lengths. Hence, no statement can be made on the linearity or non-linearity of the shifting of the POIs.

The authors of [188] also investigated the increasing ratio of iron losses at 50 Hz with decreasing sample width for one material containing 2.4 % silicon [188]. These ratios are based on a quadratic sample with 120 mm in side length [188]. The samples are cut by $CO_2$-laser and compared with guillotine-cut samples [188]. Precise information on the investigated material and the used laser settings is not provided. As with the results in this work, for small magnetic polarization, the ratios $\frac{p_{s,small}}{p_{s,wide}}$ of laser-cut samples are higher than those of the guillotine-cut samples. Considering the whole polarization range in [188], the ratios $\frac{p_{s,small}}{p_{s,wide}}$ of the laser-cut samples have a larger negative slope compared with those of the guillotine-cut samples. This is also in line with the findings of this work. This negative slope increases with decreasing sample width [188]. In contrast, the ratio $\frac{p_{s,small}}{p_{s,wide}}$ of the guillotine-cut sample also increases with decreasing sample width, but does not change strongly over the polarization range. This is confirmed by the results of this work. Also the author of [169] studied the influence of the ratio $V_{dg}/(V_{nd} + V_{dg})$ on the iron losses for guillotine-cut samples with different clearances and with different qualities of the cutting tool (sharp and blunt). This author references all results to a sample in which the hardened edges due to cutting have been eliminated by grinding [169]. The material investigated contains 1 % silicon [169]. However, the author also investigated, in addition to other sample sizes, the same sample sizes as presented in this work, but longitudinally-cut and transversely-cut samples separately. Considering and calculating the mean of the percentage change of iron losses due to the change in

cutting direction for samples with 30 mm and 7.5 mm width, no clear influence on the ratio $\frac{p_{s,\text{small}}}{p_{s,\text{wide}}}$ over the magnetic flux density is obtained. This contrasts with the findings in this work. Furthermore, the increasing ratio of losses due to the decreased sample width is about 2.4 (mean), which is larger than that of the guillotine-cut samples investigated in this work. These differences may be attributed to possible differences in guillotine settings (clearance and cutting tool quality), guillotine technique (over 25 years in difference), and/or also to the material itself (grain size, chemical composition: e.g. 1 % [169] in contrast to 1.5 to 2.8 % silicon content (see Chapter 3)).

**Magnetization curves and permeability**

**Differences due to different cutting techniques**

Considering the *B-H* curves of the *wide* samples, it is obvious that these curves of different cut samples differ predominantly in the knee point area (Fig. 5.12). With few exceptions, the *small* samples differ significantly in all parts (except high saturation; Fig. 5.4). Taking the computed relative permeability into additional consideration, the amplitudes of the differently cut samples have the following order: $\mu_{\text{max,guillotine}} > \mu_{\text{max,laser (FKL)}} > \mu_{\text{max,laser (CO}_2)}$ (Figs. 5.5 and 5.13). This agrees with the results of Chapter 4. The largest differences of these permeabilities occur at low magnetic field strengths *H*.

By just focusing on the relative permeability, the conclusion can be drawn that $CO_2$-laser cutting deteriorates the magnetic material more than FKL-laser cutting, predominantly at small magnetic field strengths *H*. However, as seen above, the specific losses do not differ significantly. Thus, the different magnetic properties are affected differently and to a different extent by the various cutting techniques. In general, with increasing frequency the difference of relative permeability of laser-cut and guillotine-cut samples at small magnetic field strengths *H* as well as the maxima of the permeability decrease. Also, a POI of the permeability of differently cut samples at higher magnetic field strengths *H* is observed (see next paragraph 'Point of intersection', p. 172 and Figs. 5.5 and 5.6). Furthermore, the maxima of the permeability are shifted to higher magnetic field strength *H* the smaller the maximum of the laser-cut samples is (see Fig. 5.13). This behavior is observed as long as a distinct maximum and no 'plateau' occurs. The difference of relative permeabilities between the different cutting techniques depends on the respective magnetic field strength *H* (see Figs. 5.13) and thus on the magnetic flux density *B*. This is also in accord with Chapter 4.

Also Dickmann [46] obtained smaller maximum permeabilities for laser-cut than for mechanically-cut specimens, with the amplitudes of the $CO_2$-laser cut samples being the smallest. Furthermore, the author observed a shifting of the maximum

permeabilities to higher magnetic field strengths $H$ with decreasing absolute values [46]. According to his literature research, this is in accordance with the behavior of soft magnetic material under machinable procedure, [46] referring to [147]. All these results confirm the results in this work. The author of [46] further showed that the maximum permeabilities of laser-cut samples vary with the laser settings. With optimum laser settings (e.g. laser speed [40, 45]) the maximum permeabilities of laser-cut samples increase [46]. Furthermore, [46] points out that the relative permeability is the magnetic property most sensitive to cutting. This most likely explains why differences between the relative permeabilites of both laser-cut samples investigated in this work still exist, in contrast to the specific losses with the samples investigated with the Epstein frame at different frequencies (Chapter 5).

Ryckebusch [162] states that the permeability is more deteriorated by laser than by mechanical cutting and that the deterioration "depends on the polarization." For low magnetic field strengths $H$, this is in line with the results of this work. Considering the diagram presented in [162], also a reversing behavior at higher magnetic flux densities $B$ is observed in which the permeabilities of laser-cut samples are larger than those of mechanically-cut specimens. This fits with the POIs in this work. However, no detailed analysis of this reversing behavior is given in [162].

Emura [51] determines the specific losses and permeabilities for differently cut samples at 1.5 T and 60 Hz. The measured results of "JCUT"[9] samples also confirm a different deterioration effect on the specific losses and on the relative permeability for differently cut samples, as the percentage change of permeability of guillotine-cut to laser-cut samples is larger than that of the total losses. The results presented in [51] also show that the permeabilities of laser-cut samples may be better than those of guillotine-cut samples. However, this depends again on the point of operation. The author of [51] investigated the permeability at 1.5 T and thus at higher magnetic field strengths $H$ (see also next section 'Point of intersection').

The maximum permeability decreases with increasing ratio $V_{\mathrm{dg}}/(V_{\mathrm{nd}}+V_{\mathrm{dg}})$ (see Tables 5.4 and 5.7). Comparing the shape of the relative permeability of the small laser-cut samples with the wide laser-cut samples (see Figs. 5.5 and 5.13), the maximum of the relative permeability of the small laser-cut samples is not well pronounced, almost plateau-like, in contrast to that of the small guillotine-cut samples with a still distinctive maximum. The plateau is moved to lower relative permeabilities, with an increasing ratio of material degraded by the cutting process to non-degraded, unaffected material. Therefore, it only occurs with the small investigated samples,

---

[9]JCUT signifies samples "just after cut" [51]. The author [51] further investigated samples which are cut and annealed, before and/or after cutting. In this discussion only the behavior of JCUT samples are of interest.

in which the ratio $V_{dg}/(V_{nd} + V_{dg})$ between degraded material to the total material volume is high.

Samples deteriorated by compressive stress show a similar effect: Above a certain compressive stress the distinct maximum disappears (cf. with [192])[10]. It may thus be interpreted that the degrading effect of laser cutting on the material is caused by induced compressive stresses. As for wide specimens the influence of laser cutting is still small; this effect is predominantly seen with the small samples. According to [59, 207], the stresses occurring at the cut edge are compressive stresses, both for punching and for laser cutting. As the guillotine-cut samples still show a distinct extrema, even for the small samples, we interpret the laser-cut induced compressive stresses to be larger than those induced by guillotine-cutting. This is in line with Chapter 4 and also with [23] in which it is mentioned that the 'main parameters for the permeability are the crystal energy, magnetostriction, grain size, number and type of lattice defects and impurities and the *internal stresses*'.

**Point of intersection**

Even for the permeability and magnetization curves, POIs between laser-cut and mechanically-cut samples occur. These occur at other magnetic field strengths $H$/magnetic flux densities $B$ than those of the specific losses. These POIs occur for both FKL-laser cut and $CO_2$-laser cut samples in the same range of magnetic field strength $H$ and thus magnetic flux density $B$ (see Table 5.6), but at different magnetic field strengths $H$ for different materials and/or frequencies investigated.[11]

The different positions ($B/H$ value) of the POIs of losses and permeability are confirmed by Dickmann [46], who also showed a different influence of (laser) cutting on losses and permeability (see p. 171). In his diagram, also a POI can be identified where the permeability of the FKL-laser cut sample is higher than that of the mechanically-cut sample. Depending on the laser settings, this POI occurs at lower field strengths $H$ for more optimized laser settings, see [46]. Also [162] presents a diagram where a POI also occurs for the permeability at higher polarizations [162]. With increasing specific cutting length this POI is shifted to lower magnetic flux densities $B$, see [162]. At large, this is also confirmed by the results of this work.

**Ratio $V_{dg}/(V_{nd} + V_{dg})$**

With increasing ratio $V_{dg}/(V_{nd} + V_{dg})$, the permeability and its amplitude decrease.

---

[10] [194] shows the change in relative permeability due to compression induced by shrink fitting. There, the shape of the relative permeability of the sample with shrink fitting does not yet show a plateau, but already the tendency to 'loose' its distinctive maximum.

[11] See POIs of the wide samples; the POIs of the small samples are not appropriate for this comparison because of the difference in sample width (see Chapter 2.1.1).

Schmidt [169] also showed this behavior by considering the specific cutting length.

Considering the ratio $V_{\mathrm{dg}}/(V_{\mathrm{nd}} + V_{\mathrm{dg}})$ for the *B-H* curve, it is remarkable that for guillotine-cut samples the largest change occurs predominantly in the knee point area (Fig. 5.20 b)). In contrast, for laser-cut samples the strongest influence occurs already in the linear range below the knee point area and extends over a larger range of flux densities *B* (see Fig. 5.19 b)) compared to that of guillotine-cut samples. Furthermore, it is observed for $B \leq 1.1\,\mathrm{T}$ that the ratio $\frac{H_{\mathrm{small}}}{H_{\mathrm{wide}}}$ of laser-cut samples is larger than that of the guillotine-cut samples. However, in most cases the extrema of the guillotine-cut samples are at higher values than those of the laser-cut samples.

In [68], magnetization curves of mechanically-cut samples are presented for different ratios $V_{\mathrm{dg}}/(V_{\mathrm{nd}} + V_{\mathrm{dg}})$. Also in [68], the most significant difference of these magnetization curves is in the knee point area [68], which is shifted to smaller magnetic flux densities *B* and larger magnetic field strengths *H* (see also [192]). The latter is also in line with the results presented in this work.

The authors of [188] also investigated the increasing ratio $\frac{H_{\mathrm{small}}}{H_{\mathrm{wide}}}$ with decreasing sample width. Here, the reference $H_{\mathrm{wide}}$ bases on a quadratic sample with 120 mm in side length and the samples are cut by $CO_2$-laser and guillotine [188]. The results presented in [188] confirm the findings of this work, in that the ratio $\frac{H_{\mathrm{small}}}{H_{\mathrm{wide}}}$ of the laser-cut samples extend over a larger range of magnetic flux density than those of the guillotine-cut sample. However, the results in [188] show that the maximum ratio $\frac{H_{\mathrm{small}}}{H_{\mathrm{wide}}}$ of laser-cut samples is a multiple larger than that of the guillotine-cut samples. This is in contrast to the findings in this work. This difference is mainly attributed to different (probably concerning the magnetic properties worse) laser settings. Unfortunately, no detailed information concerning the material or the laser settings is provided in [188]. Thus, no further evaluation is possible. The author of [169] analyzed the influence of decreasing sample width on the relative permeability for guillotine-cut samples with different clearances and different quality of the cutting tools (sharp and blunt). The hardened edges due to cutting of the reference sample are removed by grinding [169]. The material investigated contains 1 % silicon [169]. The author investigated, in addition to other sample sizes, the same sample sizes as presented in this work. Considering just these two equivalent sample sizes, the maximum relative permeability decreased in the range of 20 to 30 % (sharp and blunt cutting tool) [169]. However, the results in this work showed larger degradations for the maximum relative permeability of guillotine-cut samples. Again, this difference may be attributed to possible differences in guillotine settings (clearance and cutting tool quality), guillotine technique (over 25 years in difference), and/or to the material itself (grain size, chemical composition: e.g. 1 % [169] in contrast to 1.5 to 2.8 % silicon content (see Chapter 3)).

Conclusions:

- The 'linear' characteristic of the specific losses at moderate flux densities is more pronounced for laser-cut than for guillotine-cut samples the larger the ratio $V_{\mathrm{dg}}/(V_{\mathrm{nd}} + V_{\mathrm{dg}})$ is. Thus, it is assumed that the induced compressive stresses of laser cutting are larger than those induced by mechanical cutting. This is supported by the results on the permeability.

- Both laser cutting techniques show the same deteriorating effect on the specific losses, but different effects on the relative permeability at low magnetic field strengths $H$. Thus, the relative permeability is more sensitive to the different laser cutting techniques than the loss behavior.

- With increasing frequency and material thickness[2,p.132], the point of intersection (POI) of the specific losses is shifted to lower magnetic flux densities $B$.

- No specific relationship between the position of the POI of the specific losses and the ratio $V_{\mathrm{dg}}/(V_{\mathrm{nd}} + V_{\mathrm{dg}})$ is observed.

- With increasing frequency the difference of permeabilities of laser-cut and guillotine-cut samples decreases notably at small magnetic field strengths $H$.

- In the case of small laser-cut samples, the maxima of the relative permeabilites flattens to a 'plateau'. This is a further indication of larger compressive stresses for laser-cut samples than for mechanically-cut samples.

- The distinct maxima of the relative permeabilites as well as the 'plateau' decrease with increasing ratio $V_{\mathrm{dg}}/(V_{\mathrm{nd}} + V_{\mathrm{dg}})$.

- The ratio $\frac{p_{\mathrm{s,small}}}{p_{\mathrm{s,wide}}}$ of the laser-cut samples starts at low magnetic flux densities $B$, at higher values and decreases more strongly with increasing magnetic flux density than that of the guillotine-cut samples.

- The ratio $\frac{H_{\mathrm{small}}}{H_{\mathrm{wide}}}$ of the guillotine-cut samples show a distinct maximum in the range of 1 to 1.5 T. In contrast, the maxima of the ratios $\frac{H_{\mathrm{small}}}{H_{\mathrm{wide}}}$ of the FKL-laser cut samples extend over a larger range of magnetic flux densities.

- The ratio $\frac{\mu_{\mathrm{r,\,small}}}{\mu_{\mathrm{r,\,wide}}}$ of the laser-cut samples is more reduced at low magnetic field strengths $H$, but approaches the permeability of the wide sample at smaller magnetic field strengths $H$ than that of the guillotine-cut samples.

# Chapter 6

# Experimental results: stator measurements

In this chapter the specific losses, magnetization curves and relative permeabilities of the stator lamination stacks (explained in Chapter 2.1.1, see also Figs. 2.1 and 2.12), are determined and analyzed with regard to the influence of different cutting techniques (using the three different measurement techniques explained in Chapter 2.6). These stator samples consist of the same materials and are cut from the same MCs as the Epstein samples investigated before (Chapter 5). Subsequently, the effect of aging on the magnetic properties due to different cutting techniques is investigated as well.

In addition to the respective selected results presented in this Chapter, a more comprehensive set of results is presented in Appendix D.

## 6.1 Results of 'Epsteinframe' method

The results of the 'Epsteinframe' method are discussed first. Subsequently, the differences in results between this method and the two other techniques ('modified Epsteinframe' method and 'IEC 62044-3') are worked out (Sections 6.2 and 6.3).

**Specific losses**

*Laser versus mechanical cutting.*
First, the results for material M400-50A are discussed in detail. The measured specific losses are presented in Fig. 6.1 for the stator samples of material M400-50A for all three measured frequencies. The specific losses of both laser-cut stator samples are almost identical (see Fig. 6.1 and also Fig. 6.2 for material M270-35A; exception: material M800-65A at $250\,\mathrm{Hz}$ and $500\,\mathrm{Hz}$ from $1\,\mathrm{T}$ onward it applies $p_{\mathrm{FKL}} > p_{\mathrm{CO_2}}$,

see Fig. 6.3[1]), whereas those of the punched stack differ in shape and gradient. (This applies for all investigated materials.) The latter shows a rather quadratic relationship, whereas the specific losses of the laser-cut stacks seem to increase more 'linearly', notably in the range of (0.6...1.3) T at 50 Hz (see Fig. 6.1 a)). The 'linear' part of the laser-cut samples is reduced with increasing frequency and material thickness[2,p.132] (compare Fig. 6.1 and the Figures in Appendix D.2), see for example material M800-65A: at 50 Hz only a slight influence of the 'linear' part is noticeable, and from 250 Hz onward, no influence is detected. All these findings are in accord with the results obtained for the Epstein specimens (see Chapter 5).

Again, as with the Epstein frame measurements, *points of intersection (POIs) between laser-cut and punched stator lamination stack samples occur* after which the specific losses of the punched samples are larger than those of the laser-cut samples. Once again, the POI is shifted to lower magnetic flux densities as the frequency and/or the material thickness[2,p.132] increases. This is illustrated in Fig. 6.1, as well as in Table 6.1[2]. For material M400-50A and at 50 Hz operation (see Fig. 6.1), the specific loss curves of all different cut samples converge or are similar from 1.35 T onward. At 250 Hz, the POI occurs at 0.86 T and at 500 Hz, already at 0.71 T (see Table 6.1). The POIs of $CO_2$-laser cut and mechanically-cut samples are found to be in the same range (compare Appendix D.3). Furthermore, the difference between the specific losses of mechanically-cut and laser-cut samples in the area above the POI increases with the supply frequencies (see the differences at 1.5 T in Fig. 6.1). The same characteristics are observed for material M800-65A. Unfortunately, no investigations on a stator lamination with material M270-35A could be carried out (see Table 2.4 in Chapter 2.6).

Concerning the POIs of the specific losses of mechanically-cut and FKL-laser cut samples (Table 6.1), the shifting of the POI to lower magnetic flux densities $B$ with increasing material thickness increases with increasing frequency. Thus, for thicker[2,p.132] material and increasing frequency, the laser cutting technology becomes a viable alternative to mechanical cutting concerning specific losses.

Comparing the *occurrences of the points of intersection (POIs) of the Epstein steel strips and of the stator lamination stacks* (Table 6.1 vs. Tables 5.1 and 5.5), these points occur at lower magnetic flux densities $B$ for the stator stacks than for the rectangular samples. This was expected for the comparison of the wide Epstein samples with the stator samples. However, since the stator yoke height (12 mm) is larger than the width of the small Epstein samples (7.5 mm), this contrasts with the observation (considering just the wide and small samples) that the POI moves to lower magnetic flux densities with decreasing width of the cut specimen (see Chapter 5.2). Possible explanations

---

[1]Further explanation is given on p. 181.

[2]Table 6.1 illustrates the POIs for the FKL-laser cut and mechanically-cut samples. The points of intersection for $CO_2$-laser cut and mechanically-cut samples are shown in Appendix D.3.
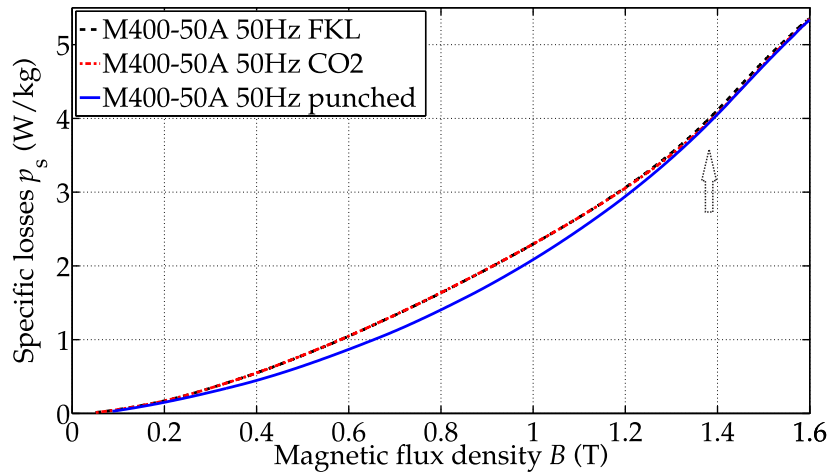
(a) 50 Hz
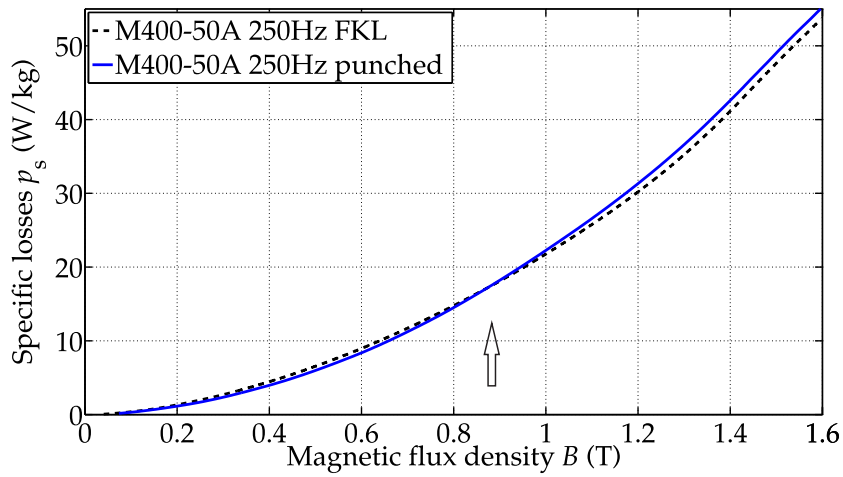


(b) 250 Hz
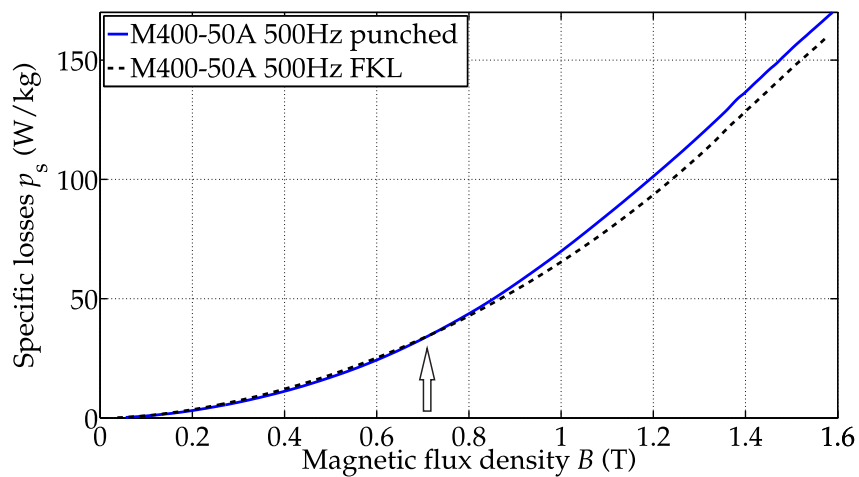


(c) 500 Hz

Figure 6.1: Specific losses of the M400-50A stator lamination stack samples at different frequencies.
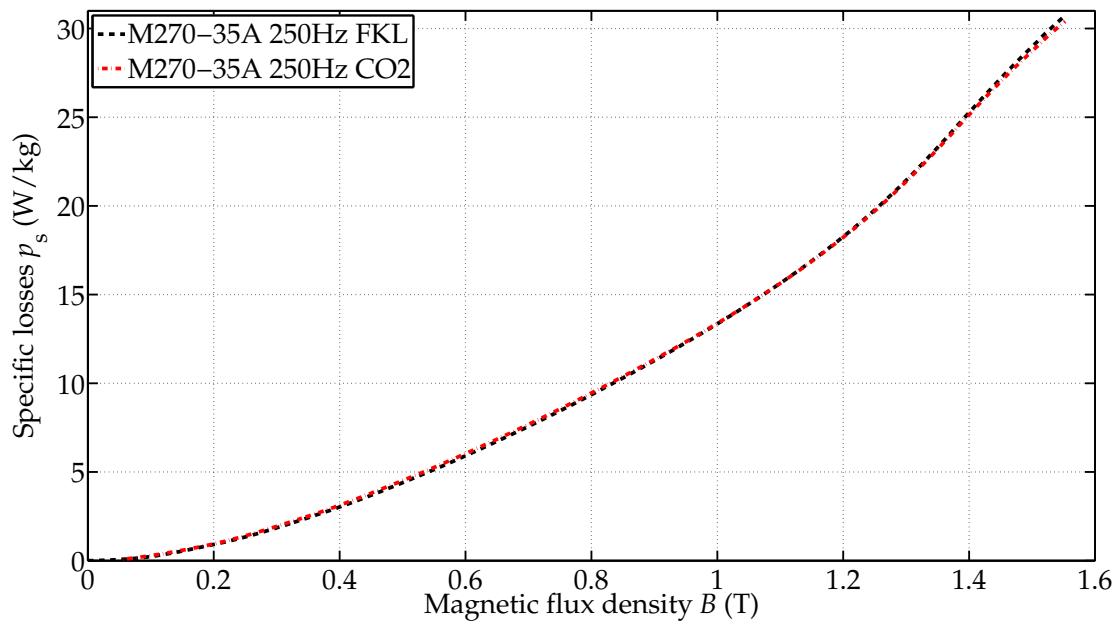
(a) Specific losses
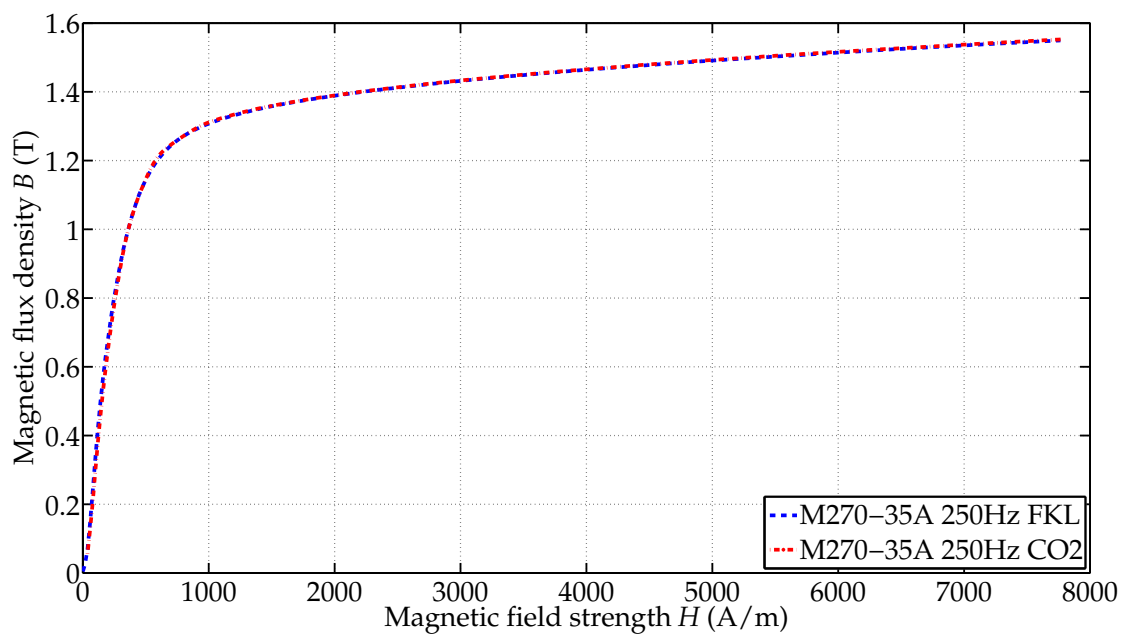


(b) Magnetization curve

Figure 6.2: Specific losses and magnetization curves of both laser-cut stators, material M270−35A. The laser-cut samples show a 'linear' influence on the loss curve.
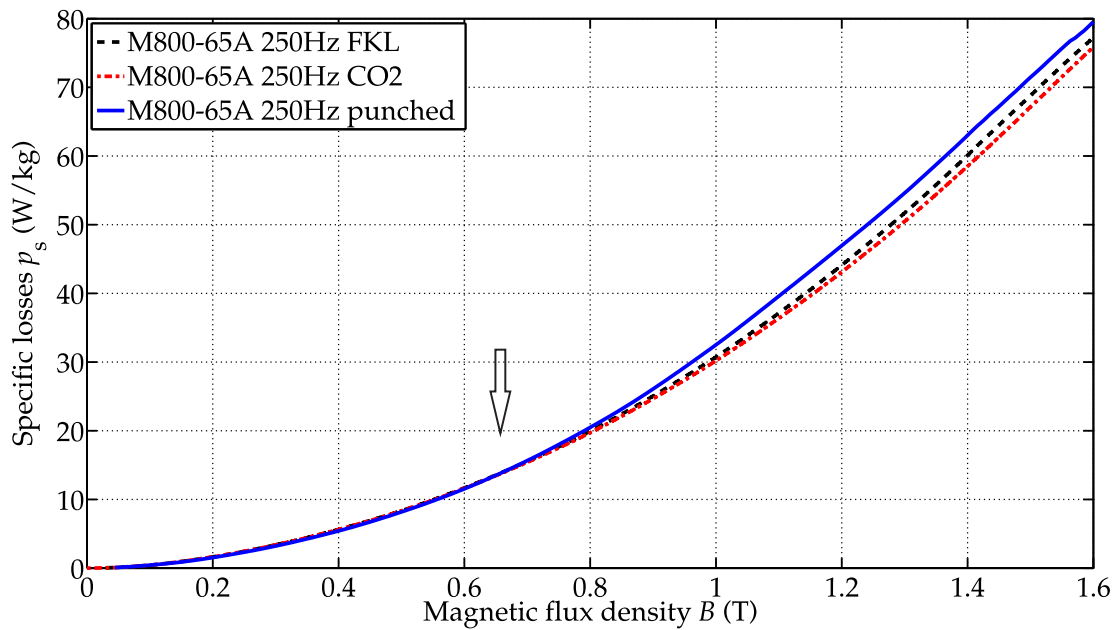
(a) 250 Hz
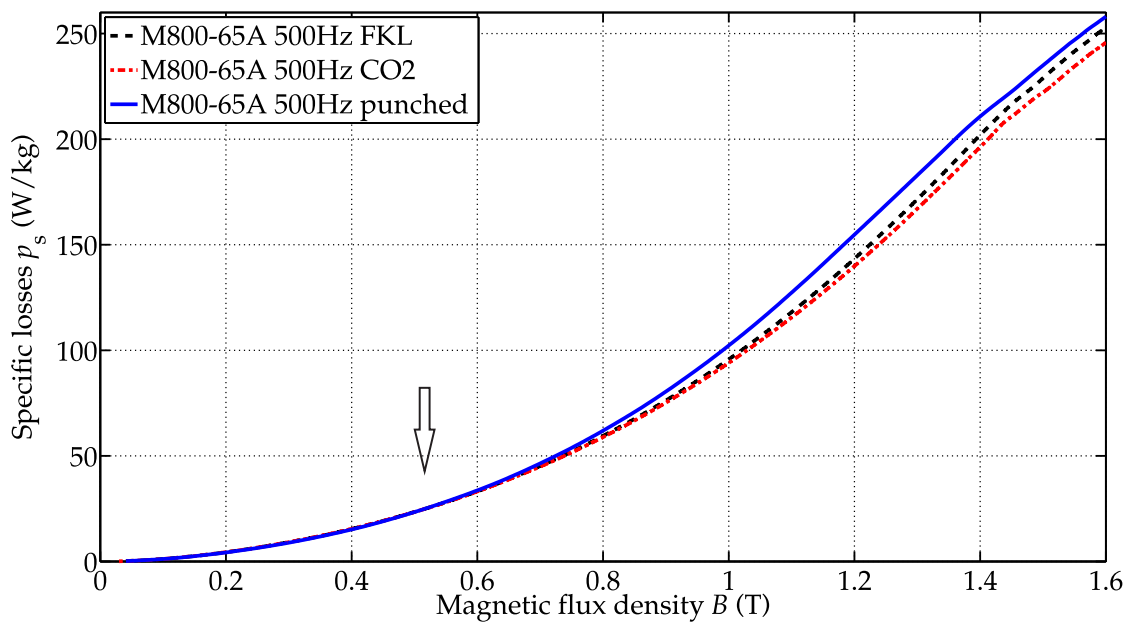


(b) 500 Hz

Figure 6.3: M800-65A: For frequencies 250 Hz and higher also the losses of both laser-cut samples differ at high magnetic flux densities $B$.

Table 6.1: Stator lamination stack measurements ('Epsteinframe' method): POIs of specific losses for the FKL-laser cut and mechanically-cut samples.

|  | **M270-35A** | **M400-50A** | **M800-65A** | Reduction of $B$ of POI from M400-50A to M800-65A in % |
|---|---|---|---|---|
| 50 Hz | N/A | 1.35 T* | 1.06 T | - |
| 250 Hz | N/A | 0.86 T | 0.65 T | −24.4 % |
| 500 Hz | N/A | 0.71 T | 0.51 T | −28.2 % |

* = no 'real' POI, rather an area where the specific losses are similar.

for this may be:

1) The different type of mechanical cutting used (punching versus guillotine cutting), the different geometries used (Epstein versus stator shape with teeth, notches, etc.), and/or the additional stress due to the compression the stators have been subjected to. The last factor mentioned may indeed be the most significant contributing factor: The stresses inside the material induced by the laser cutting may be less sensitive to additional compressive stresses into the thickness direction than those introduced into the lattice structure by mechanical cutting. Thus, the POI measured for the stator lamination stacks occurs at lower flux densities $B$ than that measured for the small Epstein samples, although the specific cutting length is smaller.

2) As shown in Chapter 5.2, even the POIs between the samples of 7.5 and 7 mm width of laser-cut samples move to higher flux densities (see Fig. 5.11). Thus, it may be assumed that the POI does not depend linearly on the sample width, ratio $V_{dg}/(V_{nd} + V_{dg})$, or specific cutting length (see Table 6.2 and Tables 5.1, 5.5, 6.1, or see for instance material M800-65A in Fig. 6.4; the calculation of the specific cutting length is presented in Appendix F.2).

To summarize, the results suggest that for machines with the size of those investigated, laser cutting provides a useful option to mechanical cutting concerning specific losses.

Table 6.2: Specific cutting lengths in m/kg of the investigated samples.

|  | **Epstein sample 30** | **Epstein sample 7.5** | **Epstein sample 7.0** | **Stator yoke** |
|---|---|---|---|---|
| **M270-35A** | 24.9 | 99.6 | 106.7 | 50.65 |
| **M400-50A** | 17.3 | 69.3 | 74.2 | 35.2 |
| **M800-65A** | 13.2 | 52.6 | 56.4 | 26.8 |

By *comparing Epstein with stator samples*, with the same material and at the same frequency, the specific losses of the stator specimens are higher than the specific losses of the wide Epstein specimens (see Fig. 6.5). This applies to all measurements
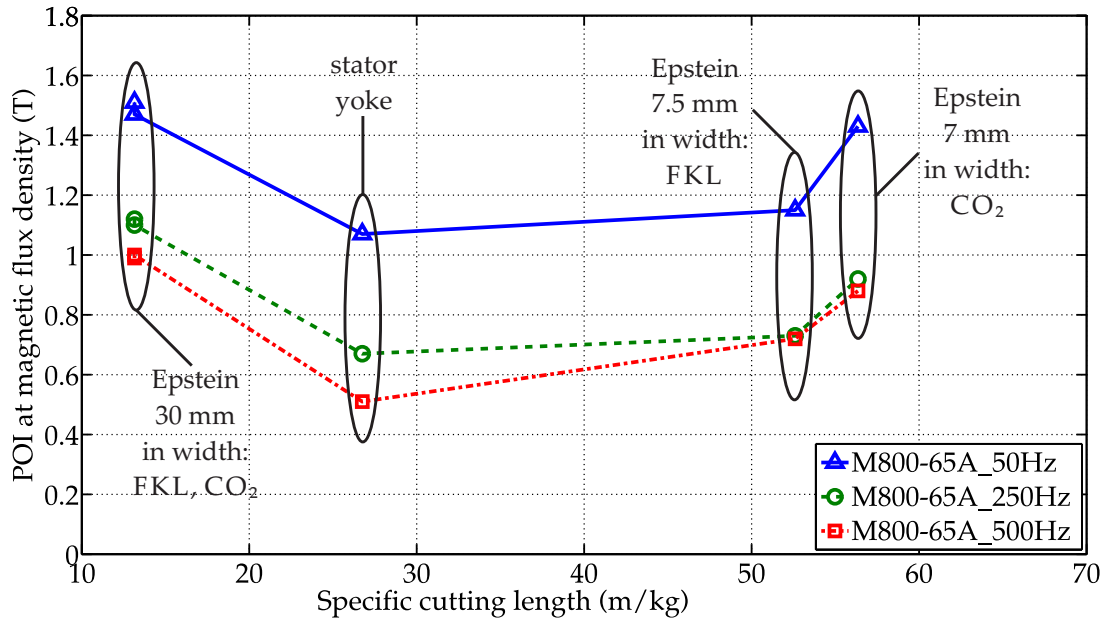
Figure 6.4: POIs as a function of the specific cutting length for material M800-65A.

performed. The specific losses of the stator specimens are closer to the small Epstein samples. This again depends on the material thickness and frequency. For example, for $CO_2$-laser cut material M400-50A at 50 Hz it applies $p_{s,stator} < p_{s,Epstein,small}$ (see Fig. 6.5). With increasing frequency a POI occurs which is again shifted to lower magnetic flux densities $B$ with increasing frequency and material thickness[2,p.132]. Considering the specific cutting length, the specific losses of the stator should be smaller than those of the small Epstein samples (see also Appendix F.2). Again, the additional processing step of the stators, the gluing and pressing, may have an influence. The pressure induces elastic stresses which result in crystal lattice deformation and thus in degraded magnetic properties [170].[3] Additionally, local short circuits may be produced because of the pressing procedure [170] (due to burrs and defects in the isolation), which increases the losses at higher magnetic flux densities and frequencies. This may be one reason for the occurrence of a POI of the small Epstein and stator samples. According to [170], the increase of losses induced by this additional processing step is rather small. However, the literature also contains accounts which show a large influence due to the pressing into the thickness direction. This is discussed in Chapter 8.3.3.

### Comparison of the two laser cutting techniques

As previously mentioned, a slight difference, if at all, between the laser-cut probes

---

[3]The differently cut samples (laser vs. mechanical cutting), with different states of internal stresses might differ in their further degradation due to additional stresses induced by pressing and gluing.
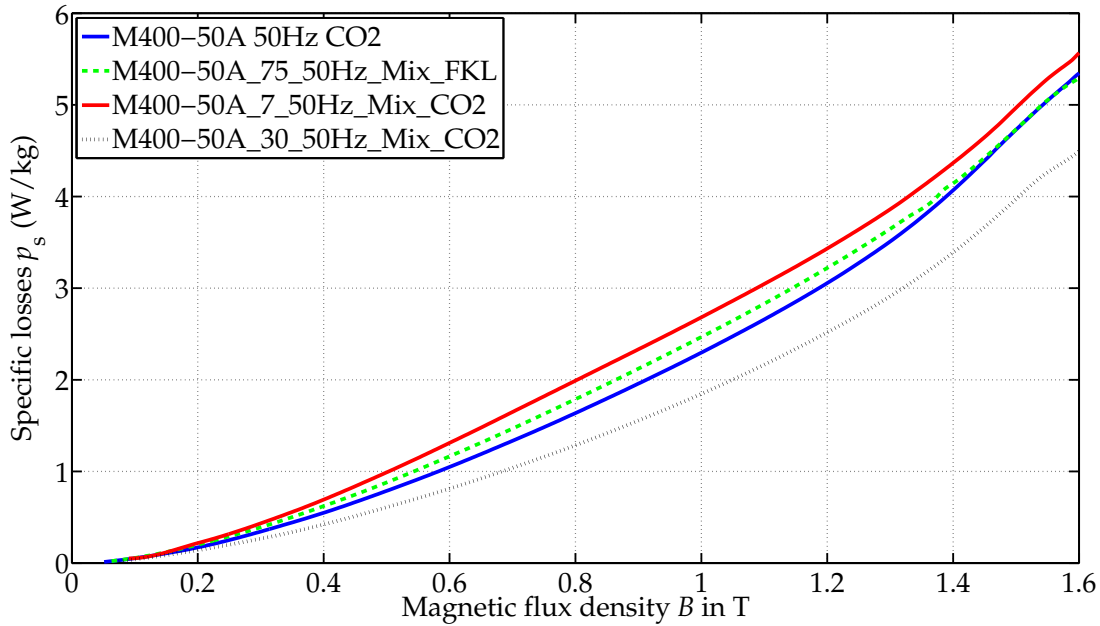
Figure 6.5: Comparison of specific losses of stator and Epstein specimens.

has been recognized at medium to high magnetic flux densities for the thick[2,p.132] material and at the higher frequencies (see Fig. 6.3). This may be explained by the laser settings. According to Table 2.1, both lasers cut the stators of material M800-65A at almost the same cutting speed. Thus, both laser methods only differ in power and mode. In both cases, the FKL-laser may have introduced more destroying energy per material volume (higher power and almost continuous mode) as the $CO_2$-laser. This, in turn, may have led to the higher determined specific losses.

**Magnetization curves and permeability**

*Laser versus mechanical cutting.*

*Magnetization curves.* Fig. 6.6 shows by way of example the magnetization curves of the laser-cut and punched stator samples for material M400-50A, obtained from the 'Epsteinframe' method, this time at 250 Hz and 500 Hz. Fig. 6.7 shows the relative permeability computed from the measurements of Fig. 6.6 a).

As with the Epstein frame measurements, the shapes of the *B-H* curves of mechanically-cut and laser-cut samples differ and thus indicate the different kind of magnetic deterioration: Again, up to the knee point of the mechanically-cut samples (see Fig. 6.6), the relative permeabilities (gradient of the *B-H* curves) of the punched samples are larger than those of the laser-cut samples (see also Fig. 6.7). The knee-point areas of the punched samples occur at lower magnetic flux densities *B* compared to the laser-cut samples. This applies to all investigated materials and is in line with the results of Chapter 5. For the chosen samples, the POI occurs at 480 A/m (Fig. 6.7).
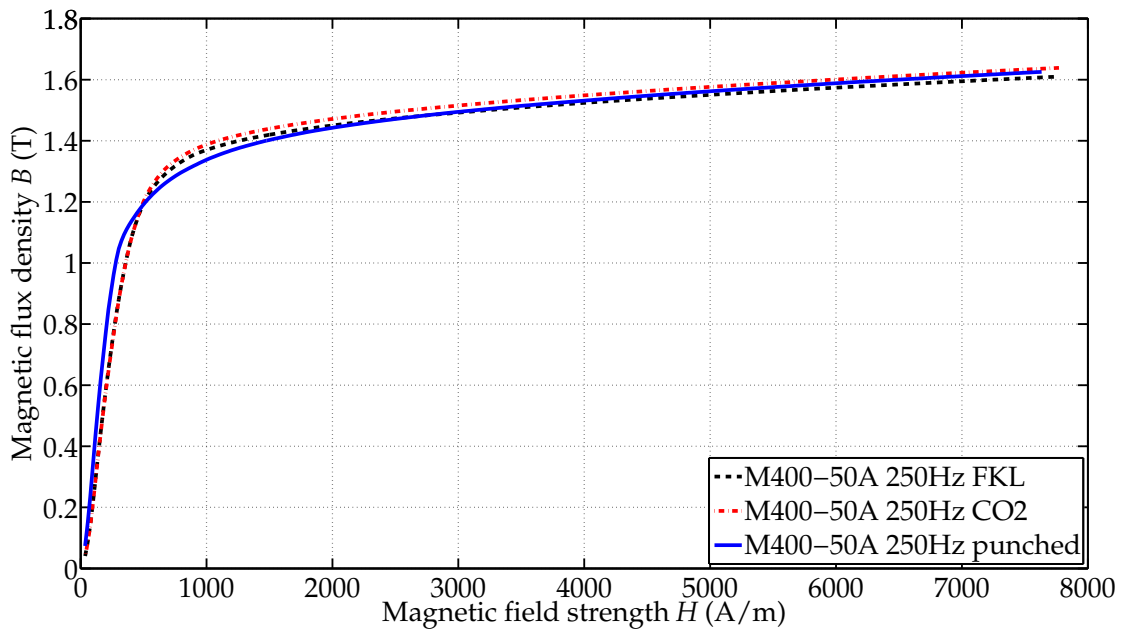
(a) 250 Hz
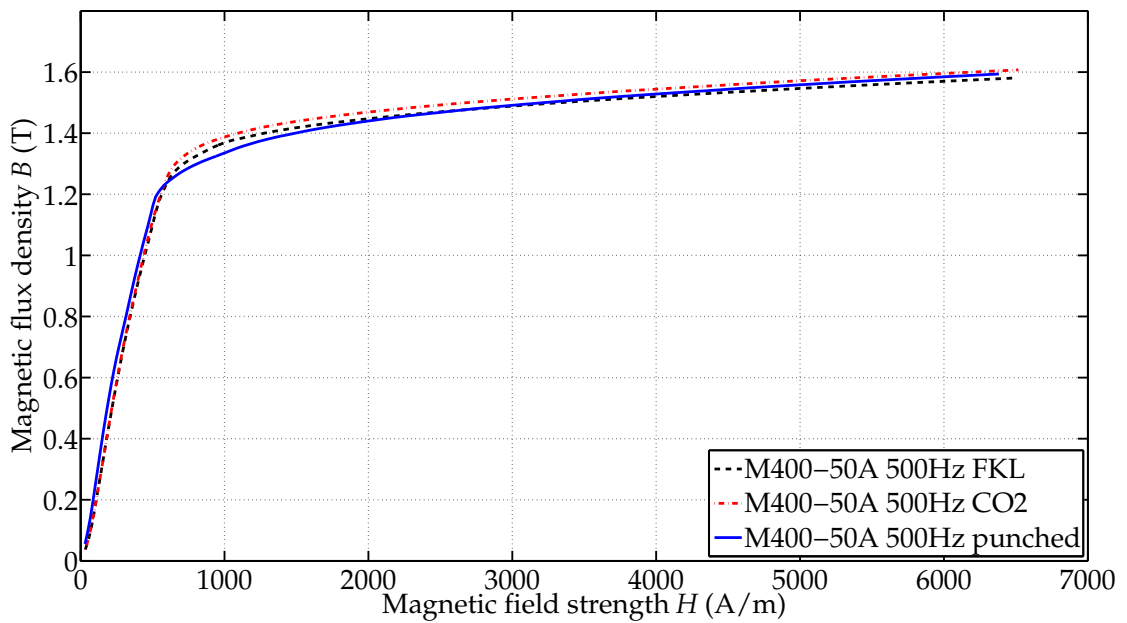


(b) 500 Hz

Figure 6.6: Magnetization curves for punched and laser-cut stator samples of M400-50A at a) 250 Hz and b) 500 Hz.
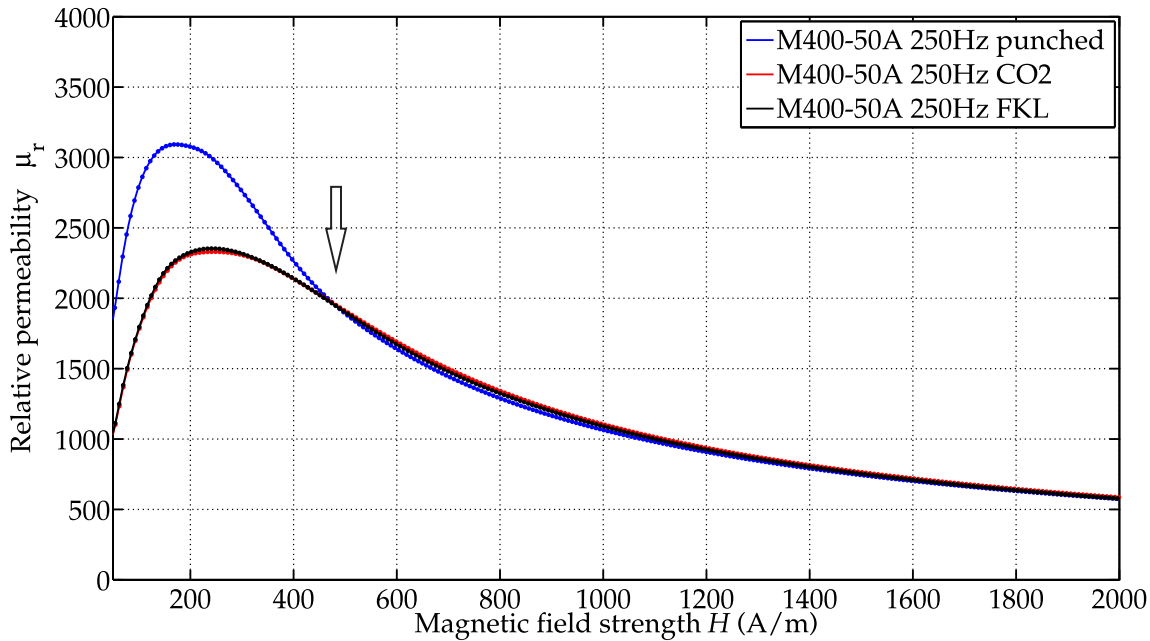
Figure 6.7: M400-50A at 250 Hz: Relative permeability $\mu_r$ for punched and laser-cut samples, computed from the measured magnetization curves.

Considering the shape of the *B-H* curves of the stator specimens concerning the comparison of the different cutting techniques (characteristics), the behavior is similar to the qualitative comparison of the different cutting techniques of the small Epstein specimens (see Fig. 6.8 or compare Appendixes C.2 and D.2), but not as distinct as those of the wide Epstein specimens (compare Appendix D.2 with Appendix C.3).

In a direct comparison of the magnetization curves of the respective stator and Epstein samples (see Fig. 6.9), the area below the knee-point area of the stator samples is close to the magnetization curve of the small Epstein samples with a width of 7.5 mm, but the knee point and saturation area differ. This applies to all measured and compared magnetization curves independent of the cutting technique. According to the specific cutting length, the degradation effect on the magnetic property, in this case the relative permeability, is assumed to be between the permeabilities of the wide and the small Epstein specimens. This is confirmed up to the knee-point area, although not with a linear decrease, as the difference of stator and small Epstein samples is small. However, this is not true for the knee-point and saturation areas. Here, the stator samples show larger material degradation for all cutting techniques, as higher magnetic field strengths $H$ are necessary to obtain the same magnetic flux density $B$; thus the saturation is decreased for the stator samples. These larger degrading effects on the magnetization curves of the stator samples might be explained by:

I) *Sample geometry.* The stator is round with smaller curvatures at the inner radius caused by notches and teeth, in contrast to the simple rectangular Epstein design. Therefore, the deterioration of the stator specimens may be worse because of the more complicated shape of the cut edges. For samples with complex and small geometries, stresses at corners submitted to several cutting processes may lead to overlapping degraded zones, which increase the stresses on a distinct material cut edge part.

II) *Further processing steps.* As previously mentioned, the stator samples are glued and pressed, in contrast to the Epstein samples (see Chapter 2.1.1) which induces additional degradation (see Chapter 1). According to [170] the differences between pressed and non-pressed steel sheets decrease with decreasing silicon content[4]. For non-silicon material, only a small deviation in the knee-point area occurs at all. In the saturation area, no difference is found for both high-silicon and non-silicon material. Thus, according to [170], the pressing process may degrade the knee-point area and the area below the knee-point. This is also in accord with the results presented in [98].

*Permeability.* For all investigated stator samples, the maximum relative permeabilities $\mu_{r,max}$ of the punched samples are larger than for the laser-cut samples (see Fig. 6.7). The maximum relative permeabilities of the laser-cut samples occurs at larger magnetic field strengths $H$ than those of the punched stator samples (see Fig. 6.7). As in the case of the investigations on the Epstein frame, the difference between the laser-cut and the mechanically-cut samples in the area of the maxima decreases (absolute values) with increasing frequency and material thickness[2,p.132] (see also Fig. 6.6), as the influence of cutting reduces with increasing eddy currents.

Even for the relative permeability a *point of intersection (POI)* occurs for the differently cut samples (see Fig. 6.7). These POIs occur for all investigated materials at all frequencies (see Tables 6.3 and D.5). As the $CO_2$-laser and FKL-laser cut samples have (nearly) the same relative permeabilities, also the POIs are in the same range. With increasing material thickness[2,p.132] the POI is shifted to lower field strengths $H$.

**Comparison of the two laser cutting techniques.**
*Magnetization curves.* For material M270-35A, the magnetization curves of both laser-cut stacks are identical (see for instance Fig. 6.2). In contrast, for materials M400-50A and M800-65A, larger magnetic flux densities $B$ are reached from the second half of the knee-point area for the $CO_2$-laser cut samples than for the FKL-laser cut samples

---

[4]This author investigated high silicon and non-silicon material. Note, in this work medium-silicon materials are studied. No detailed information is given in [170], as to which materials are investigated, which makes it difficult to evaluate, to what extent these results can be transferred to the results presented in this work.
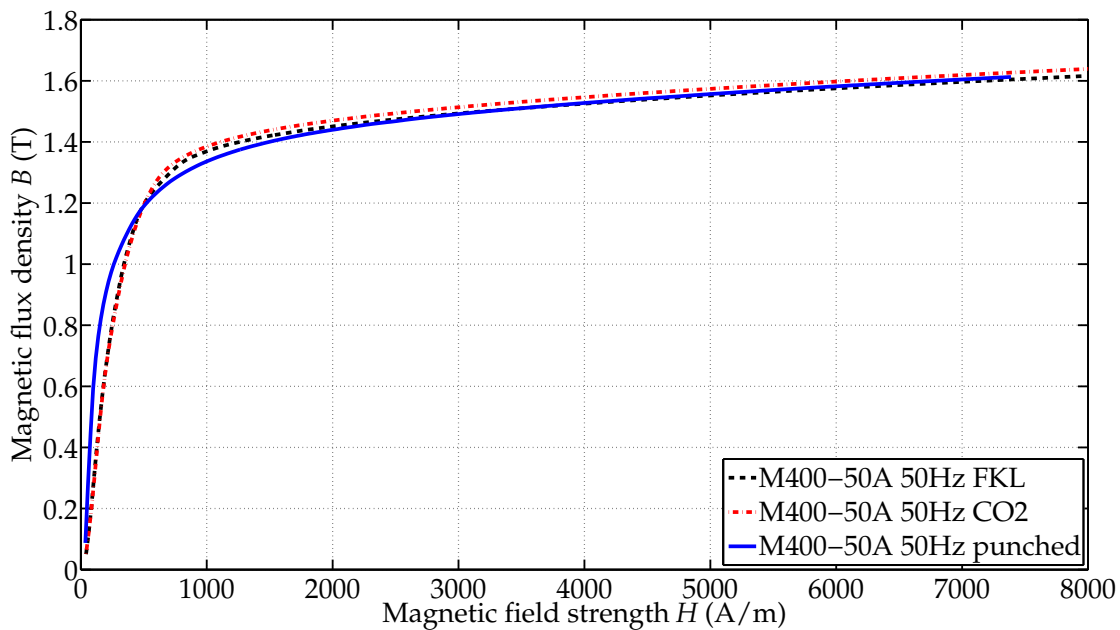
(a) M400-50A_50Hz stator sample
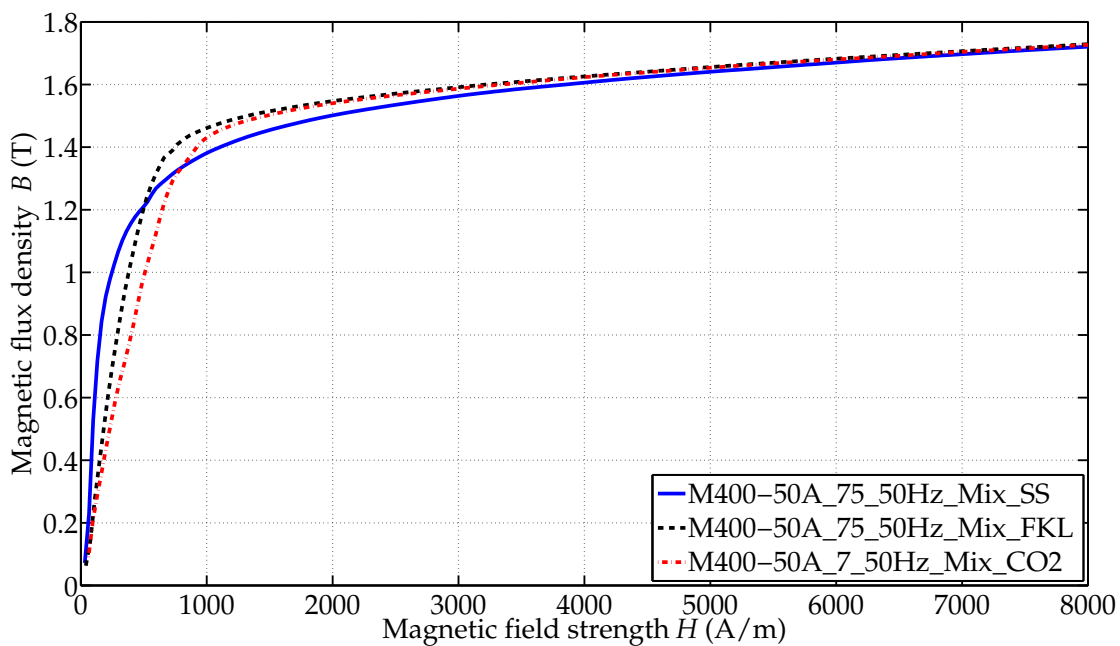


(b) M400-50A_50Hz small Epstein sample

Figure 6.8: Qualitative comparison of the *B-H* curves of different cutting techniques for a) stator samples and b) small Epstein specimens.
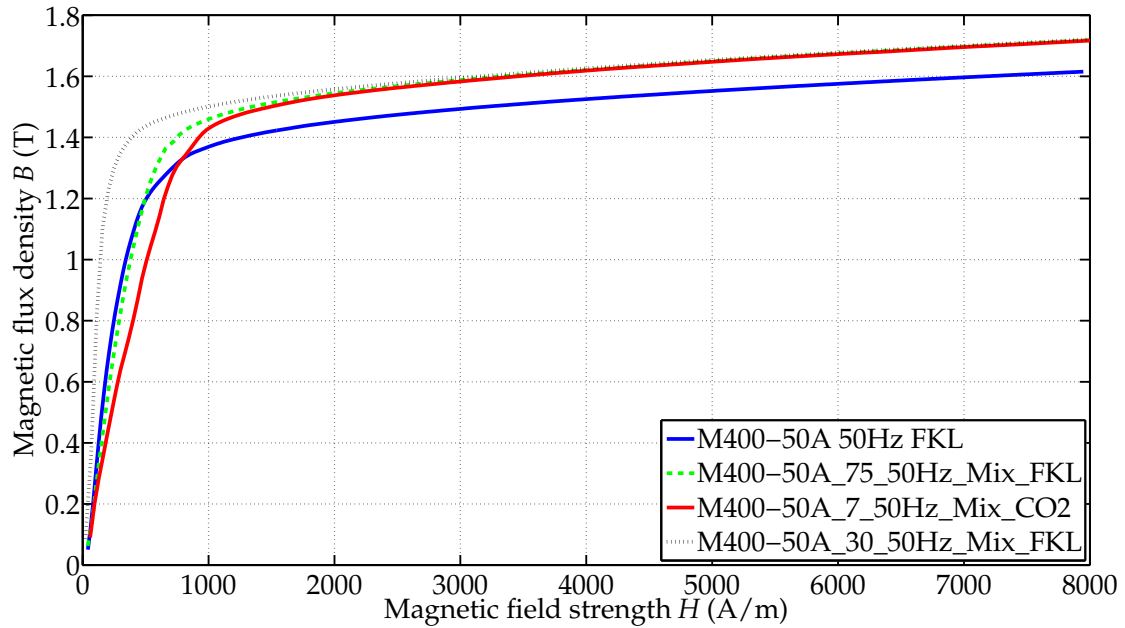
Figure 6.9: Magnetization curves of stator as well as Epstein samples for M400-50A
at 50 Hz.

Table 6.3: Stator lamination stack measurements ('Epsteinframe' method): POIs of
relative permeability for the FKL-laser cut and mechanically-cut samples.

|        | **M270-35A** | **M400-50A**      | **M800-65A**      |
|--------|--------------|-------------------|-------------------|
| 50 Hz  | N/A          | 479 A/m (1.18 T)  | 370 A/m (1.09 T)  |
| 250 Hz | N/A          | 483 A/m (1.18 T)  | 465 A/m (1.09 T)  |
| 500 Hz | N/A          | 620 A/m (1.25 T)  | 527 A/m (0.89 T)  |

considering the same magnetic field strength $H$ (see Fig. 6.6). This applies for all
investigated frequencies.

*Permeability.* In contrast to the investigations of the Epstein frame measurements,
the relative permeabilities of materials cut using different laser techniques are almost
identical (see for instance Fig. 6.7). Thus, for the stator samples the maxima of the
permeabilities are in the same range ($\mu_{r, max, FKL} \cong \mu_{r, max, CO_2}$), in contrast to the Epstein
frame measurements (see Chapter 5.2). This may be attributed to the possibly smaller
difference in cutting speed between both laser cutting techniques in the case of the
cutting of the stators in contrast to that of the Epstein samples (complex vs. simple
geometry)[5]. This effect (same versus different effect of FKL-laser vs. $CO_2$-laser) was
not observed for the specific losses (compare Figs. 5.7 and 5.13). This is in accordance
with the results presented in [45], whereby the relative permeability is most sensitive

---

[5]See Table 2.1 for the maximum cutting speeds reported. The exact cutting settings at each moment
are, however, unfortunately unknown.

to the thermal cutting techniques and their respective settings, whereas the specific losses are much less [45] affected. This observation might also be influenced by the additional manufacturing steps that the stators had been submitted to, pressing and gluing, in contrast to the Epstein specimens. Presumably, this further step reduces the difference attributed to the different laser cutting techniques. Thus, it may be possible that the differences on the magnetic properties of the different laser-cut samples become less significant with further degrading manufacturing steps.

In contrast to the case of the small Epstein frame measurements (see Fig. 5.5), the calculated relative permeabilities show a distinct maxima for both laser-cut and the punched samples. This is interpreted as follows: Since the yoke height is larger than the width of the small steel strips, the compressive stresses induced by laser cutting are not as strong as to reduce the distinct maximum to a plateau. (See Chapter 5.2 - small samples, the maximum plateau instead of a distinct maximum only appears if the sample width decreases.)

Conclusions:
- The main observations from the results of the Epstein frame in respect to the different cutting techniques are also observed with the stator samples.
- Both laser-cut stators show almost equal effects on the specific losses (including linear parts) of the material, whereas those of the punched specimens differ. This is in agreement with the findings obtained from the Epstein specimens (see Chapter 5).
- The findings on the POI of the specific losses are in line with those obtained from the Epstein frame measurements.
- Comparing the results for a given material and frequency, the POIs of the stator samples occur at lower magnetic flux densities $B$ than those of the Epstein samples.
- The POI of laser-cut and mechanically-cut samples is shifted to lower magnetic flux densities $B$ with thicker[2,p.132] material and higher frequencies.
- The *B-H* curves of the mechanically and the laser-cut samples differ. Even the laser-cut samples differ from the second part of the knee-point area onward (exception M270-35A).
- It applies: $\mu_{r,max,punching} > \mu_{r,max,laser}$ and $\mu_{r,max,FKL} \cong \mu_{r,max,CO_2}$.
- The higher the frequency and the higher the material thickness, the lower the difference of the relative permeabilities of the punched and laser-cut samples at small magnetic field strengths $H$.
- The relative permeabilities of the laser-cut samples show a distinct maximum in contrast to the investigated small Epstein samples.

- The relative permeabilities of $CO_2$-laser and FKL-laser cut samples are almost the same, even at low magnetic field strengths $H$.
- As with the Epstein strips, a POI of the measured relative permeabilities of the mechanically-cut and laser-cut stators is observed, which is shifted to lower magnetic field strengths $H$ with increasing material thickness[2,p.132].

## 6.2 Results by 'modified Epsteinframe' method

The *'modified Epsteinframe'* measurements show almost the same results as those of the *'Epsteinframe'* method (Chapter 6.1) concerning the comparison of the influence of the different cutting techniques on the magnetic material properties. The POIs listed in Table 6.4 are in the same range as those presented in Table 6.1. Furthermore, no significant differences of *these two* measured magnetization curves are observed (Fig. 6.10). This applies to all investigated magnetization curves.

Slight differences are observed for the specific losses at high magnetic flux densities (range from 1.2/1.3 T onward - consistent with the knee-point area of the magnetization curves/start of saturation effects). The *'modified Epsteinframe'* method is performed without sense lines (see Chapter 2.6). Therefore, the sinusoidal waveform of the secondary voltage (and thus also of the magnetic flux density $B$) is not ensured, which is notably relevant with increasing saturation[6]. The more the material is saturated, the more harmonics are added to the sinusoidal secondary voltage/ magnetic flux density $B$. These harmonics further increase the losses, and therefore the slope of the losses at high magnetic flux densities $B$ are larger for the measurement technique without secondary sense lines (see Fig. 6.11).

The punched samples reach the beginning of the knee point at lower magnetic flux densities $B$ than the laser-cut samples (see e.g. Fig. 6.8). Thus, also the difference in specific losses between these two different measuring methods starts at lower flux densities for the punched specimens when compared with the laser-cut specimens (see Fig. 6.11 and Appendix D.5).

Conclusions:
- The 'modified Epsteinframe' method leads to the same conclusions concerning the different cutting techniques as the 'Epsteinframe' method.
- Differences only occur with increasing saturation (above knee point) and are explained by the additional harmonics in the case of the 'modified Epsteinframe' method.

---

[6]See Chapter 2.6.
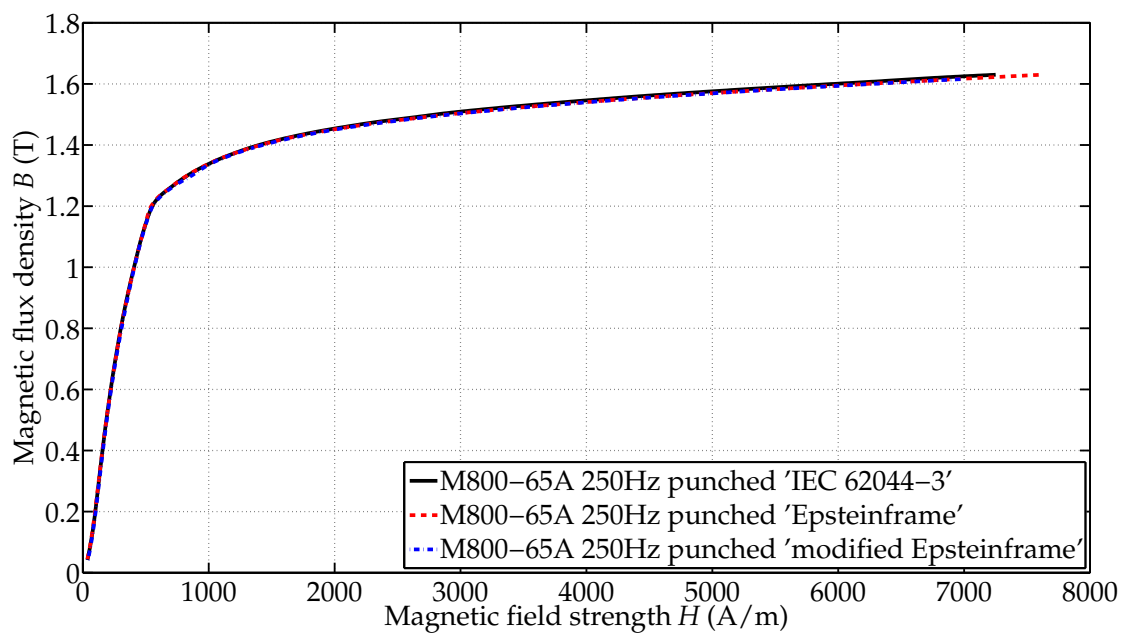
(a) M800−65A_250Hz punched
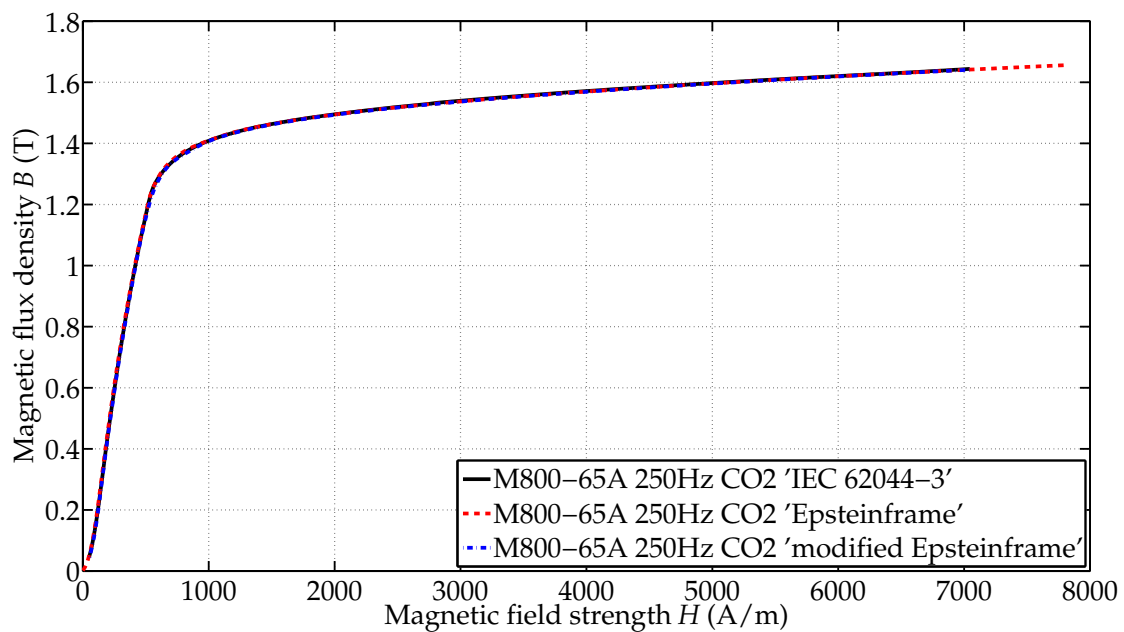


(b) M800−65A_250Hz $CO_2$

Figure 6.10: No significant differences between results of the 'Epsteinframe' and the 'modified Epsteinframe' method are observed.
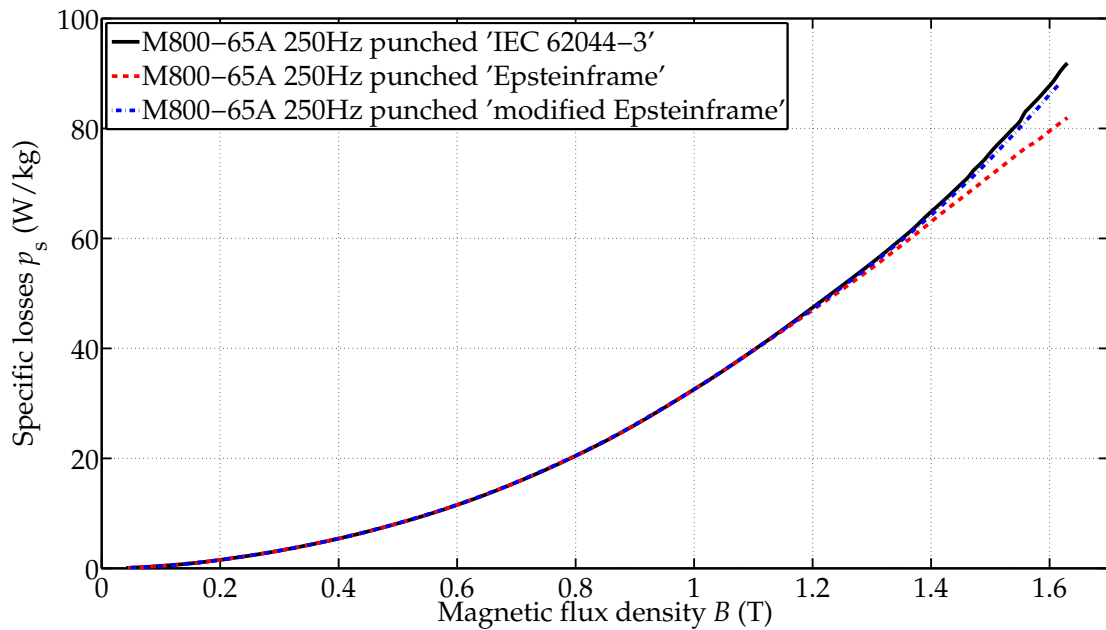
(a) M800−65A_250Hz punched
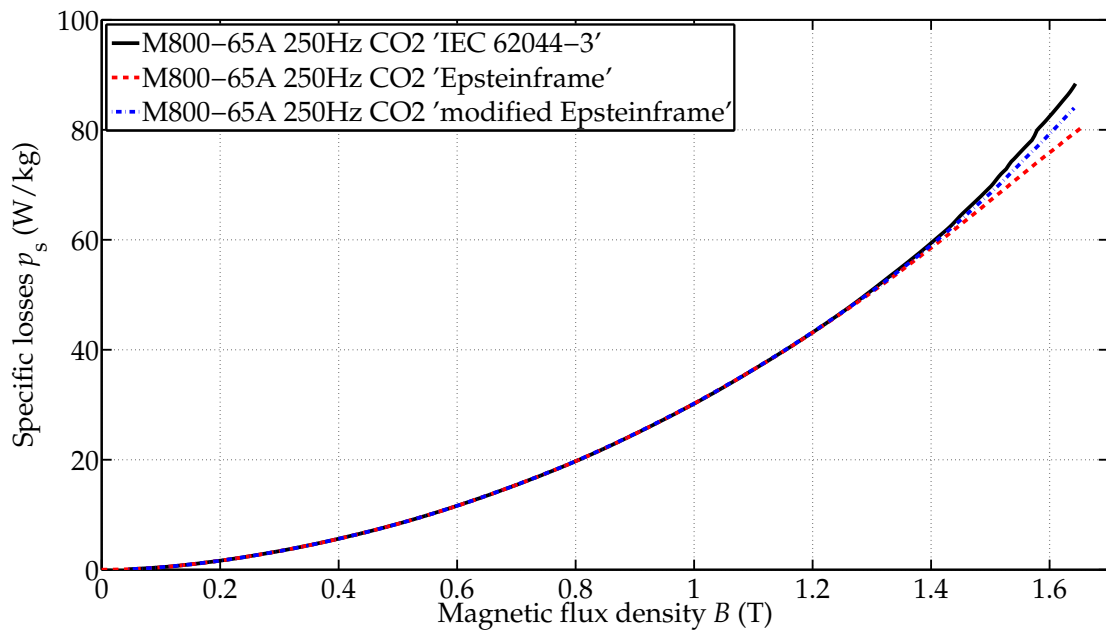


(b) M800−65A_250Hz CO$_2$

Figure 6.11: The difference of specific losses determined by the '(modified) Epsteinframe' methods starts for punched samples at lower magnetic flux densities $B$, as the knee point of punched samples occurs at lower flux densities $B$, compare with Fig. 6.8 a).

Table 6.4: Stator lamination stack measurements ('modified Epsteinframe' method): POIs of specific losses for the FKL-laser cut and mechanically-cut samples.

|  | **M270-35A** | **M400-50A** | **M800-65A** | Reduction of $B$ of POI from M400-50A to M800-65A in % |
|---|---|---|---|---|
| 50 Hz | N/A | 1.35 T* | 1.03 T | - |
| 250 Hz | N/A | 0.86 T | 0.64 T | $-25.6\,\%$ |
| 500 Hz | N/A | 0.69 T | 0.53 T | $-23.2\,\%$ |

\* = no 'real' POI, rather an area where the specific losses are similar.

## 6.3 Results by measurement method 'IEC 62044-3'

Method *'IEC 62044-3'* leads to the same results as the two *'(modified) Epsteinframe'* methods ('Epsteinframe' and 'modified Epsteinframe' method) concerning the qualitative comparison of the different cutting techniques (characteristics) (see Appendix D.5): for example the 'quadratic' specific loss shape of the mechanically-cut samples and the 'quadratic-linear' specific loss shape of the laser-cut samples (see Fig. 6.14). Even the measured POIs, as shown in Table 6.5, are almost identical (compare with Table 6.1). Again, remarkable differences only occur at higher magnetizations.

Table 6.5: Stator lamination stack measurements ('IEC 62044-3' method): POIs of specific losses for the FKL-laser cut and mechanically-cut samples.

|  | **M270-35A** | **M400-50A** | **M800-65A** | Reduction of $B$ of POI from M400-50A to M800-65A in % |
|---|---|---|---|---|
| 50 Hz | N/A | 1.35 T* | 1.05 T | - |
| 250 Hz | N/A | 0.85 T | 0.66 T | $-22.4\,\%$ |
| 500 Hz | N/A | 0.68 T | 0.51 T | $-25\,\%$ |

\* = no 'real' POI, rather an area where the specific losses are similar.

The measured *specific losses* (measured by all three different methods) deviate from about 1.4 T onward (correlating with the second part of knee-point area to (high) saturation) for all stator materials and cutting techniques (see Figs. 6.12 a)-c)). Considering this area at 50 Hz, the values taken by the *'modified Epsteinframe'* method are the highest, followed by the method according to *IEC 62044-3* and those of the *'Epsteinframe'* method (Fig. 6.12 a)). At 250 Hz, the specific losses of method *'IEC 62044-3'* and of the *'modified Epsteinframe'* method are almost equal (M270-35A, see Appendix D.5) or swapped (Fig. 6.12 b)). At 500 Hz, method *'IEC 62044-3'* determines the largest specific losses (Fig. 6.12 c)).

These differences in measured specific losses at large magnetic flux densities are attributed to the following reasons[7]:

1) These three measurement techniques differ in terms of voltage supply and control and thus deviations from the sinusoidal wave form of the magnetic flux density $B$ differ, too.

2) The different temperatures inside the stator, due to the respective measuring technique:

Method *'IEC 62044-3'* takes the loss values separately (see Chapter 2.6) to avoid self-heating of the stator samples, the two *'(modified) Epsteinframe'* methods take the reading of the different points one after another so that self-heating of the stator occurs. The larger the frequency is and the larger the magnetic flux density $B$, the higher the self-heating of the stator.

Fig. 6.13 shows: With increasing temperature of the electrical steel sheets, the specific losses decrease as shown by the result for one operating point and stator M270-35A_FKL, measured at a high magnetic flux density $B$ of 1.5 T, over a time sequence of 15 minutes. During the measurement, the stator temperature increased from 28 °C to 50 °C (measured at the outside diameter of the stator yoke[8]). In the respective case, the specific losses reduced by 0.84 $\frac{\text{W}}{\text{kg}}$ within the 15 minutes of the measurement, which corresponds to a reduction by 2.8 %. This loss behavior agrees also with literature (see Chapter 1 and [36, 185, 195]). In [185], this is explained by the increase of the material resistivity with increasing temperature.

This temperature dependence of the specific losses is (predominantly at high magnetic flux densities $B$) also reflected in the differences of the results obtained with the *'IEC 62044-3'* and the *'Epsteinframe'* methods (see for instance Fig. 6.12 a)-c)). This applies for all investigated samples and frequencies. With increasing frequency and material thickness, this difference between these two measurement methods increases, as well as the temperature inside the stator material increases with frequency and/or material thickness.

Comparing the measurement methods *'modified Epsteinframe'* and *'IEC 62044-3'* the effect of temperature firstly dominates at 250 Hz. This applies for all investigated materials. At 50 Hz the difference in temperature is still small (23 °C- 29 °C), so that the difference is mainly attributed to the voltage supply and control.

The difference between the results of the *'Epsteinframe'* and the *'modified Epsteinframe'* method at high magnetic flux densities $B$ (see Fig. 6.12 a)-c)) is explained by the different voltage controls, as both measurement methods lead to the same range of temperature inside the stator (see p. 193).

---

[7]The percentage each reason takes depends on frequency and the material investigated (e.g. thickness).

[8]Note, the temperature inside the stator is even higher.

(a) 50 Hz
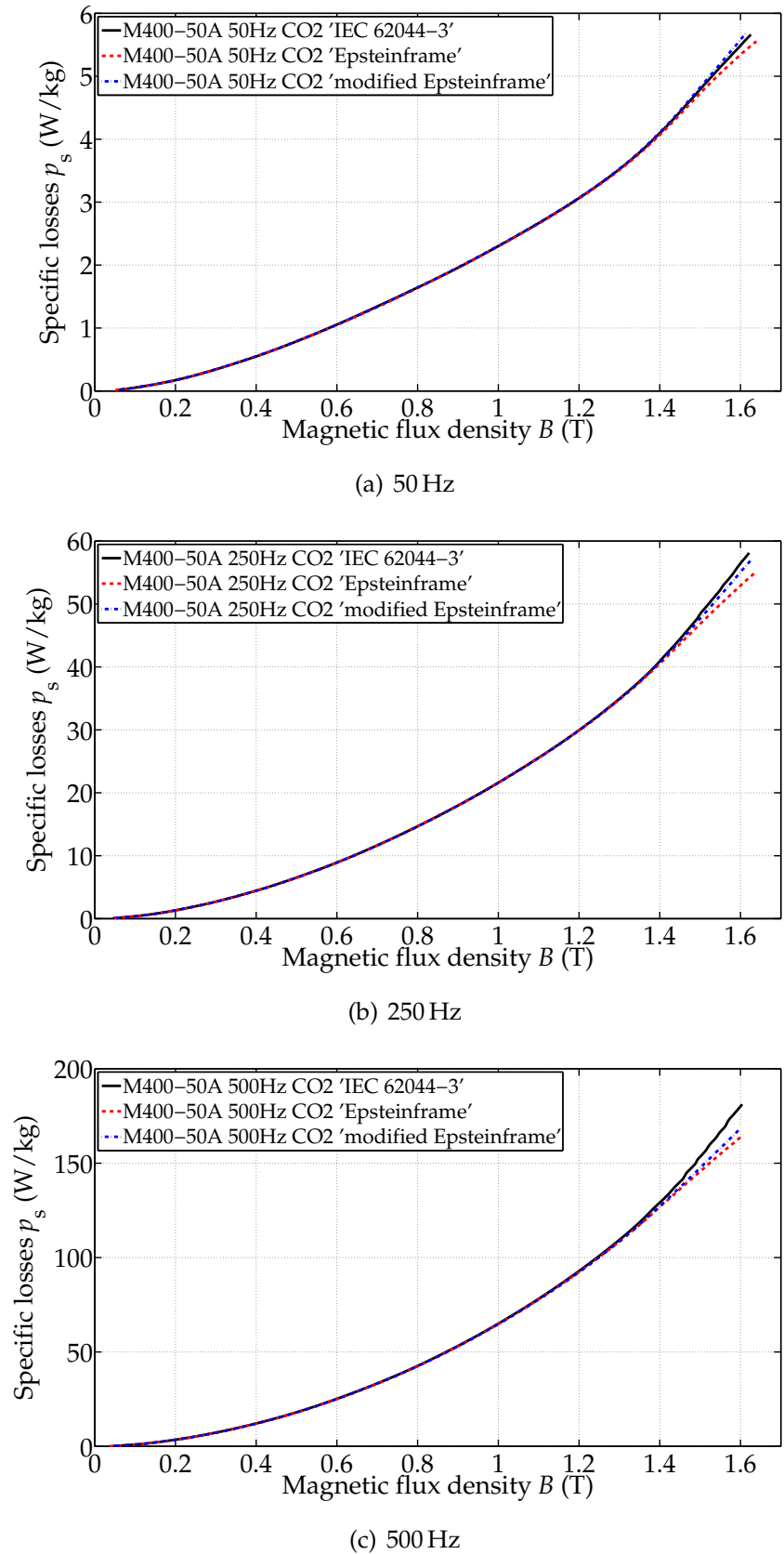


(b) 250 Hz



(c) 500 Hz

Figure 6.12: Comparison of the three different measurement methods: as shown for M400-50A_$CO_2$ at a) 50 Hz, b) 250 Hz and c) 500 Hz.
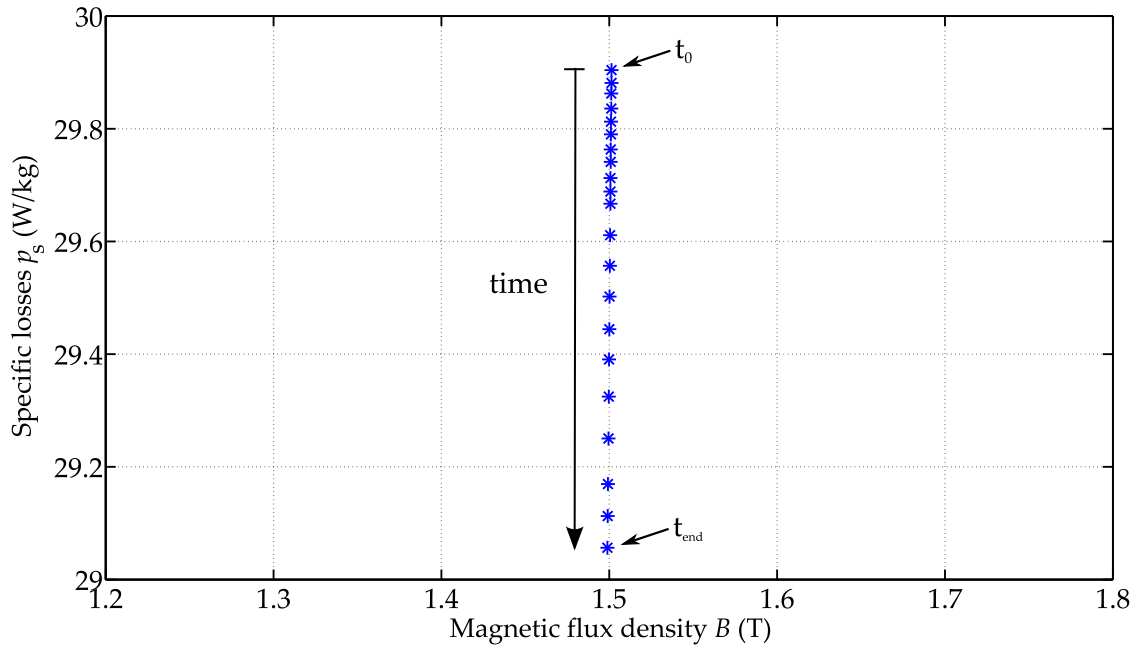
Figure 6.13: One operating point measured at 250 Hz at high magnetic flux density in a time sequence of 15 minutes for analyzing the effect of temperature on the measured specific losses.

Because of the influence of temperature and voltage supply and control, method *'IEC 62044-3'* determines higher specific losses at high frequencies and large magnetic flux densities than the other two methods.

As long as the form factor is $1.111 \pm 1\%$, the different measurement methods show a good correlation of the specific losses. Table D.8 in Appendix D.6 shows the form factor limit of each measurement and its respective measurement method.

Concerning the different measured *magnetization curves*, small differences at (high) saturation might be observed comparing the results of *'IEC 62044-3'* and the two *'(modified) Epsteinframe'* methods (M400-50A_500Hz (punched, $CO_2$), M800-65A_250Hz (punched) and M800-65A_500Hz (punched, $CO_2$, FKL)). With increasing temperature, the saturated part of the magnetization curve is reduced to smaller magnetic flux densities $B$, as the data obtained by the 'IEC-62044' method (the stator samples have about room temperature for each measurement point) show slightly larger magnetic flux densities at (high) saturation than the magnetization curves of the other two methods. This is in line with the report of [195] (consider the difference of magnetization curves for $100\,°C$ and room temperature in [195], as some of the investigated stators in this work[21,p.24] (in particular the thick material M800-65A) reached a temperature of about $100\,°C$ with the '(modified) Epstein'
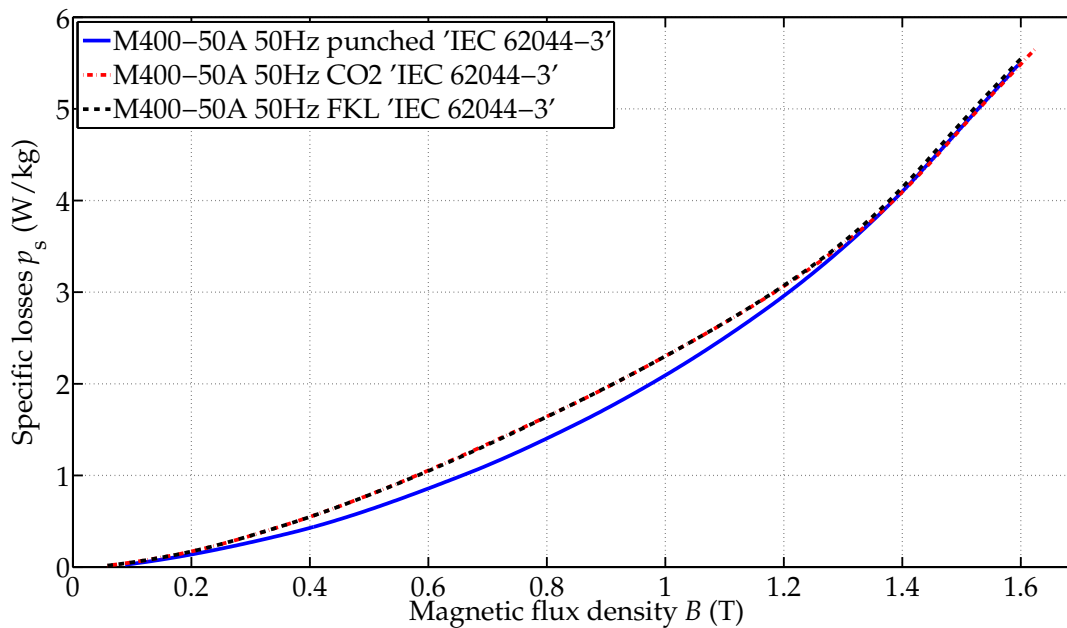
Figure 6.14: 'Quadratic' and 'quadratic-linear' specific loss shape of differently cut
　　　　　　 stators.

methods at the outer diameter [9]). Altogether, this effect of temperature on the
magnetization curve is only observed for thicker material and higher frequencies.

Conclusions:
- The specific losses determined by method 'IEC 62044-3' are larger for sam-
  ples at high frequencies and high magnetic flux densities in contrast to the
  two '(modified) Epsteinframe' methods. This is due to the temperature
  effect and voltage distortion (voltage supply and control). The deviation
  between the results obtained by the different measurement methods at high
  magnetic flux densities $B$ depends on frequency and the material investi-
  gated (e.g. thickness).
- The influence of temperature is also seen for the magnetization curves for
  thicker material and higher frequencies.
- The results obtained with the two '(modified) Epsteinframe' methods and
  the method following the procedure outlined in the standard concerning
  the qualitative comparison of the different cutting techniques are almost
  identical.

[9]The respective temperature of the investigated stators depends on the material itself and on the
　duration of the measurement. Therefore, the stator presented in Fig. 6.13 had only a temperature
　of 50 °C at the end of the measurement whereas stators of material M800-65A may reach about
　100 °C.

# 6.4 Influence of aging

In this section, the effect of aging on the steel sheet material of the stators is investigated. To this end, the stator samples had been stored for almost one year (11 months).

Some literature reported that the specific losses decrease as the material ages: According to [143], the additional losses of electric machines are expected to decrease when they are stored over several months. The effect of aging is said to depend on the material. One possible explanation for this behavior may be burrs at the cut edge [30]: Burrs (may) produce additional short circuits [110, 214] in lamination packages and thus increase the losses. After some time, these burrs may rust and thus the burrs' influence on the losses may decrease. This assumption is investigated in the following.

According to [59], non-contact cutting, and thus laser cutting, avoids burrs at the cut edge in contrast to mechanical cutting. Hence, the loss reduction caused by the aging of mechanically-cut and laser-cut samples had been expected to differ.

Measurement method 'IEC 62044-3' [90] is used for this purpose. With this method, possible differences in measured specific losses caused by the influence of temperature are almost excluded (see Chapter 2.6). The results are compared with the results obtained almost one year ago.

Figs. 6.15 and 6.16 show the magnetization curve for M800-65A at 250 Hz and the specific losses for punched, $CO_2$-laser and FKL-laser cut stators. The characteristics presented have been observed for all materials and frequencies investigated: Both the measured specific losses and the magnetization curves are (almost) identical to those measured several months ago (see Figs. 6.15 and 6.16). (If at all, a difference is observed at high magnetic flux densities $B$. However, these are within the uncertainty of the measurement equipment.)

Thus, in this work no influence of aging on the magnetic properties is found.

---

Conclusions:
- No effect of aging on the specific losses or on the magnetization curve is found. This applies to all investigated stators (materials) and cutting techniques here.

---
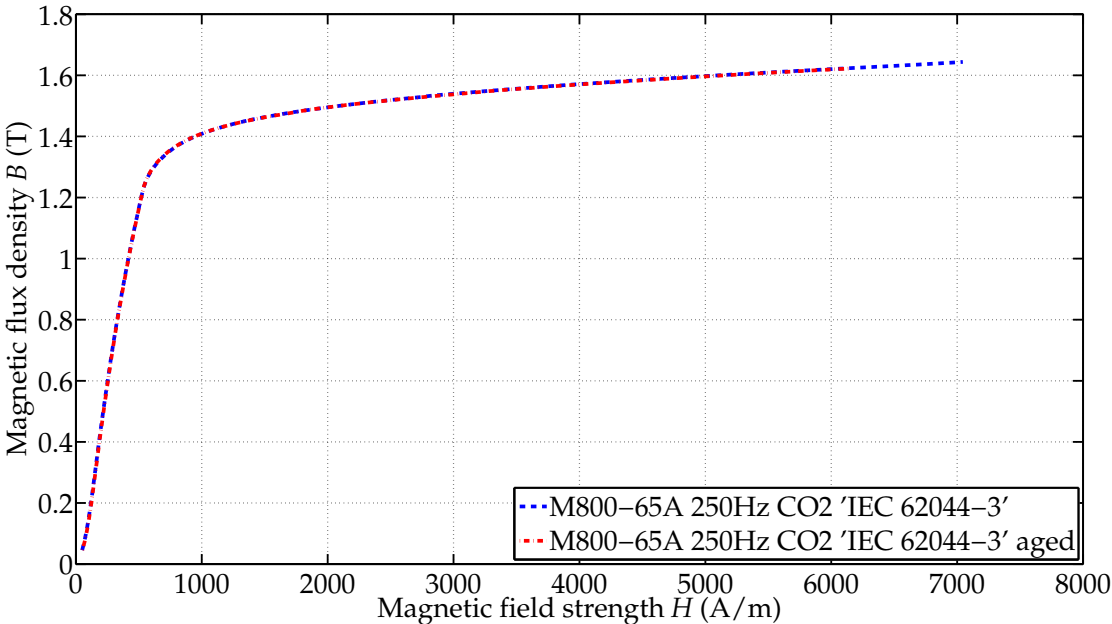
Figure 6.15: Effect of aging on the magnetization curve.
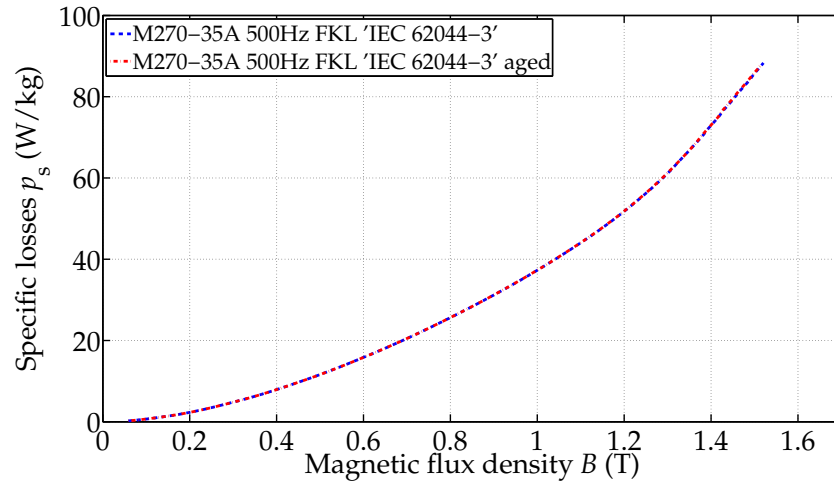
(a) M270-35A-FKL 500 Hz
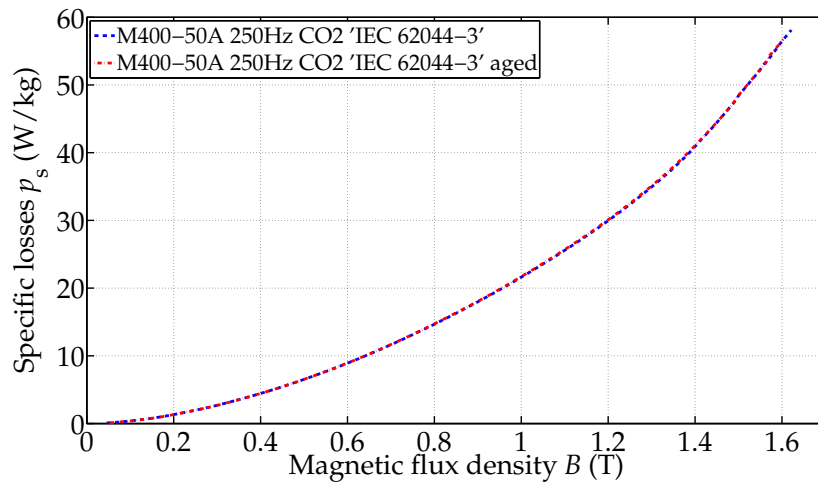


(b) M400-35A-CO$_2$ 250 Hz
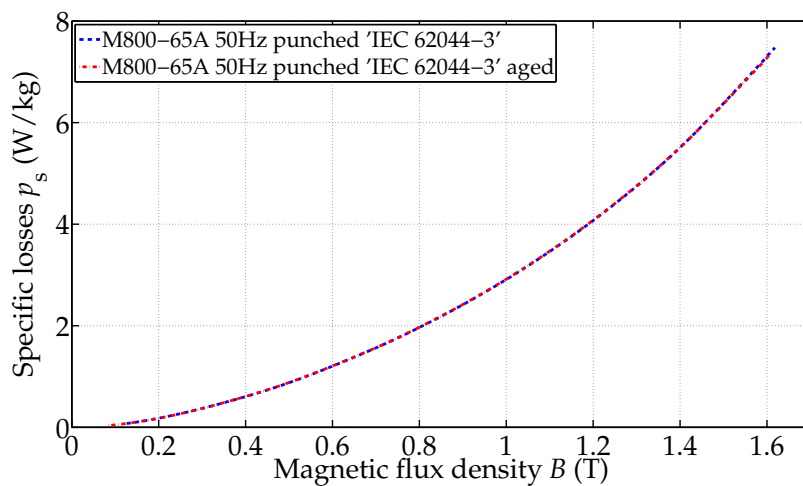


(c) M800-65A-punched 50 Hz

Figure 6.16: Effect of aging on the specific losses.

## 6.5 Discussion

In the following, the findings are further discussed in the context of the literature.

**Specific losses**

The experimental results showed that the shape of specific losses for mechanically-cut samples is more 'quadratic' compared to both laser-cut samples, where, at moderate flux densities, a 'linear' behavior becomes apparent in addition to the quadratic shape. This 'linear' part is reduced with increasing frequency and material thickness[2,p.132]. This behavior has not yet been reported explicitly by other authors concerning laser-cut samples, but only with the investigation of compressive stresses [192]. This 'linear' behavior can be only seen with laser-cut samples, suggesting that laser cutting induces more compressive stresses inside the material than mechanical cutting. This is in accord with Chapters 4 and 5.

Furthermore, the investigated materials demonstrated that at high magnetic flux densities, the specific losses of laser-cut specimens are in the same range as those of the punched samples or smaller. This finding contrasts with [59], where the total losses at 1.5 T for laser cutting are reported to be several times higher than those of punching (frequency is not mentioned), even though the investigated material M330-50A is similar to the material M400-50A investigated here. This is presumedly caused by different laser settings. (Unfortunately, the laser settings are not mentioned in [59].)

The results of the previous chapters again showed that a POI occurs at the specific losses which is shifted to lower magnetic flux densities $B$ with increasing frequency and material thickness[2,p.132]. Additionally, it is found that the POIs of stator samples occur at lower magnetic flux densities $B$ than for Epstein samples. As mentioned in Chapter 5.5, also [5, 162] showed that the losses of laser-cut samples may be smaller than those of guillotine-cut samples at higher magnetic flux densities. This work extends this knowledge by the investigation of several materials with different material thicknesses (here, also different grain sizes) and assembled stator stacks (i.e. non-Epstein samples). Furthermore, the results in this work[21,p.24] suggest that the occurrence of the POI does not depend linearly on the specific cutting length or sample width.

It was also observed that the absolute difference between specific losses in the area above the POI increases with supply frequency.

The specific losses of the stator stacks of both laser cutting techniques, are influenced in the same way. This contrasts with the findings in Chapter 4 and those published in [45], where these two laser cutting techniques are compared with ring specimens and where FKL-laser cutting is reported to produce smaller losses com-

pared to $CO_2$-laser cutting probes and a larger maximum relative permeability (up to 1.3 times larger). This contrasting conclusion of [45] may be explained by the different technical capacities of the laser technology of about 25 years ago and today, and by the respective settings. The missing difference in losses of Chapters 5 and 6, in contrast to the quasi-static hysteresis losses of Chapter 4, has already been discussed in Chapter 5 and is mainly attributed to additional eddy currents.

**Magnetization curves and permeability**

This work showed that the magnetization curves of mechanically-cut and laser-cut stator stacks and Epstein specimens differ. This indicates again the different types of deterioration of the different cutting techniques on the material, i.e. thermal deterioration (laser) against mechanical deterioration (punching) (e.g. [4, 45, 207]). Furthermore, it is observed that the maximum relative permeabilities of mechanically-cut samples are larger than those of the laser-cut specimens, $\mu_{r, max, mechanical} > \mu_{r, max, laser}$. This is in line with the results on the permeability of Chapters 4 and 5 and stated by [45] and [59]: [59] showed that the deterioration, and thus reduction of maximum permeability, is larger for laser-cut samples than for punched samples. The investigation was performed by a single sheet tester. [45] reached his results by means of ring specimens. This work additionally shows that the differences of the maxima decreases with increasing frequency and material thickness[2,p.132].

A POI of the relative permeabilities of mechanically-cut and both laser-cut samples is observed, which is shifted to lower magnetic field strengths $H$ with increasing material thickness[2,p.132]. For $CO_2$-laser and FKL-laser cut samples, this point occurs in the same range of magnetic field strength. The diagram presented in [45] also reveals a POI for the mechanically-cut and FKL-laser cut ring specimens, but not for the $CO_2$-laser cut samples[10]. This may be explained by the less sophisticated $CO_2$-laser technology at that time (late 80's). Furthermore, the diagram of [45] shows that this POI (FKL-laser cut and punched specimens) occurs already in the range of the distinctive maximum: In [45], the laser cutting settings were optimized to reach the maximum permeability with the FKL-laser technology. This demonstrates that the laser settings influence the occurrence of this POI, or, in other words: with increasing optimization of the laser settings (for minimum effect on the permeability), the POI is shifted to lower magnetic field strengths $H$.

In line with [46], no significant difference influenced by different cutting technologies on the permeabilities at (very) high magnetic field strengths is observed.

The investigations presented in [162] also indicate a POI of the relative permeabil-

---

[10]The author of [45] does not explicitly mention the occurrence of this POI in his work, it is merely seen in the diagram.

(a) M270-35A



(b) M800-65A
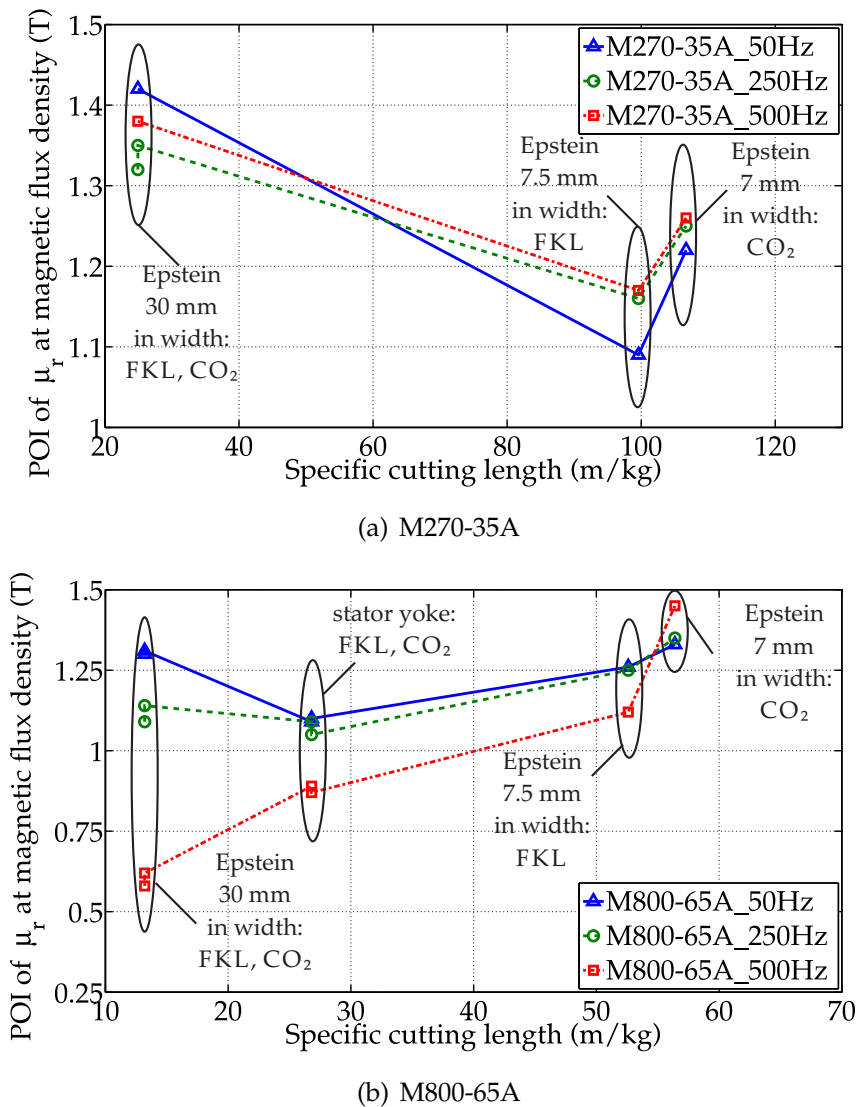
Figure 6.17: POI of permeabilities as a function of specific cutting length.

ities of laser-cut and guillotine-cut steel strips. [162] does not consider the influence of frequency, material thickness or grain size, but only sample width. According to the diagram shown in [162], the POI is shifted to lower magnetic flux densities $B$ with increasing cutting length (only two cutting lengths are investigated). In this work, more sample widths and three different materials were investigated. Considering all POIs of the relative permeabilities (see Fig. 6.17) no well defined influence (decrease/increase) with cutting length is observed.

In contrast to the results of the Epstein frame measurements (see Chapter 5.2) and of [46], the maximum relative permeability of both laser-cut stators investigated in this work are nearly the same (possible explanations have been given in Chapter 6.1).

Finally, a distinct maximum (relative permeability) for both laser-cut stator stacks is observed. This differs to the observations made with the small Epstein samples

(maximum plateau, see Chapter 5.2). This is explained by the rate of compressive stresses inside the material: The larger the ratio $V_{\mathrm{dg}}/(V_{\mathrm{nd}} + V_{\mathrm{dg}})$, the larger the induced compressive stresses. The larger the induced compressive stresses are, the more the distinct extrema disappear (compare with [192]).

**Different measurement methods**

All three methods to determine the magnetic characteristics investigated in this work lead to the same results concerning the differences of the influences of the cutting techniques and the POIs of the specific losses. Differences were observed at higher magnetic flux densities in the case of the 'Epsteinframe' method and the 'modified Epsteinframe' method. By comparing method 'IEC 62044-3' with the '(modified) Epsteinframe' methods, the differences also occur at higher magnetic flux densities and frequency. This is attributed to the difference in temperature and measurement setup (voltage supply and control).

The authors of [44] also used two different measurement methods for the investigation of E-cores. Their measurement setups are comparable with the 'Epsteinframe' and the 'modified Epsteinframe' method concerning the voltage supply and control of the primary and secondary coil. They also concluded that both measurement setups generate the same results concerning the comparison of different influences (in their case, different production steps). They additionally mention that these differences are better pronounced for the non-regulated setup (in our case, the 'modified Epsteinframe' method); a statement which was not confirmed by our work.

**Influence of aging**

Reports of literature concerning the effect of aging on electrical steel sheets differ. In this work, no influence of material aging on the specific losses and the magnetization curves is observed for all investigated stators.

According to [27], to avoid the effect of aging on the magnetic properties, the content of carbon in electrical steel sheets must be kept low [27], as carbon causes the aging process [26]. Furthermore, the authors of [42] performed an accelerated aging experiment on electrical steel sheets. That means that the aging effect is replaced by a heat treatment for several hours, in this case 24 h at 225 °C [42] (The standard aging test is composed of 100 °C and 600 h [26].); such a process "speed[s] up the natural aging process" [152]. The authors of [42] found that aging has no influence on the magnetic properties of electrical steel sheets with a carbon content of less than 0.0025 % [42]. They state an effect of aging by increased total losses, in particular hysteresis losses (see also [112]) with higher carbon content. This contrasts with our observation with material M270-35A (carbon content: 0.006 % - 0.01 %, see

Chapter 3) with no change of properties. Possibly, this accelerated aging affects the losses differently than the natural aging process.

According to [143], the specific losses decrease with the effect of aging. Possible explanations for these different results may be the following: The author of [143] performed experiments on a completed motor, not only on stator packages. Thus, also other influences may impact the aging process and subsequently the losses, as for example, the bearing, quality of grease and/or changes in air pressure and temperature, so that the ventilator may run easier [30]. Subsequently, the material of the investigated motors in [143] may contain a higher carbon content than the stator samples investigated in this work, wherefore the aging affects the losses. Unfortunately, [143] does not state the electrical steel sheet material used. Also the results of [42] (see above) are in contrast to the results of [143].

Bozorth [26] states that aging influences the core losses and that this change is "almost invariably" a change of deterioration [26] thus, this agrees more with the results of [42]. Bozorth points out that the losses of hot-rolled steels with $0.5 - 1.0\,\%$ silicon may increase about $50\,\%$ [26] with time and even so-called non-aging steel sheets with $1.5\,\%$ silicon, low carbon content and which are slowly cooled, are stated to show commonly an increase in losses of $5 - 10\,\%$ after aging[11] [26]. Thus, according to [26], the contents and impurities (e.g. silicon, carbon) of the material determine to which extent the aging effect is obvious.

However, the results of this work confirm neither the results of [26, 42] nor [143], even though the carbon content of the investigated steels should lead to a change in losses.

---

Conclusions:
- The shape of specific losses of mechanically-cut stacks is more 'quadratic' compared to both laser-cut samples, where, at moderate flux densities, an additional 'linear' behavior becomes apparent. This 'linear' part is reduced with increasing frequency and material thickness[2,p.132].
- A POI occurs both for the specific losses and the relative permeability. In the case of specific losses, this point is shifted to lower magnetic flux densities $B$ with increasing frequency and material thickness[2,p.132]. In the case of the relative permeability, it is shifted to lower magnetic field strengths $H$ with increasing material thickness[2,p.132].
- The POIs of the investigated stator stacks occur at lower magnetic flux densities $B$ than those of the Epstein samples.

---

[11]Note, the results mentioned from [26] originate from the standard test of aging ($100\,°C$ for $600$ hours).

- The difference between the specific losses of laser-cut and mechanically-cut samples above the POI increases with supply frequency.
- No linear relationship between the POI of losses and the specific cutting length was identified.
- Both laser-cut samples show the same deteriorating effect on specific losses as well as on relative permeabilities. In contrast to findings reported by other authors and the results of the Epstein samples in Chapter 5, it applies: $\mu_{\mathrm{r,max,CO_2}} \cong \mu_{\mathrm{r,max,FKL}}$.
- The results obtained with the two '(modified) Epsteinframe' methods and the 'IEC 62044-3' method concerning the qualitative comparison of the different cutting techniques are almost identical.
- In contrast to some reports in the literature, no influence of aging on the specific losses and on the magnetization curve was found for all differently cut stators and all materials investigated in this work.

# Chapter 7

# State of the art: modeling the degradation effect by cutting

## 7.1 Modeling approaches

For an overview of existing general iron loss calculation models, reference is made to the summary presented in [105]. This work focuses on iron loss modeling approaches that contain the degradation effect induced by cutting. The first section addresses previous experimental evaluations of magnetic flux density distributions caused by cutting, since these are frequently used as a starting point of the modeling of this distribution. The following sections present existing analytic and numerical approaches to compute the magnetic flux density distribution within the samples considering the degradation effect.

### 7.1.1 Distribution of magnetic flux density within cut samples

The change of the magnetic properties of a given sample due to the cutting process translates into a change of the distribution of the magnetic flux density. Understanding this distribution, i.e. the magnetization curves of the different areas of the material, is considered important for the development of a model to describe the cutting effect. Thus, this section reviews (previously) *experimentally* investigated distributions of (characteristics related to) the magnetic flux density $B$ within samples of cut electrical steel sheets.

In this work[21,p.24], direct and indirect measurements are distinguished from one another. "Indirect methods" determine parameters from which conclusions or assumptions on the distribution of the magnetic flux density can be drawn. These are, for example, the measurement of microhardness [4,12,153,154] and the method of dark field intensity [183,184]. "Direct methods" measure, as the name implies, the magnetic flux density $B$ directly, for example, by the needle probe method [153] or

by multiple search coils in the sample (method described in [138], extended in [134], used also in [119, 148, 170]).

*Microhardness measurements*

As already mentioned in Chapter 1, mechanical cutting deteriorates, in addition to the magnetic properties, also the mechanical properties of electrical steel sheets. In fact, the magnetic deterioration is a consequence of the mechanical deformation. According to [146], the microhardnesses of cut samples and the degradation of their magnetization curves are related. However, this correlation is nonlinear (see Eq. (7.10) of [146]). Furthermore, in addition to other authors, [170][1] mentions that the true zone with magnetically degraded properties, due to the mechanical cutting, is larger than the zone of deformation identified by optical microscope (the larger the deformation, the larger the microhardness). Thus, the microhardness measurements are not a quantitative, but a qualitative indication for the deterioration of the magnetic properties.

Fig. 7.1 shows different microhardness measurements as they have been presented by various authors.[2] According to these measurements, an exponential microhardness distribution for the mechanically-cut samples can be assumed. The laser-cut samples show a more evenly distributed change of the microhardness at the cut edges. This is explained by the laser cutting method itself, as predominantly thermal stresses are induced (see Chapter 1.3.4). Thus, laser cutting influences the microhardness marginally in contrast to mechanical cutting.

Assuming the magnetic flux density $B$ is related to the microhardness, it has an exponential distribution at the cut edge of mechanically-cut samples and over a sample's width decreasing characteristic for laser-cut samples.

*Neutron grating interferometer combined with dark field image technique*

The neutron grating interferometer (nGI) and the dark field image (DFI) technique are used in [183, 184] for analyzing the magnetic flux density distribution of several steel sheets. With this method, neutrons are scattered at magnetic domain walls [67] and thus "local information on the bulk domain wall density at different applied external magnetic fields is obtained" [183]. "The intensity of the dark-field signal is an inverse measure of the domain wall density distribution" [184]. "The lower the domain wall density is, the larger the average domain site will be and consequently the macroscopic magnetic flux density. The local DFI distribution represents the macroscopic flux density, the integral of the profile correlates with the magnetic

---

[1]p. 50.

[2]For completeness: Another study showing such microhardness distributions is presented in [12]. These results are in line with those presented in Fig. 7.1.
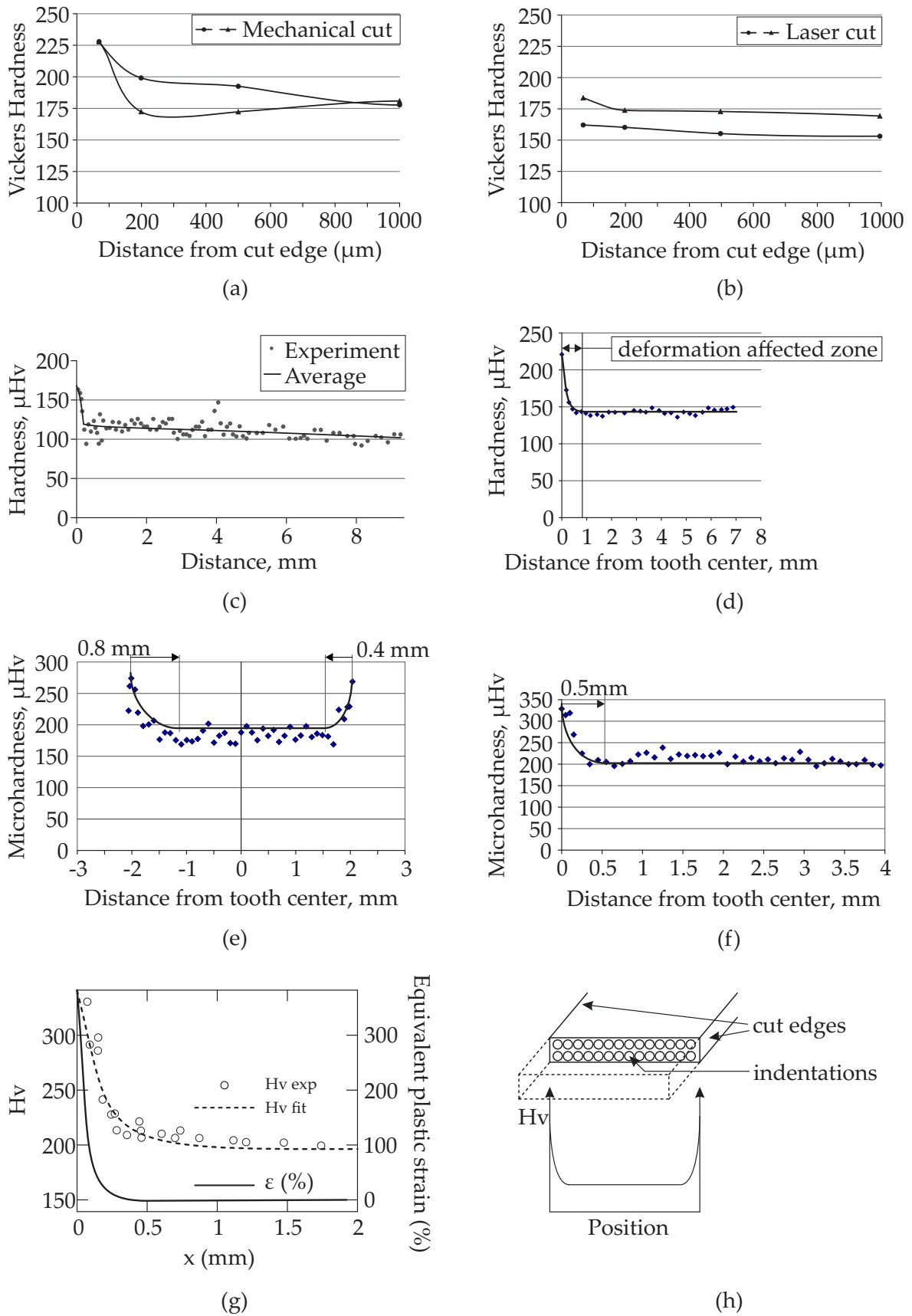
Figure 7.1: Review of microhardness measurements of the degradation effect of cutting of different authors, [4]: (a,b), [154]: (c), [153]: (d-f), [146]: (g,h).

flux density in the whole sample." [183]. The magnetic flux density distributions concluded by the authors of [183] and [184] for both mechanically-cut (guillotine and punching) and laser-cut (FKL and $CO_2$) specimens are reviewed in Fig. 7.2.

The magnetic flux density distribution for punched and guillotine-cut samples shows parabolic behavior, with its opening becoming wider with increasing sample width (see Fig. 7.2 a,d))[3]. This differs from the findings obtained from the micro-hardness measurements. But similar conclusions on the field distribution within laser-cut samples are obtained at high magnetic field strengths, characterized by a more gradual reduction ("a more linear behavior" [184]) over the whole sample and no significant extrema in the middle of the specimen (compare Figs. 7.1 and 7.2). The difference of the magnetic flux density $B$ of the two laser-cut edges (see Fig. 7.2) is explained by the fact that the edges were not cut simultaneously: At the first cut edge, higher magnetic flux densities $B$ are observed than at the second [183].

*Local magnetic measurements*

The measurement results presented in Fig. 7.3 are mostly obtained by the method presented in [138] or by modified versions of this measurement technique. This method is characterized by holes drilled through the lamination at different distances to the cut edge, in which measurement coils are placed. This (modified) method is used by [119, 138, 148, 170]. In contrast, [153] uses a non-destructive method, the so-called needle probe method.

According to these measurements, the flux density $B$ for mechanically-cut samples exponentially decreases towards the cut edge. The gradient of the curve at the cut edge decreases with increasing frequency (see Fig. 7.3 f)) and, according to [138], with increasing magnetic flux density $B$ (see Fig. 7.3 b)). This is in contrast to the measurement results of [153] and [170] (see Fig. 7.3 a,e)), in which the gradient becomes larger and steeper with increasing magnetic flux densities. This may be explained by the absolute value of the magnetic flux at the cut edge which possibly depends on the investigated material itself (see Fig. 7.3 c)), such as the silicon content (see Fig. 7.3 a)) and the grain size [170]. Results of laser-cut samples (a rather uniform distribution over the whole sample size, see Fig. 7.3 c)) confirm the results by the indirect measurements (Figs. 7.1 b) and 7.2, right).

**Conclusion of previously published experimental results**

Concerning the results of the distribution of the magnetic flux reported on in the literature, the following summary applies to the majority of curves discussed and

---

[3]The shifting to the left cut edge with increasing magnetic field strength in the case of guillotine-cut samples is attributed to the fact that "the right edge was cut without blank holder" [184].
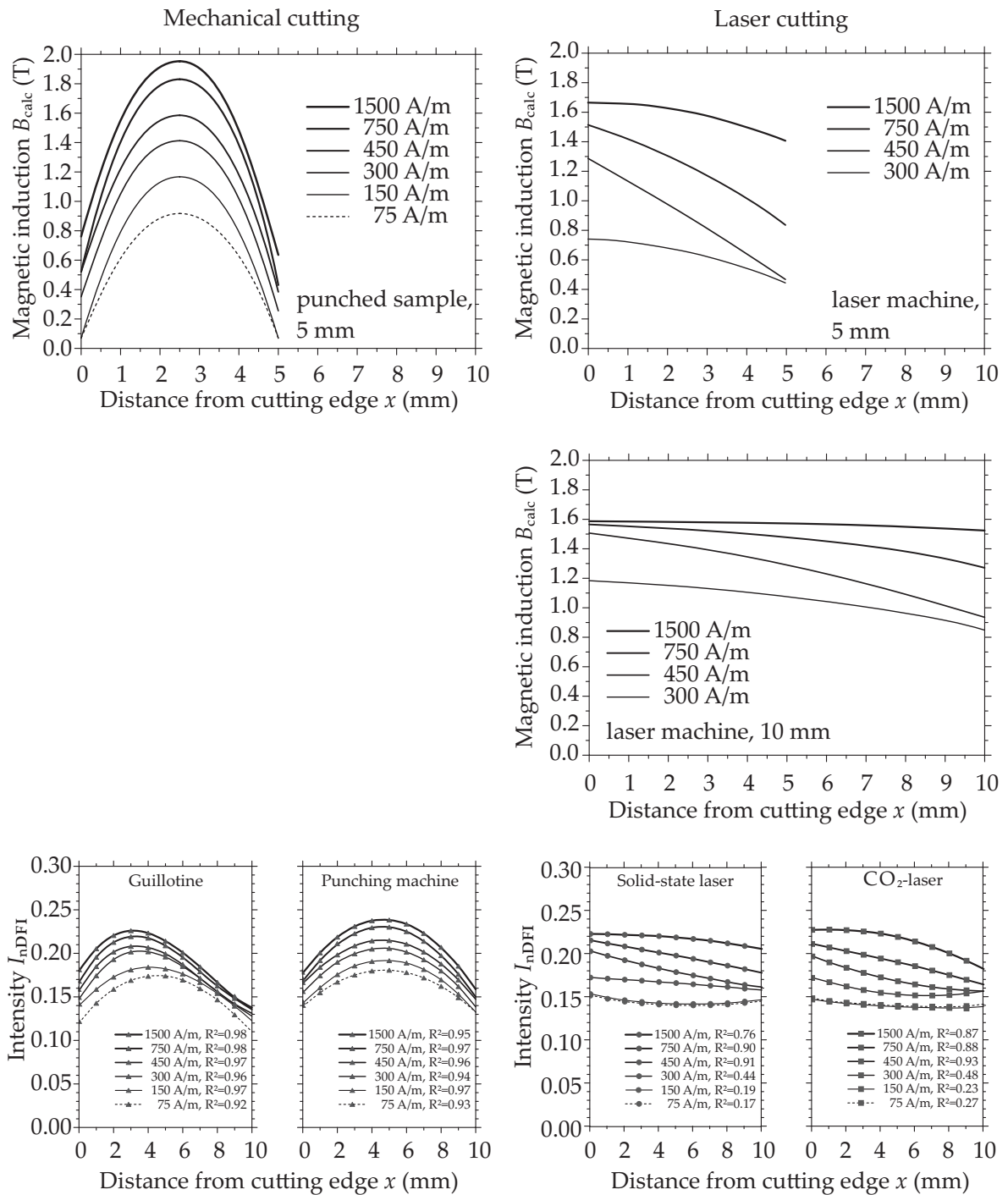
Figure 7.2: Review of dark field intensity profiles presented in [183, 184] of mechanically-cut and laser-cut specimens with different sample widths.

(a)

(b)

(c)

(d)

(e)

(f)
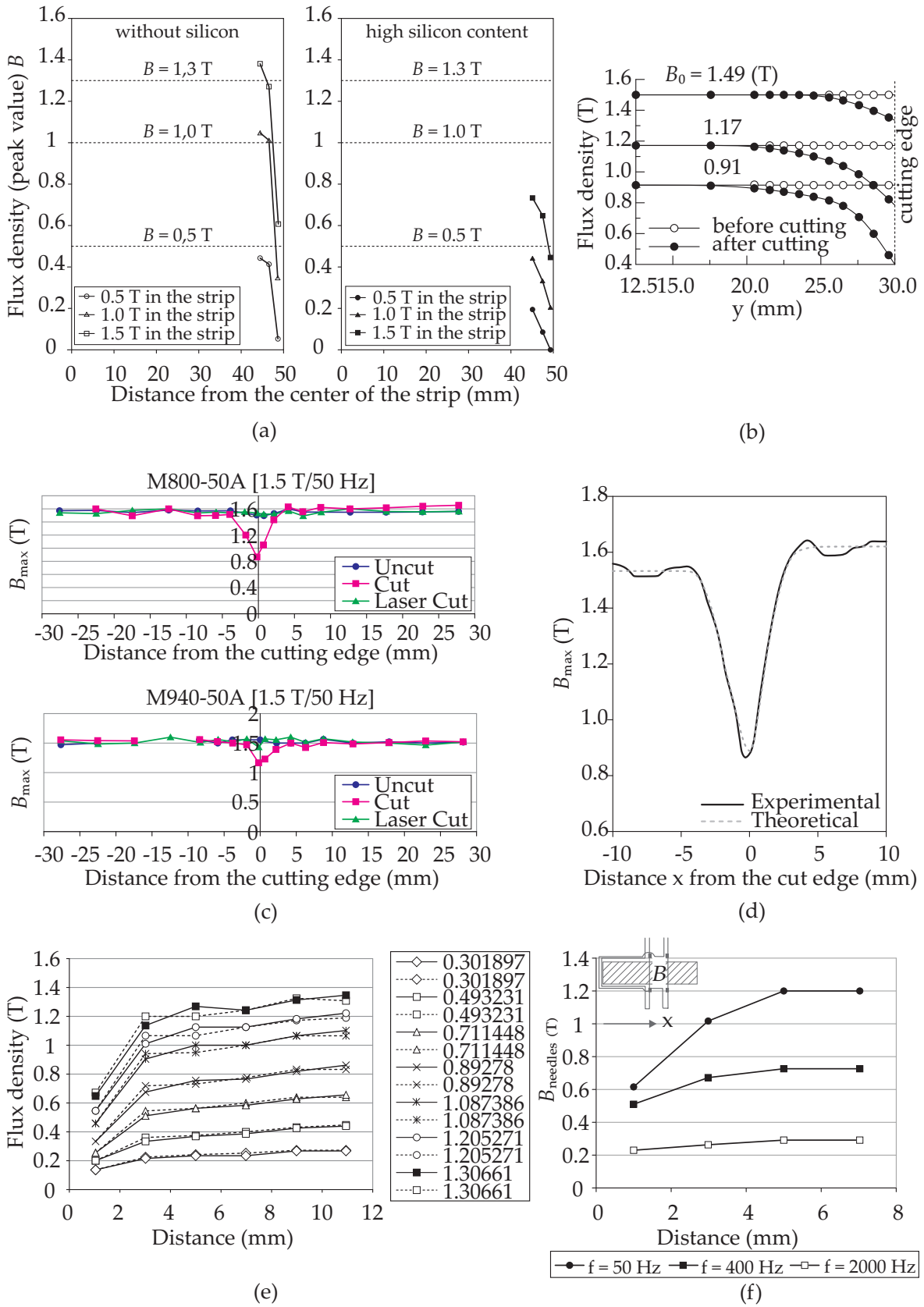
Figure 7.3: Local magnetic measurements of [170]: (a), [138]: (b), [119]: (c), [148]: (d), [153]: (e, f) for mechanically-cut and laser-cut specimens.

can be used as a starting point for mathematical modeling and simulation of the degradation effect.

Characteristics of the *magnetic flux distribution for mechanically-cut samples*:

- The magnetic flux is pushed to the sample's center because of material deterioration at the cut edge [138, 153].
- The relative width of the middle part with almost constant magnetic flux density decreases with decreasing sample width.
- With increasing saturation, the effect of flux migrating to the middle of the sample is reduced (Fig. 7.3 b)). A more uniform distribution occurs, i.e., rather a sort of area with constant flux density of increasing widths in the middle, and areas of reduced widths at the cut edges over which the flux density strongly decreases (see Fig. 7.3 a)) or only slightly reduces (see Fig. 7.3 b)), depending on the magnetic flux density at the cut edge.
- The magnetic flux density at the cut edge increases with increasing average magnetic flux density [138, 153].
- With increasing frequency, the influence of magnetic deterioration by cutting is reduced (see Fig. 7.3 f)). [153] explains this by the increasing eddy currents which "lead to skin effects, pushing the magnetic flux back to the cut edge."[4]

Thus, with increasing magnetic flux density *B* and frequency, the degrading effect by mechanical cutting loses influence.

The effect of laser cutting on the distribution of the magnetic flux within a cut sample has been much less investigated so far than mechanical cutting. The results available suggest a different distribution than in the case of mechanical cutting that can be described as follows:

Characteristics of the *magnetic flux distribution for laser-cut samples*:

- The magnetic flux is not forced to the center part, as in the case of mechanically-cut samples.
- In contrast, a steadily decreasing (see Figs. 7.1 and 7.2) distribution is observed, with a lower magnetic flux density at the second cut edge.
- With decreasing sample width, the gradient increases.
- The decrease of the magnetic flux densities from the first to the second cut edge decreases with increasing saturation.

Nevertheless, the summarized results for the magnetic flux density distribution in laser-cut samples must be used with caution, as laser cutting induces thermal stresses. Thus, the changed stress state inside the material might not be reflected by

---

[4]See also the simulated magnetic flux distribution of [37] which is influenced by high frequencies, but without considering material degradation by cutting.

the currently used indirect measurements.

Furthermore, remember the respective degradation depth $\delta$ also depends on the material properties and the settings of the cutting tool and is often a matter of definition (see Chapter 1).

## 7.1.2 Analytic and numerical approaches

*Distribution formulas*

The author of [170] proposes a "cut edge formula" (Eq. (7.1)) to model the distribution of magnetic polarization over the strip width. The distribution of the magnetic polarization provides an indication of the magnetic flux density distribution, as $B = \mu_0 H + J$. The proposed formula is based on a hyperbola function and is said to fulfill the following conditions and assumptions: same average as the measured polarization, the function is differentiable at each point, the material-dependent character is considered by parameters, the polarization $J$ at the cut edge is zero, and the degradation depth is constant along the cut edge.

$$\hat{J}_1(x) = \hat{J}_0 - \hat{J}_1 \cosh\left(A\frac{x}{x_0}\right) \tag{7.1}$$

The parameters $J_0$, $J_1$ and $A$ describe the influence of the magnetic field strength, chemical composition, and grain size and $x_0$ is half the sample width [170]. The computed distributions are shown in Fig. 7.4.

In [199], an analytic description of the magnetic polarization distribution $J(H, x)$ (Eq. (7.2)) is presented which includes the degradation effect of the magnetic properties at the cut edge. The magnetic field strength $H$ is assumed "to be uniform over the sample" [199]. $\mu_r(H, N = 0)$ is the relative permeability of a steel sheet sample without the influence of cut edges, $\Delta \mu_{cut}(H)$ is the maximal difference of the relative permeabilities of the sample (middle of the sheet vs. cut edge) and $\eta(x)$ is a distribution function according to Eq. (7.3) which includes the degradation depth $\delta$ induced by cutting, and which depends on the distance from the cut edge $x$ [199]. Both $\Delta \mu_{cut}$ and $\eta(x)$ are determined with the help of experimental data.

$$J(H, x) = \mu_0(\mu_r(H, N = 0) - \Delta\mu_{cut}(H)\eta(x))H \tag{7.2}$$

$$\eta(x) = 1 - \frac{x}{\delta} - a\frac{x}{\delta}\left(1 - \frac{x}{\delta}\right) \tag{7.3}$$

Both of these measurement-based approaches follow the distribution of the magnetic flux after mechanical cutting. No specific statements on the influence of frequency are made.

The authors of [199] further differentiate between the case in which the degradation depths $\delta$ of both cut sides do and do not overlap. In Fig. 7.5 results of computed
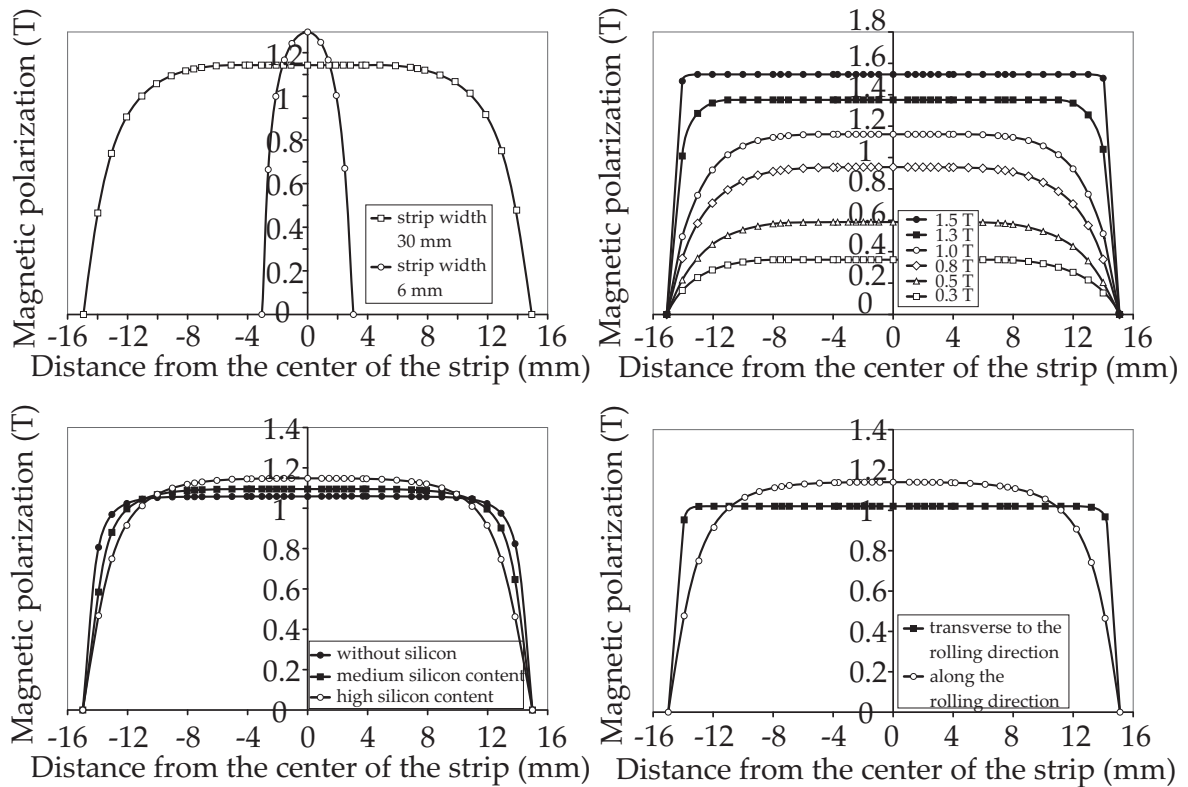
Figure 7.4: Modeled distribution of magnetic polarization over the strip width by [170].

polarization distributions of [199] are presented. For consideration of this polarization distribution, also in the iron loss calculation, a former expanded Bertotti iron loss model [94] (later also referred to as 'IEM-formula'[12, p. 228]) is further extended with the new distribution formula $J(H, x)$, and with the hysteresis loss coefficient depending on $x$.

The authors of [148] first experimentally examined the magnetic flux distribution of mechanically-cut samples using the method of drilled holes[5] on non-oriented steel samples. They then determined the function best fitting the measurement results using Matlab. This function (see Eq. (7.4)) also includes, in addition to the distance $x$ from the cut edge and the maximal magnetic flux density $B_{\max}$, material parameters *a-d* which depend on the silicon content, grain size, magnetic flux density $B$ and frequency. The material parameters *a-d* were determined for four different materials, and for two flux densities $B$, both at the frequency of 50 Hz.

$$B_{\max}(T) = \frac{a}{(1 + e^{b-cx})^{\frac{1}{d}}} \qquad (7.4)$$

Wilczynski *et al.* [207] investigated annealed and 'half-annealed' steel strips, in which the latter have one cut edge, obtained by cutting a "wide annealed strip in

---

[5]See Chapter 7.1, Local magnetic measurements.
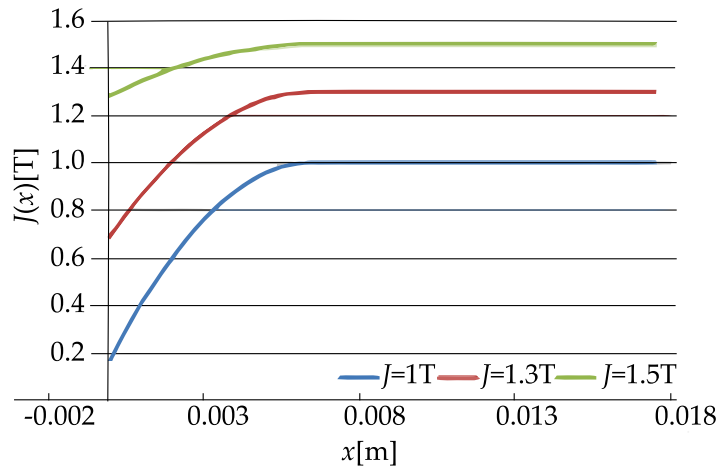
Figure 7.5: Distribution of magnetic polarization over the strip width as modeled by [199].

half" [207], so that strips with one annealed and one non-annealed cut edge are obtained [207]. The authors proposed to describe the magnetic flux density distribution for the 'half-annealed' sample by (see Eq. (7.5) and Fig. 7.6, 'half-annealed' sample),

$$B = B_a - B_\Delta e^{\frac{-(x-x_0)}{\lambda}} \tag{7.5}$$

$$x_0 < x < x_0 + a \tag{7.6}$$

$$B_a = \frac{\phi_a}{ab} \tag{7.7}$$

$$B_\Delta = \frac{\phi_\Delta}{b\lambda(1 - e^{\frac{-a}{\lambda}})} \tag{7.8}$$

with $a$ as sample width, $b$ as sample thickness, $x_0$ as starting point of the left cut edge, $\lambda$ as width of "weak magnetization zone" and thus the deteriorated zone by cutting [207]. The index $a$ indicates the annealed sample, and $\Delta$ the difference between the annealed and 'half-annealed' sample (see also Fig. 7.6) [207]. The magnetic fluxes of the annealed and 'half-annealed' samples are determined by SST[6] measurements [207]. The aim of this approach is to determine the deteriorated zone $\lambda$ of cut electrical steel sheets. The author assumes the same flux distribution, and applies his method to both punched samples as well as $CO_2$-laser cut samples. The proposed distribution (Eq. (7.5)) may be a possible model approach for the degraded zone of mechanically-cut electrical steel sheets (compare with Figs. 7.1 and 7.3). However, the authors of [207] use this equation (Eq. (7.5)) to describe the flux distribution of the whole sample, not only for the degraded zone ($\lambda < a$; in this case $a > 30\,\text{mm}$). This contrasts with the measurement results of Figs. 7.1 and 7.3, in which the flux

---

[6]Single Sheet Tester.
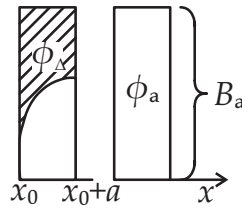
Figure 7.6: Assumed flux distribution for a 'half-annealed' sample, left, and homo-
geneous flux distribution in an annealed ("non-deteriorated") sample,
right, as presented in [207].

density in the non-degraded zone is rather constant. Even though the assumed flux
distribution after laser cutting is not in line with the one identified in Chapter 7.1.1,
the simplified modeling approach provides satisfactory results. Any influence of
frequency is not considered in this model.

*Area based models*

The author of [153] proposed a tooth model including the punching effect. Thereby,
the tooth of an induction machine is divided into a parallel and a perpendicularly
affected zone (see Fig. 7.7). In the figure, regions 1 - 3 are assumed to be parallel
to the flux; the flux is hence split "into parts favouring the regions with higher
permeability" [153]. Regions 4 - 6 represent the tooth tip. Here, the flux has to
cross all three regions. Thus, these parts are considered in series and each of such
region has a constant magnetic flux density. The zones deteriorated by punching are
selected in a way so as to prevent overlapping. The tooth is described by a lumped
parameter reluctance model: For each zone, the reluctance is derived and equalized
with the reluctance of equivalent layers obtained by local magnetic measurements.
The choice of permeabilities with different strains for the various zones of the tooth
model is arbitrary. Subsequently, a correction factor is introduced to match the
computed reluctance with measurement data. With this correction factor and the
measurement data, the permeabilities of the different zones are derived.

This, as well as the following methods, assume a symmetrical distribution of the
magnetic properties over the samples' widths.

Gmyrek *et al.* [64] measured magnetic properties on an annealed toroidal sample
(defined as "undamaged" material) and of a toroidal sample, with previously an-
nealed material, cut into five rings (providing "partially damaged" material). At
first, with simplified assumptions and measurement results, the minimum and max-
imum widths of the degraded zone are estimated. Then, in a subsequent step, the
deterioration depth is more precisely estimated based on a material strip model[7],

---

[7]The partially damaged material is modeled as material comprising two areas, both with homoge-
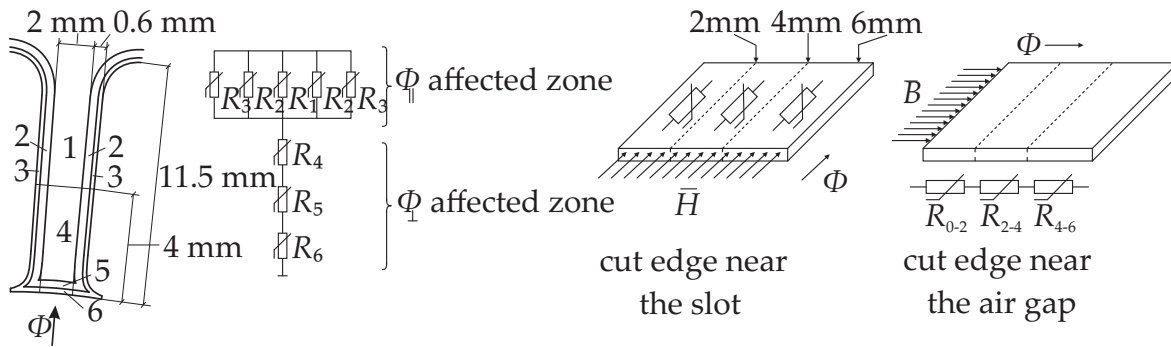
Figure 7.7: Tooth model of [153] considering the cutting effect.
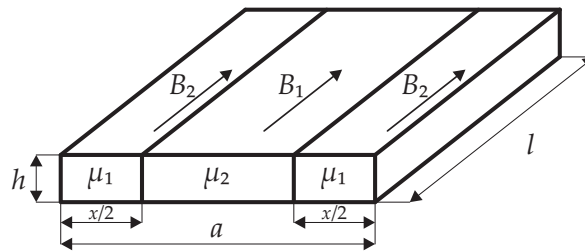


Figure 7.8: Cut steel sheet modeled as material comprising two areas with homogeneous properties, as proposed by [62].

which derives from [62] (Fig. 7.8), measurement data and further assumptions, for example, that the permeability of the deteriorated area only depends on the magnetic field strength $H$ and that the deteriorated zones have constant widths. Subsequently, with the already determined degraded width $x$, the permeability of the degraded zone is calculated (see Fig.7.9 a)). Thereafter, the specific losses of the deteriorated zone (see Fig.7.9 b)) and the magnetic flux distribution of the whole cut samples are determined (see Fig. 7.10 b)). As the magnetic field strength is assumed to be proportional to the inverse of the radius, the magnetic flux density decreases with increasing radius, see both Figs. 7.10 a) and b). This approach is illustrated for the case of 50 Hz.

The authors of [20] consider the cutting effect on the saliency ratio of a PMSM machine in FEM simulations by inserting a zone along the cut edge with width $h$, which has a different *B-H* curve assigned to it (see Fig. 7.11). In contrast to the cases of the previous works, here, the deteriorated *B-H* curve is assumed and does not result from measurements, since the authors' aim is a worst-case scenario. The influence of the cutting effect is computed for the magnetic anisotropy of the tooth tip.

---

neous properties: one with undamaged material, in the middle of the sample, with permeability $\mu_2$, and two areas of damaged material of equal width and material properties, along the cut edges, with permeability $\mu_1$ (Fig. 7.8).
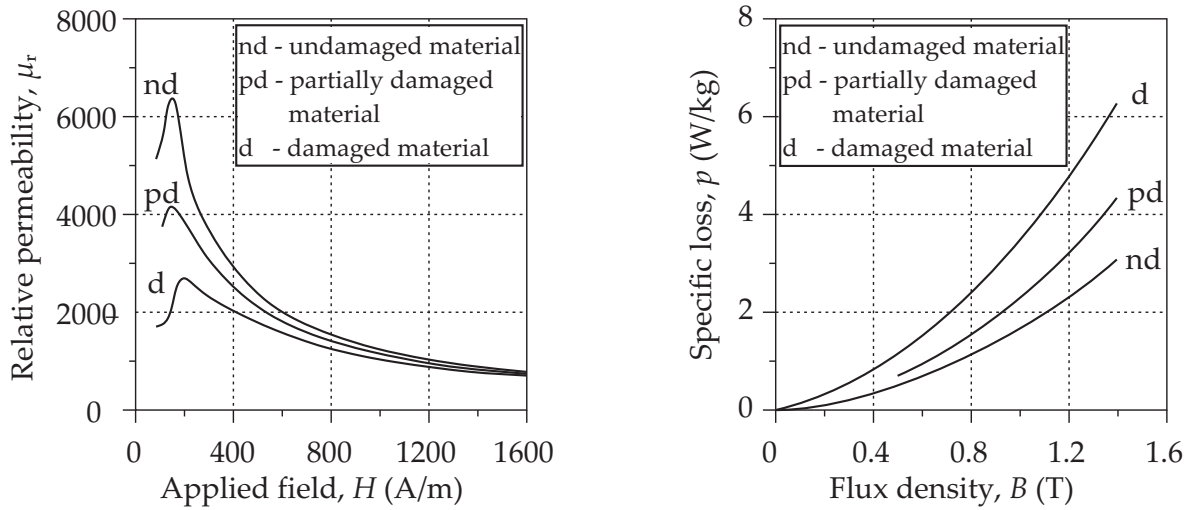
Figure 7.9: Calculated permeabilities and specific losses for the damaged, undamaged, and partially damaged material, as presented in [64].
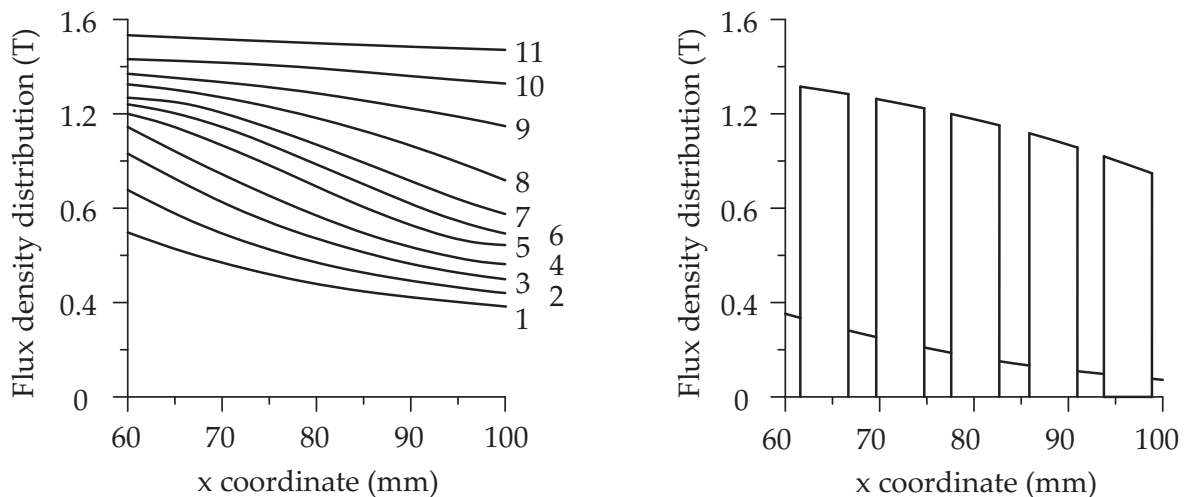


Figure 7.10: Modeled distribution of magnetic flux density $B$ of a toroidal sample "undamaged" (annealed), left, and partially damaged (sample consists of five cut rings) material, right [62, 64].
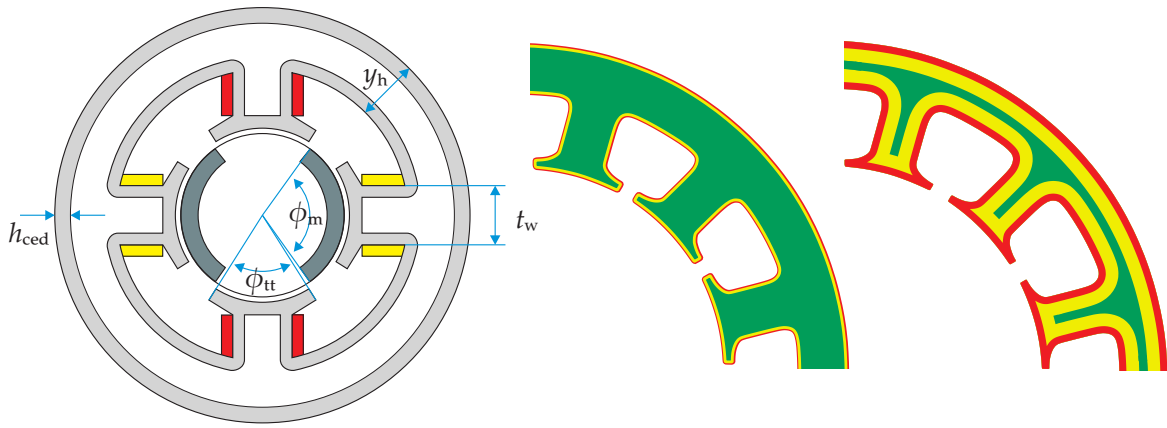
Figure 7.11: Considering the cutting effect in a FEM simulation by an additional zone with a different magnetization curve [20].

A more elaborate model, not requiring any measurements either, that considers the steel degradation due to punching by additional zones along the cut edges is presented in [6]. This method uses an exponential degradation profile (see Eq. (7.9) and Fig. 7.12 a)) derived from degradation profiles presented in the literature [82, 138, 146],

$$\gamma(s) = 1 - (1 - \hat{\gamma})e^{-s/\delta_s}. \tag{7.9}$$

At this, $\hat{\gamma}$ is the degradation factor at the cut edge, $s$ is the distance from the cut edge and $\delta_s$ is "the depth where the effect of degradation has been reduced to one third" [6]. Subsequently, the magnetization curve of non-deteriorated material $(B_i, H_i)$ is scaled to $(B_i, H_i/\gamma(s))$ (Fig. 7.12 b)) and the hysteresis loss density changes to $\sigma_{hyst}^* = \sigma_{hyst}/\gamma(s)$ for the respective distance from the cut edge. In the FE modeling, several boundary layers are set along the cut edges (Fig. 7.12 c)) and the "degradation profile is discretized by piecewise constants at a number of boundary layers" [6]. Thus, the relative permeability decreases towards the cut edges. The flux distribution in Fig. 7.12 d) illustrates how the flux is forced to flow through the middle of the teeth due to the material degradation at the cut edge [6]. This is in line with the measurement results presented for example in [138, 153].

*Extended airgaps*

If the magnetic flux flows perpendicular to the cut edge (e.g. airgap in an electric machine), the author of [170] proposes the use of an increased airgap for considering the induced deterioration. This assumption is also in line with the experimental results of Chapter 4, as with increasing ratio $V_{dg}/(V_{nd} + V_{dg})$ and thus larger relative influence of deterioration introduced by cutting, the hysteresis curve is increasingly sheared. Note that the flux enters parallel to the cut edge in the investigated samples

(a) Degradation profile at the cut edges

(b) Magnetization curves adapted



(c) Boundary layers along cut edges

(d) Machine affected by punching
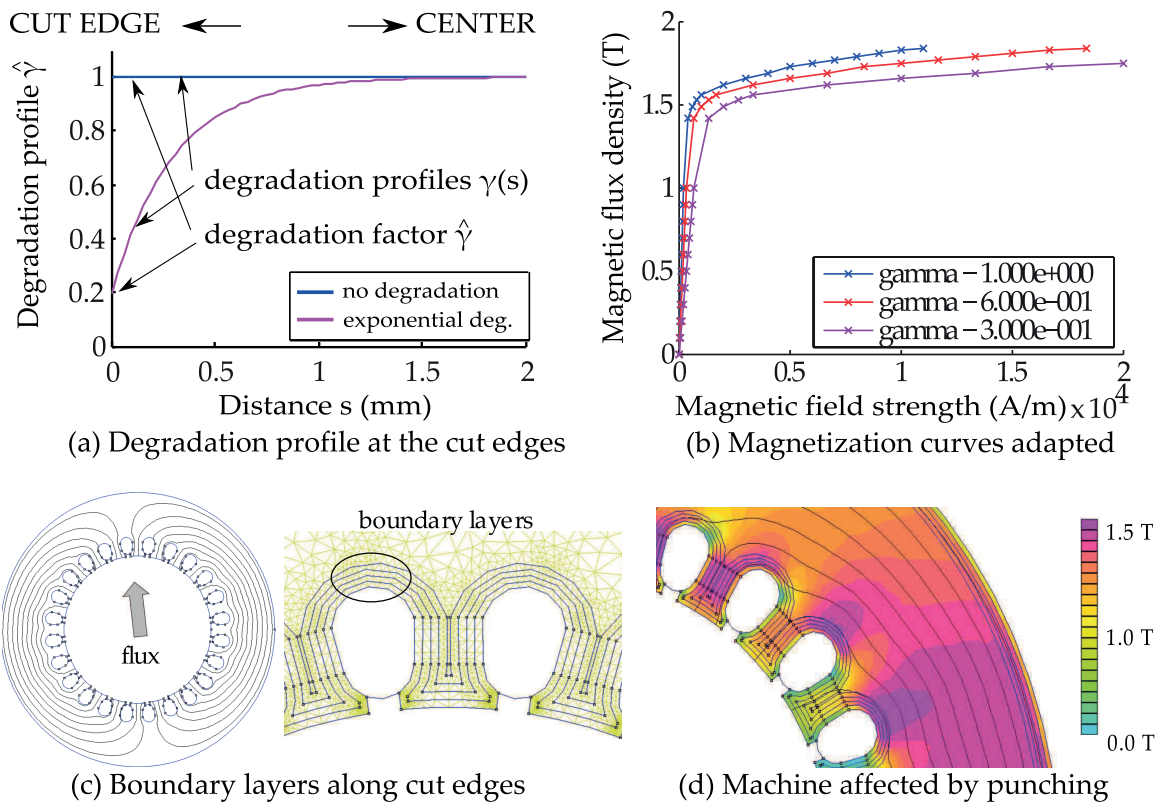
Figure 7.12: Consideration of material degradation due to punching according to [6].

in Chapter 4, in contrast to the considered case in [170]. Considering [23],[8] an increased airgap has a shearing influence on the hysteresis curve and thus a degrading influence on the relative permeability. Subsequently, the author of [170] performed some experiments in a modified, non-standardized SST with single sheets without and including an airgap. The latter was produced by cutting the single sheet transversely in the middle [170]. Of course, the larger the real airgap, the more the influence of an additional airgap caused by cutting decreases [170].

According to [154], cutting, in particular the cut edge with deteriorated magnetic properties, "leads to a virtual decrease of the cross-section of the core and [to] an increase of the air gap of rotating electrical machines." Thus, the same author proposes in [153] to consider the degradation by an "equivalent airgap" (larger than the physical airgap) which takes into account the influence of different manufacturing processes as mechanical cutting and compression. This equivalent airgap can be used in numerical simulations, "using the unaffected material properties via an appropriate modification of the airgap" [153]. This equivalent airgap is determined for a given induction machine.

This rather lumped approach requires adjustment of the equivalent permeability

---

[8]p. 50.

or airgap per material and operating point but is independent of the exact distribution of the flux within the sample.

*Stress/strain dependent parameters*

Ossart *et al.* [146] simulated (FE analysis) the magnetic flux density distribution of punched steel samples by a combination of a mechanical and a magnetic model. First, the distribution of the hardness within the sample is measured and converted into plastic strain, with a mechanical model presented in [146] (originally from [82]) for different distances from the cut edge. Then, the flux density distribution and magnetic field are simulated by using the nonlinear magnetic model,

$$B(H, \varepsilon_p) = \frac{H}{v_0(\varepsilon_p) + v_1(\varepsilon_p)H + v_2(\varepsilon_p)H^2}, \tag{7.10}$$

and a previously established strain map obtained at $0.5\,\text{Hz}$ [146]. Here, $\varepsilon_p$ represents the plastic strain, and the functions $v_i$ are given by analytic functions [146]. The mechanical model comprises material dependent parameters, thus, requiring microhardness measurements and the determination of strain maps for each new material.

Another model based on stresses and strains is presented in [128]. First, the residual stresses in punched electrical steels are analyzed [128]. Both, long-range residual stresses (i.e., stresses beyond the area of plasticity) and plasticity along the cut edge are investigated (see Fig. 7.13 a)). These results are used to determine the global magnetic behavior of the steel sheets (see Fig. 7.13 b)). For this purpose, a magneto-elastic coupled model "to determine the local permeability of the material as a function of its local mechanical state and the resulting induction" [128] is used. The author concludes that the relative influence of "residual stress is as important as the one of plasticity alone" [128]. The influence of residual stresses on the permeability itself is smaller than that of plasticity, but these affect a larger volume of material. Thus, these residual stresses on the global magnetic behavior are judged to be as important as those of plasticity [128].

The authors of [39] and [40] developed a material model to determine the magnetic properties from the plastic strain $\varepsilon_p$. The model parameters are determined by a numerical forward model using the potentials measured with the needle probe method and an Everett Preisach Distribution function [40], or a Lorentzian Preisach Distribution function [39]. Again, in addition to the needle probe method, further plastic strain measurements are needed. Thereafter, a 2D-FEM numerical model uses the previously developed material model. For this, a nonlinear diffusion equation,

$$\frac{\partial^2 H}{\partial x^2} + \frac{\partial^2 H}{\partial y^2} = \sigma \frac{\partial B}{\partial H} \frac{\partial H}{\partial t}, \tag{7.11}$$
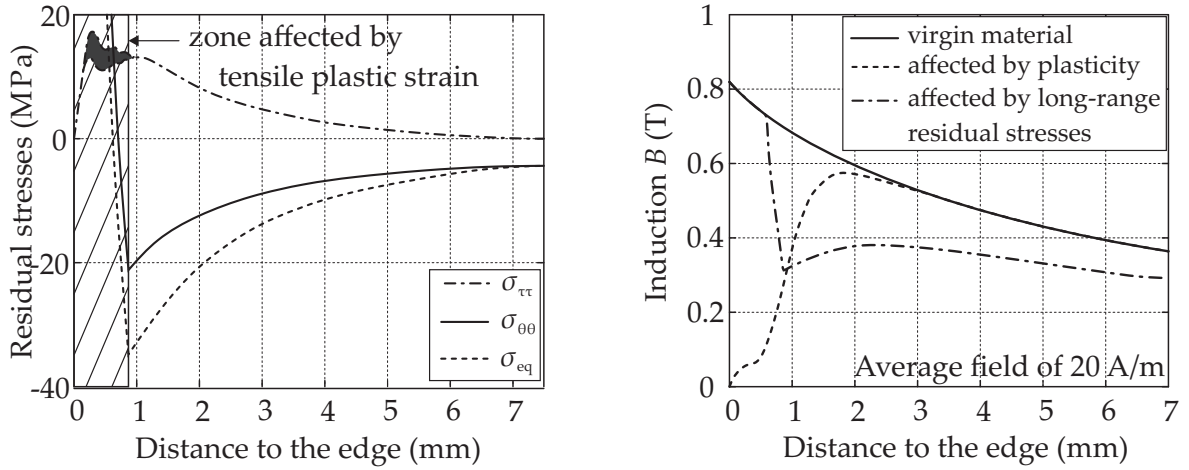
Figure 7.13: Assumed magnetic flux distribution for a punched sample at low magnetic field strengths [128].

is used. One input parameter is the differential permeability $\nu_d = \frac{\partial B}{\partial H}$ which results from the Preisach model. Afterwards, the needle potentials can be calculated depending on the distance from the edge. Subsequently, a least square minimization between simulated and measured needle signals is performed. Then, with this reconstructed material degradation, the global magnetization curve is calculated numerically.

The authors of [58] also implemented an FEM model which considers the influence of mechanical (tensile and compressive) stress on mechanical properties by the permeability. The electromagnetic field is defined by Eq. (7.12) for induction or reluctance machines[9], with $\vec{A}$ [Wb/m] as the vector potential, $V$ [V/m] as the scalar potential, $\vec{J}_0$ [A/m$^2$] as the supplied current density, $\mu$ as the permeability and $\sigma$ [S/m] as the conductivity [58].

$$\nabla \times ([\mu]^{-1} \times \nabla \vec{A}) + \sigma \left( \frac{\partial \vec{A}}{\partial t} + \nabla V \right) = \vec{J}_0. \tag{7.12}$$

The mechanical stress is taken into account in each element of the FEM calculation by the permeability $\mu$, taken from measurement data considering different amounts of stress [58]. The mechanical stress distribution is derived from structural numerical calculations or measurements. In FEM, the magnetic flux density distribution is identified with the Galerkin method. Subsequently, the iron loss distribution in the motor is calculated from the measured specific loss - mechanical stress characteristic. In this paper, the manufacturing process is not mentioned directly. But as can be seen from literature (see e.g. Chapter 7.1.1), several authors have established the correlation between material degradation by manufacturing processes and compres-

---

[9]Eq. (7.12) is simplified for DC motors to $\nabla \times ([\mu]^{-1} \times \nabla \vec{A}) = \vec{J}_0$.
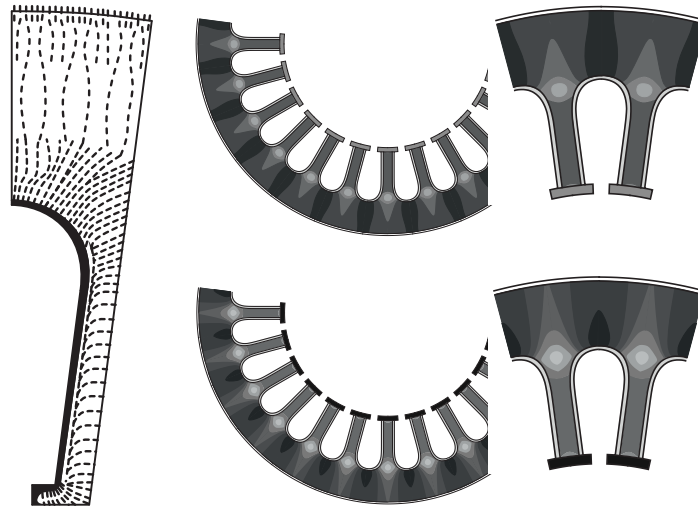
Figure 7.14: Considering the punching effect in a FEM simulation by an additional zone at the cut edge [57] [Mechanical stress distribution]. Numerical calculation for the elastic stressed zone according to [58].

sive stresses. Hence, this author [58] applies the previously presented method to an example case stator to investigate the influence of punching and of shrink fitting on the magnetic properties [57]. The stator is divided into a plastic (cut edge) and an elastically deformed area (see Fig. 7.14). The cut edge zone is defined by very poor magnetic properties [57] and the elastic stress area is characterized by the method of [58].

Note: A similar procedure is presented in [41], which also consists of a structural and magnetic field analysis. (These authors consider only the stress distribution induced by shrink fitting [41].) The pre-processing of the magnetic field analysis considers *B-H* curves measured for different mechanical stresses and a stress distribution map derived from structural analysis [41].

None of these approaches addresses the influence of frequency. Since only mechanical and not thermally induced stresses are considered, these approaches have limited applicability to laser-cut devices.

*Stochastic approaches*

In [159] and [160], material degradation induced by manufacturing processes is taken into account as a variability of magnetic properties. This method is mainly used to analyze the manufacturing influence on slinky stators, as the uncertainty (influence of manufacturing) of laser-cut stators is not found to be significant [160]. The manufacturing process is considered globally, without differentation between the individual manufacturing steps (cutting, pressing, etc.) [160]. A coefficient of variation *Cv* (see Eq. (7.13)) is introduced to describe the variability of measurement

data [160], illustrated for the case of 50 Hz.

$$Cv = \frac{\text{empirical standard deviation}}{\text{empirical mean of measured property}} \tag{7.13}$$

$$P = k_\mathrm{h} f B_\mathrm{max}^\alpha + k_\mathrm{e}(f B_\mathrm{max})^2 + k_\mathrm{exc}(f B_\mathrm{max})^{1.5} \tag{7.14}$$

$$\sum_{i=1}^{n} (P_\mathrm{measured} - P_\mathrm{predict})^2 \tag{7.15}$$

For the slinky stators, the losses are investigated by loss separation, according to [15] which includes the Steinmetz equation [190] (valid for sinusoidal supply) (see Eq. (7.14)), identifiying which variability of the different loss parts is most significant. The coefficients $\alpha$, $k_\mathrm{h}$, $k_\mathrm{e}$, $k_\mathrm{exc}$ are determined for each sample at different frequencies and magnetic flux densities by measurements. Additionally, Eq. (7.15) must be minimized [160]. A Multivariante Gaussian distribution is assumed which considers both the correlation of the parameters and their variabilities [159]. Afterwards, a Monte Carlo[10] simulation (stochastic approach) is carried out to identify the empirical Cumulative Distribution Function (CDF) of the iron losses for different flux densities [159]. The examination of experimental and identified CDF fitting and the Kolmogrov Smirnov Hypothesis Testing are performed to validate this model [159]. The author concludes that the Monte Carlo model provides good results and thus, this model could be implemented into a stochastic finite element analysis [159].

The authors of [161] extended a technique presented in [70] and applied it to a magnetoquasistatic problem which contains "uncertainties in the nonlinear material characteristic" [161]. This material uncertainty is modeled by a "monotone stochastic material model" [161], a perturbed spline model (see Eq. (7.16) and (7.17)) with $\phi(B) = \sum_{i=1}^{n} \phi_{\mathrm{j},i}$[11] and $\phi_{1,i}$ and $\phi_{2,i}$ as cubic polynomials on $[B_\mathrm{i}^\mathrm{measured}, B_\mathrm{i+1}^\mathrm{measured}]$, $\hat{\phi}(B) = \phi(B)/B$ and $\omega$ as a random parameter [161].

$$H(\omega, B) = \bar{H}(B) + s\tilde{H}^\mathrm{measured}(\omega)\phi(B) \tag{7.16}$$

$$\nu(\omega, B) = \bar{\nu}(B) + s\tilde{H}^\mathrm{measured}(\omega)\hat{\phi}(B) \tag{7.17}$$

Furthermore, a sensitivity analysis of the magnetization curve (magnetic reluctivity) is needed [161]. Here, a deterministic second-moment perturbation analysis is used [161]. Afterwards, the method is implemented into a numerical FEMM example.

The authors of [76] and [77] investigate the application of different robust topology optimization methods to minimize the torque ripple of an IPM motor, taking the magnetic deterioration induced by manufacturing processes into account. One such method is the robust genetic algorithm (RGA) in which the material parameters are

---

[10]For Monte Carlo methods, see e.g. [18] and [19].
[11]j takes the values 1 or 2.

extended by artificial random noises [76, 77]. The adjoint variable method (AVM) considers the material degradation by "the deviations in the objective and constraint functions" [77]. The material degradation is considered by the magnetic reluctivity, in the case of [76] depending on the flux density $B$ (Eq. (7.18), originally from [29]), and in the case of [77] depending on the field strength $H$ (Eq. (7.19)), where $k_i$ are constants with uncertainties that are to be assumed by the user [76, 77].

$$v(B) = k_1 exp(k_2 B^2) + k_1 \tag{7.18}$$

$$v(H) = \frac{H}{k_1[1 - exp(-k_2 H)] + \mu_0 H} \tag{7.19}$$

The derivative of the reluctivity $v$ with respect to the vector potential $A$ is then used in the nonlinear FEM calculation [77],

$$\frac{\partial v}{\partial A} = \frac{\partial v}{\partial H} \left(\frac{dB}{dH}\right)^{-1} \frac{\partial B}{\partial A}. \tag{7.20}$$

*Correction factors derived from experience*

Iron loss density is generally computed based on the established Steinmetz formula [190], sometimes expanded by additional terms (e.g. Steinmetz-Bertotti formula [15]); e.g. [83, 92, 107, 123]. The loss coefficients are typically supplied by, or can be calculated from, the manufacturer data.

Correction coefficients can be introduced to account for the degradation of the laminations during the manufacturing process of the machine [136]. These correction coefficients are based on experience and have often been determined decades ago [21, 136, 204]. Most of these correction factors presented in literature include other factors of influence, in addition to the influence of manufacturing, such as harmonics. Some of the stated coefficients refer to the total iron losses ($k_u$) while others distinguish between the individual loss components, i.e. hysteresis ($k_h$) and eddy current ($k_{ec}$) losses.

According to [204], the correction factor of the hysteresis losses $k_h$ is attributed to the degrading influence of manufacturing and further depends on the way of magnetization (alternating or rotational). [136] points out that the contribution of the cutting process on the correction factor depends on the width of the sample, and hence this value will depend on the sample's geometry.

The correction factor of the eddy current losses $k_{ec}$ also includes other manufacturing influences, such as imperfect sheet insulation and burrs, and also other aspects such as harmonics and the direction of magnetization (pure alternating versus rotational magnetization) [136, 204]. However, as known from literature (e.g. [110]), mechanical cutting also leads to changes in the average grain size in the plastically

| $k_u$ | | $k_{h, yoke}$ | $k_{ec, yoke}$ |
|---|---|---|---|
| $k_u \approx 1.3$ [54] | | | |
| $2.5 < k_u < 4$ [34] | | | |
| $1.8 < k_{u, teeth} < 2.5$ [204]* | $1.55 < k_{u, yoke} < 1.7$ [204]* | $k_{h, yoke} = 1.5$ [204]* | $1 \leq k_{ec, yoke} < 2.5$ [204]* |
| $1.7 < k_{u, teeth} < 2.5$ [136] | $1.5 < k_{u, yoke} < 1.8$ [136] | | |
| $1.8 < k_{u, teeth} < 2.5$ [156] | $1.5 < k_{u, yoke} < 2.0$ [156] | | |

\* = citing [175].

Remark: [136, 156, 204] state a range of factors to cover different types of machines.

Table 7.1: Exemplary values of correction factors presented in the literature.

deformed zone which, in turn, changes the width of the magnetic domains and thus affects the microscopic eddy currents (reflected by the excess losses). Of course, this again depends on the ratio between deformed material zone and sample width. Exemplary values of these factors as presented in the literature are shown in Table 7.1.

*Correction factors derived from steel sheet measurements*

The authors of [117] introduce a correction factor (see Eq. (7.21)) to consider the increase in iron losses if the cutting length deviates from the normal Epstein strips with a width of 30 mm (normal catalogue data).

$$K_{\text{cutting}} = C_1 + \frac{C_2}{\text{width}} \tag{7.21}$$

For this purpose, the iron losses of three different punched Epstein samples with various widths are investigated for one material (M400-50A). Curve fitting on these measurement data, results in Eq. (7.21), whereby the width is in millimeters. The coefficients $C_1$ and $C_2$ depend on the material and further on the magnetic flux density, as with different flux densities the coefficients of the fitting curve change.

The model presented in [68] extends the model of [117]. Commonly, the loss coefficients for the hysteresis losses $k_H$ and eddy current losses $k_W$ are assumed as constant [68] (see Jordan-equation (7.22)). With the help of the losses measured for three different 'Epstein' strips (differing in sample width) of one material these coefficients are determined depending on the samples' width $b$, and approximated by the functions in Eqs. (7.23) and (7.24) (compare with Eq. (7.21) of [117], $C_i$ are additional coefficients).

$$p_{\text{Fe}}(B, f) = k_H f B^2 + k_w f^2 B^2 \tag{7.22}$$

$$k_H(b) = c_{H1} + \frac{c_{H2}}{b} \tag{7.23}$$

$$k_W(b) = c_{W1} + \frac{c_{W2}}{b} \tag{7.24}$$

$$K_{\text{cut}} = \frac{1}{2}\left( \frac{k_H(b)}{k_{H,30\,\text{mm}}} + \frac{k_W(b)}{k_{H,30\,\text{mm}}} \right) \tag{7.25}$$

These sample width dependent loss coefficients are combined to give a new correction factor $K_{cut}$ (see Eq. (7.25), $k_{H,30\,mm}$ is the correction factor for 30 mm Epstein samples). According to the author, this correction factor is only accurate if hysteresis and eddy current losses are approximately the same [68].

The deterioration of magnetic properties induced by cutting is also considered by an additional correction factor $k_{Sk}$ in [151]. This correction factor results from an approximation function of measurement data of two different steel sheet materials and depends on the specific cutting length, the magnetic flux density and frequency [151]. The factor $k_{Sk}$ is then determined for each element of the degraded zone implemented in an FEM simulation and is subsequently multiplied by previously calculated iron losses [151].

The authors of [188, 205] modified the parameter $a_1$ of the hysteresis loss part of the 'IEM-formula'[12] (Eq. (7.26)) to take the effect of cutting into account. The parameters $a_i$ of Eq. (7.26) are the parameters of the respective loss parts and $\alpha$ is a parameter which must be estimated to obtain the best fitting with the measured quasi-static hysteresis loss[13]. Referring to [134], the authors state that the influence of cutting affects the hysteresis losses the most. Furthermore, it is assumed that the saturation behavior as well as "the specific electrical resistivity [...][is (]locally[)] not influenced by the cutting process" [188], whereas the parameters of the classical eddy currents ($a_2$) and of the saturation behavior ($a_3$) remain unaffected by the cutting process [188, 205].

To consider the cutting effect, the modified parameter is set in relation to the specific cutting length (CL) (Eq. (7.27)) which is the ratio of the length of the cut edge referred to the weight of the specimen [188, 205]. To evaluate the slope $m$ as well as the additional parameter $a_{ref,1}$ (Eq. (7.28)), several measurements with steel sheets of the same total width but with a different number of strips and thus different CLs must be performed (see [188, 205]).

$$P(\hat{B}, f) = a_1\hat{B}^\alpha f + a_2\hat{B}^2 f^2(1 + a_3\hat{B}^{a_4}) + a_5(\hat{B}f)^{1.5} \tag{7.26}$$

$$P(\hat{B}, f, CL) = a_1(CL)\hat{B}^\alpha f + a_2\hat{B}^2 f^2(1 + a_3\hat{B}^{a_4}) + a_5(\hat{B}f)^{1.5} \tag{7.27}$$

$$a_1(CL) = a_{1,ref} + m(CL - CL_{ref}) \tag{7.28}$$

In all of these works, the correction factors are determined for a given material (and cutting technique) only, and are expected to differ with a change of material and cutting technique.

---

[12]The 'IEM-formula' [94, 187] is an extended version of the Bertotti iron loss equation [15]: $P = k_h\hat{B}^n f + k_w\hat{B}^2 f^2 + k_a(\hat{B}f)^{1.5}$, with $k_i$ as parameters of hysteresis, eddy currents and additional losses. Most of the parameters of the 'IEM-formula' are fitted to measurements [186].

[13]The determination of the respective parameters $a_i$ of the 'IEM-formula' (measurements and/or calculation) is explained in [186, 187].

**Summary**

This chapter summarized the previous efforts to analyze and model the magnetic flux distribution in electrical steel sheets considering the cutting effect. It was shown that direct and indirect measurement methods exist to determine the flux density distribution and to identify the depth of the deteriorated material. Each method has its own advantages and disadvantages. In the case of indirect measurements, the difficulty consists in finding the correct correlation between the measured parameters and the magnetic properties. In the case of direct measurements, the material properties might be affected by the measurement, e.g., by implementing holes in the steel sheet which may falsify the measured magnetic properties. The characteristics of the flux distribution as defined by the different methods, were reviewed, showing differences between the various cutting methods.

Subsequently, the different approaches to model the degrading effect of cutting were presented. Since the effect of the cutting depends on several parameters (e.g. material investigated, cutting technique used, settings of the respective cutting technique, cut geometry), these models differ significantly with respect to their underlying approach, applicability, and need for parameter adjustment.

Both the efforts and the measurement technique required for the measurement-based approaches differ: some involve extensive development of maps, custom-designed measurement setups and/or sample preparation (e.g. annealing, winding), whereas others exploit established approaches, such as the single sheet tester or the Epstein frame. The thusly determined parameter sets typically apply to one given material. For conceptual design approaches, models that come at the price of a certain uncertainty, but that do not require additional measurements, are available.

A classification into distribution formulas, area based models, use of extended airgaps, implementation of a parameter dependence on indirect measurement data as for example stress and strain, stochastic approaches, and use of correction factors was proposed.

The next Chapter presents a new, different method to estimate the influence of different cutting techniques on the magnetic properties of electrical steel sheets with arbitrary geometries. This method is based on measurement data obtained by Epstein samples. For a set deterioration depth $d$, the magnetic properties of the deteriorated and non-deteriorated material zones are identified.

# Chapter 8

# Epstein frame based modeling of the degradation effect of cutting for arbitrary geometries

To date, the electromagnetic characteristics of the laminated steel used in electric machines are typically implemented in finite element simulations by magnetization and loss curves obtained from Epstein frame or SST measurements [86, 87] and/or provided by manufacturers. These data typically differ from those of the finished machine [5]. This Chapter focuses on the modeling of the degrading effect of the cutting process for different cutting techniques and materials. It presents a relatively easy method by which to consider the influence of material degradation in finite element computation of different, arbitrary geometries with the material properties obtained from two Epstein frame measurements (detailed information is given in Chapters 2.5 and 8.1.1), excluding additional time and cost consuming test sample preparations, such as annealing or special inserting of windings in the sample (see also Chapter 7). Indeed, the Epstein frame measurement technique provides a simple and straightforward way to quantify the input parameters (magnetization and loss curves) necessary for this modeling. Thereby, it draws only on already existing and well-established techniques. The consideration of the material degradation in the finite element method (FEM) model does not increase the computational time to a noteworthy extent.

A further advantage of this method is that it eliminates the need of knowing the deterioration depth $d$ exactly due to cutting (no agreement in literature, see Chapter 1). Consequently, the identified magnetization properties of the degraded and non-degraded material zones do not claim to be an exact image of the reality (for this, the exact value of $d$ would be required), but it claims to illustrate the magnetic behavior of arbitrary geometries with a satisfactory degree of accuracy in which both zones are considered.

First, the method is explained by which to identify the magnetization and loss curves of the degraded and the non-degraded material zones, for a specific set deterioration depth $d$, from Epstein frame measurements. Then, these material characteristics are applied to FEM modeling of other geometries, in particular stator lamination stacks. The results are verified by measured reference stators. Furthermore, the specific loss densities obtained with the proposed modeling approach are compared to those computed from the datasheet values provided by the manufacturer.

## 8.1 Identification of non-degraded and fully degraded *BH*-characteristics

### 8.1.1 Investigated samples and assumptions made

The *B-H* curves and specific loss curves of two sample sets with specimens of the same length $\ell_y$ and thickness $w_z$, but with different widths (in our case 'wide' samples with $w_1 = 30$ mm and 'small' samples with $w_2 = 7.5$ mm; $\ell_y >> w_i$, see Chapter 2.5) are determined by Epstein frame measurements (Figs. 2.9 and 8.1)[1]. Half of the measured sheet strips are longitudinally-cut and half transversely-cut, according to the described 'Mix' arrangement in the Epstein frame (see Chapter 2.5 and Fig. 2.10). Thus, the influence of the rolled, preferred direction is eliminated and subsequently the obtained information corresponds rather to stator or rotor shape geometries. In the following, the sample sets 1 and 2 are designated as samples 1 and 2.

In the case of mechanically-cut samples, the identification procedure is applied to the materials M400-50A and M800-65A. In the case of laser-cut samples, material M270-35A is also considered.[2] All investigations are carried out at three different frequencies: 50 Hz, 250 Hz and 500 Hz.

The following assumptions and simplifications have been made:

- Both cutting techniques induce equal degradation profiles on both sides of the sample.
- The degradation zone is homogeneous and has a specified depth, $d$ (Fig. 8.1).
- The degrading of the zones on the short sides of the Epstein samples is neglected as $d \ll \ell_y$.

The fractions of degraded material in samples 1 and 2 are denoted as $\gamma_1 = (2d/w_1)$ and $\gamma_2 = (8d/w_1)$, respectively.

---

[1]The first sample set consists of 16 'wide' Epstein samples and the second sample set of 64 'small' strip samples (see also Chapter 2.5).

[2]Unfortunately, no punched stator sample of the material M270-35A was available, see Table 2.4.

As discussed in Chapter 1, published results on the deterioration depth on the electrical steel sheets due to cutting vary. For the illustration of the modeling approach, a non-degraded area in the middle of the sheet and a homogeneously degraded zone with a constant deterioration depth of 2.1 mm from the cut edge for all sample strips is assumed. Note that the proposed technique also allows the setting of other degradation depths, and the computed material characteristics result accordingly.
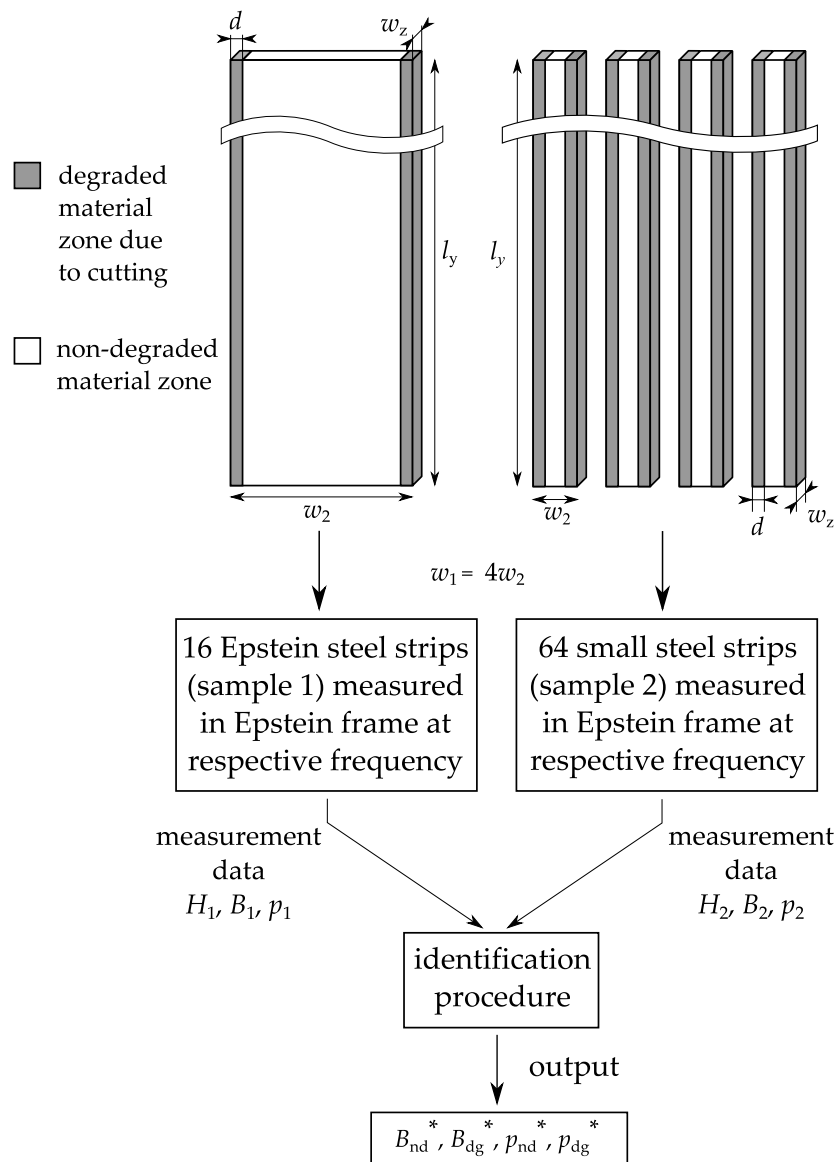


Figure 8.1: Measurement configuration and identification procedure.
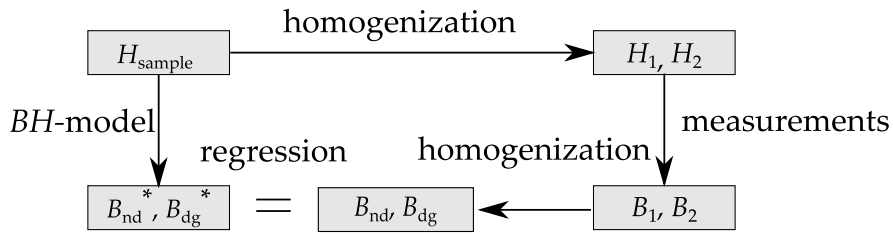
Figure 8.2: Identification of the non-degraded and degraded *B-H* curves from the *B-H* curves of small and wide samples.

## 8.1.2  Basic identification procedure

The basic idea of the identification procedure is as follows (Fig. 8.2): The measurement series $(H_1, B_1)$ and $(H_2, B_2)$ are obtained independently from the 'wide' and 'small' samples in the Epstein frame (see also Fig. 8.1). Of course, it is ensured that these samples of one set result from the same material and MC and are cut with the same cutting technique. Subsequently, data points $(H, B_{nd})$ and $(H, B_{dg})$ are calculated from

$$\begin{bmatrix} 1 - \gamma_1 & \gamma_1 \\ 1 - \gamma_2 & \gamma_2 \end{bmatrix} \begin{bmatrix} B_{nd} \\ B_{dg} \end{bmatrix} = \begin{bmatrix} B_1 \\ B_2 \end{bmatrix}. \tag{8.1}$$

The indices 1 and 2 of the magnetic flux density $B$ indicate the measured values of the two sample sets, as described in Chapter 2.5 and Fig. 8.1. Eq. (8.1) expresses the parallel connection of the flux paths through the non-degraded (nd) and degraded (dg) zones. The values $B_1$, $B_2$, $B_{nd}$ and $B_{dg}$ all correspond to the same magnetic field strength $H$. Though obviously simple, this procedure requires a few generalizations to be applicable in practice.

## 8.1.3  Interpolation and sampling

The measurement series $(H_1, B_1)$ and $(H_2, B_2)$ are obtained independently. In practice, matching values for $H_1$ and $H_2$ are difficult to obtain. As a consequence, the measured *B-H* curves have to be sampled, i.e., a distribution of sample points $H_{sample}$ has to be selected. Moreover, the measured *BH*-characteristics need to be interpolated between the sampling points. It turns out that the results of the identification procedure are quite sensitive to these choices. One possibility consists of fitting a prescribed function, e.g., the Brauer curve [29], the Bertotti curve[3] [139] or the Langevin curve [26] to the measurement data. The parameters of the curves are found by regression. This approach may fail to represent the measurement

---

[3]Strictly speaking, the function proposed in [139] is a slightly modified version of the approaches presented in [8,9,17,49].

data with sufficient accuracy. Another possibility consists of representing the *BH*-characteristics by piecewise polynomials. These attain a higher degree of precision for arbitrary *B-H* curves, but may violate physical properties, such as monotonicity, unless these properties are explicitly enforced. A common practice is the use of splines which leads to smooth curves but may cause unphysical oscillations and piecewise splines which sacrifice smoothness but suppress oscillations. In the work presented below, cubic splines have shown to be the most suitable choice for respecting all *BH*-characteristics in the model. The sampling points for the magnetic field strength are taken from the measurements of the first sample.

## 8.1.4 Rayleigh region

The measurements for small fields may lack accuracy. As a consequence, the Rayleigh effect is only marginally represented in the measurement curves. Under these circumstances, Eq. (8.1) may lead to invalid results, e.g., $B_{dg}$ may become negative. Several remedies are possible:

1. A drastic remedy consists of discarding the Rayleigh effects in the original measured *BH*-characteristics, i.e., the true characteristic is replaced by a characteristic $B = \mu_{knee}H$, $H < H_{knee}$ where $(H_{knee}, B_{knee})$ is the measured point with the highest chord permeability $\mu_{knee} = B_{knee}/H_{knee}$.

2. A less drastic remedy is to fit the model

$$B \;=\; \alpha H^2 + \beta H \qquad\qquad \text{for} \quad 0 \le H < H_{ray}, \qquad (8.2)$$

$$B \;=\; -\alpha H_{ray}^2 + \left(\beta - 2\alpha H_{ray}\right) H \quad \text{for} \quad H_{ray} \le H < H_{knee} \qquad (8.3)$$

according to the parameters $H_{ray}$, $\alpha$, and $\beta$. In both cases, the measured and interpolated *BH*-characteristics are checked for possible areas where $B_1(H)$ becomes smaller than $B_2(H)$, a situation which is fully attributed to measurement inaccuracies.

Even when the $(H_1, B_1)$-curves and $(H_2, B_2)$-curves are "cleaned" to correctly represent the Rayleigh region, this quality is not carried over by the identification procedure represented by Eq. (8.1) to the $(H, B_{nd})$-curves and $(H, B_{dg})$-curves. There, the clean-up procedure should be repeated. In fact, it makes more sense to align the Rayleigh region for the $(H, B_{nd})$-curves and $(H, B_{dg})$-curves, because these are assumed to correspond to individual materials, whereas the $(H, B_1)$-curves and $(H, B_2)$-curves are particularly averaged material properties.

For the considered materials, the Rayleigh region is small (only for magnetic flux densities below 0.2 T and almost invisible in the figures). Nevertheless, a consistent

representation of this region is of paramount importance to make sure that the Newton method embedded in the FE solver converges properly.

## 8.1.5 Full-saturation region

It is necessary to clearly define the extrapolation of the *BH*-characteristics for large fields.

- Extrapolating from the last measurement point with a differential permeability $\mu_0$ is based on physical understanding, but may introduce a discontinuity in the differential permeability which may hamper the convergence of the Newton method applied later on. As long as the $(H_1, B_1)$-curve lies above the $(H_2, B_2)$-curve, this procedure guarantees consistent results for $(H, B_{\mathrm{nd}})$ and $(H, B_{\mathrm{dg}})$.

- Another technique extends the *B-H* curves according to the slope determined by the two last measurement points. This approach may be inappropriate when the small variations of the magnetic flux density *B* are not sufficiently resolved by the measurements. Moreover, it should be verified that the final slope for $(H_1, B_1)$ is larger or equal to that of $(H_2, B_2)$.

## 8.1.6 Results of mechanically-cut samples

The identification procedure described above is applied to the measurement results for two samples of material M400-50A at 250 Hz. In Chapter 8.3.4, results for 50 Hz and 500 Hz and material M800-65A are also presented. Further results are also provided in Appendix E.1.1.

The permeability of sample 1 is substantially better than that of sample 2 (as $w_1 > w_2$, thus, the relative degraded volume ($V_{\mathrm{degraded}}/V_{\mathrm{total\ sample\ volume}}$) in sample 2 is larger than in sample 1 (Fig. 8.1)), especially in the transition region between linear regime and full saturation. When the *B-H* curves are represented by the Bertotti function[3,p.234], the standard identification procedure leads to the results shown in Fig. 8.3; differences between measurements and representation are observed. Piecewise cubic splines have been shown to represent the measured curves very accurately: However, the standard identification procedures lead to *B-H* curves for the non-degraded and degraded materials that are unphysical in the Rayleigh region (negative permeability of the degraded material) and in the region of full saturation (degraded more permeable than non-degraded material). As a remedy for these effects, the measurement data are corrected by repairing the Rayleigh region and by extrapolating the curves enforcing $\mu_0$ as differential permeability (see Chapter 8.1.4 and 8.1.5). This
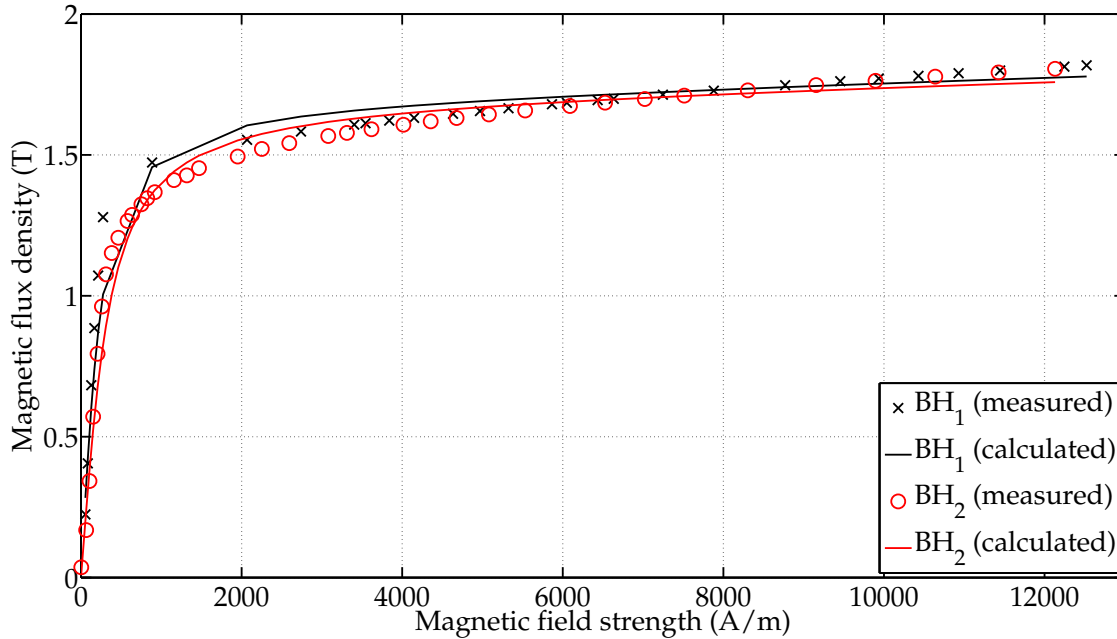
Figure 8.3: Measured and identified *B-H* curves for M400-50A at 250 Hz; represented by the Bertotti function[3,p.234].

improved procedure leads to the results shown in Fig. 8.4. The measured and calculated values of Fig. 8.4 correspond well; they can hardly be distinguished between in the figure. The further performed basic identification procedure leads to the results shown in Fig. 8.5.

As expected, the *B-H* curves are stacked such that, for all values of the magnetic field strength $H$, $B_{nd}(H) > B_1(H) > B_2(H) > B_{dg}(H)$, in all regions of the *BH*-characteristic (compare also with further results presented in Appendix E). The curves $(H, B_{nd})$ and $(H, B_{dg})$, can be used directly as part of a finite element calculation of, e.g., a machine consisting of material with a fully degraded zone at the cut edge and a non-degraded zone in the middle of the sample.

### 8.1.7 Results of laser-cut samples

The same method applied to the results of laser-cut samples of material M270-35A provides the results shown in Figs. 8.6 and 8.7 [4]. Again, the *B-H* curves are ordered such that for all values $H$ of the magnetic field strength, it holds that $B_{nd}(H) > B_1(H) > B_2(H) > B_{dg}(H)$, in all regions of the characteristic (Fig. 8.7).

Note that the model may produce unphysical behavior in the knee point area of the identified non-degraded *B-H* curve by producing an extremum (see Fig. 8.7). This may occur when the difference of the magnetic flux density $B$ or the relative

---

[4]Further results can be found in Appendix E.1.3.
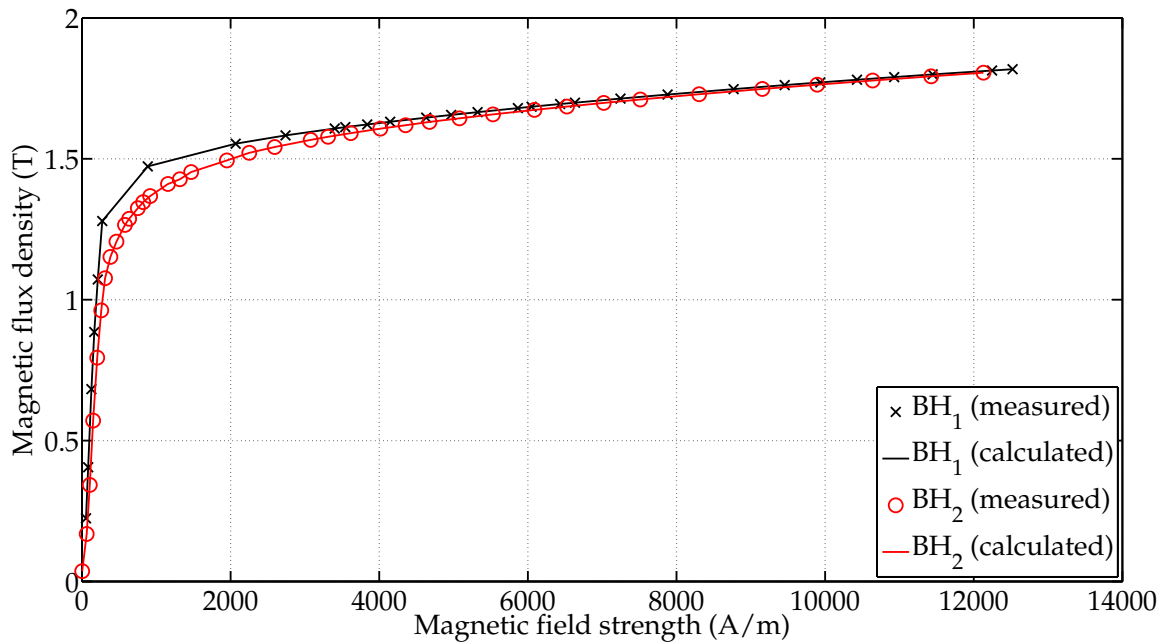
Figure 8.4: Measured and identified *B-H* curves of mechanically-cut samples for M400-50A at 250 Hz; represented by piecewise cubic splines, calculated with the improved procedure.
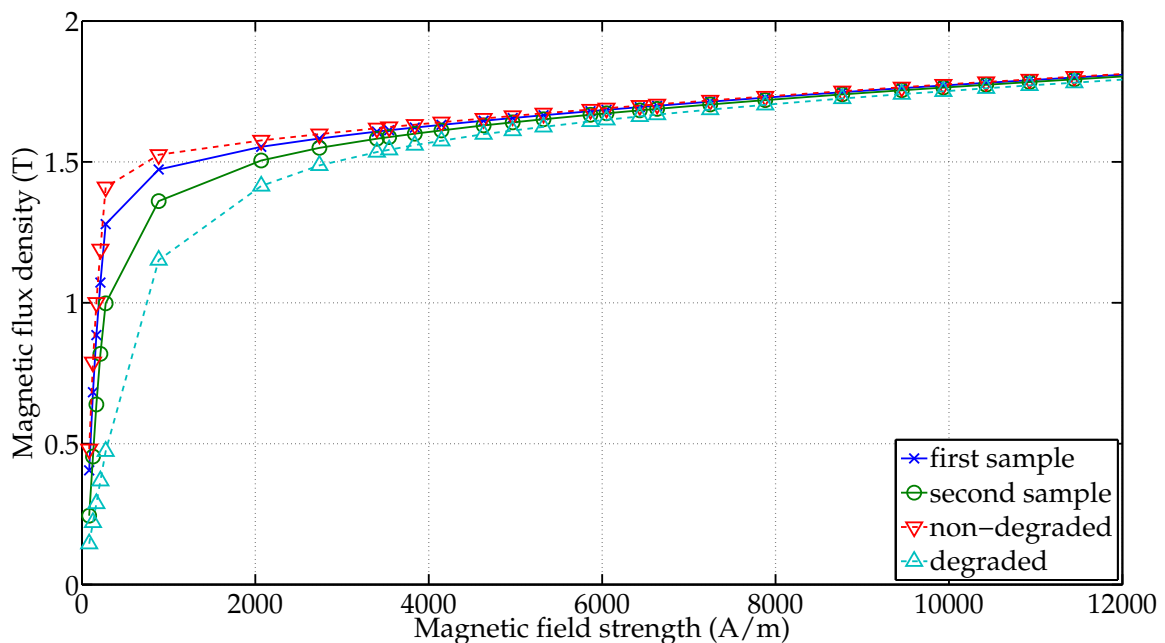


Figure 8.5: Identified *B-H* curves for the degraded and non-degraded material zone of mechanically-cut samples for M400-50A at 250 Hz; represented by piecewise cubic splines, calculated with the improved procedure.
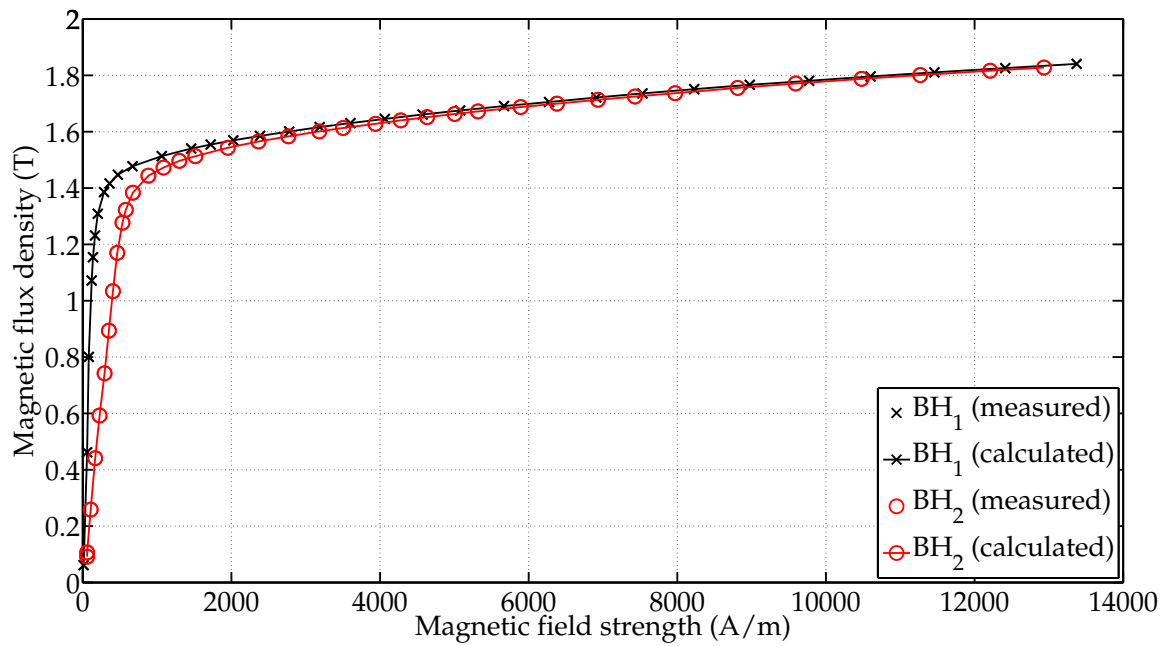
Figure 8.6: Measured and identified *B-H* curves of laser-cut samples for M270-35A at 50 Hz.
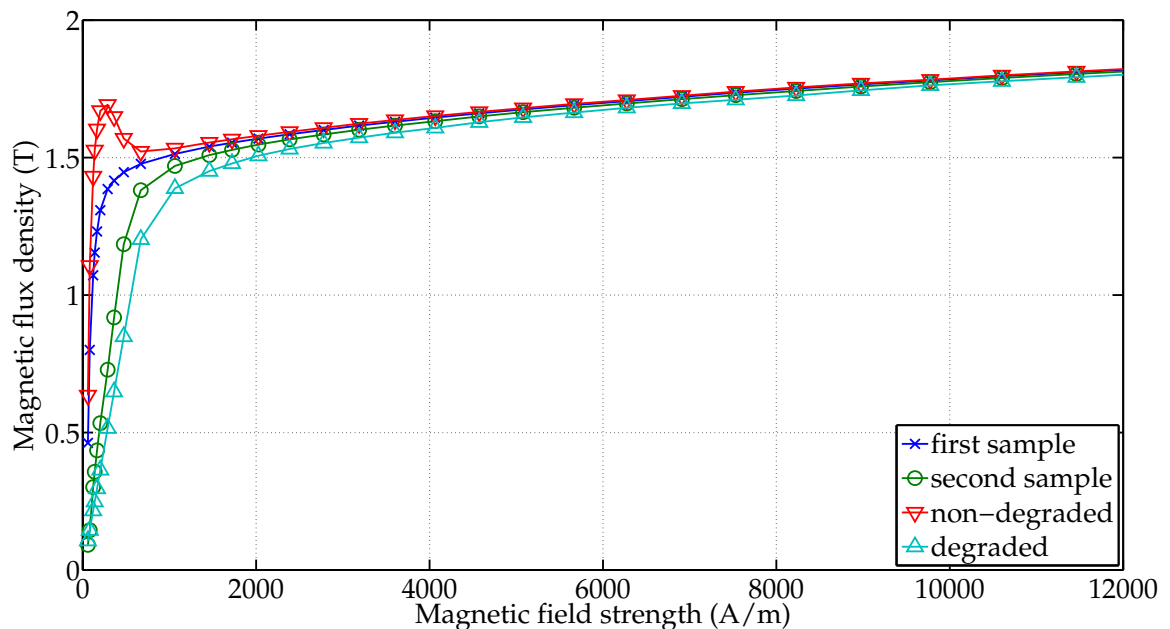


Figure 8.7: Identified *B-H* curves for the degraded and non-degraded material zone of laser-cut samples for M270-35A at 50 Hz.
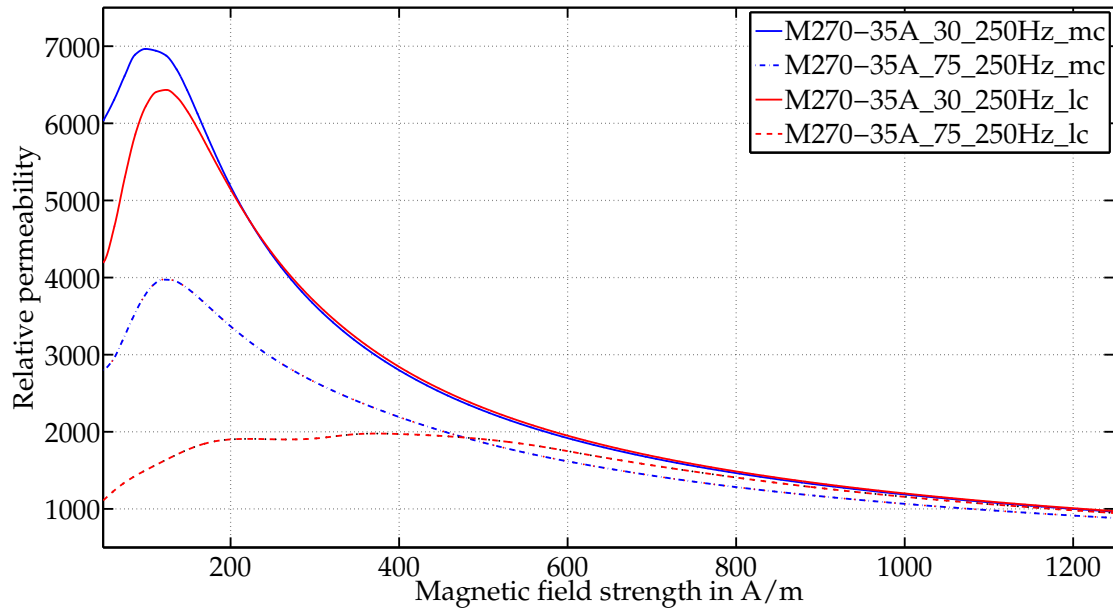
Figure 8.8: The difference in relative permeability due to the different sample sizes used is larger for laser-cut (_lc) than for mechanically-cut (_mc) samples at small magnetic field strengths.

permeability $\mu_r$ of both measured samples is very large at a respective magnetic field strength $H$: In contrast to mechanically-cut samples, the relative permeability of the small laser-cut samples is more degraded at the small magnetic field strength area (see Fig. 8.8 and Chapter 5). Additionally, the relative permeability of laser-cut samples at small magnetic field strengths $H$ is, with decreasing sample width or increasing deteriorated zone, degraded to a plateau (see for instance Fig. 8.8 and Chapter 5). Hence, the difference of relative permeabilities of samples 1 and 2 is significantly larger for laser-cut samples. Therefore, such artificial extrema may result if the method is applied to laser-cut samples of significantly different widths. This difference is smaller, for example, for material M800-65A at higher frequencies (Appendix E.1.3), wherefore the extrema disappear.

## 8.2 Identification of non-degraded and fully degraded loss characteristics

### 8.2.1 Loss model

A simple loss model is expressed by

$$p_{\text{loss}} = c_1 B + c_2 B^2 \quad , \tag{8.4}$$
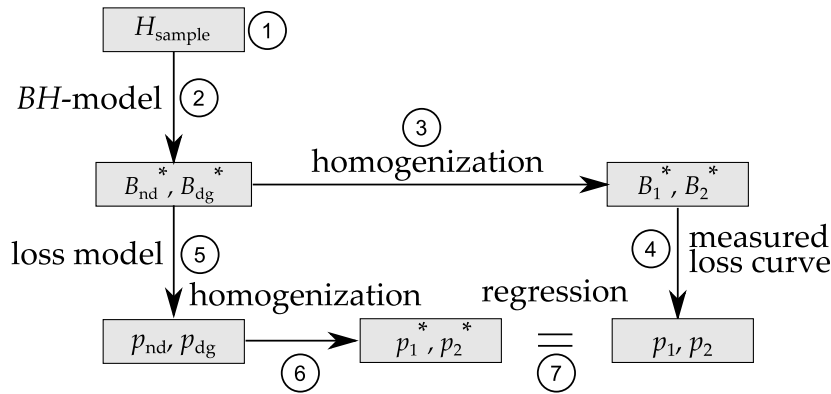
Figure 8.9: Identification of the non-degraded and degraded loss curves from the loss curves of small and wide samples.

where $p_{\text{loss}}$ is the loss density and $c_1$ and $c_2$ are two parameters to be identified by regression. Thereby, as a constraint to the regression procedure, $c_1$ is forced to be strictly positive in order to avoid an unphysical behavior of the computed non-degraded loss curves at small magnetic flux density. Although this modeling approach is quite simple, it seems to approximate the loss density quite accurately.

## 8.2.2 Basic identification procedure

The identification of the loss curves for the non-degraded and degraded material requires several steps and depends on the previously obtained *B-H* curves $B_{\text{nd}}(H)$ and $B_{\text{dg}}(H)$ (Fig. 8.9).

The steps are:
1. Choose a set of sampling points for the magnetic field strength $H_{\text{sample}}$.
2. Evaluate the $(H, B_{\text{nd}}^*)$-curves and $(H, B_{\text{dg}}^*)$ curves.
3. Calculate the corresponding averaged magnetic flux densities $B_1^*$ and $B_2^*$ in both samples, using Eq. (8.1).
4. Evaluate the measured loss curves for $B_1^*$ and $B_2^*$, leading to $p_1$ and $p_2$.
5. Evaluate the loss model for a set of model parameters and for the points $B_{\text{nd}}^*$ and $B_{\text{dg}}^*$.
6. Calculate the corresponding averaged loss densities $p_1^*$ and $p_2^*$ in both samples, using

$$\begin{bmatrix} 1 - \gamma_1 & \gamma_1 \\ 1 - \gamma_2 & \gamma_2 \end{bmatrix} \begin{bmatrix} p_{\text{nd}} \\ p_{\text{dg}} \end{bmatrix} = \begin{bmatrix} p_1^* \\ p_2^* \end{bmatrix}. \tag{8.5}$$

7. Compare $p_1^*$ and $p_2^*$ with $p_1$ and $p_2$.

Steps 1 to 4 are carried out in advance. Steps 5 to 6 are implemented in a procedure which is given as input to an optimization routine minimizing the error in step 7.
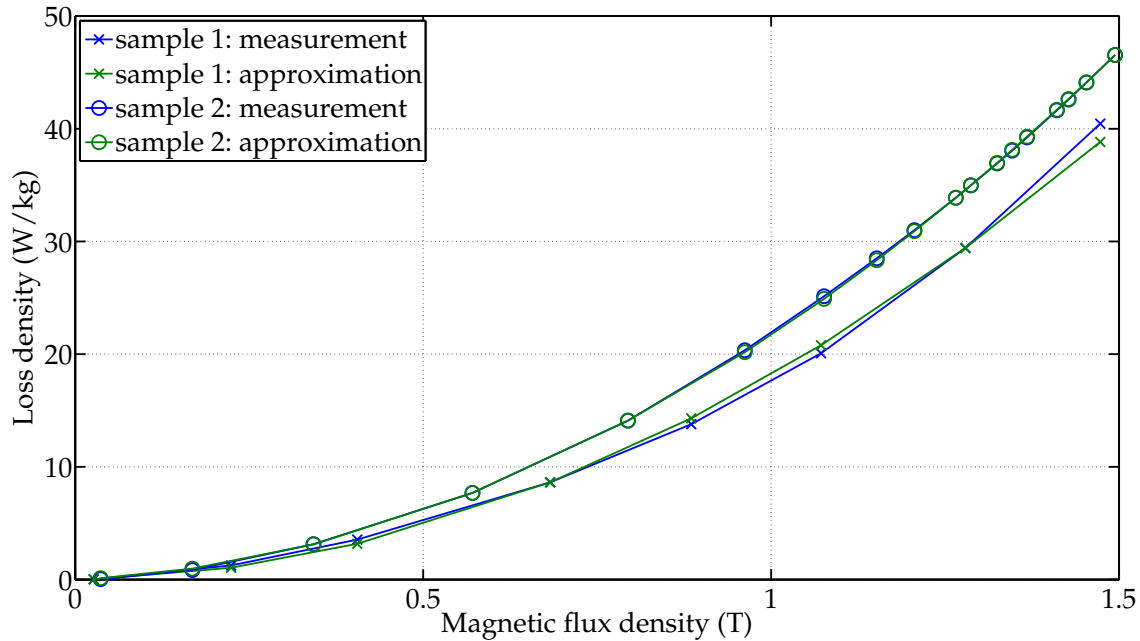
Figure 8.10: Measured and identified loss curves of mechanically-cut samples, represented by Eq. (8.4), M400-50A at 250 Hz supply frequency .

### 8.2.3 Results of mechanically-cut samples

The identification procedure for the losses is applied to the measurement results for both samples (Fig. 8.10). The modeled curves approximate the measured ones sufficiently well. Then, the losses of the degraded and non-degraded material zones are calculated according to the identification procedure presented in Fig. 8.9. As expected, the loss densities for a given magnetic flux density $B$ are ordered as $p_{nd} < p_1 < p_2 < p_{dg}$ (Fig. 8.11; further results of other materials and frequencies are provided in Appendix E.2.1).

### 8.2.4 Results of laser-cut samples

The loss identification procedure is also applied to the measurement results for 'wide' and 'small' FKL-laser cut samples. Here again, the modeled curves approximate the measured ones sufficiently well (see for instance Fig. 8.12).

The resulting loss densities for the same magnetic flux density $B$ are again stacked as $p_{nd} < p_1 < p_2 < p_{dg}$ (Fig. 8.13). This applies to all investigated samples, mechanically-cut as well as laser-cut (see also Appendix E.2).

A special characteristic occurs for the identified degraded loss curve of the laser-cut material M270-35A at 50 Hz (Appendix E.2.3). This loss curve has an almost linear character. It was observed that this behavior changes with different set degradation
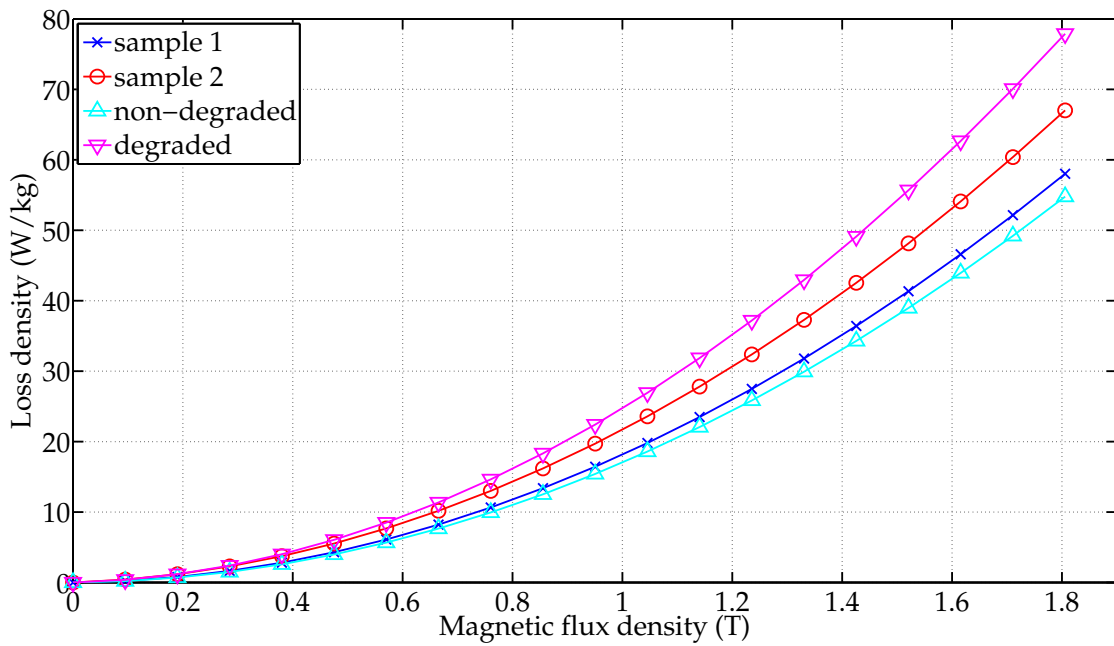
Figure 8.11: Identified loss curves for the degraded and non-degraded material parts of mechanically-cut samples, represented by Eq. (8.4), M400-50A at 250 Hz supply frequency.
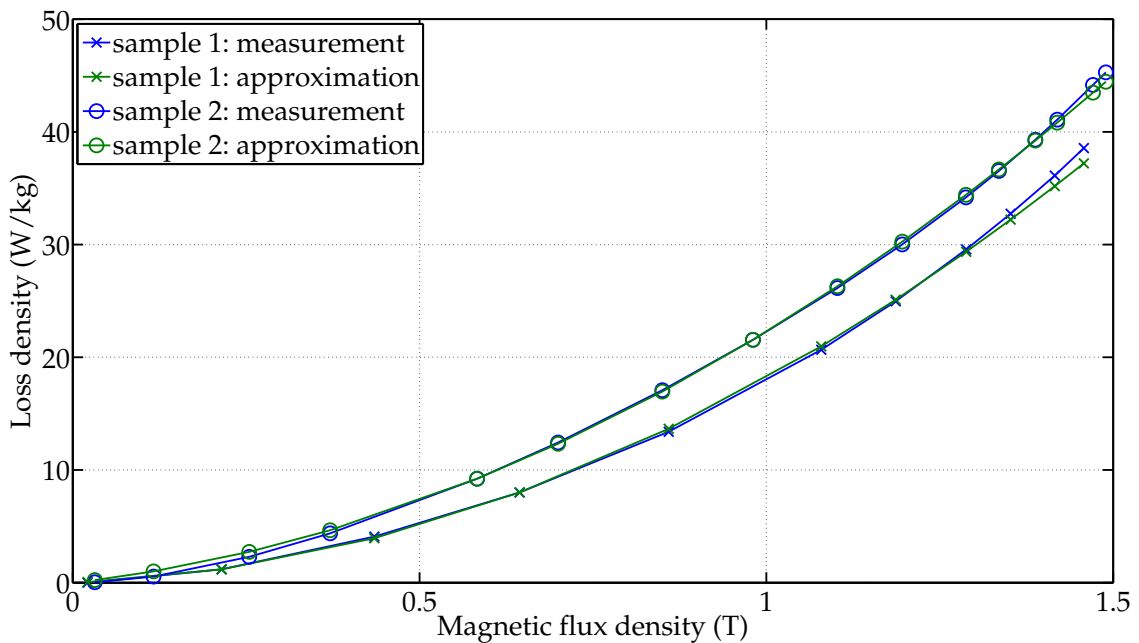


Figure 8.12: Measured and identified loss curves of laser-cut samples, M400-50A at 250 Hz supply frequency.
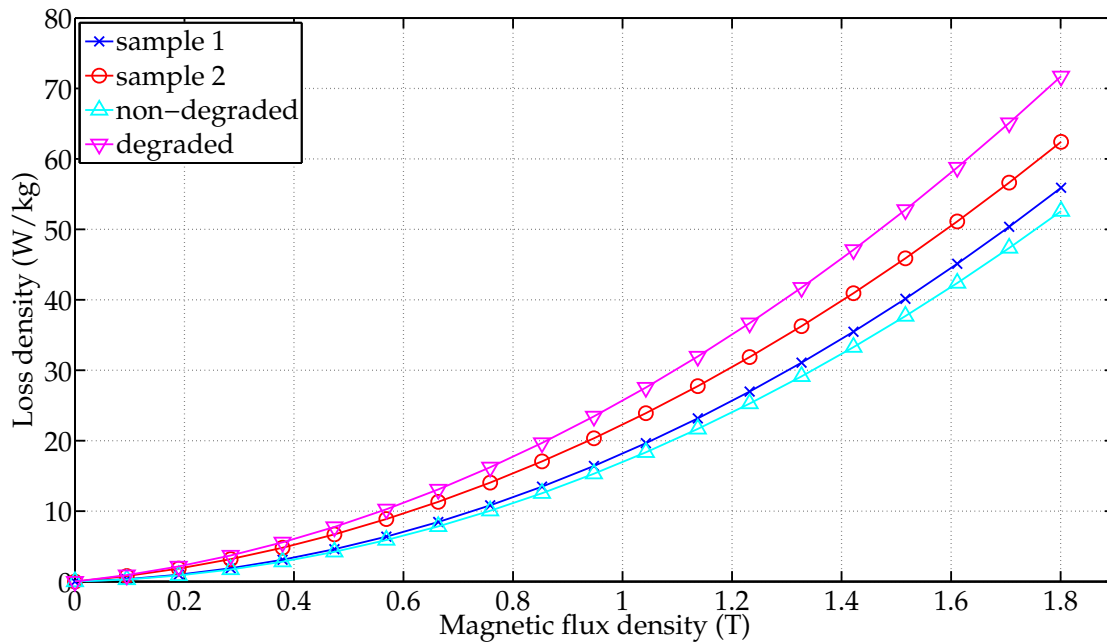
Figure 8.13: Measured and computed loss curves of laser-cut samples, M400-50A at 250 Hz supply frequency.

depths, but may also reflect the linear behavior of laser-cut samples mentioned in Chapter 5.2.1, which is also most pronounced for material M270-35A at 50 Hz (see Fig. 5.2).

## 8.3 Application to stator lamination stacks

### 8.3.1 Stator measurement setup

The electrical steel sheets of the stator lamination stacks are derived from the same MCs as the Epstein samples and have been cut with the same cutting methods[5]. Thus, possible additional deviations due to different production batches can be excluded. Further details of the measurement setup are presented in Chapter 2.6. Hence, the magnetic flux is only considered in the yoke; and an alternating field, similar to the Epstein samples, can be assumed. The results of the 'Epsteinframe' method are used (Chapter 2.6).

---

[5]Note, the mechanically-cut stators are punched and not guillotine-cut, as the Epstein samples. Both punching and guillotining refer to mechanical cutting. The subtle difference between the influences of these two cutting techniques on the magnetic properties of the material is considered of secondary importance here.
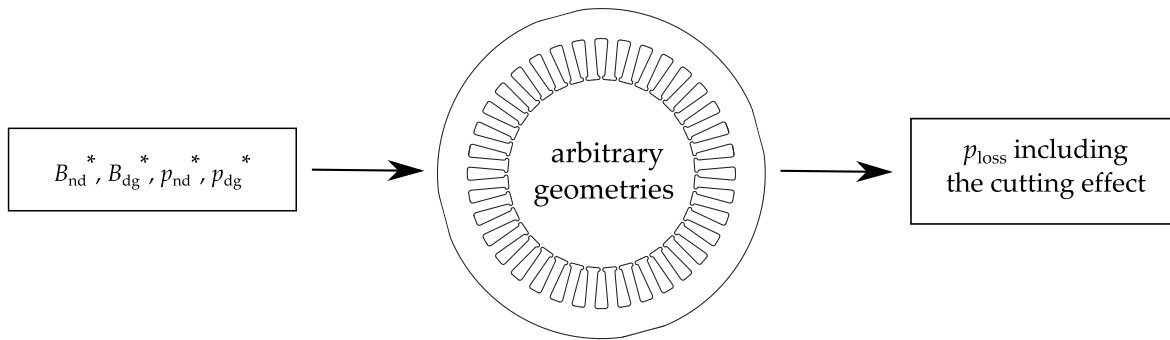
Figure 8.14: Application of computed magnetic characteristics to arbitrary geometries.

### 8.3.2 Simulation

The geometry of the stator lamination stack is implemented in an electromagnetic FE modeling program, FEMM [53], which is coupled with Matlab [125]. The identified magnetization and loss curves for the fully degraded and non-degraded zones of the Epstein samples are applied to the stator geometry (Fig. 8.14). The same degradation depth, $d$, at the cut edges as for the Epstein samples is set.

### 8.3.3 Consideration of stacking

The stator lamination stacks consist of several electrical steel sheets which are, after the cutting process, pressed and glued. Therefore, the change in specific losses due to the pressing and gluing process of the laminations is added in the computation. This change in losses can be attributed to additionally induced stresses inside the material, but are most likely also due to increasing eddy currents through short cut circuits induced by burrs at the cut edge [110].

Different results concerning the increase in losses of electrical steel sheets according to the pressing and gluing process have been presented. Most authors deal with the influence of compression along the steel sheets on rectangular samples, e.g. [97, 149, 155], or in the radial direction, for example shrink fitting (stator or ring samples), e.g. [57, 194, 212]. However [98], citing [142] and [95], states that it is assumed that the magnetic properties are changed differently if the samples are pressed into the thickness direction.

Very few studies address the influence on the losses of electrical steel sheets compressed into the thickness direction, or compressed and glued into the thickness direction. The few studies that exist show a wide range of results ranging from very small changes to a difference of over 20 % in iron losses due to pressing (e.g. [98, 132, 141, 145, 170, 213], varying of course with exact pressing force). How-

ever, the literature reports both an increase and a decrease of the specific losses by pressing: According to [170], the specific losses increase, even if only to a small extent. This extent of increase depends, for example, on the silicon content [170] and thus on the respective material composition. [141] also states that with increasing pressing force, the losses increase. However, the author also points out that the coating thickness of the steel has an influence on the extent of this increase. The authors of [132] and [145] also report an increase of the losses due to pressing. The results of [213] contrast with the finding of the other authors, reporting on decreasing losses with increasing pressing force. [98] confirms the decreasing loss behavior of [213] from 4 MPa onwards. However, below these 4 MPa [98] reports an increase of iron losses of up to 10 %. These different and partly conflicting results may be explained by the following reasons:

- Different materials investigated with different chemical compositions. [170] showed that even the silicon content[6] of the material influences the sensitivity of the material due to pressing.
- Coating thickness of the material (see results of [141]).
- Pressing force (compare results from [98, 170, 213]).
- Different measurement setups.
- Different sample sizes.

The stator lamination stacks in this work[21,p.24] were pressed with a pressure of around 0.3 MPa. After the pressure is removed, internal stresses may remain in the material, due to the gluing of the laminations [170]. These are estimated with the help of the results of [132]. Using the results presented in [132], a mean for the material JIS50A290 (material definition according to the Japanese standard [96], corresponding to material M290-50A), was calculated using the average percentage increase of the loss density from 0 MPa to 0.5 MPa at 1 T for the rolling and transverse cutting directions and added to the computation.

### 8.3.4 Results of mechanically-cut samples

Fig. 8.15 shows the computed losses for the investigated mechanically-cut stator lamination stack geometry with and without the influence of the pressing and gluing manufacturing step, as well as the measured losses of these stator stacks at 250 Hz. For these computations, the identified magnetization and loss curves of the non-degraded and fully degraded material zones, shown in Figs. 8.5 and 8.11, are used. Fig. 8.16 shows the corresponding simulated distribution of the magnetic flux density $B$ in the stator yoke. The computed and measured loss curves of the stator

---

[6]And thus potentially also the grain size, see Chapter 1.2.2.
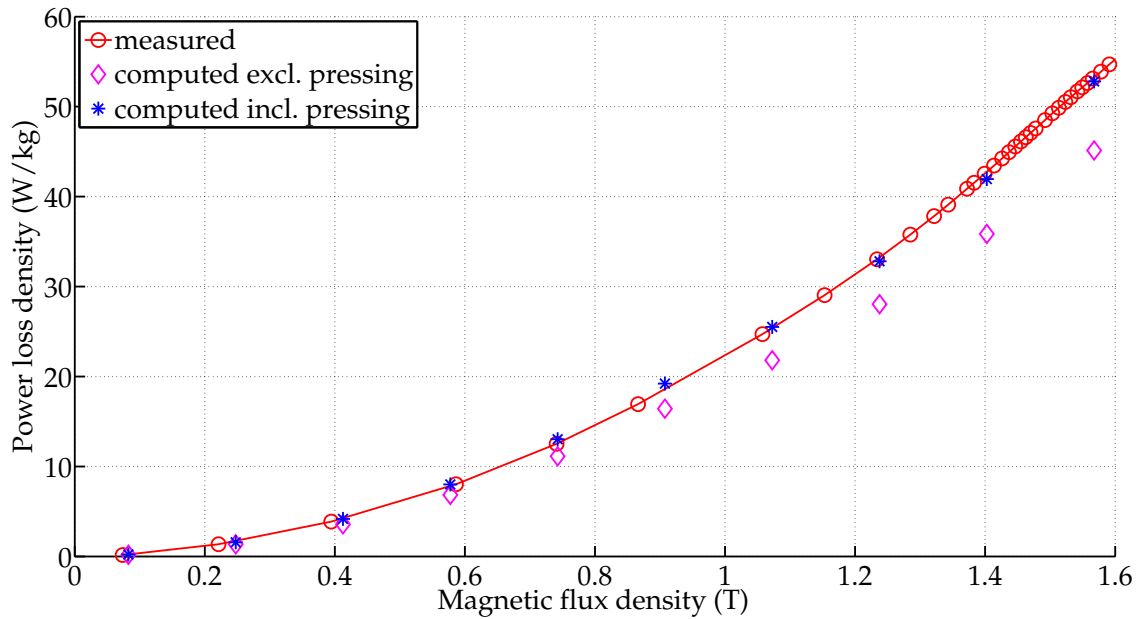
Figure 8.15: Measured and computed loss curves of the investigated mechanically-cut stator lamination stack at 250 Hz, material M400-50A.

lamination stacks concur with one another.

This identification procedure is also applied at other frequencies, 50 Hz and 500 Hz, and for another material, M800-65A. The results are presented in Figs. 8.17–8.20. Here again, the computed losses are in good agreement with the measured ones for all investigated frequencies and materials.

## 8.3.5 Results of laser-cut samples

Selected computed and measured results of the investigated stator samples are presented in Figs. 8.21-8.23. In all cases, the measured and computed specific losses of the investigated laser-cut stator lamination stacks concur well with one another, for different materials as well as different frequencies. Thus, the proposed identification procedure can serve as a helpful tool in the design process of electrical machines to obtain more accurate data of changed magnetic characteristics of electric steel sheets due to cutting for both laser-cut and mechanically-cut samples.
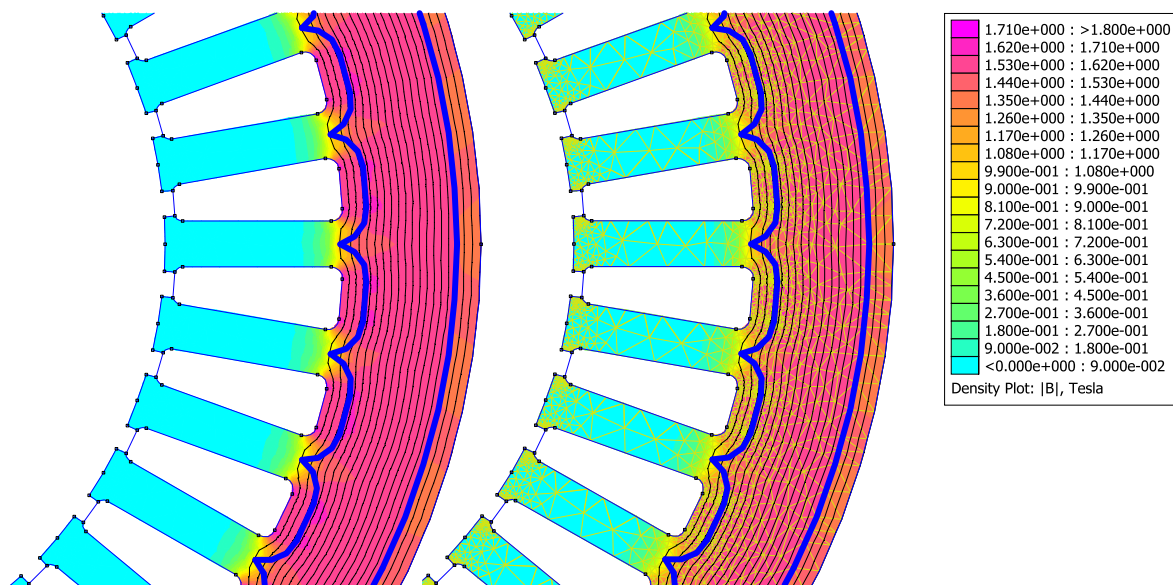
Figure 8.16: Simulated distribution of the magnetic flux density $B$ in stator yoke affected by mechanical cutting. The thick solid lines indicate the deterioration depth $d$.
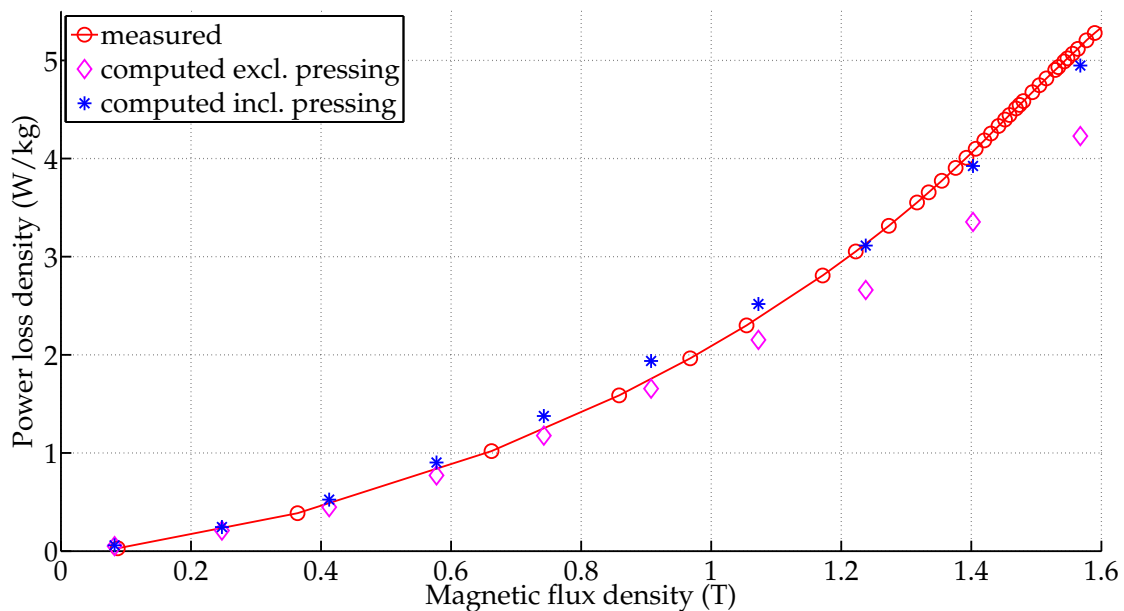


Figure 8.17: Measured and computed loss curves of the investigated mechanically-cut stator lamination stack at 50 Hz, material M400-50A.
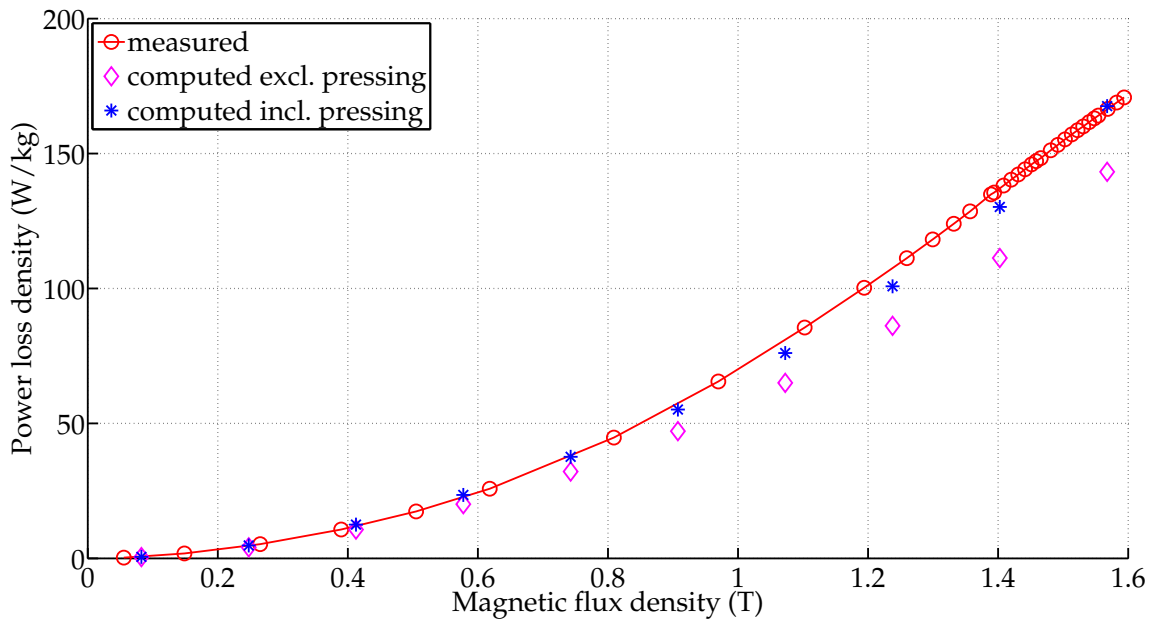
Figure 8.18: Measured and computed loss curves of the investigated mechanically-cut stator lamination stack at 500 Hz, material M400-50A.
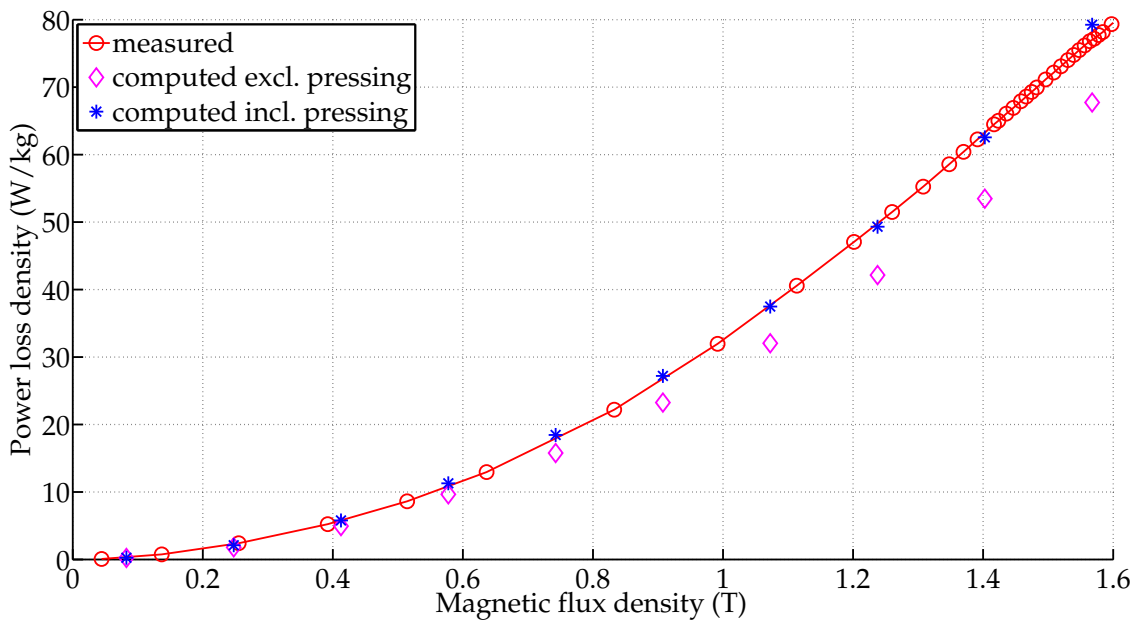


Figure 8.19: Measured and computed loss curves of the investigated mechanically-cut stator lamination stack at 250 Hz, material M800-65A.
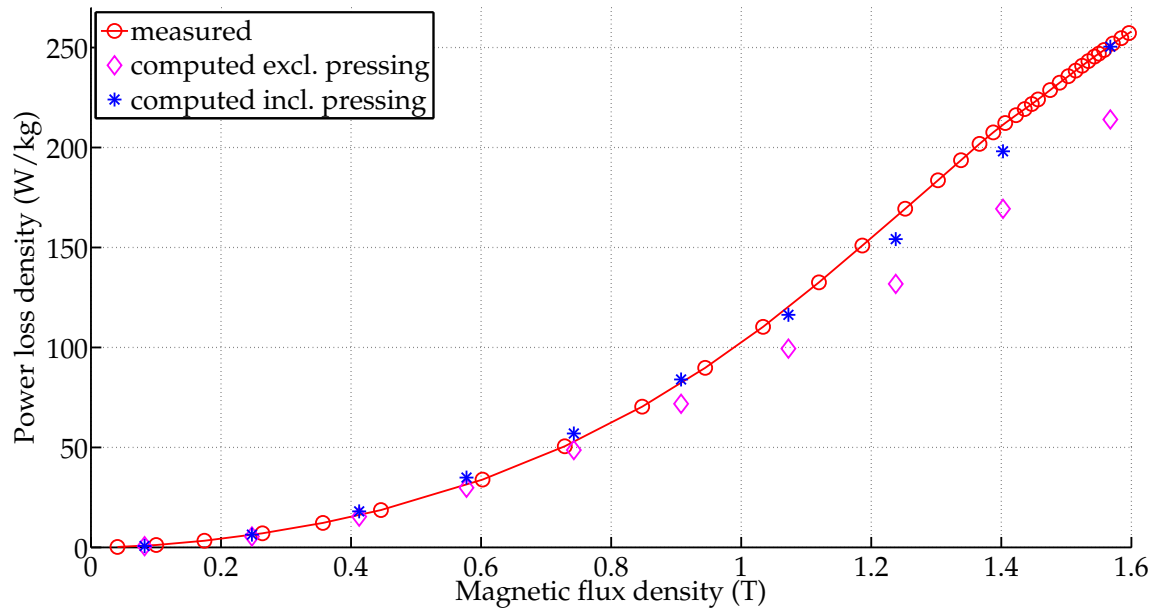
Figure 8.20: Measured and computed loss curves of the investigated mechanically-
cut stator lamination stack at 500 Hz, material M800-65A.
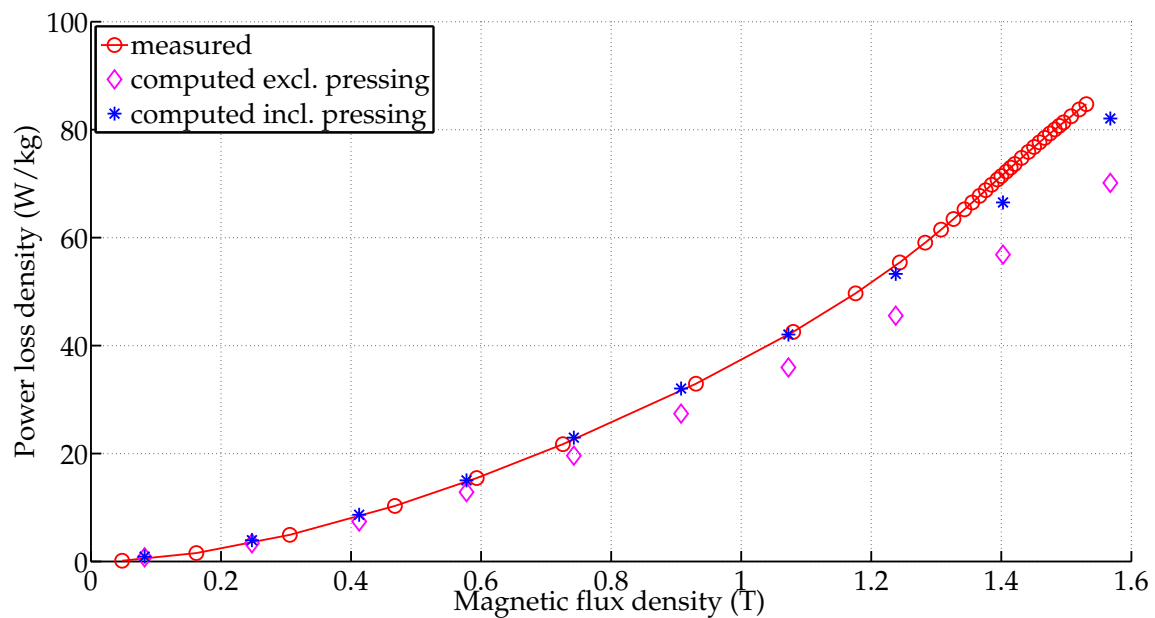


Figure 8.21: Measured and computed loss curves of the investigated laser-cut stator
lamination stack at 50 Hz, material M270-35A.
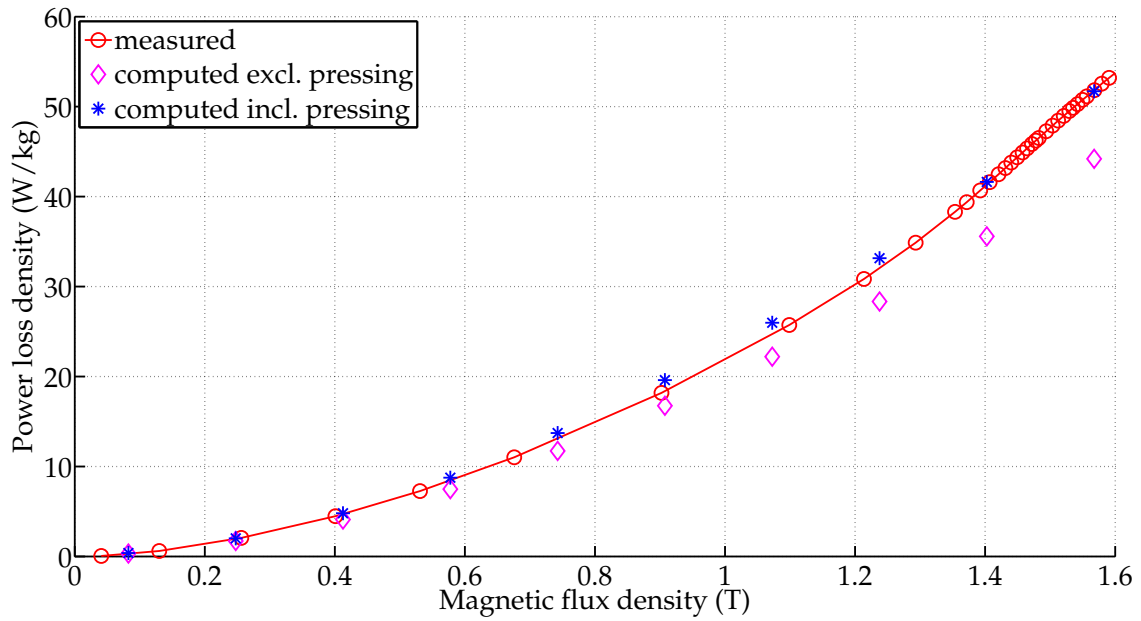
Figure 8.22: Measured and computed loss curves of the investigated laser-cut stator lamination stack at 250 Hz, material M400-50A.
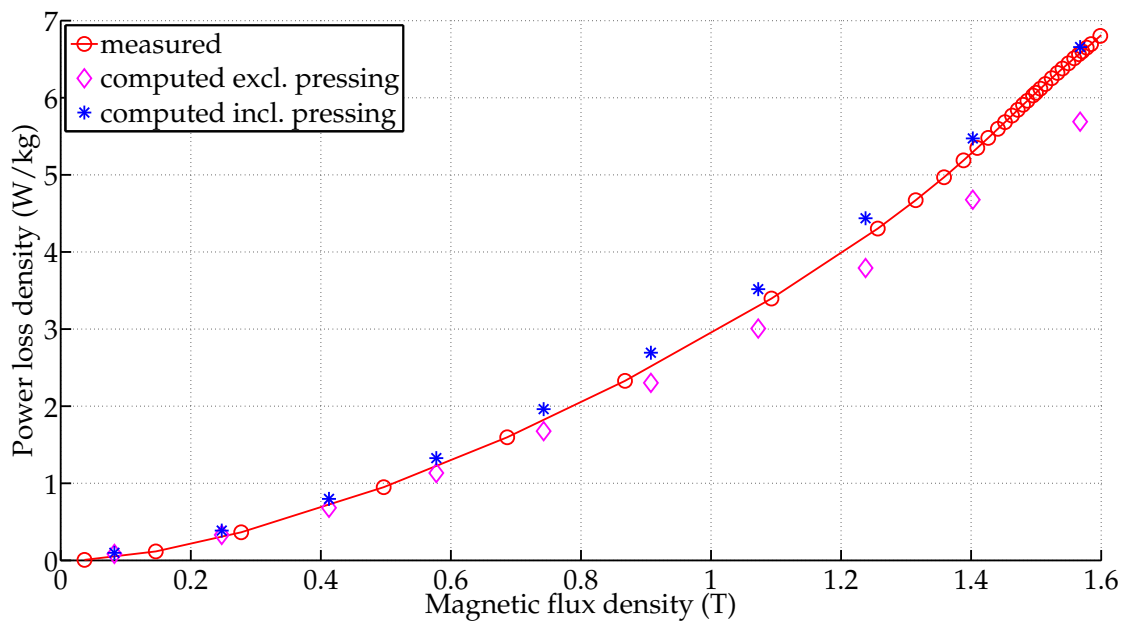


Figure 8.23: Measured and computed loss curves of the investigated laser-cut stator lamination stack at 50 Hz, material M800-65A.

## 8.4 Comparison with results from datasheet values

### 8.4.1 Motivation

The values provided by the manufacturer often differ from those obtained from the customer's own measurements [5]. These differences may be attributed to the following reasons:

1. The samples measured by the customer and those measured by the manufacturer result from different MCs and/or batches. As the authors of [38] previously stated, this may have an influence of up to 7.15 % on the final stator, as in the case of M700-65A.[7]

2. In general, the manufacturer data provided have been obtained from Epstein frame or single sheet tester (SST) measurements. Only some manufacturers do provide the information as to which measurement technique has been used. Considering, for example, standard IEC 60404-3 [87], the size of a sample used in the SST is a multiple larger (10 to 16.67 times wider) compared to the standard Epstein sample. Thus, the degrading influence of cutting and the degraded material zone of the cut edge on the samples' overall magnetic behavior are smaller in contrast to the standard Epstein sample.

3. A further uncertainty is the cutting technique used for the samples measured by the manufacturer (which may, notably for small batches, be laser cutting or guillotining). As shown by, e.g., [45, 169], also the used cutting settings have an influence on the degrading influence of the material.

In the following, the specific loss densities obtained with the proposed modeling approach are compared to those computed from the datasheet values provided by the manufacturer.

### 8.4.2 Simulation

The power loss densities for the same stator geometries are now computed from the loss data provided by the manufacturer in the materials' datasheets which result, in the respective cases, from SST measurements [201–203]. This time, no degraded zone at the cut edge is considered, but homogeneous magnetic properties for the whole material are assumed (Fig. 8.24). These simulations are performed for all investigated materials and frequencies. The material characteristics for 250 Hz are interpolated from those provided for 200 Hz and 400 Hz. The influence of the pressing and gluing is considered as described in Chapter 8.3.3.

---

[7]It is assumed that these deviations also vary with the respective material.
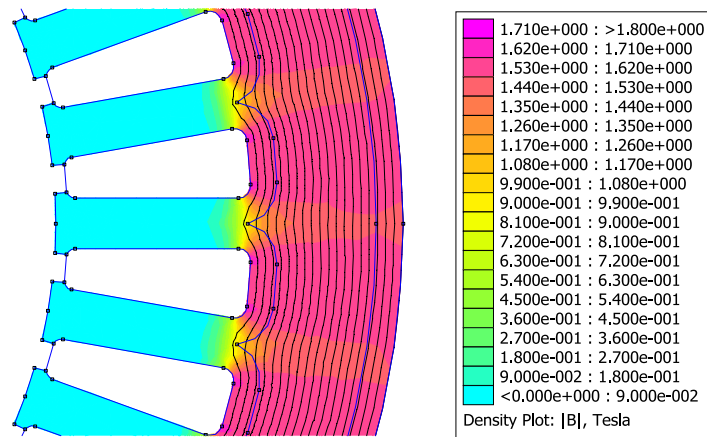
Figure 8.24: Simulated distribution of the magnetic flux density *B* in stator yoke with datasheet values, without considering the cutting effect.

### 8.4.3 Results of mechanically-cut samples

Especially for material M400-50A, significant differences are found between the losses determined by the identification and modeling procedure presented here and those computed from the datasheet values. This concerns a large range of the magnetic flux density *B* and applies to all three investigated frequencies (see Figs. 8.25-8.27).

The situation is less uniform for material M800-65A (see also Figs. E.27-E.29 provided in the Appendix E.3): For all three frequencies investigated it applies that both computed results (material characteristics obtained by the identification procedure vs. datasheet values) are aligned with the measured results until about 1.2 T. With higher magnetic flux densities *B*, the losses computed from the datasheet values increasingly differ from the measured ones. In the case of 50 Hz, this difference is the smallest.

### 8.4.4 Results of laser-cut samples

For both material M270-35A and M400-50A, noteworthy differences between the modeled stator iron losses and losses due to the datasheet values are observed for all three investigated frequencies (see Figs. 8.28-8.30 and Appendix E.3). Again, it concerns almost the whole magnetic flux density range.

This behavior is again less pronounced for material M800-65A (see Appendix E.3), especially for the frequency of 50 Hz. At higher frequencies the computed stator losses computed from datasheet values differ strongly from the measured data from about 1.2 T.

The deviations between the computed results based on the manufacturer data and
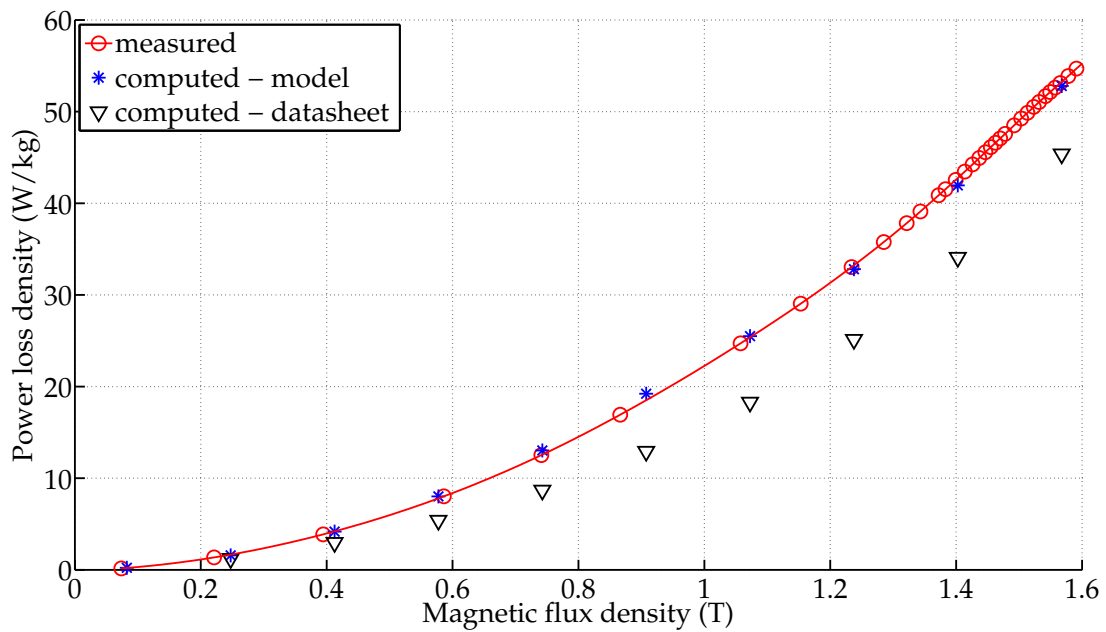
Figure 8.25: Loss curves as measured, as computed using the proposed approach and as determined from datasheet values of the investigated mechanically-cut stator lamination stack at 250 Hz, material M400-50A.
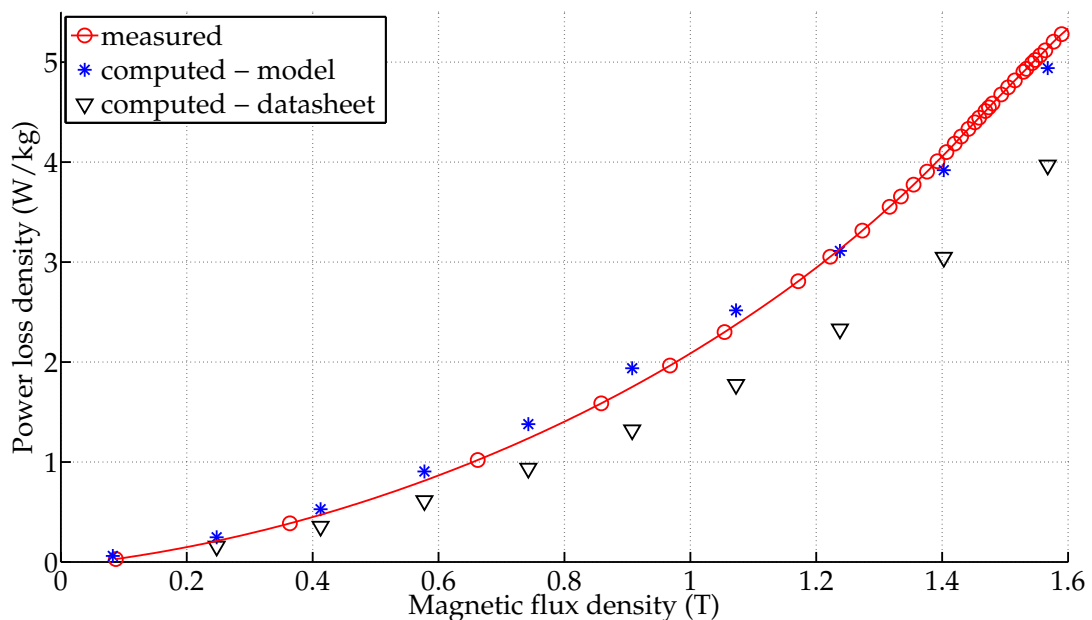


Figure 8.26: Loss curves as measured, as computed using the proposed approach and as determined from datasheet values of the investigated mechanically-cut stator lamination stack at 50 Hz, material M400-50A.
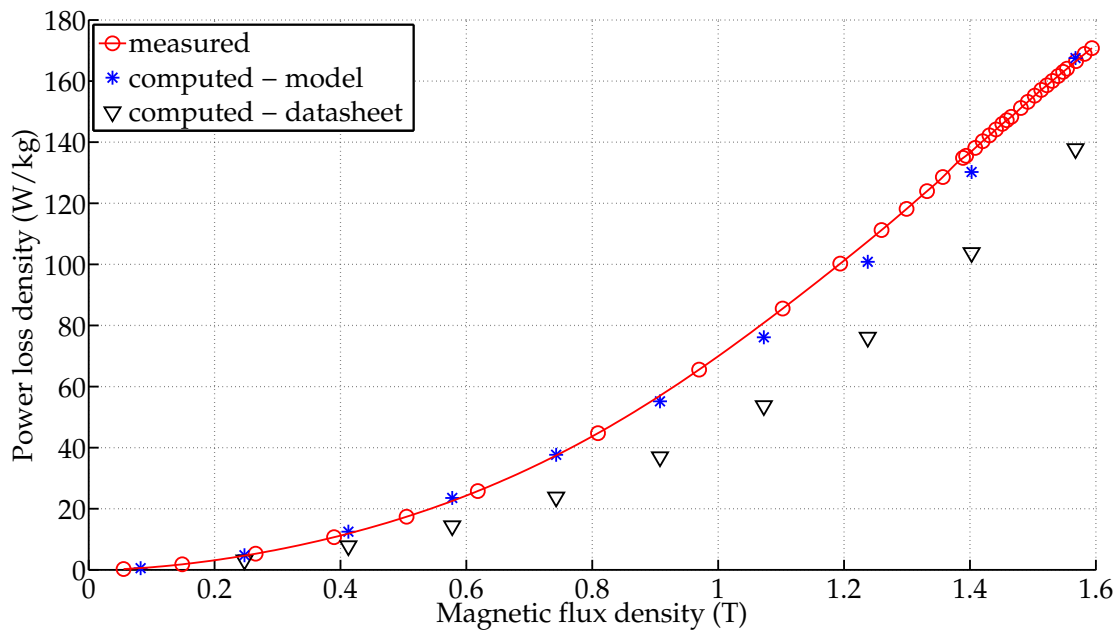
Figure 8.27: Loss curves as measured, as computed using the proposed approach and as determined from datasheet values of the investigated mechanically-cut stator lamination stack at 500 Hz, material M400-50A.
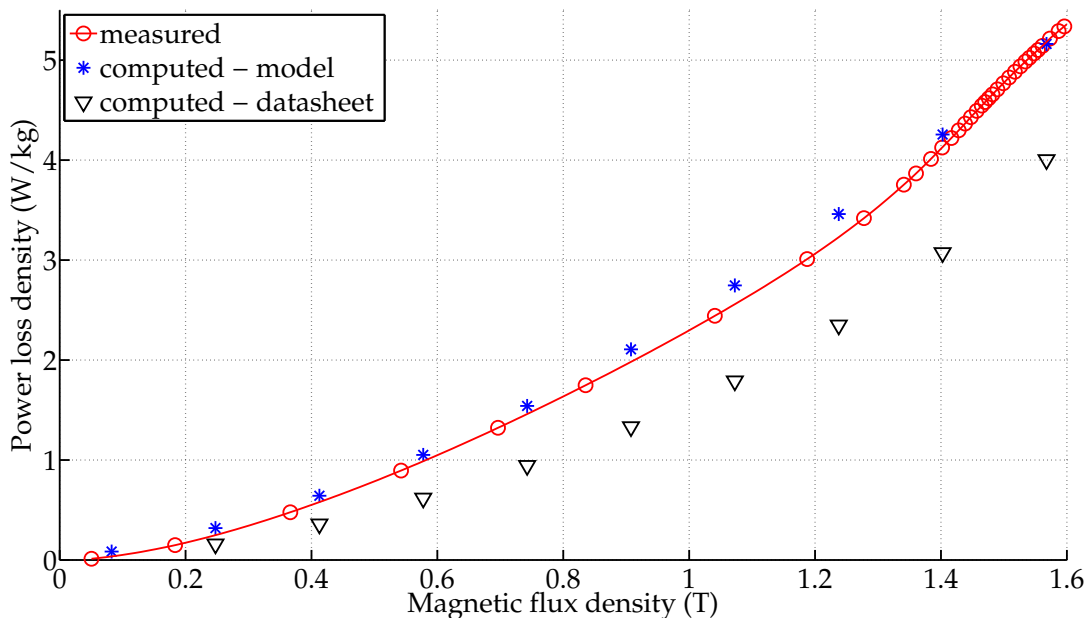


Figure 8.28: Loss curves as measured, as computed using the proposed approach and as determined from datasheet values of the investigated laser-cut stator lamination stack at 50 Hz, material M400-50A.
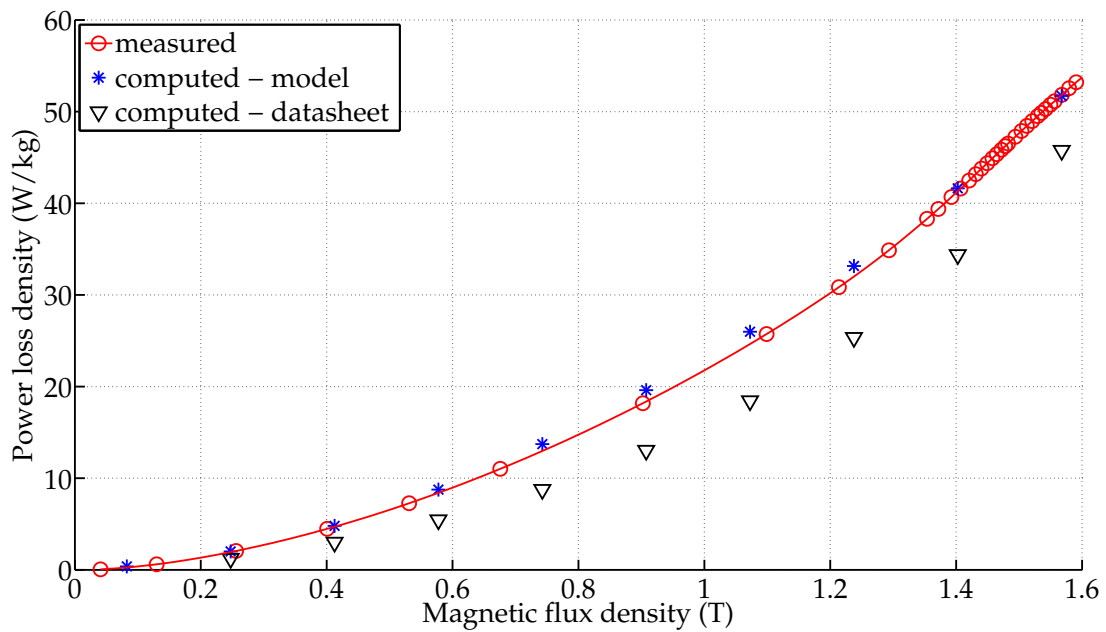
Figure 8.29: Loss curves as measured, as computed using the proposed approach and as determined from datasheet values of the investigated laser-cut stator lamination stack at 250 Hz, material M400-50A.
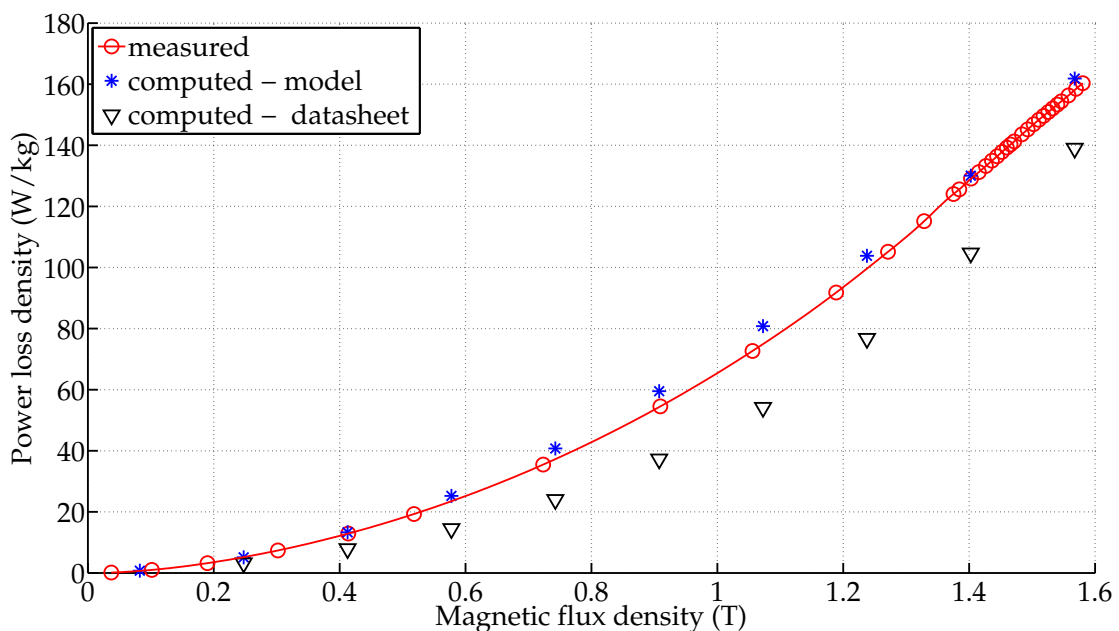


Figure 8.30: Loss curves as measured, as computed using the proposed approach and as determined from datasheet values of the investigated laser-cut stator lamination stack at 500 Hz, material M400-50A.

those resulting from the identification procedure are mainly explained by the fact that the manufacturer data result from sample geometries other than those of the final machine (e.g. stator geometry). Thus, the relative influence of the degradation on the magnetic properties due to cutting differs. For example, it can be assumed that the largest sample size allowed, according to [87] has almost no effect on the overall magnetic properties. Furthermore, the reasons motivating the comparison, outlined above (see Chapter 8.4.1), may contribute to these differences.

It is expected that the difference of measured iron losses and computed iron losses based on datasheet values increase further with increasing ratio $V_{dg}/(V_{nd} + V_{dg})$, e.g., smaller stator yokes. This will apply to laser-cut and mechanically-cut samples. Furthermore, also the difference in cutting technique will become more obvious. Hence, with smaller machine or sample sizes, the use of the presented model is increasingly important to obtain an useful iron loss estimation.

Altogether, the proposed identification and modeling approach provides significantly more accurate results. Note that the difference between the results is not constant with the magnetic flux density $B$ and also differs for various materials[8] (see results of material M400-50A and M800-65A). Furthermore, this difference will change for different geometries, as the ratio of material affected by the cutting and non-degraded material changes, illustrating the limitations of the common use of correction factors.

## 8.5 Summary

A new method is presented to estimate the influence of different cutting techniques (mechanical and laser cutting) on the magnetic properties of electrical steel sheets with geometries different from normal Epstein strips. This identification procedure is based on measurement data obtained by the wide-spread, standardized and fast-to-perform Epstein frame method [86]. The proposed approach eliminates the need of knowing the exact deterioration depth $d$, for which there is still no agreement in literature, and which also depends on the material itself, the cutting technique as well as the settings used with the cutting technique (Chapter 1). The identified magnetization and loss curves of the degraded and the non-degraded material zones with the identification procedure are subsequently implemented in FE simulations of stator lamination stacks with the same degradation depth $d$ as set for the Epstein samples. The lab referenced loss measurements on these stator stacks and the computed losses are closely in line with one another. The reference stator stacks consist of three different materials and have been cut mechanically and by laser

---

[8]Potentially, also the grain size influences this effect.

and are investigated at three different frequencies. In total, this method has been validated for frequencies of up to 500 Hz. Thus, the proposed method allows for the determination of the loss behavior of arbitrary geometries, where both zones with the identified magnetic characteristics are considered. In the last section, the power loss densities of the stator lamination stacks are also computed from datasheet material values provided by the manufacturer. For the cases investigated, using the proposed identification and modeling approach provides significantly more accurate results. Note that the difference between the results is not constant, illustrating the limitations of the common use of correction factors. Furthermore, the results underline the importance of considering the changed magnetic material properties due to different cutting techniques and the good applicability of the presented model.

The advantages of this model are as follows:
- The model bases on an easy and fast-to-perform measurement method.
- Only two measurements are necessary to obtain the needed input data.
- All important information as for example, changed grain size due to cutting and thus changed loss behavior, chemical composition, stresses and strains due to the cutting technique, are included indirectly in the measurement data (black box). Thus, these influences are then also considered in the new computed magnetic characteristics without the need of many and/or complicated material formulas or models.
- The model does not increase the computational time to a noteworthy extent.
- The model represents the loss characteristics well, even for arbitrary geometries.

# Summary

The magnetic properties of electrical steel sheets, such as those typically used in electric machines, are adversely affected by cutting. This work extensively analyzed the effects of three different cutting techniques on those magnetic properties. The samples included conventional Epstein specimens, small strip samples and stacked stator laminations, all resulting from the same mother coil, for a respective material.

This work showed that laser cutting has different effects than mechanical cutting on a sample's magnetic properties. This applies both to the absolute values and the magnetic properties when seen as functions of the magnetic flux density or the field strength. A closer examination of the curve shapes (e.g., 'plateau' of the relative permeability) indicates that laser cutting induces larger compressive stresses within the cut sample than mechanical cutting. Furthermore, the observed points of intersection (POIs), which depend on frequency, geometry and material (here, also grain size), suggest that no cutting technique is universally best. This, in turn, illustrates the need to consider the complete magnetization, loss and permeability curves for selecting the most suitable cutting technique for a given case. This work provides an overview of factors that influence the POI. It thereby provides a first database for selecting a cutting technology.

The differences between the two laser cutting techniques (carbon dioxide and solid state laser) are much smaller (and in the case of stator samples even negligible) than those between laser and mechanical cutting. In general, both laser cutting techniques have the same degrading influence on the magnetic properties with respect to the resulting shapes of the different magnetic properties. The differences observed for the small samples are mainly attributed to differences in sample size (see Chapter 2.1.1) and only to a small extent to the type of the respective laser cutting technique.

This work proposed a new modeling method to estimate the magnetic properties of cut devices of arbitrary geometries. It is based on measurement data obtained by the standardized, wide-spread and fast-to-perform Epstein frame method. The proposed approach eliminates the need to know the exact deterioration depth and is applicable to different cutting techniques. Furthermore, the approach does not require information about specific material characteristics such as (changed) grain size

and chemical composition, as this can be indirectly inferred from the measurement data. The approach uses finite-element simulations of stator lamination stacks, based on the identified magnetization and loss curves of the degraded and non-degraded material zones. It is shown that the results of those simulations corresponded well with the empirical results of the measured stator samples for both mechanical and laser cutting and for different materials and frequencies.

Promising directions for future research include the following:

- A more comprehensive understanding of the magnetic flux distribution of laser-cut samples for different sample sizes and points of operation is required.
- The impact of cutting speed dependent parameters, e.g., possible change of gas pressure and cutting power at small curvatures and edges, at more complicated geometries should be studied in detail.
- The placement of the POIs and their shifting behavior should be explored further.
- Further extensive studies are required which investigate the degrading effects of the subsequent manufacturing steps (pressing, welding, clamping, screwing, packaging), and as a function of the preceding manufacturing step, notably the cutting technique.

# Symbols and Abbreviations

**Symbols**

| SYMBOL | UNIT | NAME |
|---|---|---|
| $b_z$ | m | tooth width |
| $B$ | T | magnetic flux density |
| $B_{dg}$ | T | flux density in the degraded material zone |
| $B_{nd}$ | T | flux density in the non-degraded material zone |
| $B_r$ | T | remanent flux density |
| $c_i$ | | coefficients |
| CL | m/kg | specific cutting length |
| $d$ | mm | degradation depth |
| $d_g$ | $\mu$m | grain size diameter |
| $D_a$ | mm | outer diameter |
| $f$ | Hz | frequency |
| $h_{yoke}$ | mm | yoke height |
| $H$ | A/m | magnetic field strength |
| $H_c, H_{cB}$ | A/m | coercive magnetic field strength |
| $I$ | A | current |
| $I_1, i_1$ | A | primary current |
| $J$ | T | magnetic polarization |
| $l$ | m | length |
| $l_{Fe}$ | mm | stator sample length |
| $l_y$ | m | sample length |
| $2L$ | m | domain wall spacing in the demagnetized state |
| $m$ | kg | weight |
| $m_{yoke}$ | kg | yoke weight |
| $M$ | H | mutual inductance |
| $M$ | A/m | magnetization |
| $p_{dg}$ | T | specific losses in the degraded material zone |
| $p_a, p_{exc}$ | W/kg | anomalous or excess loss |
| $p_e$ | W/kg | eddy current loss |

| | | |
|---|---|---|
| $p_{ec}$ | W/kg | classical eddy current loss |
| $p_h$ | W/kg | hysteresis loss |
| $p_{loss}, p_s$ | W/kg | specific loss |
| $p_{nd}$ | T | specific losses in the non-degraded material zone |
| $p_s$ | W/kg | specific loss |
| $R$ | $\Omega$ | resistance |
| $s''$ | | standard deviation |
| $S_w$ | mm$^2$ | total winding cross sectional area |
| $t$ | s | time |
| $U, u$ | V | voltage |
| $U_1, u_1$ | V | primary voltage |
| $U_2, u_2$ | V | secondary voltage |
| $V_{dg}$ | m$^3$ | degraded material volume |
| $V_{nd}$ | m$^3$ | non-degraded material volume |
| $w$ | - | number of turns |
| $w_{lc}$ | A/m | loop center width |
| $w_z$ | m | thickness of electrical steel sheet sample |
| $w_1, w_2$ | m | sample width of sample 1 and 2 |
| $z$ | - | number of teeth |
| $\gamma_1, \gamma_2$ | - | fractions of degraded material in samples 1 and 2 |
| $\lambda$ | - | magnetostriction |
| $\lambda_s$ | - | saturation magnetostriction |
| $\mu_r$ | - | relative permeability |
| $\mu_{r,\,max}$ | - | peak value of the relative permeability |
| $\rho$ | kg/m$^3$ | density |
| $\rho_E$ | $\Omega$m | specific electrical resistance |

## Abbreviations

| ABBREVIATION | NAME |
|---|---|
| Al | aluminum |
| $CO_2$ | carbon dioxide laser |
| cw | continuous wave |
| EBSD | electron backscatter diffraction |
| Fe | iron |
| FEM | finite element method |

| FKL | solid state laser |
|---|---|
| HAZ | heat affected zone |
| He | helium |
| lc | laser-cut |
| LL | longitudinally-cut samples |
| mc | mechanically-cut |
| MC | mother coil |
| MIX | sample set consisting of half longitudinally-cut and half transversely-cut specimens |
| Mn | manganese |
| Nd | neodymium |
| N, $N_2$ | nitrogen |
| -o | samples clamped upwards |
| POI(s) | point(s) of intersection |
| QQ | transversely-cut samples |
| S | sulfur |
| SEM | scanning electron microscope |
| Si | silicon |
| SS | mechanical cutting: guillotine |
| -u | samples clamped downwards |
| YAG | yttrium aluminum garnet |
| Yb | ytterbium |
| wt% | weight percentage |

# Bibliography

[1] Surahammars Bruks AB, email correspondence, January 27, 2014.

[2] E. A. Abdul-Zade, A. Kh. Gasanov, and R. M. Talybov, *Influence of laser cutting on the electromagnetic characteristics of electrical steels*, Elektrotekhnika **59** (1988), no. 6, 59–60.

[3] Oxford Instruments Analytical, *Electron backscattered diffraction explained*, www.metallography.com/experts/EBSD_explained_by_OxfordInstruments.pdf, accessed on 2015.11.26.

[4] E. G. Araujo, Jürgen Schneider, Kim Verbeken, Pasquarella G., and Houbaert Y., *Dimensional effects on magnetic properties of Fe-Si steels due to laser and mechanical cutting*, IEEE Transactions on Magnetics **46** (2010), no. 2, 213–216.

[5] W. M. Arshad, T. Ryckebusch, F. Magnussen, H. Lendenmann, B. Eriksson, J. Soulard, and B. Malmros, *Incorporating lamination processing and component manufacturing in electrical machine design tools*, Industry Applications Conference, 2007. 42nd IAS Annual Meeting. Conference Record of the 2007 IEEE, Sept 2007, pp. 94–102.

[6] M. Bali, H. De Gersem, and A. Muetze, *Finite-element modeling of magnetic material degradation due to punching*, IEEE Transactions on Magnetics **50** (2014), no. 2, 745–748.

[7] J. Barros, T. Ros-Yañez, L. Vandenbossche, L. Dupré, J. Melkebeek, and Y. Houbaert, *The effect of Si and Al concentration gradients on the mechanical and magnetic properties of electrical steel*, Journal of Magnetism and Magnetic Materials **290 - 291** (2005), 1457 – 1460, Proceedings of the Joint European Magnetic Symposia (JEMS' 04).

[8] V. Basso, *Hysteresis models for magnetization by domain wall motion*, IEEE Transactions on Magnetics **34** (1998), no. 4, 2207–2212.

[9] V. Basso and G. Bertotti, *Hysteresis models for the description of domain wall motion*, IEEE Transactions on Magnetics **32** (1996), no. 5, 4210–4212.

[10] P. Baudouin, *Effect of laser and mechanical cutting on the magnetic properties of non-oriented electrical steels*, Ph.D. thesis, Universiteit Gent, 2002.

[11] P. Baudouin, A. Belhadj, F. Breaban, A. Deffontaine, and Y. Houbaert, *Effects of laser and mechanical cutting modes on the magnetic properties of low and medium Si content nonoriented electrical steels*, IEEE Transactions on Magnetics **38** (2002), no. 5, 3213–3215.

[12] P. Baudouin, M. De Wulf, L. Kestens, and Y. Houbaert, *The effect of the guillotine clearance on the magnetic properties of electrical steels*, Journal of Magnetism and Magnetic Materials **256** (2003), 32–40.

[13] A. Belhadj, P. Baudouin, F. Breaban, A. Deffontaine, M. Dewulf, and Y. Houbaert, *The effect of laser cutting in microstructure and on magnetic properties of grain non-oriented electrical steels*, Journal of Magnetism and Magnetic Materials **256** (2003), 20–31.

[14] Helmholtz Zentrum Berlin, *Texture and microstructure analysis*, https://www.helmholtz-berlin.de/forschung/oe/em/mikro/arbeitsgebiete/textur_de.html, accessed on 2016.01.14.

[15] G. Bertotti, *General properties of power losses in soft ferromagnetic materials*, IEEE Transactions on Magnetics **24** (1988), no. 1, 621–630.

[16] _____, *Hysteresis in magnetism: for physicists, materials scientists, and engineers*, Academic Press, San Diego, Calif. [u. a.], 2008 (English).

[17] G. Bertotti and M. Pasquale, *Physical interpretation of induction and frequency dependence of power losses in soft magnetic materials*, IEEE Transactions on Magnetics **28** (1992), no. 5, 2787–2789.

[18] K. Binder, *Monte Carlo simulation in statistical physics: an introduction*, vol. 80, Springer, 1992.

[19] K. Binder, *Applications of Monte Carlo methods to statistical physics*, Reports on Progress in Physics **60** (1997), no. 5, 487–559.

[20] A. Boehm and I. Hahn, *Influence of geometric parameters and cutting edge deterioration on the differential inductances*, Sensorless Control for Electrical Drives (SLED), 2014 IEEE 5th International Symposium on, May 2014, pp. 1–6.

[21] A. Boglietti, *A first approach for the iron losses building factor determination*, Industry Applications Conference, 1999. Thirty-Fourth IAS Annual Meeting. Conference Record of the 1999 IEEE, vol. 1, 1999, pp. 489–493.

[22] A. Boglietti, A. Cavagnino, L. Ferraris, and M. Lazzari, *The annealing influence onto the magnetic and energetic properties in soft magnetic material after punching process*, IEEE International, Electric Machines and Drives Conference **1** (2003), 503–508.

[23] R. Boll, *Weichmagnetische Werkstoffe, Einführung in den Magnetismus, VAC-Werkstoffe und ihre Anwendungen*, 4. Auflage, Siemens Aktiengesellschaft, Berlin und München, 1993.

[24] F. Bölling, M. Espenhahn, K. Günther, M. Hastenrath, and H. Huneus, *Trends und Ziele in der Entwicklung hochwertiger Elektrobleche*, Stahl und Eisen **107** (1987), no. 23, 1119–1124.

[25] F. Bölling, H. Pottgiesser, and K. H. Schmidt, *Hochwertiges Elektroblech für die Energietechnik*, Stahl und Eisen **102** (1982), no. 17, 833–837.

[26] R. M. Bozorth, *Ferromagnetism*, Wiley-VCH, 1993.

[27] N. Brachthäuser, *Elektromobilität - Neue Herausforderungen an den Werkstoff Elektroband*, http://www.cdw.de/home/News/Aktuelles/Elektromobilitaet

[28] F. Brailsford, *Magnetic materials, second editions*, London: Methuen & Co. LTD.; New York: John Wiley & Sons, Inc., 1951.

[29] J. R. Brauer, *Simple equations for the magnetization and reluctivity curves of steel*, IEEE Transactions on Magnetics **11** (1975), no. 1, 81–81.

[30] M. Braun, unpublished, personal discussion, 2013, Dr.-Ing. Ernst Braun GmbH.

[31] G. Buchfink, *Werkzeug Laser: Ein Lichtstrahl erobert die industrielle Fertigung, second edition*, Vogel Buchverlag, Würzburg, 2008.

[32] D. P. Bulte and R. A. Langman, *Origins of the magnetomechanical effect*, Journal of Magnetism and Magnetic Materials **251** (2002), no. 2, 229–243.

[33] M. Carlberg, 1971, Surahammars Bruks AB, Stockholm.

[34] J. J. Cathey, *Electric machines: Analysis and design applying MATLAB*, McGraw-Hill, 2001.

[35] S. Chatterjee, D. Bhattacharjee, and N. Gope, *Variation in structure and magnetic properties during decarb-annealing of electrical steel*, Scripta Materialia **49** (2003), no. 5, 355–360.

[36] C. W. Chen, *Temperature dependence of magnetic properties of silicon-iron*, Journal of Applied Physics **29** (1958), no. 9, 1337–1343.

[37] T. Chevalier, A. Kedous-Lebouc, and B. Cornut, *Influence of electrical sheet width on dynamic magnetic properties*, Journal of Magnetism and Magnetic Materials **215-216** (2000), 623–625.

[38] A. J. Clerc and A. Muetze, *Measurement of stator core magnetic degradation during the manufacturing process*, IEEE Transactions on Industry Applications **48** (2012), no. 4, 1344–1352.

[39] G. Crevecoeur, L. Dupré, L. Vandenbossche, and R. Van de Walle, *Local identification of magnetic hysteresis properties near cutting edges of electrical steel sheets*, IEEE Transactions on Magnetics **44** (2008), no. 6, 1010–1013.

[40] G. Crevecoeur, P. Sergeant, L. Dupré, L. Vandenbossche, and R. Van de Walle, *Analysis of the local material degradation near cutting edges of electrical steel sheets*, IEEE Transactions on Magnetics **44** (2008), no. 11, 3173–3176.

[41] A. Daikoku, M. Nakano, S. Yamaguchi, Y. Tani, Y. Toide, H. Arita, T. Yoshioka, and C. Fujino, *An accurate magnetic field analysis for estimating motor characteristics taking account of stress distribution in the magnetic core*, IEEE Transactions on Industry Applications **42** (2006), no. 3, 668–674.

[42] M. F. de Campos, M. Emura, and F. J. G. Landgraf, *Consequences of magnetic aging for iron losses in electrical steels*, Journal of Magnetism and Magnetic Materials **304** (2006), e593–e595.

[43] Y. Demir, O. Ocak, Y. Ulu, and M. Aydin, *Impact of lamination processing methods on performance of permanent magnet synchronous motors*, Proceedings of ICEM 2014 (ISBN: 978-1-4799-4775-1) XXIst International Conference on Electrical Machines, Berlin, 2014, pp. 1218–1223.

[44] W. Deprez, J. Schneider, T. Kochmann, F. Henrotte, and K. Hameyer, *Influence of the manufacturing process on the magnetic properties of electrical steel in e-cores*, Stahleisen (2004), 167–171.

[45] K. Dickmann, *Untersuchungen über den Einsatz von Hochleistungslasern zum Trennen von Elektroblechen*, Ph.D. thesis, Universität Hannover, 1989.

[46] _____, *Einfluss des Lasertrennens auf die magnetischen Eigenschaften von Elektroblech*, Stahl und Eisen **110** (1990), no. 12, 147–153.

[47] H.-D. Dietze and H. Thomas, *Bloch und Néel-Wände in dünnen ferromagnetischen Schichten*, Zeitschrift für Physik **163** (1961), 523–534.

[48] D. Dorner, K. Telger, A. Basteck, and M. Tietz, *Nichtkornorientiertes (NO-) Elektroband zur Herstellung von elektrischen Antrieben für Kraftfahrzeuge*, techforum (2009), no. 1, 28–33.

[49] L. Dupré, G. Bertotti, and J. Melkebeek, *Dynamic preisach model and energy dissipation in soft magnetic materials*, IEEE Transactions on Magnetics **34** (1998), no. 4, 1168–1170.

[50] Ebertshaeuser, *Technologie und Blechverarbeitung (8)*, Bänder Bleche Rohre **7** (1966), no. 9, 636/47.

[51] M. Emura, F. J. G. Landgraf, W. Ross, and J. R. Barreta, *The influence of cutting technique on the magnetic properties of electrical steels*, Journal of Magnetism and Magnetic Materials **254-255** (2003), 358–360.

[52] *DIN EN 10106, Kaltgewalztes nicht kornorientiertes Elektroblech und -band im schlussgeglühten Zustand*, Dez. 1995.

[53] Finite Element Method Magnetics (FEMM), http://www.femm.info, accessed on 2016.02.23.

[54] R. Fischer, *Elektrische Maschinen, 15th edition*, Carl Hanser Verlag München, 2011.

[55] H. Föll, *Ferromagnetismus und magnetische Domänen*, http://www.tf.uni-kiel.de/matwis/amat/mw_for_et/kap_7/backbone/r7_2_1.html, accessed on 2016.01.18.

[56] Institute for Electron Microscopy and Nanoanalysis (FELMI), 2015, Graz University of Technology.

[57] K. Fujisaki, R. Hirayama, T. Kawachi, S. Satou, C. Kaidou, M. Yabumoto, and T. Kubota, *Motor core iron loss analysis evaluating shrink fitting and stamping by finite-element method*, IEEE Transactions on Magnetics **43** (2007), no. 5, 1950–1954.

[58] K. Fujisaki and S. Satoh, *Numerical calculations of electromagnetic fields in silicon steel under mechanical stress*, IEEE Transactions on Magnetics **40** (2004), no. 4, 1820–1825.

[59] D. Gaworska-Koniarek, B. Szubzda, W. Wilczynski, J. Drosik, and K. Karas, *The influence of assist gas on magnetic properties of electrotechnical steel sheets cut with laser*, Journal of Physics: Conference Series **303** (2011), no. 1, 012091.

[60] Dr. Steingroever GmbH, *Remagraph C-500*.

[61] Prokutech GmbH, *Laserbearbeitung Leistungen*, http://www.prokutec.de/-laserbearbeitung_technologie.html, accessed on 2016.03.09.

[62] Z. Gmyrek and A Cavagnino, *Analytical method for determining the damaged area width in magnetic materials due to punching process*, IECON 2011 - 37th Annual Conference on IEEE Industrial Electronics Society, Nov 2011, pp. 1764–1769.

[63] Z. Gmyrek, A Cavagnino, and L. Ferraris, *Estimation of magnetic properties and damaged area width due to punching process: Modeling and experimental research*, Electrical Machines (ICEM), 2012 XXth International Conference on, Sept 2012, pp. 1301–1308.

[64] Z. Gmyrek, A. Cavagnino, and L. Ferraris, *Estimation of the magnetic properties of the damaged area resulting from the punching process: Experimental research and fem modeling*, IEEE Transactions on Industry Applications **49** (2013), no. 5, 2069–2077.

[65] P. Goes, E. Hoferlin, and M. De Wulf, *Calculating iron losses taking into account effects of manufacturing processes*, COMSOL Conference Hannover, Proceedings, 2008, pp. 1–6.

[66] G. P. Gogue and J. J. Jr. Stupak, *Theory & practice of electromagnetic design of dc motors & actuators*, G2 Consulting, Beaverton, OR 97007, 1993.

[67] C. Grünzweig, C. David, O. Bunk, M. Dierolf, G. Frei, G. Kühne, J. Kohlbrecher, R. Schäfer, P. Lejcek, H. M. R. Rønnow, and F. Pfeiffer, *Neutron decoherence imaging for visualizing bulk magnetic domain structures*, Phys. Rev. Lett. **101** (2008), 025504.

[68] S. Günther, R. Siebert, E. Beyer, and W. Hofmann, *Einfluss der Bearbeitung von Elektroblechen auf die Verluste elektrischer Fahrmotoren*, ETG-Fachbericht-EMA 2012, Nürnberg, 2013.

[69] P. Handgruber, *Advanced eddy currents and hysteresis loss models for steel laminations of rotating electrical machines*, Ph.D. thesis, Graz University of Technology, 2015.

[70] H. Harbrecht, *On output functionals of boundary value problems on stochastic domains*, Mathematical Methods in the Applied Sciences **33** (2010), no. 1, 91–102.

[71] S. Hartl, *Magnetic properties of deformed electrical steel*, Master's thesis, TU Wien, 2014.

[72] J. Hast, *Mobiler Analysen–Dienst an metallischen Werkstoffen, Bempflingen*, Jul. 2013.

[73] H. Hattendorf, *VDM Report Nr. 27, Weichmagnetische Werkstoffe auf Ni-Fe-Basis*, Thyssen Krupp VDM GmbH (2003), 4.

[74] J. Heath and N. Taylor, *Electron backscatter diffraction*, John Wiley & Sons Ltd., Second Edition, 2015, accessed on 2015.11.26.

[75] E. Hering and G. Schöfelder, *Sensoren in Wissenschaft und Technik*, Springer Vieweg + Teubner Verlag, 2012.

[76] Y. Hidaka, S. Furui, and H. Igarashi, *Robust optimization considering probabilistic magnetic degradation*, CEFC 2014, Annecy, France, May 2014, pp. 1–4.

[77] _____, *Robust optimization considering probabilistic magnetic degradation*, Transactions on Magnetics **51** (2015), no. 3, 1–4.

[78] R. Hilzinger and D. Rodewald, *Magnetic materials: fundamentals, products, properties, applications*, Publicis Publishing, Erlangen, 2013.

[79] A. Honda, B. Fukuda, I. Ohyama, and Y. Mine, *Effects of magnetic properties of nonoriented electrical steel sheets on motor efficiency*, Journal of Materials Engineering **12** (1990), no. 1, 41–45 (English).

[80] A. Honda, M. Kawano, M. Ishida, S. Keiji, K. Michiro, and O. Isamu, *Efficiency of model induction motor using various non-oriented electrical steels*, Journal of Materials Science and Technology **16** (2000), no. 2, 238–243.

[81] C.-K. Hou, *Effect of silicon on the loss separation and permeability of laminated steels*, Journal of Magnetism and Magnetic Materials **162** (1996), 280–290.

[82] O. Hubert and E. Hug, *Influence of plastic strain on magnetic behaviour of non-oriented Fe-3Si and application to manufacturing test by punching*, Materials Science and Technology **11** (1995), 482–487.

[83] M. Ibrahim and P. Pillay, *Advanced testing and modeling of magnetic materials including a new method of core loss separation for electrical machines*, Energy Conversion Congress and Exposition (ECCE), 2011 IEEE, 2011, pp. 706–713.

[84] *IEC 60404-1, Magnetic materials: Classification*, 2000.

[85] *IEC 60404-10, Magnetic materials - Methods of measurement of magnetic properties of magnetic steel sheet and strip at medium frequencies*, 1988.

[86] *IEC 60404-2, Magnetic materials - Part 2: Methods of measurements of the magnetic properties of electrical steel sheet and strip by means of an Epstein frame*, 1996.

[87] *IEC 60404-3, Magnetic materials - Part 3: Methods of measurement of the magnetic properties of electrical steel strip and sheet by means of a single sheet tester*, 2010.

[88] *IEC 60404-4, Magnetic materials - Part 4: Methods of measurement of d.c. magnetic properties of iron and steel*, 1995.

[89] *IEC 60404-8-6, Magnetic materials - Part 8-6: Specifications for individual materials - Soft magnetic metallic materials*, 1999.

[90] *IEC 62044-3, Cores made of soft magnetic materials - Measuring methods - Part 3: Magnetic properties at high excitation level*, 2000.

[91] Oxford Instruments, http://www.ebsd.com/ebsd-analysis/ebsd-experimental-techniques/sample-preparation, accessed on 2015.11.26.

[92] D. M. Ionel, M. Popescu, S. J. Dellinger, T. J. E. Miller, R. J. Heideman, and M. I. McGilp, *On the variation with flux and frequency of the core loss coefficients in electrical machines*, IEEE Transactions on Industry Applications **42** (2006), no. 3, 658–667.

[93] V. E. Iordache, E. Hug, and N. Buiron, *Magnetic behaviour versus tensile deformation mechanisms in a non-oriented Fe-(3 wt.%)Si steel*, Materials Science and Engineering **A359** (2003), 62–74.

[94] S. Jacobs, F. Henrotte, M. Herranz Gracia, K. Hameyer, P. Goes, and D. Hectors, *Magnetic material optimization for hybrid vehicle PMSM drives*, World Electric Vehicle Journal (www.evs24.org/wevajournal) **3** (2009), 1–9.

[95] D. C. Jiles, *Theory of the magnetomechanical effect*, Journal of Physics D: Applied Physics **28** (1995), no. 8, 1537–1546.

[96] *JIS C 2552, Cold-rolled non-oriented electrical steel strip and sheet delivered in the fully-processed state*, 2014.

[97] Y. Kai, Y. Tsuchida, T. Todaka, and M. Enokizono, *Influence of stress on vector magnetic property under alternating magnetic flux conditions*, IEEE Transactions on Magnetics **47** (2011), no. 10, 4344–4347.

[98] M. Kawabe, T. Nomiyama, A. Shiozaki, M. Mimura, N. Takahashi, and M. Nakano, *Magnetic properties of particular shape specimen of nonoriented electrical steel sheet under compressive stress in thickness direction*, IEEE Transactions on Magnetics **48** (2012), no. 11, 3462–3465.

[99] A. Kedous-Lebouc, B. Cornut, J. C. Perrier, Ph. Manifé, and Th. Chevalier, *Punching influence on magnetic properties of the stator teeth of an induction motor*, Journal of Magnetism and Magnetic Materials **254-255** (2003), 124–126.

[100] M. Kersten, *Zur magnetischen Analyse der inneren Spannungen*, Zeitschrift für Physik **76** (1932), no. 7-8, 505–512.

[101] _____, *Zur Deutung der Koerzitivkraft in: Probleme der technischen Magnetisierungskurve*, pp. 42–47, published by R. Becker, 1938.

[102] _____, *Grundlage einer Theorie der ferromagnetischen Hysterese und der Koerzitivkraft*, Verlag v. S. Hirzel/Leipzig, 1944.

[103] Dr. Brockhaus Messtechnik GmbH & Co. KG, *Brockhaus Messtechnik*.

[104] Spitzenberger & Spies GmbH & Co. KG, *data sheet, 4-Quadranten-Verstärker Typ PAS 5000*.

[105] A. Krings, *Iron losses in electrical machines*, Ph.D. thesis, KTH Royal Institute of Technology, School of Electrical Engineering, 2014.

[106] A. Krings, S. Nategh, O. Wallmark, and J. Soulard, *Influence of the welding process on the magnetic properties of a slot-less permanent magnet synchronous machine stator core*, Electrical Machines (ICEM), 2012 XXth International Conference on, 2012, pp. 1333–1338.

[107] I. Kucuk, K. Erturk, M. C. Haciismailoglu, and N. Derebasi, *Modelling of power loss in electrical steels*, Acta Physica Polonica A **113** (2008), no. 1, 147–150.

[108] K. Kunze, *State of the art in EBSD*, EMAS 2009, 11th European workshop, 2009, Electron Microscopy ETH Zürich.

[109] Kups, *Wiedemann-Franz-Lorenzsches Gesetz*, https://www.tu-ilmenau.de/-fileadmin/media/wt/Lehre/Praktikum/Werkstoffwissenschaft_WSW/1._Fach-semester/_Wiede__Wiedemann_Franz_Gesetz_v2015.pdf, accessed on 2016.02.21.

[110] Y. Kurosaki, H. Mogi, H. Fujii, T. Kubota, and M. Shiozaki, *Importance of punching and workability in non-oriented electrical steel sheets*, Journal of Magnetism and Magnetic Materials **320** (2008), 2474–2480.

[111] L. D. Landau and E. Lifshiz, *On the theory of the dispersion of magnetic permeability in ferromagnetic bodies*, Phys. Z. Sowjetunion **8** (1935), 153–169.

[112] F. Landgraf, M. Emura, J. C. Teixeira, and M. F. de Campos, *Effect of grain size, deformation, aging and anisotropy on hysteresis loss of electrical steels*, Journal of Magnetism and Magnetic Materials **215-216** (2000), no. 1, 97–99.

[113] F. J. G. Landgraf and M. Emura, *Losses and permeability improvement by stress relieving fully processed electrical steels with previous small deformations*, Journal of Magnetism and Magnetic Materials **242-245** (2002), 152–156.

[114] L. Lanotte, C. Luponio, I. De Iorio, V. Tagliaferri, and G. Tammaro, *Effect of laser cutting on magnetic properties of grain oriented Fe-Si ribbons*, Materials Science and Technology **8** (1992), 252–256.

[115] R. Laska and C. Felsch, *Werkstoffkunde für Ingenieure*, Friedr. Vieweg & Sohn Verlagsgesellschaft mbH, Braunschweig, 1987.

[116] J. Lemaitre, J. Dufailly, and R. Billardon, *Damage evaluation through microhardness measurements*, Comptes Rendus De L Academie Des Sciences Serie II **304** (1987), no. 12, 601–604.

[117] Y. Liu, S. K. Kashif, and A. M. Sohail, *Engineering considerations on additional iron losses due to rotational fields and sheet cutting*, Proceedings of the 2008 International Conference on Electrical Machines, 2008.

[118] M. LoBue, C. Sasso, V. Basso, F. Fiorillo, and G. Bertotti, *Power losses and magnetization process in Fe-Si non-oriented steels under tensile and compressive stress*, Journal of Magnetism and Magnetic Materials **215-216** (2000), 124–126.

[119] G. Loisos and A. J. Moses, *Effect of mechanical and Nd:YAG laser cutting on magnetic flux distribution near the cut edge of non-oriented steels*, Journal of Materials Processing Technology **161** (2005), 151–155.

[120] J. B. Lorenzo, T. Ros-Yanez, M. De Wulf, and Y. Houbaert, *Magnetic properties of electrical steel with Si and Al concentration gradients*, IEEE Transactions on Magnetics **40** (2004), no. 4, 2739–2741.

[121] E. Macherauch and H.-W. Zoch, *Praktikum in Werkstoffkunde, 12th edition*, Springer Vieweg, 2014.

[122] Magnettechnik Dr. Kleine, *Magnetostriktion von FeSi - Elektrobändern*, http://www.anic.de/magtech/messung.html, accessed on 2016.01.19.

[123] M. J. Manyage, T. L. Mthombeni, P. Pillay, and A. Boglietti, *Improved prediction of core losses in induction motors*, Electric Machines and Drives Conference, 2007. IEMDC '07. IEEE International, vol. 1, 2007, pp. 531–536.

[124] H. Marouani, A. Ben Ismail, E. Hug, and M. Rachik, *Rate-dependent constitutive model for sheet metal blanking investigation*, Material Science and Engineering A **487** (2008), 162–170.

[125] Matlab, http://mathworks.com/products/matlab, accessed on 2015.03.19.

[126] T. Matsubara, M. Nakata, Nakano, and Monden, IEEJ Nat'l Conv., 1988, 1665.

[127] K. Matsumura and B. Fukuda, *Recent developments of non-oriented electrical steel sheets*, IEEE Transactions on Magnetics **MAG.-20** (1984), no. 5, 1533–1538.

[128] V. Maurel, F. Ossart, and R. Billardon, *Residual stresses in punched laminations: Phenomenological analysis and influence on the magnetic behavior of electrical steels*, Journal of Applied Physics **93** (2003), no. 10, 7106–7108.

[129] R. A. McCurie, 1994, Ferromagnetic materials - structure and properties, Academic Press, San Diego, CA.

[130] M. Merkel and K.-H. Thomas, *Taschenbuch der Werkstoffe*, 5th revised ed., Fachbuchverlag Leipzig im Carl Hanser Verlag, München; Wien, 2000.

[131] L. Michalowsky, J. Schneider, and S. Siebert, *Magnettechnik: Grundlagen, Werkstoffe, Anwendungen*, p. 44, Vulkan-Verlag, 2006.

[132] D. Miyagi, Y. Aoki, M. Nakano, and N. Takahashi, *Effect of compressive stress in thickness direction on iron losses of nonoriented electrical steel sheet*, IEEE Transactions on Magnetics **46** (2010), no. 6, 2040–2043.

[133] D. Miyagi, K. Miki, M. Nakano, and N. Takahashi, *Influence of compressive stress on magnetic properties of laminated electrical steel sheets*, IEEE Transactions on Magnetics **46** (2010), no. 2, 318–321.

[134] A. J. Moses, N. Derebasi, G. Loisos, and A. Schoppa, *Aspects of the cut-edge effect stress on the power loss and flux density distribution in electrical steel sheets*, Journal of Magnetism and Magnetic Materials **215-216** (2000), 690–692.

[135] A. Mouillet, J. L. Ille, M. Akroune, and M. A. Dami, *Magnetic and loss characteristics of nonoriented silicon-iron under unconventional conditions*, Science, Measurement and Technology, IEE Proceedings - **141** (1994), no. 1, 75–78.

[136] G. Müller, K. Vogt, and B. Ponick, *Berechnung elektrischer Maschinen*, Wiley-VCH Verlag GmbH & Co. KGaA, Weinheim, Germany, 2008.

[137] R. L. Nailen, *The truth about motor core loss*, 1983.

[138] T. Nakata, M. Nakano, and K. Kawahara, *Effects of stress due to cutting on magnetic characteristics of silicon steel*, IEEE Translation Journal on Magnetics in Japan **7** (1992), no. 6, 453–457.

[139] P. Nakmahachalasint, K. D. T. Ngo, and L. Vu-Quoc, *A static hysteresis model for power ferrites*, IEEE Transactions on Power Electronics **4** (2002), no. 17, 453–460.

[140] Z. Neuschl, *Rechnerunterstüzte experimentelle Verfahren zur Bestimmung der lastunabhängigen Eisenverluste in permanentmagnetisch erregten elektrischen Maschinen mit additionalem Axialfluss*, Ph.D. thesis, Technische Universität Cottbus, 2007.

[141] E. Nitsche, *Verringerung der Ständereisenverluste*, ELIN-Zeitschrift **3/4** (1985), 92–98.

[142] A. Notoji, M. Hayakawa, and A. Saito, *Strain-magnetization properties and domain structure change of silicon steel sheets due to plastic stress*, IEEE Transactions on Magnetics **36** (2000), no. 5, 3074–3077.

[143] K. Oberretl, *13 Regeln für minimale Zusatzverluste in Induktionsmotoren*, Bulletin Oerlikon (1969), no. 389/390, 1–11.

[144] Y. Oda, Y. Tanaka, N. Yamagami, A. Chino, and K. Yamada, *Ultra-low sulfur non-oriented electrical steel sheets for highly efficient motors: NKB-CORE*, NKK Technical Review **87** (2002), 12–18.

[145] M. Oka, M. Kawano, K. Shimada, T. Kai, and M. Enokizono, *Evaluation of the magnetic properties of the rotating machines for the building factor clarification*, Przeglad Elektrotechniczny **87** (2011), no. 9b, 43–46.

[146] F. Ossart, E. Hug, O. Hubert, C. Buvat, and R. Billardon, *Effect of punching on electrical steels: Experimental and numerical coupled analysis*, IEEE Transactions on Magnetics **36** (2000), no. 5, 3137–3140.

[147] F. Özhan, *Feinbearbeitung weichmagnetischer Werkstoffe*, Ph.D. thesis, Technische Universität Berlin, Foschungsberichte für die Praxis, Bd. 36, Carl Hanser Verlag, München, 1985.

[148] A. Peksoz, S. Erdem, and N. Derebasi, *Mathematical model for cutting effect on magnetic flux distribution near the cut edge of non-oriented electrical steels*, Computational Materials Science **43** (2008), 1066–1068.

[149] V. Permiakov, A. Pulnikov, L. Dupré, M. De Wulf, and Melkebeek J., *Magnetic properties of Fe-Si steel depending on compressive and tensile stresses under sinusoidal and distorted excitations*, Journal of Applied Physics **93** (2003), no. 10, 6689–6691.

[150] H. Pfutzner and G. Krismanić, *The needle method for induction tests: sources of error*, IEEE Transactions on Magnetics **40** (2004), no. 3, 1610–1616.

[151] M. Platen, G. Henneberger, J. Schneider, and A. Schoppa, *Untersuchungen zum Einfluss des eingesetzten Elektroblechs auf den Wirkungsgrad von ausgewählten Asynchron-Normmotoren*, Electrical Engineering **82** (2000), no. 6, 291–300.

[152] H. J. Porck, *Rate of paper degradation the predictive value of artificial aging tests*, Tech. report, European Commission on Preservation and Access, Amsterdam, 2000.

[153] A. Pulnikov, *Modification of magnetic properties of non oriented electrical steels by the production of electromagnetic devices*, Ph.D. thesis, Department of Electrical Energy, Systems and Automation, Faculty of Engineering, Ghent University, 2003-2004.

[154] A. Pulnikov, P. Baudouin, and Melkebeek J., *Induced stresses due to the mechanical cutting of non-oriented electrical steels*, Journal of Magnetism and Magnetic Materials **254-255** (2003), 355–357.

[155] A. Pulnikov, V. Permiakov, M. De Wulf, and Melkebeek J., *Measuring setup for the investigation of the influence of mechanical stresses on magnetic properties of electrical steel*, Journal of Magnetism and Magnetic Materials **254-255** (2003), 47–49.

[156] J. Pyrhönen, T. Jokinen, and V. Hrabovcová, *Design of rotating electrical machines*, John Wiley & Sons. Ltd, 2008.

[157] K. Radziuk, D. Stachowiak, P. Sujka, and D. Kapelski, *Effect of geometrical dimensions and technology on magnetic properties of electrical steels*, Proceedings of EPNC 2012, June 26 - June 29, Pula, Croatia, 2012, pp. 101–102.

[158] S. A. Rahman and A. M. Knight, *Performance and core loss of concentrated winding ipmsm with different core treatment*, Proceedings of ECCE 2014, Pittsburgh, USA, 2014.

[159] R. Ramarotafika, A Benabou, and S. Clénet, *Stochastic modeling of soft magnetic properties of electrical steels: Application to stators of electrical machines*, IEEE Transactions on Magnetics **48** (2012), no. 10, 2573–2584.

[160] R. Ramarotafika, A Benabou, S. Clénet, and J. C. Mipo, *Experimental characterization of the iron losses variability in stators of electrical machines*, IEEE Transactions on Magnetics **48** (2012), no. 4, 1629–1632.

[161] U. Römer, S. Schöps, and T. Weiland, *Approximation of moments for the nonlinear magnetoquasistatic problem with material uncertainties*, IEEE Transactions on Magnetics **50** (2014), no. 2, 417–420.

[162] T. Ryckebusch, *On uncertainity of lamination properties used in electrical machines*, Master's thesis, KTH Royal Institute of Technology, 2005.

[163] R. Rygal, A. J. Moses, N. Derebasi, J. Schneider, and A. Schoppa, *Influence of cutting stress on magnetic field and flux density distribution in non-oriented electrical steels*, Journal of Magnetism and Magnetic Materials **215-216** (2000), 687–689.

[164] B. Rzany, *Laserstrahlschneiden*, Deutscher Verlag für Schweißtechnik DVS-Verlag GmbH, Düsseldorf, 1995.

[165] Kienle + Spiess GmbH Sachsenheim.

[166] C. P. Sasso, Basso, M. V. LoBue, and G. Bertotti, *Vector model for the study of hysteresis under stress*, Journal of Applied Physics **87** (2000), no. 9, 4774–4776.

[167] W. Schatt, *Einführung in die Werkstoffwissenschaft*, Dr. Alfred Hüthig Verlag, Heidelberg, 1987.

[168] S. Scheriau, M. Kiregisch, S. Kleber, N. Mehboob, R. Grössinger, and R. Pippan, *Magnetic characteristics of HPT deformed soft-magnetic materials*, Journal of Magnetism and Magnetic Materials **322** (2010), 2984–2988.

[169] K. H. Schmidt, *Influence of punching on the magnetic properties of electric steel with 1% silicon*, Journal of Magnetism and Magnetic Materials **2** (1976), 136–150.

[170] A. Schoppa, *Einfluss der Be- und Verarbeitung auf die magnetischen Eigenschaften von schlussgeglühtem, nichtkornorientiertem Elektroband*, Ph.D. thesis, Rheinisch-Westfälische Technische Hochschule Aachen, 2001.

[171] A. Schoppa, H. Louis, F. Pude, and Ch. von Rad, *Influence of abrasive water-jet cutting on the magnetic properties of non-oriented electrical steels*, Journal of Magnetism and Magnetic Materials (2003), no. 254-255, 370–372.

[172] A. Schoppa, J. Schneider, and J.-O. Roth, *Influence of the cutting process on the magnetic properties of non-oriented electrical steels*, Journal of Magnetism and Magnetic Materials (2000), no. 215-216, 100–102.

[173] A. Schoppa, J. Schneider, and C.-D. Wuppermann, *Influence of the manufacturing process on the magnetic properties of non-oriented electrical steels*, Journal of Magnetism and Magnetic Materials (2000), no. 215-216, 74–78.

[174] A. Schoppa, J. Schneider, C.-D. Wuppermann, and T. Bakon, *Influence of welding and sticking of laminations on the magnetic properties of non-oriented electrical steels*, Journal of Magnetism and Magnetic Materials **254-255** (2003), 367–369.

[175] W. Schuisky, *Berechnung elektrischer Maschinen*, Wien: Springer-Verlag, 1960.

[176] J. Schützhold and W. Hofmann, *Analysis of the temperature dependence of losses in electrical machines*, Energy Conversion Congress and Exposition (ECCE), 2013 IEEE, 2013, pp. 3159–3165.

[177] Seeberger, *Technische Information, Das Gefüge der Stähle*, seeberger.net/_assets/pdf/03_Das_Gefuege_der_Staehle.pdf, 2016.

[178] K. Senda, M. Ishida, Y. Nakasu, and M. Yagi, *Influence of shearing process on domain structure and magnetic properties of non-oriented electrical steel*, Journal of Magnetism and Magnetic Materials **304** (2006), c513–c515.

[179] P. Sergeant, F. De Belie, L. Dupré, and J. Melkebeek, *Losses in sensorless controlled permanent-magnet synchronous machines*, IEEE Transactions on Magnetics **46** (2010), no. 2, 590–593.

[180] S. B. Shah, *Finite element modeling of losses due to inter-laminar short-circuit currents in electrical machines*, Master's thesis, Aalto University School of Electrical Engineering, 2013.

[181] H. Shimanaka, Y. Ito, T. Irie, K. Matsumura, H. Nakamura, and Y. Shono, Symposium proceedings on Energy Efficient Electrical Steels, 1980, TMS of AIME, 193.

[182] H. Siebert, R. Thonig, A. Wetzig, and E. Beyer, *Applicability of various beam sources for high power laser cutting of non-oriented electrical steel*, Conference,

"High Power Laser Materials Processing - Lasers, Beam Delivery, Diagnostics, and Applications", San Francisco, Californien, 2012.

[183] R. Siebert, J. Schneider, and E. Beyer, *Laser cutting and mechanical cutting of electrical steels and its effect on the magnetic properties*, IEEE Transactions on Magnetics **50** (2014), no. 4, 1–4.

[184] R. Siebert, A. Wetzig, E. Beyer, B. Betz, C. Grunzweig, and E. Lehmann, *Localized investigation of magnetic bulk property deterioration of electrical steel: Analysing magnetic property drop thorough mechanical and laser cutting of electrical steel laminations using neutron grating interferometry*, Electric Drives Production Conference (EDPC), 2013 3rd International, Oct 2013, pp. 1–5.

[185] A. C. Smith and K. Edey, *Influence of manufacturing processes on iron losses*, Electrical Machines and Drives, 1995. Seventh International Conference on (Conf. Publ. No. 412), 1995, pp. 77–81.

[186] S. Steentjes, M. Leßmann, and K. Hameyer, *Advanced iron-loss calculation as a basis for efficiency improvement of electrical machines in automotive application*, International Conference on Electrical Systems for Aircraft, Railway and Ship Propulsion (ESARS) (Bologna,Italy), IEEE-ESARS, October 2012, pp. CD–ROM.

[187] ———, *Semi-physical parameter identification for an iron-loss formula allowing loss-separation*, Journal of Applied Physics **113** (2013), no. 17, A319–321.

[188] S. Steentjes, G. von Pfingsten, and K. Hameyer, *An application-oriented approach for consideration of material degradation effects due to cutting on iron losses and magnetizability*, IEEE Transactions on Magnetics **50** (2014), no. 11, 1–4.

[189] D. Steiner Petrovič, *Non-oriented electrical steel sheets*, Materials and Technology **44** (2010), no. 6, 317–325.

[190] C. P. Steinmetz, *On the law of hysteresis*, Transactions of the American Institute of Electrical Engineers **IX** (1892), no. 1, 1–64.

[191] S. Suwas and K. Ray, R. *Crystallographic texture of materials*, Springer London, 2014.

[192] N. Takahashi and D. Miyagi, *Examination of magnetic properties of electrical steels under stress condition*, The International Conference on Electrical Engineering 2008, 2008.

[193] N. Takahashi and D. Miyagi, *Effect of stress on iron loss of motor core*, Electric Machines and Drives Conference (IEMDC), 2011 IEEE International, 2011, pp. 469–474.

[194] N. Takahashi, H. Morimoto, Yunoki Y., and D. Miyagi, *Effect of shrink fitting and cutting on iron loss of permanent magnet motor*, Journal of Magnetism and Magnetic Materials (2008), no. 320, e925–e928.

[195] N. Takahashi, M. Morishita, D. Miyagi, and M. Nakano, *Comparison of magnetic properties of magnetic materials at high temperature*, IEEE Transactions on Magnetics **47** (2011), no. 10, 4352–4355.

[196] M. Takezawa, Y. Wada, J. Yamasaki, T. Honda, and C. Kaido, *Effect of grain size on domain structure of thin nonoriented Si-Fe electrical sheets*, IEEE Transactions on Magnetics **39** (2003), no. 5, 3208–3210.

[197] A. G. Tôrres and B. J. C. Filho, *A generalized epstein test method for the computation of core losses in induction motors*, IECON 02, Industrial Electronics Society, IEEE 2002 28th Annual Conference of the, vol. 2, Nov 2002, pp. 1150–1155 vol.2.

[198] S. Tumanski, *Handbook of magnetic measurements*, Taylor & Francis Group, LLC, CRC Press, 2011.

[199] L. Vandenbossche, S. Jacobs, F. Henrotte, and K. Hameyer, *Impact of cut edges in magnetization curves and iron losses in e-machines for automotive traction*, Proceedings of 25th World Battery, Hybrid and Fuel Cell Electric Vehicle Symposium & Exhibition, EVS (Schenzhen, China), November 2010.

[200] S. Vincenzo and F. Vincenzo, *Steel plate cutting by pulsed laser*, Ital. Mach. and Equip. **17** (1985), no. 90, 16–19.

[201] Voestalpine, *Electrical steel isovac 270-35 A data sheet*, 2015.

[202] ———, *Electrical steel isovac 400-50 A data sheet*, 2015.

[203] ———, *Electrical steel isovac 800-65 A data sheet*, 2015.

[204] K. Vogt, *Elektrische Maschinen Berechnung rotierender elektrischer Maschinen, 4th edition*, VEB Verlag Technik Berlin, 1988.

[205] G. von Pfingsten, S. Steentjes, A. Thul, T. Herold, and K. Hameyer, *Soft magnetic material degradation due to manufacturing process: A comparison of measurements and numerical simulations*, Electrical Machines and Systems (ICEMS), 2014 17th International Conference on, Oct 2014, pp. 2018–2024.

[206] E. Werner, Austrian patent no. 191 015, 1949.

[207] W. Wilczynski, A. Skopec, B. Szubzda, S. Talik, and W. Lipiec, *Aspects of the punching and laser cutting effect on the power losses and magnetic flux density distribution in electrical steel*, Stahleisen (2004), 499–503.

[208] W. Wolman, *Der Frequenzgang des Wirbelstromeinflusses bei Übertragerblechen*, Zeitschrift für technische Physik (1929), no. 12, 595–598.

[209] World Steel Association (worldsteel), *Steel statistical yearbook 2015*, worldsteel Committee on Economic Studies - Brussels (2015), 1–126.

[210] C.-D. Wuppermann and A. Schoppa, *Electrical steel sheet and strip*, Stahl-Informations-Zentrum publication 401-E (2005), no. 08.11.2011, 1–24.

[211] M. Yabumoto, T. Wakisaka, N. Suzuki, C. Kaido, and T. Kubota, *Electrical steel sheet for traction motors of hybrid/electric vehicles*, 2003, pp. 57–61.

[212] K.-I. Yamamoto, E. Shimomura, K. Yamada, and T. Sasaki, *Effects of external stress on magnetic properties in motor cores*, Electrical Engineering in Japan **123** (1998), no. 1, 15–22.

[213] K.-I. Yamamoto and S. Yanase, *Magnetic properties of non-oriented electrical steels under compressive stress normal to their surface*, Przeglad Elektrotechniczny **87** (2011), no. 9b, 97–100.

[214] M. M. Znidarich, *Hydro generators stator cores part 1 - constructional features and core losses*, 2008 Australasian Universities Power Engineering Conference, AUPEC'08, 2008, pp. 1–8.

[215] _____ , *Hydro generators stator cores part 2 - core losses, degradation mechanisms, testing and specification*, 2008 Australasian Universities Power Engineering Conference, AUPEC'08, 2008, pp. 1–9.

# List of publications

The work presented in this thesis has resulted in the following 3 journal and 7 conference publications. Some journal publications are extended versions of a conference publication (J1/C3, J2/C4, J3/C6). These papers are subjected to copyright by the particular conference organizer, mainly by the *IEEE*.

**Journal publications:**

J1 **Bali, M.**, De Gersem, H. and Muetze, A., "Determination of Original Non-Degraded and Fully Degraded Magnetic Properties of Material Subjected to Mechanical Cutting," *IEEE Transactions on Industry Applications*, vol. PP, no. 99, pp. 1-1 (9 pages), 2016.

J2 **Bali, M.** and Muetze, A., "Influences of CO2-laser, FKL-laser, and mechanical cutting on the magnetic properties of electrical steel sheets," *IEEE Transactions on Industry Applications*, vol. 51, no. 6, pp. 4446-4454, 2015.

J3 **Bali, M.**, De Gersem, H. and Muetze, A., "Finite-Element Modeling of Magnetic Material Degradation Due to Punching," *IEEE Transactions on Magnetics*, vol. 50, no. 2, pp. 745-748, 2014.

**Conference publications:**

C1 **Bali, M.**, De Gersem, H. and Muetze, A., "Epstein Frame Measurement Based Determination of Original Non-Degraded and Fully Degraded Magnetic Characteristics of Material Submitted to Laser Cutting," *IEEE Energy Conversion Congress and Exposition (ECCE)*, Montreal, Canada, pp. 6096-6101, 2015.

C2 **Bali, M.** and Muetze, A., "Influence of Different Cutting Techniques on the Magnetic Characteristics of Electrical Steels Determined by a Remagraph," *IEEE International Electric Machines and Drives Conference (IEMDC)*, Coeur d'Alene, ID, USA, pp. 1190-1196, 2015.

C3 **Bali, M.**, De Gersem, H. and Muetze, A., "Epstein Frame Measurement Based Determination of Original Non-Degraded and Fully Degraded Magnetic Properties of Material Submitted to Mechanical Cutting," *IEEE International Electric*

*Machines and Drives Conference (IEMDC),* Coeur d'Alene, ID, USA, pp. 1184-1189, 2015.

**C4 Bali, M.** and Muetze, A., "Influences of CO2 and FKL-laser cutting as well as mechanical cutting on the magnetic properties of electric steel sheets determined by Epstein frame and stator lamination stack measurements," *IEEE Energy Conversion Congress and Exposition (ECCE),* Pittsburgh, PA, USA, pp. 1443-1450, 2014.

**C5 Bali, M.**, De Gersem, H. and Muetze, A., "Determination of Original Non-Degraded and Fully Degraded B-H-Curves from Measurements of Material Submitted to Punching," *IEEE Conference on Electromagnetic Field Computation (CEFC),* Annecy, France, pp. PA2-3, 2014.

**C6 Bali, M.**, De Gersem, H. and Muetze, A., "Finite-Element Modelling of Magnetic Material Degradation Profiles due to Punching," *Compumag,* Budapest, Hungary, pp. pa3-6, 2013.

**C7 Bali, M.**, De Gersem, H. and Muetze, A., "Consideration of Steel Degradation due to Punching in Finite Element Modelling of Electric Machines," *Electromagnetic Phenomena in Nonlinear Circuits (EPNC),* Pula, Croatia, pp. 53-54, 2012.

# Appendix A

# Results of the optical emission spectrometry and EBSD

## A.1 Measured material contents in wt% with standard deviation

Table A.1: Measured material contents in wt% with standard deviation (strips as described in Chapter 2.1.1)

| % | C | Si | Mn | Cr | Ni | Mo | Cu | Pb | V | Al | Nb | Ti | S | P |
|---|---|----|----|----|----|----|----|----|---|----|----|----|---|---|
| | | | | | | **M270-35A_30_LL_SS** | | | | | | | | |
| **1 Xq** | 0.008 | 2.78 | 0.21 | <0.01 | <0.01 | <0.005 | 0.009 | <0.01 | <0.01 | 1.03 | <0.01 | <0.01 | 0.011 | 0.014 |
| **s''** | 0.001 | 0.03 | 0.003 | 0 | 0 | 0 | 0 | 0 | 0 | 0.03 | 0 | 0 | 0.002 | 0.002 |
| | | | | | | **M270-35A_30_LL_CO$_2$** | | | | | | | | |
| **2 Xq** | 0.007 | 2.82 | 0.2 | <0.01 | <0.01 | <0.005 | 0.008 | <0.01 | <0.01 | 1.05 | <0.01 | <0.01 | 0.01 | 0.012 |
| **s''** | 0.001 | 0.04 | 0.006 | 0 | 0 | 0 | 0.001 | 0 | 0 | 0.04 | 0 | 0 | 0 | 0.002 |
| | | | | | | **M270-35A_30_QQ_FKL** | | | | | | | | |
| **3 Xq** | 0.007 | 2.86 | 0.21 | <0.01 | <0.01 | <0.005 | 0.009 | <0.01 | <0.01 | 1.03 | <0.01 | <0.01 | 0.012 | 0.013 |
| **s''** | 0.001 | 0.05 | 0 | 0 | 0 | 0 | 0 | 0 | 0 | 0.04 | 0 | 0 | 0.001 | 0.002 |
| | | | | | | **M270-35A_7.5_QQ_FKL** | | | | | | | | |
| **4 Xq** | 0.009 | 2.84 | 0.21 | <0.01 | <0.01 | <0.005 | 0.01 | <0.01 | <0.01 | 1.02 | <0.01 | <0.01 | 0.009 | 0.012 |
| **s''** | 0.001 | 0.05 | 0.002 | 0 | 0 | 0 | 0 | 0 | 0 | 0.03 | 0 | 0 | 0.001 | 0.001 |
| | | | | | | **M400-50A_30_LL_SS** | | | | | | | | |
| **5 Xq** | <0.003 | 1.59 | 0.47 | <0.01 | <0.01 | <0.005 | 0.006 | <0.01 | <0.01 | 0.18 | <0.01 | <0.01 | 0.01 | 0.017 |
| **s''** | 0 | 0.02 | 0.005 | 0 | 0 | 0 | 0 | 0 | 0 | 0.05 | 0 | 0 | 0.001 | 0.002 |
| | | | | | | **M400-50A_30_LL_FKL** | | | | | | | | |
| **6 Xq** | <0.003 | 1.58 | 0.47 | <0.01 | <0.01 | <0.005 | 0.006 | <0.01 | <0.01 | 0.17 | <0.01 | <0.01 | 0.009 | 0.016 |
| **s''** | 0 | 0.02 | 0.007 | 0 | 0 | 0 | 0 | 0 | 0 | 0.004 | 0 | 0 | 0.001 | 0.002 |
| | | | | | | **M800-65A_30_QQ_SS** | | | | | | | | |
| **7 Xq** | <0.003 | 1.56 | 0.25 | <0.01 | <0.01 | <0.005 | 0.005 | <0.01 | <0.01 | 0.13 | <0.01 | <0.01 | 0.009 | 0.02 |
| **s''** | 0 | 0.008 | 0.006 | 0 | 0 | 0 | 0 | 0 | 0 | 0.002 | 0 | 0 | 0.001 | 0.002 |
| | | | | | | **M800-65A_30_LL_FKL** | | | | | | | | |
| **8 Xq** | <0.003 | 1.58 | 0.25 | <0.01 | <0.01 | <0.005 | 0.006 | <0.01 | <0.01 | 0.13 | <0.01 | <0.01 | 0.011 | 0.012 |
| **s''** | 0 | 0.017 | 0.004 | 0 | 0 | 0 | 0.001 | 0 | 0 | 0.003 | 0 | 0 | 0.001 | 0.001 |

## A.2  Average grain size diameters $d_{\mathbf{g}}$

Table A.2: Grain size diameter obtained in the steel sheet sample's center (non-deteriorated area).

| Center | Average grain size diameter in $\mu$m | Standard deviation | Number of grains | Number of measurement |
|---|---|---|---|---|
| M270-35A_SS | 78.43 | 41.58 | 365 | 1 |
| M270-35A_CO$_2$ | 77.87 | 42.01 | 367 | 2 |
| M270-35A_CO$_2$ | 83.93 | 43.78 | 320 | 3 |
| M270-35A_FKL | 83.60 | 44.34 | 342 | 4 |
| M270-35A_FKL | 80.67 | 42.97 | 367 | 5 |
| M400-50A_CO$_2$ | 50.59 | 30.4 | 366 | 1 |
| M400-50A_FKL | 57.24 | 37.4 | 261 | 2 |
| M800-65A_SS | 29.55 | 14.07 | 671 | 1 |
| M800-65A_CO$_2$ | 26.48 | 13.21 | 855 | 2 |
| M800-65A_FKL | 25.86 | 13.37 | 377 | 3 |
| M800-65A_FKL | 25.24 | 14.03 | 383 | 4 |

Table A.3: Grain size diameter obtained at the steel sheet sample's cut edge.

| Cut edge | Average grain size diameter in $\mu$m | Standard deviation | Number of grains | Number of measurement |
|---|---|---|---|---|
| M270-35A_SS | 57.41 | 42.4 | 27 | 1 |
| M270-35A_CO$_2$ | 64.88 | 36.47 | 65 | 1 |
| M270-35A_CO$_2$ | 64.02 | 34.44 | 141 | 2 |
| M270-35A_FKL | 52.48 | 34.33 | 38 | 1 |
| M400-50A_SS | 45.46 | 27.52 | 109 | 1 |
| M400-50A_CO$_2$ | 45.63 | 28.14 | 119 | 1 |
| M400-50A_FKL | 47.36 | 28.07 | 110 | 1 |
| M800-65A_SS | 29.95 | 16.39 | 408 | 1 |
| M800-65A_SS | 28.07 | 13.42 | 309 | 2 |
| M800-65A_CO$_2$ | 25.88 | 13.13 | 607 | 1 |
| M800-65A_FKL | 29.41 | 14.15 | 452 | 1 |
| M800-65A_FKL | 30.09 | 16.05 | 447 | 2 |

# Appendix B

# Results by remagraph

## B.1 Remagraph: Comparison of the different cutting techniques on the quasi-static $B$-$H$ curves

**Small samples**
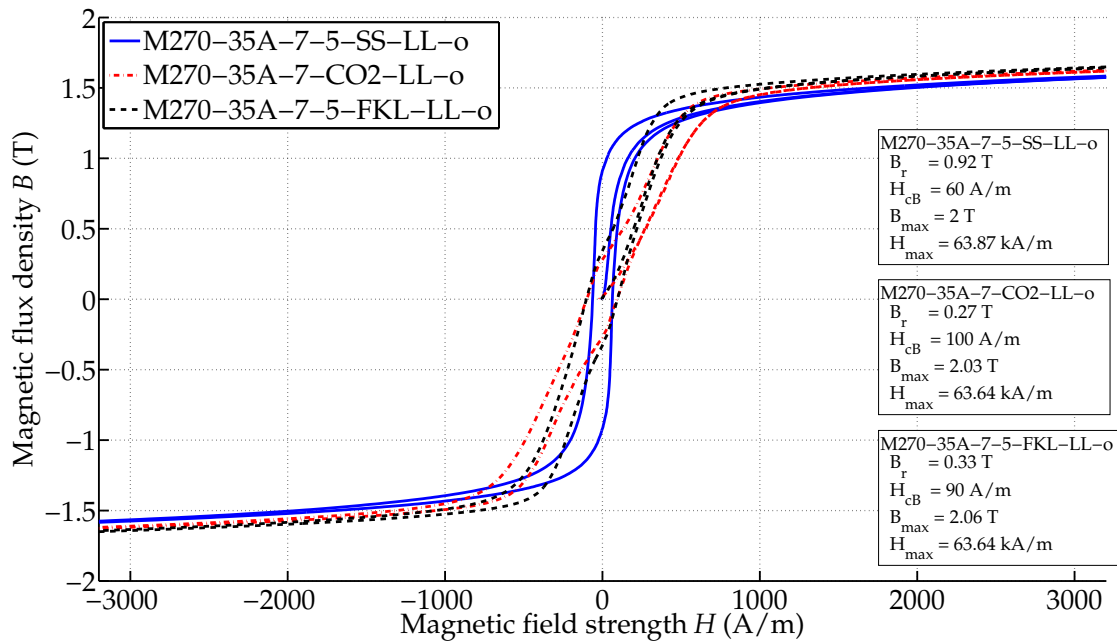


Figure B.1: *B-H* curves of M270-35A-LL-o, small samples.
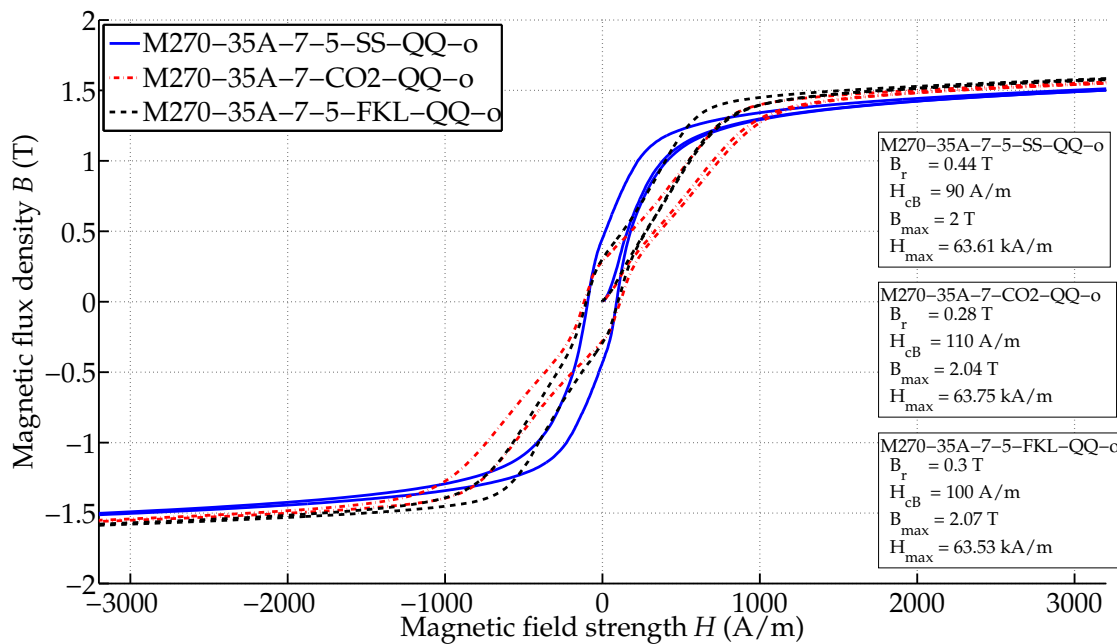


Figure B.2: *B-H* curves of M270-35A-QQ-o, small samples.
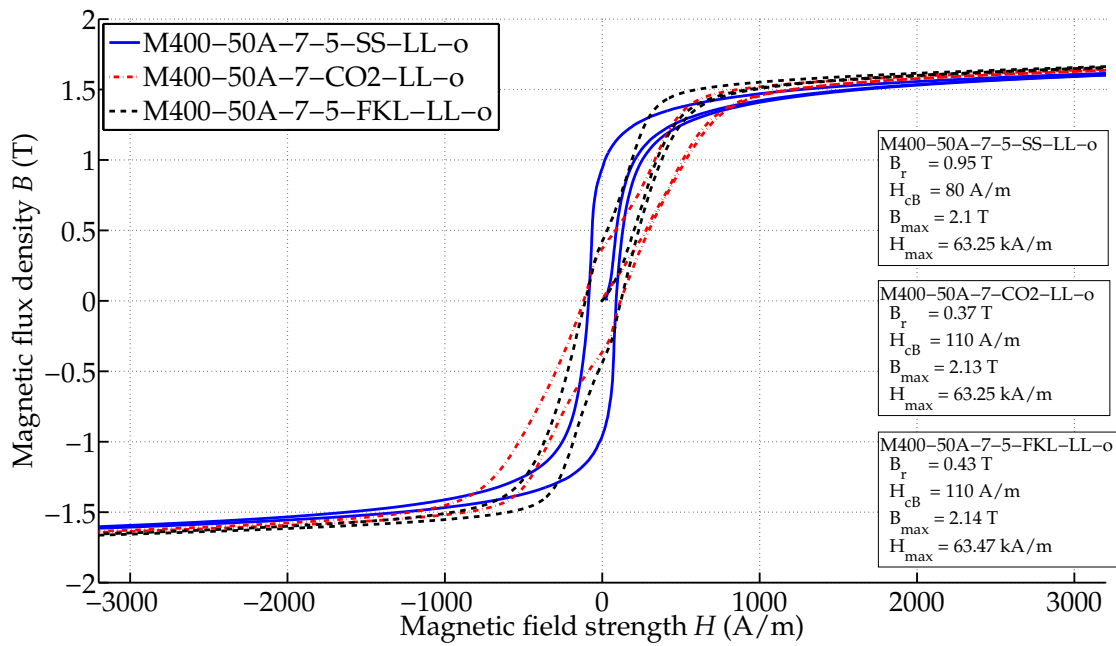
Figure B.3: *B-H* curves of M400-50A-LL-o, small samples.
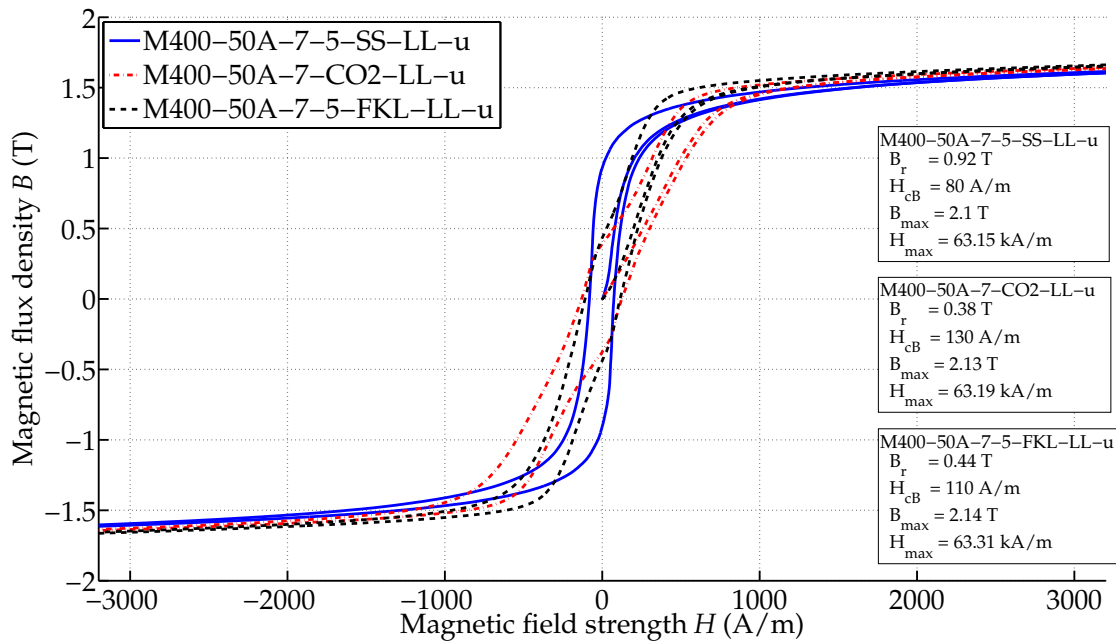


Figure B.4: *B-H* curves of M400-50A-LL-u, small samples.
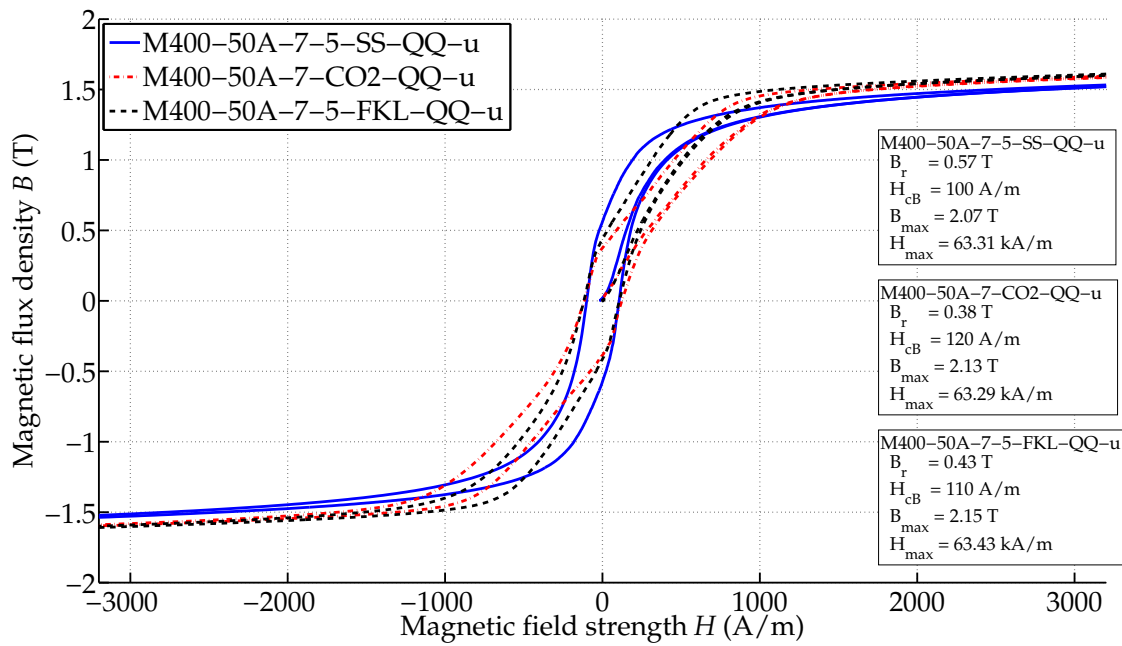
Figure B.5: *B-H* curves of M400-50A-QQ-u, small samples.
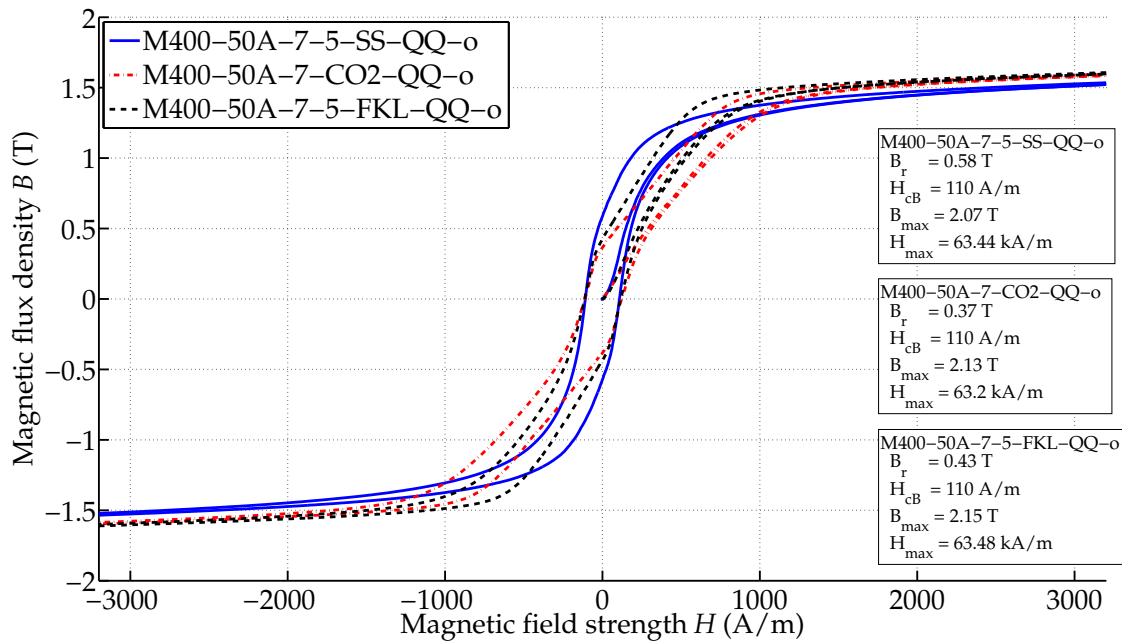


Figure B.6: *B-H* curves of M400-50A-QQ-o, small samples.
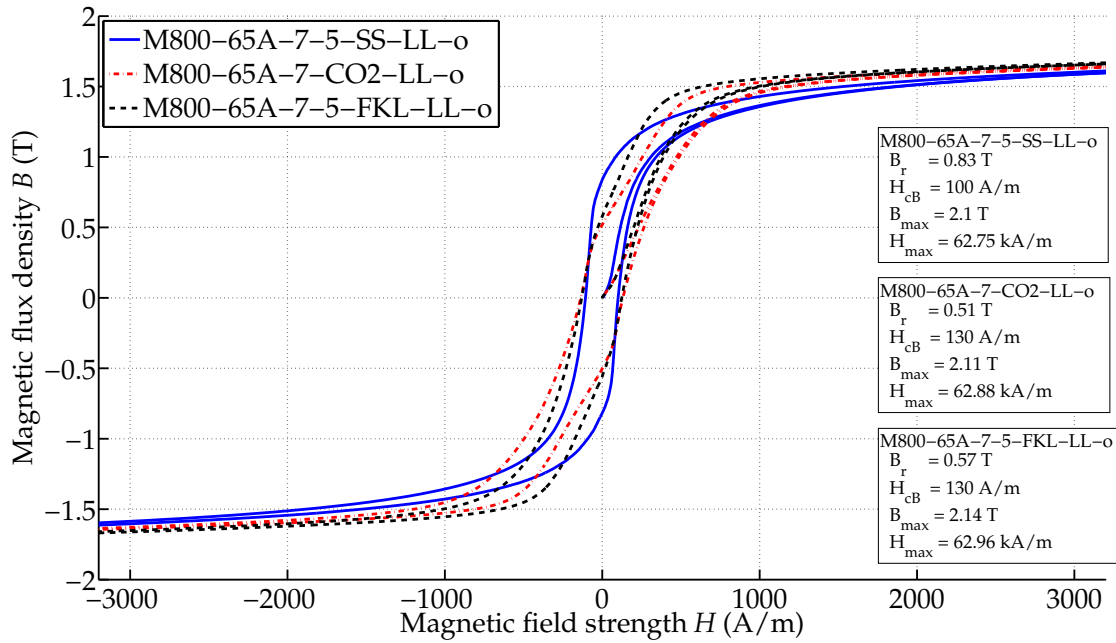
Figure B.7: *B-H* curves of M800-65A-LL-o, small samples.
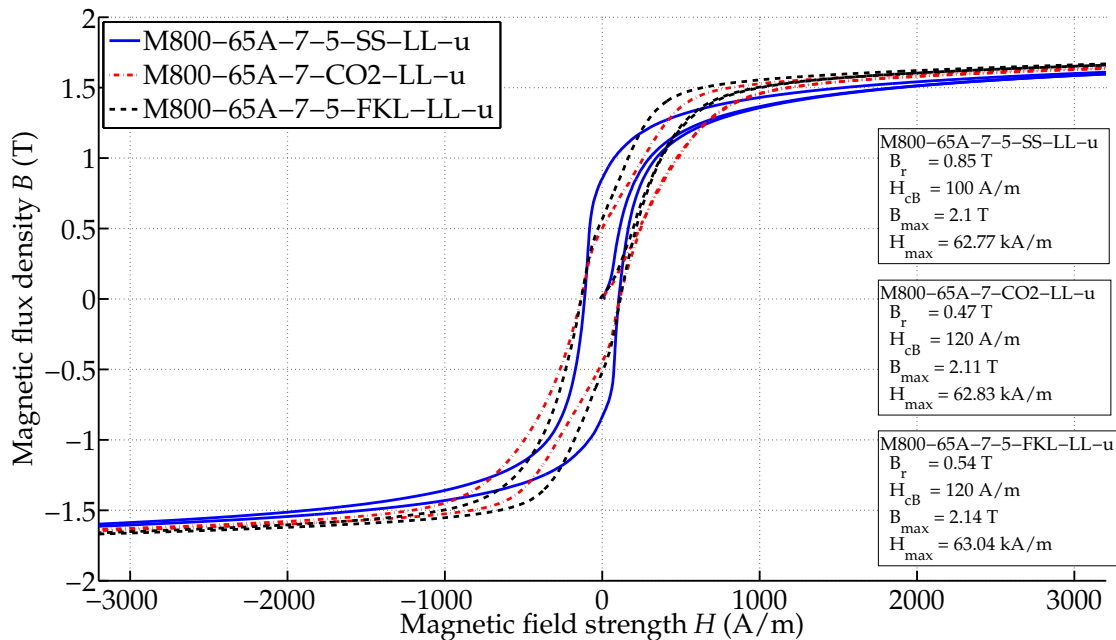


Figure B.8: *B-H* curves of M800-65A-LL-u, small samples.
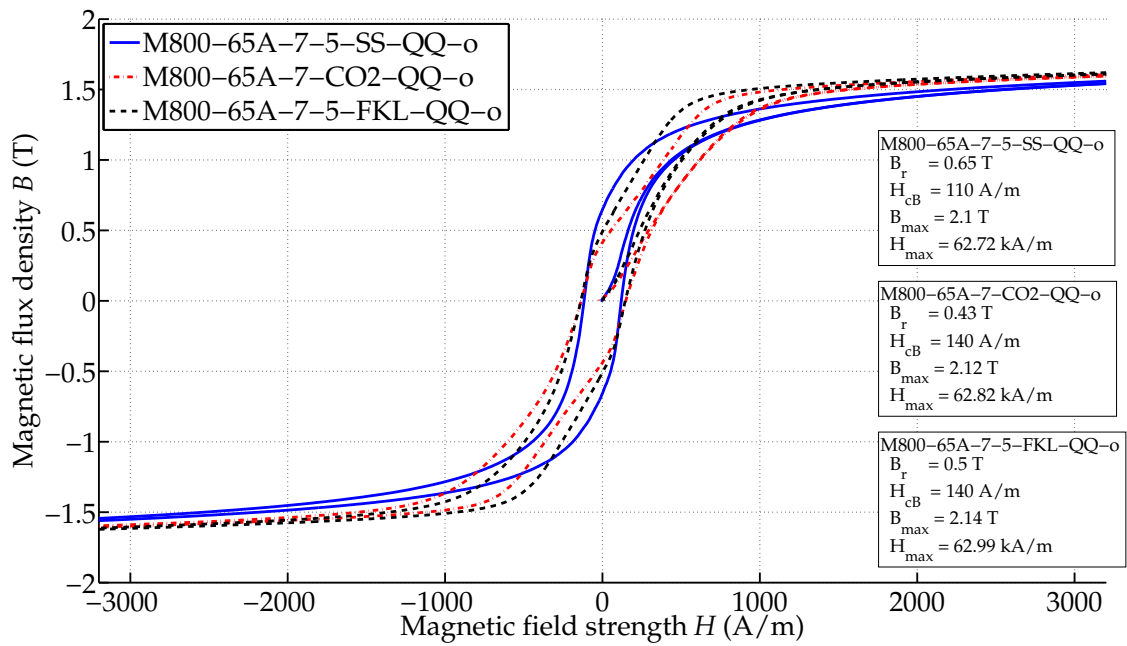
Figure B.9: *B-H* curves of M800-65A-QQ-o, small samples.
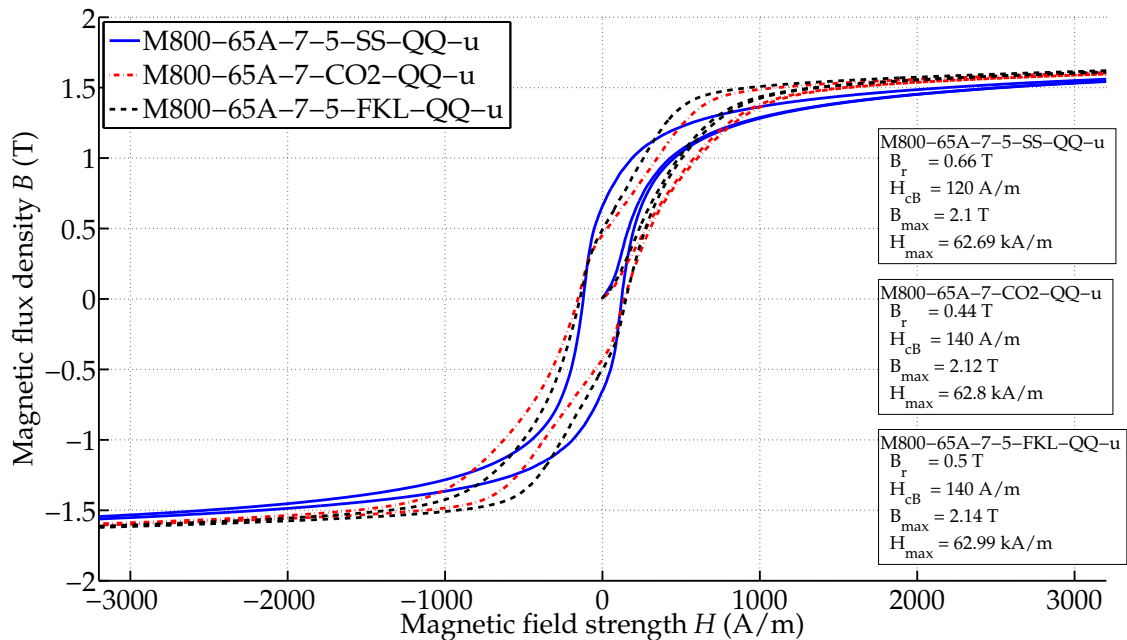


Figure B.10: *B-H* curves of M800-65A-QQ-u, small samples.

**Wide samples**
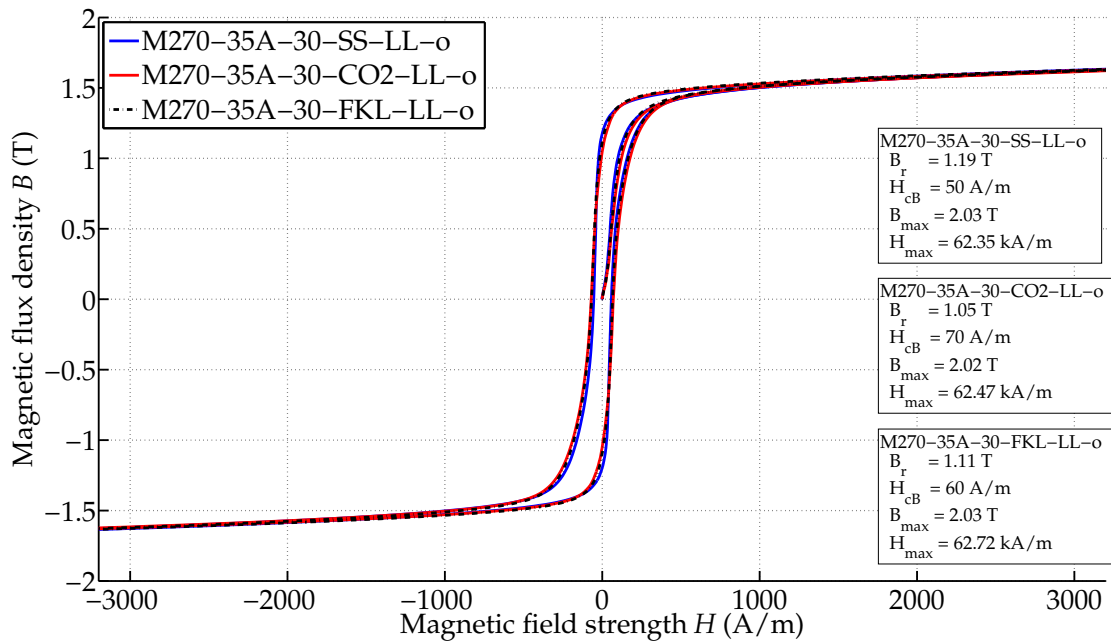


Figure B.11: *B-H* curves of M270-35A-LL-o, wide samples.
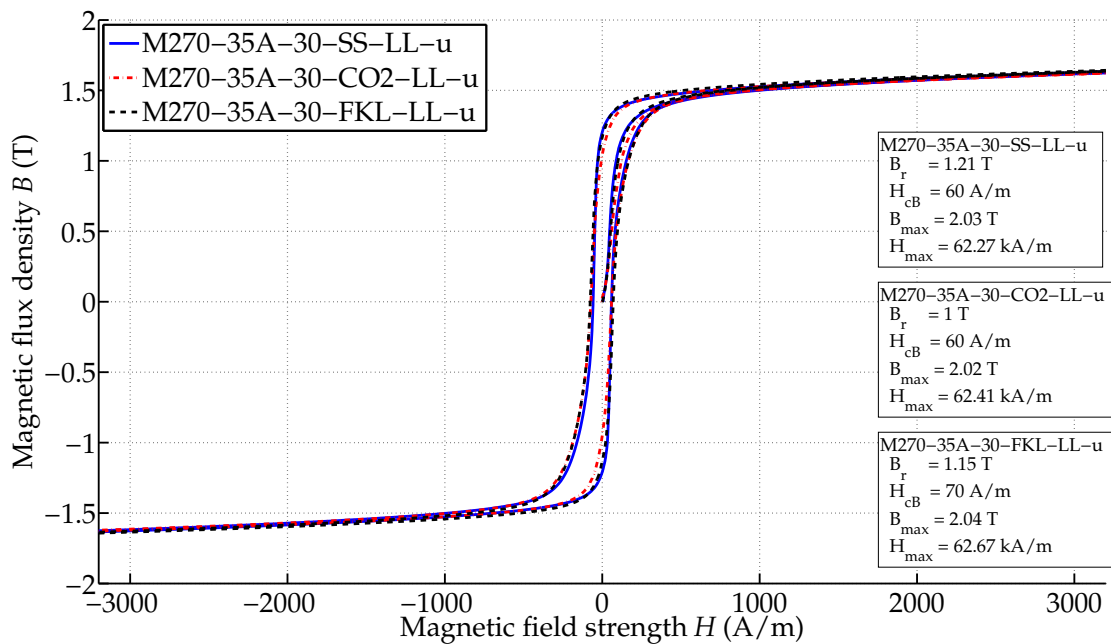


Figure B.12: *B-H* curves of M270-35A-LL-u, wide samples.
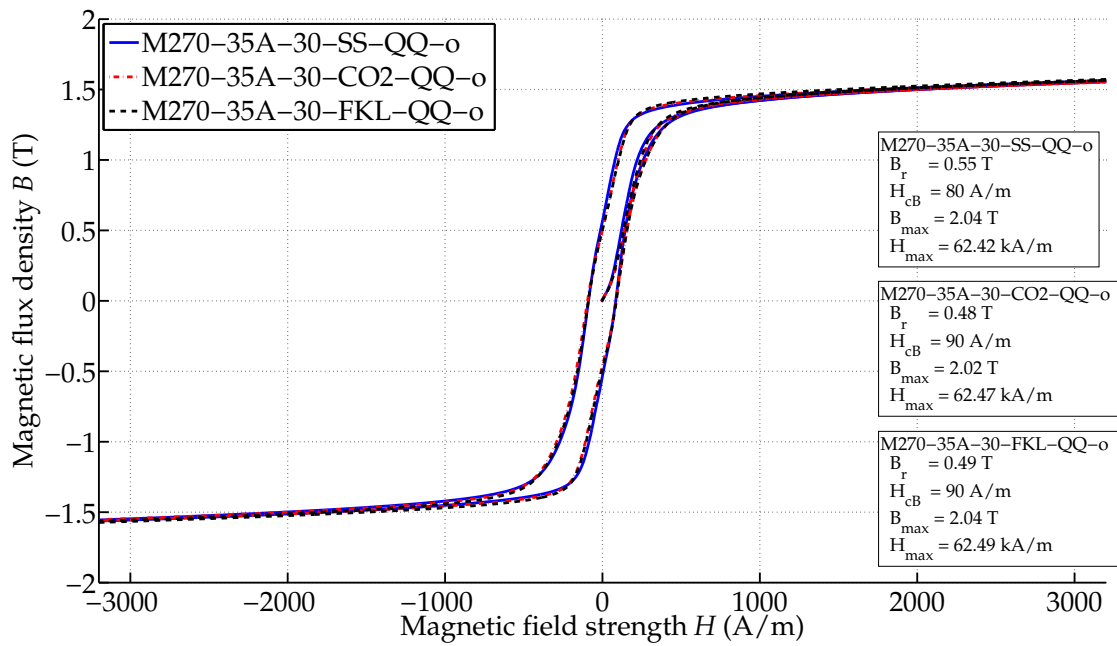
Figure B.13: *B-H* curves of M270-35A-QQ-o, wide samples.
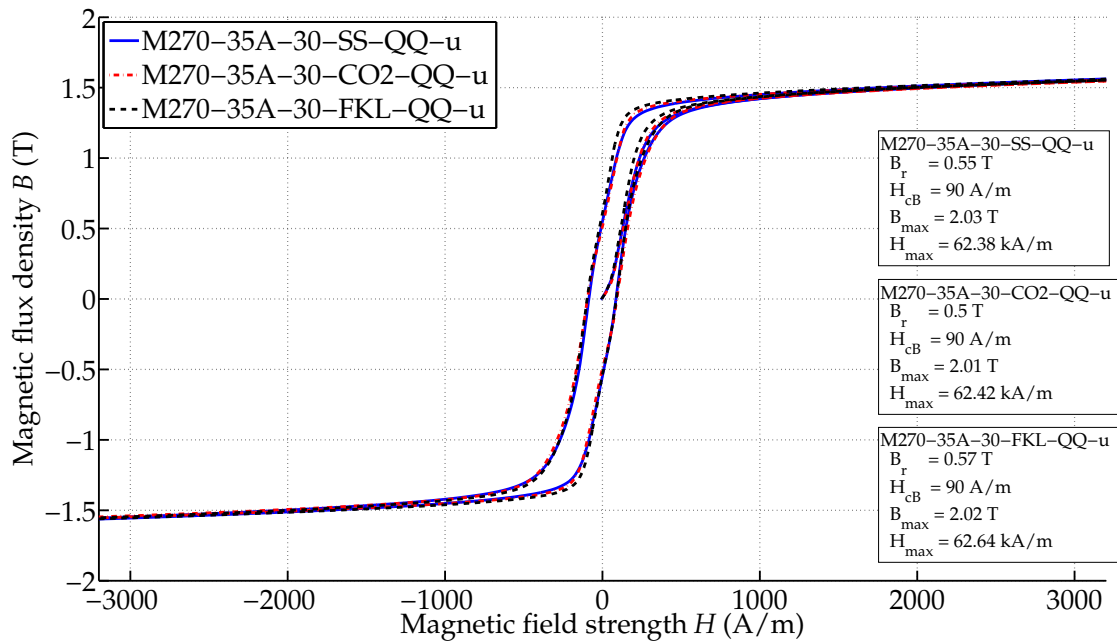


Figure B.14: *B-H* curves of M270-35A-QQ-u, wide samples.
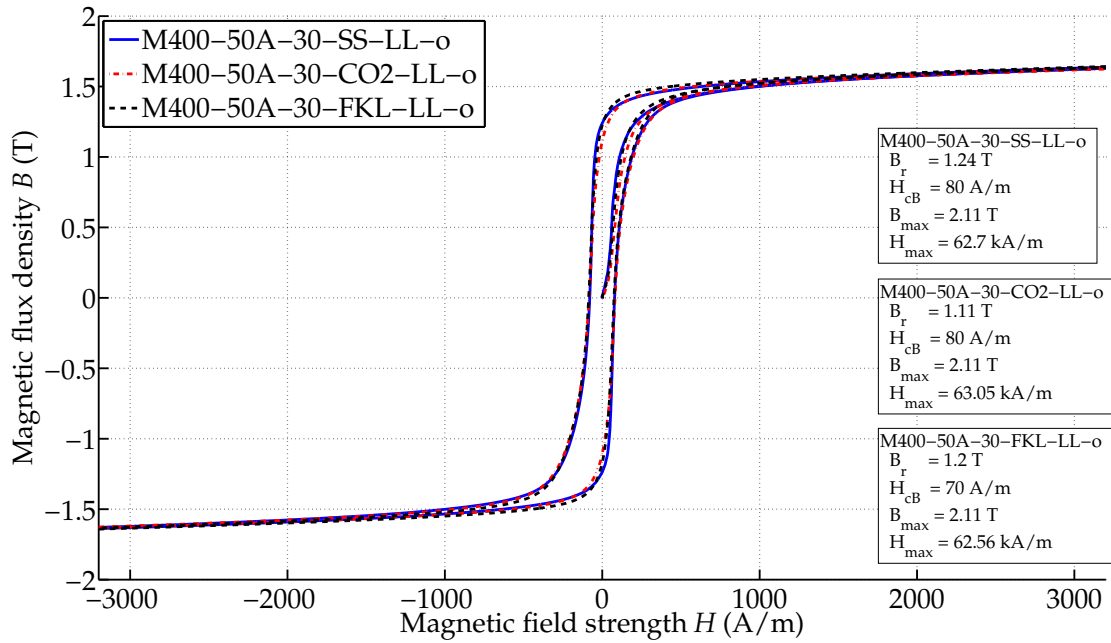
Figure B.15: *B-H* curves of M400-50A-LL-o, wide samples.
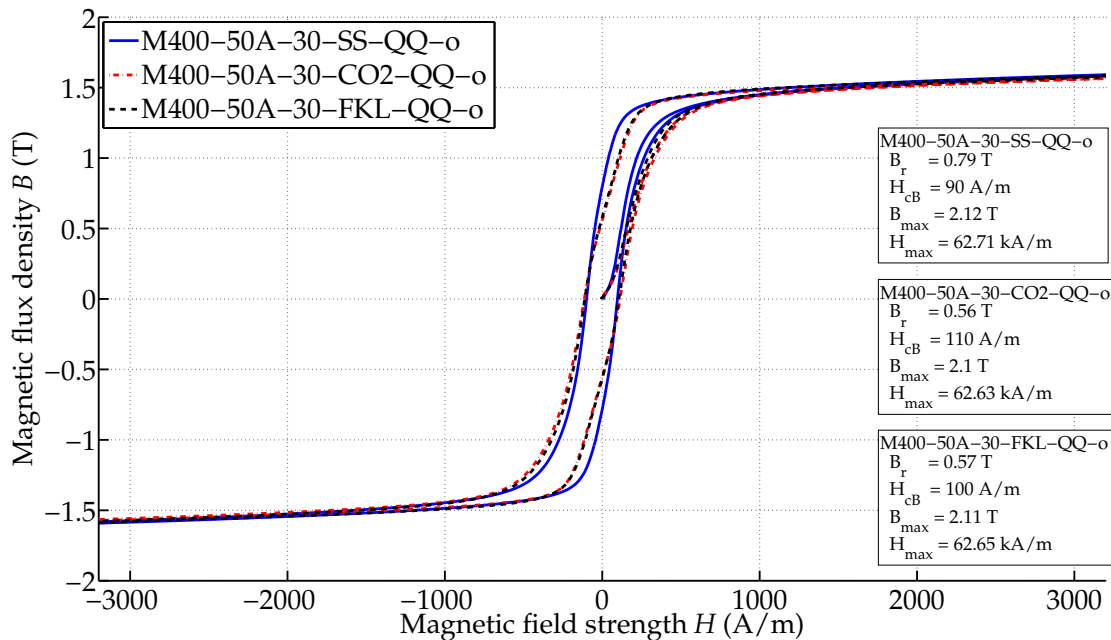


Figure B.16: *B-H* curves of M400-50A-QQ-o, wide samples.
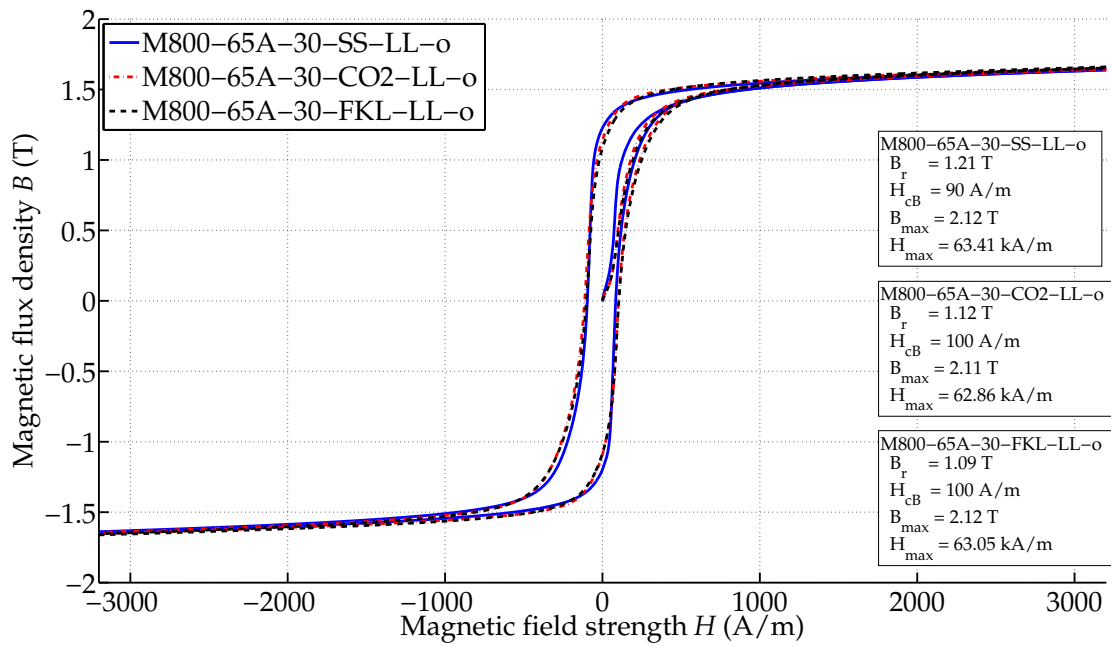
Figure B.17: *B-H* curves of M800-65A-LL-o, wide samples.
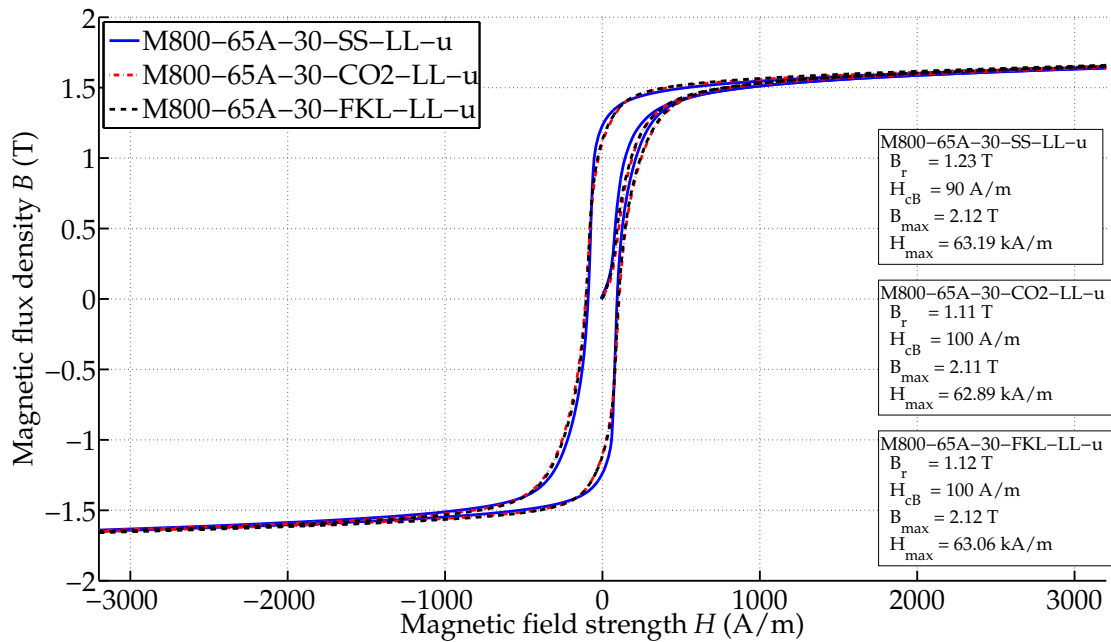


Figure B.18: *B-H* curves of M800-65A-LL-u, wide samples.
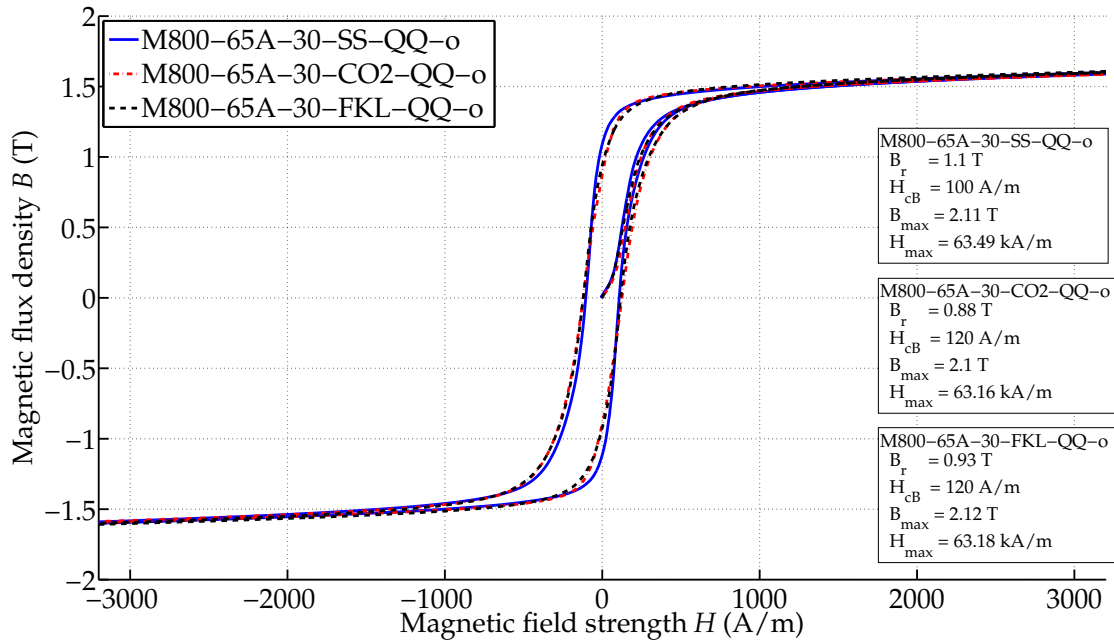
Figure B.19: *B-H* curves of M800-65A-QQ-o, wide samples.
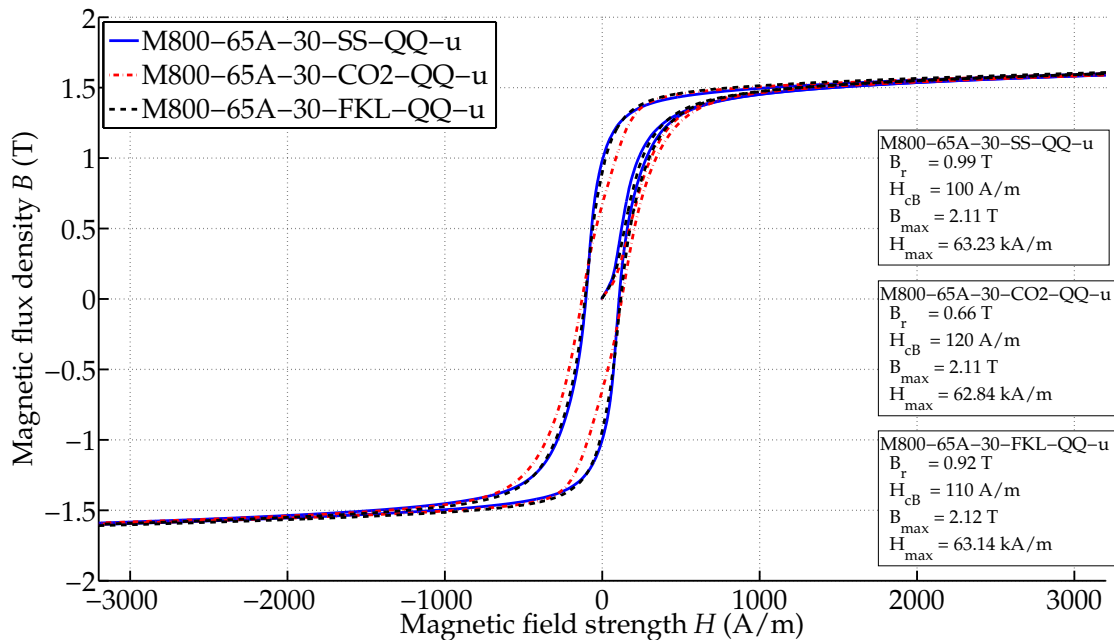


Figure B.20: *B-H* curves of M800-65A-QQ-u, wide samples.

## B.2  Remagraph: Change of the remanent flux density from longitudinally-cut to transversely-cut samples

**Small samples**

Table B.1: Change of remanent magnetic flux density from longitudinal to transverse cutting direction for small guillotine-cut samples; mean values of two measurements.

|  | M270-35A_SS | M400-50A_SS | M800-65A_SS |
|---|---|---|---|
| $B_{r\_LL}$ | 0.895 T | 0.935 T | 0.84 T |
| Standard deviation $B_{r\_LL}$ | 0.04 T/4.47 % | 0.02 T/2.1 % | 0.01 T/1.2 % |
| $B_{r\_QQ}$ | 0.46 T | 0.575 T | 0.655 T |
| Standard deviation $B_{r\_QQ}$ | 0.0 | 0.01 T/1.74 % | 0.01 T/1.53 % |
| Reduction in percent | −48.6 % | −38.5 % | −22 % |

Table B.2: Change of remanent magnetic flux density from longitudinal to transverse cutting direction for small $CO_2$-cut samples; mean values of two measurements.

|  | M270-35A_$CO_2$ | M400-50A_$CO_2$ | M800-65A_$CO_2$ |
|---|---|---|---|
| $B_{r\_LL}$ | 0.285 T | 0.375 T | 0.49 T |
| Standard deviation $B_{r\_LL}$ | 0.02 T/7.02 % | 0.01 T/2.67 % | 0.03 T/6.12 % |
| $B_{r\_QQ}$ | 0.285 T | 0.375 T | 0.435 T |
| Standard deviation $B_{r\_QQ}$ | 0.01 T/3.51 % | 0.01 T/2.67 % | 0.01 T/2.3 % |
| Reduction in percent | 0 % | 0 % | −11.2 % |

Table B.3: Change of remanent magnetic flux density from longitudinal to transverse cutting direction for small FKL-cut samples; mean values of two measurements.

|  | M270-35A_FKL | M400-50A_FKL | M800-65A_FKL |
|---|---|---|---|
| $B_{r\_LL}$ | 0.33 T | 0.435 T | 0.555 T |
| Standard deviation $B_{r\_LL}$ | 0.0 | 0.01 T/2.3 % | 0.02 T/3.6 % |
| $B_{r\_QQ}$ | 0.3 T | 0.43 T | 0.5 T |
| Standard deviation $B_{r\_QQ}$ | 0.0 | 0.0 | 0.0 |
| Reduction in percent | −9.0 % | −1.15 % | −9.9 % |

**Wide samples**

Note:  The standard deviations of $B_{r\_QQ}$ of M800-65A_$CO_2$ and M270-35A_FKL are

larger than 10 %. Thus, these values should be used with care. In the case of M800-65A_$CO_2$, the remanent flux density determined for measurement M800-65A-30-_$CO_2$-QQ-o maybe measured more correctly than the remanent flux density of M800-65A-30-_$CO_2$-QQ-u. With this assumption, the reduction of $B_r$ in percent moves from 30.9 % (see Table B.5) to 21.1 % and is similar to the reduction observed in the FKL-laser cut samples.

Table B.4: Change of remanent magnetic flux density from longitudinal to transverse cutting direction for wide guillotine-cut samples; mean values of two measurements.

|  | M270-35A_SS | M400-50A_SS | M800-65A_SS |
|---|---|---|---|
| $B_{r\_LL}$ | 1.2 T | 1.25 T | 1.22 T |
| Standard deviation $B_{r\_LL}$ | 0.01 T/0.83 % | 0.01 T/0.8 % | 0.01 T/0.82 % |
| $B_{r\_QQ}$ | 0.55 T | 0.77 T | 1.045 T |
| Standard deviation $B_{r\_QQ}$ | 0.0 | 0.03 T/3.9 % | 0.08 T/7.66 % |
| Reduction in percent | −54.2 % | −38.4 % | −14.35 % |

Table B.5: Change of remanent magnetic flux density from longitudinal to transverse cutting direction for wide $CO_2$-cut samples; mean values of two measurements.

|  | M270-35A_$CO_2$ | M400-50A_$CO_2$ | M800-65A_$CO_2$ |
|---|---|---|---|
| $B_{r\_LL}$ | 1.025 T | 1.1 T | 1.115 T |
| Standard deviation $B_{r\_LL}$ | 0.04 T/3.9 % | 0.01 T/0.91 % | 0.01 T/0.9 % |
| $B_{r\_QQ}$ | 0.49 T | 0.56 T | 0.77 T |
| Standard deviation $B_{r\_QQ}$ | 0.01 T/2.04 % | 0 | 0.16 T/20.78 % |
| Reduction in percent | −52.2 % | −49.1 % | −30.9 % |

Table B.6: Change of remanent magnetic flux density from longitudinal to transverse cutting direction for wide FKL-cut samples; mean values of two measurements.

|  | M270-35A_FKL | M400-50A_FKL | M800-65A_FKL |
|---|---|---|---|
| $B_{r\_LL}$ | 1.13 T | 1.19 T | 1.105 T |
| Standard deviation $B_{r\_LL}$ | 0.03 T/2.65 % | 0.01 T/0.84 % | 0.02 T/1.8 % |
| $B_{r\_QQ}$ | 0.53 T | 0.585 T | 0.925 T |
| Standard deviation $B_{r\_QQ}$ | 0.06 T/11.32 % | 0.02 T/3.42 % | 0.01 T/1.08 % |
| Reduction in percent | −53.1 % | −50.8 % | −16.3 % |

# B.3 Further examples of relative permeability
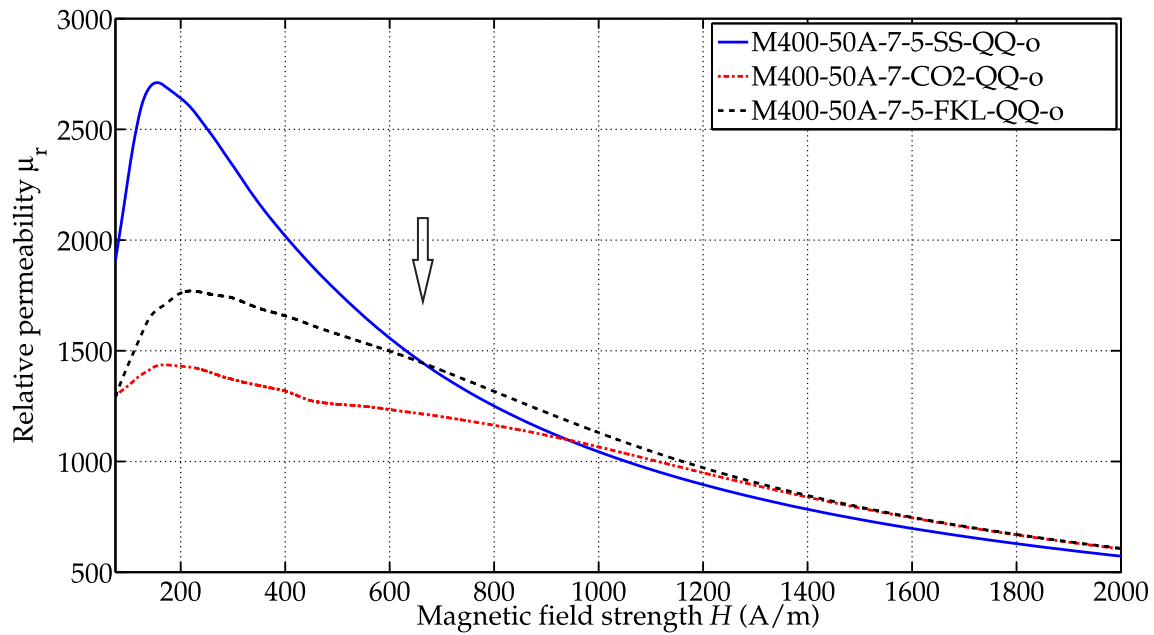


Figure B.21: Relative permeability for different cutting techniques.
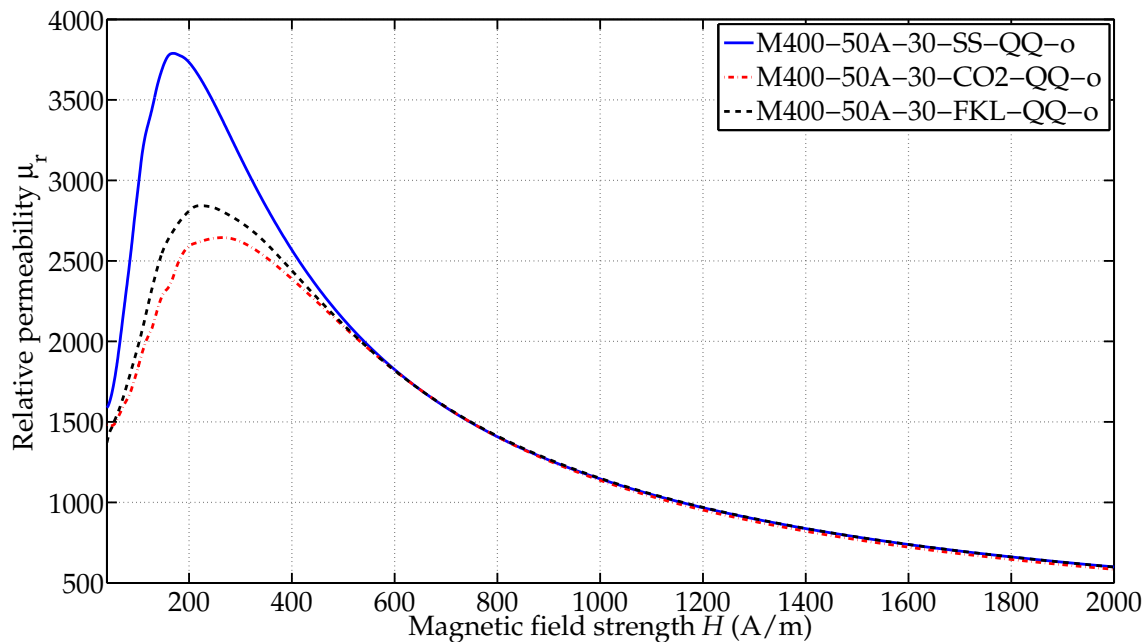


Figure B.22: Relative permeability for different cutting techniques.

# B.4 Diagrams: influence of ratio $V_{dg}/(V_{nd} + V_{dg})$
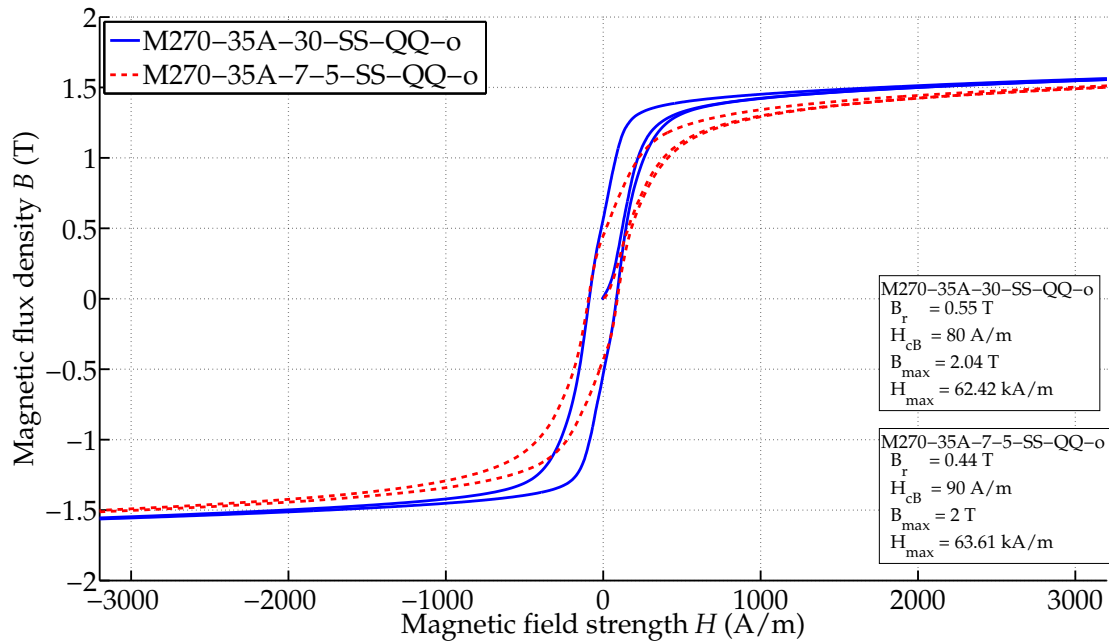


(a) M270-35A
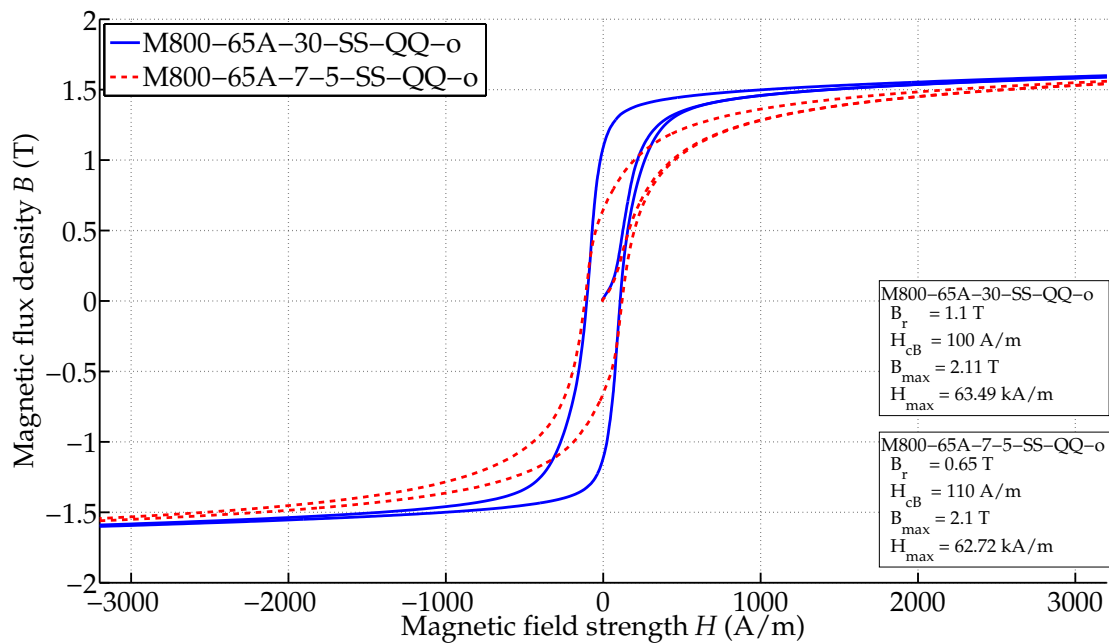


(b) M800-65A

Figure B.23: Effect of ratio $V_{dg}/(V_{nd}+V_{dg})$ on the magnetic flux density of transversely guillotine-cut samples.
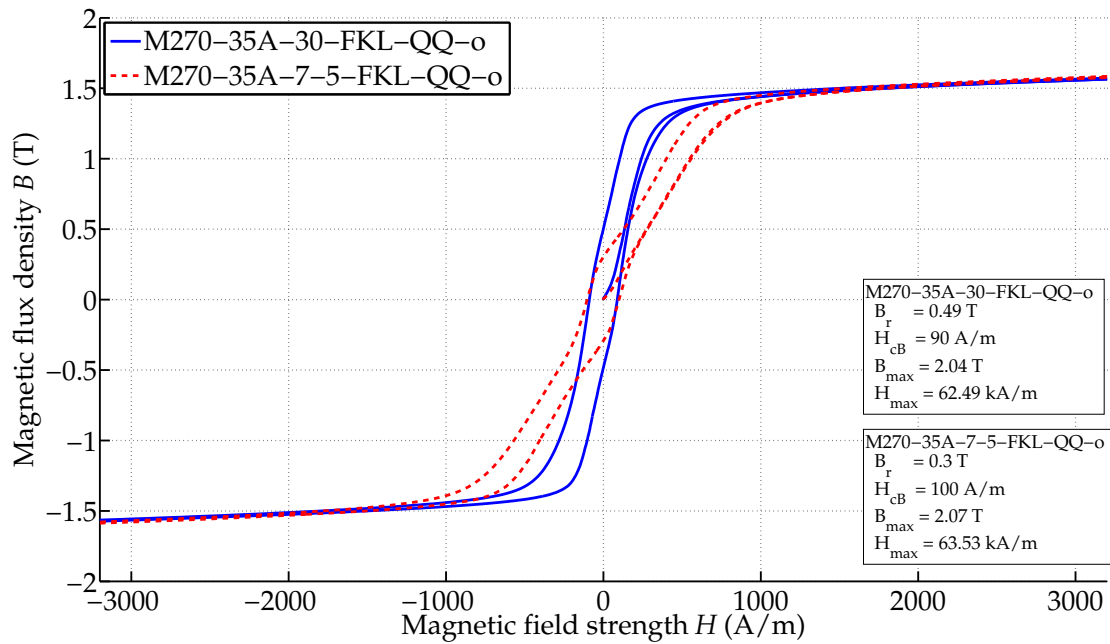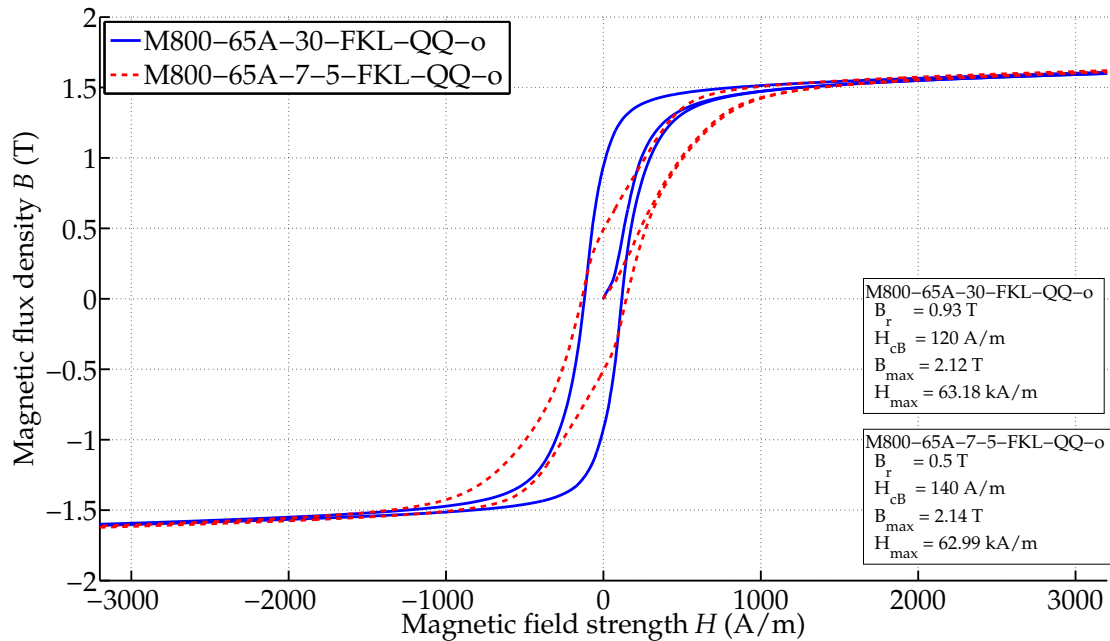
(a) M270-35A



(b) M800-65A

Figure B.24: Effect of ratio $V_{dg}/(V_{nd}+V_{dg})$ on the magnetic flux density of transversely FKL-laser cut samples.
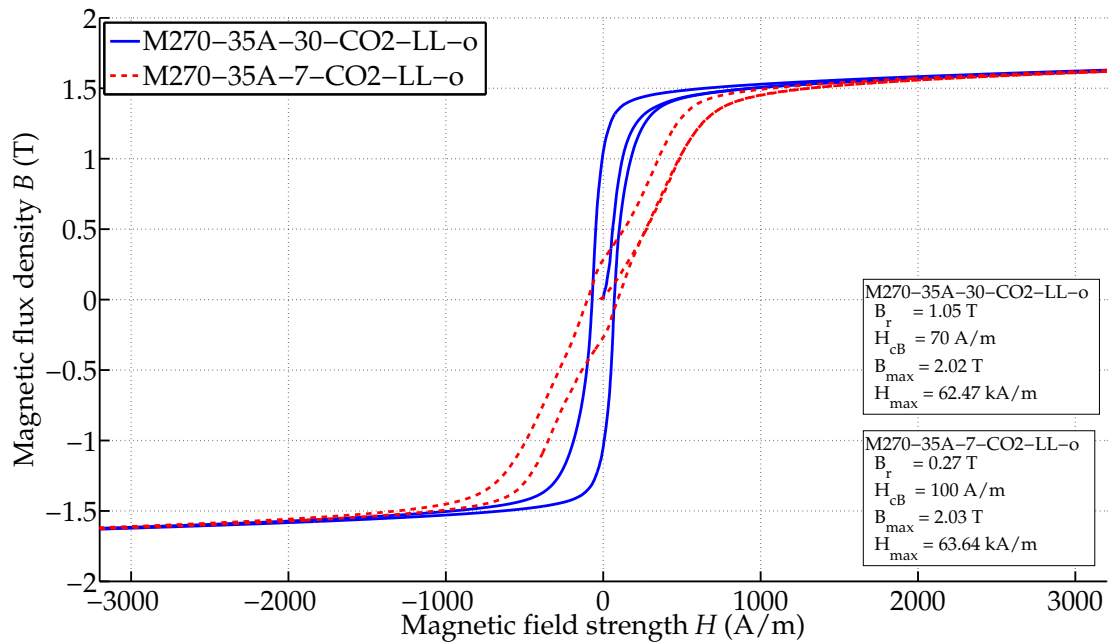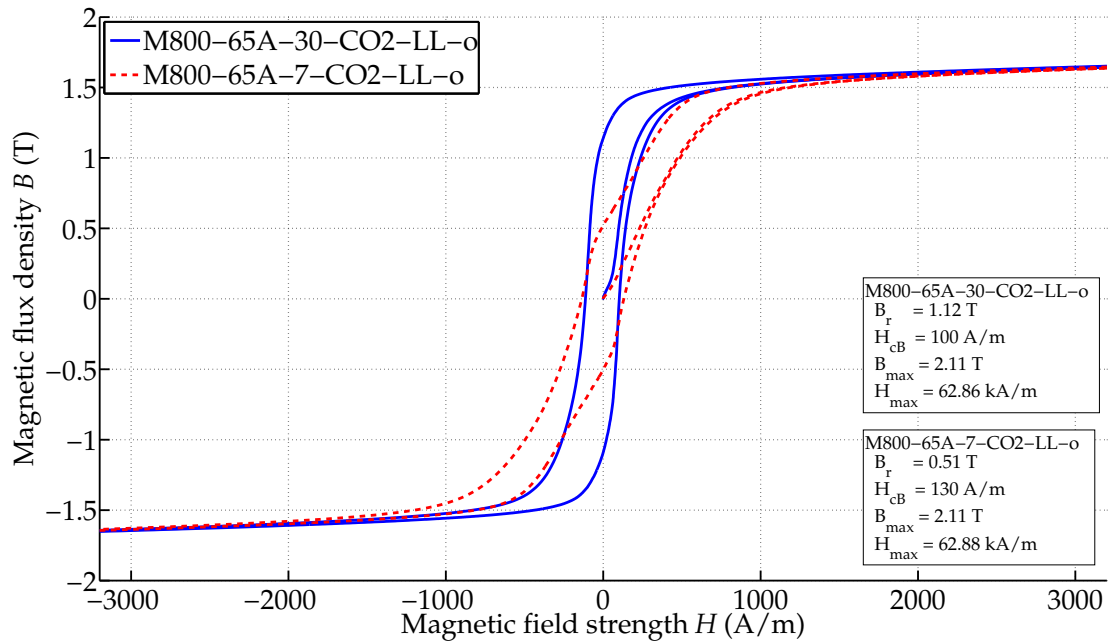
(a) M270-35A



(b) M800-65A

Figure B.25: Effect of ratio $V_{\mathrm{dg}}/(V_{\mathrm{nd}} + V_{\mathrm{dg}})$ on the magnetic flux density of longitudinally $CO_2$-laser cut samples.
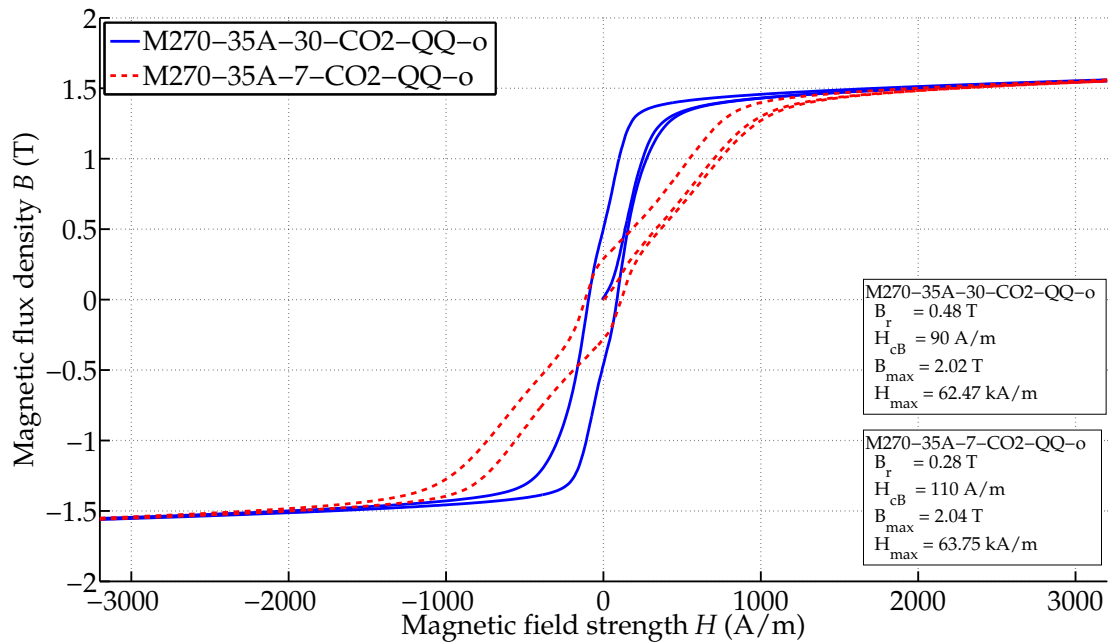
(a) M270-35A
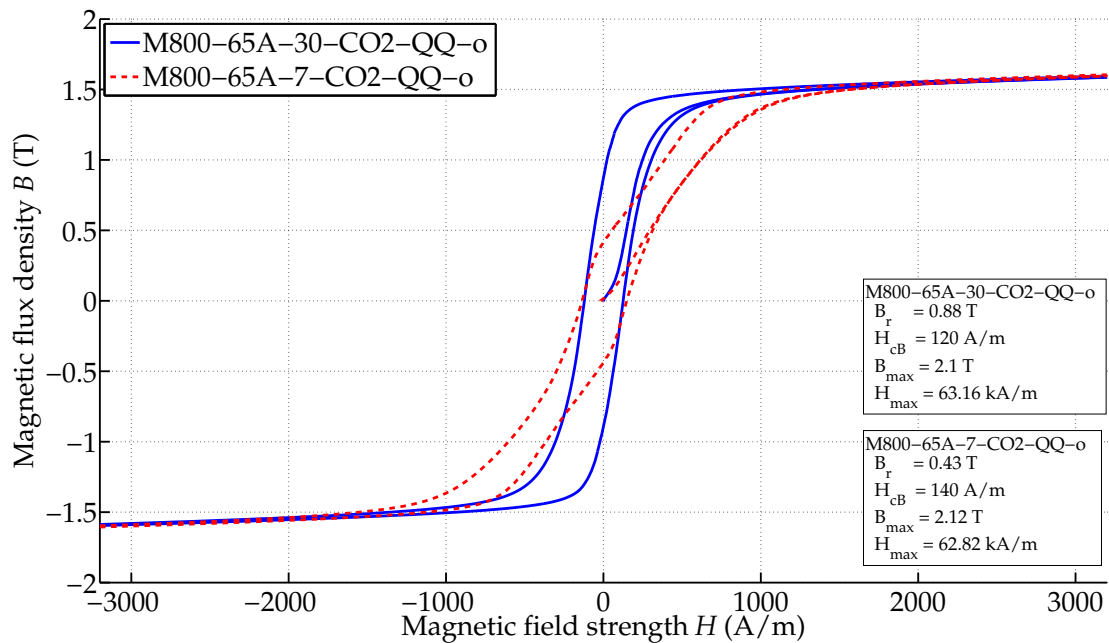


(b) M800-65A

Figure B.26: Effect of ratio $V_{\mathrm{dg}}/(V_{\mathrm{nd}}+V_{\mathrm{dg}})$ on the magnetic flux density of transversely $CO_2$-laser cut samples.

# Appendix C

# Results of the Epstein frame measurements

## C.1  Specific values of the Epstein measurements

Table C.1: Specific values of the Epstein measurements with sense lines on the secondary winding.

| Overview of the specific values of Epstein measurements with sense lines on the secondary winding | | | | | | | | |
|---|---|---|---|---|---|---|---|---|
| Bali, M. 30.04.2013 | | | Magnetic flux density at | | | | Losses at | |
| Measured specimen | Specimen | Frequency (Hz) | 2500 $\frac{A}{m}$ | 3500 $\frac{A}{m}$ | 5000 $\frac{A}{m}$ | 10000 $\frac{A}{m}$ | 1.0 T | 1.5 T |
| Mix | M270-35A_30_SS | 50 | 1.58 | 1.62 | 1.67 | 1.78 | 1.15 | 2.51 |
| Mix | M270-35A_30_SS | 250 | 1.58 | 1.62 | 1.67 | 1.79 | 9.63 | 21.58 |
| Mix | M270-35A_30_SS | 500 | 1.58 | 1.62 | 1.67 | 1.79 | 27.58 | 63.82 |
| Mix | M270-35A_30_SS | 800 | 1.58 | 1.62 | 1.67 | 1.79 | 58.70 | 139.85 |
| Mix | M270-35A_7.5_SS | 50 | 1.51 | 1.57 | 1.64 | 1.77 | 1.60 | 3.22 |
| Mix | M270-35A_7.5_SS | 250 | 1.52 | 1.58 | 1.64 | 1.77 | 12.87 | 26.35 |
| Mix | M270-35A_7.5_SS | 500 | 1.52 | 1.58 | 1.64 | 1.77 | 36.46 | 75.73 |
| Mix | M270-35A_30_$CO_2$ | 50 | 1.59 | 1.63 | 1.68 | 1.79 | 1.26 | 2.59 |
| Mix | M270-35A_30_$CO_2$ | 250 | 1.59 | 1.63 | 1.68 | 1.79 | 10.23 | 21.68 |
| Mix | M270-35A_30_$CO_2$ | 500 | 1.59 | 1.63 | 1.68 | 1.79 | 28.70 | 62.85 |
| Mix | M270-35A_30_$CO_2$ | 800 | 1.59 | 1.63 | 1.68 | 1.79 | 59.57 | 135.94 |
| LL | M270-35A_30_$CO_2$ | 50 | 1.63 | 1.66 | 1.70 | 1.82 | 1.11 | 2.30 |
| LL | M270-35A_30_$CO_2$ | 250 | 1.63 | 1.66 | 1.71 | 1.82 | 9.22 | 19.77 |
| LL | M270-35A_30_$CO_2$ | 500 | 1.63 | 1.66 | 1.71 | 1.82 | 27.13 | 58.90 |
| Mix | M270-35A_7_$CO_2$ | 50 | 1.57 | 1.61 | 1.66 | 1.78 | 1.98 | 3.48 |
| Mix | M270-35A_7_$CO_2$ | 250 | 1.57 | 1.61 | 1.66 | 1.78 | 15.16 | 28.84 |
| Mix | M270-35A_7_$CO_2$ | 500 | 1.57 | 1.61 | 1.67 | 1.79 | 40.78 | 80.66 |
| Mix | M270-35A_30_FKL | 50 | 1.59 | 1.63 | 1.67 | 1.78 | 1.24 | 2.58 |
| Mix | M270-35A_30_FKL | 250 | 1.59 | 1.63 | 1.67 | 1.79 | 10.13 | 21.73 |
| Mix | M270-35A_30_FKL | 500 | 1.59 | 1.63 | 1.68 | 1.79 | 28.76 | 62.91 |
| Mix | M270-35A_30_FKL | 800 | 1.59 | 1.63 | 1.67 | 1.79 | 59.56 | 136.29 |
| LL | M270-35A_30_FKL | 50 | 1.62 | 1.66 | 1.71 | 1.81 | 1.08 | 2.26 |
| LL | M270-35A_30_FKL | 250 | 1.62 | 1.66 | 1.71 | 1.82 | 9.23 | 19.70 |
| LL | M270-35A_30_FKL | 500 | 1.62 | 1.66 | 1.70 | 1.82 | 25.27 | 58.86 |
| QQ | M270-35A_30_FKL | 50 | 1.55 | 1.59 | 1.64 | 1.76 | 1.42 | 2.87 |
| QQ | M270-35A_30_FKL | 250 | 1.55 | 1.59 | 1.64 | 1.76 | 11.25 | 23.60 |
| QQ | M270-35A_30_FKL | 500 | 1.55 | 1.59 | 1.64 | 1.76 | 31.25 | 66.84 |
| Mix | M270-35A_7.5_FKL | 50 | 1.57 | 1.61 | 1.66 | 1.78 | 1.83 | 3.30 |
| Mix | M270-35A_7.5_FKL | 250 | 1.57 | 1.61 | 1.66 | 1.78 | 14.01 | 27.17 |
| Mix | M270-35A_7.5_FKL | 500 | 1.57 | 1.61 | 1.66 | 1.78 | 37.82 | 76.09 |

| Overview of the specific values of Epstein measurements with sense lines on the secondary winding | | | | | | | | |
|---|---|---|---|---|---|---|---|---|
| Bali, M. 30.04.2013 | | | Magnetic flux density at | | | | Losses at | |
| Measured specimen | Specimen | Frequency (Hz) | $2500\,\frac{A}{m}$ | $3500\,\frac{A}{m}$ | $5000\,\frac{A}{m}$ | $10000\,\frac{A}{m}$ | 1.0 T | 1.5 T |
| Mix | M400-50A_30_SS | 50 | 1.57 | 1.61 | 1.66 | 1.77 | 1.74 | 3.86 |
| Mix | M400-50A_30_SS | 250 | 1.57 | 1.61 | 1.66 | 1.77 | 17.66 | 42.08 |
| Mix | M400-50A_30_SS | 500 | 1.57 | 1.61 | 1.65 | 1.77 | 55.76 | 138.63 |
| Mix | M400-50A_7.5_SS | 50 | 1.53 | 1.59 | 1.64 | 1.76 | 2.22 | 4.70 |
| Mix | M400-50A_7.5_SS | 250 | 1.54 | 1.59 | 1.64 | 1.77 | 21.94 | 46.89 |
| Mix | M400-50A_7.5_SS | 500 | 1.54 | 1.59 | 1.64 | 1.76 | 66.77 | 149.44 |
| Mix | M400-50A_30_CO$_2$ | 50 | 1.57 | 1.61 | 1.66 | 1.77 | 1.85 | 3.96 |
| Mix | M400-50A_30_CO$_2$ | 250 | 1.58 | 1.61 | 1.66 | 1.77 | 18.18 | 41.31 |
| Mix | M400-50A_30_CO$_2$ | 500 | 1.57 | 1.61 | 1.65 | 1.77 | 56.16 | 134.63 |
| LL | M400-50A_30_CO$_2$ | 50 | 1.61 | 1.64 | 1.68 | 1.80 | 1.73 | 3.63 |
| LL | M400-50A_30_CO$_2$ | 250 | 1.60 | 1.64 | 1.69 | 1.80 | 17.19 | 40.27 |
| LL | M400-50A_30_CO$_2$ | 500 | 1.60 | 1.64 | 1.68 | 1.80 | 54.06 | 133.89 |
| QQ | M400-50A_30_CO$_2$ | 50 | 1.55 | 1.58 | 1.63 | 1.73 | 2.07 | 4.32 |
| QQ | M400-50A_30_CO$_2$ | 250 | 1.55 | 1.58 | 1.63 | 1.75 | 19.11 | 42.38 |
| QQ | M400-50A_30_CO$_2$ | 500 | 1.55 | 1.58 | 1.63 | 1.75 | 57.65 | 133.45 |
| Mix | M400-50A_7_CO$_2$ | 50 | 1.57 | 1.61 | 1.65 | 1.77 | 2.68 | 4.96 |
| Mix | M400-50A_7_CO$_2$ | 250 | 1.56 | 1.60 | 1.65 | 1.77 | 23.73 | 47.86 |
| Mix | M400-50A_7_CO$_2$ | 500 | 1.56 | 1.60 | 1.65 | 1.77 | 69.42 | 146.41 |
| LL | M400-50A_7_CO$_2$ | 50 | 1.59 | 1.63 | 1.68 | 1.79 | 2.58 | 4.72 |
| LL | M400-50A_7_CO$_2$ | 250 | 1.59 | 1.63 | 1.68 | 1.79 | 22.95 | 45.88 |
| LL | M400-50A_7_CO$_2$ | 500 | 1.59 | 1.63 | 1.68 | 1.79 | 67.11 | 140.74 |
| QQ | M400-50A_7_CO$_2$ | 50 | 1.54 | 1.58 | 1.63 | 1.74 | 2.80 | 5.25 |
| QQ | M400-50A_7_CO$_2$ | 250 | 1.53 | 1.58 | 1.63 | 1.74 | 24.62 | 50.16 |
| QQ | M400-50A_7_CO$_2$ | 500 | 1.54 | 1.58 | 1.62 | 1.74 | 71.89 | 152.11 |
| Mix | M400-50A_30_FKL | 50 | 1.58 | 1.61 | 1.66 | 1.77 | 1.86 | 3.94 |
| Mix | M400-50A_30_FKL | 250 | 1.58 | 1.61 | 1.66 | 1.77 | 18.05 | 41.17 |
| Mix | M400-50A_30_FKL | 500 | 1.58 | 1.61 | 1.66 | 1.77 | 54.50 | 134.50 |
| LL | M400-50A_30_FKL | 50 | 1.60 | 1.64 | 1.69 | 1.80 | 1.62 | 3.57 |
| LL | M400-50A_30_FKL | 250 | 1.61 | 1.64 | 1.69 | 1.80 | 16.73 | 40.06 |
| LL | M400-50A_30_FKL | 500 | 1.61 | 1.64 | 1.68 | 1.80 | 52.65 | 134.94 |
| QQ | M400-50A_30_FKL | 50 | 1.55 | 1.59 | 1.63 | 1.74 | 2.07 | 4.32 |
| QQ | M400-50A_30_FKL | 250 | 1.55 | 1.59 | 1.63 | 1.75 | 19.10 | 42.32 |
| QQ | M400-50A_30_FKL | 500 | 1.55 | 1.59 | 1.63 | 1.75 | 57.69 | 133.10 |
| Mix | M400-50A_7.5_FKL | 50 | 1.57 | 1.61 | 1.66 | 1.77 | 2.47 | 4.72 |
| Mix | M400-50A_7.5_FKL | 250 | 1.57 | 1.61 | 1.65 | 1.77 | 22.27 | 45.92 |
| Mix | M400-50A_7.5_FKL | 500 | 1.56 | 1.60 | 1.65 | 1.77 | 65.69 | 141.31 |

| Overview of the specific values of Epstein measurements with sense lines on the secondary winding | | | | | | | | |
|---|---|---|---|---|---|---|---|---|
| Bali, M. 30.04.2013 | | | Magnetic flux density at | | | | Losses at | |
| Measured specimen | Specimen | Frequency (Hz) | $2500\,\frac{A}{m}$ | $3500\,\frac{A}{m}$ | $5000\,\frac{A}{m}$ | $10000\,\frac{A}{m}$ | 1.0 T | 1.5 T |
| Mix | M800-65A_30_SS | 50 | 1.62 | 1.65 | 1.70 | 1.81 | 2.36 | 5.15 |
| Mix | M800-65A_30_SS | 250 | 1.62 | 1.66 | 1.70 | 1.82 | 25.65 | 65.62 |
| Mix | M800-65A_30_SS | 500 | 1.62 | 1.65 | 1.70 | 1.81 | 81.16 | 225.03 |
| Mix | M800-65A_7.5_SS | 50 | 1.58 | 1.63 | 1.69 | 1.81 | 2.99 | 6.11 |
| Mix | M800-65A_7.5_SS | 250 | 1.57 | 1.63 | 1.68 | 1.81 | 32.43 | 69.54 |
| Mix | M800-65A_7.5_SS | 500 | 1.57 | 1.62 | 1.68 | 1.80 | 99.59 | 232.43 |
| Mix | M800-65A_30_CO$_2$ | 50 | 1.63 | 1.66 | 1.70 | 1.82 | 2.51 | 5.14 |
| Mix | M800-65A_30_CO$_2$ | 250 | 1.63 | 1.66 | 1.70 | 1.82 | 26.05 | 62.49 |
| Mix | M800-65A_30_CO$_2$ | 500 | 1.62 | 1.66 | 1.70 | 1.81 | 81.81 | 216.72 |
| LL | M800-65A_30_CO$_2$ | 50 | 1.65 | 1.69 | 1.73 | 1.84 | 2.48 | 5.04 |
| LL | M800-65A_30_CO$_2$ | 250 | 1.65 | 1.68 | 1.73 | 1.84 | 26.19 | 63.83 |
| LL | M800-65A_30_CO$_2$ | 500 | 1.65 | 1.68 | 1.73 | 1.84 | 80.42 | 221.43 |
| QQ | M800-65A_30_CO$_2$ | 50 | 1.60 | 1.64 | 1.68 | 1.79 | 2.51 | 5.27 |
| QQ | M800-65A_30_CO$_2$ | 250 | 1.60 | 1.64 | 1.68 | 1.79 | 25.48 | 61.04 |
| QQ | M800-65A_30_CO$_2$ | 500 | 1.60 | 1.63 | 1.68 | 1.79 | 80.94 | 210.57 |
| Mix | M800-65A_7_CO$_2$ | 50 | 1.61 | 1.65 | 1.70 | 1.81 | 3.28 | 6.08 |
| Mix | M800-65A_7_CO$_2$ | 250 | 1.61 | 1.65 | 1.69 | 1.81 | 31.43 | 64.68 |
| Mix | M800-65A_7_CO$_2$ | 500 | 1.60 | 1.64 | 1.69 | 1.80 | 95.17 | 209.87 |
| LL | M800-65A_7_CO$_2$ | 50 | 1.63 | 1.67 | 1.72 | 1.83 | 3.24 | 5.97 |
| LL | M800-65A_7_CO$_2$ | 250 | 1.63 | 1.67 | 1.72 | 1.83 | 31.39 | 64.15 |
| LL | M800-65A_7_CO$_2$ | 500 | 1.63 | 1.67 | 1.71 | 1.83 | 95.23 | 209.24 |
| QQ | M800-65A_7_CO$_2$ | 50 | 1.58 | 1.62 | 1.67 | 1.79 | 3.39 | 6.27 |
| QQ | M800-65A_7_CO$_2$ | 250 | 1.58 | 1.62 | 1.67 | 1.79 | 31.61 | 65.72 |
| QQ | M800-65A_7_CO$_2$ | 500 | 1.58 | 1.62 | 1.67 | 1.78 | 95.53 | 210.64 |
| Mix | M800-65A_30_FKL | 50 | 1.63 | 1.67 | 1.71 | 1.82 | 2.53 | 5.16 |
| Mix | M800-65A_30_FKL | 250 | 1.63 | 1.66 | 1.71 | 1.82 | 26.21 | 63.46 |
| Mix | M800-65A_30_FKL | 500 | 1.62 | 1.66 | 1.70 | 1.81 | 81.38 | 218.89 |
| LL | M800-65A_30_FKL | 50 | 1.65 | 1.68 | 1.73 | 1.84 | 2.49 | 5.05 |
| LL | M800-65A_30_FKL | 250 | 1.65 | 1.69 | 1.73 | 1.84 | 25.84 | 64.15 |
| LL | M800-65A_30_FKL | 500 | 1.65 | 1.68 | 1.73 | 1.84 | 81.14 | 223.17 |
| QQ | M800-65A_30_FKL | 50 | 1.61 | 1.64 | 1.68 | 1.79 | 2.51 | 5.27 |
| QQ | M800-65A_30_FKL | 250 | 1.60 | 1.64 | 1.68 | 1.79 | 25.73 | 62.18 |
| QQ | M800-65A_30_FKL | 500 | 1.60 | 1.63 | 1.68 | 1.79 | 81.97 | 217.81 |
| Mix | M800-65A_7.5_FKL | 50 | 1.61 | 1.65 | 1.70 | 1.81 | 3.07 | 5.86 |
| Mix | M800-65A_7.5_FKL | 250 | 1.61 | 1.65 | 1.70 | 1.81 | 30.17 | 63.72 |
| Mix | M800-65A_7.5_FKL | 500 | 1.61 | 1.65 | 1.69 | 1.81 | 92.49 | 210.67 |

Table C.2: Specific values of the Epstein measurements without sense lines.

| Overview of the specific values of Epstein measurements without sense lines | | | | | | | | |
|---|---|---|---|---|---|---|---|---|
| Bali, M. 30.04.2013 | | | Magnetic flux density at | | | | Losses at | |
| Measured specimen | Specimen | Frequency (Hz) | 2500 $\frac{A}{m}$ | 3500 $\frac{A}{m}$ | 5000 $\frac{A}{m}$ | 10000 $\frac{A}{m}$ | 1.0 T | 1.5 T |
| Mix | M270-35A_30_SS | 50 | 1.58 | 1.62 | 1.67 | 1.78 | 1.12 | 2.53 |
| Mix | M270-35A_30_SS | 250 | 1.58 | 1.62 | 1.67 | 1.79 | 9.56 | 22.13 |
| Mix | M270-35A_30_SS | 500 | 1.58 | 1.62 | 1.67 | 1.79 | 26.94 | 65.30 |
| Mix | M270-35A_7.5_SS | 50 | 1.51 | 1.57 | 1.64 | 1.77 | 1.60 | 3.26 |
| Mix | M270-35A_7.5_SS | 250 | 1.51 | 1.57 | 1.64 | 1.77 | 12.95 | 27.18 |
| Mix | M270-35A_7.5_SS | 500 | 1.51 | 1.57 | 1.64 | 1.78 | 36.57 | 78.34 |
| Mix | M270-35A_30_CO$_2$ | 50 | 1.59 | 1.63 | 1.67 | 1.78 | 1.24 | 2.61 |
| Mix | M270-35A_30_CO$_2$ | 250 | 1.59 | 1.63 | 1.68 | 1.79 | 10.17 | 22.05 |
| Mix | M270-35A_30_CO$_2$ | 500 | 1.59 | 1.63 | 1.68 | 1.80 | 28.18 | 63.79 |
| Mix | M270-35A_7_CO$_2$ | 50 | 1.56 | 1.61 | 1.66 | 1.78 | 1.98 | 3.50 |
| Mix | M270-35A_7_CO$_2$ | 250 | 1.56 | 1.61 | 1.66 | 1.78 | 15.15 | 29.17 |
| Mix | M270-35A_7_CO$_2$ | 500 | 1.56 | 1.61 | 1.67 | 1.79 | 40.72 | 81.64 |
| Mix | M270-35A_30_FKL | 50 | 1.58 | 1.62 | 1.67 | 1.78 | 1.21 | 2.60 |
| Mix | M270-35A_30_FKL | 250 | 1.59 | 1.62 | 1.67 | 1.79 | 10.05 | 22.12 |
| Mix | M270-35A_30_FKL | 500 | 1.59 | 1.63 | 1.68 | 1.80 | 27.94 | 64.22 |
| Mix | M270-35A_7.5_FKL | 50 | 1.56 | 1.61 | 1.66 | 1.78 | 1.83 | 3.32 |
| Mix | M270-35A_7.5_FKL | 250 | 1.57 | 1.61 | 1.66 | 1.78 | 14.02 | 27.55 |
| Mix | M270-35A_7.5_FKL | 500 | 1.56 | 1.61 | 1.66 | 1.79 | 37.74 | 77.23 |

| Overview of the specific values of Epstein measurements without sense lines | | | | | | | | |
|---|---|---|---|---|---|---|---|---|
| Bali, M. 30.04.2013 | | | Magnetic flux density at | | | | Losses at | |
| Measured specimen | Specimen | Frequency (Hz) | 2500 $\frac{A}{m}$ | 3500 $\frac{A}{m}$ | 5000 $\frac{A}{m}$ | 10000 $\frac{A}{m}$ | 1.0 T | 1.5 T |
| Mix | M400-50A_30_SS | 500 | 1.57 | 1.61 | 1.65 | 1.77 | 54.86 | 142.71 |
| Mix | M400-50A_7.5_SS | 50 | 1.53 | 1.58 | 1.64 | 1.76 | 2.24 | 4.77 |
| Mix | M400-50A_7.5_SS | 250 | 1.53 | 1.58 | 1.64 | 1.76 | 22.18 | 48.23 |
| Mix | M400-50A_7.5_SS | 500 | 1.53 | 1.58 | 1.64 | 1.77 | 68.11 | 153.34 |
| Mix | M400-50A_30_CO$_2$ | 500 | 1.57 | 1.61 | 1.65 | 1.77 | 54.85 | 136.58 |
| Mix | M400-50A_7_CO$_2$ | 50 | 1.56 | 1.60 | 1.65 | 1.77 | 2.69 | 4.99 |
| Mix | M400-50A_7_CO$_2$ | 250 | 1.56 | 1.60 | 1.65 | 1.77 | 23.83 | 48.68 |
| Mix | M400-50A_7_CO$_2$ | 500 | 1.55 | 1.60 | 1.65 | 1.77 | 69.38 | 147.96 |
| Mix | M400-50A_30_FKL | 500 | 1.57 | 1.61 | 1.66 | 1.77 | 54.41 | 137.01 |
| Mix | M400-50A_7.5_FKL | 50 | 1.56 | 1.60 | 1.65 | 1.77 | 2.48 | 4.76 |
| Mix | M400-50A_7.5_FKL | 250 | 1.56 | 1.60 | 1.65 | 1.77 | 22.31 | 46.56 |
| Mix | M400-50A_7.5_FKL | 500 | 1.56 | 1.60 | 1.65 | 1.77 | 65.47 | 142.71 |

| Overview of the specific values of Epstein measurements without sense lines | | | | | | | | |
|---|---|---|---|---|---|---|---|---|
| Bali, M. 30.04.2013 | | | Magnetic flux density at | | | | Losses at | |
| Measured specimen | Specimen | Frequency (Hz) | $2500\,\frac{A}{m}$ | $3500\,\frac{A}{m}$ | $5000\,\frac{A}{m}$ | $10000\,\frac{A}{m}$ | 1.0 T | 1.5 T |
| Mix | M800-65A_30_SS | 500 | 1.61 | 1.65 | 1.70 | 1.81 | 82.80 | 227.50 |
| Mix | M800-65A_7.5_SS | 50 | 1.57 | 1.63 | 1.68 | 1.80 | 3.00 | 6.19 |
| Mix | M800-65A_7.5_SS | 250 | 1.57 | 1.63 | 1.68 | 1.81 | 32.56 | 70.96 |
| Mix | M800-65A_7.5_SS | 500 | 1.57 | 1.62 | 1.68 | 1.81 | 101.02 | 235.08 |
| Mix | M800-65A_30_$CO_2$ | 500 | 1.62 | 1.65 | 1.70 | 1.81 | 82.10 | 217.58 |
| Mix | M800-65A_7_$CO_2$ | 50 | 1.60 | 1.65 | 1.69 | 1.81 | 3.32 | 6.13 |
| Mix | M800-65A_7_$CO_2$ | 250 | 1.60 | 1.65 | 1.69 | 1.81 | 31.44 | 65.19 |
| Mix | M800-65A_7_$CO_2$ | 500 | 1.60 | 1.64 | 1.69 | 1.81 | 95.49 | 211.07 |
| Mix | M800-65A_30_FKL | 500 | 1.62 | 1.65 | 1.70 | 1.82 | 81.28 | 220.16 |
| Mix | M800-65A_7.5_FKL | 50 | 1.61 | 1.65 | 1.70 | 1.81 | 3.08 | 5.89 |
| Mix | M800-65A_7.5_FKL | 250 | 1.61 | 1.65 | 1.70 | 1.81 | 30.33 | 64.32 |
| Mix | M800-65A_7.5_FKL | 500 | 1.60 | 1.65 | 1.69 | 1.81 | 92.28 | 210.27 |

## C.2 Diagrams: cutting techniques - small samples
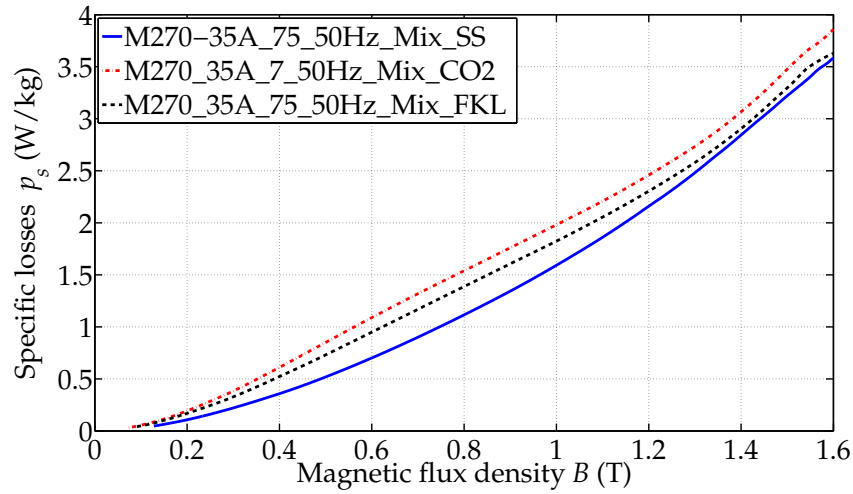


(a) 50 Hz
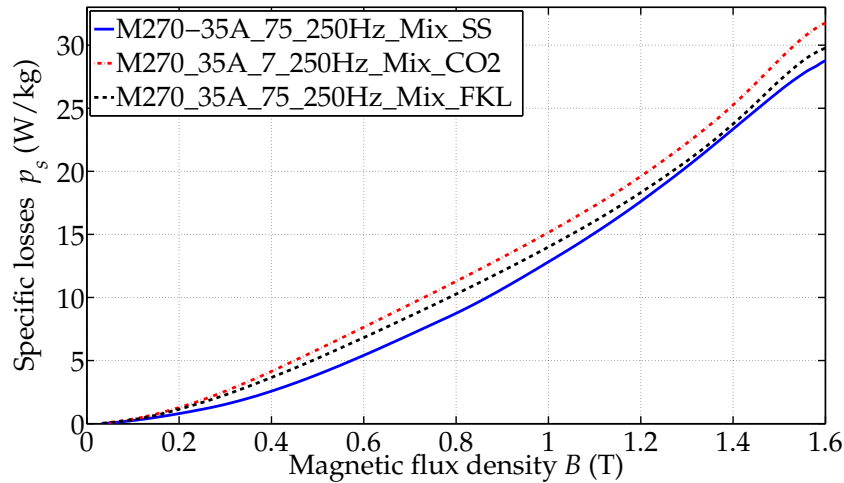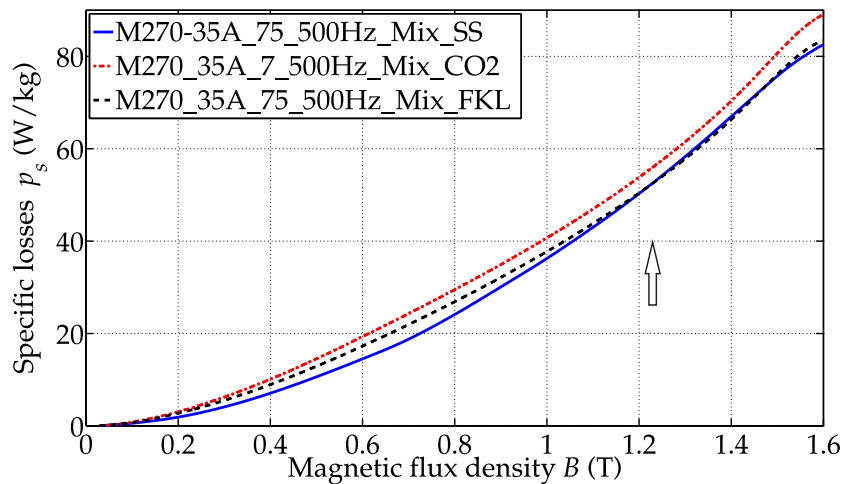


(b) 250 Hz



(c) 500 Hz

Figure C.1: Specific losses of M270-35A at different frequencies, small samples.
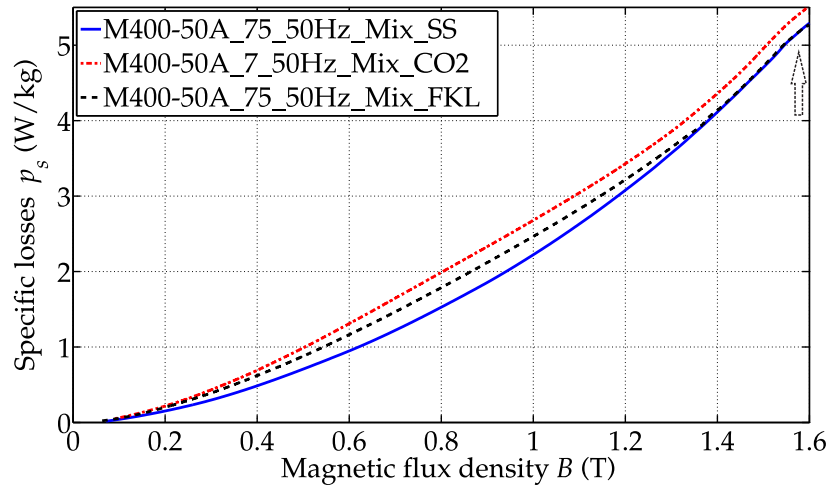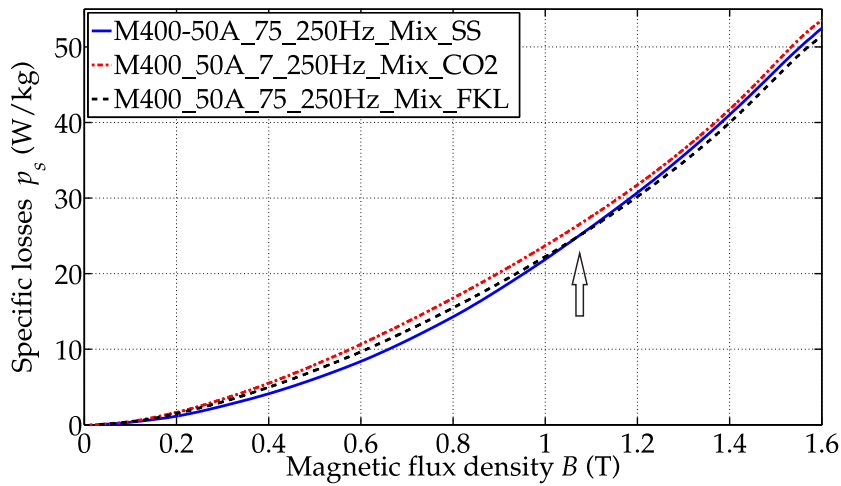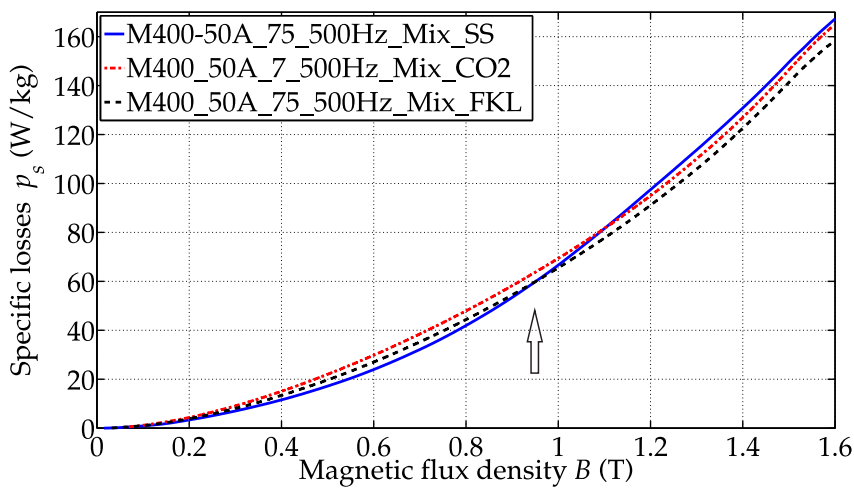
(a) 50 Hz



(b) 250 Hz



(c) 500 Hz

Figure C.2: Specific losses of M400-50A at different frequencies, small samples.
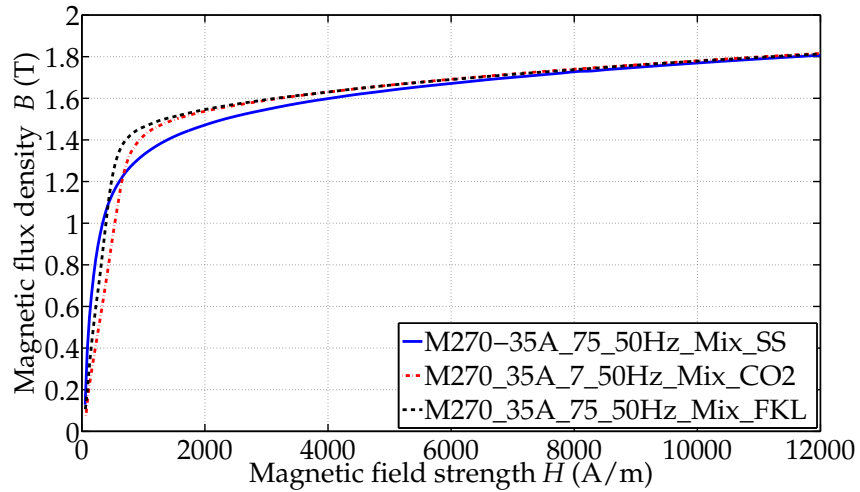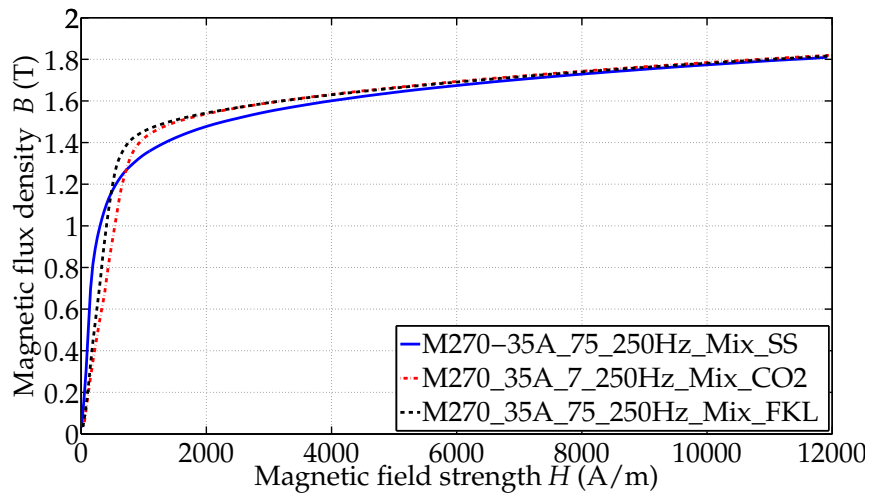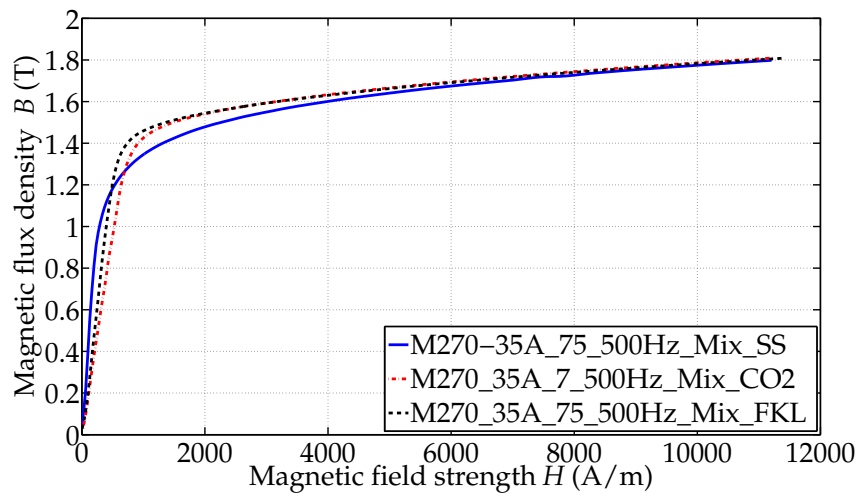
(a) 50 Hz



(b) 250 Hz



(c) 500 Hz

Figure C.3: Magnetization curves of M270-35A at different frequencies, small samples.
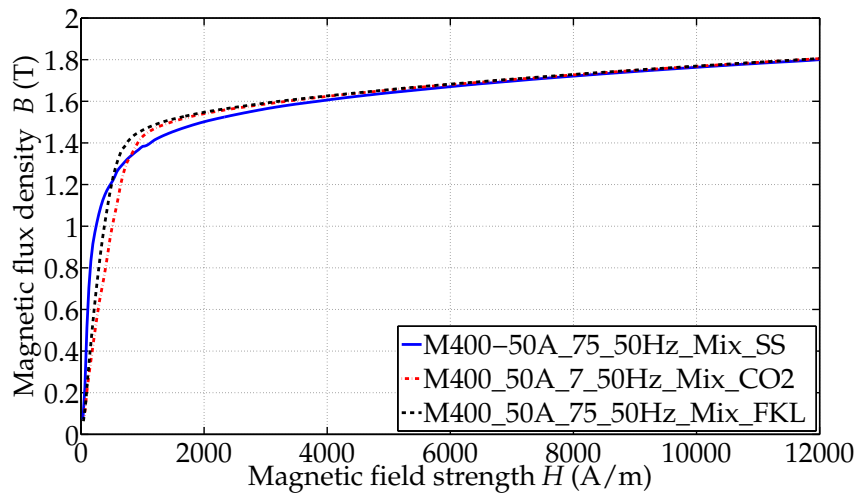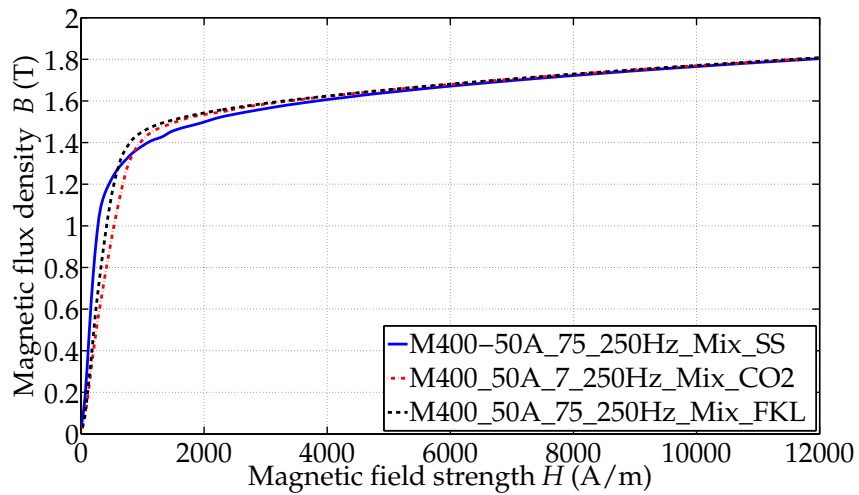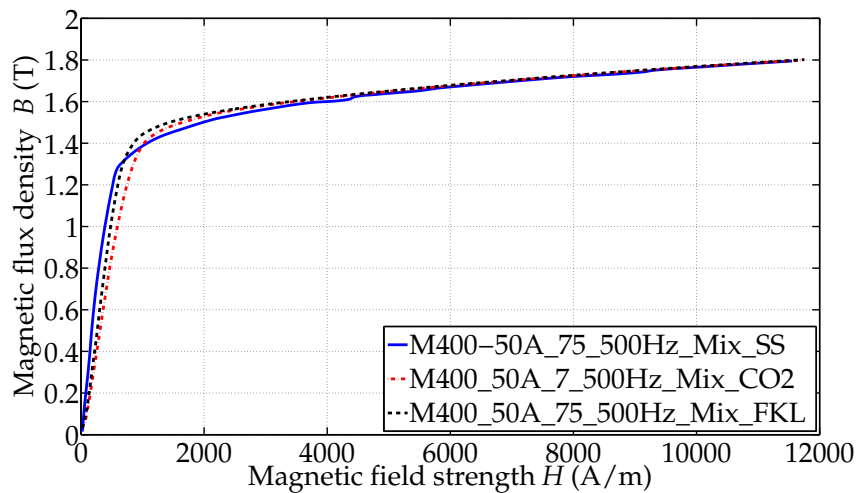
(a) 50 Hz



(b) 250 Hz



(c) 500 Hz

Figure C.4: Magnetization curves of M400-50A at different frequencies, small samples.
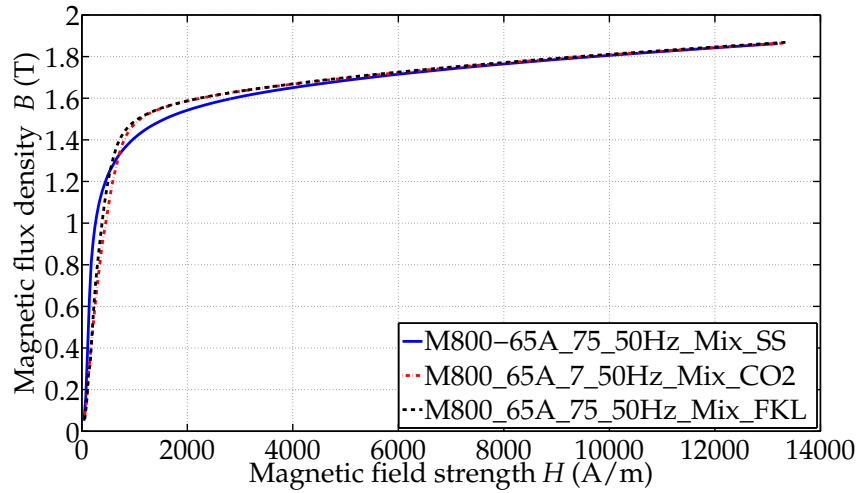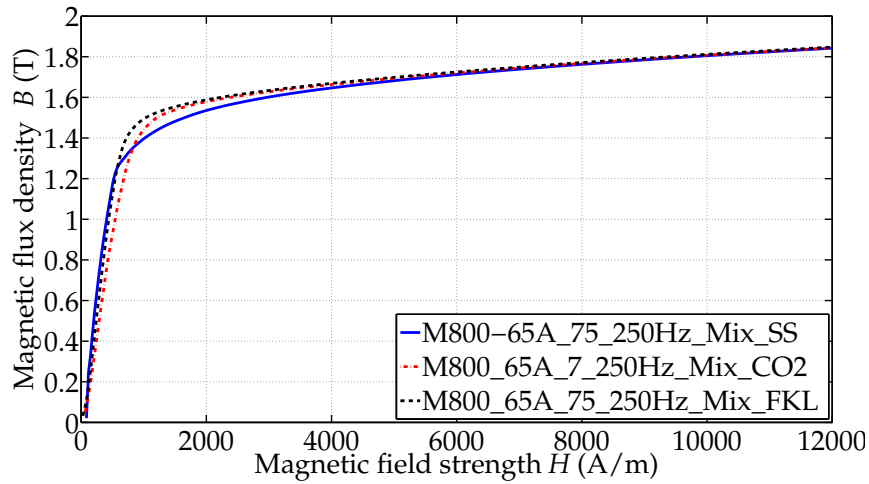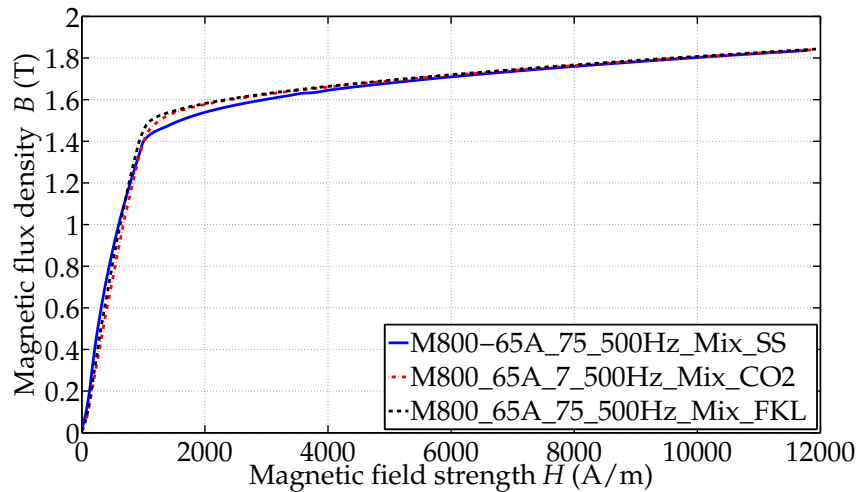
(a) 50 Hz



(b) 250 Hz



(c) 500 Hz

Figure C.5: Magnetization curves of M800-65A at different frequencies, small samples.

## C.3  Diagrams: cutting techniques - wide samples
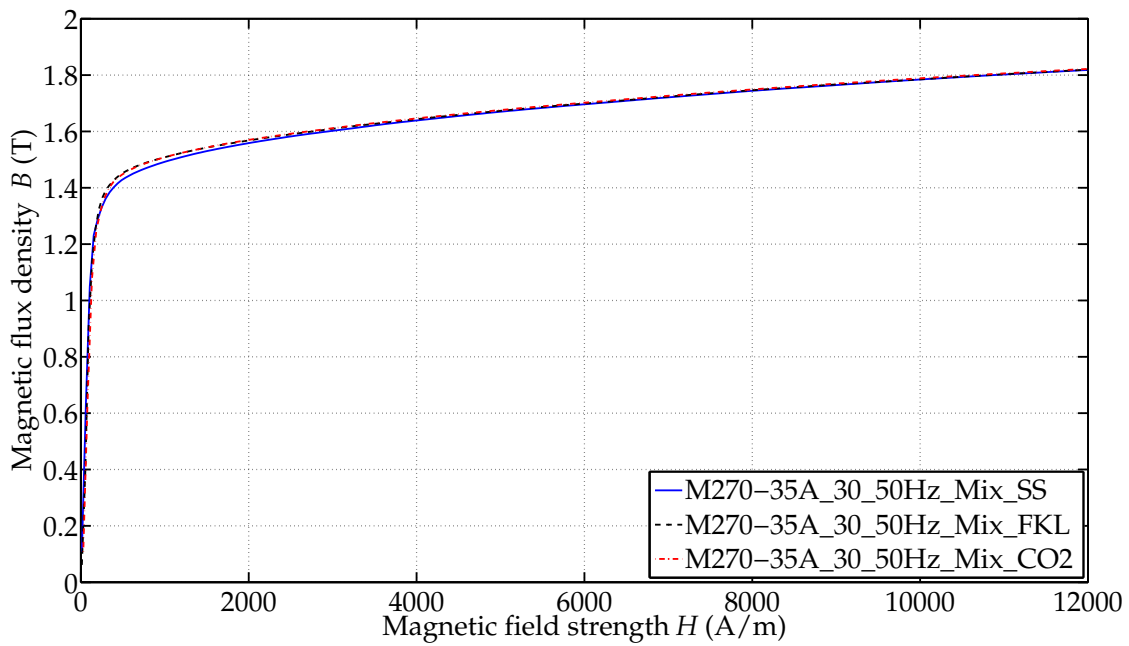


(a) 50 Hz
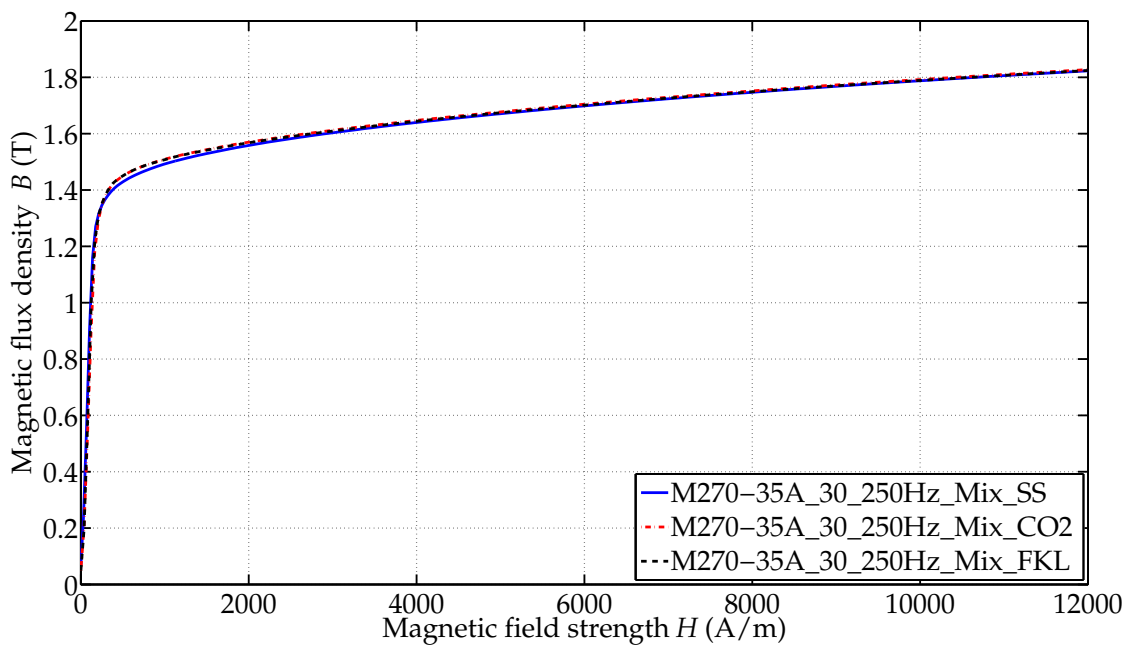


(b) 250 Hz

Figure C.6: Magnetization curves of M270-35A at 50 and 250 Hz, Mix, wide samples.
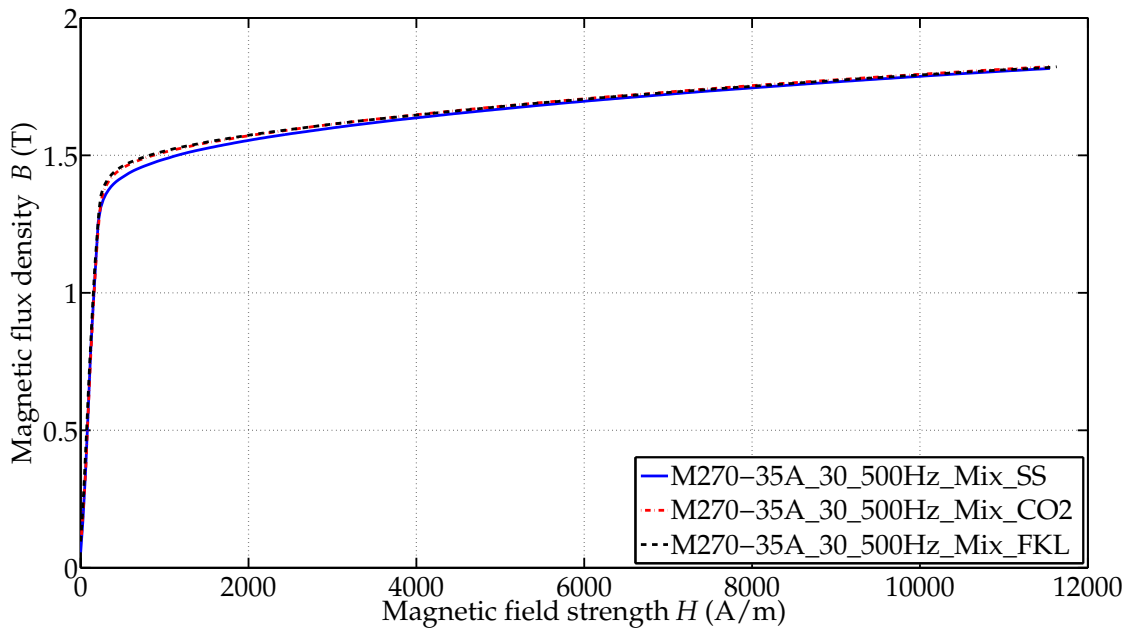
(a) 500 Hz
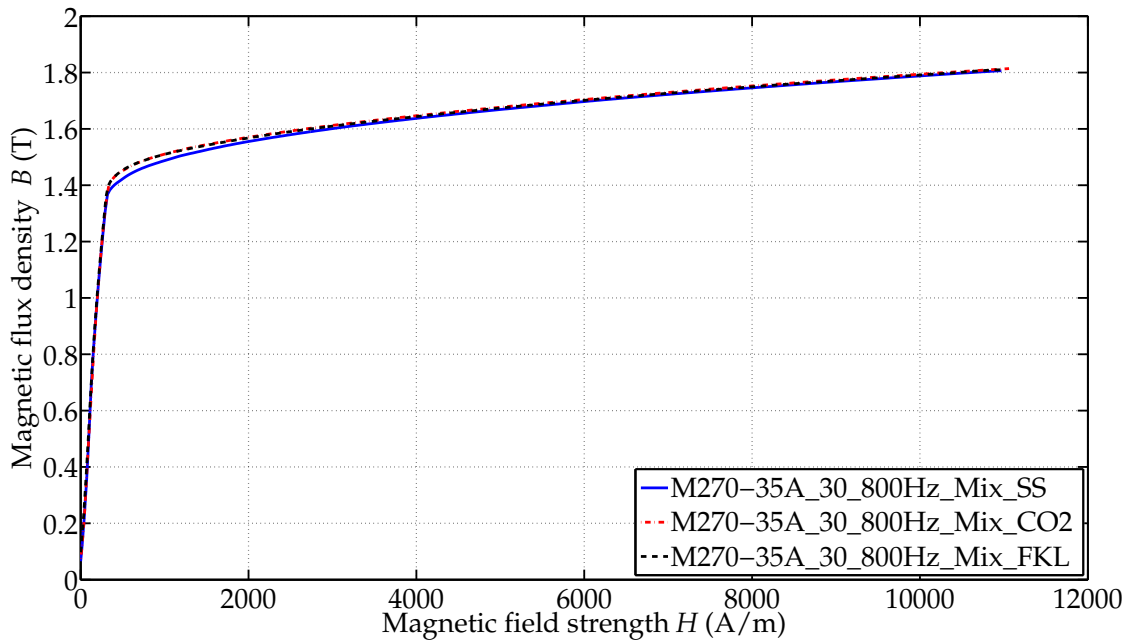


(b) 800 Hz

Figure C.7: Magnetization curves of M270-35A at 500 and 800 Hz, Mix, wide samples.
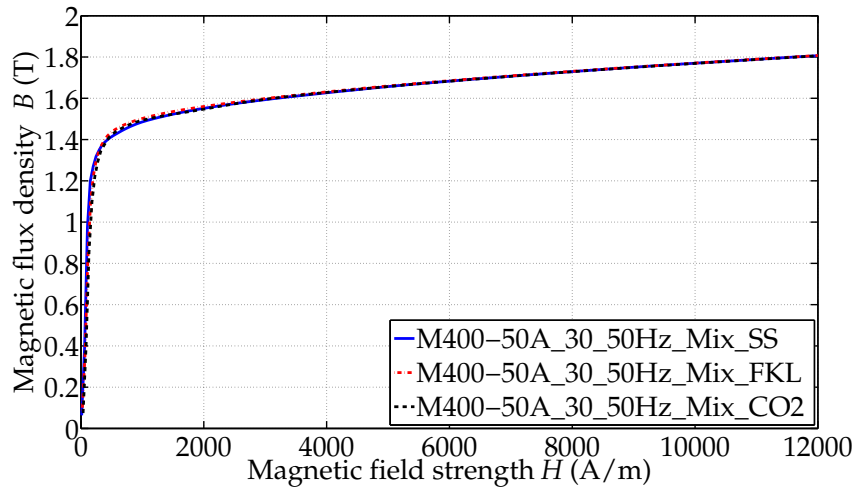
(a) 50 Hz
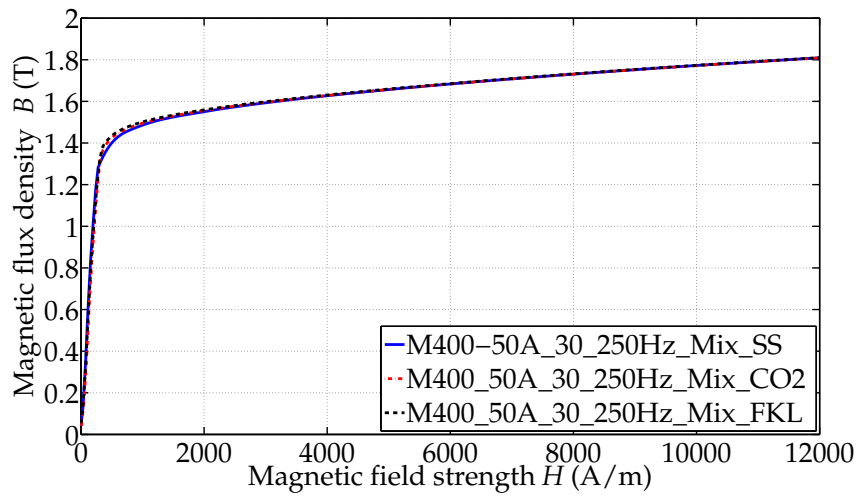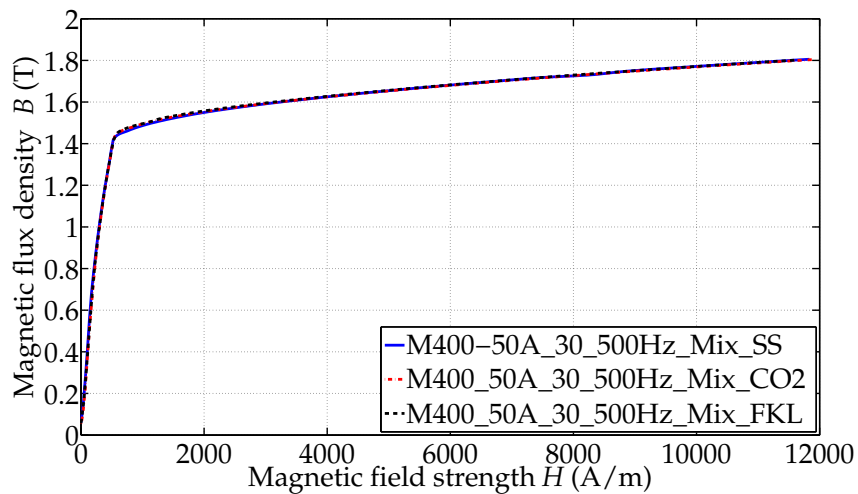


(b) 250 Hz



(c) 500 Hz

Figure C.8: Magnetization curves of M400-50A at different frequencies, wide samples.
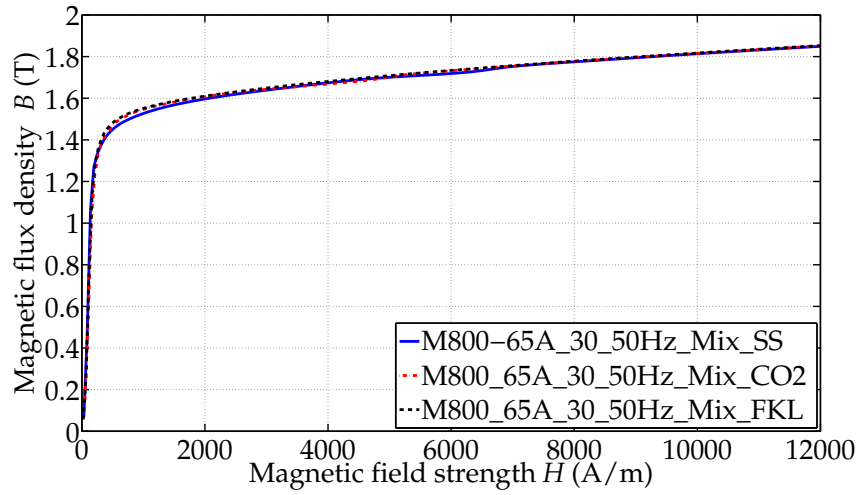
(a) 50 Hz
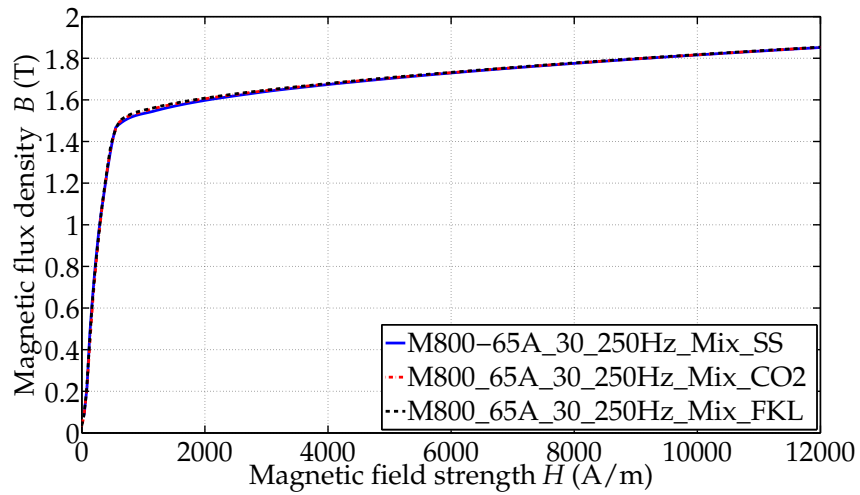


(b) 250 Hz
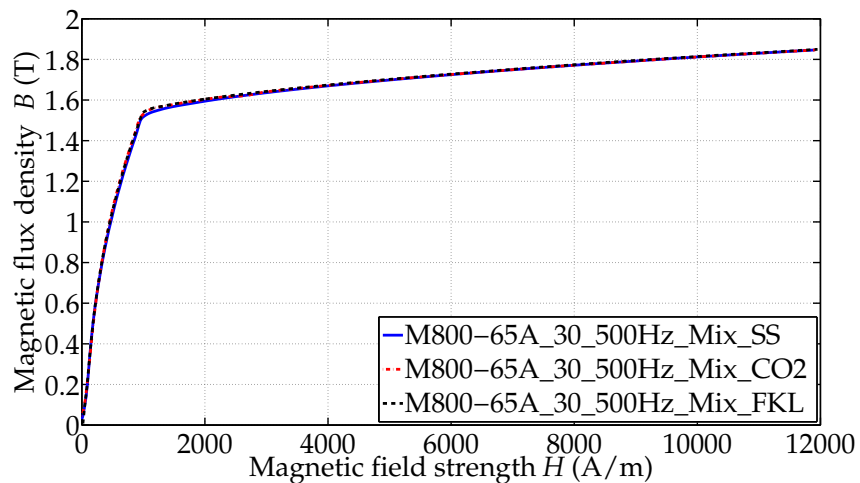


(c) 500 Hz

Figure C.9: Magnetization curves of M800-65A at different frequencies, wide samples.

# C.4  Form factor limitation - Epstein frame measurements

The following values represent the last measurement point which is still in the required form factor range of [86]. The note 'no limit' means that all measured data are within this range, the value inside the brackets is the last measured data point. '-' indicates that no measurement was performed.

Table C.3: Values of the magnetic polarization at the upper form factor limit.

| Epstein measurements with sense lines on the secondary winding | | |
|---|---|---|
| Material | Magnetic polarization $J$ in T wide samples | Magnetic polarization $J$ in T small samples |
| M270-35A_50Hz_Mix_SS | no limit (1.82) | no limit (1.80) |
| M270-35A_50Hz_Mix_$CO_2$ | 1.82 | no limit (1.81) |
| M270-35A_50Hz_Mix_FKL | no limit (1.82) | no limit (1.81) |
| M270-35A_250Hz_Mix_SS | 1.54 | 1.56 |
| M270-35A_250Hz_Mix_$CO_2$ | 1.55 | 1.55 |
| M270-35A_250Hz_Mix_FKL | 1.54 | 1.56 |
| M270-35A_500Hz_Mix_SS | 1.48 | 1.41 |
| M270-35A_500Hz_Mix_$CO_2$ | 1.50 | 1.48 |
| M270-35A_500Hz_Mix_FKL | 1.50 | 1.48 |
| M400-50A_50Hz_Mix_SS | no limit (1.81) | no limit (1.80) |
| M400-50A_50Hz_Mix_$CO_2$ | no limit (1.81) | no limit (1.81) |
| M400-50A_50Hz_Mix_FKL | no limit (1.82) | no limit (1.81) |
| M400-50A_250Hz_Mix_SS | 1.58 | 1.60 |
| M400-50A_250Hz_Mix_$CO_2$ | 1.57 | 1.59 |
| M400-50A_250Hz_Mix_FKL | 1.58 | 1.59 |
| M400-50A_500Hz_Mix_SS | 1.50 | 1.47 |
| M400-50A_500Hz_Mix_$CO_2$ | 1.51 | 1.51 |
| M400-50A_500Hz_Mix_FKL | 1.52 | 1.53 |
| M800-65A_50Hz_Mix_SS | 1.86 | no limit (1.85) |
| M800-65A_50Hz_Mix_$CO_2$ | no limit (1.87) | no limit (1.85) |
| M800-65A_50Hz_Mix_FKL | no limit (1.87) | no limit (1.85) |
| M800-65A_250Hz_Mix_SS | 1.66 | 1.68 |
| M800-65A_250Hz_Mix_$CO_2$ | 1.66 | 1.66 |
| M800-65A_250Hz_Mix_FKL | 1.66 | 1.67 |
| M800-65A_500Hz_Mix_SS | 1.55 | 1.55 |
| M800-65A_500Hz_Mix_$CO_2$ | 1.58 | 1.60 |
| M800-65A_500Hz_Mix_FKL | 1.58 | 1.58 |

Table C.4: Values of the magnetic polarization at the upper form factor limit.

| Epstein measurements without sense lines | | |
|---|---|---|
| Material | Magnetic polarization $J$ in T wide samples | Magnetic polarization $J$ in T small samples |
| M270-35A_50Hz_Mix_SS | 1.35 | 1.01 |
| M270-35A_50Hz_Mix_$CO_2$ | 1.37 | 1.41 |
| M270-35A_50Hz_Mix_FKL | 1.37 | 1.40 |
| M270-35A_250Hz_Mix_SS | 1.36 | 1.04 |
| M270-35A_250Hz_Mix_$CO_2$ | 1.37 | 1.41 |
| M270-35A_250Hz_Mix_FKL | 1.39 | 1.41 |
| M270-35A_500Hz_Mix_SS | 1.37 | 1.02 |
| M270-35A_500Hz_Mix_$CO_2$ | 1.42 | 1.39 |
| M270-35A_500Hz_Mix_FKL | 1.39 | 1.40 |
| M400-50A_50Hz_Mix_SS | - | 1.18 |
| M400-50A_50Hz_Mix_$CO_2$ | - | 1.42 |
| M400-50A_50Hz_Mix_FKL | - | 1.42 |
| M400-50A_250Hz_Mix_SS | - | 1.22 |
| M400-50A_250Hz_Mix_$CO_2$ | - | 1.40 |
| M400-50A_250Hz_Mix_FKL | - | 1.42 |
| M400-50A_500Hz_Mix_SS | 1.38 | 1.29 |
| M400-50A_500Hz_Mix_$CO_2$ | 1.44 | 1.42 |
| M400-50A_500Hz_Mix_FKL | 1.44 | 1.43 |
| M800-65A_50Hz_Mix_SS | - | 1.28 |
| M800-65A_50Hz_Mix_$CO_2$ | - | 1.48 |
| M800-65A_50Hz_Mix_FKL | - | 1.48 |
| M800-65A_250Hz_Mix_SS | - | 1.36 |
| M800-65A_250Hz_Mix_$CO_2$ | - | 1.48 |
| M800-65A_250Hz_Mix_FKL | - | 1.49 |
| M800-65A_500Hz_Mix_SS | 1.52 | 1.40 |
| M800-65A_500Hz_Mix_$CO_2$ | 1.52 | 1.52 |
| M800-65A_500Hz_Mix_FKL | 1.54 | 1.48 |

# Appendix D

# Results of the stator measurements

## D.1 Tables: specific values of the stator measurements

Table D.1: Specific values of the stators measurements - method 'IEC 62044-3'.

| Overview of the specific values of stator measurements - method 'IEC 62044-3' | | | | | | | | |
|---|---|---|---|---|---|---|---|---|
| Bali, M. 13.06.2013 | | | Magnetic flux density at | | | | Losses at | |
| Material | Cutting method | Frequency (Hz) | $2500 \frac{A}{m}$ | $3500 \frac{A}{m}$ | $5000 \frac{A}{m}$ | $10000 \frac{A}{m}$ | 1.0 T | 1.5 T |
| M270-35A | $CO_2$ | 50 | 1.41 | 1.45 | 1.49 | 1.52 | 1.67 | 3.48 |
| M270-35A | $CO_2$ | 250 | 1.41 | 1.45 | 1.49 | 1.51 | 13.42 | 29.73 |
| M270-35A | $CO_2$ | 500 | 1.41 | 1.45 | 1.49 | 1.51 | 37.41 | 85.25 |
| M270-35A | FKL | 50 | 1.41 | 1.45 | 1.49 | 1.52 | 1.65 | 3.46 |
| M270-35A | FKL | 250 | 1.41 | 1.45 | 1.49 | 1.52 | 13.37 | 29.83 |
| M270-35A | FKL | 500 | 1.41 | 1.45 | 1.49 | 1.52 | 37.48 | 85.75 |
| M400-50A | punched | 50 | 1.47 | 1.51 | 1.56 | 1.58 | 2.10 | 4.80 |
| M400-50A | punched | 250 | 1.47 | 1.51 | 1.56 | 1.59 | 22.43 | 51.01 |
| M400-50A | punched | 500 | 1.47 | 1.51 | 1.56 | - | 70.43 | 166.25 |
| M400-50A | $CO_2$ | 50 | 1.49 | 1.53 | 1.58 | 1.60 | 2.31 | 4.79 |
| M400-50A | $CO_2$ | 250 | 1.49 | 1.53 | 1.57 | 1.60 | 21.78 | 48.42 |
| M400-50A | $CO_2$ | 500 | 1.49 | 1.53 | 1.58 | 1.60 | 65.50 | 153.34 |
| M400-50A | FKL | 50 | 1.48 | 1.51 | 1.55 | 1.58 | 2.31 | 4.85 |
| M400-50A | FKL | 250 | 1.47 | 1.51 | 1.55 | 1.58 | 21.88 | 49.12 |
| M400-50A | FKL | 500 | 1.47 | 1.51 | 1.55 | 1.58 | 65.83 | 156.98 |
| M800-65A | punched | 50 | 1.48 | 1.53 | 1.57 | 1.60 | 2.91 | 6.38 |
| M800-65A | punched | 250 | 1.48 | 1.53 | 1.58 | 1.60 | 32.58 | 75.60 |
| M800-65A | punched | 500 | 1.47 | 1.53 | 1.58 | 1.60 | 103.47 | 259.72 |
| M800-65A | $CO_2$ | 50 | 1.52 | 1.56 | 1.60 | 1.62 | 2.94 | 6.05 |
| M800-65A | $CO_2$ | 250 | 1.52 | 1.56 | 1.60 | 1.62 | 30.29 | 69.62 |
| M800-65A | $CO_2$ | 500 | 1.52 | 1.56 | 1.60 | - | 94.43 | 240.05 |
| M800-65A | FKL | 50 | 1.50 | 1.54 | 1.58 | 1.60 | 2.95 | 6.15 |
| M800-65A | FKL | 250 | 1.50 | 1.54 | 1.58 | 1.60 | 30.79 | 71.79 |
| M800-65A | FKL | 500 | 1.50 | 1.53 | 1.58 | - | 96.01 | 249.20 |

Table D.2: Specific values of the stators measurements - 'Epsteinframe' method.

| Overview of the specific values of stator measurements - 'Epsteinframe' method | | | | | | | | |
|---|---|---|---|---|---|---|---|---|
| Bali, M. 13.06.2013 | | | Magnetic flux density at | | | | Losses at | |
| Material | Cutting method | Frequency (Hz) | $2500 \frac{A}{m}$ | $3500 \frac{A}{m}$ | $5000 \frac{A}{m}$ | $10000 \frac{A}{m}$ | 1.0 T | 1.5 T |
| M270-35A | $CO_2$ | 50 | 1.41 | 1.45 | 1.49 | 1.51 | 1.67 | 3.42 |
| M270-35A | $CO_2$ | 250 | 1.41 | 1.45 | 1.49 | 1.52 | 13.41 | 28.73 |
| M270-35A | $CO_2$ | 500 | 1.41 | 1.45 | 1.49 | 1.52 | 37.34 | 81.19 |
| M270-35A | FKL | 50 | 1.41 | 1.45 | 1.49 | 1.52 | 1.65 | 3.41 |
| M270-35A | FKL | 250 | 1.41 | 1.45 | 1.49 | 1.51 | 13.37 | 28.97 |
| M270-35A | FKL | 500 | 1.41 | 1.45 | 1.49 | 1.52 | 37.40 | 81.76 |
| M400-50A | punched | 50 | 1.47 | 1.51 | 1.56 | 1.58 | 2.09 | 4.72 |
| M400-50A | punched | 250 | 1.47 | 1.51 | 1.56 | 1.59 | 22.37 | 49.03 |
| M400-50A | punched | 500 | 1.47 | 1.51 | 1.56 | 1.58 | 70.10 | 154.72 |
| M400-50A | $CO_2$ | 50 | 1.49 | 1.53 | 1.57 | 1.60 | 2.30 | 4.73 |
| M400-50A | $CO_2$ | 250 | 1.50 | 1.53 | 1.58 | 1.60 | 21.74 | 46.82 |
| M400-50A | $CO_2$ | 500 | 1.49 | 1.53 | 1.57 | 1.60 | 65.20 | 145.56 |
| M400-50A | FKL | 50 | 1.47 | 1.51 | 1.55 | 1.58 | 2.30 | 4.77 |
| M400-50A | FKL | 250 | 1.47 | 1.51 | 1.55 | 1.57 | 21.93 | 47.65 |
| M400-50A | FKL | 500 | 1.47 | 1.51 | 1.55 | 1.57 | 65.75 | 146.47 |
| M800-65A | punched | 50 | 1.48 | 1.53 | 1.57 | 1.60 | 2.91 | 6.26 |
| M800-65A | punched | 250 | 1.48 | 1.52 | 1.57 | 1.59 | 32.55 | 71.46 |
| M800-65A | punched | 500 | 1.48 | 1.52 | 1.56 | 1.59 | 102.56 | 234.95 |
| M800-65A | $CO_2$ | 50 | 1.52 | 1.56 | 1.60 | 1.62 | 2.94 | 5.99 |
| M800-65A | $CO_2$ | 250 | 1.52 | 1.55 | 1.60 | 1.62 | 30.38 | 67.15 |
| M800-65A | $CO_2$ | 500 | 1.51 | 1.55 | 1.59 | 1.62 | 94.46 | 222.14 |
| M800-65A | FKL | 50 | 1.50 | 1.53 | 1.58 | 1.60 | 2.95 | 6.07 |
| M800-65A | FKL | 250 | 1.50 | 1.53 | 1.58 | 1.60 | 30.86 | 68.81 |
| M800-65A | FKL | 500 | 1.49 | 1.53 | 1.57 | 1.60 | 96.10 | 228.89 |

Table D.3: Specific values of the stators measurements - 'modified Epsteinframe' method.

| Overview of the specific values of stator measurements - 'modified Epsteinframe' method | | | | | | | | |
|---|---|---|---|---|---|---|---|---|
| Bali, M. 13.06.2013 | | | Magnetic flux density at | | | | Losses at | |
| Material | Cutting method | Frequency (Hz) | $2500\frac{A}{m}$ | $3500\frac{A}{m}$ | $5000\frac{A}{m}$ | $10000\frac{A}{m}$ | 1.0 T | 1.5 T |
| M270-35A | $CO_2$ | 50 | 1.41 | 1.45 | 1.49 | 1.51 | 1.67 | 3.52 |
| M270-35A | $CO_2$ | 250 | 1.41 | 1.45 | 1.49 | 1.51 | 13.43 | 29.75 |
| M270-35A | $CO_2$ | 500 | 1.41 | 1.45 | 1.49 | 1.51 | 37.34 | 83.31 |
| M270-35A | FKL | 50 | 1.41 | 1.45 | 1.49 | 1.51 | 1.65 | 3.52 |
| M270-35A | FKL | 250 | 1.41 | 1.45 | 1.49 | 1.51 | 13.38 | 29.83 |
| M270-35A | FKL | 500 | 1.41 | 1.45 | 1.49 | 1.51 | 37.45 | 84.07 |
| M400-50A | punched | 50 | 1.46 | 1.51 | 1.55 | 1.58 | 2.11 | 4.85 |
| M400-50A | punched | 250 | 1.47 | 1.51 | 1.56 | 1.58 | 22.38 | 50.65 |
| M400-50A | punched | 500 | 1.46 | 1.51 | 1.55 | 1.58 | 70.10 | 158.13 |
| M400-50A | $CO_2$ | 50 | 1.49 | 1.53 | 1.57 | 1.60 | 2.31 | 4.82 |
| M400-50A | $CO_2$ | 250 | 1.49 | 1.53 | 1.58 | 1.60 | 21.75 | 47.67 |
| M400-50A | $CO_2$ | 500 | 1.49 | 1.53 | 1.57 | 1.59 | 65.21 | 147.52 |
| M400-50A | FKL | 50 | 1.47 | 1.51 | 1.55 | 1.57 | 2.31 | 4.88 |
| M400-50A | FKL | 250 | 1.47 | 1.51 | 1.55 | 1.57 | 21.89 | 48.98 |
| M400-50A | FKL | 500 | 1.47 | 1.51 | 1.55 | 1.57 | 65.58 | 149.43 |
| M800-65A | punched | 50 | 1.48 | 1.52 | 1.57 | 1.60 | 2.93 | 6.41 |
| M800-65A | punched | 250 | 1.48 | 1.52 | 1.57 | 1.59 | 32.58 | 74.45 |
| M800-65A | punched | 500 | 1.47 | 1.52 | 1.56 | - | 102.46 | 238.78 |
| M800-65A | $CO_2$ | 50 | 1.52 | 1.56 | 1.60 | 1.62 | 2.94 | 6.08 |
| M800-65A | $CO_2$ | 250 | 1.52 | 1.55 | 1.60 | 1.62 | 30.35 | 68.48 |
| M800-65A | $CO_2$ | 500 | 1.51 | 1.55 | 1.59 | 1.61 | 93.94 | 225.74 |
| M800-65A | FKL | 50 | 1.50 | 1.53 | 1.57 | 1.60 | 2.96 | 6.20 |
| M800-65A | FKL | 250 | 1.50 | 1.53 | 1.57 | 1.60 | 30.79 | 70.36 |
| M800-65A | FKL | 500 | 1.49 | 1.53 | 1.57 | 1.59 | 95.67 | 228.38 |

## D.2  Diagrams: cutting techniques - 'Epsteinframe' method
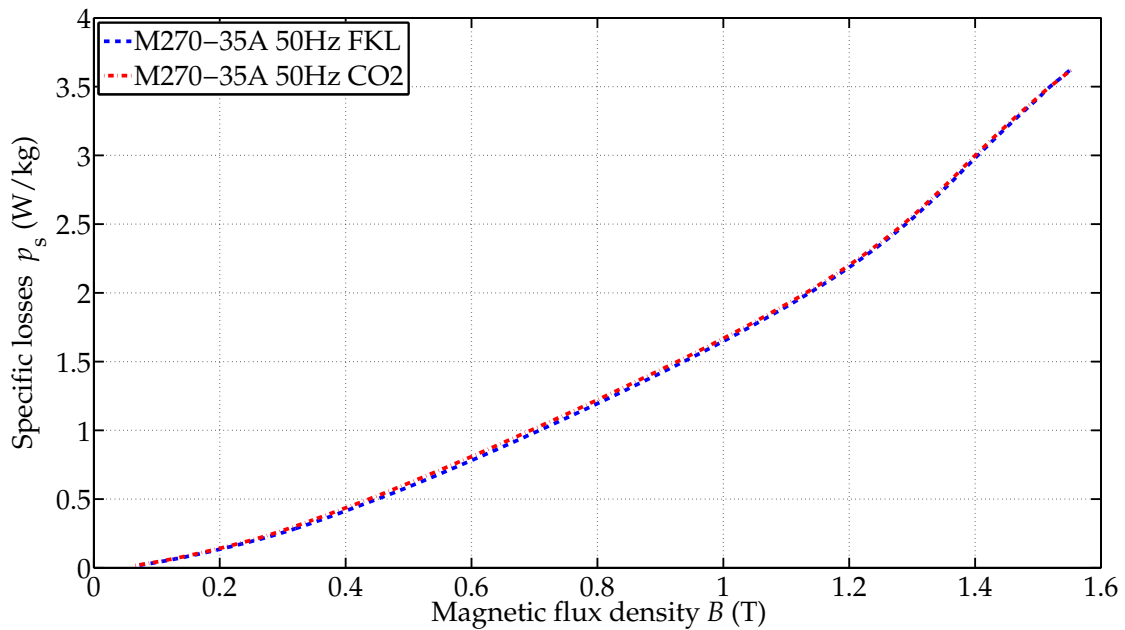


(a) 50 Hz
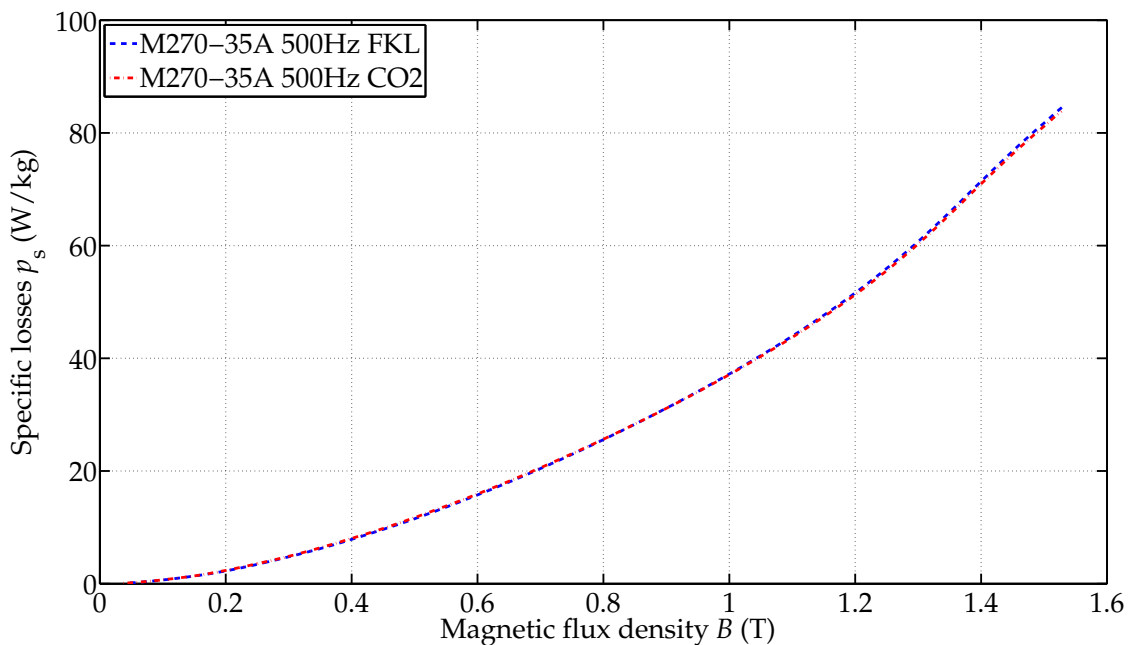


(b) 500 Hz

Figure D.1: Specific losses of M270-35A at 50 and 500 Hz.
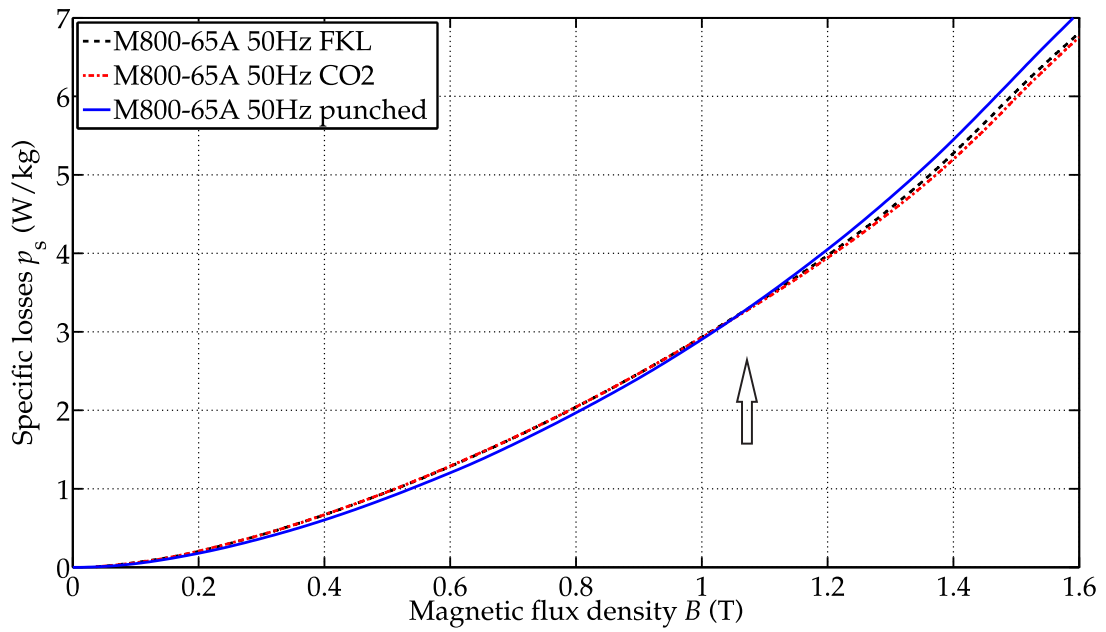
Figure D.2: Specific losses of M800-65A at 50 Hz.
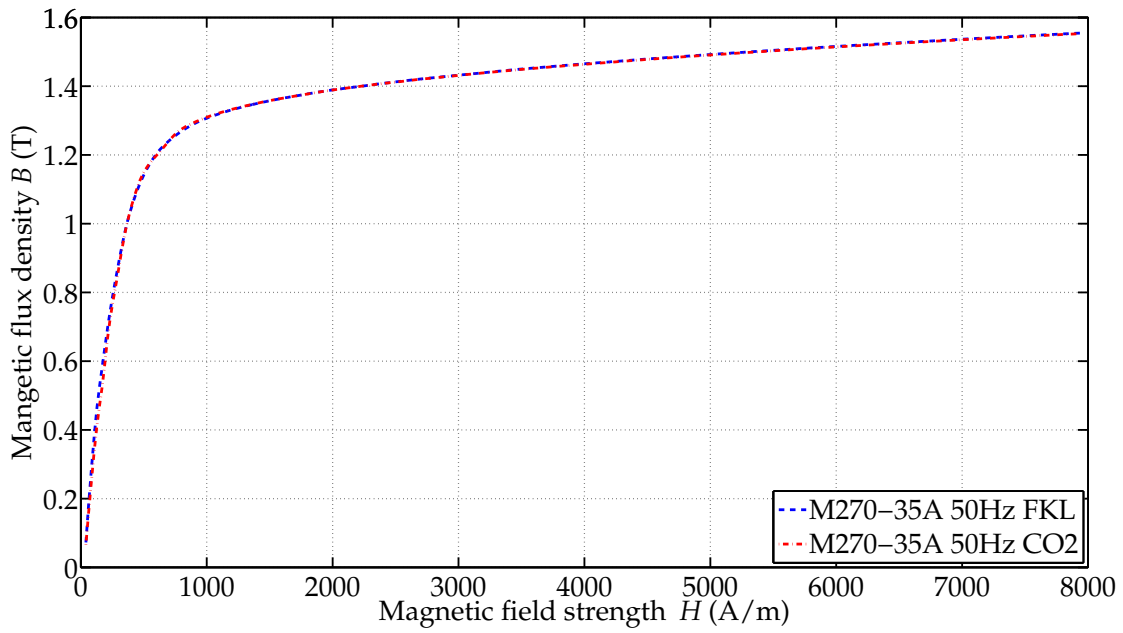
(a) 50 Hz
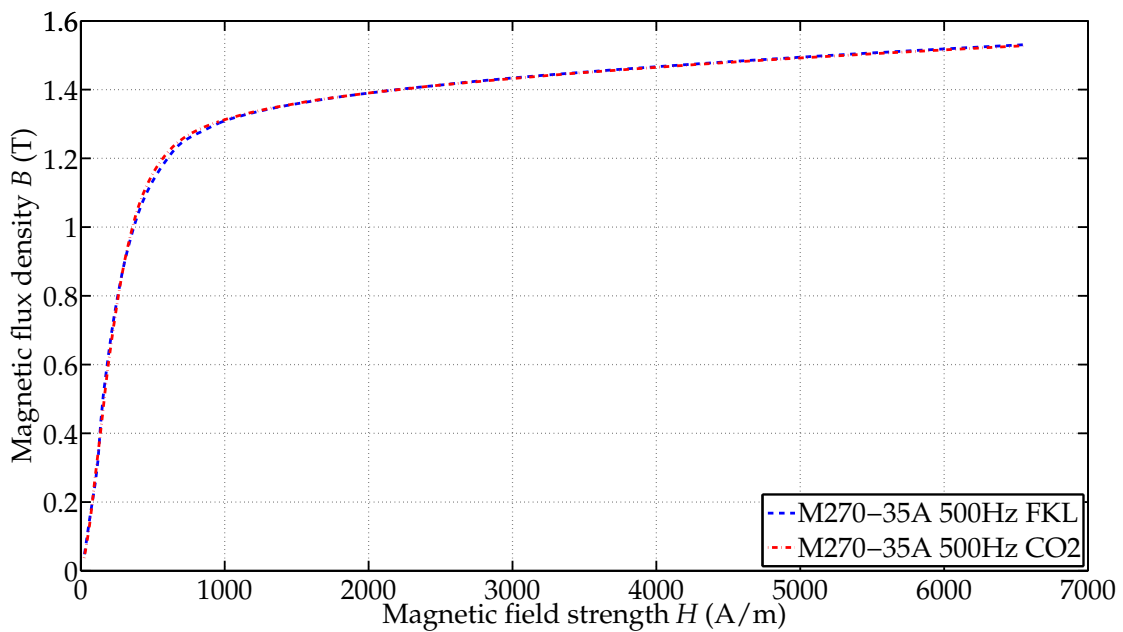


(b) 500 Hz

Figure D.3: Magnetization curve of M270-35A at 50 and 500 Hz.
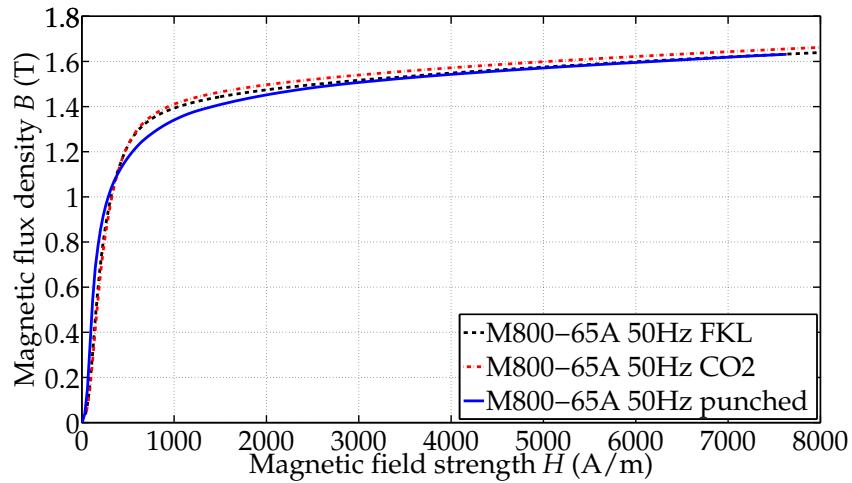
(a) 50 Hz
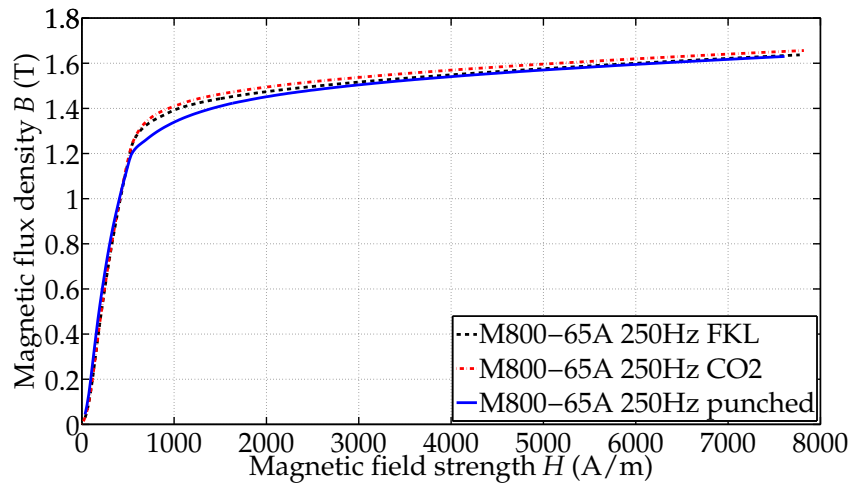


(b) 250 Hz
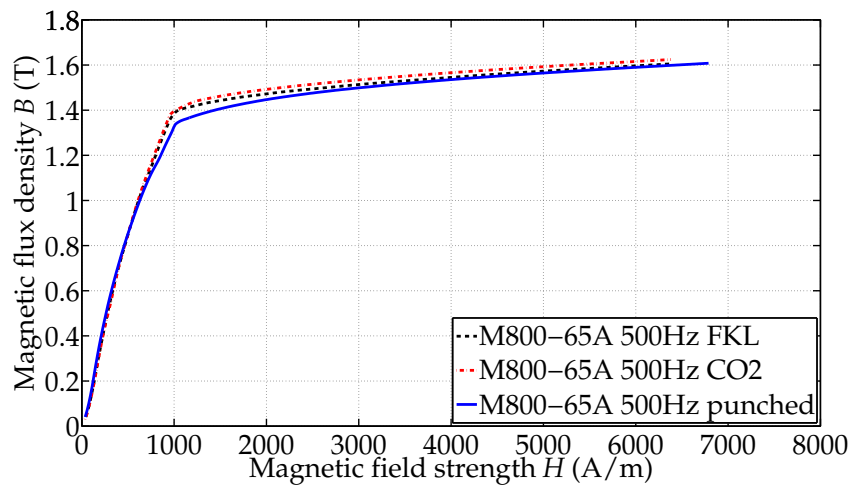


(c) 500 Hz

Figure D.4: Magnetization curves of M800-65A at 50 , 250 and 500 Hz.

# D.3  Table: points of intersection - stator samples

Table D.4: Stator lamination stack measurements ('Epsteinframe' method):  POIs of specific losses for the $CO_2$-laser cut and mechanically-cut samples.

|  | M270-35A | M400-50A | M800-65A | Reduction of B of point of intersection from M400-50A to M800-65A in % |
|---|---|---|---|---|
| 50 Hz | N/A | 1.35 T* | 1.05 T | - % |
| 250 Hz | N/A | 0.85 T | 0.63 T | −25.9 % |
| 500 Hz | N/A | 0.70 T | 0.51 T | −27.1 % |

* = no 'real' POI, rather an area where the specific losses are similar.

Table D.5: Stator lamination stack measurements ('Epsteinframe' method):  POIs of relative permeability for the $CO_2$-laser cut and mechanically-cut samples.

|  | M270-35A | M400-50A | M800-65A |
|---|---|---|---|
| 50 Hz | N/A | 492  A/m (1.19 T) | 383 A/m (1.10 T) |
| 250 Hz | N/A | 477 A/m (1.18 T) | 436 A/m (1.05 T) |
| 500 Hz | N/A | 596 A/m (1.25 T) | 513 A/m (0.87 T) |

Table D.6: Stator lamination stack measurements ('modified Epsteinframe' method): POIs of specific losses for the $CO_2$-laser cut and mechanically-cut samples.

|  | M270-35A | M400-50A | M800-65A | Reduction of B of point of intersection from M400-50A to M800-65A in % |
|---|---|---|---|---|
| 50 Hz | N/A | 1.35 T* | 1.02 T | - |
| 250 Hz | N/A | 0.83 T | 0.63 T | −24.1 % |
| 500 Hz | N/A | 0.68 T | 0.51 T | −25 % |

* = no 'real' POI, rather an area where the specific losses are similar.

Table D.7: Stator lamination stack measurements ('IEC 62044-3' method): POIs of specific losses for the $CO_2$-laser cut and mechanically-cut samples.

|  | **M270-35A** | **M400-50A** | **M800-65A** | Reduction of B of point of intersection from M400-50A to M800-65A in % |
|---|---|---|---|---|
| 50 Hz | N/A | 1.35 T* | 1.02 T | - |
| 250 Hz | N/A | 0.81 T | 0.64 T | −21 % |
| 500 Hz | N/A | 0.68 T | 0.52 T | −23.5 % |

* = no 'real' POI, rather an area where the specific losses are similar.

# D.4 Diagrams: POIs (specific losses) versus CL
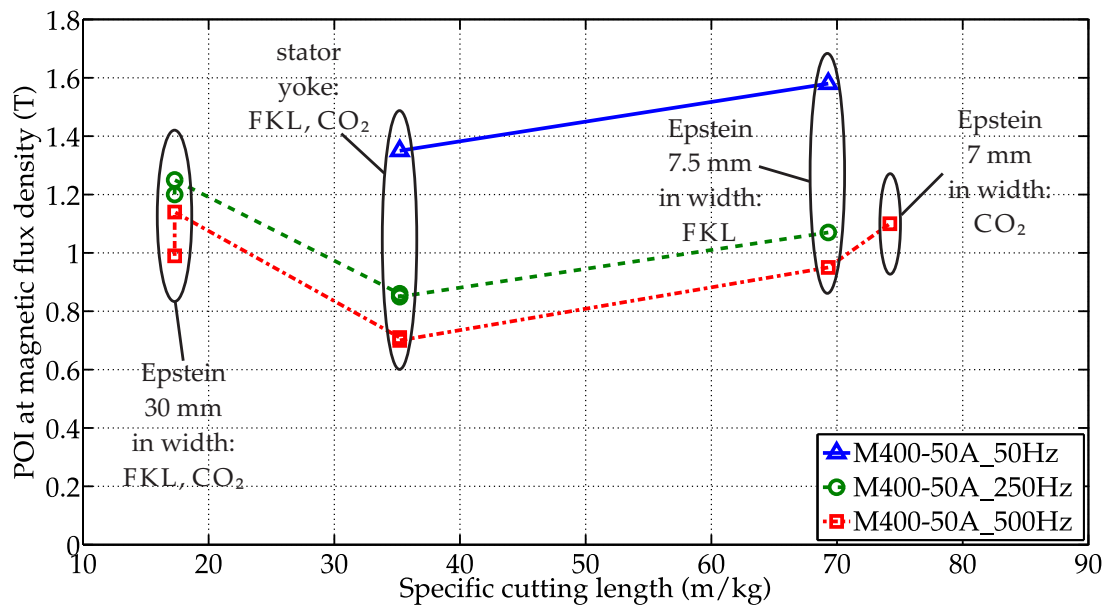


Figure D.5: POIs as a function of the specific cutting length for material M400-50A.

## D.5  Diagrams: comparison of measuring methods
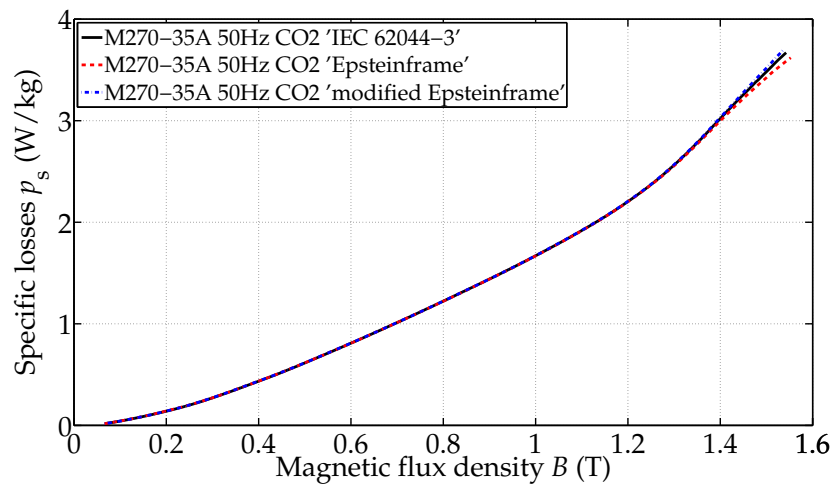


(a)  50 Hz
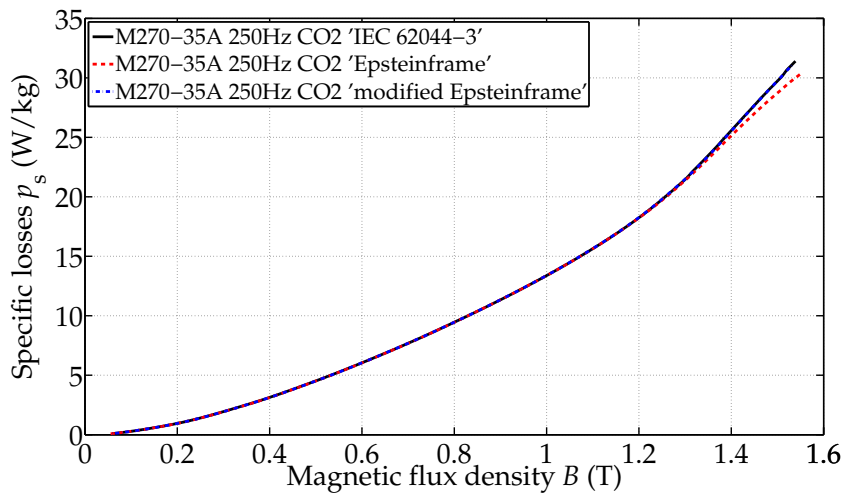


(b)  250 Hz
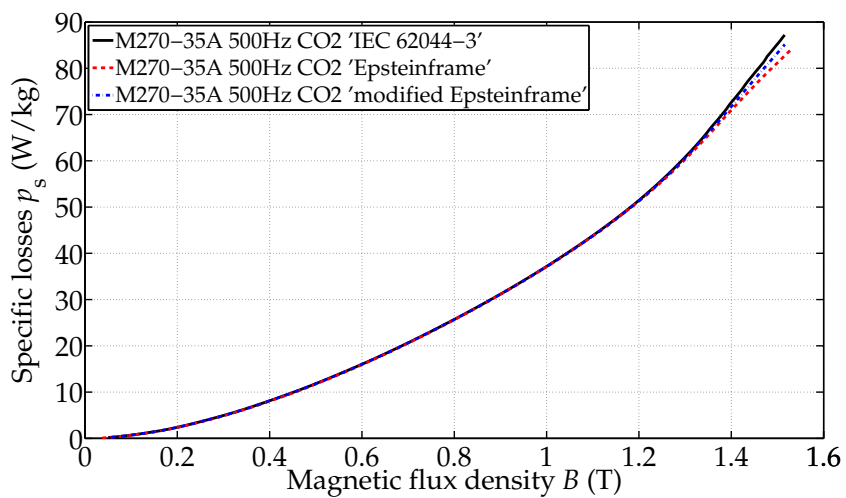


(c)  500 Hz

Figure D.6: Specific losses of M270-35A at 50 , 250  and 500 Hz, $CO_2$-laser cut.
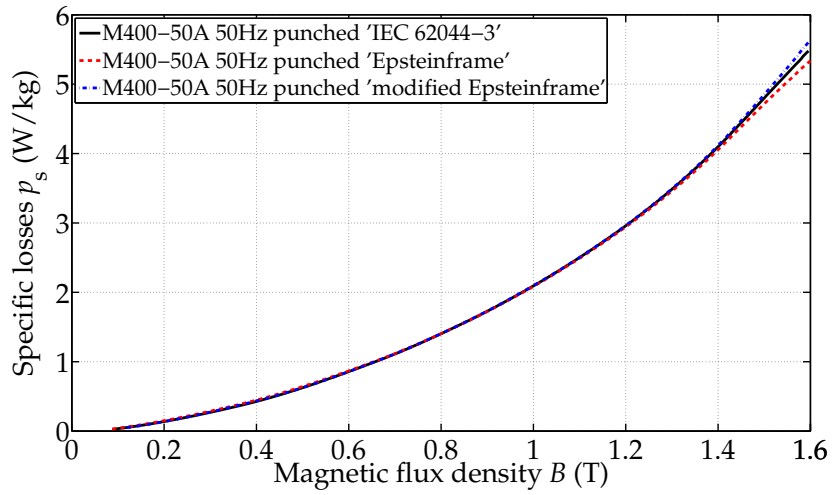
(a) 50 Hz
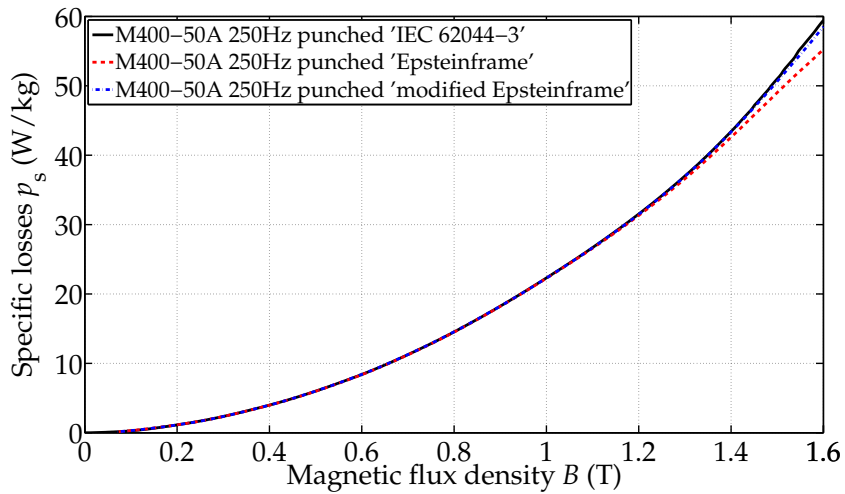


(b) 250 Hz
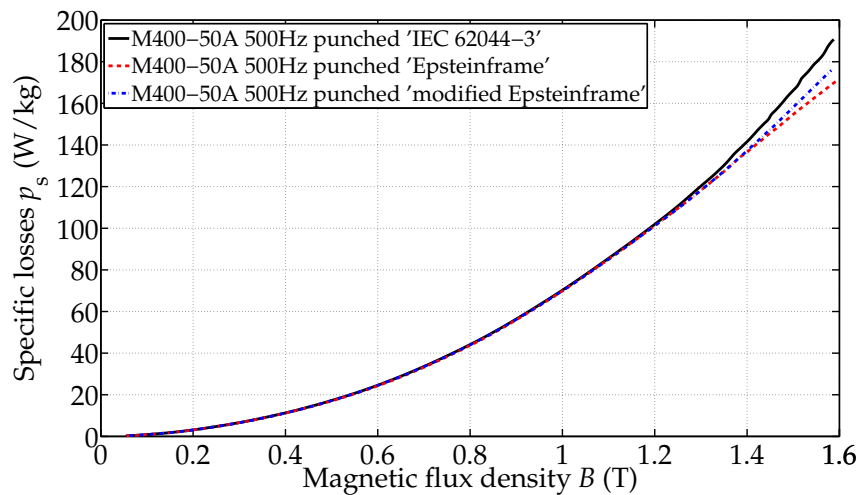


(c) 500 Hz

Figure D.7: Specific losses of M400-50A at 50 , 250  and 500 Hz, punched.
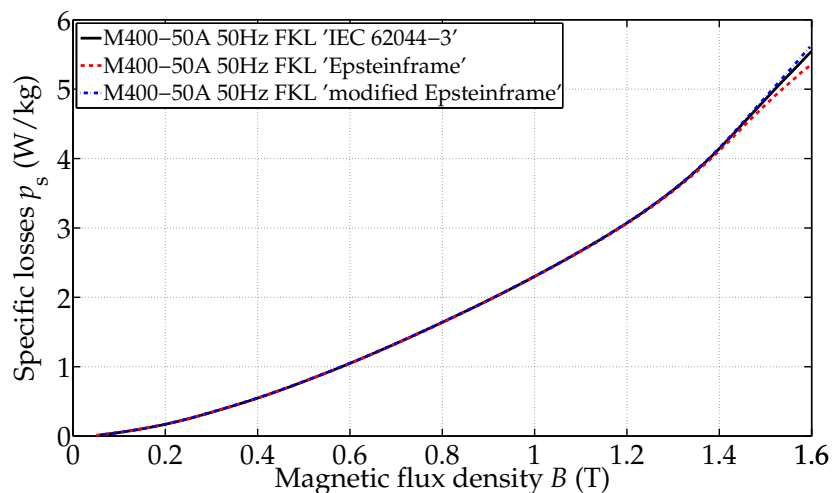
(a) 50 Hz
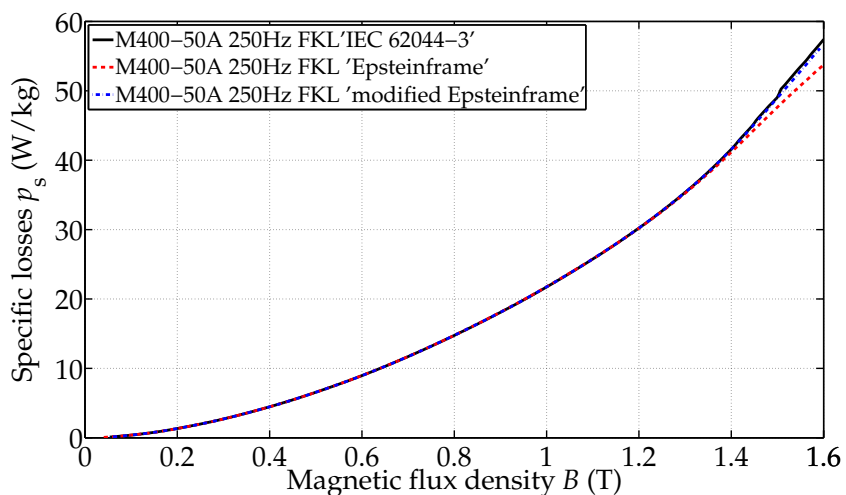


(b) 250 Hz
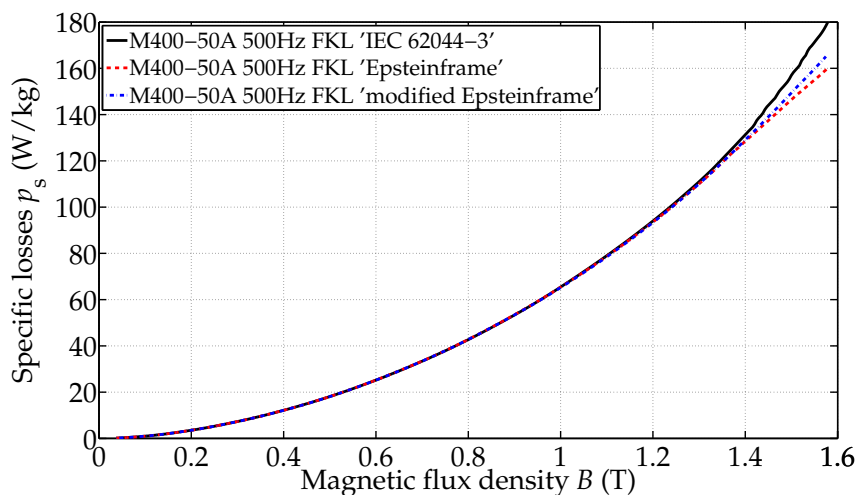


(c) 500 Hz

Figure D.8: Specific losses of M400-50A at 50 , 250  and 500 Hz, FKL-laser cut.
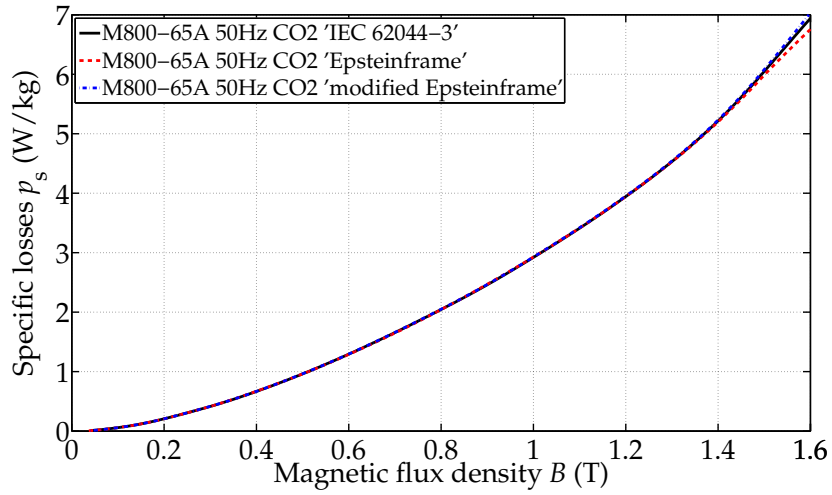
(a) 50 Hz
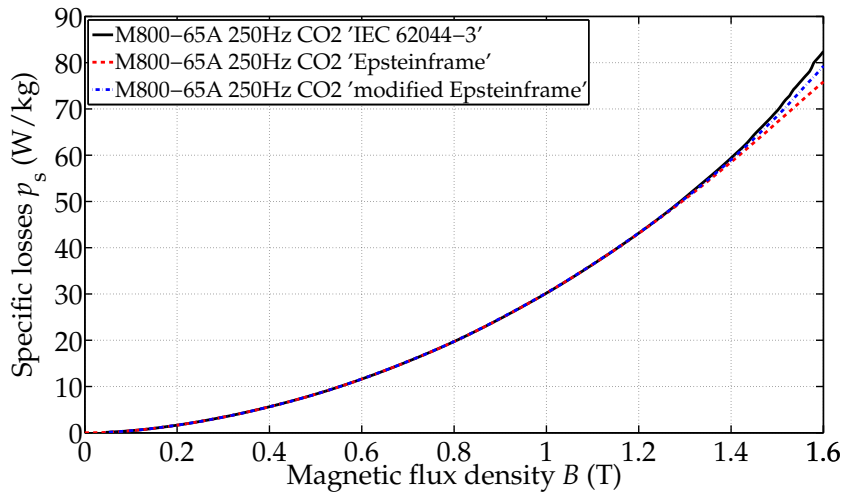


(b) 250 Hz
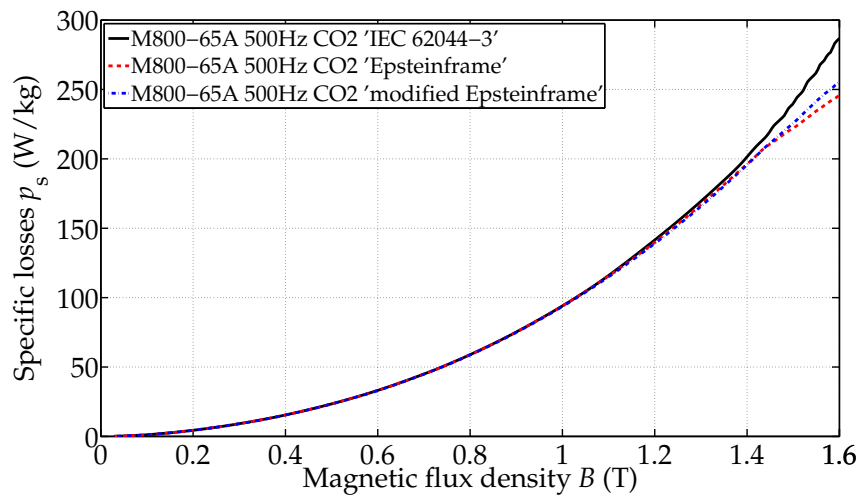


(c) 500 Hz

Figure D.9: Specific losses of M400-50A at 50 , 250  and 500 Hz, $CO_2$-laser cut.

# D.6 Form factor limitation - stator measurements

The following values represent the last measurement point which is still in the required form factor range of [86]. The note 'no limit' means that all measured data are within this range, the value inside the brackets is the last measured data point. As there is no punched stator of the material M270-35A available, no statement can be made.

Table D.8: Values of the magnetic flux density at the upper form factor limit.

| Stator measurements | | | |
|---|---|---|---|
| Material | Magnetic flux density $B$ in T 'Epsteinframe' method | Magnetic flux density $B$ in T 'IEC 62044-3' method | Magnetic flux density $B$ in T 'modified Epsteinframe' method |
| M270-35A_50Hz_punched | not available | not available | not available |
| M270-35A_50Hz_$CO_2$ | no limit (1.55) | 1.28 | no limit (1.54) |
| M270-35A_50Hz_FKL | no limit (1.55) | 1.32 | no limit (1.53) |
| M270-35A_250Hz_punched | not available | not available | not available |
| M270-35A_250Hz_$CO_2$ | no limit (1.55) | 1.32 | 1.30 |
| M270-35A_250Hz_FKL | no limit (1.55) | 1.31 | 1.31 |
| M270-35A_500Hz_punched | not available | not available | not available |
| M270-35A_500Hz_$CO_2$ | 1.45 | 1.31 | 1.31 |
| M270-35A_500Hz_FKL | 1.47 | 1.31 | 1.30 |
| M400-50A_50Hz_punched | no limit (1.61) | 1.27 | 1.18 |
| M400-50A_50Hz_$CO_2$ | no limit (1.64) | 1.35 | no limit (1.62) |
| M400-50A_50Hz_FKL | no limit (1.62) | 1.37 | no limit (1.60) |
| M400-50A_250Hz_punched | no limit (1.63) | 1.31 | 1.27 |
| M400-50A_250Hz_$CO_2$ | no limit (1.64) | 1.39 | 1.38 |
| M400-50A_250Hz_FKL | 1.60 | 1.37 | 1.34 |
| M400-50A_500Hz_punched | 1.52 | 1.33 | 1.33 |
| M400-50A_500Hz_$CO_2$ | 1.53 | 1.40 | 1.40 |
| M400-50A_500Hz_FKL | 1.49 | 1.39 | 1.38 |
| M800-65A_50Hz_punched | no limit (1.72) | 1.32 | 1.25 |
| M800-65A_50Hz_$CO_2$ | no limit (1.66) | 1.41 | 1.37 |
| M800-65A_50Hz_FKL | no limit (1.64) | 1.37 | 1.36 |
| M800-65A_250Hz_punched | no limit (1.63) | 1.35 | 1.30 |
| M800-65A_250Hz_$CO_2$ | no limit (1.66) | 1.41 | 1.41 |
| M800-65A_250Hz_FKL | no limit (1.64) | 1.40 | 1.40 |
| M800-65A_500Hz_punched | 1.50 | 1.41 | 1.39 |
| M800-65A_500Hz_$CO_2$ | 1.55 | 1.46 | 1.45 |
| M800-65A_500Hz_FKL | 1.53 | 1.43 | 1.43 |

# Appendix E

# Identified magnetic characteristics

## E.1 Diagrams: identified *B-H* curves

### E.1.1 Results of mechanically-cut samples - M400-50A
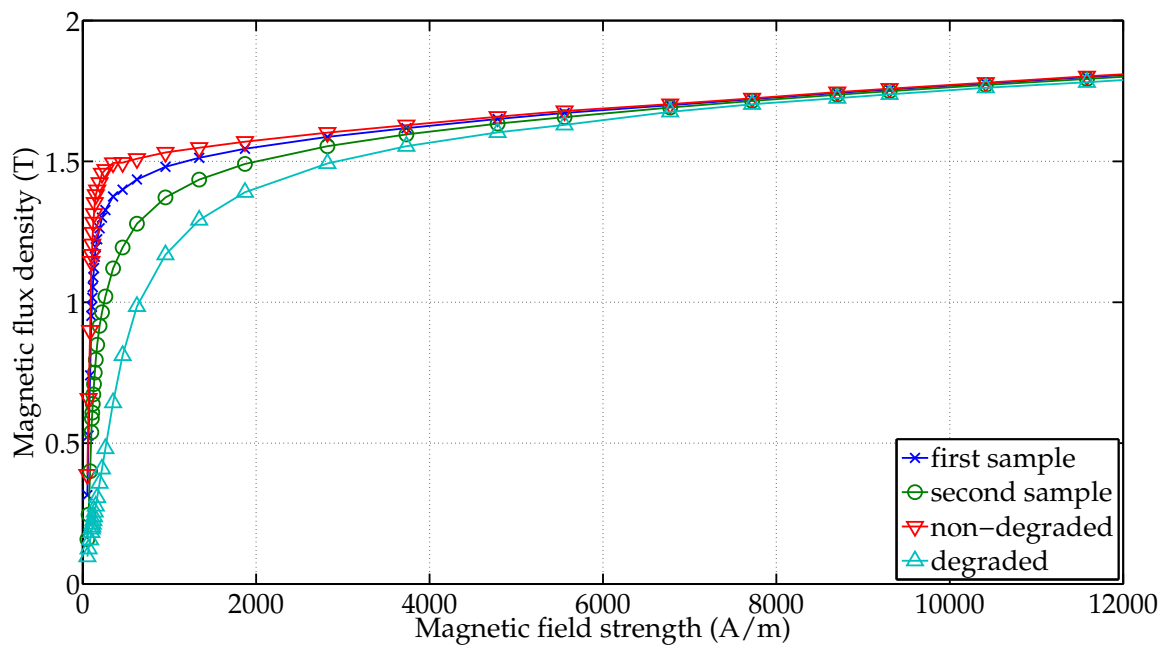


Figure E.1: Measured and identified *B-H* curves of mechanically-cut samples, M400-50A at 50 Hz supply frequency.
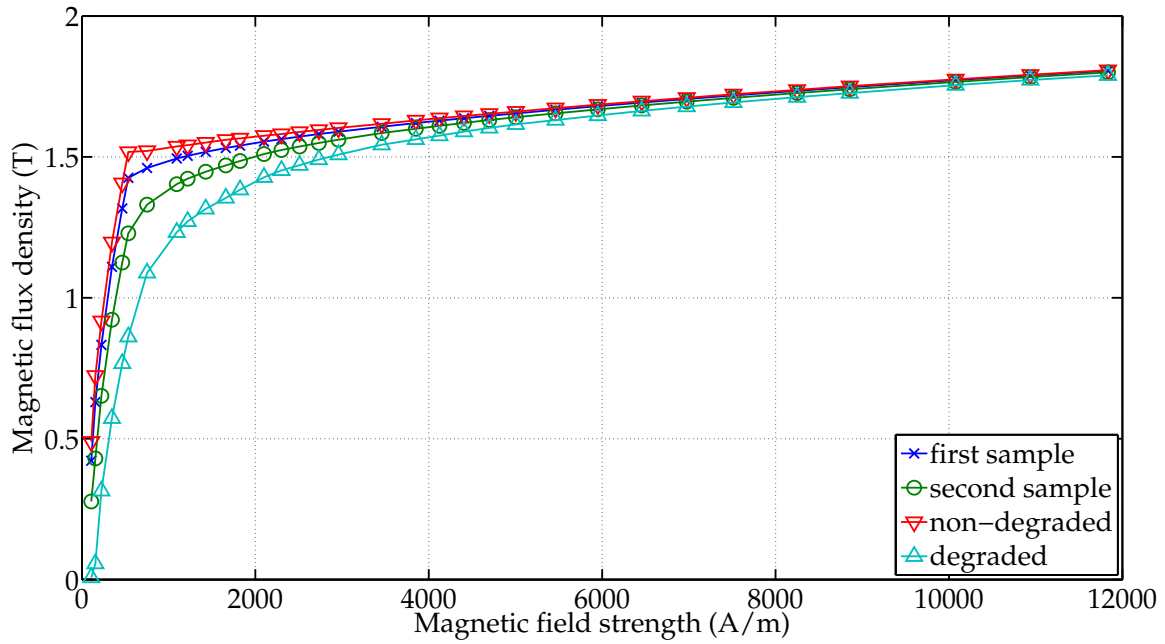
Figure E.2: Measured and identified *B-H* curves of mechanically-cut samples, M400-50A at 500 Hz supply frequency.

## E.1.2  Results of mechanically-cut samples - M800-65A
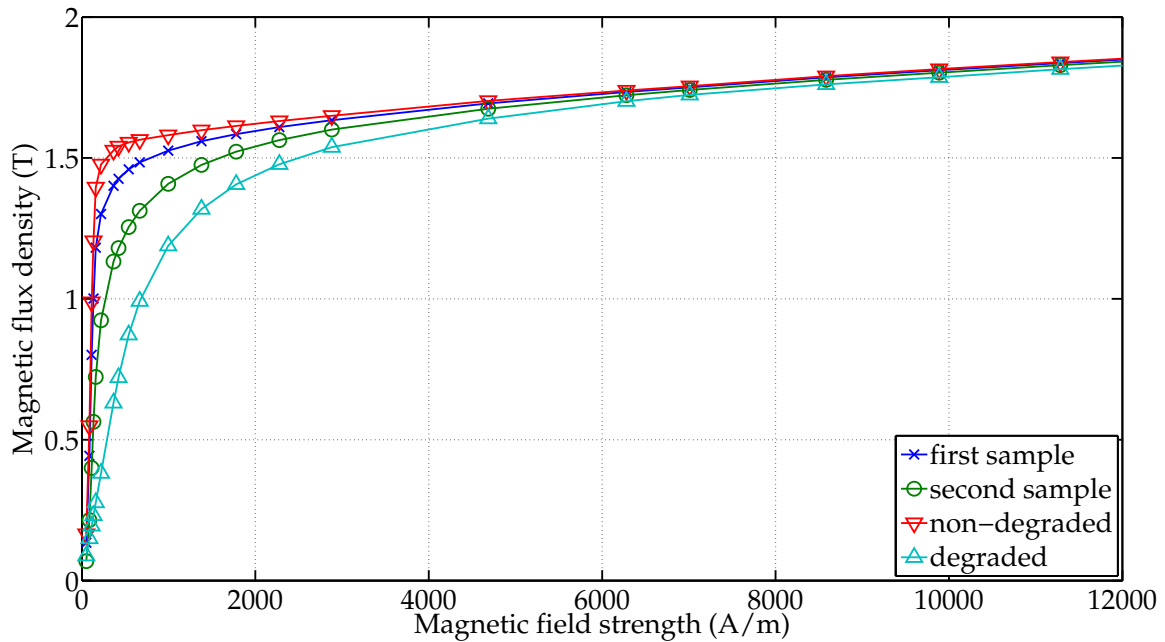


Figure E.3: Measured and identified *B-H* curves of mechanically-cut samples, M800-65A at 50 Hz supply frequency.
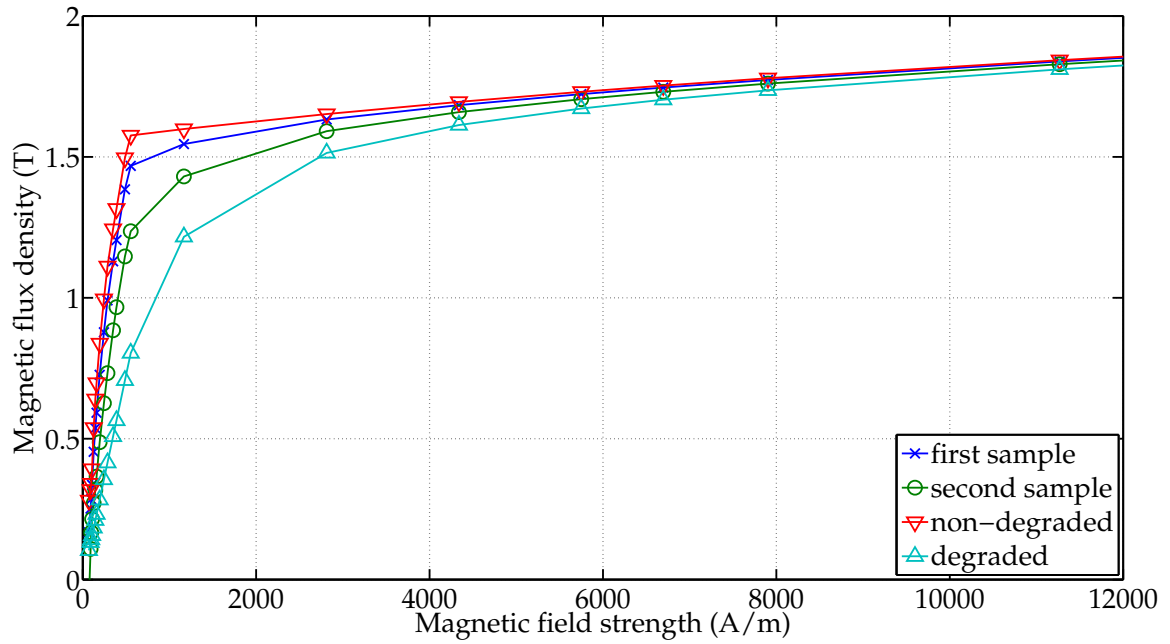
Figure E.4: Measured and identified *B-H* curves of mechanically-cut samples, M800-65A at 250 Hz supply frequency.
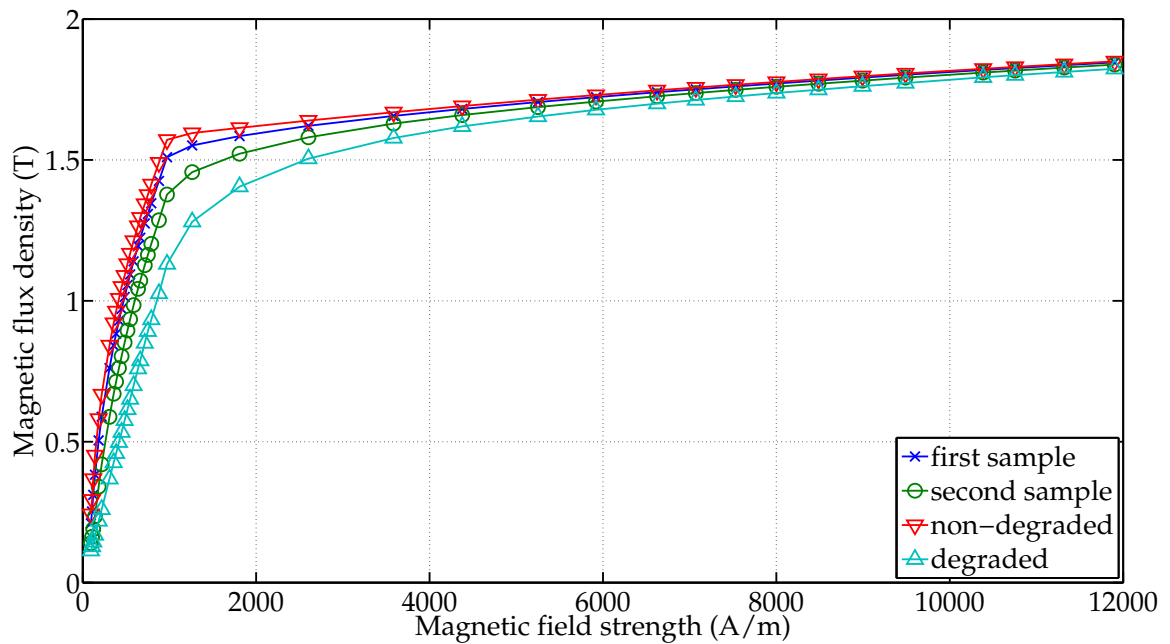


Figure E.5: Measured and identified *B-H* curves of mechanically-cut samples, M800-65A at 500 Hz supply frequency.

### E.1.3 Results of laser-cut samples - M270-35A
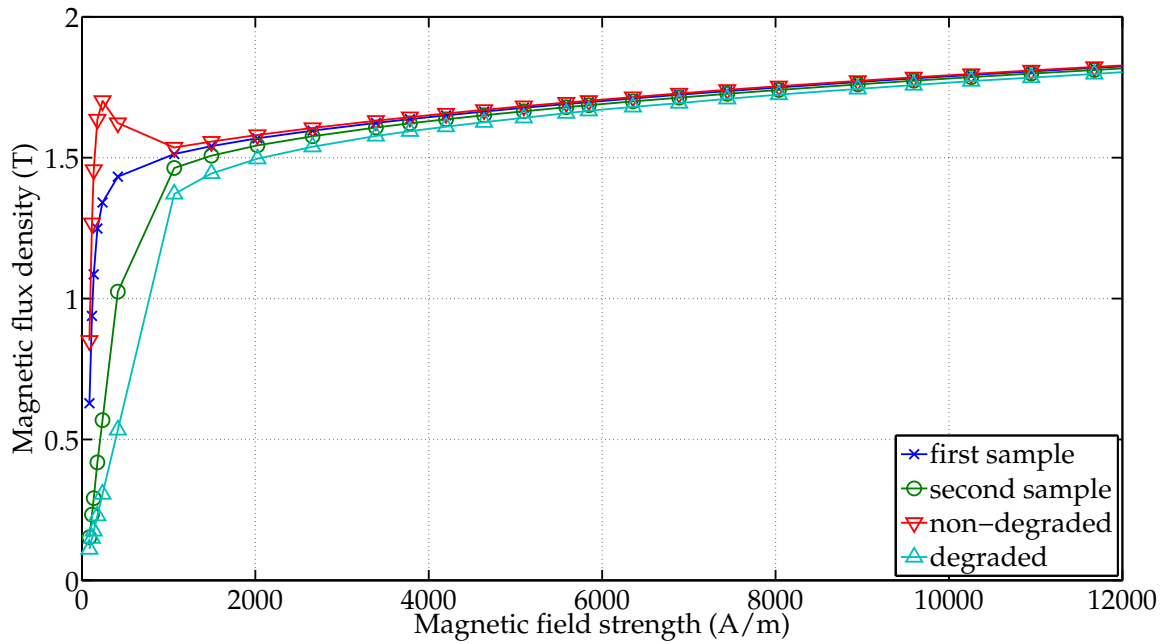


Figure E.6: Measured and identified *B-H* curves of laser-cut samples, M270-35A at 250 Hz supply frequency.
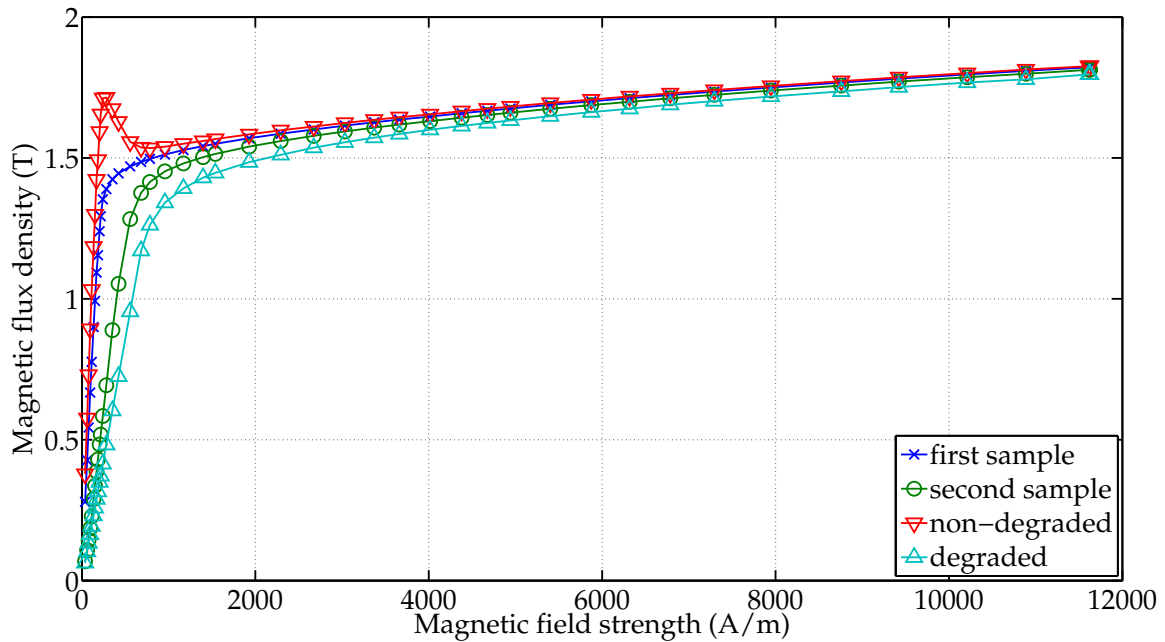


Figure E.7: Measured and identified *B-H* curves of laser-cut samples, M270-35A at 500 Hz supply frequency.

## E.1.4  Results of laser-cut samples - M400-50A
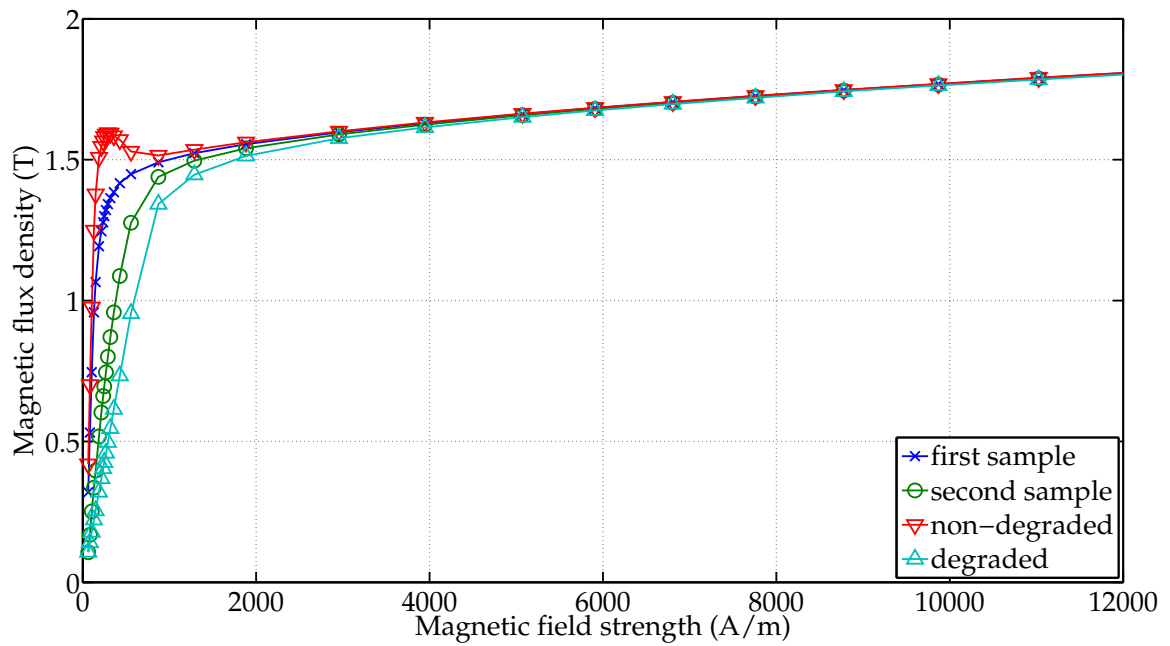


Figure E.8: Measured and identified *B-H* curves of laser-cut samples, M400-50A at 50 Hz supply frequency.
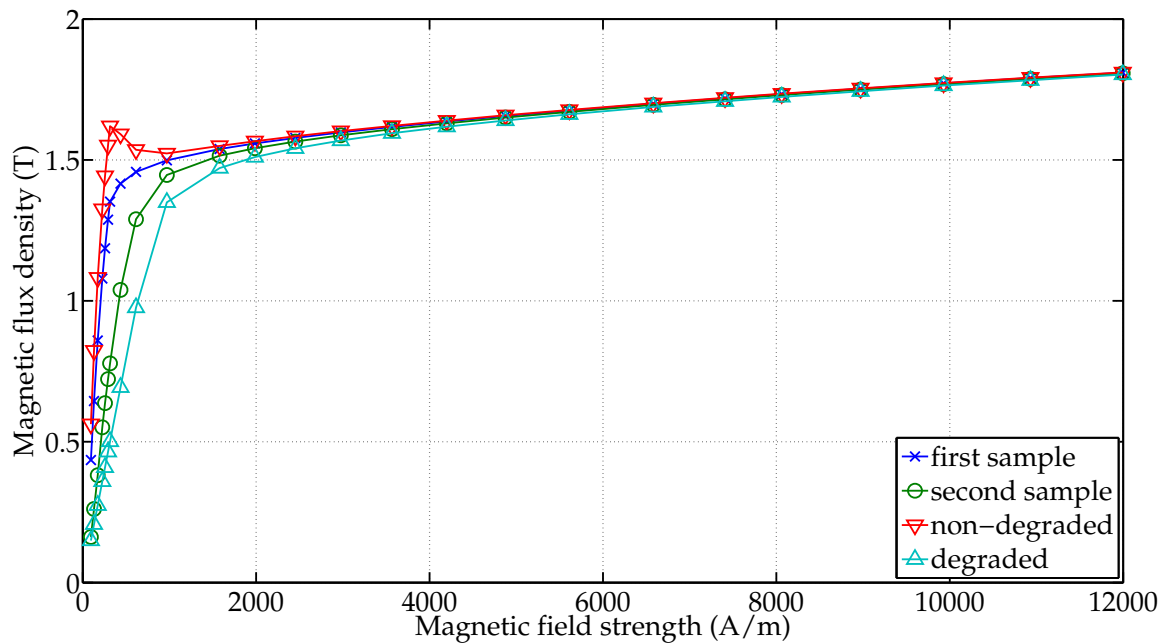


Figure E.9: Measured and identified *B-H* curves of laser-cut samples, M400-50A at 250 Hz supply frequency.
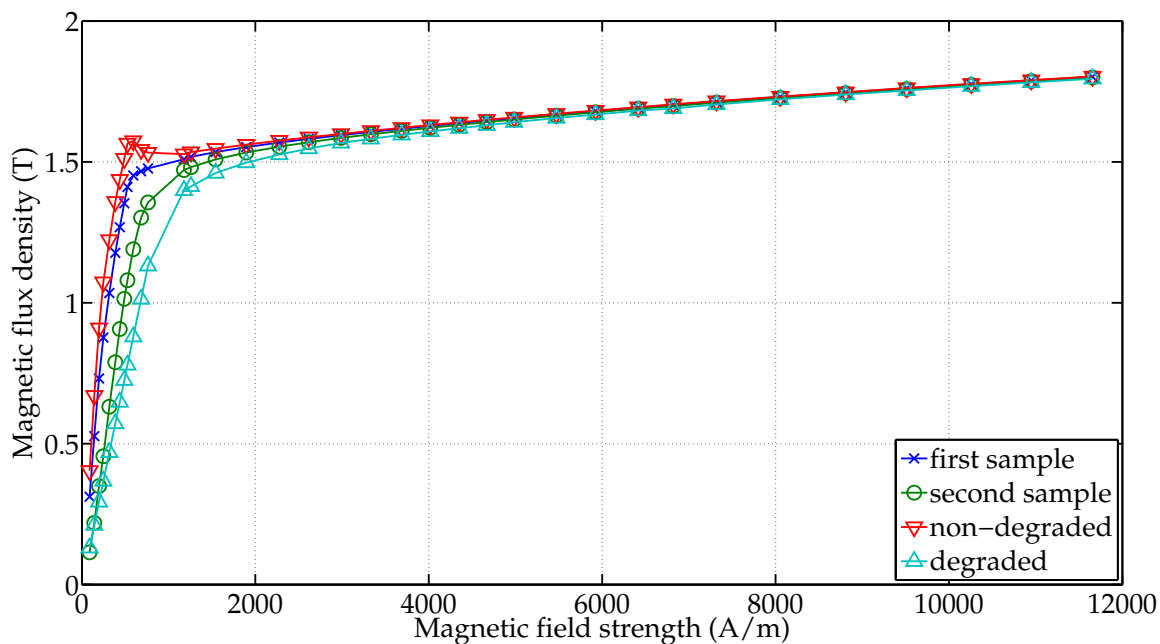
Figure E.10: Measured and identified *B-H* curves of laser-cut samples, M400-50A at 500 Hz supply frequency.

## E.1.5 Results of laser-cut samples - M800-65A
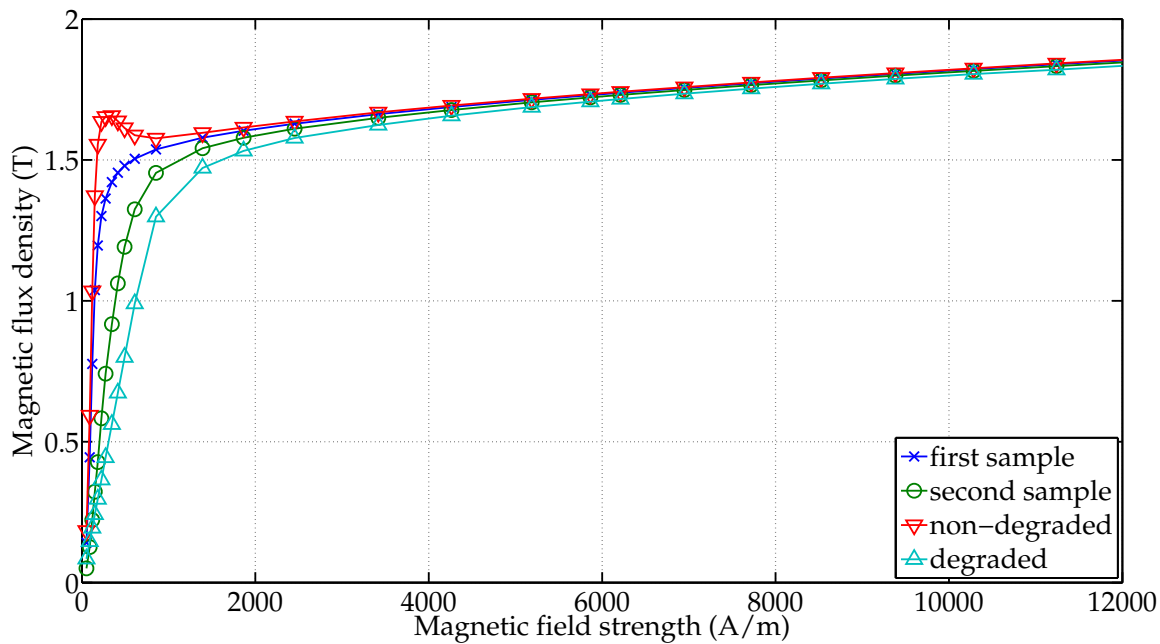


Figure E.11: Measured and identified *B-H* curves of laser-cut samples, M800-65A at 50 Hz supply frequency.
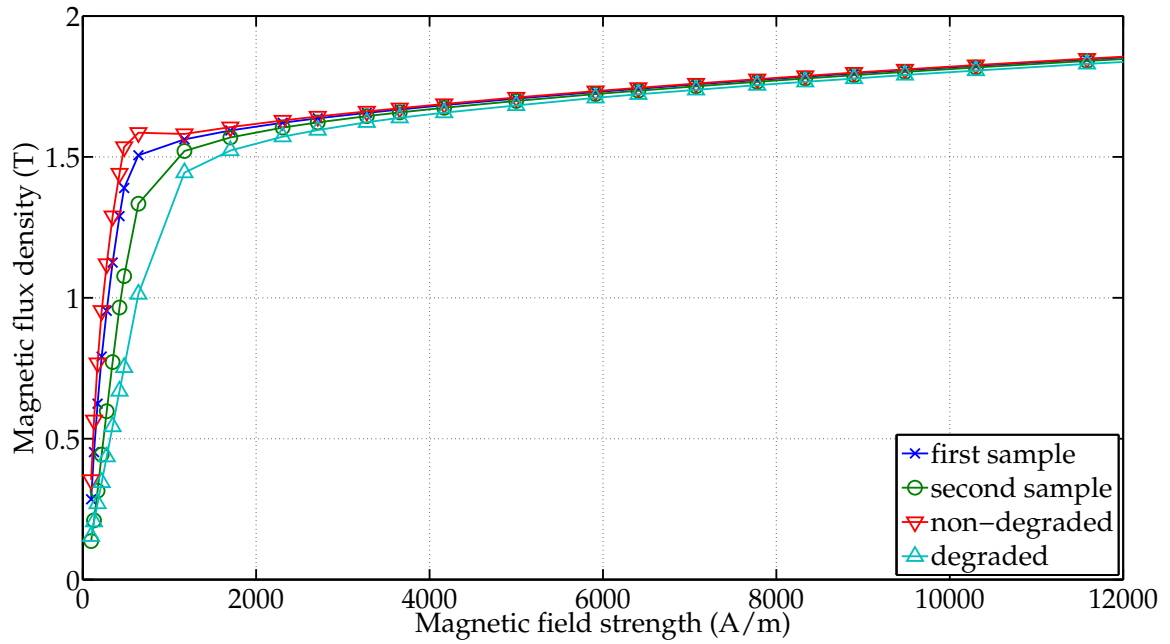
Figure E.12: Measured and identified *B-H* curves of laser-cut samples, M800-65A at 250 Hz supply frequency.
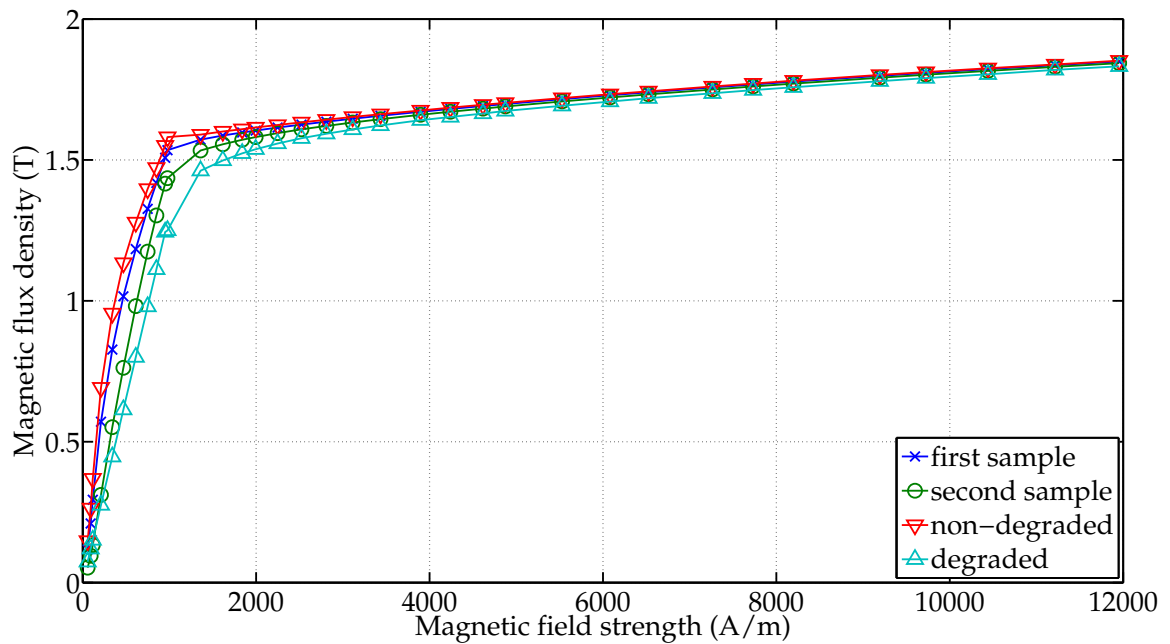


Figure E.13: Measured and identified *B-H* curves of laser-cut samples, M800-65A at 500 Hz supply frequency.

## E.2  Diagrams: identified loss curves

### E.2.1  Results of mechanically-cut samples - M400-50A
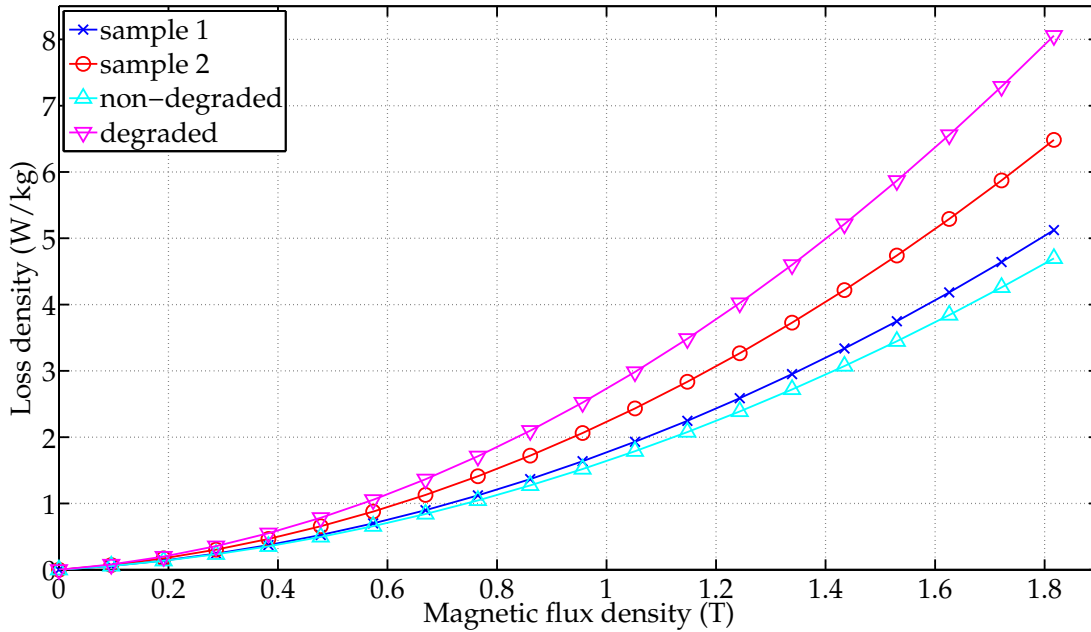


Figure E.14: Measured and computed loss curves of mechanically-cut samples, M400-50A at 50 Hz supply frequency.
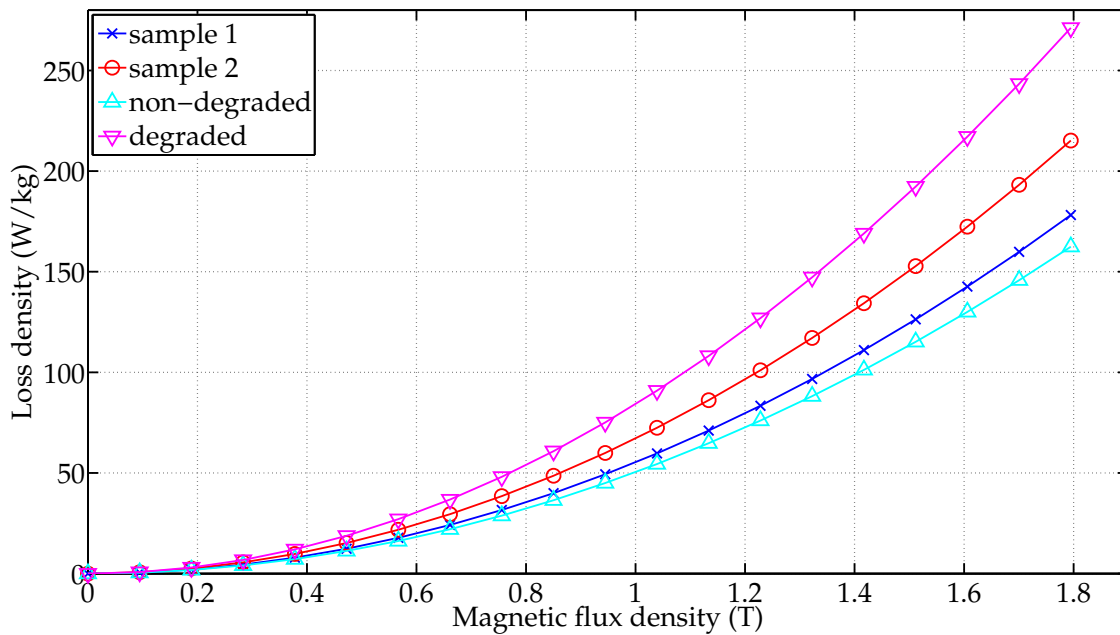


Figure E.15: Measured and computed loss curves of mechanically-cut samples, M400-50A at 500 Hz supply frequency.

## E.2.2  Results of mechanically-cut samples - M800-65A
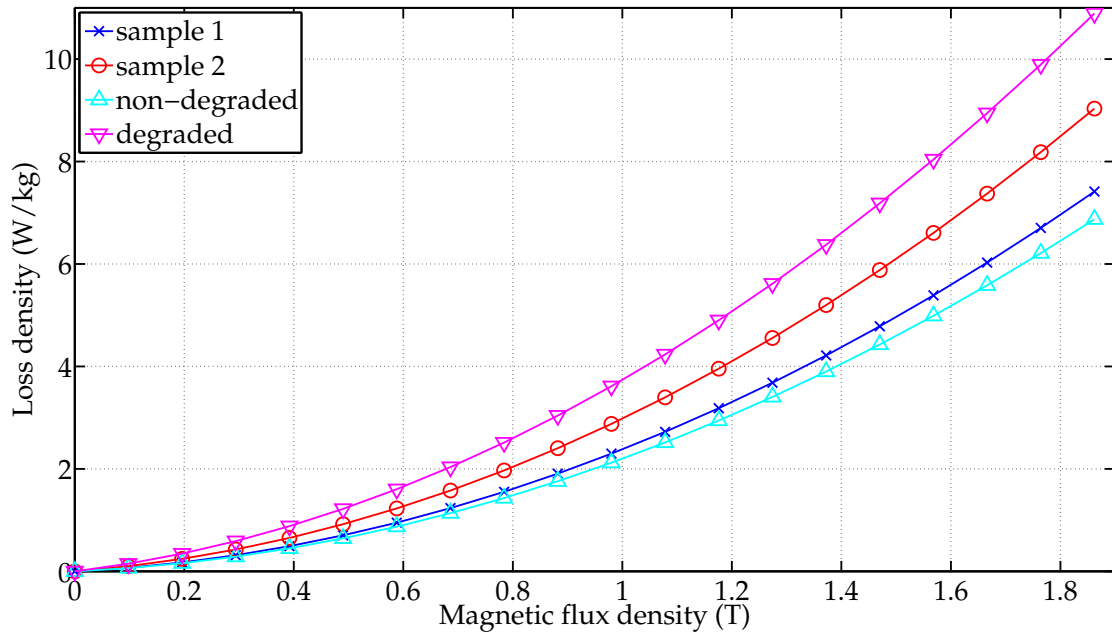


Figure E.16: Measured and computed loss curves of mechanically-cut samples, M800-65A at 50 Hz supply frequency.
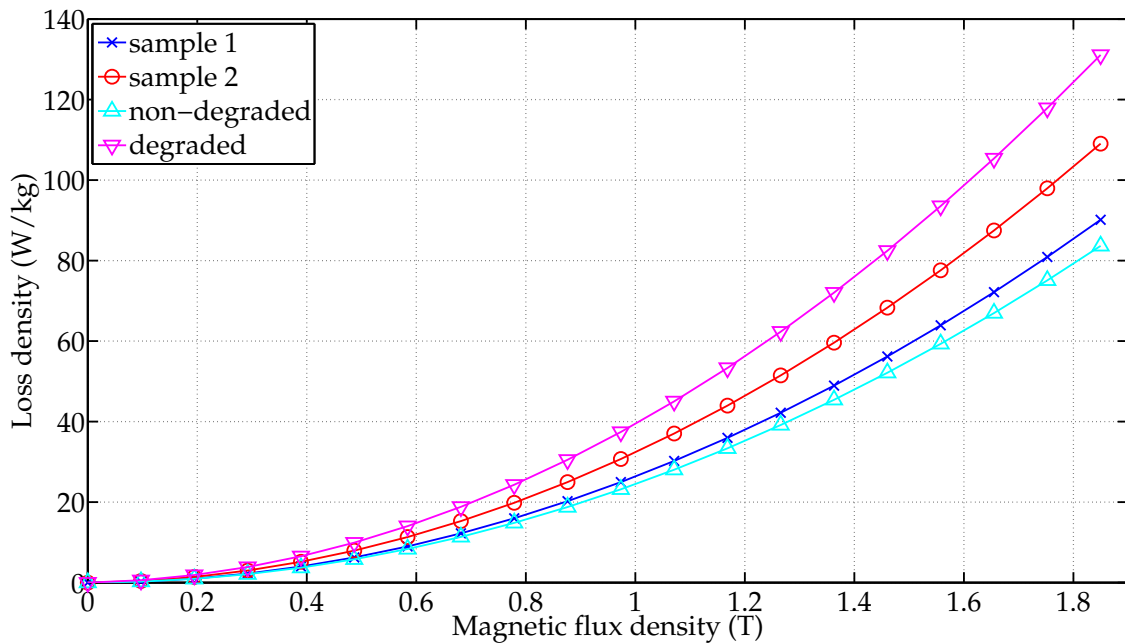


Figure E.17: Measured and computed loss curves of mechanically-cut samples, M800-65A at 250 Hz supply frequency.
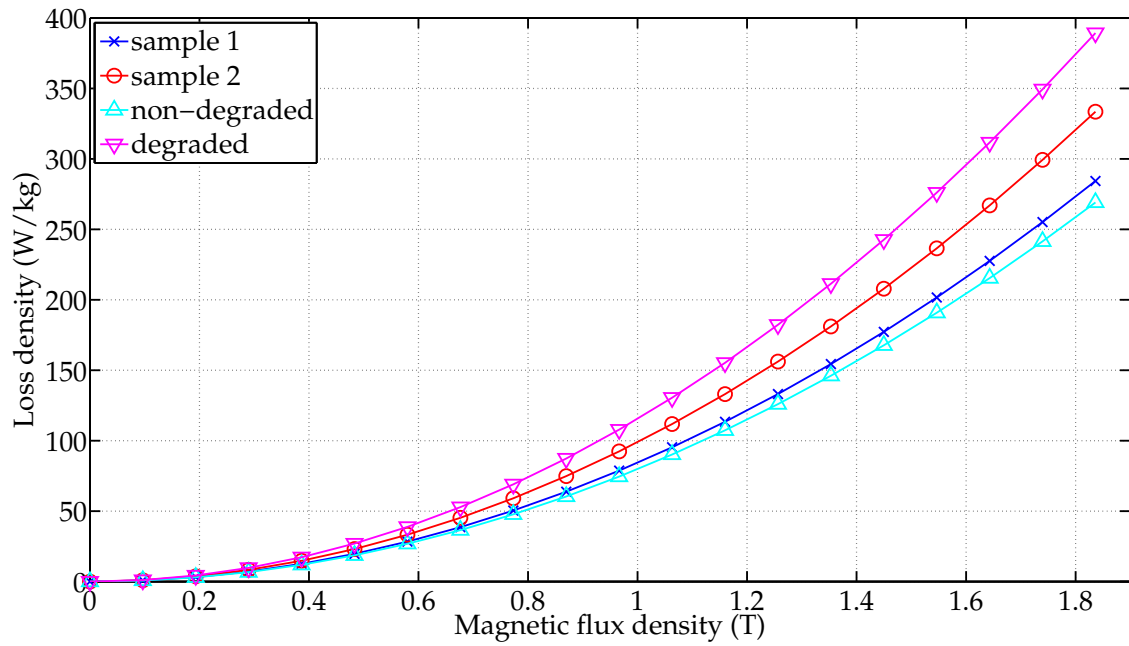
Figure E.18: Measured and computed loss curves of mechanically-cut samples, M800-65A at 500 Hz supply frequency.

## E.2.3  Results of laser-cut samples - M270-35A
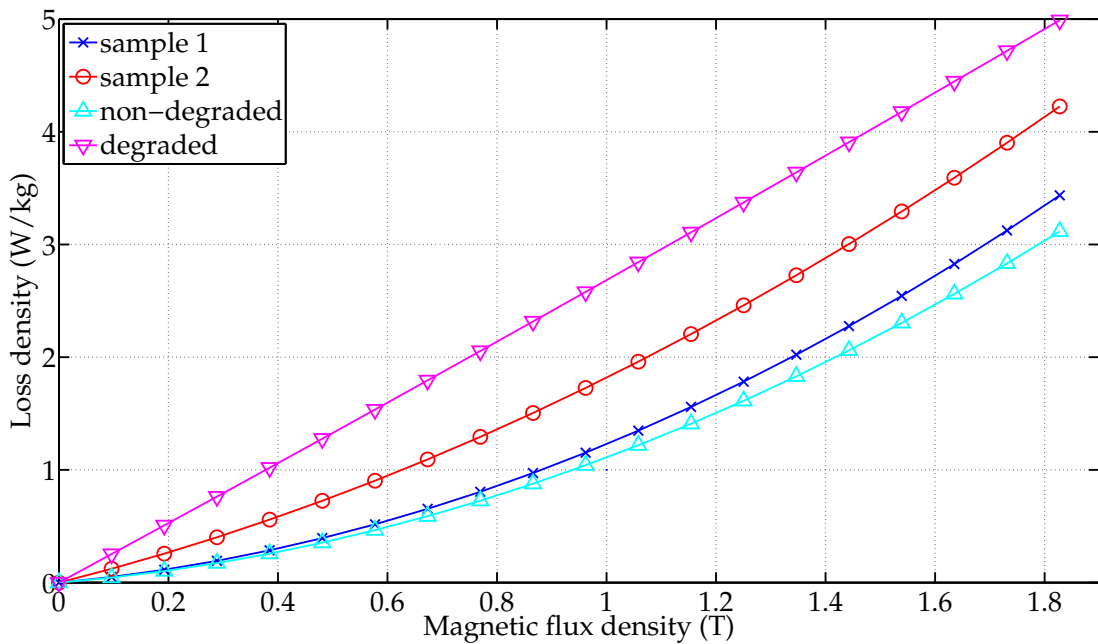


Figure E.19: Measured and computed loss curves of laser-cut samples, M270-35A at 50 Hz supply frequency.
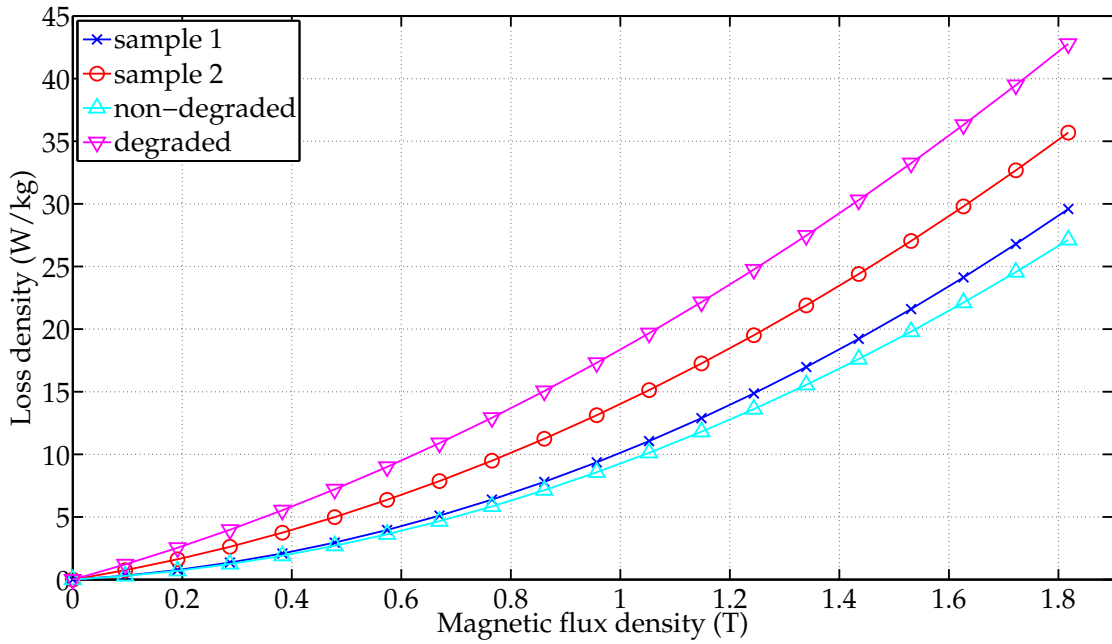
Figure E.20: Measured and computed loss curves of laser-cut samples, M270-35A at 250 Hz supply frequency.
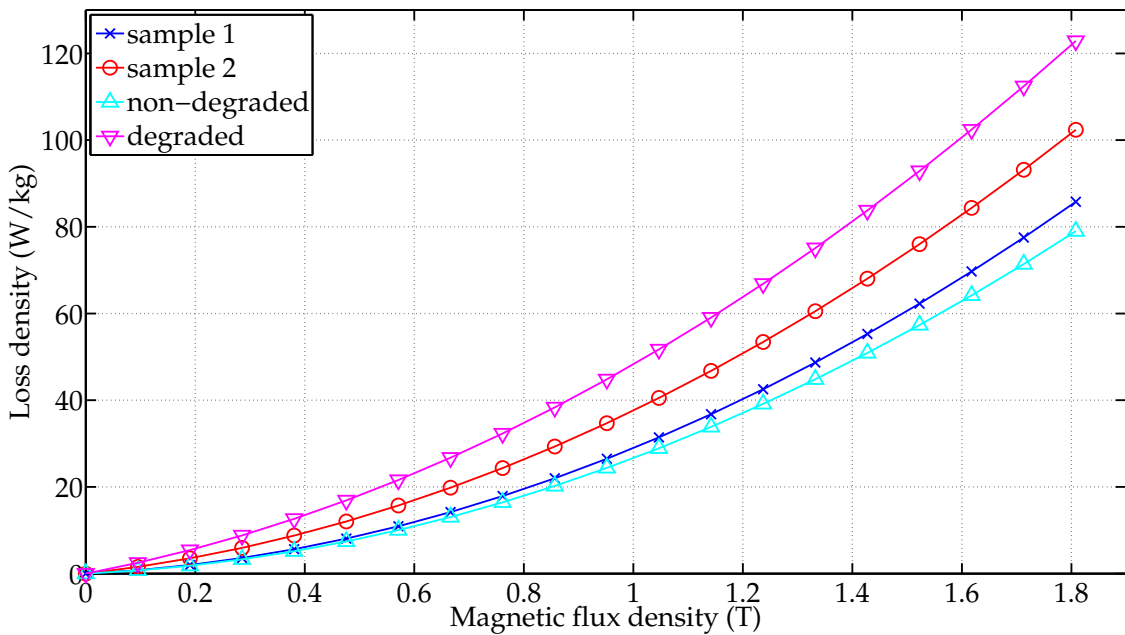


Figure E.21: Measured and computed loss curves of laser-cut samples, M270-35A at 500 Hz supply frequency.

## E.2.4  Results of laser-cut samples - M400-50A
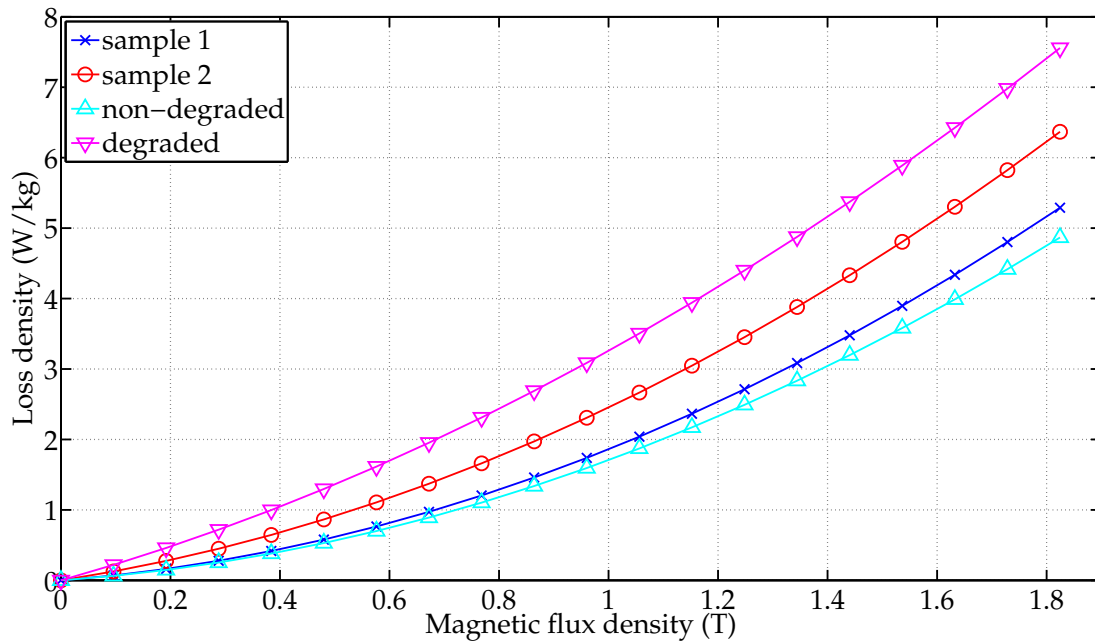


Figure E.22: Measured and computed loss curves of laser-cut samples, M400-50A at 50 Hz supply frequency.
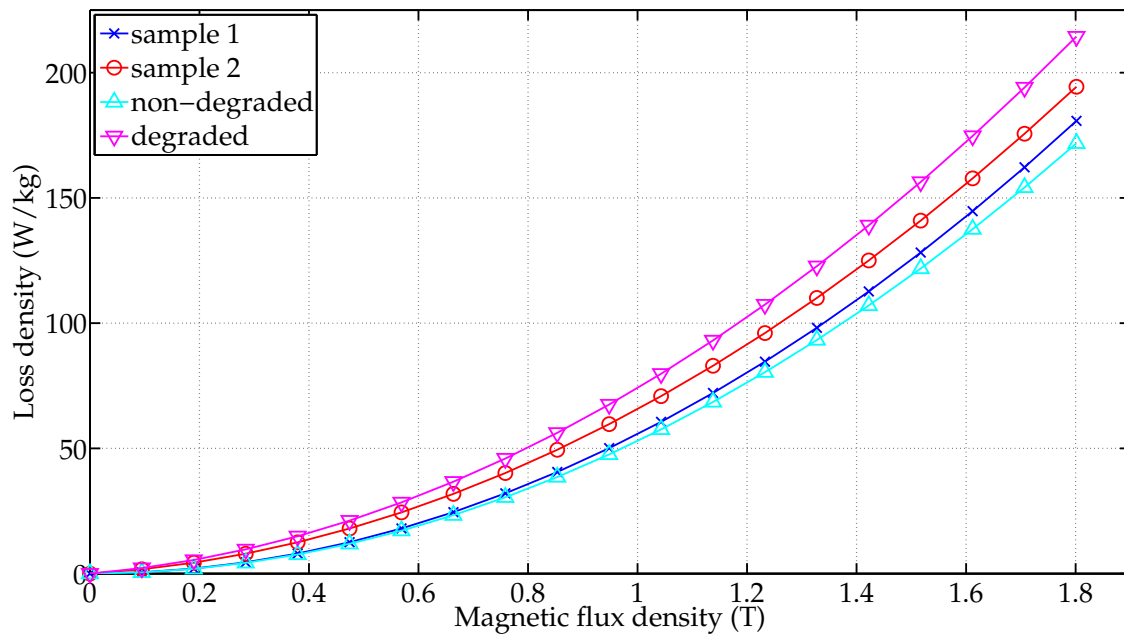


Figure E.23: Measured and computed loss curves of laser-cut samples, M400-50A at 500 Hz supply frequency.

### E.2.5 Results of laser-cut samples - M800-65A
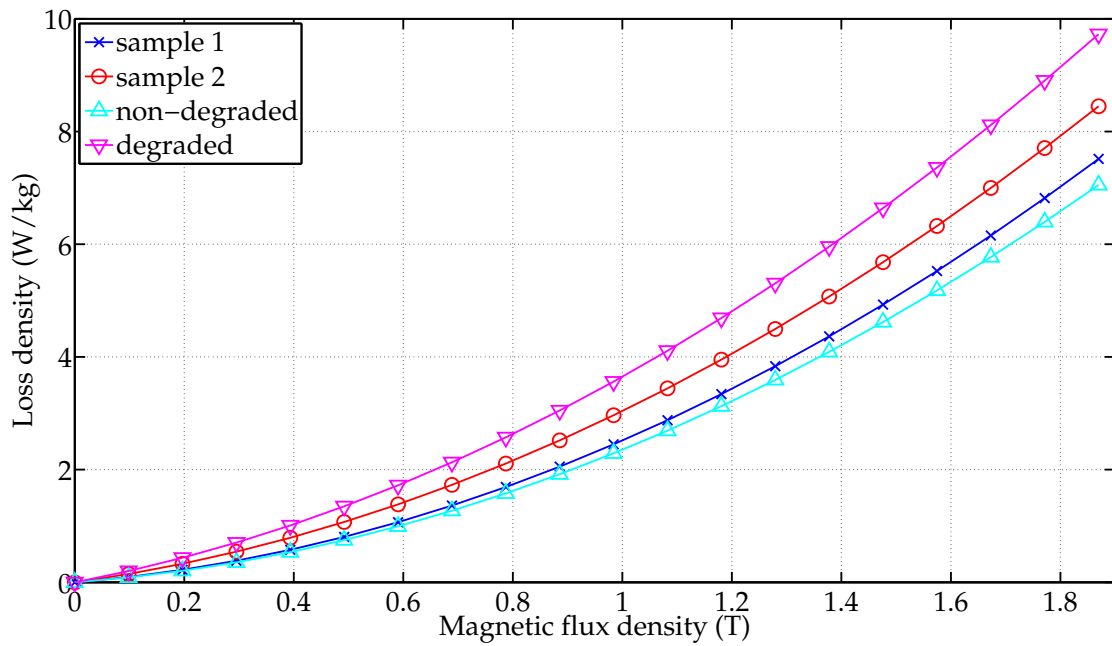


Figure E.24: Measured and computed loss curves of laser-cut samples, M800-65A at 50 Hz supply frequency.
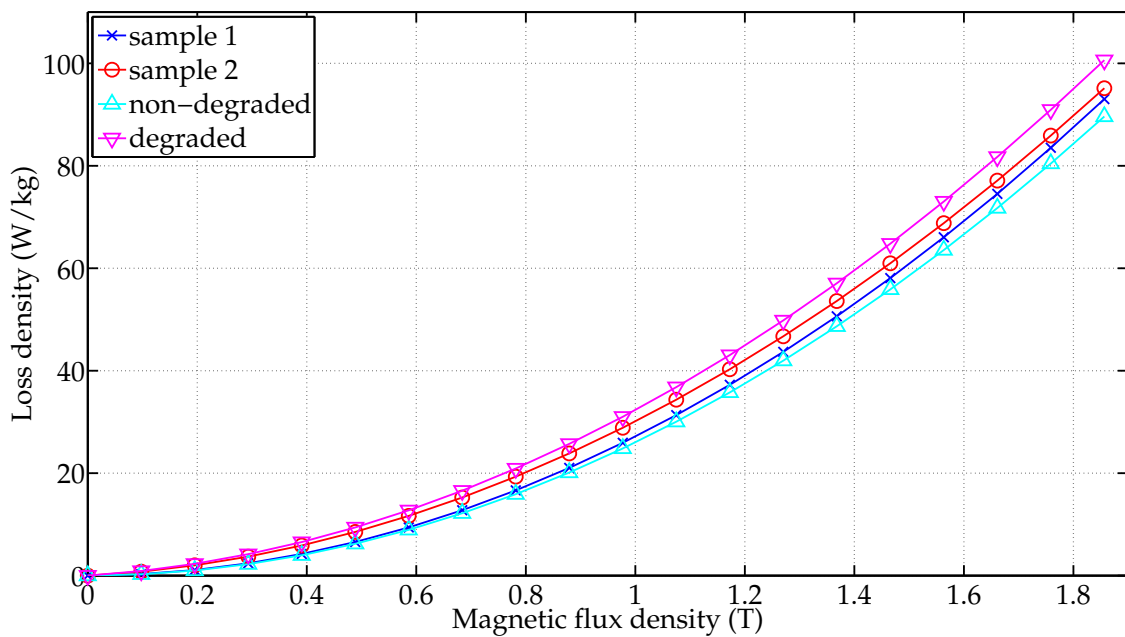


Figure E.25: Measured and computed loss curves of laser-cut samples, M800-65A at 250 Hz supply frequency.
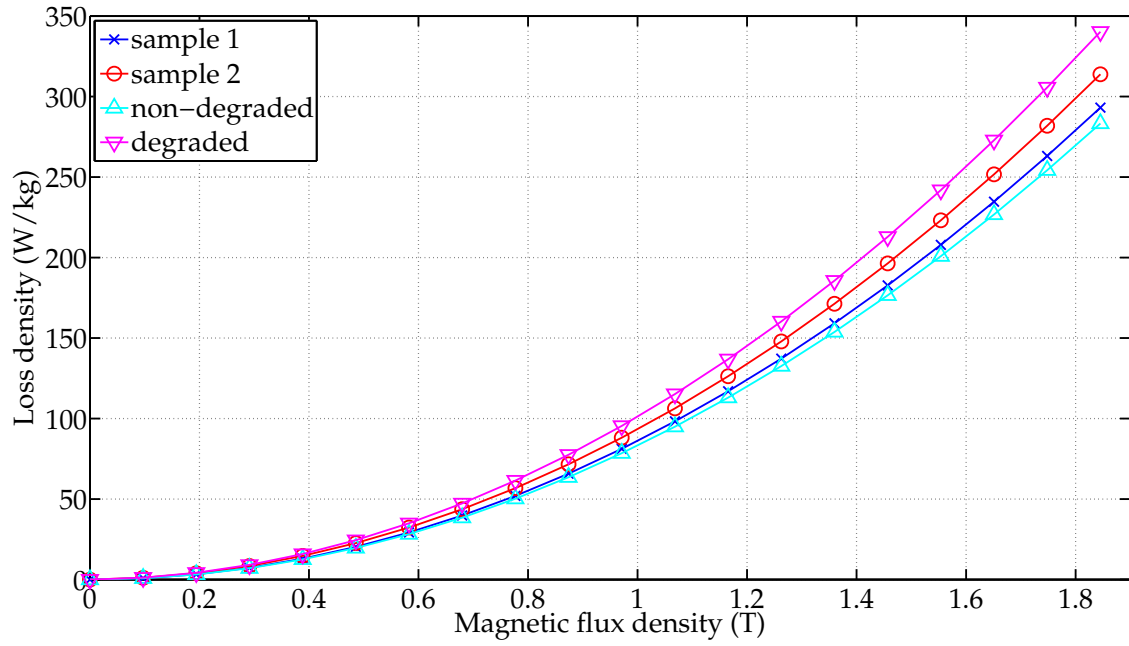
Figure E.26: Measured and computed loss curves of laser-cut samples, M800-65A at 500 Hz supply frequency.

# E.3 Diagrams: comparison with datasheet values

## E.3.1 Results of mechanically-cut samples
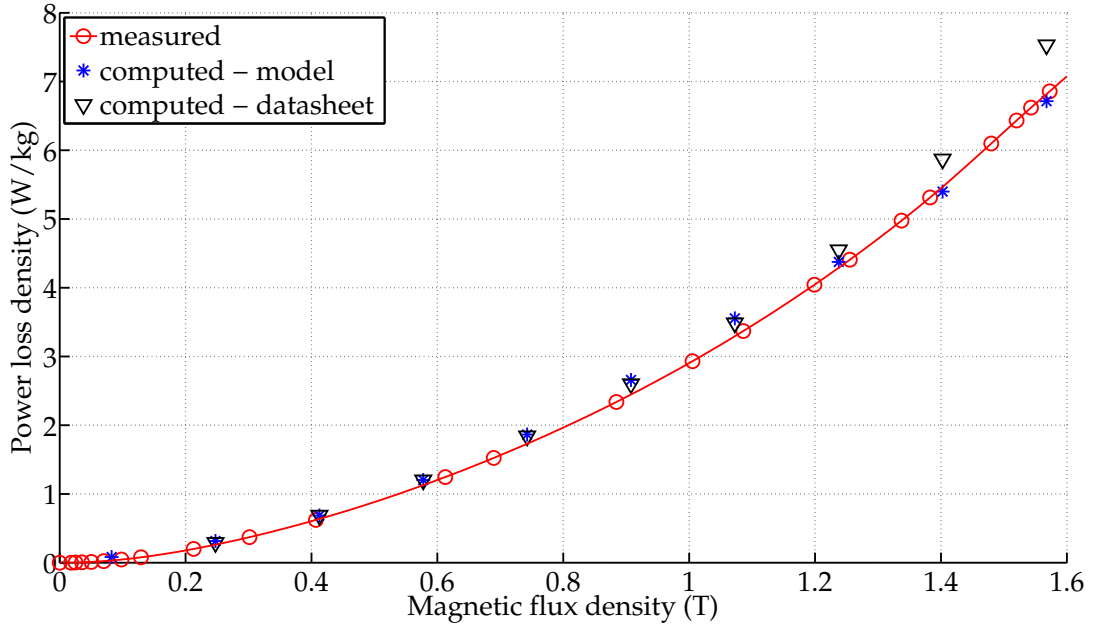


Figure E.27: Loss curves as measured, as computed using the proposed approach and as determined from datasheet values of the investigated mechanically-cut stator lamination stack at 50 Hz, material M800-65A.
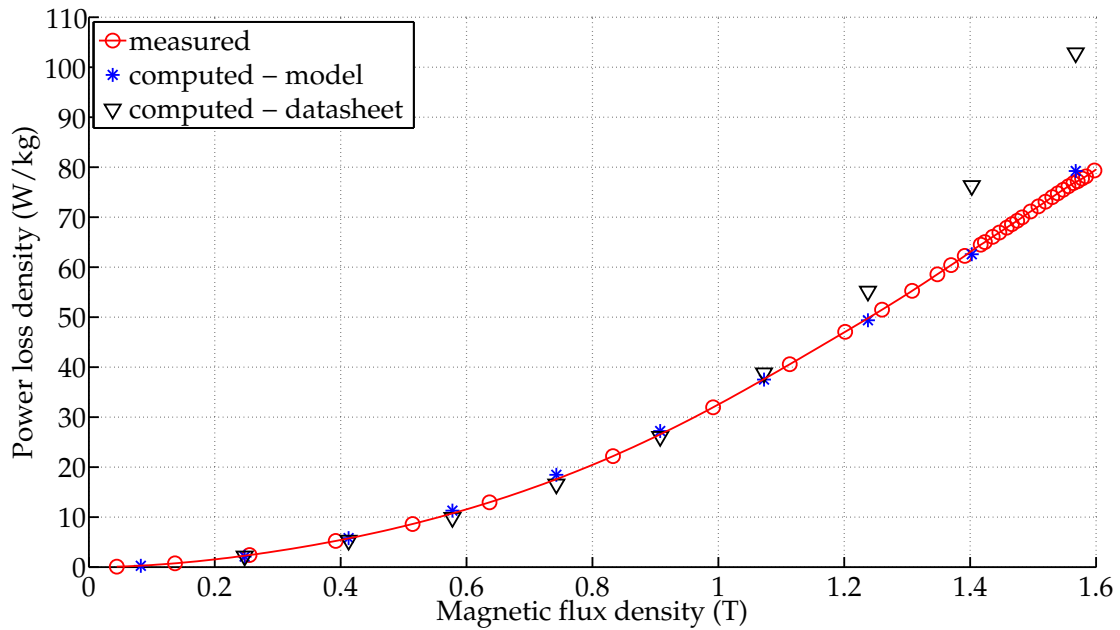
Figure E.28: Loss curves as measured, as computed using the proposed approach and as determined from datasheet values of the investigated mechanically-cut stator lamination stack at 250 Hz, material M800-65A.
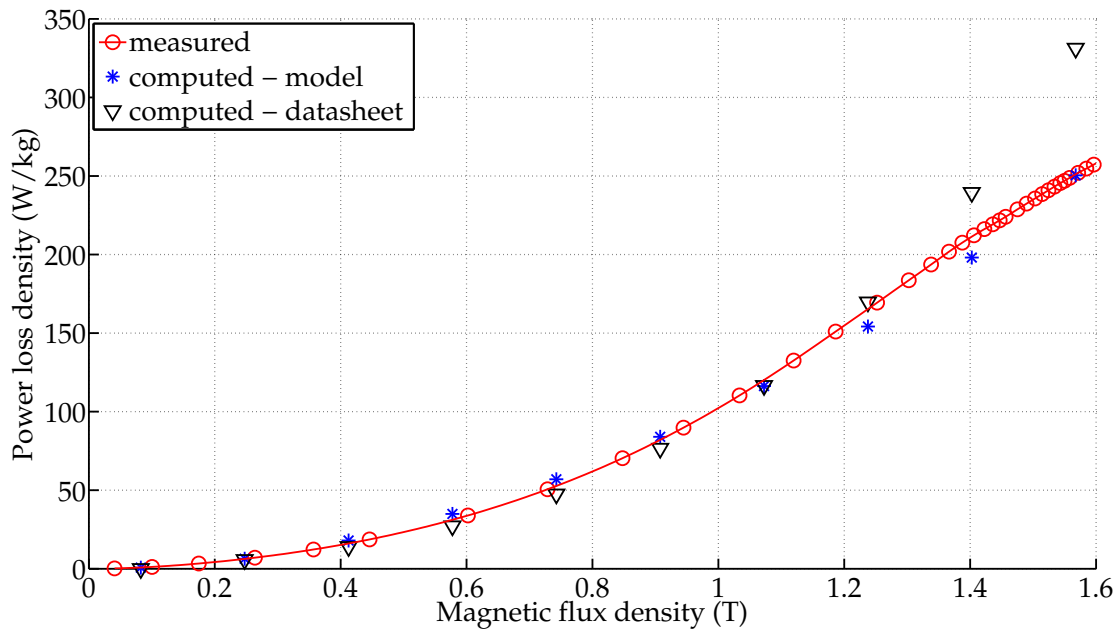


Figure E.29: Loss curves as measured, as computed using the proposed approach and as determined from datasheet values of the investigated mechanically-cut stator lamination stack at 500 Hz, material M800-65A.

## E.3.2 Results of laser-cut samples
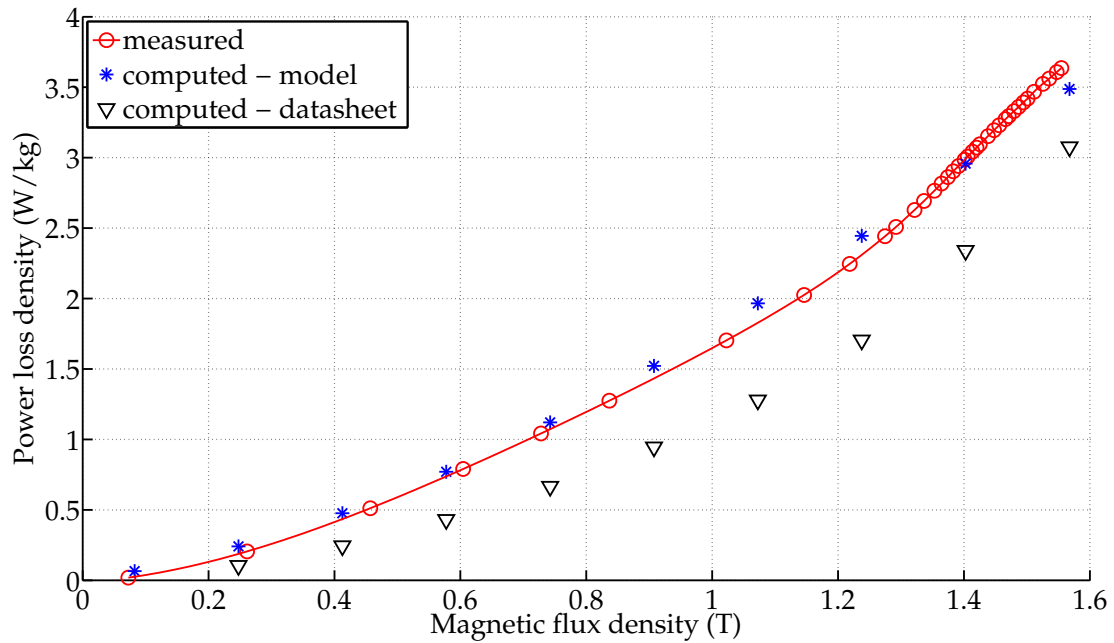


Figure E.30: Loss curves as measured, as computed using the proposed approach and as determined from datasheet values of the investigated laser-cut stator lamination stack at 50 Hz, material M270-35A.
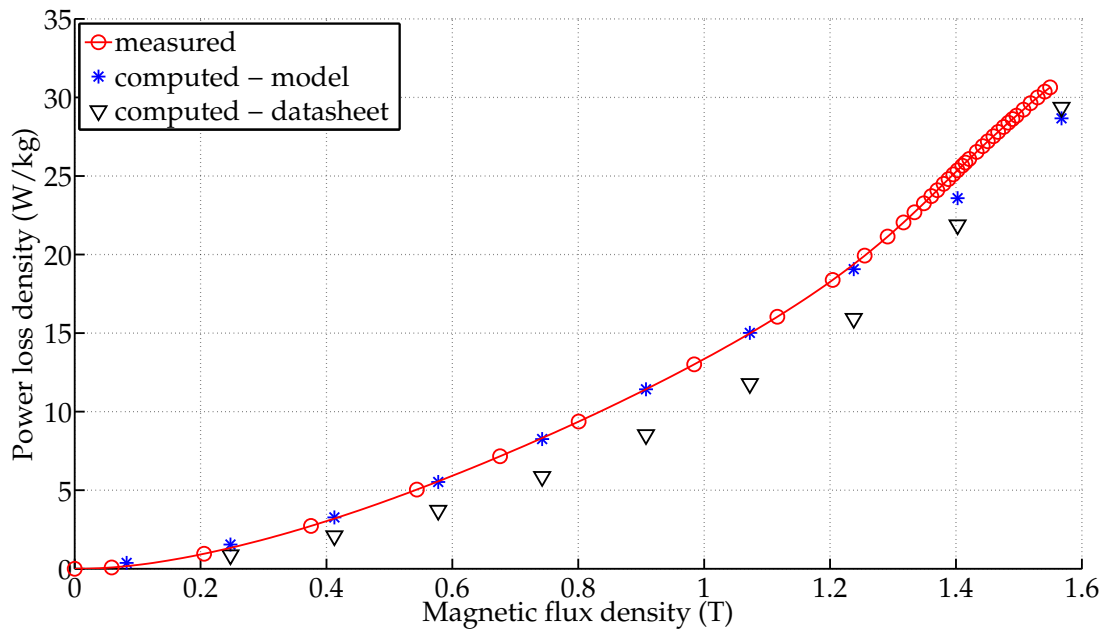


Figure E.31: Loss curves as measured, as computed using the proposed approach and as determined from datasheet values of the investigated laser-cut stator lamination stack at 250 Hz, material M270-35A.
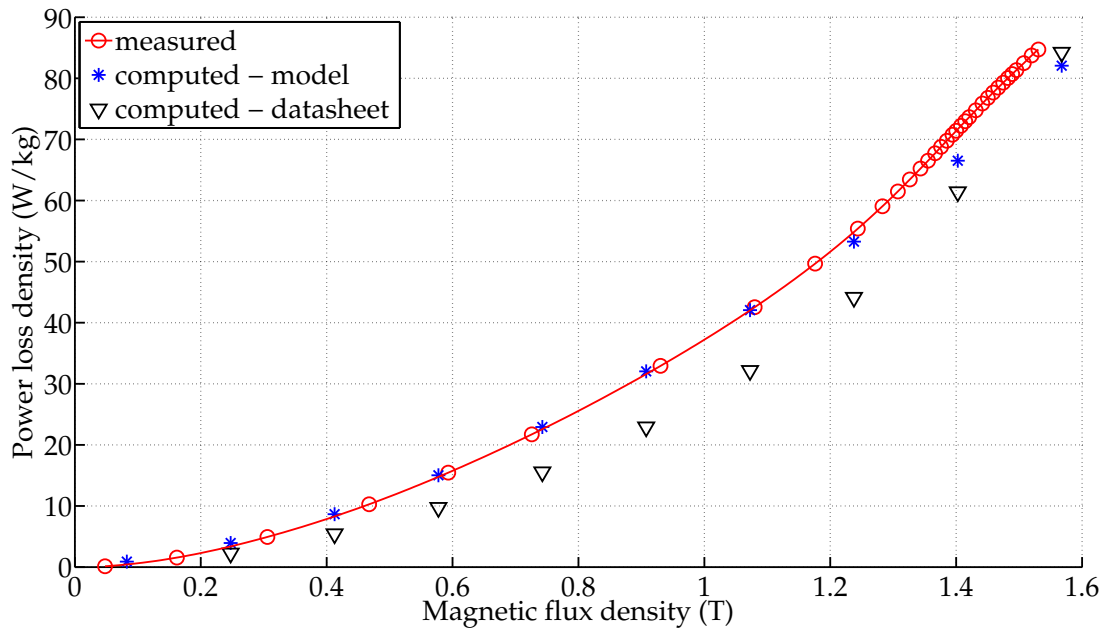
Figure E.32: Loss curves as measured, as computed using the proposed approach and as determined from datasheet values of the investigated laser-cut stator lamination stack at 500 Hz, material M270-35A.
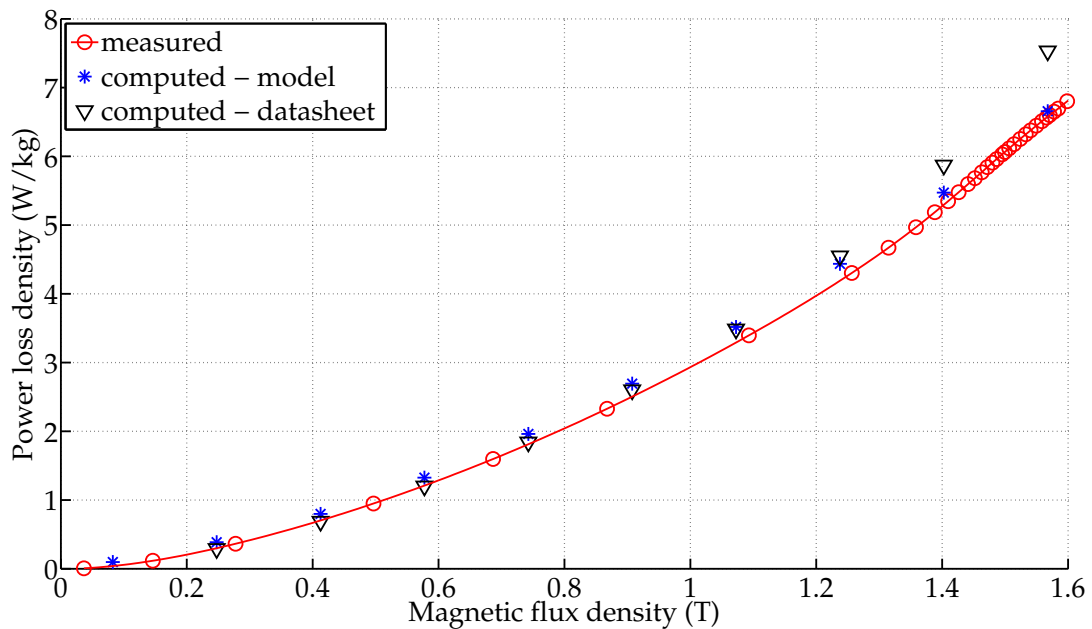


Figure E.33: Loss curves as measured, as computed using the proposed approach and as determined from datasheet values of the investigated laser-cut stator lamination stack at 50 Hz, material M800-65A.
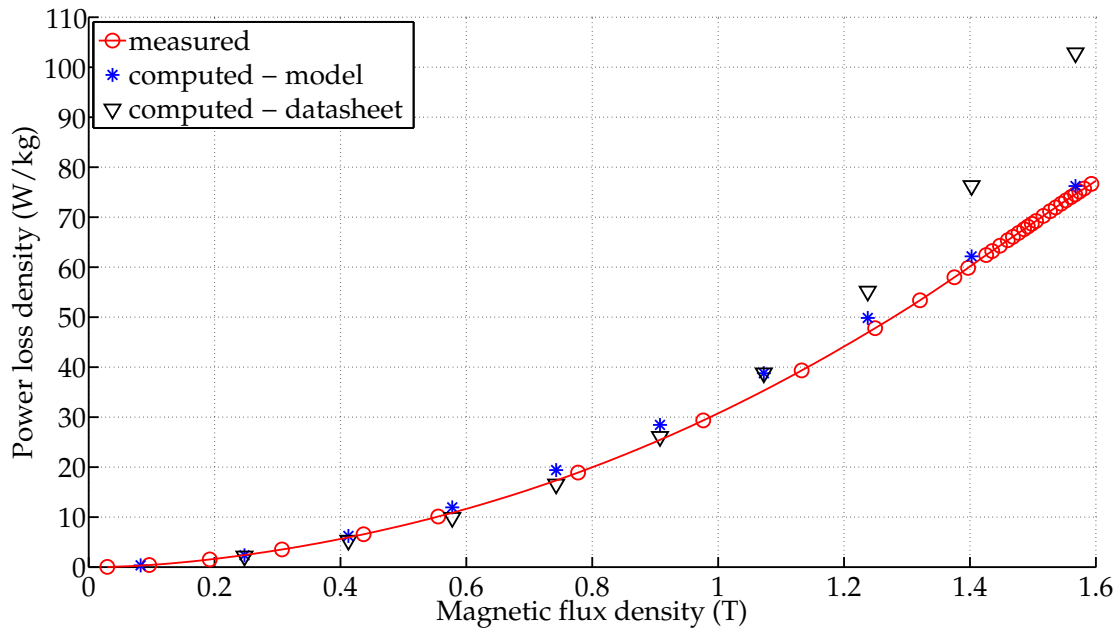
Figure E.34: Loss curves as measured, as computed using the proposed approach and as determined from datasheet values of the investigated laser-cut stator lamination stack at 250 Hz, material M800-65A.
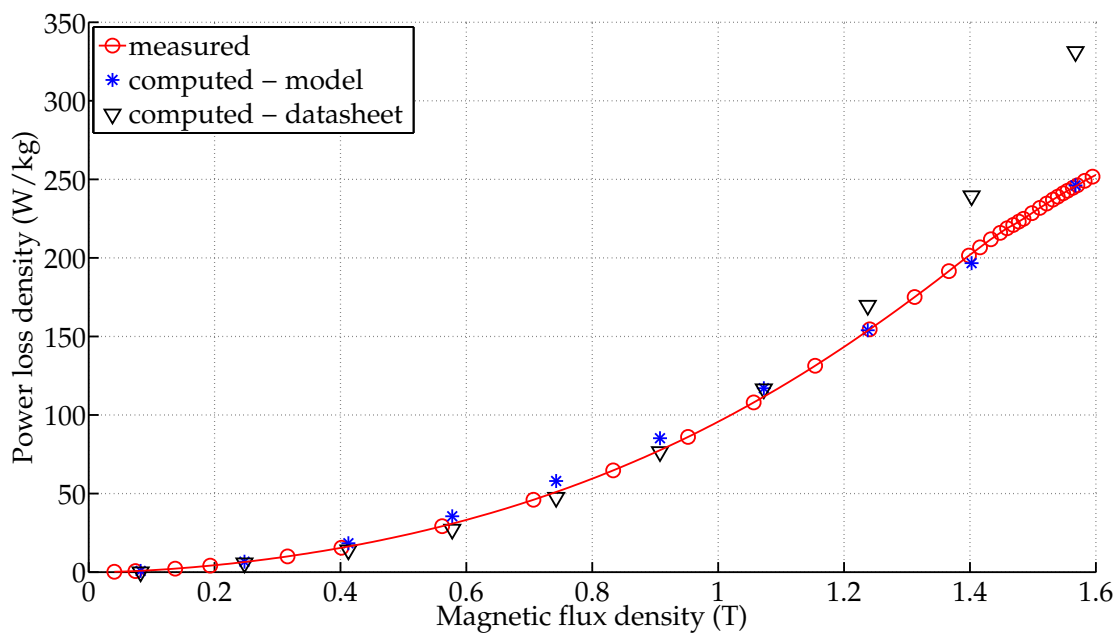


Figure E.35: Loss curves as measured, as computed using the proposed approach and as determined from datasheet values of the investigated laser-cut stator lamination stack at 500 Hz, material M800-65A.

# Appendix F

# Additional information

## F.1 Data of PAS 5000, Spitzenberger + Spiess

Table F.1: Extract from technical data PAS 5000 [104].

| | Nominal voltage | |
|---|---|---|
| | AC: 135 $V_{rms}$/270 $V_{rms}$ <br> DC: ±191 V/±382 V | 56 $V_{rms}$ |
| **Load regulation** | range/max./typ. | range/max./typ. |
| DC - 450 Hz | 135 V: 0.8 % / 0.5 % <br> 270 V: 0.3 % / 0.2 % | 56 V: 2 % / 1 % |
| 450 Hz - 5 kHz | 135 V: 4.0 % / 2.0 % <br> 270 V: 0.6 % / 0.3 % | 56 V: 6 % / 3 % |
| **Gain stability** | - 10 min: < 0.2 % at constant load and temperature <br> - 8 h: < 0.5 % at constant load and temperature | |
| **Power** | AC: continuous: 5000 VA <br> approx. 1 h: 7500 VA | AC: continuous: 2070 VA <br> approx. 1 h: 3100 VA |
| | DC: continuous: 5000 W <br> approx. 1 h: 7500 W | DC: continuous: 2700 W <br> aprox. 1 h: 3100 W |
| **Short-time power** | 10000 W for 10 min. at 270 V | 4350 W for 10 min. at 56 V |
| **Peak power** | at 135 V: 21000 $VA_p$ | 8700 $VA_p$ |
| | at 270 V: 42000 $VA_p$ | |
| **Frequency range** | DC - 5 kHz large signal bandwidth (−3 dB) | |
| | DC - 50 kHz small signal bandwidth | |
| **Harmonic distortion** | range/max./typ. | range/max./typ. |
| DC 15 Hz - 450 Hz | 135 V: 0.3 % / 0.1 % <br> 270 V: 0.1 % / 0.05 % | 56 V: 0.5 % / 0.2 % |
| 450 Hz - 5 kHz | 135 V: 2.5 % / 1.5 % <br> 270 V: 0.6 % / 0.3 % | 56 V: 3 % / 1 % |
| **Power Supply** | 230 V/400 V (+6 %/−10 %) 50 Hz - 60 Hz | |
| **Option** | Compensation of internal resistance | |
| **Option** | Special frequency range | |

## F.2  Calculation of the specific cutting length CL

The specific cutting lengths for the Epstein samples have been calculated according to the calculation used in [169] and [170] (see Eq. (F.1) for a single Epstein strip). Thus, the width of the rectangular samples is neglected for the non-specific cutting length.

$$CL = \frac{2l}{m} \tag{F.1}$$

For calculating the specific cutting length of the stator samples, only the yoke is considered, as, in the measurements, the magnetic flux flows almost exclusively in the yoke. This is due to the measurement method (see Chapter 2.6). Thus, the specific cutting length for the investigated stator sample's geometry is approximated as follows:

$$CL = \frac{\pi \left(D_{\mathrm{a}} + (D_{\mathrm{a}} - 2\,h_{\mathrm{yoke}})\right) - z\,b_{\mathrm{z}}}{m_{\mathrm{yoke}}} \tag{F.2}$$